DESY 96-235
November 1996

Future Physics at HERA

Proceedings of the Workshop 1995/96

Edited by

G. Ingelman, A. De Roeck, R. Klanner

Volume 2

http://www.desy.de/~heraws96

Future Physics at HERA

Proceedings of the workshop 1995/96

Edited by

G. Ingelman, A. De Roeck, R. Klanner

Volume 2

Diffractive Hard Scattering

Polarized Protons and Electrons

Light and Heavy Nuclei in HERA

HERA Upgrades and Impacts on Experiments

Published by

Deutsches Elektronen-Synchrotron **DESY**
Notkestraße 85
D-22607 Hamburg
Hamburg
Germany

Proceedings of the workshop on Future Physics at HERA
Volume 2

Electronic version available on http://www.desy.de/~heraws96

PRINTING COMPANY: HB-DRUCK, H. BUNG, D-22149 HAMBURG

VOLUME 1

VOLUME 2

Working Group on

Diffractive Hard Scattering

Conveners:

Halina Abramowicz (University Tel-Aviv)
Leonid Frankfurt (University Tel-Aviv)
Hannes Jung[1] (CEA, DSM/DAPNIA, CE-Saclay)

Participants:

H. Abramowicz (Tel Aviv), M. Arneodo (Torino), A. Bamberger (Freiburg), G. Barbagli (Firenze), W. Bartel (DESY), J. Bartels (Hamburg), V. Braun (NORDITA), G. Briskin (Tel Aviv), S. Brodsky (SLAC), W. Buchmüller (DESY), J. Dainton (Liverpool), V. Del Ducca (Edinburgh), M. Diehl (Cambridge), T. Doeker (Tel Aviv), Y. Dokshitzer (Milano), A. Droutskoi (Moscow), S. Eisenhardt (Freiburg), C. Ewerz (Hamburg), L. Frankfurt (Tel Aviv), E. Gallo (Firenze), E. Gotsman (Tel Aviv), D. Graudenz (CERN), M. Grothe (Bonn), T. Haas (DESY), H. Hessling (DESY), L. Iannotti (Calabria), G. Ingelman (DESY/Uppsala), H. Jung (Lund), S. Kananov (Tel Aviv), M. Kasprzak (Warsaw), W. Koepf (Columbus), B. Kopeliovich (Heidelberg, Dubna), B. Laforge (Saclay), P. Landshoff (Cambridge), E. Levin (Argonne, St. Petersburg), G. Levman (Toronto), A. Levy (Tel Aviv), H. Lotter (Hamburg), H. Mais (DESY), U. Maor (Tel Aviv), T. Massam (Bologna), M. McDermott (DESY), A. Mehta (Rutherford), T. Meng (Berlin), A. Meyer (DESY), K. Muchorowski (Warsaw), O. Nachtmann (Heidelberg), N. Nikolaev (Bonn, Moscow), C. Peroni (Torino), R. Peschanski (Saclay), J. Phillips (Liverpool), J. Pliszka (Warsaw), A. Prinias (Imperial College), H. Raach (Freiburg), J. Rahn (Santa Cruz), J. Rathsman (Uppsala), C. Royon (Saclay), M. Ryskin (Petersburg), R. Sacchi (Torino), A. Solano (Torino), H. Spiesberger (DESY), M. Strikman (Penn State), J. Terron (Madrid), T. Teubner (Durham), D. Treleani (Trieste), B. Waugh (Manchester), L. West (Birmingham), S. Wolfle (Freiburg), M. Wüsthoff (Argonne) A. Zarnecki (DESY, Warsaw)

[1] now at Lund University

Diffractive Hard Scattering — Working Group Reports:

Diffractive Hard Scattering
Summary Report of the Working Group

H. Abramowicz[a], J. Bartels[b], L. Frankfurt[ac], H. Jung[d]

[a] Raymond and Beverly Sackler Faculty of Exact Sciences
School of Physics and Astronomy
Tel-Aviv University, 69978 Tel-Aviv, Israel
[b] University Hamburg, FRG
[c] St.Petersburg Nuclear Physics Institute, Gatchina, Russia
[d] CEA, DSM/DAPNIA, CE - Saclay, Gif-sur-Yvette, France
(now at Physics Department, University of Lund, Lund, Sweden)

Abstract: This report discusses the role of hard diffractive scattering in probing new QCD phenomena expected at HERA. Within this framework it summarizes the contributions made to this workshop which cover both theoretical investigations and experimental feasibility studies.

1 Importance of Hard Diffractive Phenomena

Diffractive processes in deep inelastic scattering (DIS) of leptons with protons at small x and large Q^2 offer a unique opportunity to probe the QCD color dynamics in the intermediate region between asymptotic freedom and confinement. The very presence of a large fraction of diffractive like events at high Q^2 is a signal for the interplay of hard and soft QCD phenomena. In the language of color dynamics two effects are expected to play an important role, color transparency (color screening) for systems consisting of quarks and gluons contained within a small size configuration and color opacity for large size configurations. The interactions of small size configurations lead to reactions dominated by hard processes with a cross section rising with energy while the interaction of large size configurations is dominated by soft processes. The ability to separate clearly these two regimes is essential for testing QCD both at a quantitative and qualitative level. In particular the following issues can be addressed:

- The dynamics of compact systems, color transparency and perturbative color opacity. The appearance of a new class of hard diffractive processes calculable in QCD is expected, $\gamma^* + p \to X + p$, where X is a longitudinally polarized vector meson or a system consisting of two high p_T jets. If confirmed experimentally, this would lead to a direct determination of the gluon distribution in the proton as well as the distribution of bare quarks within the vector meson.

- QCD predictions for the high momentum behavior of wave functions of hadrons consisting of light quarks and QCD physics of heavy quarkonia. In this respect the big advantage of hard diffractive processes is that they have large cross sections and provide a variety of new information.

- Violation of DGLAP evolution equation. Theoretical estimates suggest that the increase of parton densities at small x will slow down and that this effect can be observed at HERA in hard diffractive processes, in the measurements of the proton structure functions at moderate Q^2, as well as in the measurements of the structure functions of nuclei.

- Semi-classical approximation to high energy interactions. In the limit of strong color fields which are typical in the HERA kinematical regime, new developments and tests of the semi-classical approach are possible.

Let us repeat that, in order to test and improve our understanding of QCD, it is important to separate small and large size configurations in the diffractive final state. The two regions are described by quite different dynamical mechanisms. On the other hand, the diffractive structure function is an inclusive quantity which contains an integral over the final state configuration. From a theoretical point of view, therefore, this structure function is more difficult than some of the individual final states. This is why in this report the inclusive diffractive structure function can be discussed only after having analysed the small and large size final state configurations. This is quite in contrast to the experimental point of view: inclusive measurements of the diffractive cross section are easier to perform than the measurement of final states e.g. the hard di - jet events.

The outline of the report is the following. The second section gives a glossary and notation. The third section is devoted to the introduction of the theoretical framework which allows to understand the role of hard diffractive processes in testing the mechanism of high energy interactions in perturbative QCD and beyond. The experimental prospects for measuring the properties of the suggested large rapidity gap processes are then discussed in section 4. Section 5 outlines the expected theoretical implications and their significance for understanding the role of QCD in high energy processes.

2 Glossary and Notation

In the course of the presentation we will use a customary notation for variables used in describing deep inelastic and diffractive phenomena. For convenience we define them once for all in this section.

In the process (the momentum vectors are given in brackets):

$$e(l) + p(p) \to e'(l') + X + p'(p')$$

the center of mass energy squared is given by: $s = (l+p)^2$. The center of mass energy squared of the hadronic system is given by:

$$W^2 = (q+p)^2 = -Q^2 + 2pq + m_p^2 = Q^2\left(\frac{1}{x} - 1\right) + m_p^2 ,$$

with $q = (q_0, \vec{q})$ and $Q^2 = -q^2$ being the 4 - momentum of the virtual photon. The Bjorken variable x is given by:

$$x = \frac{Q^2}{2pq} ,$$

with p being the 4 - momentum of the incoming proton.

For the description of the diffractive interactions we use X to denote the final state corresponding to the photon dissociation. If also the proton dissociates we denote its state by Y to indicate that it is still separated from the state X. The kinematical variables are given in the following. The square of the momentum transfer at the proton vertex,

$$t = (p - p')^2 ,$$

where p' is the 4-momentum of the outgoing proton. In the more general case of proton dissociation p' should be replaced by the 4-momentum of the outgoing system Y.

The fraction of the proton momentum carried by the Pomeron is:

$$x_{I\!P} = \frac{(p - p') \cdot q}{p \cdot q} = \frac{M_X^2 + Q^2 - t}{W^2 + Q^2 - m_p^2} ,$$

where M_X is the invariant mass of the hadronic system produced as the outcome of photon dissociation, and m_p stands for the proton mass. For large Q^2 and W^2 the influence of t and m_p on $x_{I\!P}$ is negligible. It should be noted that the subscript $I\!P$ may not always be adequate, although it still make sense to talk about the fraction of proton momentum in the interaction. This is particularly true for models where there is no object such as a Pomeron.

In analogy to x we define β as the Bjorken variable related to the Pomeron,

$$\beta = \frac{Q^2}{2(p - p') \cdot q} = \frac{x}{x_{I\!P}} = \frac{Q^2}{Q^2 + M_X^2 - t} .$$

Here again t is only included for completeness.

In the splitting of the photon into a $q\bar{q}$ we will denote by z the fraction of the photon momentum carried by one of the quarks of the pair, and by k_t their transverse momentum relative to the photon direction. The transverse momenta of jets in the final state are denoted by p_T.

3 Theoretical framework

This section reviews the theoretical ideas discussed during this workshop pertaining to the hard diffractive scattering and its potential in clarifying and exploring the properties of QCD. It is not meant to be a complete review of all the phenomenological activities developing very dynamically in this area of research. Its main purpose is to outline the fundamentals of QCD that can potentially be probed in diffractive processes.

3.1 Classification of high energy processes

In order to understand the issue of the interplay of hard and soft physics in high energy processes it is fruitful to classify them according to the number of involved scales [1].

Soft QCD - Physics of the Pomeron: Soft hadron collisions are usually considered as processes with one scale $\approx$ 1 fm. At high energy these processes have been successfully described by Pomeron [2, 3] exchange or by Pomeron cuts as advocated since the sixties and seventies [4] (for a review see [5]). The basic feature of this class of processes is the Pomeron pole factorization, by which we mean that at high enough energy the energy dependence of any hadronic cross section should be given by a universal Pomeron trajectory. With a universal Pomeron the ratio of single to double diffractive cross sections is independent of the projectile [6, 7]. This universal trajectory of the Pomeron described by $\alpha(t) = \alpha_0 + \alpha' t$ with $\alpha_0 = 1.08$ and $\alpha' = 0.25$ GeV^{-2} [8] gives a reasonable phenomenological description of the energy dependence of cross sections. The universal energy dependence of cross sections is also natural in the semi-classical approximation of [9] to quantum field theory.

Hard QCD evolution: The second class consists of hard processes which are determined by two or more different scales involved in the interaction. Deep inelastic lepton scattering off protons as well as all hard diffractive processes belong to this class. The hard scale is supplied by the virtuality of the photon or jets and the soft scale on the proton side is determined by its size of $\approx$ 1 fm.

In order to be able to use perturbative QCD, it is important to prove that the short distance physics factories from the soft one. For the total cross section and for special hard diffractive processes this is achieved using the factorization theorem in QCD which leads to the DGLAP equations describing the evolution from the large Q^2 scale to the scale of soft QCD processes. The soft physics (and in particular the soft Pomeron) then enters the boundary conditions to these equations.

The characteristic feature of two scale processes is the violation of the Pomeron pole factorization. In hard processes at high energies one may observe different energy dependences for different external particles and that the energy dependence may change as Q^2 changes. Thus to avoid confusion the word Pomeron will be used in this report for the soft QCD processes described by a universal trajectory, as it has been originally suggested.

BFKL evolution In its original form the BFKL equation is derived assuming a small but fixed value of the strong coupling constant. The scale of α_s is that of the external particle, e.g. for onium-onium scattering the scale is defined by the heavy quark of the onium state. The BFKL approximation therefore applies to processes with one large momentum scale. At HERA, a clean test of BFKL would be provided by the measurement of high-p_T forward jets, with $p_T^2 \approx Q^2$, in low-x deep inelastic scattering, as suggested by A.Mueller [10].

Whether the BFKL can be used for predicting the x dependence of the gluon structure function at small x is a topic of heated debate: the structure functions have not only the scale Q^2, but, through the initial conditions, also contain the hadronic momentum scale, and therefore do not provide a clean BFKL application. In deep inelastic diffractive scattering, a promising place to look for the BFKL Pomeron is semi-inclusive diffractive vector production $\gamma^* + p \to V + X$ with a large momentum transfer t.

Color transparency and Perturbative Color Opacity: Color transparency is a phenomenon which describes within QCD the interaction of a small size color neutral parton configuration with a hadronic target. The essence of color transparency is expressed in the formula [11, 12, 13] which follows from the factorization theorem for hard processes in QCD.

$$\sigma_T^{q\bar{q}} = 2\alpha_s \pi^2 b^2 \frac{1}{N_c} Tr\left(\frac{F^2}{8}\right) xG_T(x, 9/b^2), \quad (1)$$

where b is the transverse separation between the $q\bar{q}$ system, F^2 is the Casimir operator of the SU(3) color group and G_T stands for the gluon distribution in the target.

The name derives from the fact that high energy processes are dominated by gluon exchanges and that the cross section for a small configuration is proportional to its size in the impact parameter space (color screening). The decrease of the cross section with decreasing size is partly compensated by the known increase of the gluon density. At fixed size b the cross section increases with increasing energy. At very high energy, when the number of gluons becomes very large, the interaction cross section also becomes large and that leads naturally to perturbative color opacity. Both phenomena are particularly relevant for photon induced high energy interactions as the photon fluctuates into a $q\bar{q}$ pair and most of these fluctuations lead to a small size, large relative k_t quark pair where the partons screen each other. An important consequence of color transparency is that in the region of its applicability initial and final state interactions are suppressed. Color transparency and perturbative color opacity phenomena can be used to probe the diffusion of a small size configuration into a normal hadron size. This diffusion is characteristic for quantum field theory phenomena and is one of the sources of leading twist nuclear shadowing at small x. At sufficiently small x the impact parameter unitarity condition and perturbative color opacity put dynamical limit on the region of applicability of existing pQCD methods to hard processes. In this respect color transparency and color opacity are new phenomena, on top of perturbative QCD.

A few more words might be in place about the BFKL approximation in the diffractive structure function. It is immediately clear that the use of BFKL approximation across the rapidity gap faces the same problem as for the gluon structure function, i.e. it has two scales: the hadronic scale at the coupling to the proton, the other scale characterizing the diffractive system at the other end of the Pomeron. In addition, this latter scale is not necessarily the same as the photon virtuality Q^2. It rather depends upon details of the final state of the diffractive system. As for the diffractive structure function, it has recently [14] been observed that, as a result of its built-in diffusion mechanism, the BFKL itself pushes this upper scale into the infrared region, i.e. into a region of phase space where non-leading corrections to the BFKL approximation are expected to be large.

Beyond these more subtle difficulties in the application of the BFKL approximation to multi-scale processes it is also not clear whether in diffractive dissociation at HERA there is enough phase space available for building up the power-law behavior expected from the BFKL equation. Namely, in order to achieve a multi-Regge type regime in which the BFKL approximation is valid, i.e. where only small correlations between the subsequent parton emissions exist, the rapidity interval available for radiation has to be large. Let us estimate the effective order of terms containing $\ln 1/x$ within the kinematics of HERA. The interval in rapidity covered by HERA is $\Delta y = \ln 1/x + \ln Q/m \sim 12$. A typical correlation length in rapidity space between

particles in multi-particle interactions has been measured to be of the order of 2 to 3 units in rapidity. Thus the photon and proton fragmentation regions will occupy typically about 5 units of rapidity. In the multi-Regge kinematics the rapidity interval between adjacent partons should be greater than the typical correlation length. Thus assuming a rapidity separation of 3 units, the BFKL ladder at HERA may contain not more than 2 to 3 steps. In the DGLAP evolution or within the multi-peripheral pQCD kinematics the ladder can be somewhat longer. It is thus not clear whether there is enough phase space available at HERA for building up the power-law behavior expected from the BFKL equation. To unambiguously observe the BFKL asymptotics it is necessary to find a trigger which ensures only one hard scale. Such a kinematical condition will prevent the impact parameter space evolution to larger sizes and will facilitate the search for the behavior predicted by the BFKL approximation (see above).

In reality, the distinction between these four types of physics is not always clear. For example the spatial size of known hadrons varies from the proton having a radius of ≈ 0.8 fm to the Υ whose radius is ≈ 0.1 fm. Thus the J/ψ or Υ scattering of a proton belongs, in a wide kinematical range, to the second class of processes [15]. However, with the increase of the energy of these interactions (i.e. in the Regge limit) the soft regime would dominate in most of the rapidity space as a result of diffusion from the large scale provided by the mass of the heavy vector mesons to the scale of soft QCD processes.

3.2 The physical picture underlying LRG events

The interest generated by the observation in DIS of a significant proportion of events with large rapidity gaps (LRG) in the hadronic final state is easy to understand within the pQCD wisdom. In perturbative QCD [16, 17] the probability for a gap to occur is $P_{gap} \sim \exp(-\Delta y \omega)$, where Δy is the length of the gap in units of rapidity and

$$\omega = N_c \int_{Q_0^2}^{Q_{max}^2} \frac{\alpha_s(k_t^2)}{k_t^2 \pi} dk_t^2, \quad (2)$$

where $N_c = 3$. At low Q_{max}^2 ω is of the order of unity and it increases with Q^2. Of course the lower limit of integration is sensitive to non-perturbative physics and thus in practice the numerical value of ω is uncertain. However one expects an exponential suppression of large rapidity gaps and this fact is reproduced in the MC generators for DIS events. In the Lund Model the confinement forces produce quark-antiquark pairs which fill the rapidity gap [18].

This apparent contradiction stimulated interest in the role of non-perturbative "color rearrangement" QCD effects in the final states. Models [19, 20] have been suggested where LRG events arise as the result of non-perturbative random soft color interactions between the ejected parton and proton remnants (hard radiation is accounted for using pQCD methods). Within these models the ratio of cross section for diffraction in DIS to the total cross section is expected to weakly decrease with increasing Q^2. The decrease of this ratio with Q^2 seems to be a model independent prediction of QCD since as Q^2 is increased at fixed x, the radiation region will expand to fill up the whole phase space and LRG events will be suppressed. The model of [20, 21, 22], in which the perturbative phase of radiation is described by the DGLAP evolution is capable of describing the gross features of the data on diffraction in DIS. However QCD radiation in terms of a BFKL type approach has been found to lead to much larger radiation [23]. It seems that the probability of gap survival in the production of high p_T dijets

separated by a large rapidity gap can provide an effective testing ground for these ideas. Such processes have been observed by ZEUS [24], CDF [25] and D0 [26].

It is of interest to consider the deep inelastic processes at small x in the reference frame where the proton is at rest, a relatively new idea in QCD. In fact, this approach is closer to the theoretical ideas formulated in 1970's for generalizing the then more familiar model of vector meson dominance to the parton model. In principle, the target rest frame description is equivalent to the Breit frame description of Feynman in which the photon has no structure. The difference in the interpretation reflects the fact that the time interval is not Lorentz invariant. Obviously it is only the space-time interval which is Lorentz invariant. However the QCD formulae for the hard diffractive processes clearly reveal the equivalence between both approaches.

In DIS, in the proton rest frame, the virtual photon fluctuates into a quark-antiquark pair at distances $l_c = 1/2m_p x$ upstream from the proton (of mass m_p). A formation or interaction length can be measured when the cross section depends on the masses of the interacting particles [27]. The existence of a large interaction length in DIS has been established by Ioffe [28, 29] based on the decrease of the total cross section with Q^2. Theoretically such an interaction length is a basic property of the parton model- 'ladder diagrams' which dominate the pQCD regime. At fixed x when Q^2 increases pQCD cascades tend to be relevant for most of the phase space of the final state. In this case the interaction length is a measure of the spatial distances occupied by perturbative QCD in DIS.

In the HERA energy range "macroscopic" interaction lengths of up to 1000 fm can be reached, while fixed target experiments reach at most $l_c \sim 10$ fm; in other words, in the HERA kinematics, it is a quark-antiquark pair rather than a photon that interacts with the proton. This knowledge has deep implications for the existence of coherent phenomena in DIS at low x [30] and is the reason why from now on the interaction length will be called coherence length.

Semi-classical calculations of the space-time evolution of a $q\bar{q}$ pair created with size $1/Q^2$ at the origin show that the transverse size b of the $q\bar{q}$ pair upon arrival on the target is $b^2 \approx 1/k_t^2$ [31, 32, 33] where k_t is the transverse momentum of the quarks from the photon. Thus DIS at small x probes the interaction of different quark configurations in the photon wave function with the target. This observation helps to establish the equivalence between the parton model and the proton rest frame description which is in essence the "aligned jet model" (AJM) [31, 32, 33] for DIS. In the AJM the large k_t, $q\bar{q}$ configurations of the virtual photon are inactive and the interaction occurs predominantly through $q\bar{q}$ pairs with small relative k_t, with one of the constituents carrying practically the whole of the projectile momentum. This assumption is necessary to reconcile Bjorken scaling with the laboratory frame description and to avoid the Gribov unitarity limit [34] saying that $\sigma(\gamma^* N)$ would be independent of Q^2 or even increase as $\ln Q^2$, if all quark-gluon configurations were to interact with the same cross section.

These quark-antiquark pairs with large transverse separation, resulting from an asymmetric sharing of the photon momentum generate a strong color field and behave essentially like hadrons. Thus both the parton model and the AJM naturally predict a large leading twist cross section for diffraction in DIS - similar to that observed in soft hadronic interactions.

The modeling of diffraction with the AJM approach [35] has been implemented in the NIKZAK generator [36] and gives a fair agreement with the data. LRG events can also be reasonably well described in terms of diffractive interactions as given by a phenomenological Pomeron exchange. The basic idea is that the Pomeron has a parton content which can be

probed in hard scattering processes [37]. This approach is realized in Monte Carlo generators such as POMPYT [38] and RAPGAP [39]. We want to stress that the contribution of naive AJM- configurations of quarks having transverse momenta $k_t \ll \sqrt{Q^2}$ is suppressed in QCD by Sudakov type form factor. This suppression is compensated to a large extent by bremsstrahlung. Thus within QCD the number of jets in the photon fragmentation region should increase with increasing Q^2 [40].

The $q\bar{q}$ configurations with sufficiently small transverse separation in space, i.e. with large relative transverse momenta, interact with a hadronic target, T, with a small cross section given by eq. (1). The presence of the gluon density in eq.(1) $G_T(x, 9/b^2)$ shows another distinctive property of the dynamics of small objects - small objects interact with small cross section which however increase fastly with energy due to the evolution of partons in the target. The presence of the gluon structure function $G_T(x, 9/b^2)$ distinguishes eq.(1) (derived in QCD) from a similar equation suggested within the constituent quark model of hadrons for quarks interacting through two gluon exchange [41, 42, 43].

For the small $q\bar{q}$ configurations diffractive scattering is driven by two gluon exchange. It is important to consider the suppression of gluon radiation from the pair of exchanged gluons. The issue is the coherence in the radiation from a color neutral system when the color charges are almost at the same impact parameter. In this case radiation of gluons with small transverse momenta is known to be suppressed [44, 45] since such a gluon can not resolve a colorless object. Radiation of gluons with large transverse momenta is suppressed by the smallness of the coupling constant. This reasoning is directly applicable to hard diffractive processes initiated by small size $q\bar{q}$ pairs where the exchange of a colorless pair of a hard and a relatively soft gluon can be calculated in QCD. These processes are still of a leading twist type because QCD factorization theorem is modified for processes with diffractive final states [46]. The smallness of the relative impact parameters is the property of QCD evolution. The amplitude of processes with large rapidity gap is generally suppressed due to the fact that all color exchanges have to be at the same impact parameter.

To summarize the following scenario emerges for the energy dependence of hard diffractive scattering. In the soft QCD regime, the parton model predicts the usual Pomeron type behavior somewhat modified by Q^2 evolution. In QCD, in contrast to the parton model, the contribution of $q\bar{q}$ pairs with small relative distances b, (large relative momenta k_t) is only suppressed by α_s/k_t^2 but their interaction cross section increases quickly at small x. Thus, due to the presence of the so called anomalous photon contribution, $\sigma_{\gamma^* N}$ may increase faster with W^2 as compared to cross sections for hadron collisions since the probability of small configurations in the wave function of a hadron is significantly smaller than in the photon wave function. This physics is naturally incorporated in the models for the production of $q\bar{q}$ pairs from a gluon field [40, 47]. Calculation of these diagrams leads to a reasonable interpolation formulae between soft and hard QCD. For the small transverse momenta configuration this approach is more or less equivalent to the AJM. At large transverse quark momenta these diagrams lead to high p_T dijet production calculable in QCD. The smooth matching of the contributions of these two types of physics predicts the violation of universality of the intercept and of the slope of the "effective Pomeron". At large β, small diffractive masses, the result may become closer to that characteristic for the pQCD regime [30, 48].

Finally, a few words should be said about the possibility of observing deviations, in the cross section given by eq.(1) at small x, from the DGLAP evolution equations (often referred to as " saturation effects"). There is very little doubt that the DGLAP-predicted small x behavior

of the gluon distribution cannot be correct for arbitrarily small x; similarly, also the BFKL approximation needs larger and larger corrections when x becomes very small. Qualitatively we expect these corrections to tame the increase at small x. The observation and theoretical understanding of such unitarization effects is widely considered to be one of the main challenges of low x physics. Empirically we know that the rate of the increase of the gluon structure function at small x changes with the transverse size of the $q\bar{q}$ pair: for small b^2 we observe a stronger increase and, most likely, will have to go to smaller x before we can see the onset of corrections, whereas for larger sizes of the $q\bar{q}$ system we move into the regime of the non-perturbative (soft) Pomeron with very strong corrections already at not so small x. Hard diffractive scattering, which, at fixed small x, allows to probe different ranges of b^2, therefore offers the exciting possibility of observing the onset of deviations from DGLAP evolution. Compared to F_2, these corrections should become visible already at larger values of x, i.e. at HERA hard diffractive scattering may be the most promising way of addressing this fundamental issue!

3.3 How to distinguish between Soft and Hard Diffractive Processes

Let us now highlight the features that can differentiate between soft and hard QCD diffractive processes. For simplicity let us parameterize the elastic or diffractive cross section for $\gamma^{(*)}p$ in the form

$$\frac{d\sigma}{dt} \propto W^{4n} \exp\left(B_o\, t + 2\alpha'_{I\!P}\, t \ln\frac{W^2}{s_o}\right), \qquad (3)$$

where as usual W is the c.m. energy of the $\gamma^{(*)}p$ collision and t the momentum transfer at the proton vertex.

Energy dependence of the cross sections: The analysis of soft processes shows that n is universal, determined to be $n \approx 0.08$ and $\alpha' \approx 0.25 GeV^{-2}$ [8]. These observations can be interpreted either as evidence for the exchange of a Pomeron with small re-scattering effects [49, 50] or by saying that the observed behavior is a combination of a Pomeron with $n \geq 0.2$ and big re-scattering effects [51, 52]. In the latter case the effective W dependence is expected to vary from process to process.

For the hard diffractive processes we have $d\sigma/dt \approx [xG_p(x, Q^2_{eff})]^2$ where Q^2_{eff} depends on the process (for a discussion see [53, 12, 54]). For the vector meson production $Q^2_{eff} = Q^2\langle b_L^2\rangle/\langle b_V^2\rangle \ll Q^2$ [55], for diffractive dijet production $Q^2_{eff} = p_T^2/(1-\beta) \geq p_T^2$ [56, 57, 58] (for the same process within the constituent quark model of the nucleon see also [59]). The quantity $\langle b_V^2\rangle$ is the effective size of the $q\bar{q}$ pairs in the diffractive production of vector meson V while $\langle b_L^2\rangle$ is the effective size of $q\bar{q}$ pairs in the total cross section for the longitudinally polarized photon. Thus cross sections of hard diffractive processes should increase with W considerably faster than the soft ones with a scale dependent power as dictated by the QCD evolution equations. Hard diffractive physics corresponds to the limit when both $\ln Q^2$ and $\ln(1/x)$ increase at the same time. At fixed Q^2 and M_X^2 (Pomeron type kinematics) and at sufficiently small x the energy dependence of cross section should be again dominated by soft QCD.

The BFKL approximation predicts an even faster increase with energy of the cross sections for the hard diffractive processes, but taking into account energy conservation and coherent effects in radiation tends to diminish n [60, 61, 62, 63].

Higher twist hard processes should be specially enhanced in the diffractive production of states with masses $Q^2 \gg M_X^2$ and in the processes initiated by longitudinally polarized photons.

t dependence of the cross sections: The energy dependence of the slope B of the t distribution $\sim \exp(Bt)$ and its universality is a sensitive probe of soft and hard QCD [30, 64]. When soft QCD phenomena dominate B is expected to increase with energy $B_{\rm soft} = B_o + 2\alpha'_{I\!P} \ln(W^2/s_o)$, where $\alpha'_{I\!P}$ is the slope of the vacuum pole as given above. Within the HERA kinematical range the slope should change typically by 2 units if indeed soft QCD dominates. [65]

In the hard QCD regime one expects $\alpha' \approx 1/Q^2$ and $s_o \approx Q^2$. Also the value of B_o should be significantly smaller for hard diffractive processes compared to the soft ones. For ρ meson photo-production the measured value is $B \sim 10$ GeV^{-2} [66] and is well understood in terms of vector dominance model and the similarity between ρN and πN scattering. For hard diffractive processes B should be significantly smaller since the scale of the t dependence at the hard vertex is given by Q^2. At small x it should be practically independent of W, $B = B_o$, and the same for all hard diffractive processes [30]. This seems to be not far from the current data on diffractive electro-production of ρ, ϕ and in particular J/ψ mesons [67]. A unsolved question concerns the kinematical region where Pomeron regime is restored in the limit of $x \to 0$ and large but fixed Q^2 . The signature of this regime is a value for $\alpha'_{I\!P}$ which should be the same as in the soft hadron interactions.

Diffractive production of light quarks by transversely polarized photon is beyond the control of hard QCD, and therefore its theoretical description is model dependent at present. One of the ways to investigate the interplay of hard and soft QCD in such processes is to observe a difference in the behavior of reactions initiated by transversely polarized photons as compared to those initiated by longitudinally polarized photons: a larger value of the slope of the t dependence and its noticeable energy dependence. Another feature of the soft diffractive processes is the presence of maxima and minima in the t dependence of the differential cross section which are due to the interference between the impulse approximation and the re-scattering terms. For the hard diffractive processes the re-scattering term should be suppressed. Thus for hard diffractive processes such structures in the differential cross section should disappear with increasing Q^2.

The phenomena discussed above can also be used to investigate the onset of deviations from the DGLAP equation. Near the unitarity limit two phenomena are expected, a slowing down of the increase of the parton densities with decreasing x and a fast increase with energy of the t slope (significantly faster than for the soft regime) and its growth with t.

Diffractive charm production: Diffractive charm production may appear as an effective probe of the hardness of the interaction processes [36, 58, 59, 68, 69, 70, 71]. If diffraction is dominated by hard QCD and the masses of the quarks can be neglected, the fraction of diffractive charm production is given by the ratio of the squares of the quark electric charges: $e_c^2/\sum e_i^2 = 0.4$. If soft QCD dominates in diffraction, for example by the exchange of two soft non-perturbative gluons [68] or via boson gluon fusion with a gluon coming from a non-perturbative partonic Pomeron a la Ingelman - Schlein [37], the production of charm is expected to be smaller. An estimate of charm production can be obtained assuming a universal structure of the Pomeron. For a typical transverse momentum of a quark in the soft QCD regime of $\sim$ 0.4 GeV and a bare mass of the c quark of $m_c = 1.2$ GeV, the ratio F^D_{2charm}/F^D_2 is proportional to $(4/9 \cdot k_t^2/m_c^2)/(6/9 + 4/9 \cdot k_t^2/m_c^2) \approx 0.07$. A larger yield can be obtained if the structure of the parton ladder relevant for the process depends on the channel. In reality the expected yield of charm should be larger since QCD evolution leads to diffractive production of high p_T jets which should be enriched by charmed particles [36, 58, 59, 68, 69, 70] The

first experimental indications are that charm production at HERA [72] is not small. Thus the absolute value, the energy and t dependence of diffractive charm production are sensitive probes of interplay of soft and hard QCD.

Azimuthal distribution: Hard physics should manifest itself in very specific azimuthal distributions for the process $e + p- > e + q\bar{q} + p$ [73, 74, 75]. The azimuthal distribution in exclusive two jet production will be different for boson gluon fusion than for a two gluon exchange mechanism. Thus the study of azimuthal distributions should help in differentiating between hard and soft diffractive physics.

Thus we conclude that the competition between soft and hard QCD requires attention in the comparison between results of different groups and of different measurements of the same group. This is because in the different kinematical ranges different physics may dominate.

3.4 Semi-classical approach to diffractive processes

In [69] a semi-classical approach to diffraction is proposed in which the proton is treated like a classical background field. Working in the proton's rest frame, the contributions of different configurations of the $q\bar{q}$ pair in the virtual photon to diffractive and inclusive structure functions are calculated. A physical picture emerges that is very similar to Bjorken's aligned-jet model. As the very fast partons of the pair pass through the proton they interact, essentially elastically, with its color field, which is treated as a classical background field. This leads to non-abelian eikonal factors in their wave-functions which allow the possibility of diffractive scattering. Leading twist diffraction is dominated by the configuration in which one of the partons in the pair carries most of the momentum of the photon and a large transverse distance develops between the partons by the time they arrive at the proton. Unlike the inclusive cross section, it has no logarithmic enhancement at large Q^2. The approach has a few features similar to the more phenomenological model advocated in [19], in which diffractive events are kinematically dominated by single gluon exchange and non-perturbative soft color interactions allow the formation a color singlet final state.

In [76] the model is expanded to include an additional gluon in the final state. Leading twist diffractive processes appear when at least one of the partons has a small transverse momentum and carries a small fraction of the longitudinal momentum of the proton. The other two partons may have large transverse momentum, i.e. they stay close together as they move through the proton, acting effectively as one parton. This high k_T jet configuration produces the only leading twist contribution to F_L^D at this order (which is constant) and $\ln Q^2$ enhancement of F_2^D. This signals that F_2^D also has leading twist contribution from the configuration in which the transverse momenta of the partons interacting with the target transverse momenta are small. Phenomenologically one expects the ratio F_2^D/F_2 to decrease like $1/\ln Q^2$. There should be fewer jets in F_2^D, since they appear only at order α_s, than in F_2 where they appear at leading order. In F_L^D the leading twist diffraction appears at order α_s which will be dominated by jets.

3.5 Hard diffractive processes calculable in QCD

It has been understood recently that hard diffractive processes, in particular elastic electroproduction of vector mesons by longitudinally polarized photons at large Q^2, $\gamma^* + p \to V + p$, and high p_T dijet production, $\gamma^* + p \to q(p_T)\bar{q}(-p_T) + p$, are calculable in QCD. Although

these processes are higher twist effects, QCD factorization theorem justifies factorization of the hard blob from the soft blob [77]. The large interaction length at low x justifies the use of completeness of hadron states produced in the intermediate step and as the outcome, the calculation of the cross sections for the hard diffractive processes in terms of quarks and gluons. Therefore, as for the deep inelastic processes, the scattering amplitude can be expressed by the distribution of the gluons in the nucleon and in case of vector mesons by the bare quarks inside the vector meson.

A feature particular to these new hard processes is that as a result of energy-momentum conservation the fractions of proton momentum carried by the exchanged partons are not equal [53, 46, 30, 78] leading to non-diagonal parton distribution. At sufficiently small x within the leading $\alpha_s \ln x$ approximation of QCD the non-diagonal gluon distribution tends to the diagonal one [79]. However this result could be valid even beyond this approximation since it is the property of both multi-Pomeron [79] and multi-peripheral kinematics. Within the leading $\alpha_s \ln Q^2$ approximation the difference between diagonal and non-diagonal distributions, at sufficiently small x, is calculable in pQCD because as a result of QCD evolution, in the non-perturbative distribution, only partons with large fraction of the proton momentum are important. The radiation from asymmetric gluons is a small correction since the gluons are effectively at the same impact parameter. This is a particular case of Gribov's theorem [44] which states that, as a result of gauge invariance radiation of vector particles with small p_T in high energy processes is predominantly from large distances and insensitive to the interior structure of amplitude. For a colorless exchange only gluons with large p_T can be radiated but this radiation is suppressed by the smallness of the coupling constant. Thus there is a definite possibility to measure the same gluon distribution in different hard diffractive processes.

The investigation of these processes will provide a novel information on the hadron structure and on the space-time development of QCD processes at high energies. They offer the possibility to measure parton distributions in hadrons in a new way, to establish the three-dimensional distribution of color in hadrons as opposed to the one-dimensional one from the leading twist phenomena and to check the predictions of QCD for the asymptotic behavior of the light-cone wave functions of hadrons. This field is rather young, but progress in the theory and in the experiment is rather fast.

The processes of this type which have been considered at this workshop are diffractive vector meson production by longitudinally polarized photons, diffractive production of two high p_T jets, and large t diffractive J/ψ production.

One of the striking experimental observations at HERA is the qualitative difference in the energy dependence of diffractive photo-production of J/ψ meson as compared to electroproduction of ρ meson. This fact is in line with the significant high momentum tail of the wave function of J/ψ which follows from realistic models of charmonium. As a result, in the processes determined by the first power of charmonium wave function, color in the $c\bar{c}$ pair is strongly localized. This explains the precocious applicability of pQCD to the diffractive photo-production of J/ψ [55]. This process is an effective probe of relativistic effects in the charmonium wave function. The fact that such effects are large has been known long ago from the calculation of QCD radiative corrections to the decay of J/ψ into leptons.

Other processes which have been considered are diffractive production of masses $M^2 \ll Q^2$ [30, 80] and diffractive open charm production [68, 71, 58]. Both belong to a class of processes where special care has to be taken for the contribution of the transversely polarized virtual photon. The theoretical description of diffractive processes initiated by transversely polarized

photons is model dependent [81, 80]. This is because the contribution of soft physics is not suppressed for such processes up to extremely large Q^2 where it becomes suppressed by Sudakov type form factors.

The pQCD calculation of diffractive reactions initiated by longitudinally polarized photons can in principle be applied to a more general case of low mass hadronic final states. However the presence of crossed diagrams (4 gluon exchange) leads to the end-point, non-perturbative QCD contribution which may spoil the predictive power of the calculation unless it is restricted to the region of exclusive states with $(1-\beta) \leq \mu^2/Q^2$ where μ is a Q^2 independent hadronic scale. This is not an issue for vector meson production as the end-point contribution is suppressed by the the decrease of the wave function of vector mesons as $\sim z(1-z)$ or faster [30, 79].

3.6 Color transparency phenomenon and possible signatures

Not unexpectedly the low x physics and hard diffraction in particular indicate the importance of color dynamics in QCD. It seems that certain aspects of hard diffraction are easier to understand in the language of color dynamics than in the quark-parton language. The important starting point is to view the deep inelastic scattering in the rest frame of the proton. As explained earlier, in this frame the photon fluctuates into a $q\bar{q}$ pair long before reaching the target. The interaction of this photon with the target depends on the initial configuration of the $q\bar{q}$. In order to achieve scaling a la Bjorken, one has to assume that certain configurations, those in which the pair of quarks have a large relative k_T are inactive [31, 32, 33] (this is the assumption of the AJM).

In QCD the pseudo-neutrality of the large k_t configurations is explained by the fact that they occupy a small transverse area in which color is screened. It turns out that the interaction cross section of such a small size configuration is not zero but proportional to the square of the transverse distance between the partons and the gluon density in the target (see formula 1). Thus the QCD corrections to scaling find a natural explanation. Since the interaction cross section for a small size object is small this leads to the notion of color transparency (CT). CT in QCD is the consequence of color screening and asymptotic freedom.

In low x processes (large coherence length) CT is expected when Q^2 is large and its role will increase with increasing Q^2. Albeit even at large fixed Q^2 when x decreases CT may disappear. Due to QCD evolution the number of gluons increases with decreasing x and even for an interaction of a small object the cross section may become very large and reach the unitarity bound. Thus the regime of color transparency will lead to perturbative color opacity. A way to enhance the role of CT is either to go to very large Q^2 or to select photons with longitudinal polarization for which the $q\bar{q}$ tends to have a large relative k_t. Note that the picture which emerges in this language of color optics is very consistent with the one forged on ideas of the QCD improved quark-parton model.

CT leads naturally to the appearance of hard diffractive processes where a color neutral small objects traverses the target without disturbing it too much and reappears either as a small mass diffractive final state (a vector meson in particular) or as a two jet configuration. The fact that these interactions can be described as due to two perturbative gluon exchange without form factor suppression requires further theoretical insight as explained in one of the previous sections.

One the consequence of CT is that the process of re-scattering of a small object within a target should be suppressed and thus in general initial and final state interactions should be suppressed in a wide range of high energy interactions (see discussion and references in [82]). This striking prediction of QCD can be hardly understood in terms of pre-QCD ideas. This is why CT phenomena are at present searched for at all high energy accelerators. Another important role of CT is that it will allow to probe the onset of saturation expected at very low x.

One of the recent experimental confirmations of ideas leading to CT phenomenon is the observation by H1 and ZEUS of a fast increase of cross sections of hard diffractive ρ, ϕ, ψ meson production with decreasing x [79]. The slope of the t distribution is also found to be smaller compared to photo-production data. The E665 experiment at FNAL has found some evidence for color transparency [83] in the ρ meson production. However, the data have low statistics, cover a rather restricted range of x and Q^2 and cannot reliably separate events without hadron production.

In the context of vector meson production a direct consequence of CT would be the disappearance at large Q^2 of maxima and minima in the t distribution which for soft processes are due to the interference between the impulse approximation and the re-scattering terms.

The suppression of initial and final state interactions should be observed also in the diffractive processes in DIS off the proton. This is because at small x the initial and final state interactions of the small size $q\bar{q}$ pair with proton remnants should be suppressed by an additional power of the size of the quark-gluon configuration b^2. But there are no firm conclusions to be drawn as yet.

A generic example of a process in which CT can be tested is the production of jets separated by a large rapidity gap in photo-production. A real or virtual photon contains with a significant probability an unresolved photon defined as a small size quark-gluon configuration where color is well screened (anomalous contribution to the photon structure function and direct contribution to the photo-production cross section). Hence CT should be important in any process induced by the contribution of the unresolved photon. If CT is a viable phenomenon the probability of survival of large rapidity gaps between jets is expected to be higher for jet production initiated by the unresolved photon contribution than for the hadronic component.

The gap survival probability P accounts for the soft interactions of the constituents which do not participate in the hard process. The estimate of P for $p\bar{p}$ collisions within the eikonal approximation has been made in [84, 85] and leads to the universal function of dimensionless parameter: $\frac{\sigma_{tot}}{B}$ where B is the slope of the t dependence of the scattering amplitude. The universality follows from the fact that hard partons are concentrated at considerably smaller impact parameters as compared to the soft ones [86]. The dependence of P on the projectile is seen to be rather weak. Gluon radiation should be also projectile independent since its effects cancel out in the ratio of events with and without large rapidity gap. Thus the expectation of CT is very different from the above [86]. A significant difference in the gap survival probability for projectiles of different size would have to be interpreted as evidence for CT.

The recent measurements of ZEUS [24] show a substantially larger gap survival probability than observed in CDF [25] and D0 [26]. In the kinematics of the ZEUS experiment one of the jets carries a significant fraction (≈ 0.7) of the photon momentum, a configuration which favors the direct photon contribution. This observation could well be the first experimental hint that

small size configurations for which initial and final state interactions are suppressed lead to a larger gap survival probability.

These data are in line within the assumption that color of a hard gluon can be neutralized in hard diffractive processes by the exchange of a relatively soft gluon located at the same impact parameter [53, 87, 88, 84, 89, 46, 79].

In particular the observed practical independence of the ratio on pseudo-rapidity implies that the LRG events follow a $\frac{1}{t^2}$ Rutherford scattering distribution, just like the non-gap dijet events to which they are normalized and which are dominated by single gluon exchange in the t channel [45].

To demonstrate in a model independent way that the explanation lays within CT it is necessary to measure the gap survival probability as a function of the resolved photon contribution. The advantage of using a photon target is that the kinematical region in which one of the jets carries a significant fraction ($z \approx 0.7$) of the photon momentum [90] enhances the small size configurations while requesting $z \leq 0.4 - 0.5$ will enhance the resolved contribution. Note that the region of large z is suppressed in the wave function of hadrons. The gap survival probability for the resolved contribution should be smaller. A naive estimate would lead to reduction of a factor two.

3.6.1 Proton fragmentation region

The proton fragmentation region in the reactions $\gamma^* + p \to X + Y$, where X and Y, the states corresponding to the dissociation of the photon and proton respectively, are separated by a large rapidity gap are expected to be sensitive to the previously unexplored features of QCD.

By definition the Pomeron type factorization means that the ratio of diffractive events with state X accompanied by proton dissociating into state Y and with the proton scattered elastically,

$$R_X = \frac{d\sigma(\gamma^* + p \to X + Y)/dt}{d\sigma(\gamma^* + p \to X + p)/dt}, \qquad (4)$$

should not depend on the choice of the hadronic state X. This factorization follows from the assumption that high energy processes are dominated by the exchange of a Regge pole - the Pomeron [6]. As a first step, it is important to check this Pomeron type factorization for soft diffractive processes as a test of possible shadowing effects.

The violation of the Pomeron type factorization is expected as a consequence of QCD evolution from large to small scale. As is known the evolution leads to a Q^2 dependence of the slope of the energy dependence. As a result the total DIS cross section as well as cross sections for hard diffractive processes cannot really be described as the exchange of one or several vacuum poles. It is also expected, in line with the experimental measurements, that the slope of the t distribution depends on the hardness of the process. In particular the slope for elastic photo-production of ρ mesons at HERA energies is $B \simeq 10$ GeV^2 [66, 91] while for larger Q^2 it turns out to be smaller $B \simeq 5 - 7$ GeV^2 [92, 93]. Both effects may influence the value of R_X when going from the soft regime to the harder one [90]. Approximate factorization may be also valid in the hard regime where two gluon exchange dominates. This is because in R_X the non-universal x and t dependence cancel out to large extent.

In QCD, the proton is represented at a given light-cone time $\tau = t + z$ as a superposition of quark and gluon Fock states $|uud>, |uudg>, |uudgg>, |uudQ\bar{Q}>$, etc. Thus when the proton

is expanded on a free quark and gluon basis, it is a fluctuating system of arbitrarily large particle number [94]. The light-cone wave-functions $\psi_n(x_i, k_{\perp i}, \lambda_i)$ are the probability amplitudes which describe the projections of the proton state on this Hilbert space. The structure functions measured in deep inelastic lepton scattering are directly related to the light-cone x momentum distributions of the quarks and gluons determined by the $|\psi_n|^2$.

Fluctuations in the wave-functions of the proton can be studied in hard diffractive processes as diffraction is a measure of color fluctuations. Using completeness of the hadron states resulting from the fragmentation of the proton one can deduce the following relation between the fluctuations of the gluon distribution in the proton and the hard diffractive cross sections:

$$\frac{\sum_n < p|G(x,Q^2)|n >^2}{< p|G(x,Q^2)|p >^2} = \frac{< p|G(x,Q^2)^2|p >}{< p|G(x,Q^2)|p >^2} = \sum_Y \frac{d\sigma(\gamma_L^* + p \to X + Y)/dt}{d\sigma(\gamma_L^* + p \to X + p)/dt}|_{t=0}, \qquad (5)$$

where G is the two gluon operator whose diagonal matrix element gives the gluon distribution in the proton, and the state $|n>$ is a product of the proton fragmentation. The state X can be any state produced by a small size configuration of the initial photon. Let us consider a kind of a bag model where a proton consists of 3 bare quarks (or models where the color is concentrated within the constituent quarks). At sufficiently large Q^2 the transverse momenta of the exchanged gluons become large and as a result both gluons scatter from the same quark. In this case only diagonal transitions would survive at sufficiently large Q^2. Thus within this model the ratio in eq.(5) should tend to one at large Q^2. In general non-diagonal transitions are non zero at large Q^2, because quarks and gluons belong to different representations of SU(3) color group. The left hand side of the equation can be treated as a measure of the fluctuations of color density in the proton. Preliminary HERA data suggest a value of 2 for the ratio on the right hand side. This is an indication that color fluctuations may indeed be large.

4 Experimental Aspects

In the first part of this section we shall discuss the implications of present data in deep inelastic diffractive scattering on our understanding of diffractive physics. The second part of this section is devoted to a discussion of future aspects.

4.1 Indication for non-trivial QCD dynamics in HERA data

The measured diffractive cross section [95, 95, 96, 97] as a function of Q^2 shows a significant leading twist effect. This observation indicates that there is an important contribution from non-perturbative QCD effects for the following reasons:

- Unless the Pomeron is introduced by hand, DGLAP evolution starting at rather low scale Q_0^2, as advocated by GRV [98], would lead to a very small fraction of diffractive scattering in DIS: the radiation of gluons, governed by DGLAP evolution would fill the gap in rapidity, thus leading to an exponentially suppressed probability of finding large rapidity gap events.
- Processes in hard diffractive scattering (initiated by a projectile in a spatially small configuration), that can be calculated in QCD, like vector meson - or high p_T dijet production, turn out to be higher twist processes.

Thus the only way to obtain a significant leading twist effect is by assuming AJM [31, 32, 33], or QCD AJM [40], by scattering on partons in a non perturbative Pomeron [37], or by introducing a non-perturbative mechanism to recover a rapidity gap after pQCD radiation has taken place [19, 20].

On the other hand there are also hints in the present HERA data for an onset of hard diffractive scattering, which cannot be explained with the assumption of a soft Pomeron, but can be explained within the framework of QCD and CT. Present data on electro-production of vector mesons (ρ, ω and ϕ at sufficiently large Q^2 and J/ψ even in photo-production) [92, 93] are in disagreement with the assumption of a soft Pomeron and can be broadly described with:

$$\sigma(\text{hard diffractive}) \approx \left[xG_p(x, Q^2_{eff})\right]^2 \tag{6}$$

A fast increase of the cross section with energy, as in eq.(6) due to the strong increase of the number of gluons at small x, is a signature of a hard QCD process and a signature of color transparency.

Another observation beyond a soft Pomeron is the significant fraction of high p_T dijet events with a large rapidity gap between the jets compared to those without, as observed in photo-production in ZEUS [24] and in $p\bar{p}$ by CDF [25] and D0 [26]. The factor of seven enhancement in the rapidity gap survival probability for photon initiated processes, as compared to $p\bar{p}$ scattering, can be hardly explained as due to the difference in the cross sections of $p\bar{p}$ and Vp scattering, or due to gluon bremsstrahlung. This enhancement has a natural explanation within CT where the interaction cross section is proportional to the transverse volume occupied by color in the projectile.

If this interpretation is correct, it means that we start to understand the role of perturbative QCD in diffraction and its connection to inclusive deep inelastic scattering. Moreover a variety of new processes is expected.

4.2 Future Prospects

Inclusive measurements of the diffractive cross sections are relatively easy to perform, and do not require highest luminosity, since the cross section is about 10% of the inclusive deep inelastic cross section. However the interpretation in terms of QCD is more difficult: even if there is a regime of hard diffractive scattering, that can be calculated in QCD, one expects a mixture of soft and hard QCD processes, since the inclusive cross section will be dominated by small k_t processes where pQCD calculations are not applicable. Since we aim to study pQCD in diffraction, we discuss first diffractive processes like high p_T jet, open charm and vector meson production, since there pQCD calculations can be attempted. Then we discuss inclusive measurements and the importance of measuring the proton fragmentation region. At the end we mention a interesting class of processes in diffraction, the charged current interactions.

4.2.1 Diffractive high p_T dijet production

The calculation of diffractive dijet production can be performed using pQCD for large photon virtualities Q^2 and high p_T of the $q(\bar{q})$ jets [48, 57, 59, 68, 80]:

$$e + p \rightarrow e' + q\bar{q} + p \tag{7}$$

The process is mediated by two gluon exchange. Different assumptions on the nature of the exchanged gluons have been made: in [57] they are taken from a NLO parameterization of the proton structure function [98], in [68] the gluons are non perturbative and in [48] they are a hybrid of non perturbative and perturbative ones. The cross section is essentially given by

$$d\sigma \sim \left[x_{I\!P} G_p\left(x_{I\!P}, \mathrm{k}_t^2 \frac{Q^2 + M_X^2}{M_X^2}\right)\right]^2 \tag{8}$$

at the scale explicitly given.

Due to the different gluon densities a different $x_{I\!P}$ dependence of the cross section is expected and further discussed in [99], where also numerical estimates are presented. Thus by itself the measurement of the dijet cross section as a function of $x_{I\!P}$ would yield information on the gluons involved in the process.

A striking feature of the dijet production via two gluon exchange is the azimuthal asymmetry between one of the jets and the electron in the jet - jet center of mass system. This asymmetry is present, independent of the nature of the gluons, i.e. calculated for both perturbative [73] and non-perturbative [74] gluons. Moreover this azimuthal asymmetry is completely different from the one known for boson gluon fusion processes, where only one hard gluon interacts.

However one has to worry about the experimental separation of this processes: due to jet finding algorithms there could be a contribution of processes $ep \rightarrow e' + q\bar{q}g + p$, where one of the quarks or the gluon has small k_t, which could possibly be interpreted as a Pomeron remnant. By requiring exclusively 2 jets, where the 2 jets take all available M_X, or equivalently selecting $x_g^{I\!P} \simeq 1$, the contribution from processes with additional particles becomes small [100]. Here we defined $x_g^{I\!P}$ as $x_g^{I\!P} = (Q^2 + \hat{s})/(Q^2 + M_X^2)$ with $\hat{s}$ being the invariant mass of the two jets. For $Q^2 > 10$ GeV^2 and $p_T^2 > 5$ GeV^2 the measurement can be performed for $x_{I\!P} > 10^{-3}$. With an estimated overall selection efficiency of ~ 70 % a statistical error of ~ 10 % can be achieved with an integrated luminosity of ~ 100 pb^{-1} and at least 4 bins per decade in $x_{I\!P}$. With such a measurement one can clearly distinguish between the soft non-perturbative gluon input and the perturbative approach [100].

To differentiate between the azimuthal asymmetry for the two gluon exchange process and the boson gluon fusion with the gluon originating from a partonic Pomeron, a statistical error of ~ 10 % in 7 bins in ϕ is needed corresponding to an integrated luminosity of ~ 250 pb^{-1}. With such a statistical error the separation between one or two gluon exchange mechanisms can be made at the $4\,\sigma$ level. Both measurements, the $x_{I\!P}$ dependence and the ϕ asymmetry are of great importance. The ultimate prove of the 2 gluon exchange mechanism would be the observation of the specific ϕ asymmetry, which is completely different from the one expected from boson gluon fusion models. The $x_{I\!P}$ dependence of the cross section would give more inside on the nature of the gluons involved in the hard interaction.

The calculations so far are restricted to a region of relatively large $\beta > 0.1$. For small β, or equivalently large M_X, gluon radiation is expected to play a important role and final states like $q\bar{q}g$ have to be considered. The inclusion of these higher order diagrams is difficult and various approaches exist to estimate the next-to-leading order contributions [48, 80, 101, 102]. A systematic investigation of $q\bar{q}g$ jets is a urgent and important task.

4.2.2 Diffractive Open Charm Production

Diffractive open charm production can be a significant contribution both to hard and soft QCD [59, 68, 58, 71]. Having in mind that preliminary data on diffractive charm production [72] are in broad agreement with the expectations from a partonic Pomeron, the measurements to differentiate between hard and soft gluon exchange would require measurements of the $x_{I\!P}$, Q^2 and β dependence of the cross section. Most probably there is no way to select exclusive 2 charm final states, since due to the mass threshold charm production can only happen at relatively large masses M_X and therefore higher order corrections like radiation of hard gluons which transform into a $c\bar{c}$ pair are expected to be non negligible.

A Monte Carlo [39] simulation of the process $e + p \rightarrow e' c\bar{c}g + p$ with subsequent decay $c \rightarrow D^* \rightarrow D^0\pi$ was used together with the H1[103] parameterization of the gluon density in the Pomeron to to identify charm production and to determine efficiencies and acceptances [104]. The criteria to identify the decay products of the D^{*+} are given in [104]. With an overall detection efficiency of ~ 50 % it was shown that for 2 bins per decade in $Q^2 > 25$ GeV^2 and $x_{I\!P}$ and 3 bins in $0.01 \leq \beta \leq 0.9$ a 30 % statistical error can be achieved for a integrated luminosity of ~ 30 pb^{-1}. A more precise measurement at high β values can be made with ~ 250 pb^{-1}, but for a precision measurement with 5 bins per decade in Q^2 and $x_{I\!P}$ and 7 bins in $0.01 \leq \beta \leq 0.9$ and a statistical error of 10 % a luminosity of ~ 2000 pb^{-1} is needed.

With a measurement of F^D_{2charm} the gluon dominance in hard diffractive scattering can be demonstrated and a decision whether soft or perturbative gluons interact can be easily made. However special care has to be taken for higher order corrections which might be important.

4.2.3 Vector Meson Production

Diffractive vector meson production $e + p \rightarrow e' + \mathrm{VM} + p$ is another example of processes where pQCD calculations are expected to be applicable, at high Q^2 for the light vector mesons, and for heavy vector mesons like J/ψ or Υ even in photo-production (for a discussion see [54, 79, 105]). Strictly speaking for the case of vector mesons, built of light quarks, the QCD calculation can only be performed for longitudinally polarized photons. This is just because of the spatially small configuration occupied by the $q\bar{q}$ pair which then forms a vector meson. In such a configuration again the cross section is driven by $\left[xG_p(x, Q^2_{eff})\right]^2$. The extension of the QCD calculations beyond this approach is model dependent and there is no consensus on the applicability of all the predictions [105].

In all calculations the γ^* couples to the vector meson through the same quark loop. There is agreement on helicity conservation and that at large Q^2 the longitudinal cross section dominates. The different approaches differ in the way the gluons couple to the proton and to the wave function of the vector meson which is poorly known. The advantage of vector meson production is the possibility to select experimentally the contribution of longitudinal photons and therefore the possibility to enter the hard pQCD regime.

Another group of processes calculable in QCD are reactions $\gamma^* + p \rightarrow V + Y$ with large momentum transfer squared t to the vector meson V and with Y representing the state in which the proton dissociates. The idea is that at sufficiently large t the contribution of spatially small configurations in the wave function of the photon and the vector meson would dominate. (The soft Pomeron exchange should be highly suppressed due to the steeply falling t distribution.)

As a result of screening of color charge and asymptotic freedom it would be possible to justify applicability of the methods of pQCD to calculate cross sections of discussed processes [53, 30, 106, 107]. The prospective kinematical region is $-t > 2 - 4$ GeV^2 where the phenomena characteristic for soft diffraction disappear.

Depending on the kinematical restrictions on the proton dissociation different hard QCD phenomena may reveal themselves such as the scattering off valence, sea quarks or gluons of the proton target [30, 106, 56]. The contribution of the BFKL type dynamics is enhanced in this case due to larger intercept for the x dependence [106, 56]. It is worth to note that if the running of coupling constant is taken into account the intercept for the x dependence of BFKL amplitude depends on t.

In order to distinguish soft Pomeron initiated vector meson production from the pQCD region the following measurements are important:

- the absolute value, the x and the Q^2 dependence of the longitudinal and transverse photon absorption cross sections,
- the relative yields of various vector meson production including their excited states in photo-production and electro-production,
- the slope of the t dependence as a function of x and Q^2 and polarization of the vector meson,
- the energy dependence of the large t vector meson production.

Based on an extrapolation of existing data to a integrated luminosity of 250 pb^{-1} we expect 60000 ρ, 6000 Φ and 3000 J/ψ events with $Q^2 > 7$ GeV^2 giving a reasonable small statistical error up to $Q^2 \sim 20 - 30$ GeV^2. The total systematic errors are presently ~ 13 % and could be reduced to ~ 7 % by better understanding of reconstruction errors, errors related to non-resonant background and proton dissociation. The largest error comes from proton dissociation background. If the proton is tagged by a Leading Proton Spectrometer, this sort of background might be negligible, but the acceptance of such a device is only ~ 10 % in the best case, leading to a much lower rate of tagged events. Thus the understanding of proton dissociation is important for all the conclusions drawn from the energy and t dependence of the cross sections.

The measurement of the t distribution should allow to distinguish clearly between soft and hard pQCD regime, since the B slope in soft interactions is energy dependent because of $\alpha' \simeq 0.25$ whereas in pQCD $\alpha' \simeq 0$. Again the error on the determination of α' is dominated by the proton dissociation background, and is estimated to be of the order of $\Delta\alpha' \simeq 0.1$ requiring tagging of proton dissociation down to 1.5 mrad. If tagging is possible only down to 6 mrad, then the error on α' is twice as large, and no conclusion on shrinkage can be drawn [108]. This shows clearly the importance of the ability to measure in the very forward region of the HERA detectors.

The model independent measurement of the longitudinal cross section or the ratio $R = \sigma_L/\sigma_T$ can be done best with a reduced e beam energy ($E_e = 12$ GeV), since the fluxes of transverse and longitudinal photons differ most strongly at high y. With only 10 pb^{-1} at each electron beam energy the statistical error will be above 50 %. With 100 pb^{-1} the error in the highest W bin is reduced to 25 % [108].

Production of J/ψ vector mesons at large t, $e+p \to e'+J/\psi+Y \to e'+\mu^+\mu^-+Y$, has a reasonable high cross section: $\sigma \sim 6$ nb in photo-production for $0.01 < y < 0.3$, $0.003 < x < 1$, $Q^2 < 4$ GeV^2 and $2 < -t < 100$ GeV^2 ($\sigma \sim 0.4$ nb for $Q^2 > 4$ GeV^2) for the leptonic decay of the J/ψ and the leptons within the detector acceptance [108]. Interesting here is the measurement of the t distribution, which should show no shrinkage, as well as its energy dependence. However a precise determination of t requires a measurement of the scattered electron unless the measurement is restricted to very low Q^2. The large cross section should enable us to measure this process in the very near future.

4.2.4 Inclusive diffractive cross sections at high Q^2

The measurements of the inclusive diffractive cross section show that it is predominantly a leading twist phenomena. As discussed earlier in this report, processes calculated using perturbative QCD are of higher twist. Thus we expect the inclusive diffractive cross section to be dominated by soft, non perturbative effects. However in the region of large β, or equivalently in the small mass region, perturbative effects could be important, analogous to vector meson production by longitudinally polarized photon or high p_T jet production. The small β region, on the other hand, could be dominated by soft Pomeron exchange processes and QCD evolution of parton densities in the Pomeron. This would lead to the following picture:

- $\beta \lesssim 0.1$: Exchange of a soft Pomeron with a partonic substructure dominates. The partons in the Pomeron evolve according to the DGLAP evolution equation. Due to soft Pomeron exchange, factorization is expected,

$$F_2^D(\beta, Q^2, x_{I\!P}, t) = f(x_{I\!P}, t) F_2^{I\!P}(\beta, Q^2, t)\,. \qquad (9)$$

- $\beta \gtrsim 0.8$: Hard pQCD processes contribute significantly, leading to a violation of the factorization in eq.(9) and to large higher twist effects.

- $0.1 \lesssim \beta \lesssim 0.8$: Intermediate region. The amount of factorization breaking depends on the interplay between soft Pomeron physics and hard pQCD physics.

To clearly establish the above picture, the $x_{I\!P}$ dependence of the cross section as a function of β has to be measured precisely in a region of $x_{I\!P} \lesssim 0.01$ where no significant contribution from other possible Regge trajectories is expected. In such a scenario one could expect for $\beta < 0.1$ $f(x_{I\!P}, t) \sim x_{I\!P}^{1-2\alpha_{I\!P}}$. Another important ingredient for soft Pomeron exchange is the measurement of the t distribution. If soft Pomeron exchange dominates, then shrinkage of the t - slope is expected, whereas in the hard pQCD regime $\alpha' \simeq 0$.

The relative cross sections for large and small β also yield information on the underlying mechanism. In the soft Pomeron picture the cross section at large β should decrease with increasing Q^2. Within pQCD calculations in the large β region a large contribution from longitudinally polarized virtual photons is expected [35, 48, 109, 99, 110, 30, 80] which is absent in the partonic soft Pomeron picture.

Recent measurements of F_2^D show a deviation of factorization at large $x_{I\!P}$ [103], which could be interpreted as a contribution from higher Regge trajectories. However to safely exclude such a contribution we will restrict our discussion to the region $x_{I\!P} < 0.01$.

Thus the following measurements are needed:

- Measurement of $F_2^D(x_{I\!P}, t, \beta, Q^2)$ with $x_{I\!P} < 0.01$ and largest possible range in β and Q^2.

- Measurement of $F_L^D(x_{I\!P}, t, \beta, Q^2)$ with special emphasis on the large $\beta > 0.8$ region.

Since the inclusive diffractive cross section is large ($\sigma_{diff} \sim 4$ nb for $Q^2 > 10$ GeV^2 and $x_{I\!P} < 0.01$) the Leading Proton Spectrometer can be used to identify diffraction. A systematic error of ~ 7 % can be achieved with the LPS [111]. A measurement of $F_2^D(x_{I\!P}, t, \beta, Q^2)$ with 2 bins in $0.07 < |t| < 0.0.35$ GeV^2, 3 bins in $4 < Q^2 < 30$ GeV^2, 7 bins in $0.001 < \beta < 0.3$ and 5 bins in $0.001 < x_{I\!P} < 0.1$ is possible for 20 pb^{-1} with a statistical error of ~ 10 % in each bin [111].

For a measurement of $F_2^{D(3)}(x_{I\!P}, \beta, Q^2)$ (integrated over t) using the present experience one can hope to achieve an overall systematic error (except for the error coming from proton dissociation) of ~ 5 %. To achieve a statistical error of ~ 5 % with 5 bins per decade in Q^2 and $x_{I\!P}$ and 7 bins in $0.01 < \beta < 0.9$ an integrated luminosity of 8 pb^{-1} is needed for F_2^D. To achieve $\sim 3(1)$ % statistical errors one would need 22 (200) pb^{-1} [104].

If factorization is proven to be valid, one can measure $F_L^{I\!P}$ directly using the wide band beam of Pomerons by changing $x_{I\!P}$. With a luminosity of 15 pb^{-1} and a fine granularity at high y one can measure $R^{I\!P}$ within 50 % for $y < 0.8$ [104].

If factorization does not hold, then a measurement of the longitudinal cross section can be performed only by lowering the proton beam energy (from $E_p = 820$ GeV to $E_p = 500$ GeV). Changing the proton beam energy would lead to better acceptance in the high mass region. On the other hand, as stated in the section on vector mesons, changing the electron beam energy gives better acceptance in the low mass region (at high β). A luminosity of 2 pb^{-1} for $E_p = 500$ GeV is required to achieve a precision of the ratio of transverse to longitudinal cross section of the order of ~ 50 % [104].

4.2.5 Proton fragmentation region

So far we considered only processes (the ones that can be calculated within pQCD as well as processes mediated by soft Pomeron exchange) where a quasi elastic proton can be found (at least in principle) in the hadronic final state. This is easiest done by using the Leading (Forward) Proton Spectrometers, where both energy and transverse momentum of quasi-elastic protons can be measured, at the expense of event rates. Experimentally it is necessary to have clear measurements of the proton fragmentation region in order to subtract possible contributions from double dissociation and to control the background from non-diffractive events.

Proton dissociation is interesting on its own for the following reasons:

- If the cross section for inclusive diffractive scattering is mainly due to soft Pomeron exchange, then one should observe that the ratio $R_X = \sigma(e+p \to e'+X+Y)/\sigma(e+p \to e'+X+p)$, where Y is the proton dissociation system separated in rapidity from the system X, should not depend on the system X.

- In the hard diffractive regime, when spatially small size configurations are selected (high p_T dijets or vector mesons), it is interesting to test the factorization hypothesis. A change of regime cannot be a priori excluded.

- In going from large rapidity gaps between X and Y in $e+p \to e'+Xq+Y$ to smaller and vanishing rapidity gaps, the transition between diffraction and inclusive deep inelastic scattering can be studied [112].

- In the spirit of studying the fluctuations in the wave function of the proton it has been advocated that the intrinsic charm contribution may not be negligible [113]. Intrinsic heavy quarks Fock states could be materialized by the virtual photon probe and released in the proton fragmentation region. This effect if present would lead to spectacular events with two muons produced in the very forward region.

Experimentally the proton dissociation system can be effectively measured with tagging devices in a rapidity range of $\eta < 5.9$ with ~ 100 % efficiency for masses $M_Y > 3$ GeV starting with an efficiency of ~ 10 % at masses $M_Y > 1$ GeV. In order to determine the slope of the distribution:

$$\frac{d\sigma}{dM_Y^2} = C\left(\frac{1}{M_Y^2}\right)^a \tag{10}$$

one needs to measure M_Y at least in 2 ranges. The dominant uncertainty comes from the badly known multiplicity and p_T distributions of the particles in the system M_Y. The error on a is estimated to be $\Delta_a \simeq 0.14$ for tagging up to rapidities of $\eta < 5.9$ [114]

High efficiency tagging of proton dissociation or even better performing calorimetric measurements in $\eta < 5.9$ requires detector upgrades'[115]. In addition one has to ensure as little dead material as possible in front of the tagging device or calorimeter.

It should be stated very explicitly that if magnets for an improvement of the HERA luminosity [116] are installed in a region of $\eta > 3.5(\simeq 70\text{mrad})$ then even tagging of the system M_Y is made difficult.

4.2.6 Charged Currents

So far we discussed only neutral current processes, but also charged current processes (via W exchange) should occur in diffraction at large $x_{I\!P}$. As in inclusive deep inelastic scattering, only at very high Q^2 the cross sections for neutral current and charged current processes are of similar size. Since the Pomeron is a flavor singlet system, one would expect the charged current cross sections for electron and positron beams to be the same.

The cross section can be estimated [117] using the present knowledge of the diffractive structure function F_2^D,

$$\sigma_{CC}^{Diff.} \sim 2\text{pb} \tag{11}$$

for $x_{I\!P} < 0.1$. The rapidity gap for charged current events is smaller than for neutral current events since high diffractive masses are involved due to the W mass. With cuts on the transverse momentum and the transverse energy and a missing transverse momentum of 4 GeV the diffractive charged current efficiency is ~ 35 %. With a luminosity of 1000 pb^{-1} the cross section could be measured with a precision of ~ 5 %. With such a luminosity also the β dependence of the cross section can be determined with a $20-30$ % statistical error. This measurement requires an efficient tagging of the non-diffractive background. The use of the LPS is impossible because of the small acceptance and therefore devices to tag proton dissociation and non-diffractive background are essential.

5 Expected Significance of Hard Diffractive Scattering: Limit of Applicability of the DGLAP Evolution Equation

It is widely expected that the fast increase of parton distributions at small x cannot be sustained without running into conflict with the unitarity of the S matrix (see e.g. [118]) for the interaction of small size wave packages, that is with the positiveness of probabilities for physical processes. However the most stringent restriction on the region of applicability of the DGLAP or BFKL equations follows from the requirement of positiveness for single particle density in the central rapidity region [55].

At sufficiently small x, LO and NLO $\alpha_s \ln \frac{Q^2}{\Lambda^2_{QCD}}$ approximations as well as the leading $\alpha_s \ln x$ approximation predict a fast increase of the amplitudes for hard processes which run in conflict with probability conservation. The restriction on the applicability of the DGLAP evolution is that the leading twist contribution to the cross section of a small size $q\bar{q}$ pair scattering off a proton target should be much larger than the next-to-leading twist effect. Since this cross section is well formulated only in the pQCD regime, the reasoning below may only give restriction on the region of applicability of conventional QCD methods. To estimate this restriction let us consider the scattering of a $q\bar{q}$ pair off a target . Let us decompose the cross section in powers of $1/Q^2$. Let us denote by σ_1 the inelastic single scattering cross section due to the exchange of one ladder and by σ_2 the double scattering inelastic cross section due to the exchange of two ladders. The application of the Abramovsky, Gribov and Kanchely cutting rules [119] leads to the following relations between the cross sections:

$$\sigma_{tot} = \sigma_1 - \sigma_2\,, \tag{12}$$

$$\sigma_2 = \sigma_{el} + \sigma_{diff}\,, \tag{13}$$

$$\sigma_1 \geq 4\sigma_2\,, \tag{14}$$

where the subscripts el and $diff$ denote the elastic and diffractive cross sections. The last equation follows from the requirement of positiveness of single particle densities. One of the consequences of the above equations is that in models in which shadowing is due to the exchange of two ladders (due to triple BFKL type diagrams [118, 109]) it may cause not more than 25% depletion in parton distributions. That is to say that shadowing calculated within these models is unable to prevent the increase of parton densities without violating the positiveness of single particle densities. Further eikonal diagrams cannot be used since more than two rescatterings of the $q\bar{q}$ pair leads to violation of energy conservation in multi-particle production.

The optical theorem implies that

$$\sigma_2 = \frac{\sigma_{tot}^2}{16\pi B}(1+\eta^2)(1+\kappa)\,, \tag{15}$$

where

$$\eta = \frac{ReA}{ImA}\frac{\pi}{2}\frac{d}{d\ln x}\ln x ImA(x,Q^2)\,, \tag{16}$$

with A – the amplitude for $q\bar{q}$ pair scattering off the proton, κ – the fraction of events due to inelastic proton dissociation and B – the slope of the t dependence as measured in hard

diffractive processes. This can now be used to put restrictions on the region of applicability of QCD evolution equation by requiring that

$$\sigma_1 \geq 4\frac{\sigma_{tot}^2}{16\pi B}(1+\eta^2)(1+\kappa)\,. \tag{17}$$

Numerical estimates indicate that, for Q^2 of the order of few GeV^2, the kinematical region where the DGLAP equation becomes inapplicable for the diffractive processes and for the structure functions seems to be within the kinematics of HERA. To conclude, the decomposition over powers of Q^2 may be violated at small x in the HERA regime. Since the numerical estimates rely also on experimental measurements of B and κ the improvement in those will make the limits tighter.

Another restriction on the region of validity of the pQCD evolution follows from the unitarity of the S matrix applied to hard processes,

$$\sigma_{\rm tot} \gg \sigma_{\rm el} + \sigma_{\rm proton\ dissociation}\,. \tag{18}$$

Using the optical theorem we obtain an estimate for the kinematics where the increase of parton distributions should slow down [30],

$$\sigma_{tot} \geq \frac{\sigma_{tot}^2}{16\pi B}(1+\eta^2)(1+\kappa)\,. \tag{19}$$

One may even include the increase of B with energy, $B = r_N^2/4 + 2\alpha_s[\ln s/s_o]^n$ to obtain a strict inequality. For Pomeron exchange $n = 1$ while $n = 2$ for the Froissart regime. Again numerical estimates suggest that for hard diffractive processes this boundary may be within the HERA kinematics.

Both constraints leads to the expectation that we may become sensitive to the unitarity limit within HERA kinematics [30, 55] (see also [120]). The features which are being investigated include the x and Q^2 dependence of the diffractive jet photo-production, charm production and production of vector mesons.

Characteristic features of unitarity corrections near the unitarity limit are the slowing down of the increase of parton distributions at small x and a fast increase of the effective slope of the t dependence with energy and t [30].

The interesting question remains whether the manifestation of the unitarity limit can also be reached for $\sigma(\gamma^* p) = \frac{4\pi\alpha}{Q^2}F_2 \sim \pi r_n^2$. There is no doubt that for small Q^2 higher-twist contributions become important and participate in the transition from the strong rise of F_2 to the soft Pomeron in the photo-production cross section. It is not yet clear at which Q^2 values this transition will start. On the one hand it has been demonstrated that one can find input distributions to the DGLAP equations which describe the data down to $Q^2 \sim 1$ GeV^2 [98]. However it would be premature to draw from this the conclusion that higher twist corrections are negligible. So far no systematic analysis of higher twist corrections at small x has been performed. Furthermore, it has been shown that for flat input distributions the DGLAP is sensitive to higher order corrections (re-summation of singular terms in the anomalous dimension). All this leads to the impression that the issue of unitarity corrections to F_2 at low Q^2 is still waiting for clarification. The reason why hard diffraction may be a better place to look for a manifestation of the unitarity limit is that, by varying the final state

we have a handle on the transverse size of the $q\bar{q}$ pair, whereas in F_2 the size is always small (of the order of $b^2 \sim 1/Q^2$).

The behavior of small x processes at extremely small x is still a challenge for theory. Theoretical investigations of one hard scale processes like onium-onium scattering [121] suggest the existence of a new QCD regime of large parton densities where all interactions can be described in terms of pQCD. In the two scale processes (for example F_2 at small x) soft QCD physics is probably not suppressed: this follows from the analysis of the multiple (≥ 3) rescatterings of a small size $q\bar{q}$ pair off a nucleon. However the elastic eikonal approximation is known to have problems with probability and energy conservation in multi-particle processes [122] and ignores the leading diagrams in pQCD. It therefore seems likely that the unitarization of F_2 at small x is a non-perturbative issue.

6 Summary

The scientific program that emerges from the studies and discussions in the Working Group is as follows:

1. Inclusive measurements of $F_2^{D(3)}$ and $F_L^{D(3)}$ as a function of x, Q^2, $x_{I\!P}$, β and t in as wide a range of variables as possible. One should be able to establish the region of dominance of soft and hard physics. Assuming that we need to differentiate $\alpha_{I\!P}$ in the range of 1.05 to 1.25, it would be desirable to measure $\alpha_{I\!P}$ with a precision of $\Delta\alpha_{I\!P} = 0.04$. The required luminosity, assuming the forward tagging capability down to $\eta \simeq 6$, are:

Q^2 [GeV^2]	luminosity $\int Ldt$ [pb^{-1}]
$Q^2 < 100$	~ 10
$100 < Q^2 < 500$	~ 60
$2000 < Q^2 < 3500$	~ 250

   The cross section for charm production depends strongly on the regime of the physics behind diffractive processes. The predictions vary between 10 to 40 % of the inclusive cross section. For the integrated luminosities above, given the low tagging efficiency, a statistical error of 30% is achievable by decreasing the number of bins.

   Hard physics should be accompanied by a change in the Q^2 dependence, from a leading twist to higher twist effect. The most sensitive probe is given by the measurements of F_L. A model independent determination of F_L requires running at lower energies. The error is determined by the run with lowest luminosity. An error of 25% on $F_L/(F_2 - F_L)$ requires an integrated luminosity of 10 pb^{-1} with the proton beam energy of 500 GeV.

   The t dependence is essential to establish whether the observed tendencies are due to the change from soft to hard physics. This can be done only with the forward/leading proton spectrometers. It is estimated on the basis of existing data that for an integrated luminosity of 40 pb^{-1} in the present running conditions one could expect 20000 events with the proton tagged by the LPS for $4 < Q^2 < 30$ GeV^2). That would allow to establish the lack of shrinkage at the 3σ level and to determine $\alpha_{I\!P}$ with the same precision as in the inclusive case down to $\beta \simeq .001$. To cover the region of $Q^2 > 100$ GeV^2 with the same precision a 10 fold increase in luminosity would be required.

2. To test in depth the dynamics of vector meson production we need to measure the longitudinal cross section as a function of x, Q^2 and t for at least the ρ, ϕ and J/ψ vector mesons. To achieve a precision of $\Delta\alpha_{I\!P} = 0.06$ about 100 events per Q^2 are required. In order to probe the region of $Q^2 > 30$ GeV^2, be it for the ρ meson, an integrated luminosity of 100 pb^{-1} is required. An integrated luminosity of 250 pb^{-1} would allow measurements for the ϕ and J/ψ in the same region with comparable significance. For the latter luminosity also few Υ events are expected in the higher Q^2 region. A meaningful measurement of shrinkage could be performed only for the ρ meson and up to $Q^2 \simeq 30$ GeV^2. Assuming SCHC and 100 events per bin an error of 40 % on R can be achieved. A similar precision without assuming SCHC would require running at lower electron beam energy with at least 10 pb^{-1} integrated luminosity. All the estimates are obtained assuming that proton dissociation can be controlled at a 5% level. A useful cross check could be done with the LPS for low Q^2, ρ production. Here again the ideal measurement would be with a tagged proton in the LPS.

   The large t vector meson production does not require any special environment. For large t diffraction the expected cross sections are relatively large.

3. For diffractive exclusive large p_T jet production the region of interest is that of $M_X^2 \lesssim Q^2$. Since color is well localized in the wave function function of the projectile photon and the hard scale is defined as $p_T^2/(1-\beta)$ relatively low p_T jets (with $p_T \approx$ few GeV) can be considered. A typical integrated cross section for $p_T^2 > 5$ GeV^2, $Q^2 > 10$ GeV^2 and in the range $50 < W < 220$ GeV turns out to be of the order of 20 pb assuming a two perturbative gluon exchange as the dominant mechanism and is about 2.5 times larger than expected from non-perturbative gluons. For an integrated luminosity of 250 pb^{-1} about 2500 events identified in the detectors are expected in the best case. To be able to establish the two gluon exchange mechanism the azimuthal asymmetry has to be measured and in order to exclude an asymmetry typical of boson-gluon fusion whole statistics is necessary.

   Here again not only the $x_{I\!P}$ and Q^2 dependence is of interest but also the t dependence which is the barometer for the hardness of the interaction. However this is beyond the reach of HERA experiments unless the LPS would be operational throughout the whole integrated luminosity.

4. Study of large rapidity gap events in charged current interactions offers many attractive possibilities to study the parameters of the Standard Model. The main advantages are due to the isoscalar nature of the Pomeron and the point-like coupling of the W boson to quarks. One could imagine that by tagging for example $W \to cs$ transition with a large rapidity gap one could measure the V_{cs} element of the Kobayashi-Maskawa mixing matrix without the uncertainty of final state interactions.

   However estimates of the detectable cross section for CC diffractive scattering lead to an number of events of the order of 1/pb^{-1}. This estimate would decrease by factor 2 if the forward taggers in the proton fragmentation region were not available.

5. Two options for measuring the invariant mass of the proton dissociation system have been considered. Assuming high efficiency forward taggers covering the region down to $\eta = 5.9$ the mass distribution can be determined at best with a systematic error of 13%, mainly due to the uncertainty in the hadronization process. This error can be substantially improved by introducing calorimetry and running at lower proton energy. This knowledge is of interest in its own right. It affects all the inclusive diffractive measurements without LPS tagging. In the present estimates this is the major source of systematic error. Tagging of the forward region with high efficiency could decrease this error by factor 3. This is of particular importance if diffractive measurements are to be continued after the HERA upgrade.

The polarization options have not been discussed in depth. The expressed opinions were very much in favor of diffractive measurements with polarized beams. It was felt that it could have an impact on a deeper understanding of the diffractive mechanism.

The emerging scenario is the following:

- The inclusive measurements of the diffractive structure functions could be completed with 100 pb^{-1}. Roughly speaking this would lead to an understanding of hard diffractive physics similar to what was known about the DIS structure of the proton before HERA. An integrated luminosity of 10 pb^{-1} at lower proton energy is highly recommended for model independent measurements of the longitudinal structure functions.

- The program of hard diffractive physics, vector meson and exclusive jet production at high Q^2, could in principle be continued after the HERA upgrade. This will have to be investigated further. However, based on the present understanding, this will not be meaningful unless the tagging of the forward region is preserved and unless there is a good understanding of the systematics acquired before the upgrade. Given the importance of diffractive scattering in understanding QCD we recommend that the design of the upgrade takes into account the need for preserving high efficiency forward tagging.

Acknowledgments

We are indebted to all those who contributed to make this workshop a success, either by participating actively or by expressing their encouraging interest. The list is very long and goes far beyond the list of contributions to this workshop, suffice to say that the mailing list consisted of more than 100 names. Very special thanks go to W. Bartel who kept us informed on the progress made in the accelerator upgrade group.

References

[1] A. Mueller, in *Proceedings of the Conference on Hard Diffractive Scattering* (Eilat, 1996).

[2] V. Gribov, *Sov. Phys. JETP* **8** (1961) 40.

[3] V. Gribov, *Sov. Phys. JETP* **14** (1962) 478.

[4] V. Gribov, *Sov. Phys. JETP* **26** (1968) 414.

[5] L. Caneschi, in *Regge Theory of low p_T hadronic interactions*, edited by L. Caneschi (North-Holland, 1989).

[6] V. Gribov, I. Pomeranchuk, *Sov. Phys. JETP* **4** (1962) 42.

[7] V. Gribov, I. Pomeranchuk, *Phys. Rev. Lett.* **2** (1962) 195.

[8] A. Donnachie, P. Landshoff, *Nucl. Phys. B* **267** (1986) 690.

[9] H. Cheng, J. Walker, T. Wu, *Phys. Lett. B* **44** (1973) 97.

[10] A. Mueller, *Nucl. Phys. B (Proc. Suppl.)* **18C** (1991) 125.

[11] B. Blättel et al., *Phys. Rev. Lett.* **70** (1993) 896.

[12] L. Frankfurt, G. Miller, M. Strikman, *Phys. Lett. B* **304** (1993) 1.

[13] L. Frankfurt, A. Radushkin, M. Strikman, in preparation.

[14] J. Bartels, H. Lotter, M. Wüsthoff, *Z. Phys. C* **68** (1995) 121.

[15] L. Frankfurt, V. Khoze, in *Proceedings of the Leningrad School on Particle Physics* (1975).

[16] Y. Dokshitzer, Materials of this Workshop.

[17] Y. Dokshitzer, in *Proceedings of the Conference on Hard Diffractive Scattering* (Eilat, 1996).

[18] B. Andersson et al., *Phys. Rep.* **97** (1983) 31.

[19] W. Buchmüller, A. Hebecker, *Phys. Lett. B* **355** (1995) 573.

[20] A. Edin, G. Ingelman, J. Rathsman, *Phys. Lett. B* **366** (1996) 371.

[21] A. Edin, G. Ingelman, J. Rathsman, *J. Phys. G* **22** (1996) 943.

[22] A. Edin, G. Ingelman, J. Rathsman, *DESY 96-060*

[23] L. Lönnblad, *J. Phys. G* **22** (1996) 947.

[24] ZEUS Collaboration; M. Derrick et al., *Phys. Lett. B* **369** (1996) 55.

[25] CDF Collaboration; F. Abe et al., *Phys. Rev. Lett.* **74** (1995) 855.

[26] D0 Collaboration; S. Abbachi et al., *Phys. Rev. Lett.* **72** (1994) 2332.

[27] V. Gribov, B. Ioffe, I. Pomeranchuk, *Sov. J. Nucl. Phys.* **2** (1969) 549.

[28] B. Ioffe, *Phys. Lett. B* **30** (1969) 123.

[29] C. Llewellyn-Smith, *Phys. Rev. D* **4** (1971) 2392.

[30] H. Abramowicz, L. Frankfurt, M. Strikman, *DESY 95-047*

[31] J. Bjorken, in *Proceedings of the International Symposium on Electron and Photon Interactions at High Energies* (Cornell, 1971), p. 281.

[32] J. Bjorken, J. Kogut, *Phys. Rev. D* **8** (1973) 1314.

[33] J. Bjorken, in *Proceedings of the Colloqium on High Multiplicity Hadronic Interactions*, edited by A. Krzywicki (Paris, 1994).

[34] V. Gribov, *Sov. Phys. JETP* **10** (1969) 57.

[35] N. Nikolaev, B. Zakharov, *Z. Phys. C* **53** (1992) 331.

[36] A. Solano, contribution to this workshop.

[37] G. Ingelman, P. Schlein, *Phys. Lett. B* **152** (1985) 256.

[38] P. Bruni, G. Ingelman, *DESY 93-187*

[39] H. Jung, *Comp. Phys. Comm.* **86** (1995) 147.

[40] L. Frankfurt, M. Strikman, *Phys. Rep.* **160** (1988) 235.

[41] F. Low, *Phys. Rev. D* **12** (1975) 163.

[42] S. Nussinov, *Phys. Rev. Lett.* **334** (1975) 1286.

[43] J. Gunion, D. Soper, *Phys. Rev. D* **15** (1977) 2617.

[44] V. Gribov, *Yad. Fiz.* **5** (1967) 399.

[45] D. Zeppenfeld, *MADPH-95-933* (1995).

[46] J. Collins, L. Frankfurt, M. Strikman, *Phys. Lett. B* **307** (1993) 161.

[47] J. Bartels, M. Wüsthoff, *J. Phys. G* **22** (1996) 929.

[48] M. Wüsthoff, *DESY 95-166*

[49] A. Donnachie, P. Landshoff, *Phys. Lett. B* **202** (1988) 131.

[50] A. Donnachie, P. Landshoff, *Phys. Lett. B* **296** (1992) 227.

[51] A. Capella et al., *Phys. Lett. B* **37** (1994) 358.

[52] A. Capella, in *Proceedings of the Conference on Hard Diffractive Scattering* (Eilat, 1996).

[53] L. Frankfurt, M. Strikman, *Phys. Rev. Lett.* **64** (1989) 1914.

[54] M. Ryskin, *Z. Phys. C* **57** (1993) 89.

[55] W. Koepf, contribution to this workshop.

[56] J. Bartels, in *Proceedings of the Conference on Hard Diffractive Scattering* (Eilat, 1996).

[57] J. Bartels, H. Lotter, M. Wüsthoff, *Phys. Lett. B* **379** (1996) 239.

[58] E. Levin et al., *DTP/96/50*, hep-ph/9606443.

[59] M. Genovese, N. Nikolaev, B. Zakharov, *Phys. Lett. B* **378** (1996) 347.

[60] S. Catani, F. Fiorani, G. Marchesini, *Phys. Lett. B* **234** (1990) 339.

[61] S. Catani, F. Fiorani, G. Marchesini, *Nucl. Phys. B* **336** (1990) 18.

[62] P. Landshoff, in *Proceedings of the Conference on Hard Diffractive Scattering* (Eilat, 1996).

[63] P. Landshoff, contribution to this workshop.

[64] V. D. Duca, contribution to this workshop.

[65] V.Khoze, Talk at Durham Workshop on HERA physics.(1965).

[66] ZEUS Collaboration; M. Derrick et al., *Z. Phys. C* **69** (1995) 39.

[67] H. Abramowicz, in *Proceedings of the International Conference on High Energy Physics* (Warsaw, 1996), (see references there in).

[68] M. Diehl, Charm versus Light Flavors in Diffraction: Jet Production and the Diffractive Structure Function, Talks at this workshop, 1996.

[69] W. Buchmüller, A. Hebecker, *DESY 95-208, SLAC-PUB-7064*, hep-ph/9512329.

[70] T. Teubner, Diffractive Open Charm Production at HERA, contribution to this workshop.

[71] H. Lotter, PhD thesis (to be published).

[72] H1 Collaboration, A Measurement of the Production of $D^{*\pm}$ Mesons in Deep–Inelastic Diffractive Interactions at HERA, ICHEP 1996, pa02-60, 1996.

[73] J. Bartels et al., *DESY 96-085*, hep-ph/9605356.

[74] M. Diehl, Azimuthal Angles and Photon Helicity, Talk at proc96, 1996.

[75] T. Arens et al., *HD-THEP-96-06*

[76] W. Buchmüller, A. Hebecker, M. F. McDermott, *DESY 96-126, SLAC-PUB-7204*, hep-ph/9607290.

[77] J. Collins, L. Frankfurt, M. Strikman, in preparation (unpublished).

[78] A. V. Radyushkin, *hep-ph* (1996).

[79] S. Brodsky et al., *Phys. Rev. D* **50** (1994) 3134.

[80] E. Gotsman, E. Levin, U. Maor, *CNBPF-NF-021/96, TAUP 2333896/96*, hep - ph 9606280.

[81] H. Dosch et al., *HD-THEP-96-31* (1996).

[82] L. Frankfurt, G. Miller, M. Strikman, *Ann. Rev. Nucl. Part. Sci.* **44** (1994) 501.

[83] E665 Collaboration; M. Adams et al., *Phys. Rev. Lett.* **74** (1995) 1525.

[84] J. Bjorken, *Int. J. Mod. Phys. A* **7** (1992) 4189.

[85] E. Gotsman, E. Levin, U. Maor, *Phys. Lett. B* **309** (1993) 199.

[86] L. Frankfurt, M. Strikman, contribution to Working Group: Light and Heavy Nuclei in HERA, this workshop.

[87] A. Mueller, W. Tang, *Phys. Lett. B* **284** (1992) 123.

[88] L. Frankfurt, Hard diffractive processes at colliders, in *Proceedings of the FAD meeting* (Dallas, 1992).

[89] J. Bjorken, *Phys. Rev. D* **47** (1993) 101.

[90] M. Strikman, This Workshop.

[91] H1 Collaboration, Elastic ρ' Electroproduction at High Q^2, ICHEP96, pa01-088.

[92] H1 Collaboration; S. Aid et al., *Nucl. Phys. B* **468** (1996) 3.

[93] ZEUS Collaboration, ICHEP96, pa02-028.

[94] S. Brodsky, in materials of the working group (unpublished).

[95] H1 Collaboration; T. Ahmed et al., *Nucl. Phys. B* **249** (1994) 477.

[96] ZEUS Collaboration; M. Derrick et al., *Phys. Lett. B* **315** (1993) 481.

[97] ZEUS Collaboration; M. Derrick et al., *Z. Phys. C* **68** (1995) 569.

[98] M. Glück, E. Reya, A. Vogt, *Z. Phys. C* **53** (1992) 127.

[99] J. Bartels et al., Quark - Antiquark Jets in DIS Diffractive Dissociation, in *this workshop* (Hamburg, 1996).

[100] M. Grothe et al., Studies of Diffractive Dijet Production in DIS, contribution to this workshop.

[101] M. Ryskin, M. Besancon, Heavy Photon Dissociation in Deep Inelastic Scattering, in *Proceedings of the workshop Physics at HERA*, edited by W. Buchmüller, G. Ingelman (Hamburg, 1991).

[102] E. M. Levin, M. Wüsthoff, *Phys. Rev. D* **50** (1994) 4306.

[103] H1 Collaboration, A Measurement and QCD Analysis of the Diffractive Structure Function $F_2^{D(3)}$, ICHEP 1996, pa02-61, 1996.

[104] J. Phillips, A. Mehta, B. Waugh, Future Diffractive Structure Function Measurements at HERA, in *this workshop* (Hamburg, 1996).

[105] W. Koepf et al., Vector Meson Production in $ep \to epV$, in *this workshop* (Hamburg, 1996).

[106] J. Forshaw, M. Ryskin, *Z. Phys. C* **68** (1995) 137.

[107] J. Bartels et al., *Phys. Lett. B* **375** (1996) 301.

[108] H. Abramowicz et al., Future Aspects of Vector Meson Production at HERA, in *this workshop* (Hamburg, 1996).

[109] E. Laenen, E. Levin, *Ann. Rev. Nucl. Part. Sci.* **44** (1994) 199.

[110] M. Diehl, *Z. Phys. C* **66** (1995) 181.

[111] E. Gallo et al., Measurements with the Leading Proton Spectrometer, in *this workshop* (Hamburg, 1996).

[112] E. Edin, G. Ingelman, J. Rathsman, QCD in the Forward Region, in *this workshop* (Hamburg, 1996).

[113] S. Brodsky, W. Tang, P. Hoyer, *Phys. Rev. D* **52** (1995) 6285.

[114] H. Abramowicz et al., Proton Diffractive Dissociation at HERA. Studying Proton Dissociation using Forward Taggers or Calorimeters, in *this workshop* (Hamburg, 1996).

[115] A. Bamberger et al., Diffractive and Jet Physics with a Forward PLUG Calorimeter at ZEUS, in *this workshop* (Hamburg, 1996).

[116] W. Bartel, HERA Machine Upgrade, in *this workshop* (Hamburg, 1996).

[117] J. Pliszka, A. Zarnecki, Diffraction in Charged Current DIS, in *this workshop* (Hamburg, 1996).

[118] L. Gribov, E. Levin, M. Ryskin, *Phys. Rep.* **100** (1983) 1.

[119] V. Abramovsky, V. Gribov, O. Kanchely, *Sov. J. Nucl. Phys.* **18** (1973) 388.

[120] E. Gotsman, E. Levin, U. Maor, *Nucl. Phys. B* **464** (1996) 251.

[121] A. Mueller, G. Salam, *CU-TP-746*

[122] H. Cheng, T. Wu, *Expanding Protons: Scattering at High Energy* (MIT-Pr, 1987).

Quark-Antiquark Jets in DIS Diffractive Dissociation

J. Bartels*, C. Ewerz*, H. Lotter*
M. Wüsthoff†
M. Diehl‡

*II. Institut für Theoretische Physik, Universität Hamburg,
Luruper Chaussee 149, D-22761 Hamburg, FRG
†High Energy Physics Division, Argonne National Laboratory,
Argonne, USA
‡Department of Applied Mathematics and Theoretical Physics,
University of Cambridge, Cambridge CB3 9EW, England

Abstract: We report on investigations concerning the production of large transverse momentum jets in DIS diffractive dissociation. These processes constitute a new class of events that allow for a clean test of perturbative QCD and of the hard (perturbative) pomeron picture. The measurement of the corresponding cross sections might possibly serve to determine the gluon density of the proton.

1 Introduction

The subject of this report is the production of jets with large transverse momenta in diffractive deep inelastic scattering. We will concentrate on events with two jets in the final state, i. e. events with a quark- and an antiquark jet. Due to the high photon virtuality Q^2 and the large transverse momenta of the jets we can use perturbative QCD to describe this process. From a theoretical point of view, diffractive jet production should allow an even better test of pQCD than diffractive vector meson production since it does not involve the uncertainties connected with the wave function of the meson.

After defining the kinematic variables we will present in some detail the main results of our analysis that was performed for the production of light quark jets. A more extensive account of these results can be found in [1, 2]. Related and in part similar work on quark–antiquark jet production has been reported in [3, 4]. We will close this report with a comment on open charm production.

2 Kinematics

We assume the total energy s to be much larger than the photon virtuality $Q^2 = -q^2$ and much larger than the squared invariant mass $M^2 = (q + x_{I\!P} p)^2$ of the jet pair. We constrain our analysis to events with a rapidity gap and we require the momentum fraction $x_{I\!P}$ of the

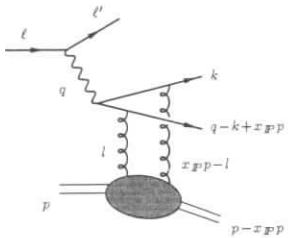

Figure 1: *One of the four diagrams contributing to the hard scattering* $\gamma^* + p \to q\bar{q} + p$. *The outgoing (anti)quark momenta are held fixed.*

proton's momentum carried by the pomeron to be small, $x_{I\!P} \ll 1$. $x_{I\!P}$ can be expressed as $x_{I\!P} = (M^2 + Q^2)/(W^2 + Q^2)$ where W is the invariant mass of the final state (including the outgoing proton). We keep the transverse momentum $\mathbf{k}$ of the jets fixed with $\mathbf{k}^2 \geq 1\,\mathrm{GeV}^2$. It will be convenient to use also $\beta = x_B/x_{I\!P} = Q^2/(M^2 + Q^2)$. The momentum transfer t is taken to be zero because the cross section strongly peaks at this point. An appropriate t–dependence taken from the elastic proton form factor is put in later by hand.

For large energy s (small $x_{I\!P}$) the amplitude is dominated by perturbative two gluon exchange as indicated in fig. 1, where the kinematic variables are illustrated. In fig. 2 we define the angle ϕ between the electron scattering plane and the direction of the quark jet pointing in the proton hemisphere (jet 1 in the figure). The angle ϕ is defined in the γ^*–$I\!P$ center of mass system and runs from 0 to 2π.

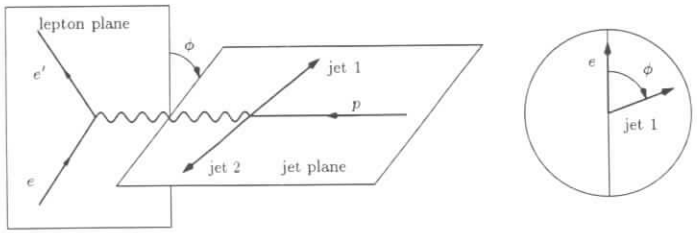

Figure 2: *Definition of the azimuthal angle* ϕ *in the* γ^*–$I\!P$ *CMS*

3 Results

In the double logarithmic approximation (DLA), the amplitude of the process can be expressed in terms of the gluon structure function. The cross section is therefore proportional to the square of the gluon structure function. The momentum scale of the latter can be calculated. We thus find as one of our main results

$$d\sigma \sim \left[x_{I\!P} G_p \left(x_{I\!P}, \mathbf{k}^2 \frac{Q^2 + M^2}{M^2} \right) \right]^2 . \tag{1}$$

Performing our numerical estimates, however, we include some of the next–to–leading corrections (proportional to the momentum derivative of the gluon structure function) which we expect to be the numerically most important ones.

From (1) one can deduce that, in our model, Regge factorization à la Ingelman and Schlein [5] is not valid, i. e. the cross section can *not* be written as a $x_{I\!P}$–dependent flux factor times a β– and Q^2–dependent function.

In the following we present only the contribution of transversely polarized photons to the cross section. The corresponding plots for longitudinal polarization can be found in [1, 2]. As a rule of thumb, the longitudinal contribution is smaller by a factor of ten. Only in the region of large β it becomes comparable in size.

Figure 3 shows the $x_{I\!P}$–dependence of the cross section for $Q^2 = 50\,\mathrm{GeV}^2$, $\beta = 2/3$ and $\mathbf{k}^2 > 2\,\mathrm{GeV}^2$. We use GRV next–to–leading order parton distribution functions [6]. Our prediction is compared with the cross section obtained in the soft pomeron model of Landshoff and Nachtmann [7, 8] with nonperturbative two–gluon exchange. Its flat $x_{I\!P}$–dependence, characteristic of the soft pomeron, is quite in contrast to our prediction.

Further, we have included (indicated by *hybrid*) a prediction obtained in the framework of the model by M. Wüsthoff [9]. This model introduces a parametrization of the pomeron based on a fit to small x_B data for the proton structure function F_2. In this fit, the pomeron intercept is made scale dependent in order to account for the transition from soft to hard regions. The $x_{I\!P}$–dependence is not quite as steep as ours but comparable in size.

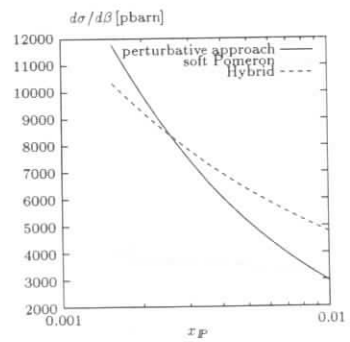

Figure 3: $x_{I\!P}$*–spectrum*

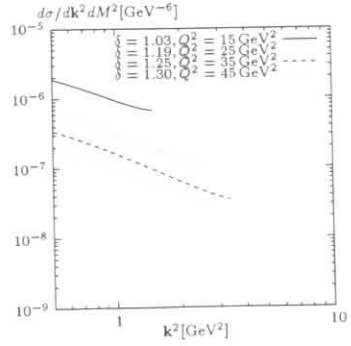

Figure 4: $\mathbf{k}^2$*–spectrum*

Figure 4 presents the $\mathbf{k}^2$–spectrum for different values of Q^2 between $15\,\mathrm{GeV}^2$ and $45\,\mathrm{GeV}^2$. Here we have chosen $x_{I\!P} = 5 \cdot 10^{-3}$ and $\beta = 2/3$. The quantity δ given with each Q^2 value

describes the effective slope of the curves as obtained from a numerical fit of a power behaviour $\sim (\mathbf{k}^2)^{-\delta}$. We have taken $\mathbf{k}^2$ down to 0.5 GeV^2. For $\beta = 2/3$ the effective momentum scale of the gluon structure function in (1) equals $\mathbf{k}^2/(1-\beta) = 1.5$ GeV^2.

Integrating the cross section for different minimal values of $\mathbf{k}^2$ we find that the total cross section is dominated by the region of small $\mathbf{k}^2$. If we choose, for instance, $x_{I\!P} < 0.01$, $10\,\mathrm{GeV}^2 \leq Q^2$ and $50\,\mathrm{GeV} \leq W \leq 220\,\mathrm{GeV}$, the total cross section is

$$\begin{aligned} \sigma_{\mathrm{tot}} &= 20\,\mathrm{pb} \quad \text{for } \mathbf{k}^2 \geq 5\,\mathrm{GeV}^2 \\ \sigma_{\mathrm{tot}} &= 117\,\mathrm{pb} \quad \text{for } \mathbf{k}^2 \geq 2\,\mathrm{GeV}^2 . \end{aligned}$$

In the hybrid model of [9] the corresponding numbers are

$$\begin{aligned} \sigma_{\mathrm{tot}} &= 28\,\mathrm{pb} \quad \text{for } \mathbf{k}^2 \geq 5\,\mathrm{GeV}^2 \\ \sigma_{\mathrm{tot}} &= 108\,\mathrm{pb} \quad \text{for } \mathbf{k}^2 \geq 2\,\mathrm{GeV}^2 . \end{aligned}$$

In accordance with fig. 4 these number show that the cross section is strongly suppressed with $\mathbf{k}^2$. We are thus observing a higher twist effect here. For comparison, we quote the numbers which are obtained in the soft pomeron model [7]. With the same cuts the total cross section is

$$\begin{aligned} \sigma_{\mathrm{tot}} &= 10.5\,\mathrm{pb} \quad \text{for } \mathbf{k}^2 \geq 5\,\mathrm{GeV}^2 \\ \sigma_{\mathrm{tot}} &= 64\,\mathrm{pb} \quad \text{for } \mathbf{k}^2 \geq 2\,\mathrm{GeV}^2 . \end{aligned}$$

The β–spectrum of the cross section is shown in fig. 5 for three different values of Q^2. Here we have chosen $x_{I\!P} = 5 \cdot 10^{-3}$ and $\mathbf{k}^2 > 2\,\mathrm{GeV}^2$. The curves exhibit maxima which, for not too large Q^2, are located well below $\beta = 0.5$. For small β we expect the production of an extra gluon to become important. First studies in this direction have been reported in [9, 10] and in [11], but a complete calculation has not been done yet.

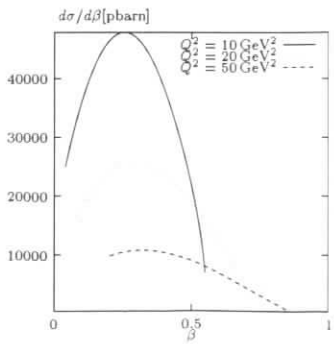

Figure 5: *β–spectrum*

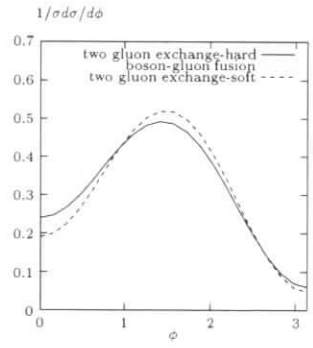

Figure 6: *Azimuthal angular distribution*

The most striking observation made in [2] concerns the azimuthal angular distribution, i. e. the ϕ–distribution of the jets. It turns out that the jets prefer a plane *perpendicular* to the electron scattering plane. This behaviour comes as a surprise because in a boson gluon fusion process the jets appear dominantly *in* the electron scattering plane [12]. The azimuthal angular distribution therefore provides a clear signal for the two gluon nature of the exchanged pomeron. This is supported by the fact that a very similar azimuthal distribution is obtained in the soft pomeron model by M. Diehl [7, 13]. Figure 6 shows the ϕ–dependence of the ep–cross section for the hard pomeron model, the soft pomeron model and for a boson gluon fusion process. We have normalized the cross section to unit integral to concentrate on the angular dependence. Thus a measurement of the azimuthal asymmetry of quark–antiquark jets will clearly improve our understanding of diffractive processes.

Finally, we would like to mention the interesting issue of diffractive open charm production. It is in principle straightforward to extend our calculation to nonvanishing quark masses [14]. A similar computation was done in [15]. A more ambitious calculation has been performed in [16] where also higher order correction have been estimated. The cross section for open charm production is again proportional to the square of the gluon density, the relevant scale of which is now modified by the charm quark mass

$$d\sigma \sim \left[x_{I\!P} G_p \left(x_{I\!P}, (m_c^2 + \mathbf{k}^2)\, \frac{Q^2 + M^2}{M^2} \right) \right]^2 . \tag{2}$$

Integrating the phase space with the same cuts as above the charm contribution to the jet cross section is found to be [14]

$$\begin{aligned} \sigma_{\mathrm{tot}} &= 8\,\mathrm{pb} \quad \text{for } \mathbf{k}^2 \geq 5\,\mathrm{GeV}^2 \\ \sigma_{\mathrm{tot}} &= 29\,\mathrm{pb} \quad \text{for } \mathbf{k}^2 \geq 2\,\mathrm{GeV}^2 . \end{aligned}$$

In the case of open charm production one can even integrate down to $\mathbf{k}^2 = 0$ since the charm quark mass sets the hard scale. One then finds for the $c\bar{c}$ contribution to the total diffractive cross section

$$\sigma_{\mathrm{tot}} = 101\,\mathrm{pb} \quad \text{for } \mathbf{k}^2 \geq 0\,\mathrm{GeV}^2 .$$

In the soft pomeron model the corresponding numbers read [7]

$$\begin{aligned} \sigma_{\mathrm{tot}} &= 4.8\,\mathrm{pb} \quad \text{for } \mathbf{k}^2 \geq 5\,\mathrm{GeV}^2 \\ \sigma_{\mathrm{tot}} &= 17\,\mathrm{pb} \quad \text{for } \mathbf{k}^2 \geq 2\,\mathrm{GeV}^2 \\ \sigma_{\mathrm{tot}} &= 59\,\mathrm{pb} \quad \text{for } \mathbf{k}^2 \geq 0\,\mathrm{GeV}^2 . \end{aligned}$$

In [16], where corrections from gluon radiation are taken into account, the relative charm contribution to the diffractive structure function is estimated to be of the order of 25–30%.

4 Summary and Outlook

We have presented perturbative QCD calculations for the production of quark–antiquark jets in DIS diffractive dissociation. The results are parameter free predictions of the corresponding cross sections, available for light quark jets as well as for open charm production. The cross

sections are proportional to the square of the gluon density and the relevant momentum scale of the gluon density has been determined. The azimuthal angular distribution of the light quark jets can serve as a clean signal for the two–gluon nature of the pomeron in hard processes.

The two–jet final state is only the simplest case of jet production in diffractive deep inelastic scattering. The next steps should be the inclusion of order–α_s corrections and the extension to processes with additional gluon jets. Such processes become dominant in the large–M^2 region.

References

[1] J. Bartels, H. Lotter, M. Wüsthoff, *Phys. Lett.* **B 379** (1996), 239

[2] J. Bartels, C. Ewerz, H. Lotter, M. Wüsthoff, *Phys. Lett.* **B** (in press), preprint DESY 96-085, hep-ph 9605356

[3] M. G. Ryskin, M. Besancon, Proceedings of the HERA workshop 'Physics at HERA', Vol. 1 (W. Buchmüller and G. Ingelman, eds.), Hamburg 1991

[4] N. N. Nikolaev, B. G. Zakharov, *Phys. Lett.* **B 332** (1994), 177;
M. Genovese, N. N. Nikolaev, B. G. Zakharov, *Phys. Lett.* **B 380** (1996), 213

[5] G. Ingelman, P. E. Schlein, *Phys. Lett.* **B 152** (1985), 256

[6] M. Glück, E. Reya, A. Vogt, *Z. Phys.* **C 67** (1995), 433

[7] M. Diehl, *Z. Phys.* **C 66** (1995), 181; and PhD thesis, Cambridge 1996, in preparation

[8] P. V. Landshoff, O. Nachtmann, *Z. Phys* **C 35** (1987), 405;
A. Donnachie, P. V. Landshoff, *Nucl. Phys.* **B 311** (1988/89), 509

[9] M. Wüsthoff, PhD thesis, Hamburg 1995, DESY preprint DESY 95-166;
J. Bartels, M. Wüsthoff, *J. Phys. G: Nucl. Part. Phys.* **22** (1996), 929

[10] E. M. Levin, M. Wüsthoff, *Phys. Rev.* **D 50** (1994), 4306.

[11] E. Gotsman, E. Levin, U. Maor, CBPF-NF-021/96, TAUP-233896/96, hep-ph 9606280

[12] H. Georgi, J. Sheiman, *Phys. Rev.* **D 20** (1979), 433;
Ch. Rumpf, G. Kramer, *Phys. Lett.* **B 89** (1980), 380;
Ch. Rumpf, G. Kramer, J. Willrodt, *Z. Phys.* **C 7** (1981), 327

[13] M. Diehl, in preparation;
T. Arens, O. Nachtmann, M. Diehl, P. V. Landshoff, HD-THEP-96-06, hep-ph 9605376

[14] H. Lotter, PhD thesis, Hamburg 1996, in preparation

[15] M. Genovese, N. N. Nikolaev, B. G. Zakharov, *Phys. Lett.* **B 378** (1996), 347

[16] E. M. Levin, A. D. Martin, M. G. Ryskin, T. Teubner, Durham DTP/96/50, hep-ph 9606443

Vector Meson production in $ep \to epV$

W. Koepf[a], P. V. Landshoff[b], E. M. Levin[c,d], N. N. Nikolaev[e,f]

[a] Department of Physics, Ohio State University, Columbus, OH 43210, USA
[b] DAMPT, University of Cambridge, Cambridge CB3 9EW, UK
[c] Physics Division, Argonne National Laboratory, Argonne, IL60439, USA
[d] Theory Department, Petersburg Nuclear Physics Institute, 188350 Gatchina St. Petersburg, Russia
[e] ITKP, Universität Bonn, Nußallee 14-16, Bonn D-53115, FRG
[f] L.D.Landau Inst. Theor. Physics, Kosygina 2, 117334 Moscow, Russia

Abstract: The diffractive production of vector mesons in ep interactions at low x is a subject of heated debates. This chapter consists of four contributions written by the original authors and expresses the possible scenarios which are to be investigated experimentally.

1 Hard diffractive vector meson production

contributed by **L. Frankfurt, W. Koepf and M. Strikman**

The derivation of our QCD formulas [1] consists of three essential steps:
(i) The process factorizes into three stages: the creation of a quark-gluon wave packet, the interaction of this packet with the target, and the formation of the vector meson. The wave packet's large coherence length, $\frac{1}{2m_N x}$, justifies using completeness over the intermediate states.
(ii) For longitudinal polarization, the end point contribution is suppressed by $1/Q^2$, which supports applying the factorization theorem. This important result follows from the well known light-cone wave function of a photon and conformal symmetry of PQCD, which dictates the dependence of the vector meson's asymptotic wave function on the momentum fraction carried by the quarks. For transverse polarizations, the onset of the hard regime is expected at much larger Q^2 since large distance effects are suppressed only by the square of a Sudakov type form factor, $exp(-\frac{4\alpha_s}{3\pi}\ln^2\frac{Q^2}{k_t^2})$.
(iii) As a result of the QCD factorization theorem, the hard amplitude factorizes from the softer blob [2]. Thus, within the leading $\alpha_s \ln Q^2$ approximation, the cross section of hard diffractive processes can be written in terms of the distribution of bare quarks within the vector meson and the gluon distribution in the target.

The respective cross section can thus be expressed through the light-cone wave function of the vector meson, $\psi_V(z, b = 0)$, a well defined and intensively researched object in QCD. In addition, there is not much freedom in the choice of this wave function since the absolute normalization of the cross section is related to the vector meson's leptonic decay width, $\Gamma_{V\to e^+e^-}$. Our numerical analysis has found a number of distinctive features of these hard diffractive processes (see Ref.[3] and references therein):

1. A significant probability of small transverse size ($b_{q\bar{q}} \approx 3/Q$) minimal Fock $q\bar{q}$ configurations within the vector meson's light-cone wave function.

2. A fast increase of the cross section at small x and a relatively slow Q^2 dependence, both resulting from the Q^2 evolution of the parton distributions.

3. To avoid contradiction with b-space unitarity, the increase of the cross section with decreasing x should slow down. For $Q^2 \sim 5$ GeV^2, this is expected at $x \sim 10^{-3}$ [3].

4. For longitudinal polarization, an almost flavor and energy independent t-slope, while for transverse polarizations, soft QCD may reveal itself in a larger value as well as an energy dependence of the latter.

5. At large Q^2, the diffractive electroproduction ratio of ρ and ϕ mesons follows from the form of the e.m. current in the standard model, i.e. restoration of $SU(3)$ symmetry. Some enhancement of the relative yield of the ϕ meson is expected due to its smaller size.

6. The diffractive photoproduction of J/ψ meson is dominated by relativistic $c\bar{c}$ configurations. Significant diffractive photoproduction of Υ mesons.

7. Large cross sections for the production of excited states, $ep \to epV'$, with a ratio proportional to $M_{V'}\,\Gamma_{V' \to e^+e^-}$, in qualitative difference from photoproduction processes.

8. Model estimates found large $1/Q^2$ corrections to the basic formulas resulting from quark Fermi motion within the vector meson and from shadowing effects evaluated within the eikonal approximation. However, the reliability of these estimates is still unclear since similar corrections follow from the admixture of $q\bar{q}g$ components to the vector meson's wave function and because the elastic eikonal approximation is inappropriate. Note that, in an exact calculation, the contribution of more than two rescatterings by the $q\bar{q}$ pair should be zero due to energy-momentum conservation.

2 γ^* p $\to$ V p at small t

contributed by **P. V. Landshoff**

All models [4, 5, 6, 7, 8, 9] couple the γ^* to the vector meson V through a simple quark loop, to which is attached a pair of gluons which interact with the proton. The models differ in two essentials: what they assume about the wave function that couples V to the $q\bar{q}$, and what they assume about how the gluons interact with the proton.

Because the models have the same quark loop, there is general agreement that the γ^* and the V should have the same helicity, and that

$$\frac{\sigma_L}{\sigma_T} \propto \frac{Q^2}{m_V^2} \qquad (1)$$

so that at large Q^2 longitudinal production dominates. Presumably the detailed dependence of σ_L/σ_T on Q^2 is sensitive to the form of the wave function. The very simple form assumed by DL fits the data reasonably well [10], but more theoretical work is needed to decide just how much can be learnt about the wave function from this. Also, according to (1), for heavier flavours it will need a larger Q^2 to achieve dominance of the longitudinal polarisation; it is likely that most of the J/ψ production at HERA will be transverse.

The way in which the gluons couple to the proton will determine the W-dependence. If they couple through a soft pomeron, then

$$\frac{d\sigma}{dt} = f(t, Q^2)\, e^{4(\epsilon - \alpha'|t|)\log W} \qquad (2)$$

with $\epsilon \approx 0.08$ and $\alpha' = 0.25$ GeV^{-2}. If the data find a larger value of ϵ, this may be a sign of the BFKL pomeron (though this is unlikely [11]), or of whatever other mechanism is responsible for the rapid rise seen in νW_2 at small x. Some of the models seek to make a direct connection between the energy dependence of exclusive vector electroproduction and the rise of νW_2 at small x, but there are theoretical problems in this. The soft-pomeron form (2) predicts that the t-slope changes with W in a particular way; if the soft pomeron is not involved the forward-peak shrinkage will surely not ocurr at the same rate and is likely to be significantly slower, though this is not understood. Notice that $f(t, Q^2)$ contains the square of the elastic form factor of the proton and so is not a simple exponential: the t-slope will vary with t. Notice also that its measurement is particularly sensitive to any contamination from nonelastic events, which become increasingly important as $|t|$ increases.

3 Shadowing corrections in diffractive QCD leptoproduction of vector mesons

contributed by **E.Gotsman, E. Levin and U. Maor**

In our paper [12] the formulae for the shadowing corrections (SC) for vector meson diffractive dissociation (DD) in DIS have been obtained within the framework of the DGLAP evolution equation in the region of low x. It is shown that the rescatterings of the quarks is concentrated at small distances ($r_\perp^2 \propto \frac{1}{Q^2 z(1-z)+m_q^2}$) and can be treated theoretically on the basis of perturbative QCD.

The numerical calculation of the damping factor defined as:

$$D^2 = \frac{\frac{d\sigma(\gamma^* p \to Vp)}{dt}[\,with\ SC\,]}{\frac{d\sigma(\gamma^* p \to Vp)}{dt}[\,without\ SC\,]}\Big|_{t=0} \qquad (1)$$

shows that the SC (i) should be taken into account even at HERA kinematic region and they generate the damping factor of the order of 0.5 for J/Ψ production at $W = 100 - 200GeV$ for $Q^2 = 0 - 6GeV^2$ (see [12] for details); (ii) t he value of the SC is bigger than uncertainties related to the unknown nonperturbative part of our calculations, and (iii) DD in vector meson for DIS can be used as a laboratory for investigation of the SC.

The calculation of the SC for the gluon structure function depends on a wide range of distances including large ones ($r_\perp^2 > \frac{1}{Q^2 z(1-z)+m_q^2}$). This causes a large uncertainty in the pQCD calculations which, however become smaller at low x. We show that the gluon shadowing generates damping, which is smaller or compatible with the damping found in quark sector.

The cross section of the vector meson DD is shown to be proportional to $(\frac{dF_2^{exp}}{d\ln Q^2})^2$ [12]. This formula takes into account all possible SC and it is derived in the leading log approximation of pQCD (for the GLAP evolution). It means that the experimental data for DD for vector meson production provides information about $dF_2/\ln Q^2$, from which we could extract the gluon structure function in the DGLAP evolution equation in the region of low x.

4 Vector mesons

contributed by **N. N. Nikolaev and B. G. Zakharov**

The amplitude of exclusive vector meson production [14, 15, 16, 17, 18] reads (we suppress the polarization subscripts T and L) $\mathcal{M} = \int d^2\vec{r}dz\Psi_V^*(z,\vec{r})\sigma(x,r)\Psi_{\gamma^*}(z,\vec{r})$, where Ψ_{V,γ^*} are the color dipole distribution amplitudes and $\sigma(x,r)$ is the color dipole cross section. On top of the gBFKL component which dominates $\sigma(x,r)$ at $r \lesssim R_c = 0.3\,\mathrm{fm}$, at larger r in $\sigma(x,r)$ there is a soft component. The non-negotiable prediction as that at a sufficiently small x the rising gBFKL component takes over at all r. The small but rising gBFKL contribution provides a viable description of the rise of soft cross sections. $\mathcal{M}_{T,L}$ are dominated by $r \approx r_S = 6/\sqrt{Q^2+m_V^2}$. The large value of the scanning radius r_S is non-negotiable and makes vector meson production at best semiperturbative, unless $Q^2 + m_V^2 \gtrsim$20-40 GeV^2, i.e., unless $r_S \lesssim R_c$. Because the scanning radius r_S is so large, the formulas for the production amplitudes in terms of the vector wave function at the origin are of limited applicability at the presently studied Q^2. When $r_S \lesssim R_c$ and the soft contribution is small, one can relate $\mathcal{M}_{T,L}$ to the gluon density in the proton but at a very low factorization scale $q_{T,L}^2 = \tau(Q^2+m_V^2)$ with τ =0.05-0.2 depending on the vector meson. The energy dependence of vector meson production at $r_S \sim 0.15\,\mathrm{fm}$, i.e., $Q^2(\Upsilon) \sim 0$ and $Q^2(J/\Psi) \sim 100\,\mathrm{GeV}^2$ and $Q^2(\rho) \sim 200\,\mathrm{GeV}^2$ probes the asymptotic intercept of the gBFKL pomeron. The major gBKL predictions are:

1. A steady decrease of R_{LT} with Q^2 in $\sigma_L/\sigma_T = R_{LT}Q^2/m_V^2$ with $R_{LT} \sim 1$.

2. When fitted to $W^{4\Delta}$, the effective intercept Δ is predicted to rise with Q^2. It also rises with W and flattens at a Q^2 independent $\Delta \approx 0.4$ at a very large W. The universal energy dependence is predicted for all vector mesons if one compares cross sections at identical $\bar{Q}^2$.

3. Comparing the Q^2 dependence of $\mathcal{M}_{T,L}$ makes no sence, the real parameter is r_S and/or $\bar{Q}^2 = Q^2 + m_V^2$, the ratios like $(J/\Psi)/\rho$ exhibit wild Q^2 dependence but we predict the flavor dependence disappears and these ratios are essentially flat vs.$\bar{Q}^2$. The Q^2 dependence must follow the law $\propto \bar{Q}^{2n}$, where n is about flavor independent, typically $n \sim 2.2$ at HERA. The $\propto \bar{Q}^{2n}$ fits are strongly recommended.

4. Strong suppression of the $2S/1S$ cross section ratios by the node effect is a non-negotiable prediction, these ratios are predicted to rise steeply and then level off on a scale $Q^2 \lesssim m_V^2$. Steady rise of these ratios with energy is predicted. For the D-wave vector mesons the ratio $D/1S$ is pedicted to have a weak Q^2 dependence in contrast to the $2S/1S$ ratio.

5. The gBFKL pomeron is a moving singularity and we predict the conventional Regge shrinkage of the diffraction cone. The rise of diffraction slope by ~ 1.5 GeV^{-2}, which is about universal for all vector mesons and at all Q^2, is predicted to take place from the CERN/FNAL to HERA energies. An inequality of diffraction slopes $B(2S) < B(1S)$ is predited. For the $\rho'(2S)$ and $\phi'(2S)$ the diffraction cone can have a dip and/or flattening at $t = 0$. For the 1S states, the diffraction cone for different vector mesons must be equal if compared at the same $\bar{Q}^2$.

References

[1] S. J. Brodsky, L. Frankfurt, J. F. Gunion, A. H. Mueller and M. Strikman, *Phys. Rev.* D **50** (1994) 3134

[2] J. C. Collins, L. L. Frankfurt and M. Strikman, *Phys. Lett.* **B307** (1993) 161

[3] L. Frankfurt, W. Koepf and M. Strikman, *Phys. Rev.* D **54** (1996) 3194

[4] A. Donnachie and P. Landshoff, *Phys. Lett.* **B185** (1987) 403

[5] A. Donnachie and P. Landshoff, *Nucl. Phys.* **B 311** (1989) 509

[6] J. R. Cudell, *Nucl. Phys.* **B 336** (1990) 1

[7] J. M. Laget and R. Mendez-Galain, *Nucl. Phys.* **A 581** (1995) 397

[8] I. F. Ginzburg and D. Yu. Ivanov, hep-ph/9604437

[9] H. G. Dosh, T. Gousset, G. Kulzinger and H. J. Pirner, hep-ph/9608203

[10] A. Donnachie and P. Landshoff, *Phys. Lett.* **B348** (1995) 213

[11] J. R. Cudel, A. Donnachie and P. Landshoff, hep-ph/9602284

[12] E. Gotsman, E. Levin and U. Maor: *Nucl. Phys.* **B 464** (1996) 251

[13] M.G. Ryskin, R.G. Roberts, A.D. Martin and E. M. Levin, *DTP-95-96*, hep-ph/9511228

[14] B. Z. Kopeliovich et al., *Phys. Lett.* **B309** (1993) 179

[15] B. Z. Kopeliovich et al., *Phys. Lett.* **B234** (1994) 469

[16] J. Nemchik et al., *Phys. Lett.* **B339** (1994) 194

[17] J. Nemchik et al., *Phys. Lett.* **B374** (1996) 199, hep-ph/9605231

[18] N. Nikolaev et al., *Phys. Lett.* **B366** (1996) 337

Future aspects of Vector Meson production at HERA

H. Abramowicz[a], T. Doeker[a1], L. Iannotti[b], S. Kananov[a], A. Levy[a] and L. West[c]

[a] School of Physics and Astronomy, Raymond and Beverly Sackler Faculty of Exact Sciences, Tel Aviv University
[b] Physics Department, Calabria University
[c] School of Physics, University of Birmingham

Abstract: The analysis of exclusively produced vector mesons in deep inelastic scattering offers the opportunity for detailed tests of QCD predictions. This report gives an overview of the expected rates for vector meson production and investigates the accuracy which can be achieved with an increase in statistics and a better understanding of the existing detector components of the H1 and ZEUS experiments. Requirements for the HERA luminosity and detector upgrades are described for several vector meson related measurements.

1 Introduction

The study of the exclusive production of vector mesons provides important information on the hadronic structure of the photon and the nature of diffraction. The simplicity of the final state makes this process attractive for almost parameter-free QCD calculations. Several recent QCD based approaches are available to predict the cross section for exclusive vector meson production [1, 2, 3, 4]. These calculations require the presence of a hard scale to be applicable. In addition phenomenological models also give estimates for this process [5]. The comparison of the HERA data with these estimates will help to test those models and to determine the kinematic range in which they are reliable.

The aim of this report is to determine which of the theoretical predictions can be tested by experiment (and in which kinematic range), which accuracy is needed to distinguish between different models and what are the demands for the HERA machine and experiments to perform such measurements. The focus of this work is on the vector meson production at high Q^2 or t.

Throughout this paper we assume that the central detectors of the H1 and the ZEUS experiments are available in their present setup and that the ongoing improvement of the detector understanding will allow to use the full tracking systems of the two experiments. The *forward* components of the detectors are of special interest for the estimate of the proton dissociation contribution to the cross section. The limits to the measurements due to the layout of these components are investigated.

This article is organized as follows: Chapter 2 gives an introduction to the kinematic variables and a brief overview of some QCD models for elastic vector meson production. Based on these models, estimates for the rates of exclusively produced vector mesons are given. Chapter 3 describes the detector setup, the expected acceptance in the kinematic range and the expected systematic uncertainties of the measurements. In Chapter 4 the accuracy of future measurements is evaluated. Chapter 5 summarizes the requirements for HERA.

[1]Supported by MINERVA

2 Cross section estimates

2.1 Vector meson production at large Q^2

In this section some general aspects of elastic vector meson electro-production,

$$e(k) + p(P) \rightarrow e(k') + V(v) + p(P') \tag{1}$$

will be briefly discussed.

The kinematic variables which are used throughout the paper are defined as follows:

- $Q^2 = -q^2 = -(k - k')^2$,
- $x = \frac{Q^2}{2(P \cdot q)}$,
- $t = (q - v)^2 = (P - P')$,
- $s = (P + k)^2$,
- $y = \frac{q \cdot P}{k \cdot P}$,
- $W = \sqrt{ys}$,

where Q^2 is the negative square of the 4-momentum transfer at the electron vertex, y is the inelasticity parameter, t is the 4-momentum transfer squared between the photon and the vector meson, x is the Bjorken variable, s is the ep center-of-mass energy squared and W is the $\gamma^* p$ center-of-mass energy.

The ep cross section is related to the $\gamma^* p \rightarrow Vp$ cross section:

$$\frac{d^2\sigma_{tot}(ep \rightarrow eVp)}{dy\, dQ^2} = \Gamma_T\, \sigma_{tot}(\gamma^* p \rightarrow Vp), \tag{2}$$

where Γ_T is the flux of transverse virtual photons given by

$$\Gamma_T = \frac{\alpha_{em}\,(1 - y + y^2/2)}{\pi y Q^2}. \tag{3}$$

Hard diffractive electro-production of longitudinally polarized vector mesons has been studied recently in the framework of perturbative QCD [2], where the cross section of the $\gamma^* p \rightarrow Vp$ process was calculated within the leading $\alpha_s \ln \frac{Q^2}{\Lambda^2_{QCD}}$ approximation of QCD using the leading order parton densities within the proton. V denotes any vector meson (e. g. $\rho, \rho', \phi, J/\Psi, \Upsilon$). When the momentum transferred to the target t tends to zero and $Q^2 \gg M_V^2$, where M_V is the vector meson mass, the cross-section for the hard diffractive electro-production has the form:

$$\left.\frac{d\sigma^L_{\gamma^* p \rightarrow Vp}}{dt}\right|_{t=0} = \frac{4\pi^3 \Gamma_{V \rightarrow e^+e^-} M_V \alpha_s^2(Q^2) T(Q^2) \eta_V^2 \left|\left(1 + i\frac{\pi}{2}\frac{d}{d\ln x}\right) xG(x, Q^2)\right|^2}{3\alpha_{EM} Q^6}, \tag{4}$$

where $\Gamma_{V \rightarrow e^+e^-}$ is the decay width of the vector meson into an e^+e^- pair. The parameter η_V is defined as $\eta_V \equiv \frac{1}{2}\frac{\int \frac{dz\, d^2k_t}{z(1-z)}\, \phi_V(z,k_t)}{\int dz\, d^2k_t\, \phi_V(z,k_t)}$, and ϕ_V is the light-cone wave function of the $q\bar{q}$ component of the vector meson. $xG(x, Q^2)$ is the gluon distribution in the proton and $T(Q^2)$ is a factor connected with the Fermi motion of the quarks within the vector meson.

The predictions of pQCD for diffractive electro-production of vector mesons have been partly compared with the existing experimental results [6, 7, 8]:

- A fast increase of the cross section of electro-production of vector mesons with the $\gamma^* p$ center of mass energy W, $\sigma \sim W^{0.8-0.9}$. The rise is connected with the behavior of the gluon density with decreasing x. The non-perturbative two-gluon-exchange model of Donnachie and Landshoff [5] predicts a cross section rising as $\sim W^{0.32}$ which, after taking into account the shrinkage of the forward diffractive peak becomes $\sim W^{0.22}$.

- The dominance of the longitudinal polarization, $\sigma_L/\sigma_T \propto Q^2/M_V^2$.

- The absolute magnitude of the cross section is reasonably well explained, though uncertainties in the knowledge of $xG(x,Q^2)$ are too large to make a quantitative comparison.

- The account of Fermi motion of the quarks within the vector meson leads to a strong suppression of the cross section. The dependence of the suppression factor $T(Q^2)$ on the Q^2 for light and heavy mesons was presented in [2].

- The Q^2 dependence of the cross section can be parameterized as Q^{-n} with $n \sim 4$. The difference of n from the asymptotic value of 6 is changed by the Q^2 dependence of the factors $[\alpha_s(Q^2)xG(x,Q^2)]^2 \sim Q$ and of $T(Q^2)$.

Based on equation (4) with the GRV94 LO gluon distribution [9], we have calculated the cross section[2] for production of longitudinally polarized vector meson states $\sigma_L(\gamma^* p)$ as a function of W for the different ranges of Q^2 for the following vector mesons: $\rho(770)$, $\rho(1700)$, $\phi(1020)$, $J/\psi(3097)$ and $\Upsilon(9460)$. The kinematic ranges were chosen as $20-150$ GeV^2 for Q^2 and 40 - 220 GeV for W. The cross section (4) was integrated over t between $t_{min} = 0$ and $t_{max} = 1$ GeV^2 assuming the e^{bt} behavior of the cross section with slope $b = 5$ GeV^{-2}. The total cross section $\sigma_{tot}(\gamma^* p \to Vp)$ is defined as: $\sigma_{tot}(\gamma^* p \to Vp) = \sigma_L(\gamma^* p \to Vp)(1/R + \varepsilon)$, where ε is the polarization parameter, $\varepsilon = \frac{1-y}{1-y+y^2/2}$, $R = \sigma_L/\sigma_T$, and σ_T is the transverse $\gamma^* p$ cross section.

In fig. 1 the total $(\gamma^* p \to \rho p)$ cross section as a function of energy W is displayed. One can see the predicted [1, 2] strong rise of the cross section with W.
Using the electro-production cross sections we have calculated the expected number of vector mesons N_V:

$$N_V = \sigma(ep \to Vep) \times \mathcal{L} \times \mathrm{Br}; \quad (5)$$

where $\mathcal{L}$ denotes the integrated luminosity and Br the branching fraction of vector mesons. We have considered the following decay channels : $\rho(770), \rho(1700) \to \pi^+\pi^-$, $\phi \to K^+K^-$, J/Ψ, $\Upsilon \to e^+e^-$ and $\mu^+\mu^-$. The value of $Br = 0.3$ was assumed for $\rho(1700) \to \pi^+\pi^-$ decay.

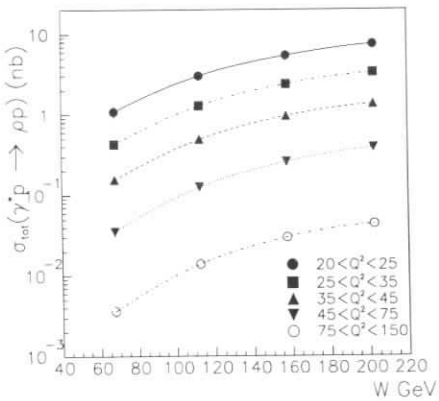

Figure 1: *Predicted cross section of ρ^0 production as function of W and Q^2 [1,2].*

In table 1 the estimated rates of events with $\mathcal{L}$=250 pb^{-1} are displayed. In addition we show in the table the extrapolated number of events for 250 pb^{-1}, based on the currently available event statistics.

[2]In case of heavy mesons production Q^2 was replaced by $Q^2 + M_V^2$.

Q^2[GeV^2]	20-25	25-35	35-45	45-70	70-150	Total	$Q^2 > 7$GeV^2 estim. from data
$\rho(770)$	1100	800	250	170	30	2350	60000
$\phi(1020)$	150	100	40	20	5	315	6000
$\rho(1700)$	17	40	13	11	4	95	-
$J/\psi(3097)$	130	130	60	30	10	360	3000
$\Upsilon(9460)$	1.7	1.6	1.3	0.8	0.5	6	-

Table 1: *Estimated number of events in the measurable W range for different Q^2 ranges. We would like to thank E. Gallo for preparing the estimated number of events from the current data.*

2.2 Vector meson production at large t

The process $\gamma p \to V + X$, where V is a vector meson and X is a hadronic state originated by the diffractive dissociation of the proton (fig. 2(a)), in the limit of large t, has been described in the BFKL formalism in terms of the exchange of a perturbative QCD pomeron [11, 4]. In such a model, the vector meson is produced quasi-elastically, i.e. in the proton rest frame it carries nearly all the energy of the photon. The photon can be either quasi-real ($Q^2 \simeq 0$) or virtual ($Q^2 > 0$).

2.2.1 Kinematics and cross section

In addition to the standard kinematic variables, the model [11, 4] uses two extra variables. These are the scaling variable, τ, and the 'energy' variable z defined as:

$$\tau = \frac{-t}{(Q^2 + M_V^2)} \quad \text{and} \quad z = \frac{3\alpha_s}{2\pi} \log\left(\frac{x_g \cdot W^2}{-t + Q^2 + M_V^2}\right) ,$$

where x_g is the fraction of the proton momentum carried by the struck parton. The variable z is proportional to the rapidity gap between the produced vector meson and the scattered parton. The differential cross section for the process $\gamma p \to VX$, when the photon is transversely polarized, is written as:

$$\frac{d^2\sigma_T(\gamma p \to VX)}{dt dx_g} = \left(G(x_g,t) + \frac{16}{81}\sum_f (q(x_g,t) + \bar{q}(x_g,t))\right) \frac{\pi\alpha_s^4}{t^4} \mid \mathcal{F}(z,\tau) \mid^2 ,$$

where G, q and $\bar{q}$ represent the gluon, quark and anti-quark densities respectively, and $\mathcal{F}$ is the product of the two-gluon scattering amplitude and the form factor associated with the γV vertex [11, 4]. The cross section for longitudinal photons is assumed to be $\sigma_L = (Q^2/M_V^2)\sigma_T$.

2.2.2 Monte Carlo Generators

Two Monte Carlo generators have been written which simulate the large t vector meson production process, named HITVM [15] and RHODI [16]. The available vector mesons are ρ, ω, ϕ, J/ψ or Υ in both generators. However, as a non-relativistic wave function is used in the calculations, the predictions for the ρ, ω and ϕ mesons are not as reliable as for the heavier vector mesons. The two Monte Carlo generators agree in their results for both the γp and ep cross sections. The main difference between the two generators is the modeling of the proton remnant:

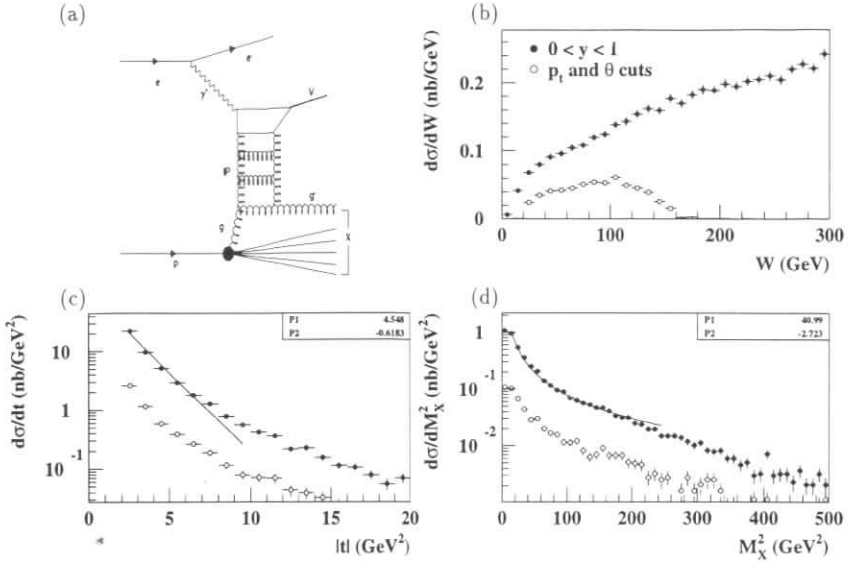

Figure 2: *For the process $ep \to e'VX$ at large t, (a) shows the Feynman diagram, (b) the W distribution, (c) the $|t|$ distribution fitted with $p_1 \cdot e^{p_2 t}$ and (d) the M_X^2 distribution fitted with $p_1 \cdot (M_X)^{p_2}$ when $V = J/\psi$. The closed and open circles represent the generated distributions and the distributions after applying the p_t and θ cuts indicated in the text, respectively. For these plots the HITVM generator was used.*

- In RHODI the multiplicity and momentum distribution of the hadrons produced from the proton dissociation are generated using parameterizations of the $\bar{p}p \to \bar{p}(p)X$ results from the UA5 experiment [12] and imposing two requirements on M_X: $M_X^2/W^2 \leq 0.1$ (to ensure that the interaction be diffractive) and $M_X \geq m_p + m_\pi$ (to remove the events with only a proton in the diffractive state X).

- In HITVM, the struck parton can be either a valence quark, gluon or sea quark and in each case the proton remnant is a diquark, quark+diquark or quark+baryon respectively (based on the method used by PYTHIA [13]). Then the resulting particles are given to JETSET [13] to hadronize.

2.2.3 Cross section predictions

Table 2 summarizes the ep cross sections expected for J/ψ production and also the expected number of $J/\psi \to \mu^+\mu^-$ (or e^+e^-) events for a luminosity of $100\,\mathrm{pb}^{-1}$. In order to simulate the apparatus acceptance, events were accepted only if both muons are in the range $6° < \theta < 155°$ and $p_t > 1.0$ GeV. The predictions are calculated in the region $0.01 < x_g < 1.0$, $|t| > 2.0$ GeV^2 and using $\alpha_s = 0.3$ and the structure functions MRSA [14]. The predictions are very sensitive to the value of α_s: for example when $\alpha_s = 0.2$ the cross section is reduced by a factor of 20.

The generated and accepted distributions in W, $|t|$ and M_X^2 for $Q^2 < 4\,\mathrm{GeV}^2$ are shown figures 2(b), 2(c) and 2(d), respectively. Note the strong increase of the cross section with W and that this model predicts a very small W-dependence of the t-slope ($\alpha' < 0.1$ GeV^{-2}).

Kinematic Range	$\sigma(ep \to e'J/\psi X)$ (nb)		$N(J/\psi \to \mu^+\mu^-)$	
	$Q^2 < 4$ GeV^2	$Q^2 > 4$ GeV^2	$Q^2 < 4$ GeV^2	$Q^2 > 4$ GeV^2
$0.000 < y < 1.00$	46.	1.4	250000	8000
$0.015 < y < 0.60$	30.	1.0	150000	6000
$0.010 < y < 0.30$	17.	0.67	100000	4000
Muon p_t and θ cuts	5.90	0.36	35000	2000

Table 2: *Cross section predictions and the expected number of $J/\psi \to \mu^+\mu^-$ events for $100\,\mathrm{pb}^{-1}$.*

3 Detector performance

This study is based on the present layout of the two multi-purpose detectors at HERA H1 and ZEUS. It is assumed that in the near future the full tracking system of both experiments will be available and that during the HERA upgrade no changes to the tracking chambers are needed. The acceptance of the tracking systems of the two detectors is similar. In case of the ZEUS detector the polar coverage of the central drift chamber is $16° - 165°$, the forward tracking chambers cover the region $7° - 28°$ and the rear tracking system the region $160° - 170°$.

Like for the selection of all diffractive processes at HERA, an efficient tagging of very forward particles is needed to distinguish between single and double dissociative events.

The identification of all vector meson decay products and of the scattered electron allows the complete and precise reconstruction of the event kinematics. However, the additional detection of the scattered proton selects an almost proton dissociation free subsample and allows additional important cross checks. Due to the small acceptance of a leading proton spectrometer ($\sim 5\%$), measurements are limited to the low Q^2 region.

More important for future vector meson selections at large Q^2 is the tagging of proton fragments in the very forward region. This method to separate single from double dissociative events has the advantage of high acceptance and is not limited to a small t-region. We will discuss the importance of tagging particles as forward as possible in the context of systematic errors.

We assume for the study that the trigger for the vector meson events will not be a basic problem. The clean topology of the events should help to select such events already in a very early trigger stage.

3.1 Acceptance

The understanding of the detector acceptance increases normally slowly with time. Using the DIPSI Monte Carlo generator [10] we checked with the standard simulation of the ZEUS detector that the average acceptance of vector mesons is above 60% in the relevant W range. For the following we used the simple approximation that the chance to identify a vector meson is high if its original direction is within the acceptance range of the tracking chambers.

Figure 3 shows the pseudo-rapidity ($\eta = -\ln\tan\frac{\theta}{2}$) of the vector mesons as function of W with Q^2 as additional parameter; the dependence of the acceptance on t and M_V is in case of large Q^2 very small. For example using the complete tracking system for $Q^2 = 20$ GeV^2, the

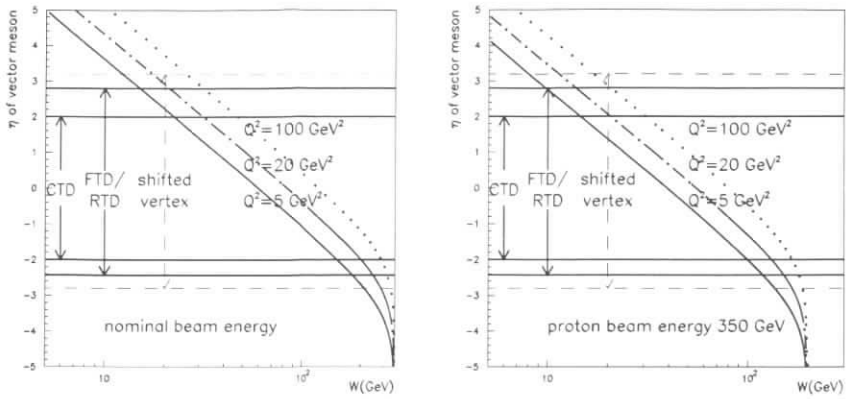

Figure 3: *Rapidity of scattered vector meson as function of W and Q^2 for nominal beam energies (left, $E_p = 820$ GeV, $E_e = 27.5$ GeV) and reduced proton energy (right, $E_p = 350$ GeV). The full lines indicate the acceptance of the tracking chambers. The dashed line shows the acceptance of the full tracking system for shifted vertex runs (± 70 cm).*

accepted W range for vector mesons is roughly $25 - 220$ GeV. Additional shifted vertex runs (with z $\pm$ 70 cm) can extend the η range by $\pm$ 0.4 units and increase the W range slightly.

Changing the proton beam energy to lower values helps to extend the measurements to smaller values (see fig. 3 for a proton beam of 350 GeV). Measurements down to $W = 10$ GeV will be possible and therefore the results of the NMC collaboration can be cross-checked. A change of the electron beam energy does influence the direction of the vector meson only at very large W values, close to the kinematic limit, but it shifts the events to higher values of y. Measurements with a reduced electron beam energy can therefore be used to estimate R, the ratio of transverse to longitudinal cross section, directly, without the assumption of s-channel helicity conservation.

The acceptance as function of Q^2 depends mostly on the layout of the detector responsible for tagging the scattered electron. The main calorimeters of the H1 and ZEUS experiments can be used for this purpose down to Q^2 values of a few GeV^2. Events with smaller Q^2 values can be selected with additional taggers along the beam pipe. For the full reconstruction of the event kinematics at least the measurement of the direction of the scattered electron is required.

3.2 Systematic errors

The systematic uncertainties will become more important for the measurements at high luminosity. The sources of uncertainties can be divided into the following subgroups: reconstruction of the final state particles, non-resonant background, proton-dissociation and other sources like luminosity measurement, radiative corrections, non-physical background. The following estimates are based on the two presently available publications on vector meson production at high Q^2 [7, 8].

1. **Reconstruction:** The present error estimate in the cross section measurements related to uncertainties in the acceptance and the reconstruction of the event kinematic is about 7%. A large effort is underway by both collaborations to get a better determination of the position of the scattered electron, a better understanding of the track reconstruction efficiency and of the sources of calorimeter noise. This certainly will reduce the systematic error soon. The usage of additional components (tracking chambers in the forward and rear region, new components in the very forward region) will create new sources of uncertainties. Overall a reduction of this error down to 4% should be possible.

2. **Non-resonant background:** Neither the shape of e. g. the resonant ρ-mass peak nor of the underlying non-resonant background is known for the production of vector mesons at large Q^2 values. So far different assumptions about the shape of the non-resonant mass distributions were used to fit the data and to estimate this background source (6%). The higher statistics in future measurements will help to constrain the assumptions about the shape and the fit result. An estimate of 4% seems reasonable.

3. **Proton-dissociation:** With an uncertainty of about 8% the estimate of the contribution of events where the proton dissociates is the largest source for the systematic error. The contribution (and therefore the error estimate) can be reduced either by tagging the outgoing proton or by tagging excited proton states of very low masses. Due to the higher acceptance the second method is favored for the vector meson selection. The main problem for the cross section measurement is the a priori unknown mass-spectrum of the excited proton states.

   Monte Carlo simulations are used to estimate the untagged mass distribution of the proton fragments for different detector layouts. We studied the two cases that the tagging device has an acceptance down to 1.5 mrad or only down to 6 mrad (the lower limit of 1.5 mrad is given by the fact that for a momentum transfer squred (t) on the proton of about 1GeV^2 the proton is scattered by 1.2 mrad!). In the first case, excited states of the proton above 1.8 GeV, while in the second case above 2.2 GeV are rejected. Assuming a mass dependence of the excited proton state $\sim M_N^{-2.0}$ such devices can veto 92% (84%) of the events where the proton dissociates. Assuming the cross section for proton dissociation to be of the same order as for the elastic scattering, the remaining background of about 8% (16%) can be constrained by assumptions about the M_N or t dependence. We assume one half of this contribution as a conservative estimate of the systematic error.

   For the determination of the t-slope, this error leads to an uncertainty of the measured slope of about ± 0.2 GeV^{-2} (± 0.4 GeV^{-2}).

4. **Other sources:** Compared to the errors above, the uncertainties of the luminosity measurement should be negligible and the improved knowledge of the Q^2-dependence will reduce the uncertainties in the calculation of radiative corrections.

The following table summarizes the estimates of systematic errors:

error	93/94	future estimate
reconstruction related	7%	4%
non-resonant background	6%	4%
proton-diss. background tagged at 1.5 / 6 mrad	8%	4% / 8%
other sources	5%	-
	13%	7% / 10%

The overall systematic error is therefore expected to be about 7% (or about 10% if only proton fragments above 6 mrad are tagged). Since the dependence of the background on the

kinematic variables is not known, for cross section measurements the error contribution has to be taken into account for each measured bin independently, rather than using an overall normalization uncertainty. In case of the measurement of R, cross section ratios are measured at the same W and Q^2 values (but different y), it can be therefore assumed that the systematic errors partly cancel and a systematic error of 5% is reasonable.

4 Accuracy of measurements

In this section the accuracy is estimated for future measurements related to elastic vector meson production under the assumptions explained previously [3]. We consider the measurement of the power δ of the W-dependence, the change of the t-slope described by the value of α' and the ratio of $\sigma_L/\sigma_T = R$. Different theoretical predictions for these observables are available. The aim of this section is to define the luminosity needed to distinguish between the predictions.

In order to minimize the error of the measurement, some time was spent to optimize the bin sizes. As long as the statistical error dominates, the chosen bin size has almost no influence on the resulting error. If only two or three bins in W are used for the δ and α' measurement, the loss of "lever arm" in W gives a slightly higher error. If the systematic error becomes important, the best results are observed if the bin size is adjusted such that the systematic error is smaller or equal to the statistical error in each bin.

The estimate of the error of the δ and α' measurement is almost independent on the assumed model. Once the W and t range is given by the detector acceptance, the error depends only on the number of events which are available in a given Q^2-interval. Following the ideas of Frankfurt et al. [2], in the range of large Q^2 (> a few GeV^2) the dynamics of vector meson production will vary only slowly with Q^2, thus relatively large bins in Q^2 can be used. See tables 1 and 2 for the expected number of events in the given Q^2 ranges.

4.1 W-dependence

Equidistant W-bins were used and a systematic error of 7% was added to the statistical error in each bin. The resulting error for δ is shown in fig. 4. The lines correspond to the accessible W range at $Q^2 = 20$ GeV^2 if either only the central tracking chambers of the experiments are used or the full tracking systems are available. In the second case with about 100 events in a given Q^2 interval the error on δ is ≈ 0.2. HERA data can therefore very soon discriminate between the very different predictions of e.g. Donnachie-Landshoff and QCD approaches for the ρ meson. With an integrated luminosity of about 250 pb^{-1} this accuracy can be expected for Q^2 values up to 35 GeV^2 also for ϕ and J/ψ mesons. Above 1000 events the systematic error dominates and limits the precision on δ to 0.05. This limit is important at low Q^2 values for ρ, ϕ and J/ψ production.

4.2 α'-measurement

The (non-) observation of "shrinkage" requires a detailed understanding of the t-dependence of the cross section. The slope of the t distribution of proton dissociative events is smaller than the slope of the elastic sample. Therefore proton dissociation becomes important at large t values and limits the accuracy of the measurement of the t-slope.

[3]The following study is done for the elastic vector meson production; however, the results are in principle also valid for the production of vector mesons at large t.

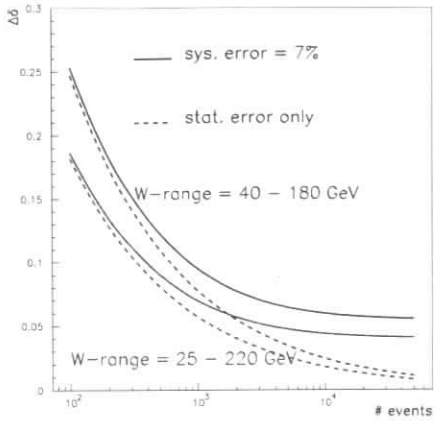

Figure 4: *Estimate of the error for a δ measurement as function of the number of events in a given Q^2 range.*

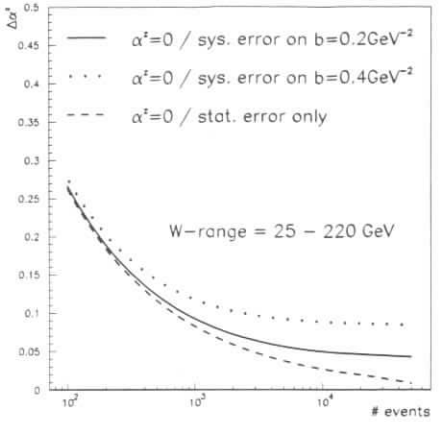

Figure 5: *Estimate of the error for a α' measurement as function of the number of events in a given Q^2 range.*

In each W-bin the statistical error for the t-slope measurement was calculated. We used for the t-fit the range $0.1 - 1.0$ GeV^2. The lower limit is given by the expected beam emittance for the low β optics of HERA, the upper limit by the influence of proton dissociation background. To the statistical error we add the systematic error of $\Delta b = \pm 0.2$ GeV^{-2} (0.4 GeV^{-2}). The error of the α'-fit is shown in fig. 5.

The value of α' in soft physics is about 0.25 GeV^{-2}. To establish that this value is excluded by 2 standard deviations, the error of the measurement should be below 0.12 GeV^{-2}. From fig. 5 it can be seen that at least 1000 events are needed. From table 1 it can be concluded that only the ρ cross section at higher Q^2 values is large enough to enable such a measurement. With a luminosity of 1000 pb^{-1} the requested accuracy can be achieved also for the ϕ and J/ψ mesons at intermediate Q^2 values.

If proton fragments can only be tagged above 6 mrad the resulting error is almost twice as high. It is then impossible to measure α' with the requested accuracy. This result demonstrates very clearly the importance of a good tagging of proton fragments in the very forward region.

4.3 Measurement of R

The measurement of the ratio between the cross section of longitudinally and transversely polarized photons gives additional information about the structure of a virtual photon. Two different approaches are available to measure R: either comparing the cross sections at fixed W and Q^2, but at different beam energies (the ratio of the transverse to the longitudinal photon flux changes with the ep center-of-mass-energy) or assuming s-channel helicity conservation (SCHC) and measuring the helicity distribution of the final state particles.

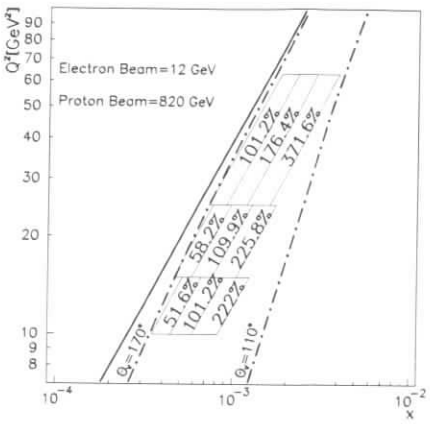

Figure 6: *Error estimate for R. The cross section is measured in the shown W, Q^2-bins at two different electron beam energies (27.5, 12 GeV) with about 10 pb^{-1} luminosity. The dotted lines indicate constant values of the VM scattering angle.*

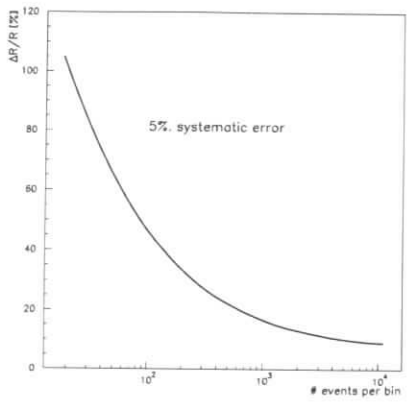

Figure 7: *Error estimate for the measurement of R from the helicity distribution of the final state particles. For the estimate of the systematic uncertainty a flat distributed background with an uncertainty of 5% is assumed.*

4.3.1 Reduced beam energy

At the nominal beam energy, the acceptance of the central tracking limits the measurements of exclusive vector meson production to small and intermediate values of y ($4 \cdot 10^{-3} < y < 0.5$). The transverse and longitudinal photon fluxes differ significantly only at very high y values. The practical way for the selection of vector mesons at high y values is the reduction of the electron beam energy. The error estimate of R for some W- and Q^2- bins is given in fig. 6. For this estimate we used the cross section prediction for the ρ^0-meson of section 2.1, assumed a 5% error between the two cross section measurements at high and low beam energies and considered the case that about 10pb^{-1} are available at each energy. The error, which is mostly of statistical nature, is in all bins above 50%. If 100pb^{-1} are taken at each energy, the error in the highest W-bins is reduced to about 25%.

4.3.2 Assuming SCHC

The helicity distribution of the vector meson decay products contains information about the polarization of the vector meson. If one assumes that the helicity is conserved in the diffractive interaction, the vector meson has the same polarization as the original photon. The fraction of transversely to longitudinally polarized photons can therefore be estimated. The assumption of SCHC has been proven for small values of t and Q^2. But an indication was seen, that this assumption is not true at large values of t [17].

The acceptance for vector mesons is reduced if $\cos(\theta_h)$, θ_h being the polar angle of one decay product of the vector meson in the vector meson c.m. system, is close to ± 1. In that case typically one of the decay particles has only a very small momentum. However, the region of $|\cos(\theta_h)| < 0.8$ is unaffected. The error of a fit to the helicity distribution is plotted in fig.7. The accuracy of this method is better than the one described in 4.3.1. A combination of both methods might be used to check SCHC.

5 Conclusions

The analysis of exclusively produced vector mesons at HERA provides important tests of QCD predictions. Significant differences exists in the predictions between phenomenological and perturbative QCD models. We concentrate in this report on the QCD predictions available at large values of t and Q^2. We studied the requirements for the HERA accelerator and the two experiments H1 and ZEUS to enable measurements which can distinguish between those models. As examples we focused on the obtainable accuracy in the measurement of the W-dependence, the observation of shrinkage and the measurement of the ratio between the longitudinal and the transverse cross section.

For a luminosity of about 250pb^{-1} the measurements with heavy vector mesons are limited by the available statistics. The high luminosity option of HERA is therefore favored. For measurements with the ρ^0 vector meson, and with the heavier vector mesons at very high luminosity, the main systematic uncertainty becomes the estimate of proton dissociation. A very good tagging of the forward proton or proton fragments is needed. Tagging devices sensitive to an angle of 1.5 mrad relative to the proton direction are needed to reduce this error to the level of other uncertainties. It is recommended to have a redundant system of tagging devices with decreasing angular acceptance to be able to study the angular distribution of the proton fragments and to separate scattered protons at large momentum transfers from dissociated protons.

References

[1] M. G. Ryskin, Z. Phys. C57 (1993) 89; M. G. Ryskin *et al.*, HEP-PH 9511228
[2] S. J. Brodsky *et al.*, Phys. Rev. D50 (1994) 3134; L. L. Frankfurt, W. Koepf, M. Strikman, HEP-PH 9509311
[3] J. Nemchik *et al.*, HEP-PH 9605231
[4] J. Bartels *et al.*, Phys. Lett. B375 (1996) 301
[5] A. Donnachie, P. V. Landshoff, Phys. Lett. B185 (1987) 403; Nucl. Phys. B311 (1989) 509
[6] NMC Collaboration, M. Arneodo *et al.*, Z. Phys. C51 (1991) 387
[7] ZEUS Collaboration, M. Derrick *et al.*, Phys. Lett. B356 (1995) 601
[8] H1 Collaboration, S. Aid *et al.*, Nucl. Phys. B468 (1996) 3
[9] M. Glück, E. Reya, A. Vogt, Z. Phys. C67 (1994) 433
[10] M. Arneodo, L. Lamberti, M. G. Ryskin, DESY 96-149
[11] J. R. Forshaw, M. Ryskin, Z. Phys. C68 (1995) 137
[12] UA5 Coll., G. J. Alner *et al.*, Nucl. Phys. B291 (1987) 445
[13] T. Sjöstrand, Comp. Phys. Comm. 82 (1994) 74
[14] A. D. Martin *et al.*, Phys. Rev. D50 (1994) 6734
[15] L. West, to be published
[16] A. Garfagnini, L. Iannotti, L. Lamberti, to be published
[17] T. H. Bauer *et al.*, Rev. Mod. Phys. 50 (1978) 261

Diffractive structure functions in DIS

M.F. McDermott[a] and G. Briskin[b1]

[a] Deutsches Elektronen-Synchrotron DESY, Notkestrasse 85, D-22603 Hamburg, FRG
[b] School of Physics and Astronomy, Raymond and Beverly Sackler Faculty of Exact Sciences, Tel Aviv University, Israel.

Abstract: A review of theoretical models of diffractive structure functions in deep inelastic scattering (DIS) is presented with a view to highlighting distinctive features, that may be distinguished experimentally. In particular, predictions for the behaviour of the diffractive structure functions $F_2^D, F_L^D, F_2^{D(\mathrm{charm})}$ are presented. The measurement of these functions at both small and high values of the variable β and their evolution with Q^2 is expected to reveal crucial information concerning the underlying dynamics.

1 Models of hard diffractive structure functions in DIS

It is natural to start with a definition of what we mean by the terms 'hard' and 'diffractive' when applied to scattering of electrons and protons. High energy scattering processes may be conveniently classified by the typical scales involved. By hard scattering we mean that there is a least one short distance, high momentum, scale (e.g. high p_T-jet, boson virtuality, quark mass) in the problem that gives one the possibility of using factorization theorems and applying perturbative QCD. In case of diffractive DIS this is the photon virtuality, Q^2, however this hard scale is not necessarily enough and indeed QCD factorization may not even be applicable to all hard diffractive scattering in DIS (see [1, 2, 3] for discussions and refs). It has been shown to be applicable to diffractive production of vector mesons initiated by a longitudinally polarized photon [4]. For the time being we will use the definition, due to Bjorken, that a diffractive event contains a non-exponentially suppressed rapidity gap. Rapidity is the usual experimental variable related to the trajectory of an outgoing particle relative to the interaction point: given approximately by $\eta \approx -\ln(\tan(\theta/2))$ (in a cylindrical system of co-ordinates centered on the interaction point, with the z-axis along the beam pipe and polar angle θ). This rather obscure sounding definition results from the fact that within perturbative QCD large rapidity gaps (LRG) *are* suppressed because a coloured particle undergoing a violent collision will emit radiation that would fill up the gap. The suppression factor increases with the interval of rapidity but it's absolute magnitude for diffractive processes in DIS is uncertain. An additional source of rapidity gap supression comes from an overall damping factor associated with multiple interactions. The amount of damping is found to be much smaller in DIS than that typical for soft processes (e.g. proton proton collisions see [5]) making LRG events more likely.

[1]Supported by MINERVA

Theoretically, for 'diffractive' electron proton scattering in DIS one must observe the proton in the final state. In practice this is very difficult for HERA kinematics since the highly energetic scattered proton disappears down the beam pipe in most events. This means that the current measurements also contain contributions from interactions in which the scattered proton dissociates into higher mass states. This uncertainty is considerably alleviated by the advent of the Leading Proton Spectrometer (LPS) which will provide crucial information about diffraction (for the first data from the LPS see [6]). The significance of the difference between the experimental working definition of diffraction and the theoretical one is an interesting but as yet unresolved problem (it is certainly possible to produce large gaps in rapidity in 'non-diffractive' processes, e.g. via secondary trajectory exchanges).

Such LRG events occur naturally in processes known to be governed by soft processes (e.g proton anti-proton scattering at high energies). This is explained naturally in the context of Regge theory : at high enough energies one reaches the so-called Regge limit ($s \gg t$ and $s \gg$ all external masses) and *all* hadronic total cross sections are expected to be mediated by Pomeron exchange and to exhibit *the same* energy behaviour. This expectation is born out by the data (see e.g. [7]), which shows that a wide variety of high energy total elastic cross sections have the same energy dependence which is attributed to the trajectory of the soft pomeron. The energy dependence for diffraction in these processes is discussed in e.g. [8].

Scattering of virtual photons and protons at small enough x corresponds to the Regge limit of this subprocess ($\hat{s} \gg \hat{t}, \hat{s} \gg Q^2, M^2_{\mathrm{Proton}}$). It is natural to ask if the diffractive events observed in the DIS sample also exhibit the universal behaviour even though we are now considering off-shell scattering for which, strictly speaking, Regge theory does not necessarily have to apply. One of the reasons why hard diffraction at HERA at small x is so interesting is that as x decreases, for fixed large Q^2 there should be a transition between the hard short distance physics associated with moderate values of x and the physics of the soft pomeron which is widely believed to dominate at very small x. It is a theoretical and experimental challenge to establish whether LRG events in DIS in the HERA range are governed by hard or soft processes or whether they are actually a mixture of both. The purpose of this report is to discuss the current theoretical models for diffractive structure functions in an attempt to address this problem, and, in particular, to outline the benchmark characteristics of the various approaches to facilitate the search for appropriate experimental tests.

In analogy to the total DIS cross section, the diffractive cross section in DIS can be written,

$$\frac{d\sigma^D}{dx_{I\!P}dtdxdQ^2} = \frac{4\pi\alpha^2_{\mathrm{e.m}}}{xQ^4}\left[1 - y + \frac{y^2}{2[1 + R^D(x, Q^2, x_{I\!P}, t)]}\right] F_2^D(x, Q^2, x_{I\!P}, t) \qquad (1)$$

where D denotes diffraction, $R^D = F_L^D/(F_2^D - F_L^D)$ and $y = Q^2/sx$; $t = 0$ is usually assumed since the cross section is strongly peaked here.

Ingleman and Schlein [9] suggested on the basis of expectations from Regge theory that the diffractive structure functions could be factorized as follows:

$$F_2^D(x, Q^2, x_{I\!P}, t) = f(x_{I\!P}, t)F_2^{I\!P}(\beta, Q^2, t), \qquad (2)$$

where Q^2 is the photon virtuality, $x_{I\!P}$ is the fraction of the proton's momentum carried by the diffractive exchange and t is the associated virtuality, $\beta = Q^2/(M_x^2 + Q^2) = x/x_{I\!P}$, with M_x^2 the mass of the diffractive system. The last relation for β in terms of x, the Bjorken variable,

is a good approximation but only holds for negligible t and proton mass [10]. Due to lack of information on the remnant proton both $x_{I\!P}$ and t can only be estimated indirectly or have to be integrated out.

The 1993 HERA data [11, 12, 13] confirmed the presence of events with large rapidity gap between the proton direction and the nearest significant activity in the main detector, in the total DIS cross section at the leading twist level (i.e. this contribution persisted to high values of Q^2). These events constitute approximately 10 % of the total sample (compared to $\sim$ 40% in photo-production). As has been known for many years and as Bjorken has recently pointed out [14] the fact the diffractive cross section is present in the total sample as a leading twist effect (i.e. it 'scales') at large Q^2 and small x does not necessarily imply that the mechanism that creates these events is point-like. For a careful discussion of the kinematics of hard and soft diffraction in a variety of different reference frames see [15].

The observed events were also not inconsistent with the Regge factorization of eq.(2). Since the cross section had the same power-like $x_{I\!P}$ dependence (in f) over a the wide range of (β, Q^2) that were measured it was tempting to postulate that a single mechanism or 'exchange' was responsible for these events. The presence of the gap tells us that this object is a colour singlet and since the centre of mass energy was very high, the exchanged object became known as the 'Pomeron'. From this observation it is natural to ask, following [9], if the partonic content of this 'particle' may be investigated by changing β and Q^2, with β interpreted as the momentum fraction of the pomeron carried by the struck parton; f in this picture is interpreted as 'the flux of pomerons in the proton'.

This approach has led to a plethora of theoretical papers in which the parton content of the Pomeron at some small starting scale, Q_0^2, is treated in various physically motivated ways (relying strongly on Regge theory). The DGLAP [16] equations of perturbative QCD (to a given logarithmic accuracy) are then used to investigate the evolution with Q^2 of this parton content. Formally the use of the DGLAP equations is inapplicable for the description of diffraction because the presence of the gap makes it impossible to sum over all possible final hadronic states. Their use in this context is at the level of a plausible assumption. In some papers an analogy is drawn with the proton [10, 17, 18] and a momentum sum rule may be imposed on the parton content. Others models [10, 19, 20] take the view that that the Pomeron may be more like the photon and so can have, in addition, a direct coupling to quarks within the virtual photon. Although it is no longer clear once a direct coupling has been introduced whether the concept of a Pomeron structure function has any meaning.

Fits [10, 17, 21] to the 1993 data on diffraction reveal a partonic structure that is harder (more partons at high β) than the proton and that gluons contain a large fraction of pomeron momentum (up to 90 %) with a large fraction of these at high β. Clearly in a quantitative sense such statements will depend on the physical assumptions used to parameterize the input distribution. However qualitatively these statements are reasonable. The paper of Gehrmann and Stirling [10] is particularly useful in discussing Pomeron structure function models in that it discusses and compares two models: model 1 which has only resolved component and imposes a momentum sum rule on the parton content and model 2 which also allows a direct coupling of the Pomeron to quarks. This leads to rather different predictions for the Q^2 evolution of these two models (see curves labelled 'GS(I), GS(II)' in fig.(1)). Model 1 evolves in a way familiar to the evolution of the proton structure function in QCD, i.e. as Q^2 increases there is a migration of partons from high to low β. In model 2, as a result of the direct coupling of the pomeron to quarks (at '$\beta = 1$'), the high β distribution is supplemented and, provided

the direct component is large enough, one expects an increase of parton densities with Q^2 over the whole β range, which is also an expectation of the boson-gluon fusion model of [22] (see fig.(1)).

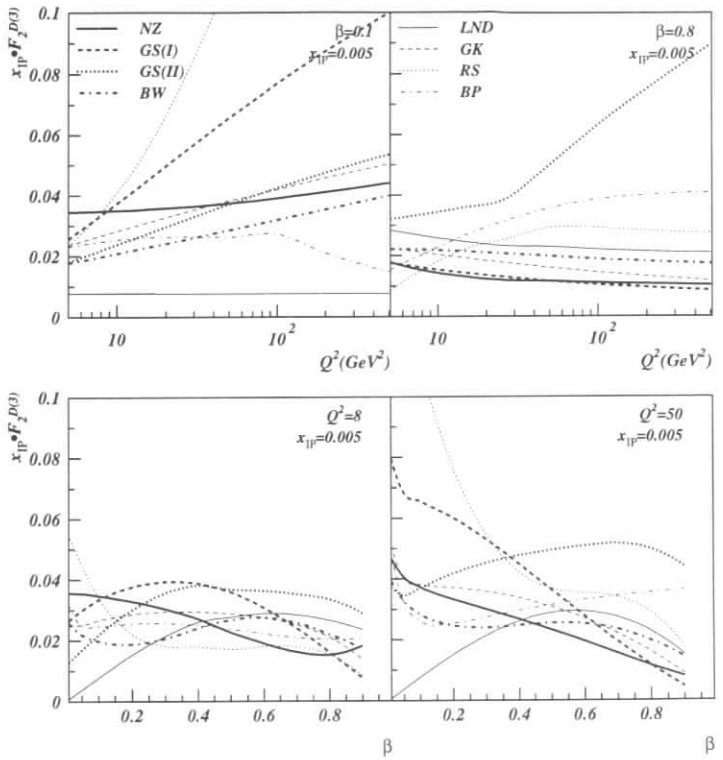

Figure 1: *Distribution of $x_{I\!P}F_2^D(\beta, Q^2, x_{I\!P})$ as a function of β and Q^2, at fixed $x_{I\!P} = 0.005$, for various models. For key assignments - see text.*

The high gluon content of the pomeron that comes out of the LO QCD factorizable pomeron models indicate that the pomeron structure R-factor, $R^D(\beta, Q^2, x_{I\!P}) = F_L^D(\beta, Q^2, x_{I\!P})/F_T^D(\beta, Q^2, x_{I\!P})$, where $F_T^D = F_2^D - F_L^D$, may be considerably bigger ($R^D \sim 1$) than that for the proton ($R^p \sim O(\alpha_s)$). Clearly in order to provide a theoretically consistent prediction for F_L^D a NLO QCD calculation is required. Such a calculation has been performed by Golec-Biernat and Kwieciński [17] who consider a model with resolved partons in the pomeron subject to a momentum sum rule. For high β, R is small in such models but it can reach 0.5 for $\beta < 0.1$. It has a much softer dependence on β than F_2^D (see 'GK' in figs.(1,2)).

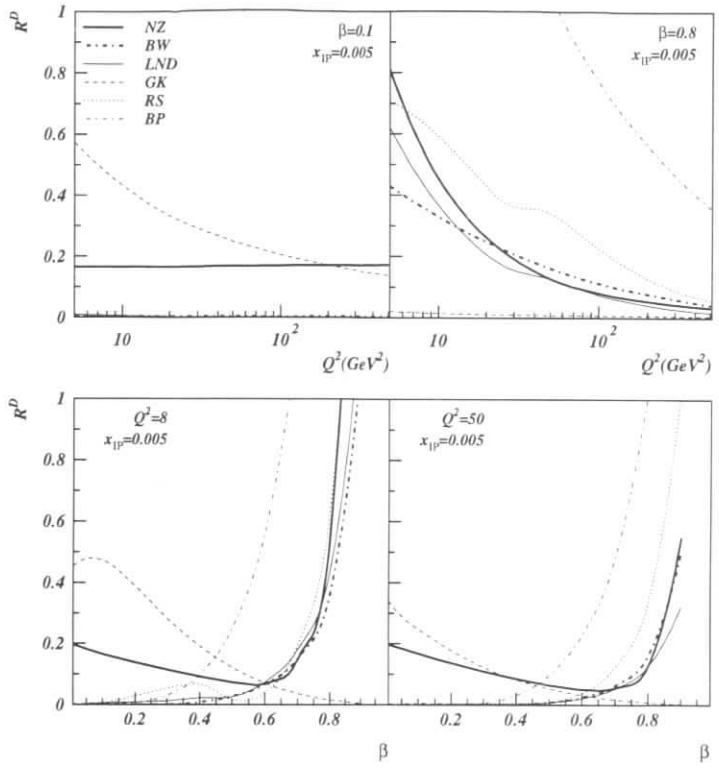

Figure 2: R^D *as a function of* β *and* Q^2 *for* $x_{\mathbb{P}} = 0.005$. *The pomeron structure function model 'GK' differs markedly from the two gluon exchange models 'NZ,BW, LND,RS,BP' at high and low* β. *Of these, those based on the dipole approach to BFKL, 'NZ,BP', produce markedly different* β *and* Q^2 *behaviour to 'RS,BW,LND'.*

This picture of the pomeron structure function has been discussed in detail elsewhere and will not be repeated in further detail here. For a lucid account of this picture and of the 1993 data see [21]. The latest results from H1 [23, 24] on the 1994 data (which has a factor of 10 increase in statistics and covers a broader kinematical range) suggest that single particle factorization no longer holds over the full kinematical range and that particularly for small β it breaks down, i.e. f in eq.(2) become β (but not Q^2) dependent. A possible explanation of this is that sub-leading Regge exchanges play an important rôle [23, 24, 25].

The paper by Ellis and Ross [26] calls into question the validity of these parton model approaches using kinematical arguments concerning the virtuality of the struck parton. They

stress the importance of measuring diffractive events at high β and predict a slow power-like increase with Q^2 in this region in contrast to the logarithmic decrease that may expect from a naive QCD evolution.

This and others models are, broadly speaking, similar in spirit to the old aligned jet model (AJM), which is a kind of parton model approximation to the wavefunction of the photon (see [14, 15] and refs.), and it's QCD improved formulation (see [27] and refs.). Consider virtual-photon proton scattering at high energies (small x) in the proton's rest frame. In this frame the virtual photon, whose energy, q_0, is the largest scale, fluctuates into a $q\bar{q}$ at a large distances, $l_c = 1/2M_p x = q_0/Q^2$, from the proton. As Ioffe [28] observed many years ago these large distances are important in determining the DIS structure functions. For the HERA energy range this 'coherence length' can be as large as 1000 Fm. In other words, at enough high energies we may consider DIS as the interaction of the quark anti-quark pair with the proton. The transverse size of the pair on arrival at the proton is $b_T^2 \approx 1/k_T^2$.

In the configuration in which one of the quarks carries most of the momentum of the photon a large transverse distance develops between the fast and the slow quark by the time it arrives at the proton. This large system, in which the pair is initially 'aligned' along the direction of the original photon, essentially interacts with the proton like a hadron. This aligned configuration gives a leading twist contribution to F_2 and F_2^D, the latter being interpreted as the fraction of events where the produced pair is in a colour singlet state. Since the slow quark is almost on shell, the AJM is similar to the parton model and there is no leading twist contribution to F_L from this configuration.

In the configuration in which the momentum is shared more equally the quarks can stay closer together in transverse space and may interact with the proton perturbatively. These configurations contribute at leading twist to $F_2(x, Q^2)$ and $F_L(x, Q^2)$. In the former the integration over the momentum fraction leads to the logarithm in Q^2 (coming directly from the box diagram). For such small configurations colour transparency phenomena are expected: the emission of initial and final state radiation is suppressed [27].

A semi-classical calculation [29, 30] in which the proton is treated like a classical background field, leads to results very similar to those of the AJM. Working in the proton's rest frame, one considers the interaction of different kinematical configurations of the highly energetic partons in the virtual photon with the soft colour field of the proton. These interactions induce non-abelian eikonal factors in the wavefunctions of the partons which can lead to diffractive final states. In [30] the addition of gluon to the final state is considered. Leading twist diffractive processes appear when at least one of the three partons has a small transverse momentum and carries a small fraction of the longitudinal momentum of the proton. The other two partons may have large transverse momentum, this means they stay close together as they move through the proton, acting effectively as one parton. This high k_T jet configuration, produces the only leading twist contribution to F_L^D at this order (which is constant) and $\ln Q^2$ enhancement of F_2^D. This signals that F_2^D also has leading twist contribution from the configuration in which all the transverse momenta are small. Several qualitative phenomenological predictions come out of this picture. One expects the ratio F_2^D/F_2 to decrease like $\ln Q^2$ and there to be fewer high-p_T jets in F_2^D than in F_2 (they appear only at order α_s in the former). Leading twist diffraction appears at order α_s in F_L^D which will be dominated by jets.

Buchmüller and Hebecker [22] present a model of diffraction in DIS based on the dominant process being boson gluon fusion, with the colour singlet state being formed by soft colour interactions (SCI). The main point is that diffractive and non-diffractive events differ only by

SCI, the kinematics are expected to be similar since one gluon carries most of the momentum of the exchanged system. This idea has also been developed in [31, 32] which provides a Monte Carlo simulation of SCI.

The simplest QCD model for diffractive exchange is a pair of t-channel gluons in a colour singlet state. Such an exchange is a common feature of many models [33, 34, 35, 36, 37, 38, 39] and leads to a diffractive structure functions which are proportional to the gluon density squared. The dynamical content of these models differ in the treatment of QCD corrections and choice of gluon density and will be discussed in more detail below.

It may be possible to distinguish these models from those in which soft colour interactions play a rôle [29, 22, 30] by comparing $F_2^D(x, Q^2, x_{I\!P})$ with $F_2(x_{I\!P}, Q^2)$ for fixed Q^2 and intermediate β. For the latter the following scaling relation is predicted:

$$F_2^D(x, Q^2, x_{I\!P}) \simeq \frac{C}{x_{I\!P}} F_2(x_{I\!P}, Q^2) \tag{3}$$

where C is a constant.

In [33] where diffraction is governed by two gluon exchange one expects this behaviour to be multiplied by a factor $x_{I\!P}^{-\lambda}$, where $\lambda \geq 0.08$ and will depend on k_T^2 (see below). In the dipole approach to BFKL [38, 39], in which the dipoles couple via two gluon exchange a similar result is expected but with a larger power $x_{I\!P}^{-\Delta}$, $\Delta \equiv \alpha_{I\!P} - 1 = 12\alpha_s \ln(2)/\pi$ possibly softened by inverse powers of logarithms in $1/x_{I\!P}$ [38, 40]. Of course, in this case, the individual energy dependences of F_2 and F_2^D is expected to be a lot harder.

In the perturbative QCD approach advocated by Bartels and Wüsthoff [33] the coupling of the pomeron to the hadronic final state can be derived without any additional parameters except the strong coupling. The following ansatz is used for the unintegrated gluon density:

$$\psi(x, k_T^2, Q_0^2) \sim \frac{1}{k_T^2 + Q_0^2} x^{1-\alpha_{I\!P}(Q^2)}, \tag{4}$$

with the effective scale-dependent pomeron intercept (which explicitly, albeit mildly, breaks the factorization of eq.(2) since it depends of Q^2) $\alpha_{I\!P}(Q^2) = 1.08 + 0.1 \ln[\ln(Q^2/1\mathrm{GeV}^2) + 3]$ for $Q^2 > 0.05\mathrm{GeV}^2$ and 1.08 below this. This gluon density is then fitted to the available data on F_2. Predictions for the diffractive cross section (which is proportional to $[\psi(x_{I\!P}, k_T^2, Q_0^2)]^2$ integrated over k_T^2) with $q\bar{q}$ and $q\bar{q}g$ in final state are then presented over a wide range of β. Now the relevant scale in $\alpha_{I\!P}$ is the virtuality k_T^2.

In the limit $\beta \to 1$ the longitudinal contribution, which is formally 'higher twist', is finite so is expected to dominate over the transverse part which goes like 1 - β. This highlights the fact that the concept of 'twist' must be applied very carefully in diffraction - contributions which naively appear higher twist may in fact dominate at high Q^2 in certain regimes. With an additional gluon in the final state one finds a $(1-\beta)^3$ behaviour at large β. For small β this configuration dominates and the cross section diverges like $1/\beta$. In summary, a characteristic β spectrum is found that shows that emission of the additional gluon is bound to the small β region whereas the large β is dominated by the longitudinal photon. Numerical results, labelled 'BW', using the ansatz of eq.(4) for F_2^D, and R^D as function of β and Q^2 are shown in figs.(1,2).

The large mass, small β or triple Regge regime ($s \gg M_x^2 \gg Q^2 \gg \Lambda_{QCD}^2$) has also been investigated in detail by Bartels and Wüsthoff (see [41, 42, 43] and refs). Theoretically the

emergence of a 4 gluon t-channel state which builds up the large diffractive mass is expected. Experimentally, this region is hard to investigate since the requirement of a large mass tends to close up the rapidity gap making it difficult to distinguish experimentally from the non-diffractive background and also because the diffractive final state may not be fully contained in the main detector. This situation is improving now that the first data collected with the LPS is becoming available [6]. For the purpose of this report we will discuss expectations in the not-too-small β regime.

Diehl [34] has calculated the contribution of $q\bar{q}$ in the final state to the diffraction cross section in the non-perturbative two gluon exchange model of Nachtmann and Landshoff [36, 44]. Numerical predictions for this model (applicable for not-too-small β), labelled 'LND', are shown in figs.(1,2,3). This model predicts a relatively small contribution of charm in diffraction (less than 10 % over a wide range of $x_{I\!P}, \beta, Q^2$).

The high β, small mass regime of diffraction is considered explicitly in [37] who work in co-ordinate space of the transverse distance between the quark and the anti-quark. They claim that at high enough β (≥ 0.4) only the $q\bar{q}$ contributes (in agreement with [33]) and that for $\beta \geq 0.7$ diffractive scattering from the longitudinal photon dominates for which only small distances ($b_T \sim 1/Q$) contribute. The effective scale of the gluon density relevant to diffraction is $k_T^2/(1-\beta)$ (see also [45]) which is clearly hard for high β. This implies that for high β (see fig.(2)) R^D becomes greater than unity in sharp contrast to the Pomeron structure function model of [17]. For the transverse photon distances of $b_T \sim 1\mathrm{GeV}^2$ dominate which is used to justify the use of perturbative QCD and the use of evolution equations, using GRV input distributions, for the diffractive structure functions.

The series of papers by Genovese, Nikolaev and Zakharov [46, 47, 48, 49] provides a model for diffraction inspired by the QCD dipole approach [50, 39, 51] to the generalised BFKL [52] equation. In [48] they strongly reject the factorizable pomeron model and instead suggest that a two component structure function for the pomeron with valence and sea partons having different pomeron flux factors. The absolute normalizations of these components of the diffractive structure function are substantially the same as evaluated in 1991 [39], before the HERA data have become available. In recent papers for this Regge factorization breaking model specific predictions for F_L [46] and charm [47] are given (see 'NZ' in figs.(1,2,3)).

The curves, labelled 'RS', shown in figs.(1,2,3) are from a Monte Carlo simulation developed by A.Solano and M.Ryskin, for the dissociation of the virtual photon to two and three jets [53]. The formulae used are the same as those in the LMRT [35] model but use a GRV [54] gluon distribution and a simplified version of the NLO corrections.

Bialas and Peschanski also present predictions for hard diffraction [38, 40] based on the QCD dipole picture of the BFKL equation. In this picture they find that most of the diffractive cross section comes from the interaction of $q\bar{q}$ pairs whose transverse size is of the order of the target size as seen by the virtual photon. The perturbative QCD prediction is enhanced by the BFKL resummation and by the number of dipole configurations in the initial proton state. In the factorized picture they find a strong $x_{I\!P}$ dependence modified by log corrections. They expect R^D to be a strongly varying function of β and to go above unity for large β. The number of diffractive events increases with Q^2 over the whole range. At small β, i.e. large masses, they expect a scaling violation to be similar to that seen in F_2 at small x. Predictions of this model for F_2^D and R_D have been presented recently [55] and are shown, labelled 'BP', in figs.(1,2).

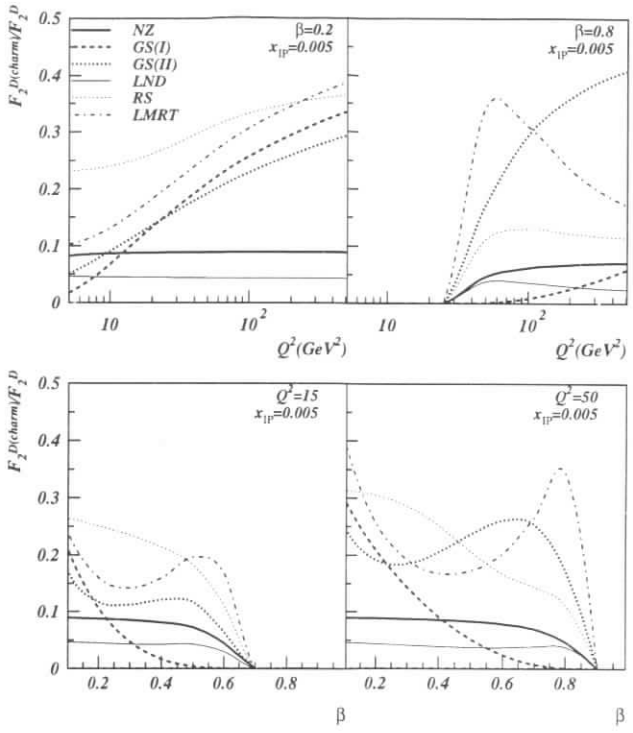

Figure 3: *Predictions for the charm content in diffraction, as a fraction on the total diffractive sample, as a function of β and Q^2 for $x_{\mathbb{P}} = 0.005$. The maximum value of β reflects the charm threshold and increases with Q^2.*

2 F_2^D (Charm)

The ratio of charm events observed in the diffractive structure function is in principle a very good test of the hardness of the processes feeding the $c\bar{c}$ production. Clearly a measurement of the β and Q^2 spectra for these charm events will provide a lot more information.

If hard QCD dominates in diffraction, i.e. the transverse momenta of the $q\bar{q}$ in the loop are large, $k_T^2 \sim Q^2$, the relative yield of charm in diffraction is determined by the electric charges of the quarks and should be about 40 %. In the Pomeron structure function models of [10] the charm contribution comes from boson gluon fusion and is indeed large. Model 2 predicts that it

should also be large at high β in comparison to model 1 (compare 'GS(I)' and 'GS(II)' in fig.(3)). Also since diffraction is a higher twist effect one would expect the $F^{D(\text{charm})}/F(\text{total charm})$ to decrease quickly as a function of Q^2.

In the naive AJM, since the quark transverse momenta are small, one would expect a very small charm content. Within the QCD-improved AJM this may be expected to increase with Q^2 and for sufficiently high Q^2 the charm contribution to diffraction should approach that anticipated from hard physics.

The early paper of Nikolaev and Zakharov [49], predicts that the diffractive contribution to open charm is around 1 %. In a recent paper [47], they present predictions for the charm contribution to diffraction and suggest a very steep rise at small $x_{\mathbb{P}}$ strongly breaking Regge factorization; at $x_{\mathbb{P}} = 0.005$ this leads to a charm content of about 10 % (see 'NZ' in fig.(3)).

In a numerical study of the influence of the small k_T region in the BFKL equation, in [56], it is shown that the dominant contribution to diffraction comes from the region of small transverse quark momenta, even for large Q^2. This would seem to favour a small charm contribution in this model.

The LMRT approach [35] is based on the same Feynman graphs for $\gamma \to q\bar{q}$ and $\gamma \to q\bar{q}g$ dissociation as [33, 37, 41, 42] and [37, 39, 46, 47, 48, 49, 51]. [2] However in the LMRT case the most realistic MRS(A') gluon distribution (which fits all the present data) were used and the main NLO corrections, including an estimate of the K-factor in the $O(\frac{\alpha_s}{\pi}\pi^2)$ approximation, were taken into account. Thanks to the large anomalous dimension γ of the gluon structure function $g(x, k_T^2) \propto (k_T^2)^\gamma$ at small $x = x_{\mathbb{P}}$ the infrared divergence is absent from the k_T-integral and, even for the transverse part originated by the light quarks, the dominant contribution comes mainly from small distances (see also [37]) and doesn't depend too much on the value of the infrared cutoff. This short distance dominance is reflected in the large charm content of the Monte Carlo [53] and of [35] (see curves 'RS' and 'LMRT' in fig.(3), respectively). The LMRT predictions are normalised using a phenomenological fit to the '93 ZEUS data and show a significant threshold behaviour for β approaching the kinematical limit. The sharp increase for low values of β comes from the inclusion of real gluon emission (see [35]), which is not taken into account in LND.

The measurement of the charm contribution in diffraction, which should be available in the near future (at least for D^* production [57]), will certainly help our understanding of the interplay of hard and soft physics in diffraction.

Acknowledgments

We would like to thank H. Abramowicz, J. Bartels, W. Buchmüller, L. Frankfurt, H. Jung and M. Ryskin for discussions and suggestions for this report. We're also grateful to M. Diehl, T. Gehrmann, K. Golec-Biernat, N. Nikolaev, C. Royon, A. Solano, M. Wüsthoff for providing numbers for the figures at short notice.

[2] these perturbative QCD formulae were first derived in [39] for $\gamma \to q\bar{q}$ and in [43] for $\gamma \to q\bar{q}g$

References

[1] J. Collins *et al.*, Phys. Rev. **D51**, 3182 (1995).

[2] J. Collins, L. Frankfurt, and M. Strikman, Phys. Lett. **B307**, 161 (1993).

[3] A. Berera and D. Soper: Phys. Rev. **D50**, 4328 (1994) ; E Levin, *DIS and related subjects*, talk at Eilat Conference on Diffractive Scattering, February 1996, Eilat, Israel.

[4] S. Brodsky *et al.*, Phys. Rev. **D50**, 3134 (1994).

[5] E. Gotsman, E. Levin, and U. Maor, Phys. Lett. **B309**, 199 (1993); E. Levin, Phys. Rev. **D48**, 2097 (1993).

[6] Zeus Collab., *Measurement of the cross section and t distribution in diffractive DIS events with leading protons at HERA*, XVIII International Conference on High Energy Physics, Warsaw, July 1996.

[7] A. Donnachie and P. V. Landshoff, Phys. Lett. **B296**, 227 (1992).

[8] E. Gotsman, E. Levin, and U. Maor, Phys. Rev. **D49**, 4321 (1994).

[9] G. Ingleman and P. Schlein, Phys. Lett. **B152**, 256 (1985).

[10] T. Gehrmann and W. Stirling, Z.Phys **C70**, 89 (1996).

[11] T. Ahmed *et al.*, H1 Collab., Phys. Lett. **B348**, 681 (1995).

[12] M. Derrick *et al.*, Zeus Collab., Z.Phys **C68**, 569 (1995).

[13] M. Derrick *et al.*, Zeus Collab., DESY 96-018, 1996.

[14] J. Bjorken, *Rapidity Gaps in DIS* , talk at ITEP, Moscow, October 1995, SLAC-PUB-7096.

[15] J. Bjorken, *Collisions of constituent quarks at collider energies*, lectures at Lake Louise Winter Institute: Quarks and Colliders, Lake Louise, Canada, 1995, SLAC-PUB-95-6949.

[16] V. Gribov and L. Lipatov, Sov. J. Nucl. Phys. **15**, 438,675 (1972); G. Altarelli and G. Parisi, Nucl. Phys. **B126**, 298 (1977); Y. Dokshitzer, Sov. Phys. JETP **46**, 641 (1977).

[17] K. Golec-Biernat and J. Kwiecinski, Phys. Lett. **B353**, 329 (1995).

[18] A. Capella *et al.*, Z.Phys **C65**, 657 (1995).

[19] H. Kohrs, hep-ph/9512372 **DESY 95-248**, (1995).

[20] A. Donnachie and P. V. Landshoff, Phys. Lett. **B191**, 309 (1987).

[21] J. Phillips, *Rapidity Gap Events at HERA and the structure of the Pomeron*, Workshop on Deep Inelastic Scattering, Paris, 1995.

[22] W. Buchmüller and A. Hebecker, Phys. Lett. **B355**, 573 (1995).

[23] A. Mehta, H1 Collab., talk at Eilat Conference on Diffractive Scattering, February 1996, Eilat, Israel.

[24] H1. Collab., *A measurement and QCD analysis of the diffractive structure function* $F_2^{D(3)}$, XVIII International Conference on High Energy Physics, Warsaw, July 1996.

[25] K. Golec-Biernat and J. Kwieciński, INP Cracow 1734/PH, hep-ph/9607399 (1996).

[26] J. Ellis and G. Ross, CERN-TH/96-101, OUTP-96 20P, hep-ph/9604360, (1996).

[27] H. Abramowicz, L. Frankfurt, and M. Strikman, 1995, published in SLAC Summer Inst. 1994.

[28] B. Ioffe, Phys. Lett. **30**, 123 (1968).

[29] W. Buchmüller and A. Hebecker, hep-ph/9512329 **SLAC-PUB-95-7064**, (1995).

[30] W. Buchmüller, M. F. McDermott, and A. Hebecker, hep-ph/9607290 **SLAC-PUB-7204, DESY-96-126**, (1996).

[31] A. Edin, J. Rathsman, and G. Ingelman, Phys. Lett. **B366**, 371 (1996).

[32] A. Edin, J. Rathsman, and G. Ingelman, DESY-96-060 , **hep-ph/9605281**, (1996).

[33] J. Bartels and M. Wüsthoff, J. Phys. G: Nucl. Part. Phys. **22**, 929 (1996).

[34] M. Diehl, Z.Phys **C66**, 181 (1995).

[35] E. Levin, A. Martin, M. Ryskin, and T. Teubner, hep-ph/9606443 **DTP/96/50**, (1996).

[36] P. V. Landshoff and O. Nachtmann, Z.Phys **C35**, 405 (1987).

[37] E. Gotsman, E. Levin, and U. Maor, hep-ph/9606280 (1996).

[38] A. Bialas and R. Peschanski, Phys. Lett. **B378**, 302 (1996).

[39] N. Nikolaev and B. Zakharov, Z.Phys **C49**, 607 (1991).

[40] A. Bialas and R. Peschanski, hep-ph/9605298 **TPJU-8/96 (Krakow)**, (1996).

[41] J. Bartels and M. Wüesthoff, Z.Phys **C66**, 157 (1995).

[42] M. Wüsthoff, DESY-95-166 **Doctoral Thesis**, 62pp (1995).

[43] E. Levin and M. Wüsthoff, Phys. Rev. **D50**, 4306 (1994).

[44] A. Donnachie and P. V. Landshoff, Nucl. Phys. **B311**, 509 (1988).

[45] J. Bartels, H. Lotter, and M. Wüsthoff, Phys. Lett. **B379**, 239 (1996).

[46] M. Genovese, N. N. Nikolaev and B. G. Zakharov, Phys. Lett. **B380**, 213 (1996).

[47] M. Genovese, N. N. Nikolaev and B. G. Zakharov, Phys. Lett. **B378**, 347 (1996).

[48] M. Genovese, N. N. Nikolaev and B. G. Zakharov, J.Exp.Theor.Phys **81**, 625 (1995).

[49] N. Nikolaev and B. Zakharov, Z.Phys **C53**, 331 (1992).

[50] A. Muller, Nucl. Phys. **B415**, 373 (1994).

[51] N. Nikolaev and B. Zakharov, Z.Phys **C64**, 651 (1994).

[52] E. A. Kuraev, L. N. Lipatov, and V. Fadin, Zh. Eksp. Teor. Fiz **72**, 373 (1977); Sov. Phys. JETP **45**, 199 (1977); Y. Y. Balitskij and L. N. Lipatov, Sov. J. Nucl. Phys. **28**, 882 (1979); L. N. Lipatov, in *Perturbative QCD*, edited by A. Mueller (World Scientific, Singapore, 1989).

[53] M. Ryskin, S. Sivoklokov, and A. Solano, Monte Carlo studies of diffractive processes in deep inelastic scattering, proc. of Int. Conf. on Elastic and Diffractive Scattering (5th Blois Workshop), Providence, USA, 8-12 June 1993, Edited by H.M. Fried, K. Kang and C-I. Tan, World Scientific.

[54] M. Gluck, E. Reya and A. Vogt, Z. Phys. **C53**, 127 (1992).

[55] Ch. Royon, *QCD dipole predictions for DIS and diffractive structure functions*, XVIII International Conference on High Energy Physics, Warsaw, July 1996.

[56] J. Bartels, H. Lotter, and A. Vogt, Phys. Lett. **B379**, 239 (1996).

[57] H1. Collab., *A Measurement of the Production of $D^{*\pm}$ Mesons in Deep-Inelastic Diffractive Interactions at HERA*, XVIII International Conference on High Energy Physics, Warsaw, July 1996; L. Lamberti (Zeus Collab.), private communication.

Future Diffractive Structure Function Measurements at HERA

A. Mehta[a], J. Phillips[b], B. Waugh[c]

[a] Rutherford-Appleton Laboratory
[b] University of Liverpool
[c] University of Manchester

Abstract: The purposes and possibilities of future diffractive structure function measurements at HERA are presented. A review of the current range and accuracy of the measurement of $F_2^{D(3)}(\beta, x_{I\!P}, Q^2)$ is presented and an estimate of the precision of future measurements is given. A feasibility study is performed on the measurement of the structure functions $F_2^{D(4)}(\beta, x_{I\!P}, Q^2, t)$, $F_{2\ charm}^{D}$, $R^{D(3)}$, $R^{D(4)}$ and $F_L^{I\!P}$. Included in this study are estimates of the integrated luminosity required, the analysis techniques to be employed and values of systematic error that could be expected.

1 Introduction

The first pioneering measurements of the deep inelastic diffractive cross section at HERA have yielded great insight into the mechanism of diffractive exchange and the partonic structure of the pomeron [1, 2, 3, 4]. The precision of present measurements is, however, inadequate for the study of many quantitative aspects of this picture. The origin of the gluonic structure of the pomeron and the interface between soft and hard physics are unresolved questions that would benefit from the higher luminosity offered by HERA in the years to come. In addition, the substantially different partonic structure of the pomeron in comparison to usual hadrons makes diffraction a challenging test for perturbative QCD [5]. Furthermore, it has been suggested that the emerging data from HERA may provide fundamental insight into the non-perturbative aspects of QCD, leading to a complete understanding of hadronic interactions in terms of a Reggeon Field Theory [6].

In this paper we study the measurements that can be made of inclusive diffractive cross sections with the luminosities which may be achieved in the future running of HERA. We evaluate what precision is possible for these measurements, and attempt to highlight those measurements which will be of particular relevance to achieving significant progress in our understanding of QCD .

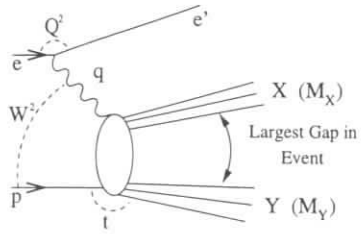

Figure 1: Schematic illustration of the method of selecting events to define a diffractive cross-section, showing the definitions of the kinematic variables discussed in the text. The systems X and Y are separated by the largest gap in true rapidity in the γ^*-p centre of mass system. The system Y is nearest to the direction of the incident proton in this frame of reference.

2 Experimental Signatures of Diffractive Dynamics

A prerequisite for any precision measurement of a hadronic cross section is that it must be defined purely in terms of physically observable properties of the outgoing particles. Since there is, as yet, only the beginnings of a microscopic understanding of the mechanism responsible for diffractive dynamics, and since there are a plethora of wildly different predictions for how the diffractive cross section should depend on all of the kinematic variables, it is the experimentalist's job to provide a well defined measurement unfettered by any *ad hoc* assumptions about how the cross section should behave.

For the interaction $ep \to eX$ (X =*Anything*) the cross section is usually measured differentially as a function of the two kinematic variable x and Q^2 defined as follows:

$$x = \frac{-q^2}{2P \cdot q}, \qquad Q^2 = -q^2, \tag{1}$$

where q and P are the 4-momenta of the exchanged virtual boson and incident proton respectively, and y is the fractional energy loss of the electron in the rest frame of the proton. The differential cross section $\frac{\mathrm{d}^2\sigma}{\mathrm{d}x\mathrm{d}Q^2}$ may then be related to the proton structure functions F_2 and $F_L = F_2 \cdot R/(1+R)$ by:

$$\frac{\mathrm{d}^2\sigma}{\mathrm{d}x\mathrm{d}Q^2} = \frac{2\pi\alpha_{em}^2}{xQ^4}\left[2(1-y) + \frac{y^2}{1+R}\right] \cdot F_2(x,Q^2). \tag{2}$$

Such an interaction may be further characterised by dividing the total hadronic final state (i.e. the final state system excluding the scattered lepton) into two systems, X and Y, separated by the largest gap in true rapidity distribution of particles in the γ^*-p centre of mass system, as shown in figure 1. When the masses of these two systems, M_X and M_Y, are both much smaller than the γ^*p centre of mass energy W then a large rapidity gap between the two systems is kinematically inevitable, and the interactions are likely to be dominantly diffractive.

The two additional kinematic degrees of freedom may be specified by introducing the variables t, β and $x_{I\!P}$:

$$t = (P - Y)^2, \tag{3}$$

$$x_{I\!P} = \frac{Q^2 + M_X^2 - t}{Q^2 + W^2 - M_p^2} \simeq \frac{Q^2 + M_X^2}{Q^2} \cdot x, \tag{4}$$

$$\beta = \frac{Q^2}{Q^2 + M_X^2 - t} \simeq \frac{Q^2}{Q^2 + M_X^2}, \tag{5}$$

The hadronic cross section to be measured is therefore $\frac{\mathrm{d}^4\sigma_{ep\to eXY}}{\mathrm{d}x\,\mathrm{d}Q^2\,\mathrm{d}x_{I\!P}\,\mathrm{d}t}$. The presence of a rapidity gap may then be identified experimentally by use of the calorimeters and forward detectors of the experiments. For sufficiently small values of M_X, the system X will be completely contained in the central calorimeters, allowing an accurate determination of β and $x_{I\!P}$. Tagging of energy in the very forward direction allows both the mass of system Y and the magnitude of $|t|$ to be constrained, but does not allow a direct measurement of t.

A leading proton spectrometer (LPS) "tags" particles which follow closely the path of the outgoing proton beam separated by only a very small angle. By tagging the particle at several points along it's trajectory and with detailed knowledge of the magnetic field optics between the interaction point and the tagging devices, it is possible to reconstruct the original vector momentum of the particle. Thus it is possible to select a sample of events containing a "leading" proton with $E_p \sim E_p^{beam}$. An LPS permits an accurate measurement of t, and provides an independent method of selecting interactions sensitive to diffractive dynamics. Since there is no need for all the hadrons of system X to be contained within the main calorimeter it is possible to make measurements at higher values of $x_{I\!P}$, so that subleading contributions to the cross section may be confirmed and further investigated.

Regge phenomenology has been highly successful in correlating many features of the data for both elastic and inelastic hadron–hadron cross sections [7]. At high energies (low $x_{I\!P}$) the data are dominated by the contribution from the leading trajectory of intercept $\alpha(0) \gtrsim 1$. The most simple prediction of Regge phenomenology is that at fixed M_X the cross section should vary $\propto x_{I\!P}^{-n}$ where n is related to the intercept of the leading trajectory by $n = 2\alpha(t) - 1$.[1] The size of the rapidity gap is kinematically related to the value of $x_{I\!P}$ by $\Delta\eta \sim -\ln x_{I\!P}$ [8]. It is easy to show that at fixed M_X the rapidity gap distribution is then related to $\alpha(t)$ by:

$$\frac{\mathrm{d}N}{\mathrm{d}\Delta\eta} \propto (e^{-\Delta\eta})^{2-2\alpha(t)}. \tag{6}$$

Hence for $\alpha(t) < 1$ the production of large rapidity gaps is exponentially suppressed, whilst for $\alpha(t) > 1$ it is exponentially enhanced [9]. With $x_{I\!P}$ fixed, then extensions of the simple Regge model are necessary to predict the M_X dependence. For sufficiently large masses, it is perhaps possible to use Müller's extension of the optical theorem [10] ("Triple Regge") to achieve this aim, and for small masses the vector meson dominance model [11] may be appropriate.

There is much evidence from hadron–hadron data [7], and some from ep data [4] that additional ("sub-leading") trajectories are necessary to reproduce the measured hadronic cross sections. The Regge formalism permits t dependent interference between some of the different contributions rendering problematic any theoretical predictions for the dependence of the measured hadronic cross sections on M_X, $x_{I\!P}$, W^2 or t.

Estimates of the diffractive contribution to both deep-inelastic and photoproduction cross sections have been made using the M_X dependence at fixed W [2].

[1] It is worth pointing out that at $Q^2 > 0$ then $x_{I\!P}$ is the basic Regge variable, not W^2 as is sometimes assumed.

3 Future Measurements of $F_2^{D(3)}$

The 1994 H1 data [3, 4], corresponding to ~ 2 pb^{-1}, have allowed a measurement of $F_2^{D(3)}$ to be made in the kinematic region $2.5 < Q^2 < 65$ GeV^2, $0.01 < \beta < 0.9$ and $0.0001 < x_{I\!P} < 0.05$. For $Q^2 < 8.5$ GeV^2 this was achieved by taking data with the nominal interaction point shifted by +70 cm allowing lower angles to be covered by the backward electromagnetic calorimeter.

The dependence of $F_2^{D(3)}$ on $x_{I\!P}$ was found not to depend on Q^2 but to depend on β, demonstrating that the factorisation of the $\gamma^* p$ cross section into a universal diffractive flux (depending only on $x_{I\!P}$) and a structure function (depending only on β and Q^2) is not tenable. These deviations from factorisation were demonstrated to be consistent with an interpretation in which two individually factorisable components contribute to $F_2^{D(3)}$. These two components could be identified with pomeron ($I\!P$) and meson contributions $\propto x_{I\!P}^{-n_{I\!P}}, x_{I\!P}^{-n_M}$ where $n_{I\!P} = 1.29 \pm 0.03 \pm 0.07$ and $n_M = 0.3 \pm 0.3 \pm 0.6$. Scaling violations, positive with increasing $\log Q^2$ for all β, were observed and could be interpreted in terms of a large gluon component in the diffractive exchange, concentrated near $x_{g/I\!P} = 1$ at $Q^2 \sim 2.5$ GeV^2 [12, 13, 3, 4].

Given the significant progress in the understanding of diffractive dynamics that has been achieved with the existing data, the goal of future measurements is twofold: to extend the kinematic regime of existing measurement, and to achieve highest possible precision, particularly where existing measurements have uncovered interesting physics. In the 1994 measurement, with 5 bins per decade in both Q^2 and $x_{I\!P}$, and 7 bins in β between 0.01 and 0.9, then in the interval $8.5 < Q^2 < 65$ GeV^2 there were an average of ~ 100 events per bin, corresponding to a statistical accuracy of $\sim 10\%$[2]. The different sources of systematic error for the 1994 measurement are shown in table 1, along with an estimate of the level to which they may be reduced in the future. The largest single error arises from the combination of limited Monte Carlo statistics (10%) and different possible final state topologies leading to varying corrections for finite efficiency and resolution (10%). The latter contribution was estimated from the difference in the correction factors calculated for two possible $\gamma^* I\!P$ interaction mechanisms:

- a quark parton model process in which the γ^* couples directly to a massless quark in the exchange with zero transverse momentum,
- a boson–gluon fusion process in which the γ^* couples to a gluon in the diffractive exchange through a quark box.

Numerous experimental measurements of diffractive final state topologies at HERA are now available [4] which constrain the data to lie between these two possibilities. Therefore, it is reasonable to assume that the error arising from a lack of knowledge of the final state topologies may be reduced by a factor of ~ 2 such that it no longer dominates the total error. Monte Carlo statistics can obviously be increased. Therefore, it is reasonable that in the future a measurement may be made with a total systematic uncertainty of 5% or less. To reduce the statistical error to 5% (3%) would require 8 pb^{-1} (22 pb^{-1}) of data.

Less luminosity is required to achieve the same statistical precision at lower Q^2. However, to reach the lowest possible Q^2 with the widest possible range in x (and hence in $x_{I\!P}$) it

[2]The variation of the cross section with Q^2 of approximately Q^{-4} was partially offset by an increasing bin size with increasing Q^2.

H1 1994 Preliminary		H1 Future
Error Source	$\delta F_2^{D(3)}/F_2^{D(3)}$	$\delta F_2^{D(3)}/F_2^{D(3)}$
Main Calo' Hadronic E Scale: $\pm 5\%$	3%	$\lesssim 1\%$
Backward Calo' Hadronic E Scale: $\pm 15\%$	3%	$\lesssim 0.5\%$
Backward Calo' Elec. E Scale: $\pm 1.5\%$	5%	$\lesssim 3\%$
Tracking Momentum Scale $\pm 3\%$	2%	$\lesssim 1\%$
Scattered Lepton Angle: ± 1 mrad	2%	1%
t dependence: $e^{6 \pm 2t}$	1%	0.5%
$x_{I\!P}$ dependence: $x_{I\!P}^{n \pm 0.2}$	3%	1%
β dependence	3%	1%
$M_X/x_{I\!P}$ resolution	4%	2%
Background (photoproduction and non-ep)	0.1%	$< 0.1\%$
MC Statistics/Model Dependence	14%	4%

Table 1: Sources of systematic error for the H1 1994 Preliminary measurement of $F_2^{D(3)}$. The results of calculations to estimate the extent to which these uncertainties may be reduced are shown in the right hand column. These calculations take cognisance of the new SPACAL backward calorimeter installed by H1 [14], and rely upon future measurements made using the LPS and forward neutron calorimeter based upon a minimum luminosity of 10 pb^{-1}.

is advantageous to run with the interaction vertex shifted forwards along the proton beam direction. We calculate that 2 pb^{-1} of such data would give a statistical accuracy of 5% in the region of overlap between nominal and shifted vertex data, allowing a precise cross check of the two analyses. It is important to note that the HERA magnets are not optimised for a shifted vertex configuration, and so such data take twice as long to collect as for the nominal configuration.

Theoretically, and consequently experimentally, the region of high β is of particular interest. The evolution of $F_2^{D(3)}$ with Q^2 at high β is expected to depend crucially upon which evolution equations are pertinent to diffractive dynamics. In particular, a DGLAP [15] QCD analysis [13, 3, 4] demonstrates that the H1 data are consistent with a large gluon distribution, concentrated near $x_{g/I\!P} = 1$ at $Q^2 \sim 2.5 GeV^2$. In this case then $F_2^{D(3)}$ should begin to fall with increasing Q^2 at $\beta = 0.9$ for $Q^2 \gg 10$ GeV^2. The presence of a sufficiently large "direct" term in the evolution equations would lead to a indefinite increase with Q^2 [16]. Thus a measurement of $F_2^{D(3)}$ at high β to the highest possible Q^2 is desirable.

At fixed ep centre of mass energy $\sqrt{s}$ the range of β that may be accessed decreases with increasing Q^2 such that:

$$\beta > \frac{Q^2}{s x_{I\!P}^{max} y^{max}}. \qquad (7)$$

The acceptance for a measurement of $F_2^{D(3)}$ at $\beta = 0.9$, based upon the interval $0.8 < \beta < 1$, therefore extends to a maximum Q^2 of $\sim 3500 GeV^2$ for $x_{I\!P} < 0.05$, where the cross section is likely to be dominantly diffractive. To achieve 10% statistical precision in a measurement in the interval $2000 < Q^2 < 3500$ GeV^2 (bin centre $Q^2 = 2600$ GeV^2) would require ~ 200 pb^{-1}. However, a measurement of 30% statistical precision, requiring only ~ 20 pb^{-1}, would already be significant in light of theoretical calculations which differ by more than a factor of 2 in this region.

4 Measurement of $F_2^{D(4)}$

For particles with $E \ll E_P$ (here E_P is the proton beam energy) then the HERA magnets separate them from the proton beam allowing particles to be tagged for $t \sim t_{min}$. For particles with $E \sim E_P$ then only those particles with transverse momentum $P_T^2 \gtrsim 0.07\,\mathrm{GeV}^2$ may be tagged [18]. Consequently, for diffractive measurements then the acceptance in t is limited to $t \lesssim -P_T^2/(1-x_{I\!P}) = -0.07\,\mathrm{GeV}^2$. For a process with a highly peripheral t dependence then this limitation results in the loss of 30 to 40% of the total cross section. The geometrical acceptance of the current ZEUS detectors is $\sim 6\%$ [17], giving an overall acceptance in the region $x_{I\!P} < 0.05$ of $\sim 4\%$.

Tantalising first measurements of the t dependence of deep–inelastic events with a leading proton have been presented by the ZEUS collaboration [18]. The observed dependence on t of $\mathrm{d}\sigma/\mathrm{d}t \propto e^{bt}$, $b = 5.9 \pm 1.2^{+1.1}_{-0.7}\,\mathrm{GeV}^{-2}$, lends strong support to a diffractive interpretation of such interactions. The measurements of b differential in $x_{I\!P}$, β and Q^2 that will be possible with increased luminosity are eagerly awaited.

A preliminary measurement $F_2^{D(3)}$ using an LPS has also been made [19]. In order to use measurements of $F_2^{D(4)}$ to estimate $F_2^{D(3)} = \int_{t_{min}}^{t_{max}} \mathrm{d}t\, F_2^{D(4)}$ it is necessary to extrapolate from the measured region at high $|t|$ into the region of no acceptance to t_{min}. To make this extrapolation with the minimal assumptions about the t dependence, it is necessary to have at least three bins in t for each bin in β, Q^2 and $x_{I\!P}$. This means that $\sim 150\,\mathrm{pb}^{-1}$ of data are required to make a measurement of similar accuracy to the existing data for $F_2^{D(3)}$. Obviously it would be possible to study the t dependence in aggregate volumes of phase space and make a measurements with a factor 3 fewer statistics, relying upon model assumptions about the variation of the t dependence with β, Q^2 and $x_{I\!P}$. Even with $150\,\mathrm{pb}^{-1}$ of data, the extrapolation into the t region of no acceptance relies on the assumption that the t dependence is the same in the measured and unmeasured regions. It is not clear that the resultant theoretical uncertainty will be less than the 5% uncertainty in the overall normalisation resulting from proton dissociation for existing measurements of $F_2^{D(3)}$.

The primary purpose of the LPS is the diffractive "holy grail" of measuring $F_2^{D(4)}(\beta, Q^2, x_{I\!P}, t)$. Measurements of any possible "shrinkage" of the forward diffractive scattering amplitude (increasing peripherality of the t dependence with decreasing $x_{I\!P}$) are likely to have unique power for discriminating between different theoretical models of diffractive dynamics [5]. In addition, the ability to select subsamples of events in which there is an additional hard scale at the proton vertex is of great theoretical interest [5]. It is therefore of the utmost importance that the 100 to $150\,\mathrm{pb}^{-1}$ of data necessary to make an accurate measurement of $F_2^{D(4)}(\beta, Q^2, x_{I\!P}, t)$ are collected by both collaborations with the LPS devices fully installed.

The LPS also allows measurements at higher $x_{I\!P}$ for which the rapidity gap between the photon and proton remnant systems X and Y becomes too small to observe in the main calorimeter. This will allow the contributions to the measured hadronic cross section from subleading trajectories to be further investigated. Combining information from the scattered lepton and proton will allow the invariant mass M_X to be reconstructed in the region $x_{I\!P} \gg 0.05$, where it would otherwise be impossible.

Tagged particles with $E \ll E_P^{beam}$ will provide information about the way in which protons dissociate into higher mass systems. Particles thus produced are kinematically unlikely to generate a significant background in the region $x_{I\!P} < 0.05$, but for larger $x_{I\!P}$ then this background will become increasingly important.

5 On the Determination of $F_L^{I\!P}$

A fundamental question in the study of hard diffractive processes is the extent to which perturbative QCD dynamics may be factorised from the proton vertex. Some recent calculations of diffractive cross sections [20, 21] consider the interaction in terms of a hard (perturbative) phase producing a coloured partonic system which subsequently interacts with the colour field of the proton via the exchange of non-perturbative gluons. Such "soft colour interactions" [21] allow colour to be exchanged between the photon and proton remnant systems such that in some fraction of the events both will become colour singlet states separated by a potentially large rapidity gap. In such models the evolution of the effective parton distribution functions (PDFs) will be driven by the evolution of the PDFs of the proton. Alternatively, it is possible that the presence of a large rapidity gap will confine any evolution dynamics to within the photon remnant system X. The effective PDFs will then depend only upon β and Q^2, and not upon $x_{I\!P}$ as in the former case.

The 1994 H1 data have been demonstrated to be consistent with a factorisable approach in which a large gluon distribution is attributed to the pomeron in the region $x_{I\!P} < 0.01$ or over the whole kinematic range for the sum of two individually factorisable components [4]. At next to leading order (NLO) then a large gluon distribution $G^{I\!P}(\beta, Q^2)$ necessitates a large longitudinal structure function, $F_L^{I\!P}(\beta, Q^2)$:

$$F_L^{I\!P}(\beta, Q^2) = \frac{\alpha_s(Q^2)}{4\pi} \cdot \beta^2 \int_\beta^1 \frac{\mathrm{d}\xi}{\xi^3} \left[\frac{16}{3} F_2^{I\!P}(\xi, Q^2) + 8 \sum_i e_i^2 (1 - \frac{\beta}{\xi})\, \xi G^{I\!P}(\xi, Q^2) \right]. \qquad (8)$$

A prediction for $F_L(\beta, Q^2)$ based upon a NLO QCD analysis of the data could be tested directly since the wide range in $x_{I\!P}$ accessible at HERA leads to a wide variation in the $e I\!P$ centre of mass energy $\sqrt{s_{e I\!P}} = \sqrt{x_{I\!P} s}$. This means that in factorisable models, at fixed β and fixed Q^2 the same partonic structure of the pomeron may be probed at different values of $x_{I\!P}$, corresponding to different values of y:

$$y = \frac{Q^2}{s\beta} \cdot \frac{1}{x_{I\!P}}. \qquad (9)$$

If the dependence of the diffractive structure function can be factorised such that

$$F_2^{D(3)}(\beta, Q^2, x_{I\!P}) = f(x_{I\!P}) F_2^{I\!P}(\beta, Q^2) \qquad (10)$$

and $F_L^{I\!P}$ is non-zero, then a measurement of $F_2^{D(3)}$ assuming $F_L^{I\!P}$=0 is lower than the correct value of $F_2^{D(3)}$ by the factor $\delta(y, \beta, Q^2)$:

$$\delta = \frac{F_2^{D(3)}(Measured)}{F_2^{D(3)}(True)} = \frac{2(1-y) + y^2/[1 + R^{I\!P}(\beta, Q^2)]}{2(1-y) + y^2} \qquad (11)$$

Thus under the assumption of factorisation, a measurement of $F_L^{I\!P}(\beta, Q^2)$ is possible by measuring the extent of the deviation from a simple $x_{I\!P}^{-n}$ extrapolation from higher $x_{I\!P}$. The size of this effect is shown for different values of $R^{I\!P} = F_L^{I\!P}/(F_2^{I\!P} - F_L^{I\!P})$ in figure 2. Also shown is the range covered by the existing 1994 data and the range that could be covered by future

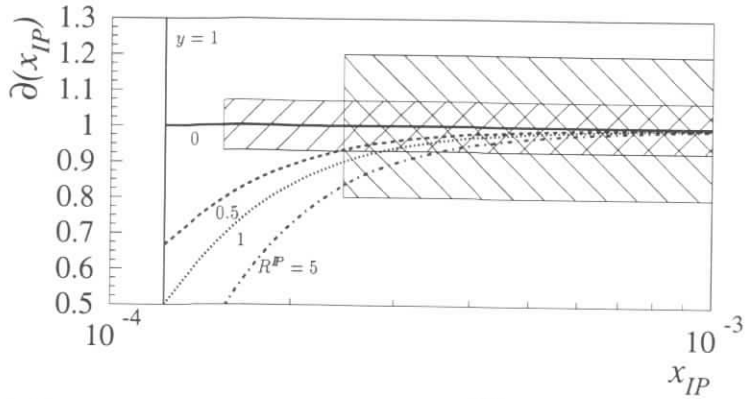

Figure 2: The expected fractional deviation $\delta(x_{I\!P})$ of $F_2^{D(3)}$ from an extrapolation from high $x_{I\!P}$ for $R^{D} = 0$ (horizontal solid line), $R^{D} = 0.5$ (dashed line), $R^{D} = 1.0$ (dotted line) and $R^{D} = 5.0$ (dash-dotted line) for $Q^2 = 10\,\mathrm{GeV}^2$, $\beta = 0.5$. The vertical solid line indicates the kinematic limit of $y = 1$. The larger box indicates the area covered by the preliminary 1994 H1 measurements, which extended up to $y \sim 0.5$ with an accuracy of $\sim 20\%$. The smaller box represents a future measurement with a total error of 7% extending to $y = 0.8$.

measurements at HERA. It is clear that in order to see this effect it is necessary to make a measurement at y values above 0.7 with a total error of less than 10%. For high values of β the extrapolation of $F_2^{D(3)}$ into the high y region of interest should not be significantly compromised by the possible presence of subleading trajectories, which contribute only at high $x_{I\!P}$ (low y).

A comparison between the values of F_L^{D} determined from such apparent deviations from factorisation and the values expected from a QCD analysis of $F_2^{D(3)}$ constitutes a powerful test of both the validity of factorisation and the applicability of NLO QCD to diffraction at high Q^2.

6 Measurements of $R^{D(3)}$ and $R^{D(4)}$

Since an evaluation of F_L^{D} using the techniques described in the previous section require theoretical assumptions concerning factorisation, such an analysis is clearly no substitute for a direct measurement of the ratio of the longitudinal to transverse diffractive cross sections, $R^{D}(x_{I\!P}, \beta)$. A good measurement of this quantity is vital for a full understanding of the diffractive mechanism and should provide an exciting testing ground for QCD. There is at present no theoretical consensus on what values to expect for R^{D}, although all models suggest a substantial dependence on β with most suggesting an extreme rise as $\beta \to 1$ [5]. A measurement of R^{D} to any precision leads us into unexplored territory.

Measurements of R^{D} have so far been restricted to DIS exclusive vector mesons production [22] by a direct measurement of the polarisation of the final state resonance. This method could perhaps be used for the bulk data if the directions of the final state partons could be inferred, but is likely to be difficult due to the problems of running jet analyses on low mass final states. Instead we investigate a slightly modified version of the method used to determine $R(x, Q^2)$ for inclusive DIS [23].

The general form relating the structure functions F_2^{D} and F_1^{D} to the ep differential diffractive cross section can be written in analogy to the inclusive cross sections [24].

$$\frac{\mathrm{d}^4\sigma_{ep}^{D}}{\mathrm{d}x_{I\!P}\,\mathrm{d}t\,\mathrm{d}x\,\mathrm{d}Q^2} = \frac{4\pi\alpha^2}{xQ^4}\left(1 - y + \frac{y^2}{2(1 + R^{D(4)}(x, Q^2, x_{I\!P}, t))}\right) F_2^{D(4)}(x, Q^2, x_{I\!P}, t), \qquad (12)$$

where $R^{D(4)} = (F_2^{D(4)} - 2xF_1^{D(4)})/(2xF_1^{D(4)}) = \sigma_L^{D}/\sigma_T^{D}$. Although a measurement of $R^{D(4)}$ as a function of all 4 variables is the most desirable measurement and must be an experimental goal, statistical limitations are likely to mean that initial measurements must be made without a reliance on a leading proton spectrometer (LPS) and so t is not measured. In this case we define $F_2^{D(3)}$ and $R^{D(3)}$ as

$$\frac{\mathrm{d}^3\sigma_{ep}^{D}}{\mathrm{d}x_{I\!P}\,\mathrm{d}x\,\mathrm{d}Q^2} = \frac{4\pi\alpha^2}{xQ^4}\left(1 - y + \frac{y^2}{2(1 + R^{D(3)}(x, Q^2, x_{I\!P}))}\right) F_2^{D(3)}(x, Q^2, x_{I\!P}), \qquad (13)$$

In this case $R^{D(3)}$ is the ratio of the longitudinal to transverse cross section only if $R^{D(4)}$ has no dependence on t.

Analysis of equation 13 reveals that in order to make a measurement of R^{D} independent of F_2^{D} at least two ep cross sections must be compared at the same values of x, Q^2 and $x_{I\!P}$ but different values of y. This is achieved by varying the ep centre of mass energy, $\sqrt{s}$. There are of course many possible running scenarios for which either or both beam energies are changed to a variety of possible values. A full discussion on this point is given in [23]. For the present study we examine the case when the proton beam is roughly halved in energy from 820 GeV to 500 GeV and the electron beam remains at a constant energy of 27.5 GeV so that data is taken at the 2 values of s of $s = 90200\ \mathrm{GeV}^2$ and $s = 55000\ \mathrm{GeV}^2$. This setup allows for a reasonable luminosity at the low proton beam energy and enables systematic uncertainties concerned with detection of the scattered electron to be minimised. In this scheme we make a measurement of the ratio of the ep differential cross sections, $r = \sigma_{hi}^{D}/\sigma_{lo}^{D}$, for two values of y, y_{hi} and y_{lo} (corresponding to the high and low values of s) for fixed x, Q^2, $x_{I\!P}$ and (if measuring $R^{D(4)}$) t. Equation 12 or 13 is then used to determine R^{D}.

It is also apparent from equation 13 that in order to have the greatest sensitivity to R^{D} measurements must be made at the highest y_{lo} possible (and thus lowest electron energy). This is illustrated in figure 3, where it can be seen that for values of $y_{lo} = 0.5$ (or lower) there is little change of r for different values of R^{D}. The upper limit in y_{lo} is crucially dependent on the ability of the detectors to discriminate and veto against photoproduction events in which a pion is misidentified as an electron. Experience has shown, however, that for the diffractive events the low mass of the final state reduces the chance of faking electron when compared to the more energetic non-diffractive events. For this study we take a central value of $y_{lo} = 0.8$ with a lower (upper) bin limit of 0.75 (0.85) so that good electron identification for energies above 4.15 GeV is assumed.

The kinematic range of the measurement projected onto the x–Q^2 plane is shown in figure 4 for both CMS energies. To ensure that the scattered electrons are well contained within the backward detectors we place a maximum θ_e cut of 174°. This restricts us to $Q^2 > 5\ \mathrm{GeV}^2$ and $x > 10^{-4}$. In order to ensure good acceptance in the forward region we impose a cut of $x_{I\!P} < 0.01$.

For low electron energies the kinematic variables are well reconstructed and have good resolutions if the electron only method is used [25, 26]. Since the major problem with this

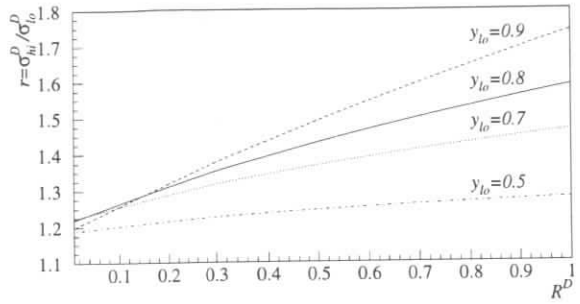

Figure 3: Dependence of the ratio, r, of the ep cross sections at $s = 90200$ and $s = 55000$ with R^D for various values of y at $s = 55000$.

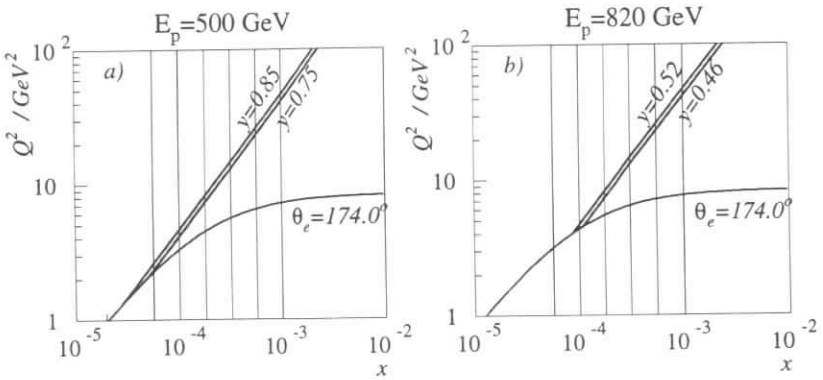

Figure 4: A projection of the kinematic range onto the x–Q^2 plane for a) a proton beam of $E_p = 500$ GeV and b) a proton beam of $E_p = 820$ GeV for an electron beam of 27.5 GeV. The shaded region represents the proposed region of study. Also shown is the restriction on the kinematic range imposed by a maximum θ_e cut of 174°.

measurement will be in reducing the statistical error we select bins as large as possible whilst maintaining enough bins to investigate any variation of R^D with the kinematic quantities. A suitable choice would be 4 bins per decade in x, 4 bins in β and if the LPS is used 2 bins in t. The bins in β and t are optimised so as to contain approximately equal numbers of events at each x value. Identical bins in these variables are used for both CMS energies.

In order to estimate the statistical errors on the measurement we used the RAPGAP gen-

$\log_{10} x$	Number of Events without LPS		Number of Events with LPS	
	$E_P = 820$ GeV	$E_P = 500$ GeV	$E_P = 820$ GeV	$E_P = 500$ GeV
-4.125	41	28	0.82	0.56
-3.875	36	25	0.72	0.50
-3.625	19	13	0.38	0.27
-3.375	9	6	0.18	0.12

Table 2: The estimated number of events in each bin for an integrated luminosity of 1 pb^{-1} for the 2 proton beam energies and an electron beam energy of 27.5 GeV, assuming 4 bins per decade in x, 4 bins in β and (for measurements with the LPS) 2 bins in t. R^D was set to 0.5.

erator [27] with a fit to the measured H1 $F_2^{D(3)}$ [3] at $s = 90200$ GeV^2 and used equation 12 to determine the statistics at $s = 55000$ GeV^2. We assumed 100% efficiency for measurements made without any LPS and 4% efficiency for those with. The expected number of events per integrated luminosity in each bin is summarised in table 2 for an example $R^D = 0.5$.

For systematic errors we estimate an error of $\delta(r)/r$ of 5%. This error is conservatively evaluated by taking the estimated error on F_2^D (see above) and assuming any improvement that arises from taking a ratio is offset by increased uncertainty in the photoproduction background and radiative corrections.

An example of the sort of precision which may be obtained for a measurement of $R^{D(3)}$ and $R^{D(4)}$ is shown in figure 5. For this study we assumed that many more data would be obtained at the high CMS energy. It can be seen that for an integrated luminosity of 10 pb^{-1} at the lower s value a measurement of $R^{D(3)}$ is statistically dominated with an error around 60% if $R^{D(3)} = 0.5$ for the lowest value of x. For an integrated luminosity of 50 pb^{-1} at the lower s value statistical and systematic errors become comparable and $R^{D(3)}$ can be measured to 40% accuracy. For measurements of $R^{D(4)}$ very high integrated luminosities are required – at least a factor of 50 is needed for a similar precision to $R^{D(3)}$.

7 Measuring $F_2^D{}_{charm}$

Since the leading mechanism in QCD for the production of charm quarks is the boson gluon fusion process, the diffractive charm structure function $F_{2\,charm}^D$ is very sensitive to the gluonic component of the diffractive exchange. It is important to establish whether the measured $F_{2\,charm}^D$ is consistent with that expected from a QCD analysis of the scaling violations in $F_2^{D(3)}$. In addition, it has already been observed in the photoproduction of J/ψ mesons that the charm quark mass provides a sufficiently large scale to generate the onset of hard QCD dynamics. The extend to which the charm component of $F_2^{D(3)}$ exhibits a different energy ($x_{I\!P}$) dependence to that of the total will provide insight into the fundamental dynamics of diffraction.

The method used here for tagging charm events uses the D^{*+} decay[3] $D^{*+} \to D^0\pi^+_{slow} \to (K^-\pi^+)\pi^+_{slow}$. The tight kinematic constraint imposed by the small difference between the D^{*+}

[3]Charge conjugate states are henceforth implicitly included.

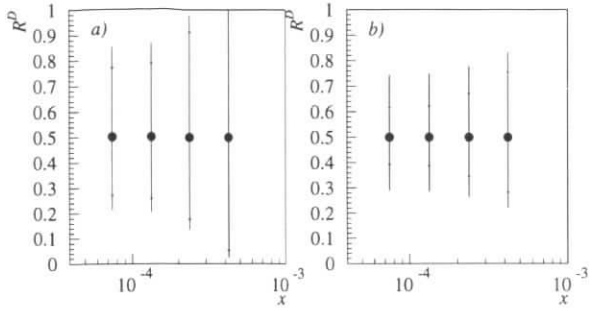

Figure 5: The estimated errors for an example central value of $R^D = 0.5$ for a) 10(500) pb^{-1} at $s = 55000$ GeV^2 and 50(2500) pb^{-1} at $s = 90200$ GeV^2 and b) 50(2500) pb^{-1} at $s = 55000$ GeV^2 and 250(12500) pb^{-1} at $s = 90200$ GeV^2 for a measurement of $R^{D(3)}$ ($R^{D(4)}$). The inner error bar represents the statistical error and the outer the statistical and systematic error added in quadrature.

and D^0 masses means that the mass difference $\Delta M = M(K\pi\pi_{slow}) - M(K\pi)$ is better resolved than the individual masses, and the narrow peak in ΔM provides a clear signature for D^{*+} production. The chosen D^0 decay mode is the easiest to use because it involves only charged tracks and because the low multiplicity means that the combinatorial background is small and that the inefficiency of the tracker does not cause a major problem.

A prediction of the observed number of events is obtained using RAPGAP with a hard gluon dominated pomeron structure function taken from a QCD analysis of $F_2^{D(3)}$ [3]. The cross section predicted by this model for $D^{*\pm}$ production in diffractive DIS is compatible with the value measured in [4]. The acceptance of the detector is simulated by applying cuts on the generated direction (θ) and transverse momentum ($p_\perp$) of the decay products and on the energy of the scattered lepton (E'_e). The $p_\perp$ cut used is 150 MeV, which is approximately the value at which the H1 central and forward trackers reach full efficiency. This cut has a major influence on the acceptance for D^{*+} mesons, because the momentum of the slow pion π_{slow} is strongly correlated with that of the D^{*+}, so a D^{*+} with $p_\perp$ much less than 150 MeV$\times M_{D^{*+}}/M_{\pi^+} \approx 2$ GeV cannot be detected. The $p_\perp$-dependence of the acceptance is shown in figure 6a. There is no obvious way of extending the tracker acceptance to lower $p_\perp$, so this cut is not varied.

Figure 6b shows the average acceptance for a D^{*+} over the region 10 GeV^2 < Q^2 < 100 GeV^2 and all values of β and for $p_\perp > 2$ GeV. It can be seen that extending the angular coverage from the present $25 < \theta < 155°$ range in the backward direction to 170° in conjunction with lowering the scattered lepton energy cut used in present analyses significantly improves the acceptance, especially at low $x_{I\!P}$. Figure 7 shows the number of $D^{*\pm}$ which one might expect to detect in the low- and high-Q^2 regions with a total integrated luminosity of 750 pb^{-1}. It can

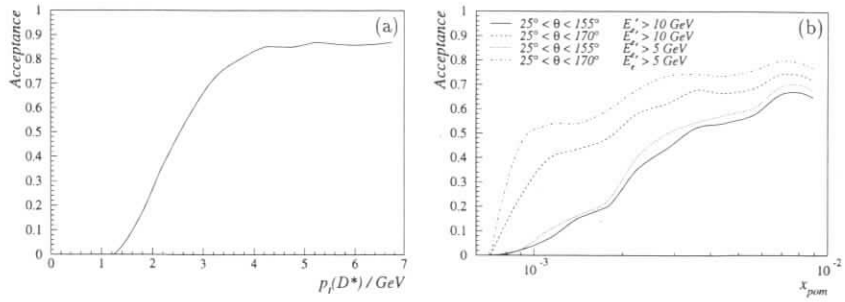

Figure 6: The acceptance for D^{*+} in the region 10 GeV^2 < Q^2 < 100 GeV^2, shown as a function of (a) $p_\perp$ and (b) $x_{I\!P}$. The continuous line in (b) shows the results with central tracking only and a requirement $E'_e > 10$ GeV. The other lines show the effect of extending track coverage in the backward direction and including E'_e down to 5 GeV.

be seen that even with this large integrated luminosity, cross section measurements can only be made with an accuracy of 10% in this binning.

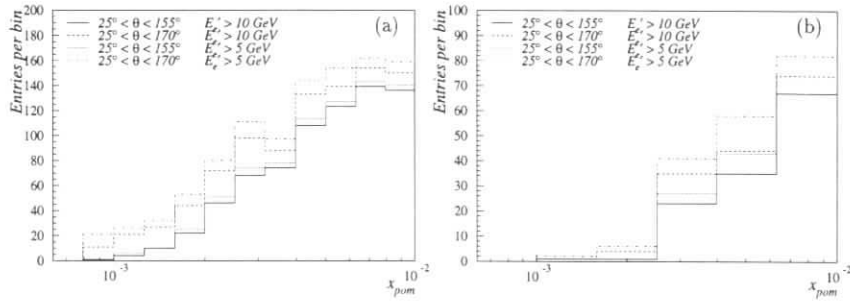

Figure 7: The number of $D^{*\pm}$ expected to be observed in 750 pb^{-1} in the range (a) 10 GeV^2 < Q^2 < 25 GeV^2 and (b) 50 GeV^2 < Q^2 < 100 GeV^2, predicted using RAPGAP with a hard-gluon-dominated pomeron.

Whilst one waits for 750 pb^{-1}, it may be worthwhile attempting to increase the statistics by investigating other decay modes which are experimentally more demanding. The D^{*+} decay to $D^0\pi^+_{slow}$ has a branching fraction of nearly 70% [28] and is the only decay mode giving a charged track in addition to the D^0 decay products. However, the D^0 decay to $K^-\pi^+$ has a branching fraction of slightly less than 4% [28], so there is clearly room for a large improvement in statistics if other channels can be used. For example the use of a silicon vertex detector close to the interaction point, such as that already partly installed in H1, should enable the secondary vertex from the decay of the D^0, which has a decay length $c\tau = 124$ μm [28], to be tagged. This could be used to extend the analysis to other channels, including semileptonic decays, which are otherwise difficult to use. The gain in statistics, neglecting the vertex-tagging inefficiency, can be up to a factor of ~ 20 (if all channels are used), with a further factor of ~ 2 available if inclusive D^0 production is used rather than relying on the D^{*+} decay.

8 Summary and Conclusions

We have argued that a precise hadron level definition of the cross section to be measured is essential in order that future high precision measurements of diffractive structure functions may be treated in a consistent theoretical manner. Although $20\,\mathrm{pb}^{-1}$ of integrated luminosity will be enough to achieve precision in the measurement of $F_2^{D(3)}$ at moderate Q^2, in excess of $100\,\mathrm{pb}^{-1}$ is necessary to make a comprehensive survey of diffractive structure within the kinematic limits of HERA. An attempt to determine $F_L^{\boldsymbol{P}}$ will be an important tool in establishing the validity of both factorisation and NLO QCD in diffractive interactions. A direct measurement of $R^{D(3)}$ is shown to be feasible with $10\,\mathrm{pb}^{-1}$ of integrated luminosity taken at lower proton beam energy. A substantial integrated luminosity is demonstrated to be necessary to complete an exhaustive study of the diffractive production of open charm, although statistics can be markedly improved by exploiting the full range of possible charm decays.

References

[1] H1 Collaboration, T. Ahmed et al., Phys. Lett. **B348**(1995) 681-696.
ZEUS Collaboration, M. Derrick et al. , Z. f. Physik **C68**(1995).

[2] ZEUS Collaboration, M. Derrick et al. , Z. f. Physik **C70**(1996).

[3] A. Mehta, Proceedings of the Topical Conference on Hard Diffractive Processes, Eilat, Israel, February 1996.
P. Newman, Proceedings of the International Workshop on Deep–Inelastic Scattering and Related Phenomena, Rome, Italy, April 1996, DESY-96-162.

[4] J. Phillips, Proceedings of the *XXVIII* International Conference on High Energy Physics, Warsaw, Poland, July 1996. See also contributed papers **pa02-061**, **pa02-060**, **pa02-063** and **pa02-068**.

[5] M. McDermott, G. Briskin, *Diffractive Structure Functions in DIS*, these proceedings, and references therein.

[6] A. R. White, "The Hard Gluon Component of the QCD Pomeron", hep-ph/9609282.

[7] A. Kaidalov, Phys. Rep. **50**(1979) 157.
G. Alberi, G. Goggi, Phys. Rep. **74** (1981) 1.
K. Goulianos, Phys. Rep. **101** (1983) 169.
N. Zotov, V. Tsarev, Sov. Phys. Usp. **31**(1988) 119.

[8] E. L. Berger et al. , Nucl. Phys. **B286**(1987) 704.

[9] J. D. Bjorken, "Hadronic Final States in Deep–Inelastic Processes", in "Current Induced Reactions: International Summer Institute in Theoretical Particle Physics in Hamburg 1975", ed. J. G. Kröner, G. Kramer, and D. Schildknecht, Lecture Notes in Physics, Springer Verlag 1976.

[10] A. Müller, Phys. Rev. **D2** (1970) 2963.

[11] J. J. Sakurai, Phys. Rev. Lett. **22** (1969) 981
J. J. Sakurai and D. Schildknecht, Phys. Lett. **40B** (1972) 121,
T. H. Bauer, R. D. Spital, D. R. Yennie, F. M. Pipkin, Rev. Mod. Phys. **50** (1978) 261.

[12] K. Golec–Biernat and J. Kwiecinski, Phys. Lett. **B353**.

[13] J. Dainton and J. Phillips, Proceedings of the Workshop on Deep-Inelastic Scattering and QCD, Paris, France, April 24-28 1995.

[14] H1 SpaCal Group, T. Nicholls et al., DESY preprint 95-165 (1995) and DESY preprint 96-013 (1996).

[15] Yu. L. Dokshitzer, JETP **46** (1977) 641.
V. N. Gribov and L. N. Lipatov, Sov. Journ. Nucl. Phys. **15** (1972) 78.
G. Altarelli and G. Parisi, Nucl. Phys. **B126** 1977 298.

[16] T. Gerhmann and W. Stirling, Z. Phys **C70**, 89 (1996).

[17] E. Gallo, M. Grothe, C. Peroni, J. Rahn, R. Sacchi, A. Solano, these proceedings.

[18] G. Wolf, Proceedings of the Topical Conference on Hard Diffractive Processes, Eilat, Israel, February 1996.

[19] E. Barberis, Proceedings of the International Workshop on Deep–Inelastic Scattering and Related Phenomena, Rome, Italy, April 1996.

[20] W. Buchmüller and A. Hebecker, Phys. Lett. **B355**, 573 (1995),
W. Buchmüller and A. Hebecker, hep-ph/9512329 (1995),
W. Buchmüller, M. F. McDermott, and A. Hebecker, DESY preprint 96-126 (1996).

[21] A. Edin, J. Rathsman and G. Ingelman, Phys. Lett. **B366**, 371 (1996),
A. Edin, J. Rathsman and G. Ingelman, DESY-96-060 (1996).

[22] ZEUS Collaboration, M. Derrick et al. , Physics Letters B 356 (1995) 601-616,
H1 Collaboration, S. Aid et al. , Nucl.Phys. **B463** (1996) 3.

[23] L. Bauerdick et al. , "F_L: Experiment and Theory", these proceedings.

[24] G. Ingelman and K. Janson–Prytz, "The Pomeron Structure Function and QCD at Small–x", in Proceedings of the Workshop "Physics at HERA", p. 233, October 1991, ed. W. Buchmüller and G. Ingelman,
G. Ingelman and K. Prytz, Zeit. Phys. **C58** (1993) 285.

[25] H1 Collaboration, S. Aid et al. , Nucl. Phys. **B470** (1996) 3.

[26] ZEUS Collaboration, M. Derrick et al. , DESY 96-076 (1996).

[27] H. Jung, Comp. Phys. Comm.**86** (1995) 147,
H. Jung, RAPGAP 2.2 Program Manual, to appear in Comp. Phys. Comm.

[28] R. M. Barnett et al. (Particle Data Group): Phys. Rev. D54 1 (1996).

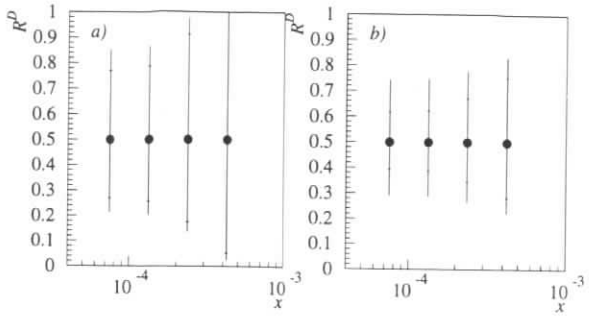

Figure 5: The estimated errors for an example central value of $R^D = 0.5$ for a) 10(500) pb^{-1} at $s = 55000$ GeV^2 and 50(2500) pb^{-1} at $s = 90200$ GeV^2 and b) 50(2500) pb^{-1} at $s = 55000$ GeV^2 and 250(12500) pb^{-1} at $s = 90200$ GeV^2 for a measurement of $R^{D(3)}$ ($R^{D(4)}$). The inner error bar represents the statistical error and the outer the statistical and systematic error added in quadrature.

and D^0 masses means that the mass difference $\Delta M = M(K\pi\pi_{slow}) - M(K\pi)$ is better resolved than the individual masses, and the narrow peak in ΔM provides a clear signature for D^{*+} production. The chosen D^0 decay mode is the easiest to use because it involves only charged tracks and because the low multiplicity means that the combinatorial background is small and that the inefficiency of the tracker does not cause a major problem.

A prediction of the observed number of events is obtained using RAPGAP with a hard gluon dominated pomeron structure function taken from a QCD analysis of $F_2^{D(3)}$ [3]. The cross section predicted by this model for $D^{*\pm}$ production in diffractive DIS is compatible with the value measured in [4]. The acceptance of the detector is simulated by applying cuts on the generated direction (θ) and transverse momentum ($p_\perp$) of the decay products and on the energy of the scattered lepton (E'_e). The $p_\perp$ cut used is 150 MeV, which is approximately the value at which the H1 central and forward trackers reach full efficiency. This cut has a major influence on the acceptance for D^{*+} mesons, because the momentum of the slow pion π_{slow} is strongly correlated with that of the D^{*+}, so a D^{*+} with $p_\perp$ much less than 150 MeV$\times M_{D^{*+}}/M_{\pi^+} \approx 2$ GeV cannot be detected. The $p_\perp$-dependence of the acceptance is shown in figure 6a. There is no obvious way of extending the tracker acceptance to lower $p_\perp$, so this cut is not varied.

Figure 6b shows the average acceptance for a D^{*+} over the region 10 GeV^2 < Q^2 < 100 GeV^2 and all values of β and for $p_\perp > 2$ GeV. It can be seen that extending the angular coverage from the present $25 < \theta < 155°$ range in the backward direction to 170° in conjunction with lowering the scattered lepton energy cut used in present analyses significantly improves the acceptance, especially at low $x_{I\!P}$. Figure 7 shows the number of $D^{*\pm}$ which one might expect to detect in the low- and high-Q^2 regions with a total integrated luminosity of 750 pb^{-1}. It can

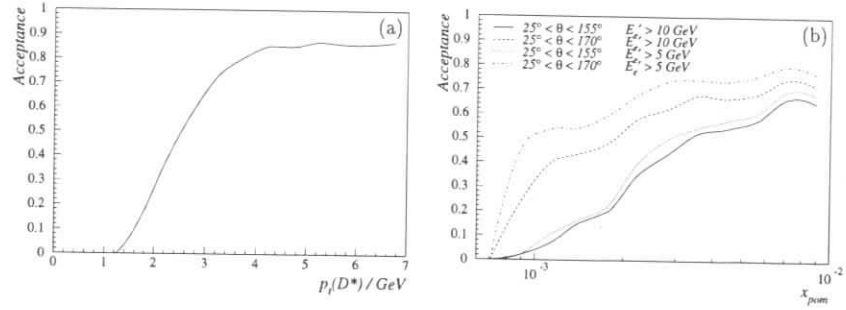

Figure 6: The acceptance for D^{*+} in the region 10 GeV^2 < Q^2 < 100 GeV^2, shown as a function of (a) $p_\perp$ and (b) $x_{I\!P}$. The continuous line in (b) shows the results with central tracking only and a requirement $E'_e > 10$ GeV. The other lines show the effect of extending track coverage in the backward direction and including E'_e down to 5 GeV.

be seen that even with this large integrated luminosity, cross section measurements can only be made with an accuracy of 10% in this binning.

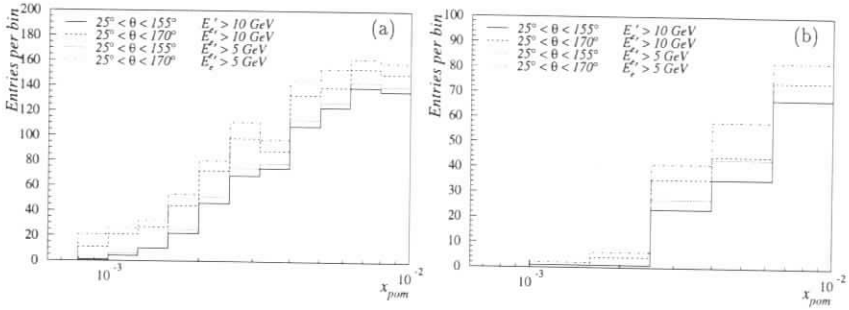

Figure 7: The number of $D^{*\pm}$ expected to be observed in 750 pb^{-1} in the range (a) 10 GeV^2 < Q^2 < 25 GeV^2 and (b) 50 GeV^2 < Q^2 < 100 GeV^2, predicted using RAPGAP with a hard-gluon-dominated pomeron.

Whilst one waits for 750 pb^{-1}, it may be worthwhile attempting to increase the statistics by investigating other decay modes which are experimentally more demanding. The D^{*+} decay to $D^0\pi^+_{slow}$ has a branching fraction of nearly 70% [28] and is the only decay mode giving a charged track in addition to the D^0 decay products. However, the D^0 decay to $K^-\pi^+$ has a branching fraction of slightly less than 4% [28], so there is clearly room for a large improvement in statistics if other channels can be used. For example the use of a silicon vertex detector close to the interaction point, such as that already partly installed in H1, should enable the secondary vertex from the decay of the D^0, which has a decay length $c\tau = 124$ μm [28], to be tagged. This could be used to extend the analysis to other channels, including semileptonic decays, which are otherwise difficult to use. The gain in statistics, neglecting the vertex-tagging inefficiency, can be up to a factor of ~ 20 (if all channels are used), with a further factor of ~ 2 available if inclusive D^0 production is used rather than relying on the D^{*+} decay.

8 Summary and Conclusions

We have argued that a precise hadron level definition of the cross section to be measured is essential in order that future high precision measurements of diffractive structure functions may be treated in a consistent theoretical manner. Although $20\,\mathrm{pb}^{-1}$ of integrated luminosity will be enough to achieve precision in the measurement of $F_2^{D(3)}$ at moderate Q^2, in excess of $100\,\mathrm{pb}^{-1}$ is necessary to make a comprehensive survey of diffractive structure within the kinematic limits of HERA. An attempt to determine $F_L^{\boldsymbol{P}}$ will be an important tool in establishing the validity of both factorisation and NLO QCD in diffractive interactions. A direct measurement of $R^{D(3)}$ is shown to be feasible with $10\,\mathrm{pb}^{-1}$ of integrated luminosity taken at lower proton beam energy. A substantial integrated luminosity is demonstrated to be necessary to complete an exhaustive study of the diffractive production of open charm, although statistics can be markedly improved by exploiting the full range of possible charm decays.

References

[1] H1 Collaboration, T. Ahmed et al., Phys. Lett. **B348**(1995) 681-696.
ZEUS Collaboration, M. Derrick et al. , Z. f. Physik **C68**(1995).

[2] ZEUS Collaboration, M. Derrick et al. , Z. f. Physik **C70**(1996).

[3] A. Mehta, Proceedings of the Topical Conference on Hard Diffractive Processes, Eilat, Israel, February 1996.
P. Newman, Proceedings of the International Workshop on Deep–Inelastic Scattering and Related Phenomena, Rome, Italy, April 1996, DESY-96-162.

[4] J. Phillips, Proceedings of the *XXVIII* International Conference on High Energy Physics, Warsaw, Poland, July 1996. See also contributed papers **pa02-061**, **pa02-060**, **pa02-063** and **pa02-068**.

[5] M. McDermott, G. Briskin, *Diffractive Structure Functions in DIS*, these proceedings, and references therein.

[6] A. R. White, "The Hard Gluon Component of the QCD Pomeron", hep-ph/9609282.

[7] A. Kaidalov, Phys. Rep. **50**(1979) 157.
G. Alberi, G. Goggi, Phys. Rep. **74** (1981) 1.
K. Goulianos, Phys. Rep. **101** (1983) 169.
N. Zotov, V. Tsarev, Sov. Phys. Usp. **31**(1988) 119.

[8] E. L. Berger et al. , Nucl. Phys. **B286**(1987) 704.

[9] J. D. Bjorken, "Hadronic Final States in Deep–Inelastic Processes", in "Current Induced Reactions: International Summer Institute in Theoretical Particle Physics in Hamburg 1975", ed. J. G. Kröner, G. Kramer, and D. Schildknecht, Lecture Notes in Physics, Springer Verlag 1976.

[10] A. Müller, Phys. Rev. **D2** (1970) 2963.

[11] J. J. Sakurai, Phys. Rev. Lett. **22** (1969) 981
J. J. Sakurai and D. Schildknecht, Phys. Lett. **40B** (1972) 121,
T. H. Bauer, R. D. Spital, D. R. Yennie, F. M. Pipkin, Rev. Mod. Phys. **50** (1978) 261.

[12] K. Golec–Biernat and J. Kwiecinski, Phys. Lett. **B353**.

[13] J. Dainton and J. Phillips, Proceedings of the Workshop on Deep-Inelastic Scattering and QCD, Paris, France, April 24-28 1995.

[14] H1 SpaCal Group, T. Nicholls et al., DESY preprint 95-165 (1995) and DESY preprint 96-013 (1996).

[15] Yu. L. Dokshitzer, JETP **46** (1977) 641.
V. N. Gribov and L. N. Lipatov, Sov. Journ. Nucl. Phys. **15** (1972) 78.
G. Altarelli and G. Parisi, Nucl. Phys. **B126** 1977 298.

[16] T. Gerhmann and W. Stirling, Z. Phys **C70**, 89 (1996).

[17] E. Gallo, M. Grothe, C. Peroni, J. Rahn, R. Sacchi, A. Solano, these proceedings.

[18] G. Wolf, Proceedings of the Topical Conference on Hard Diffractive Processes, Eilat, Israel, February 1996.

[19] E. Barberis, Proceedings of the International Workshop on Deep–Inelastic Scattering and Related Phenomena, Rome, Italy, April 1996.

[20] W. Buchmüller and A. Hebecker, Phys. Lett. **B355**, 573 (1995),
W. Buchmüller and A. Hebecker, hep-ph/9512329 (1995),
W. Buchmüller, M. F. McDermott, and A. Hebecker, DESY preprint 96-126 (1996).

[21] A. Edin, J. Rathsman and G. Ingelman, Phys. Lett. **B366**, 371 (1996),
A. Edin, J. Rathsman and G. Ingelman, DESY-96-060 (1996).

[22] ZEUS Collaboration, M. Derrick et al. , Physics Letters B 356 (1995) 601-616,
H1 Collaboration, S. Aid et al. , Nucl.Phys. **B463** (1996) 3.

[23] L. Bauerdick et al. , "F_L: Experiment and Theory", these proceedings.

[24] G. Ingelman and K. Janson–Prytz, "The Pomeron Structure Function and QCD at Small–x", in Proceedings of the Workshop "Physics at HERA", p. 233, October 1991, ed. W. Buchmüller and G. Ingelman,
G. Ingelman and K. Prytz, Zeit. Phys. **C58** (1993) 285.

[25] H1 Collaboration, S. Aid et al. , Nucl. Phys. **B470** (1996) 3.

[26] ZEUS Collaboration, M. Derrick et al. , DESY 96-076 (1996).

[27] H. Jung, Comp. Phys. Comm.**86** (1995) 147,
H. Jung, RAPGAP 2.2 Program Manual, to appear in Comp. Phys. Comm.

[28] R. M. Barnett et al. (Particle Data Group): Phys. Rev. D54 1 (1996).

The LPS in diffractive physics with HERA upgrade.

T. Massam

August 27, 1996

The functions of the LPS in the analysis of diffractive events are twofold:

1. To measure the transverse momentum of the proton and thus obtain a direct measurement of t.
2. To measure the mass, M_X of the diffractively produced state and/or tag its diffractive nature.

To perform either of these tasks well requires a good geometric acceptance for the proton.

This contribution contains an updated summary of the verbal presentation and further information is appended to the ZEUS interaction region study.

1 Transverse momentum measurement

The conclusions are that a HERA upgrade with a low-β solution will introduce serious and probably unacceptable systematic errors in measurements of $t-$slope parameters. Because these uncertainties are due to the transverse momentum spread (??) within the emittance of the incident proton beam, they will be present in any method of measuring $t-$distributions so measurements of slope parameters should be completed before the upgrade.

There may remain some possibilites of measuring lower slopes if they are found above $p_T = 1GeV$ since in the low-*beta* upgrade the LPS acceptance will extend above $1GeV$, but with reduced acceptance.

Table 1: Emittance parameters of the proton beam

Normalized emittance		2.000e-5	metres
Quantity	Horizontal	Vertical	units
β	3.00	0.15	metre
σ_{space}	0.131	0.0293	mm
σ_{angle}	0.0437	0.1953	milli radian
$\sigma_{transverse-momentum}$	0.036	0.160	GeV

2 M_X measurement.

Measurements of x_L on the other hand will not deteriorate with the upgrade. At lower values of M_X the kinematics are such that a measurement showing that the proton momentum is close to 1.0 (e.g. ¿0.99) gives a clear tag of a quasi two-body low-t event. At higher values of M_x and provided that Q^2 is not very high, M_X can be measured using the LPS momentum measurement.

These statements are quantified by the expression:

$$M_X^2 = Sy(1-x-x_L) + t - 2p_T^{proton} p_T electron \tag{1}$$

where x and y are the deep inelastic parameters, x_L is the leading proton momentum/incident proton momentum, p_T are the momentum components transverse to the incident beam.

The uncertainty in M_X resulting from the transverse momentum spread in the beam is then

$$\Delta M_X = \frac{\Delta p_T^{beam}}{M_X}\left\{\frac{p_T^{leading-proton}}{x_L} + p_T^{scattered-electron}\right\} \tag{2}$$

3 Statistical accuracy

Geometrical acceptance in the spectrometer is restricted by the aperture between the beam and the vacuum system. Detectors cannot be placed closer to the beam line than the beams 10σ profile. When a low-β optics is introduced, it modifies the phase space in such a way that the minimum p_T which can be accessed by the detectors is increased and for the proposed upgrade this results in about a factor of two loss in events rate. For events which will need pre-scaling with the higher luminosities, this can be recuperated by introducing a suitable trigger and reducing the scaling factor.

The upper limit to the aperture affects the upper limit of t which can be reached. It depends on the details of the magnet and vacuum chamber design and this is being studied in collaboration with the upgrade designers.

Measurements with the ZEUS Leading Proton Spectrometer

E. Gallo[a], M. Grothe[b], C. Peroni[c], J. Rahn[d], R. Sacchi[e], A. Solano[c]

[a] INFN Firenze, Largo E. Fermi 2, I-50125 Firenze, Italy
[b] Physikalisches Institut der Universität Bonn, Bonn, Germany
[c] Università di Torino and INFN, via P. Giuria 1, I-10125 Torino, Italy
[d] University of California, Santa Cruz, CA, USA
[e] INFN Torino, via P. Giuria 1, I-10125 Torino, Italy

Abstract: The measurements that can be achieved with the use of the ZEUS Leading Proton Spectrometer are reviewed, focussing on the diffractive physics. Estimates of the systematic errors on some of the measurements are given, together with an estimate of the integrated luminosity needed.

1 Introduction

The two experiments H1 and ZEUS at HERA are equipped with forward spectrometers to detect the scattered proton in ep interaction. This study concentrates on the physics program in diffractive physics achievable with the ZEUS Leading Proton Spectrometer (LPS).

The LPS consists of six stations of silicon microstrip detectors placed along the proton beam line at distances of 23 to 90 m from the interaction point. The LPS detects protons scattered at small angles with respect to the beam, corresponding to proton transverse momenta $p_T \lesssim 1$ GeV. The HERA beam magnets are used to determine the proton momentum. The resolution on the fractional longitudinal proton momentum, $x_L = p'/p$, where p is the incoming proton beam momentum and p' is the momentum of the scattered proton measured in the spectrometer, is 0.4% at high x_L. The p_T resolution of 5 MeV is less than the beam transverse spread at the interaction point of $\lesssim 100$ MeV. The LPS selects a clean sample of single diffractive dissociation events $ep \to epX$ and measures the square of the four-momentum transfer t at the proton vertex directly.

The first physics results achieved are based on the 1994 data [1], [2], when the three stations S4, S5 and S6, extending from 63 to 90 m, were operational. In this configuration the LPS geometrical acceptance extends approximately from $x_L \simeq 0.5$ to $x_L = 1$ and from $p_T \simeq 0$ to $p_T = 0.8$ GeV, and it varies as a function of x_L and p_T. For $x_L > 0.97$, that is for single photon diffractive dissociation events, the t range covered is between 0.05 and 0.4 GeV^2, with $t \simeq -p_T^2/x_L$. In this range the geometrical acceptance is approximately 6%.

With the complete installation of all six stations, the LPS can measure in an extended region and the acceptance in the region at high x_L is approximately a factor two larger. The resulting acceptance is shown in figure 1, and it will be used in the estimation of the integrated luminosity needed for the LPS measurement.

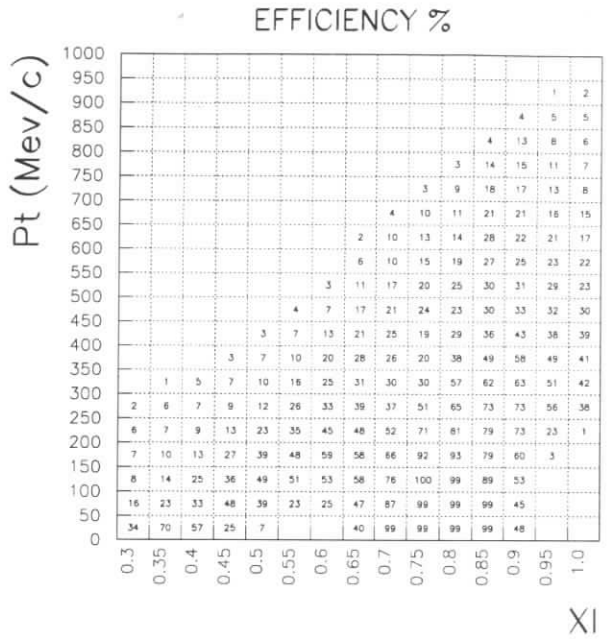

Figure 1: *Acceptance table in the x_L, p_T plane for coincidences between any two stations of the LPS out of six.*

2 Measurements with the LPS

The list of topics of interest in hard diffractive scattering is long and is discussed in detail in the summary [3]. Among all the processes of interest there are some which cannot be explored fully without the use of the LPS.

The t distribution is claimed to be the testing ground for the hardness of diffractive processes. The LPS is the unique tool for measuring the t distribution for all inclusive processes in which the p_T resolution achieved with the main calorimeter is larger than the typical width of the t distribution itself.

Another area which cannot be explored without heavy use of Monte Carlo simulation is the large mass diffraction, where the existing detectors, except for the LPS, loose their sensitivity to the presence of large rapidity gaps.

Thus this report concentrates on the measurement of the diffractive structure function $F_2^{D(4)}$

and of the t dependence in DIS. The numbers presented here for these specific cases can then be easily rescaled to estimate the luminosity requirements for any diffractive processes.

3 Diffractive Cross Section in DIS

The differential cross section for diffractive DIS events can be written in terms of the diffractive structure function $F_2^{D(4)}$ as:

$$\frac{d^4\sigma_{diff}}{d\beta dQ^2 dx_{I\!P} dt} = \frac{2\pi\alpha^2}{\beta Q^4}\left(1+(1-y)^2\right) F_2^{D(4)}(\beta, Q^2, x_{I\!P}, t), \qquad (1)$$

where α is the electromagnetic coupling constant, y is the fractional energy transferred to the proton in its rest frame; in the expression above the contributions of the longitudinal structure function and of Z^0 exchange have been neglected. Assuming that diffractive interactions are due to pomeron exchange, $x_{I\!P}$ is the momentum fraction of the proton carried by the pomeron and β is the momentum fraction of the struck quark with respect to $x_{I\!P}$.

Diffractive DIS events are selected in the LPS requiring a well reconstructed proton track with $x_L > 0.97$. The uniqueness of the LPS for the determination of the diffractive cross section is due to four reasons:

- the ability to select a clean sample of single diffractive dissociation events through the proton tagging (estimates are that the background due to other physics processes is below 5%);
- the ability to measure t directly;
- good resolution in β and $x_{I\!P}$, in the region $0.001 < \beta < 0.1$;
- the ability to determine the background to diffraction by extending the measurement of the proton at low x_L ($x_L < 0.97$).

As shown in the formula above, the differential cross section is a function of four variables, $Q^2, t, x_{I\!P}$ and β. The quantities Q^2 and y are reconstructed from the electron variables (electron angle and energy) or from the double angle variables, as for the inclusive F_2 measurement. The quantities $x_{I\!P}$ and β are reconstructed from the variables at the electron vertex and from the mass M_X of the final hadronic system into which the virtual photon diffractively dissociates:

$$\beta = \frac{Q^2}{Q^2+M_X^2}; \qquad x_{I\!P} = \frac{x}{\beta} \simeq 1 - x_L \qquad (2)$$

where W is the $\gamma^* p$ centre-of-mass energy and x the Bjorken scaling variable. With the LPS, the measurement can extend to higher masses (therefore to lower values of β and higher values of $x_{I\!P}$) compared to measurements based on rapidity gap selection. In the high mass region, M_X can be reconstructed from the momenta of the electron and the proton, $M_X = sy(1-x-x_L)$, achieving a very good resolution (for $M_X \gtrsim 25$ GeV the resolution is 15%, for $M_X \simeq 80$ GeV it is 6%).

3.1 Measurement of $d\sigma/dt$

One of the first measurements performed with the LPS has been the determination of the t dependence in diffractive DIS events. The measurement was performed integrating over the kinematical region $4 < Q^2 < 30$ GeV^2, $70 < W < 210$ GeV, $0.02 < \beta < 0.4$ and $x_L > 0.97$, and for $0.07 < |t| < 0.35$ GeV^2. The resulting distribution is exponential and expressed as $d\sigma/d|t| \sim \exp(-b|t|)$ leads to a value of b which is within errors in agreement with what is expected for the soft pomeron, although on the low side.

One of the prediction of models based on the soft pomeron is the shrinkage of the diffractive peak with increasing c.m. energy. Measuring in two W bins around 50 GeV and 200 GeV, at an average Q^2 of 10 GeV^2 and an average mass of 10 GeV, one expects:

$$b\,(W) \simeq b_0 + 2\alpha' \ln(W^2/(M_X^2+Q^2))\ \text{GeV}^{-2} \simeq 6\ \text{GeV}^{-2}, \qquad (3)$$

$$b\,(W \simeq 200) - b\,(W \simeq 50) \simeq 2\alpha' \ln(200^2/50^2) \simeq 1.4\ \text{GeV}^{-2}, \qquad (4)$$

where $b_0 \simeq 4.5$ GeV^{-2} and $\alpha' \simeq 0.25$ GeV^{-2} is the slope of the soft pomeron trajectory. For the hard pomeron the expectations are that $\alpha' \simeq 0$ (no shrinkage), which means that $b\,(W \simeq 200) = b\,(W \simeq 50)$.

In order to measure a difference between the two values at the 3σ level in these two W bins, the error on b should be of the order of 0.3 GeV^{-2}, i.e. of the order of 5% for $b \simeq 6$ GeV^{-2}. With 20 pb^{-1}, about 4000 tagged LPS events can be collected for each W point, obtaining a statistical error on $b\,(W)$ of $3 \div 4$%. The dominant systematic errors are due to the alignment of the LPS with respect to the beam and to the unfolding of the proton beam transverse momentum spread. The estimate is that, with the present configuration, a systematic error of 3% on b could be achieved, giving the possibility to measure the shrinkage with the required precision. The HERA luminosity upgrade by means of low-β quadrupoles would restrict the range in t where there is acceptance for the LPS, moving the lower $|t|$ limit from 0.07 GeV^2 to 0.27 GeV^2 [4], reducing the statistics. In addition the low β quadrupoles increase the beam dispersion in transverse momentum at the interaction point, thus increasing the systematic error on b. The effect is shown in fig. 2. The observed t distribution is a convolution of the p_T^2 exponential folded with the p_T dispersion caused by the beam emittance represented by a 2-dimensional gaussian in transverse momentum space, whose width increases slowly during the lifetime of the beam. Therefore, the observed p_T^2 distribution is also a 2-dimensional gaussian and can be approximated by an exponential whose slope changes with time. The size of this effect is shown in fig. 2 for the 1994 HERA optics ($\beta_x = 7; \beta_y = 0.7$) and for the proposed low β quadrupoles configuration ($\beta_x = 3; \beta_y = 0.2$); for a slope of 6 GeV^{-2} in the proposed configuration, the beam emittance would change the slope by as much as 20%, with a strong dependence on the size of the emittance of the beam. The systematic error on b induced by this correction is estimated to increase to $7 - 12$%.

3.2 Measurement of $F_2^{D(4)}$

The systematic errors on $F_2^{D(4)}$ are limited by the kinematic reconstruction of x, Q^2, the M_X reconstruction, the background subtraction and the LPS acceptance. The systematic errors due to the acceptance of DIS events and x, Q^2 reconstruction are the same as for the inclusive F_2 measurement. In the intermediate y region a systematic error below 5% has been achieved [5]

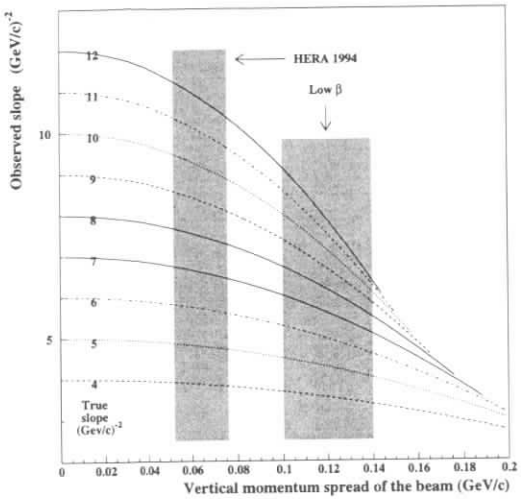

Figure 2: *Effect of the low β optics on the measurement of the diffractive slope b with the LPS. The bands are the range of variation induced by the growth of the emittance during the lifetime of the proton beam.*

and could be reduced to 3% with a better measurement of the electron and hadronic variables in the next years. The M_X reconstruction, as already mentioned, is well under control at high masses, $M_X \gtrsim 10$ GeV, where the LPS information is used, and should provide a precise measurement for $\beta \lesssim 0.1$. A systematic error of 3% could be achieved. The background is due mainly to two processes. The beam halo background comes from interactions of beam protons with the residual gas in the beam pipe or with the beam collimators, accidentally overlapping with genuine DIS events. This type of background can be easily subtracted and estimated requiring energy and longitudinal momentum conservation and can be controlled at the level of 1%. The second type of background is due to processes where the proton does not remain intact, like proton dissociation, Reggeon exchange other than the pomeron and non-diffractive interactions. In this case the x_L spectrum peaks at low values, and study of the low x_L data can shed light on the nature of the remaining background under the diffractive peak. An error due to this background of 2% could be achieved. Finally the error due to the LPS acceptance (LPS alignment and calibration and run-to-run dependence of the acceptance) can reach an ultimate precision of 5%. Summing in quadrature all the above contributions, a systematic uncertainty of 7% could be achieved in each bin. The HERA upgrade would severely affect the LPS acceptance increasing the systematic error due to this contribution.

The LPS allows measurement of the structure function $F_2^{D(4)}$ in the four variables t,$x_{I\!P}$,β,Q^2. If a measurement were made in two t bins ($0.07 < |t| < 0.12$ GeV^2, $0.12 < |t| < 0.35$ GeV^2), in three Q^2 bins in the range $4 < Q^2 < 30$ GeV^2, in seven β bins in the range $0.001 < \beta < 0.5$

and in three to six $x_{I\!P}$ bins in the range $4 \times 10^{-4} < x_{I\!P} < 3 \times 10^{-2}$, 70 events on average per bin are expected with 20 pb^{-1} (in those bins within kinematic range at HERA). This results in an average statistical error of the order of 12% for each bin, to be compared with the systematic error of 7%. Fitting the $x_{I\!P}$ dependence with $(1/x_{I\!P})^a$ for every Q^2, t and β interval, the statistical error on the slope a could be measured with a statistical precision of 5 to 15% and a systematic precision of less than 3%, testing if factorization holds in the mentioned β range. Table 3.2 shows the error on a in individual β bins. The error at low β is larger because the HERA kinematics limit the accessible range in $x_{I\!P}$.

β	Number of $x_{I\!P}$ bins	Number of events per bin	Statistical error (in%) on a
$\simeq 0.01$	3 ($10^{-2} < x_{I\!P} < 3 \times 10^{-2}$)	50	$\pm 15\%$
$\simeq 0.03$	3 ($2 \times 10^{-3} < x_{I\!P} < 3 \times 10^{-2}$)	70	$\pm 10\%$
$\simeq 0.1$	5 ($4 \times 10^{-4} < x_{I\!P} < 3 \times 10^{-2}$)	70	$\pm 6\%$
$\simeq 0.3$	5 ($4 \times 10^{-4} < x_{I\!P} < 3 \times 10^{-2}$)	70	$\pm 5\%$

Table 1: *Estimated number of events in β intervals for 20 pb^{-1} of collected LPS data, for 3 Q^2 bins, 2 t bins and 3-5 $x_{I\!P}$ bins, and relative statistical error on the power a of the $x_{I\!P}$ dependence.*

4 Summary

The LPS provides a very powerful tool to study diffraction at HERA. In particular it provides the direct measurement of t, it allows the selection of a clean sample of single diffractive dissociation events and it extends the measurement to low β and high $x_{I\!P}$. The proposed HERA upgrades would severely limit the LPS acceptance, especially at low t as shown in [4]. An estimated integrated luminosity of 20 pb^{-1} collected with the LPS would allow a measurement of the differential diffractive structure function $F_2^{D(4)}$ in a reasonable binning in $x_{I\!P}$,β,Q^2,t for $Q^2 < 30$ GeV^2, with a statistical error of 12% and a systematic error of the order of 7%. Note that the LPS efficiency compared to the luminosity delivered by HERA is of the order of 50%: 20 pb^{-1} collected by the LPS correspond to 40 pb^{-1} delivered by HERA. The factorization breaking could be tested with a precision of $5 - 15\%$. The shrinkage of the diffractive peak could be tested unambigously in two W bins, integrating over Q^2, with 4000 events per bin, obtaining a precision of 0.3 GeV^{-2} on the slope b and of 0.1 GeV^{-2} on α'.

References

[1] ZEUS Collaboration, M. Derrick et al., paper submitted to the XVIII International Conference on High Energy Physics, Warsaw July 25-31 1996, Ref. pa 02-050.

[2] ZEUS Collaboration, M. Derrick et al., paper submitted to the XVIII International Conference on High Energy Physics, Warsaw July 25-31 1996, Ref. pa 02-026.

[3] H. Abramowicz et al., these proceedings.

[4] T. Massam, *Possible effects of the HERA luminosity improvement on the forward spectrometers*, these proceedings.

[5] ZEUS Collaboration, M. Derrick et al., DESY 96-076.

Diffraction in Charged Current DIS

J.Pliszka[a], A.F.Żarnecki[ab]

[a] Institute of Experimental Physics, Warsaw University, ul. Hoża 69, 00-681 Warszawa, Poland
[b] currently at DESY, Notkestraße 85, 22603 Hamburg, Germany

Abstract: Following the observation of one large rapidity gap CC DIS event by ZEUS in 1994 dedicated studies were made on theoretical and experimental aspects of diffractive CC scattering. The theoretical estimate of the cross section is $\sigma^{(diff)}_{ep\to\nu X}(x_{I\!P} < 0.1) = 2.1\ ^{+1.0}_{-0.7}$ pb. Monte Carlo study shows that the signature of these events is sufficiently unique to enable good background rejection at about 35% signal efficiency. With 1 fb^{-1} of integrated HERA luminosity measurement of the diffractive CC interaction should give a significant contribution to our understanding of diffractive phenomena.

1 Introduction

Within the ZEUS sample of charged current DIS events, selected from the 1994 e^+p data, one event was found satisfying a large rapidity gap (LRG) selection as used in the NC DIS analysis [1]. This corresponds to the cross section [2]:

$$\sigma^{(LRG)}_{e^+p\to\bar{\nu}X}(Q^2 > 200GeV^2) \;=\; 0.8\ ^{+1.8}_{-0.7}(stat.) \pm 0.1(syst.)\ \text{pb}. \tag{1}$$

This event is interpreted as a diffractive charged current DIS event, where the W^+ exchange occurs between positron and pomeron. Following this observation dedicated studies were made on both theoretical and experimental aspects of diffractive CC scattering. Perspectives of precise diffractive CC DIS measurement after the planned HERA upgrade were also investigated.

2 Cross section estimate

The cross section for diffractive CC DIS can be expressed, similarly as in the case of NC DIS, in terms of the diffractive structure functions $F^{CC}_{2\,D}$ and $F^{CC}_{3\,D}$,

$$\frac{d^3\sigma^{CC}_{diff}}{d\beta dQ^2 dx_{I\!P}} = \frac{G_F^2}{4\pi}\,\frac{M_W^4}{(Q^2+M_W^2)^2}\,\frac{1}{\beta}\cdot \tag{2}$$
$$\left[(1+(1-y)^2)\,F^{CC}_{2\,D}\,(\beta,Q^2,x_{I\!P}) \;\pm\; (1-(1-y)^2)\,\beta\,F^{CC}_{3\,D}\,(\beta,Q^2,x_{I\!P})\right],$$

where $x_{I\!P}$ is the fraction of proton momentum carried by the pomeron, whereas β is the fraction of the pomeron momentum carried by the parton coupling to the W. The cross section is integrated over the undetected four-momentum transfer to the proton system.

In the studies presented here factorization of diffractive structure functions is assumed, i.e. they are decomposed into a pomeron flux factor independent of the hard scattering process and into parton distributions in the pomeron. The calculations were performed in QPM approximation, neglecting higher order QCD contributions as well as any scaling violation of diffractive structure functions.

Assuming that the pomeron contains an equal amount of up and down quarks and antiquarks the $F_{3\,D}^{CC}$ structure function vanishes and $F_{2\,D}^{CC}$ can be related to the diffractive structure function measured in NC DIS,

$$F_{2\,D}^{CC} = \frac{18}{5} F_2^D \ . \tag{3}$$

In the following the parameterization of the ZEUS diffractive structure function measurement[1] was used,

$$F_2^{D(3)} = (1/x_{I\!P})^a \cdot b \cdot (\beta(1-\beta) + \frac{c}{2} \cdot (1-\beta)^2), \tag{4}$$

where the values of parameters fitted to data are

$$\begin{aligned} a &= 1.30 \pm 0.08\ (stat)^{+0.08}_{-0.14}\ (sys), \\ b &= 0.018 \pm 0.001\ (stat) \pm 0.005\ (sys), \\ c &= 0.57 \pm 0.12\ (stat) \pm 0.22\ (sys). \end{aligned}$$

Integration of the cross section formula 2 using relation 3 yields[1]

$$\sigma^{(diff)}_{ep\to\nu X}(x_{I\!P} < 0.1) = 2.1\ ^{+1.0}_{-0.7}\ pb. \tag{5}$$

The error on the cross section is dominated by the uncertainty in the slope parameter a, to which the cross section is very sensitive. This is shown in figure 1, together with the error band on the value of a measured by ZEUS. Precise measurement of the diffractive CC cross section can significantly constrain the description of the pomeron flux factor.

The integration of the cross section was limited to $x_{I\!P} < 0.1$, as for higher $x_{I\!P}$ diffraction is not well defined. In case of diffractive CC DIS this is a significant constraint, since, due to the W mass in the propagator term (eq. 2), the diffractive CC cross section decreases very slowly with $x_{I\!P}$, approximately like $(\frac{1}{x_{I\!P}})^{a-1}$. It also means that, in contrast to what we observe in NC diffractive scattering, the cross section is dominated by events with high M_x (invariant mass of the pomeron-W system).

3 Experimental signature

In 1995 a dedicated trigger was implemented at ZEUS to select diffractive CC events. The selection is based on two basic requirements: the event should have a rapidity gap in the

[1]The assumption of equal u and d contents of the pomeron also implies that the e^-p and e^+p CC diffractive cross sections are equal.

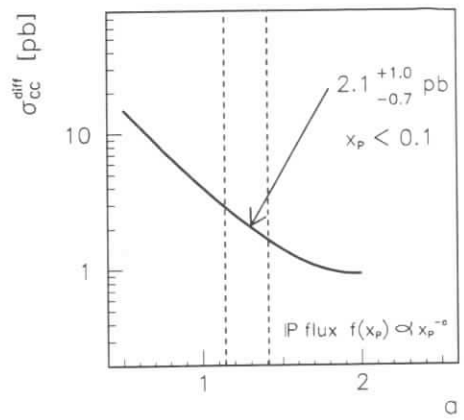

Figure 1: *Total cross section for diffractive CC scattering as a function of the pomeron slope parameter a. The arrow indicates the value of σ_{CC}^{diff} corresponding to a measured by ZEUS [1]. The vertical dashed lines indicate the quoted error on a.*

forward direction (to select diffractive events) and a significant missing transverse momentum (to select CC events).

Due to the high diffractive masses involved, the expected rapidity gap is much smaller than in diffractive NC DIS. Hence we require a minimal rapidity gap observable in the main detector, corresponding to no energy deposits in the calorimeter cells adjacent to the beam pipe hole. This cut can be slightly released, thus increasing the selection efficiency, if the contribution of nondiffractive events is additionally suppressed by use of scintillator counters placed behind the main calorimeter very close to the beam pipe. This so called Proton Remnant Tagger tags charged particles produced in the pseudorapidity interval $4.3 < \eta < 5.8$.

To select CC events it was required that there is missing transverse momentum of at least 4 GeV. Monte Carlo studies showed that both photoproduction and NC DIS background can be very efficiently suppressed by additional cuts based on the transverse momentum – p_T and the transverse energy[2] – E_T of the event, measured both in the calorimeter and in the tracking detectors:

$$\begin{aligned} \left.\frac{p_T^2}{E_T}\right|_{Calorimeter} &> 3\ GeV^2 \\ \left.\frac{p_T^2}{E_T}\right|_{Tracking} &> 2\ GeV^2 \end{aligned}$$

With the additional requirement that the direction of the transverse momentum measured in the calorimeter and from the tracking detectors agree, the efficiency of the diffractive CC selection is of the order of 35% with a purity of the final sample of about 60%. Most of the background comes from non-diffractive CC DIS.

[2]The transverse energy E_T is defined as the scalar sum of the transverse momenta over all calorimeter energy deposits, or over all tracks coming from the primary vertex, respectively.

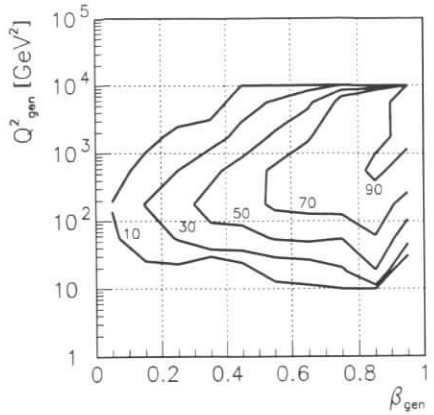

Figure 2: *Selection efficiency (indicated in percents) of diffractive CC DIS events as a function of the kinematic variables Q^2 and β.*

Figure 2 shows the efficiency of the proposed diffractive CC selection as a function of the kinematic variables Q^2 and β. The efficiency improves significantly towards high β. The proposed cuts select events in a relatively narrow Q^2 range of about $10^2 - 10^3$ GeV^2.

4 Perspectives

With the proposed upgrade schedule, HERA should be able to deliver about 1000 pb^{-1} of luminosity until the year 2005. This would open a wide range of possibilities in studying diffractive CC interactions. Figure 3 shows the expected number of events observed after selection cuts, as a function of the kinematic variables Q^2 and β. The total cross section could be measured with precision of the order of 5%, which corresponds to an error on the pomeron flux parameter a of the order of 2%. This measurement will be very sensitive to the pomeron flux description at high $x_{I\!P}$ as well as to the assumed factorization of the diffractive cross section itself.

With 1000 pb^{-1} of data also the measurement of the differential cross section becomes possible. The cross section in β can be measured with 20–30% statistical error, as shown in figure 4. Although the diffractive CC DIS events populate (after selection cuts) a relatively narrow Q^2 range, this measurement can be used to test the evolution of the diffractive structure function, when compared to low Q^2 NC DIS results.

High statistics of diffractive CC events should also allow a precise jet rates study. The fraction of two jet events should be sensitive to the gluon contents of the pomeron, as they are expected to result from the W-gluon fusion.

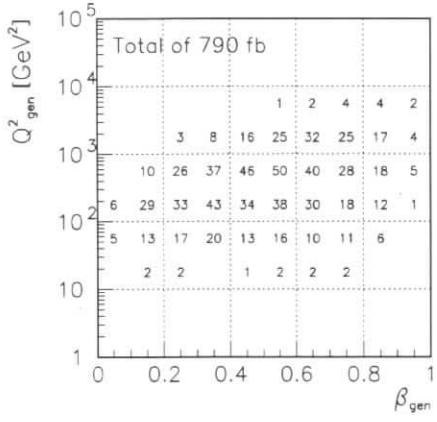

Figure 3: *Cross section in fb, after selection cuts, for diffractive CC DIS in bins of the kinematic variables Q^2 and β. The values correspond to the expected number of events for an integrated HERA luminosity of 1000pb^{-1}.*

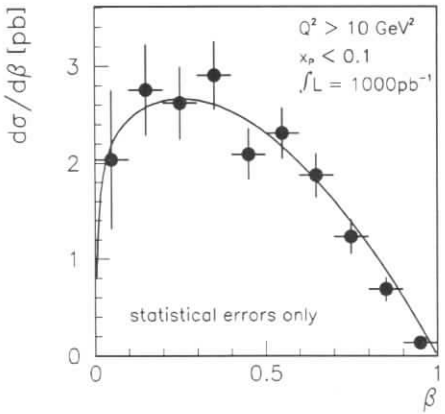

Figure 4: *Measured differential cross section for diffractive CC DIS as a function of β. Only statistical errors are shown, corresponding to an integrated HERA luminosity of 1000pb^{-1}.*

5 HERA upgrade

Results presented in the previous section were obtained with the assumption that the efficiency for the diffractive CC event selection after the HERA upgrade will remain the same as before. Using the Monte Carlo simulation it was checked that the proposed HERA and detector modifications should not have much influence on the measurement of CC events in the ZEUS detector. However, the proposed modification of the HERA magnet system is incompatible

with the present design of the Proton Remnant Tagger. It is not clear at the moment if the installation of new tagging device will be possible, nor if its efficiency in vetoing nondiffractive events will be compatible to the present design. If the proton remnant can not be tagged, stronger selection cuts will have to be applied in the central detector, resulting in the reduction of selection efficiency by a factor of about 2.

Acknowledgments

I would like to thank Juan Terron for supplying the MC sample for diffractive CC events [3]. Many thanks are due to Halina Abramowicz for encouraging me to take part in this workshop, and for many useful discussions. I would also like to thank the DESY directorate for the support of my work at DESY.

References

[1] ZEUS Collaboration; M.Derrick *et al.*, *Z. Phys.* C **68**, 569 (1995).

[2] ZEUS Collaboration; M.Derrick *et al.*, DESY 96-104, submitted to *Z. Phys.* C.

[3] J.Terron, see materials contributed to this workshop.

Proton Diffractive Dissociation at HERA. Studying the Proton Dissociation Using Forward Taggers or Calorimeters

H.Abramowicz[a], G.Barbagli[b], M.Kasprzak[c], A.Levy[a].

[a] Raymond and Beverly Sackler Faculty of Exact Sciences
School of Physics and Astronomy
Tel-Aviv University, 69978 Tel-Aviv, Israel
[b] Istituto Nazionale di Fisica Nucleare, Sezione di Firenze, Firenze, Italy
[c] Warsaw University, Institute for Experimental Physics,Warsaw, Poland

Abstract: The potential of the HERA colliding experiments for studies of diffractive proton dissociation is investigated. Two measurement methods are considered. The first one relies on a set of tagging devices detecting particles emitted from the proton dissociation, while the second one involves a calorimetric measurement. The possible accuracy of the measurement of the dissociated mass spectrum and the measurement of the fraction of diffractive events where the proton did not dissociate is estimated. The effect of lowering the proton beam energy is also studied.

1 Introduction

The processes under consideration are $ep \to eVY, eXY$, where V denotes a vector meson, X is a dissociated photon system and Y is the excited nucleonic state. They compete with reactions where the proton stays intact, namely $ep \to eVp, eXp$. An efficient way of separating the two classes of events is essential for the measurements of the elastic and photon dissociation cross sections. It is also of primary importance to test the factorization of the diffractive proton vertex, i.e. to verify whether the probability for the proton to dissociate to a system of a given mass, M_Y, is the same in ep as in pp collisions and whether it depends on Q^2 or M_X.

In a naive approach, it should be easiest to study the proton dissociation in processes involving the production of vector mesons which decay into charged particles. One could estimate the energy, momentum and the mass of the nucleonic system from the difference between that of the initial and scattered electron and the vector meson decay products measured in tracking devices. One could also distinguish events with an intact proton by means of a simple mass cut. Unfortunately, the kinematics at HERA strongly disfavors this method. The only other possibility is by measuring the particles from the proton dissociation or the protons that stayed intact in the scattering process. The scattered protons are already measured by ZEUS using a leading proton spectrometer [1]. The acceptance is limited for geometric reasons and the momentum range restricted. The leading proton spectrometer can be used to select events

with intact protons or to describe qualitatively proton dissociation events, but it is not suitable as a tagger of proton dissociation.

In the following we investigate the potential accuracy that may be reached in measurements of the proton dissociation by recording the particles originating from the Y system in detectors installed in the proton fragmentation region. The fraction of the events where the proton stayed intact may be estimated by selecting the events where no particles were detected in these devices. The precision of such measurements is also analyzed.

2 Modelling the proton dissociation

The creation of the Y system may be modelled as a collision of the proton with the pomeron. Since the proton momentum is fixed the mass and the total momentum of the dissociated nucleonic state is determined by the energy and the momentum of the pomeron. The transverse momentum of the pomeron is practically zero compared to the longitudinal momenta involved, as $p_T^2 \approx t$, where t is the exponentially suppressed squared four momentum of the pomeron. Therefore in practice the kinematics of the nucleonic system is solely determined by the longitudinal momentum of the pomeron or equivalently by the mass $M_Y^2 \approx 4 \cdot p_p \cdot p_{I\!P}$.

The properties of the hadronization of the dissociated proton system depend mainly on the mass M_Y. Within the discussed model it corresponds to the centre–of–mass of the pomeron–proton collision. Fig. 1 shows the dependence of the average total transverse energy and the average charged multiplicity on the dissociated proton mass, according to PYTHIA 5.7 Monte Carlo program [2].

At HERA the particles from the proton dissociation are emitted under small angles in the direction of flight of the proton beam due to the strong Lorenz boost of the whole Y system. The angular distributions of final state hadrons, expressed in terms of pseudorapidity [1] for different intervals of the dissociated proton mass are shown in fig. 2. These distributions were obtained using the EPSOFT [3] MC program. It models the proton dissociation as a soft hadronic collision of the pomeron and the proton. The following assumptions define the properties of the final state:

- charged multiplicity according to the parametrization of $pp \rightarrow pN$ data;
- exponential suppression of transverse momenta with $\langle p_T \rangle \approx 300$ MeV;
- longitudinal momenta uniformly distributed in phase space.

Fig. 2 shows also how the distributions change if the average multiplicity is lowered by 30% or the average transverse momentum is increased by 30%. The reduction of the proton beam energy to $E_p = 450$ GeV shifts the distributions towards lower pseudorapidities which is equivalent to larger opening angles.

[1] The pseudorapidity, η, is derived from the relation $\eta = -log(tan(\theta/2))$, where θ is the polar angle calculated with respect to the proton beam direction

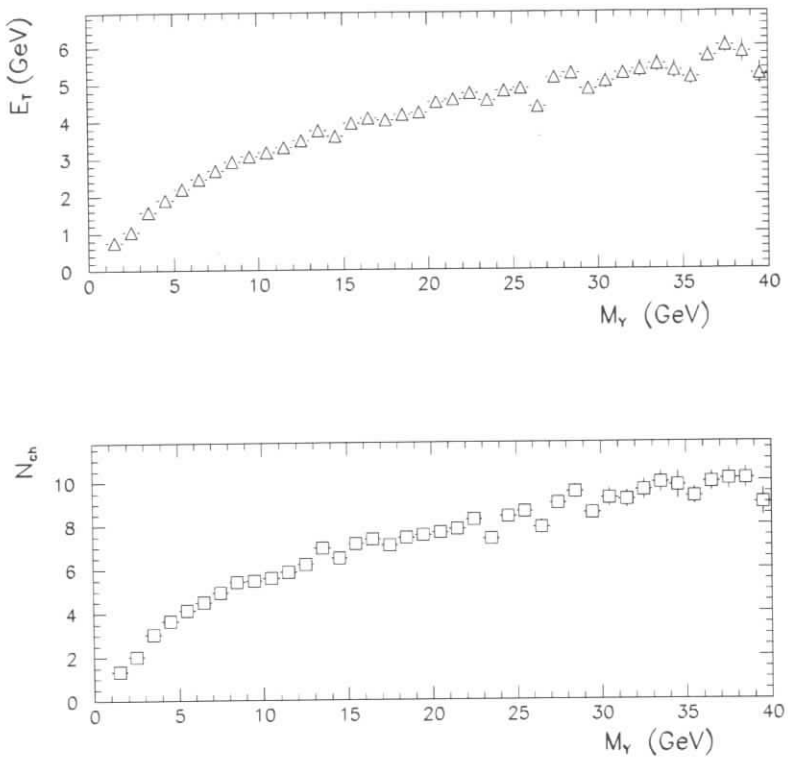

Figure 1: *Dependence of the average transverse energy (top) and the average charged multiplicity (bottom) on the dissociated proton mass in events generated with PYTHIA 5.7.*

3 Tagging the proton dissociation

In this section we investigate the possibility of tagging events with diffractive proton dissociation by detecting particles from the Y system with tagging devices installed in the forward region. For this study it was assumed that the central calorimeter, CAL, measures up to $\eta < 4$. The forward region was assumed to be instrumented with two counter rings symmetric around the beam axis covering the angles $4 < \eta < 4.9$ (tagger 1) and $4.9 < \eta < 5.9$ (tagger 2). There is a significant amount of inactive material in front of the taggers (up to one interaction length), concentrated mainly at $Z \approx 2.5$ m, where in the present design of the ZEUS interaction region the C4 collimator is installed. The preshowering effects may lead to significant distortions of the spectra in the taggers. This was simulated assuming that a shower of 7 cm radius may start

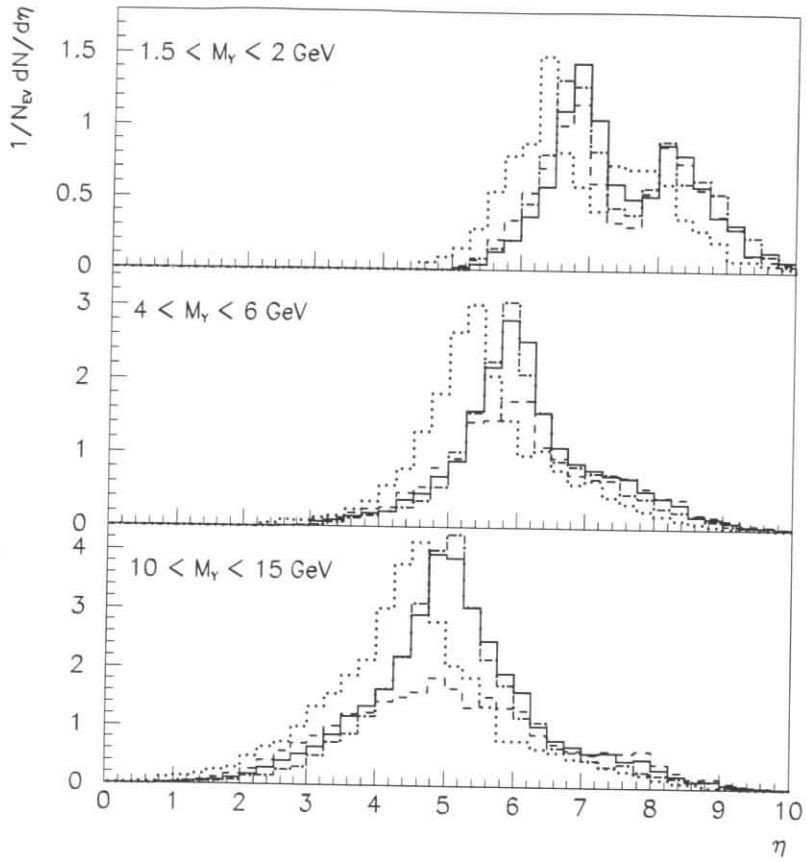

Figure 2: *Pseudorapidity distributions of particles from proton dissociation for different intervals of M_Y (solid histogram) according to EPSOFT. Dashed and dashed-dotted lines correspond to the distributions obtained if the charged multiplicities are reduced by 30 % or if the transverse momenta are increased by 30 %, respectively. The dotted line corresponds to lower proton beam energy, $E_p = 450$ GeV.*

at that place. Since the preshowering effect ensures high multiplicity of secondaries reaching the detectors, a 100 % efficiency for tagging such events was assumed. Fig. 3 shows the fraction of the proton dissociation events tagged by these devices as a function of the mass M_Y. Most of the events with $M_Y < 2$ GeV escape the detection in any of the devices, however masses $M_Y > 4$ GeV will almost certainly produce particles within the geometrical acceptance of the taggers.

The most straightforward application of forward taggers is the selection of diffractive processes where the proton stayed intact. This is done by rejecting all events with a signal in the

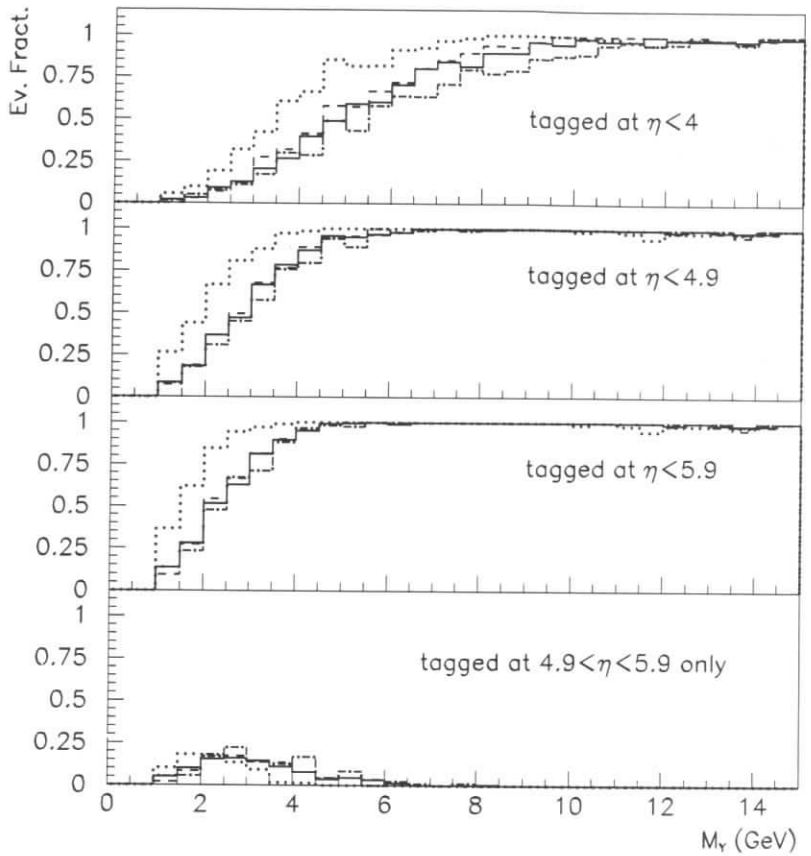

Figure 3: *The fraction of the proton dissociation events tagged by the counting devices covering different pseudorapidity regions as a function of the mass M_Y (solid histogram) according to EPSOFT. Dashed and dashed-dotted lines correspond to the distributions obtained if the charged multiplicities are reduced by 30 % or if the transverse momenta are increased by 30 %, respectively. The dotted line corresponds to lower proton beam energy, $E_p = 450$ GeV.*

forward detectors. Assuming that the probability for the proton in a diffractive ep interactions to stay intact or to dissociate to a given mass M_Y is the same as in the pp collisions one can estimate the fraction of the events with proton dissociation with no signal in the taggers. If only the central detector with $\eta < 4$ is used as veto, the contamination of single photon diffractive processes by proton dissociation is 16 ± 5 %. The error was estimated by varying the multiplicities and the transverse momenta assumed in the hadronization model by 30 %. The result is a large fraction known with a relatively poor precision. This uncertainty directly translates into a large error on the measured cross sections for the processes $ep \to eVp, eXp$.

The fraction of events with untagged proton dissociation may be reduced to 5.7 ± 1.4 %, if all the tagging devices at $\eta < 5.9$ are used. A significant reduction of the remaining proton dissociation fraction is possible only with devices reaching smaller polar angles, or by running with a lowered proton beam energy. The geometrical acceptance of the taggers for the beam energy of $E_p = 450$ GeV is also shown in fig. 3. In that case only 2.1 ± 0.6 % of the accepted events are accompanied by an untagged proton dissociation, allowing for very precise measurements of the cross sections for the single diffractive processes $ep \to eVp, eXp$.

To conclude, the fraction of single diffractive dissociation events contaminated by untagged double dissociation can be reduced by factor 3 by extending the forward tagging capabilities from $\eta = 4$ down to $\eta = 5.9$. A 30% uncertainty in the average multiplicity and transverse momenta of particles in proton dissociation results in similar uncertainty in the contamination.

4 Measuring the $d\sigma/dM_Y$ spectrum using taggers

It is also of interest to measure the mass spectrum of the diffractive proton dissociation in ep collisions at HERA and verify the factorization in diffractive process by comparing to pp interactions. Such a measurement is very difficult at HERA due to the strong forward boost of the whole Y system. Nevertheless one may attempt to estimate the behaviour of the M_Y spectrum even if only tagging devices are installed in the forward region. For example, one can measure the ratio of the number of proton dissociated events detected only in tagger 2 covering $4.9 < \eta < 5.9$ to the number of events tagged only in the main CAL, $\eta < 4$. As shown in fig. 3, the former cut selects events with c.a. $2 < M_Y < 5$ GeV, while the latter picks up those with roughly $M_Y > 8$ GeV. Assuming the distribution of the nucleonic mass in the form,

$$\frac{d\sigma}{dM_Y^2} \propto \left(\frac{1}{M_Y^2}\right)^a \tag{1}$$

it is possible to estimate the value of a from the measured ratio of the events. However, the region of Y masses selected by requiring signals in the tagging devices depends strongly on the assumptions of the fragmentation model. We have verified, that if the assumed average multiplicities are off by 30 %, the obtained value of a will be shifted by 0.11. This should be compared to 1.08, which is the absolute value expected for a from triple–pomeron phenomenology [4, 5]. The sensitivity of a to the p_T of the produced hadrons is similar. Therefore, considering the ideal case of 100 % efficient taggers the error on the measured value of a is $\sigma_a > 0.13$ due only to uncertainties in the hadronization process. If the energy of the proton beam is reduced to $E_p = 450$ GeV the acceptance of the tagging improves, but the uncertainty on a due to model assumptions does not.

5 Measuring the $d\sigma/dM_Y$ spectrum using calorimeters

The situation can be improved by installing calorimeters instead of the tagging devices in the forward region. To evaluate the potential of this solution we performed a MC study assuming that the region $4 < \eta < 5.9$ is instrumented with a calorimeter having a resolution of $\sigma_E/E = 60\ \%/\sqrt{E}$. The granularity is assumed to be such, that one cell corresponds to $\Delta\theta = 7$ mrad for angles $\theta < 28$ mrad and $\Delta\theta = 40$ mrad beyond that. Additionally, a position reconstruction

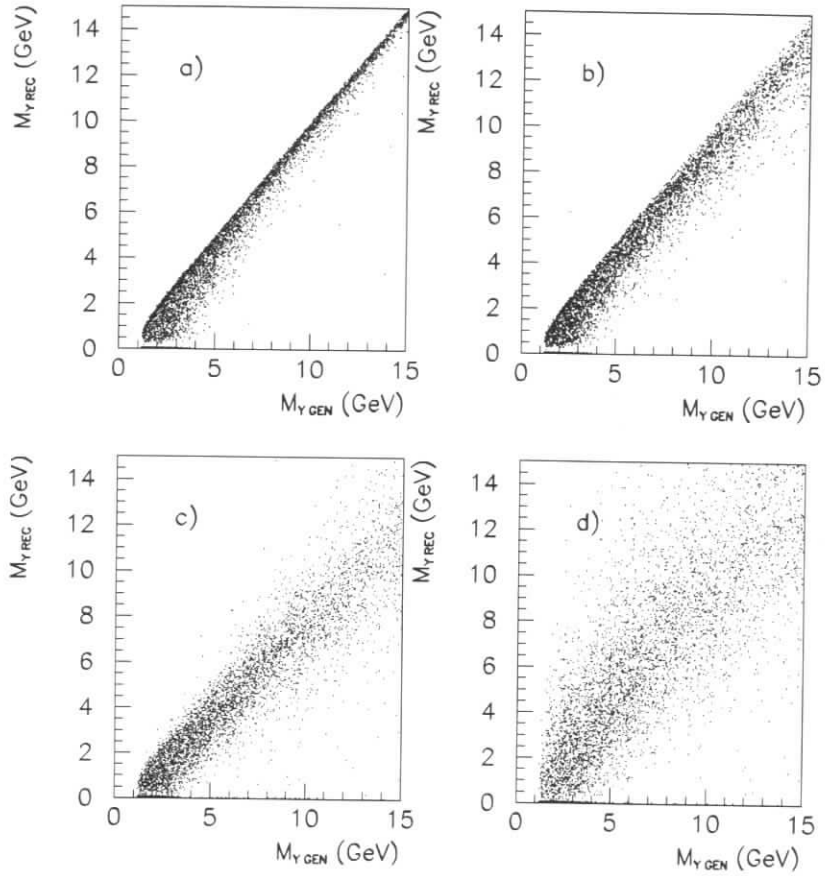

Figure 4: *Relation between the reconstructed and the true mass of the dissociated proton system according to EPSOFT MC program: a) taking into account only the effect of geometrical acceptance of the forward calorimeters, b) assuming in addition that particle momenta are approximated by their energy, c) after including the energy smearing due to losses in inactive material and calorimeter resolution, d) and after the position reconstruction smearing is also included.*

smearing due to the transverse size of the hadronic shower was included. The showers were assumed to begin at the C4 collimator at $Z \approx 2.5$ m and have a radius of 7 cm. The large amount of inactive material in the forward beam pipe region may also significantly distort the energy measurement. This was simulated assuming that every second particle may lose some energy before entering the calorimeter. This energy loss was generated from a flat distribution spanning from 0 to the particle energy. The rough estimate is based on the measurement of energy lost by hadrons in the EMC section of the ZEUS calorimeter [1]. The main calorimeter covering $\eta < 4$ was assumed to have a resolution of $\sigma_E/E = 40\ \%/\sqrt{E}$ and a granularity

of $\Delta\theta = 40$ mrad. The following relation was used to reconstruct the invariant mass of the nucleonic system Y:

$$M_{Y\,REC} = \sqrt{E^2 - P^2} \approx \sqrt{(E - P_Z) \cdot (E + P_Z)} \approx \sqrt{\sum_i E_i(1 - cos\theta_i) \cdot 2E_p}, \qquad (2)$$

where the summation runs over all the energy deposits measured in the forward region. Fig. 4 illustrates the expected quality of the dissociated proton mass reconstruction. The four plots show how the different factors degrade the mass resolution. Based on this simplified MC simulation one can estimate the resolution expected for the M_Y reconstruction of $\sigma_{M_Y}/M_Y \approx$ 100-120 $\%/\sqrt{M_Y}$. However, if the energy of the beam is reduced to $E_p = 450$ GeV the resolution can improve to about $\sigma_{M_Y}/M_Y \approx$ 70-80 $\%/\sqrt{M_Y}$, since the particles are emitted under larger angles.

Given this quality of the dissociated proton mass reconstruction we estimated the systematic precision one can achieve in measuring the mass spectrum. We assumed that the experimental method is similar to that considered for the case of taggers, namely by measuring the ratio of the number of events with mass $2 < M_Y < 5$ GeV and those with $M_Y > 8$ GeV. This time, the events were selected by requiring the reconstructed mass to fall into the intervals $0 < M_{Y\,REC} <$ 3 GeV and $M_{Y\,REC} > 7$ GeV. The thresholds applied on the reconstructed quantity are lower than what is expected for the true masses, since $M_{Y\,REC}$ is not corrected for energy lost in inactive material and carried by the particles that escaped the detection.

Assuming the form of Eq. 1 for the nucleonic mass spectrum we estimated the sensitivity of the measured value of a to the details of the hadronization of the Y system. Assuming that the average multiplicities and the transverse momenta are known to 30% the systematic uncertainty on a can not be smaller than 0.09. However, if the beam energy is reduced to $E_p =$ 450 GeV the precision on the measurement of a improves significantly, to about 0.03.

In this analysis we have not considered the uncertainties of the acceptance due to imprecise simulation of the effects of the dead material which may be large. Most probably, it is easier to control these effects if a calorimeter is installed in the forward region, as the calorimetric measurement is less sensitive to preshowering effects. A more realistic comparison of the two scenario would require further investigation of these aspects as well, as the questions of calibration, aging, radiation damage, etc.

6 Conclusions

We investigated the potential of forward detectors covering the pseudorapidities of $\eta < 5.9$ in the HERA colliding experiments for the studies of diffractive processes involving proton dissociation and those where the proton stays intact.

The processes with an elastically scattered proton, $ep \to eVp, eXp$, are measured by selecting events with no signal deposited in the forward detectors covering a range in η up to 5.9 units. Due to limited tagging acceptance, 5.7 $\pm$ 1.4 % of the events may still involve proton dissociation. If lower proton beam energy of $E_p = 450$ GeV was used the contribution from proton dissociation would reduce to 2.1 $\pm$ 0.6 %. For this type of studies the instrumentation of the forward region with tagging devices is as good as the calorimetric measurement since the geometrical acceptance is the decisive factor.

If the mass spectrum of the dissociated nucleonic states is to be measured, instrumenting the forward region with a calorimeter is preferable. The power a of the $d\sigma/dM_Y^2 \propto (1/M_Y^2)^a$ form of the mass spectrum may be measured with an error of 0.10 using calorimeters compared to that of 0.15 if tagging devices are used. The real potential of calorimetry with respect to tagging becomes apparent only if the beam energy is reduced. At $E_p = 450$ GeV the calorimetric resolution becomes $\sigma_{M_Y}/M_Y \approx$ 70-80 $\%/\sqrt{M_Y}$ instead of $100 - 120\%/\sqrt{M_Y}$ at the nominal beam energy and the systematic error on a may be reduced to roughly 0.03. The precision of the measurement using taggers does not significantly improve if the beam energy is reduced.

Acknowledgements

We would like to thank A.Droutskoi, T.Haas and A.Mehta for comprehensive presentation of the existing detectors in the forward regions of H1 and ZEUS experiments and their current understanding.

References

[1] ZEUS Coll., Status Report 1993.

[2] T. Sjöstrand, Z. Phys. C42 (1989) 301;
H-U. Bengtsson and T. Sjöstrand, Comput. Phys. Commun. 46 (1987) 43;
T. Sjöstrand, CERN-TH. 6488/92 (1992).

[3] M.Kasprzak, paper in preparation.

[4] K.Goulianos, Phys.Rep. 101 (1983) 169.

[5] A.Donnachie and P.V.Landshoff, Nucl. Phys. B244 (1984) 322.

Diffractive and Jet Physics with a Forward PLUG Calorimeter at ZEUS

A. Bamberger[a], S. Eisenhardt[a], H. Heßling[b], H. Raach[a], S. Wölfle[a]

[a] Universität Freiburg, Fakultät für Physik, D-79104 Freiburg, FRG
[b] Deutsches Elektronen-Synchrotron DESY, D-22603 Hamburg, FRG

Abstract: It is suggested to upgrade the forward ZEUS calorimeter in the current beam hole by a FPLUG calorimeter. The foreseen layout of the FPLUG would increase the acceptance of the ZEUS detector in the forward direction by 1.6 units in pseudorapidity. The calorimetric properties of the FPLUG are studied and its potential for diffractive physics and jet physics is analyzed.

1 Introduction

The complete coverage of phase space in the physics of lepton-proton scattering at HERA is one of the objectives of a multipurpose detector such as ZEUS or H1.
Since the observation of diffractive processes in deep inelastic scattering events with rapidity gaps have been interesting in various ways. An increase in acceptance is advantageous for the study of these processes. The very forward detection by the forward neutron spectroscopy (e.g. FNC at ZEUS) and the leading proton spectrometers (e.g. LPS at ZEUS) is successfully implemented. Their acceptance covers typically small momentum transfers, since they are integrated into the beam guiding systems. However, the transition region of forward calorimetry and the beam guiding systems is more difficult to equip with detectors because a number of boundary conditions have to be met. One option is the implementation of detectors wherever the beam elements allow to do so. This has been pursued by H1 and realised as a cascaded version of calorimetry. The other option is the implementation of the forward detection by "smooth" continuation of the calorimetry near the beam modifying the beam pipe and some of the vital elements as collimators and pumps.
Here we present a part of the results of this activity. The possible realisation (section 2) and the improvement for the detection of scattering processes are discussed. Among a variety of possible fields of interest we concentrate on the detection of diffractive DIS via the calorimetric measurement of diffractively produced masses (section 3) and the jet detection in the forward direction (section 4).

2 The FPLUG Calorimeter

2.1 Physics Requirements and Layout of the FPLUG Calorimeter

The requirements for a FPLUG calorimeter are:

- angular acceptance as close as possible at the proton beam,
- energy resolution similar to the energy resolution of the main calorimeters,
- small distortion of the response at the boundary of the calorimeters,
- small amount of dead material in front of the FPLUG.

The most efficient way to realise this is a FPLUG calorimeter integrated into the existing calorimeter. Transition effects at the boundary between the calorimeters are minimized this way. Shadowing effects as would be the case in a cascaded version are avoided. The cross talk due to leakage, especially for the hadronic cascade, is intrinsically present. The closest approach to the proton and electron beam is limited by its sizes, the various injection conditions and synchrotron radiation fan accompanying the electron beam, in our case typically 2 cm.
The requirements for the angular resolution are moderate, since the invariant mass resolution of M_X is mainly determined by the energy resolution. However, the angular resolution and granularity is of importance for the separation of diffractively excited proton system.

2.2 General Layout

The FPLUG calorimeter would be positioned inside the current beam hole of the ZEUS forward calorimeter (FCAL) with a dimension of 20×20 cm^2. Leaving a hole for the beam pipe of 4×4 cm^2 the acceptance in pseudorapidity η could be increased from 3.8 to 5.4 at the front face of the calorimeter.

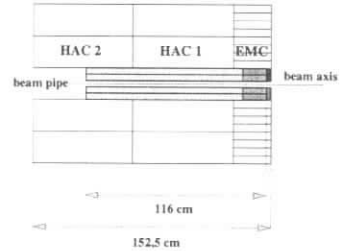

Figure 1: *Layout of the FPLUG inside FCAL (DU-version).*

The general layout of the FPLUG calorimeter inside the ZEUS FCAL is given in Fig. 1. A possible realization of the FPLUG calorimeter could be a spaghetti type calorimeter with tungsten as absorber medium. Tungsten has a very short nuclear interaction length λ of 10.3 cm which would allow for a rather compact hadron calorimeter. Space considerations would limit the amount of fibres to 10%.
The scintillating fibres would run along the beam axis and could be read out both from the direction of the interaction point and from the back, thus defining the electromagnetic and

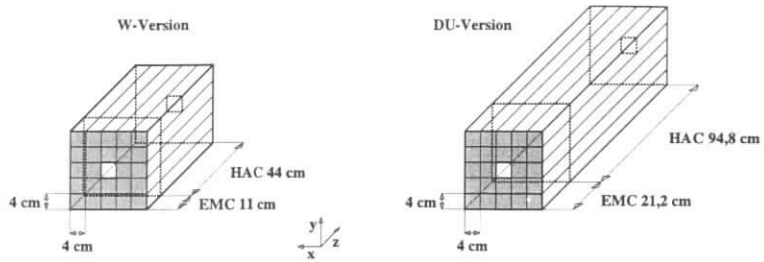

Figure 2: *Readout granularity of the FPLUG.*
Only the lognitudinal layout differs between W and DU-version.

hadronic sections of the calorimeter. The electromagnetic part would have the length of 1 λ, the hadronic part of 4 λ, giving a total length of 55 cm. This is two interaction lengths shorter than the FCAL, but sufficient as will be shown in Fig. 5
The usage of scintillating fibres would allow a flexible readout granularities. Our studies were employing a cell structure of 5×5 with a square cross section of each cell of 4×4 cm^2 and the center cell replaced by the beam pipe, cf. Fig. 2.

2.3 Monte Carlo Studies of the Calorimetric Properties

General features of a W–scintillating fibres calorimeter such as sampling fraction, energy resolution and leakage were studied by a "stand alone" simulation. In order to save computing time the fibre geometry was replaced by a sandwich structure of alternating layers of 9 mm W and 1 mm polystyrene as scintillator material preserving the 10% of active volume foreseen.
The simulation of the electromagnetic showers was performed with the GEANT 3.21 package [1]. For a detailed simulation of hadronic showers we used the GEANT–GCALOR interface [2]. The CALOR89 program package simulates hadronic interactions down to 1 MeV for nucleons and charged pions and into thermal regions for neutrons, for higher energies the FLUKA model [3] is employed.
The transport of neutrons down to thermal energies and the use of cross section tables for the various elements is expected to make the simulation of the response of hadronic calorimeters (which is especially sensitive to neutrons) rather reliable, cf. Ref. [4].
The response of the calorimeter was determined by hitting a very large calorimeter with monoenergetic particles (electrons or positive pions), incident at the center, perpendicular to the layer orientation. Sampling fractions are energy dependent and lie in the range of 0.7%, cf. Fig. 3a, the calorimeter is slightly overcompensating.
The electromagnetic energy resolution could be parametrized in the following form

$$\frac{\sigma_E}{E} = \frac{(31.1 \pm 1.2)\,\%}{\sqrt{E[\mathrm{GeV}]}} \,.$$

A detailed study that took into account the precise fibre geometry (1 mm diameter, 3.2 mm spacing) showed a more complicated behaviour due to the small number of fibres participating in an electromagnetic shower. This was confirmed by test beam measurements [5].

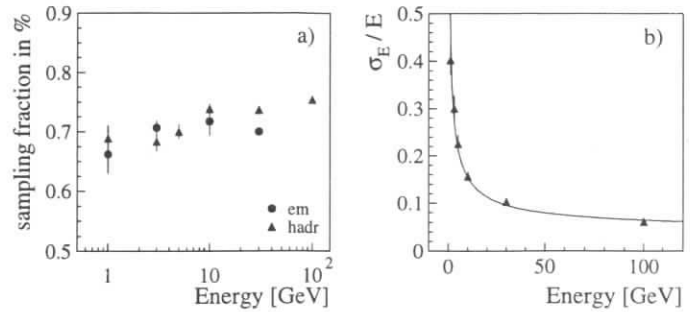

Figure 3: *a) Electromagnetic and hadronic sampling fractions,*
b) Hadronic energy resolution.

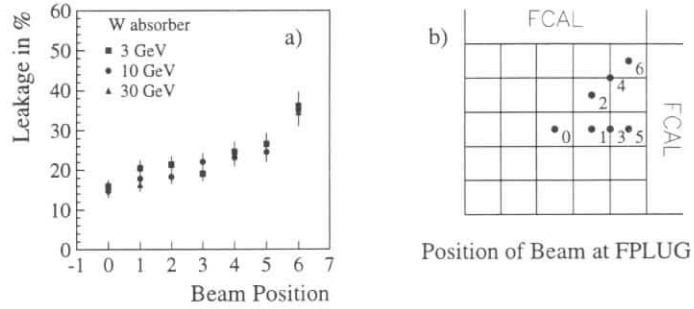

Figure 4: *a) Energy dependent leakage of W–FPLUG into FCAL.*
b) Incident points for leakage study on W and DU–FPLUG.

The energy resolution for hadronic showers was found to be

$$\frac{\sigma_E}{E} = \frac{(45.2 \pm 1.7)\,\%}{\sqrt{E[\mathrm{GeV}]}} \oplus (4.6 \pm 0.6)\,\% \,,$$

with the two contributions added in quadrature.
As the foreseen dimensions of the FPLUG are rather small for a hadronic calorimeter, especially in lateral direction, leakage into the FCAL cannot be neglected. Fig. 4a gives the leakage[1] for various energies from the FPLUG into the FCAL. The different entrance positions of the beam are indicated in Fig. 4b.
The energy resolution as a function of the calorimeter length was also extracted from the simulations. For this, no hole for the beam pipe was modelled, the particles were hitting the FPLUG at the center (point 0 in Fig. 4b). The results for 10, 30 and 100 GeV are shown in Fig. 5. One can see that there is no significant gain in the energy resolution for $\lambda > 5$.

[1] Leakage always denotes the fraction of energy deposited in the FCAL divided by the total energy deposition both in FPLUG and FCAL.

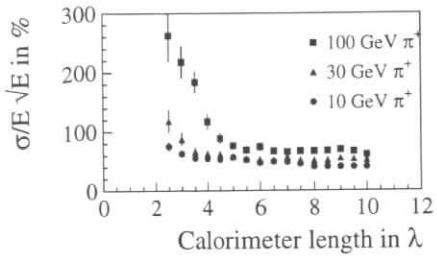

Figure 5: *Dependence of energy resolution on calorimeter length.*

2.4 Simulation of the FPLUG within the ZEUS Detector

The physics results presented in the next sections were gained with a simulation routine where the FPLUG calorimeter was implemented in the general ZEUS Monte Carlo routine MOZART. As a detailed simulation of hadronic showers in tungsten within the MOZART environment would be too time consuming and not reliable[2] we chose the same DU–scintillator "porridge" which is used as tracking material for the FCAL. The length of the FPLUG was adapted to the larger interaction length of 23.3 cm by increasing it to 116 cm as displayed in Fig. 1, again corresponding to 5 λ.
To take into account dead material (pump and flanges), a layer of 3 cm iron was situated just in front of the FPLUG.

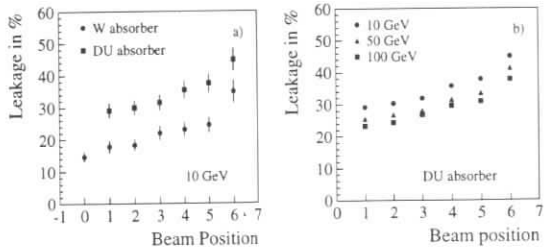

Figure 6: *a) Leakage from the FPLUG into FCAL for W and DU–absorber.*
b) Leakage from a DU–FPLUG into FCAL for different energies.
For the beam positions cf. Fig. 4b.

An idea of the different behaviour of tungsten and uranium as absorber can be obtained by looking at figure Fig. 6a where the larger leakage of DU with respect to W for 10 GeV pions is displayed. The lower leakage of the W configuration is caused by the smaller shower spread due to the higher density. The energy dependence of the leakage for DU is plotted in Fig. 6b.

2.5 Monte Carlo Programs

The relevant event generators are DJANGO6 and POMPYT2.2 [6] for the non-diffractive and diffractive events, respectively. DJANGO6 2.1 (2.2) [7] is an interface between LEPTO 6.1 (6.3) [8] and HERACLES 4.4 (4.5) [9]. In this section the non-diffractive process $ep \to eX$ is simulated with LEPTO6.1. The following parameters for POMPYT were taken: slope of the pomeron exchange to be 8 GeV^{-2}, no excitation of the diffractive scattered proton system, flat pomeron structure function $F_2^{I\!P}(\beta, Q^2) = 1$. Note, that for this investigation the proton dissociation option within POMPYT was switched OFF. The version used for MOZART was NUM12.3, which does include the C4 collimator for realistic comparison.

[2]The GEANT version in MOZART is too old to be used with the GCALOR interface.

3 Diffractive Physics

Diffractive physics in deep inelastic electron–proton scattering has become popular since rapidity gap events have been identified at HERA in 1993 [10].
The discrimination of diffractive events from normal DIS can be achieved in different ways, for example by rapidity gaps or by the invariant mass accepted by the detector being small as compared with "normal" deep inelastic events. In the following we assume the latter definition.
The topology of diffractively produced events is of major interest because the exchange of a pomeron at the proton vertex reveals QCD properties of the exchanged object.
The interest in the extention of the acceptance of the calorimetric detector has many reasons, of which in this section mainly the diffractive physics is discussed. Aspects of non-diffractive physics are insofar relevant as they represent the major part of the cross section and cover in certain kinematical ranges the diffractive events as background.

3.1 Outline of Physics Processes

3.1.1 Definition of the Variables used

The diagrams of the physics processes and some kinematic variables are indicated in Fig. 7. The mass of the hadronic final state, W, can be expressed in terms of Q^2 and Bjorken–x:

$$W^2 = Q^2(1/x - 1) + m_p^2 \approx Q^2/x \quad \text{for} \quad x \ll 1. \tag{1}$$

The following argument uses the rapidity variable y approximated by the pseudorapidity η:

$$y = \frac{1}{2} \ln \frac{E + p_{||}}{E - p_{||}} \quad \text{and} \quad \eta = -\ln \tan \frac{\theta}{2},$$

where $\tan\theta = p_t/p_z$ and $\theta, E, p_{||}$ and p_t are the angle with respect to the proton beam, the particle energy, the longitudinal and transversal momentum.

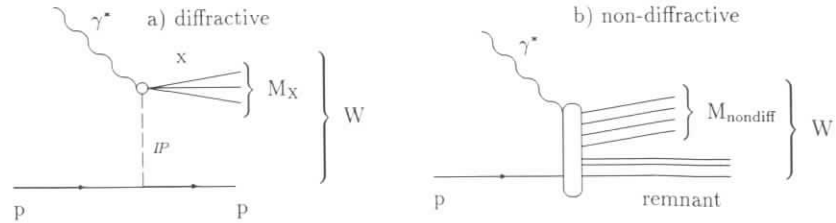

Figure 7: *Diagrams for the subprocess of diffractive scattering (a) and non-diffractive scattering (b). The M_X and $M_{nondiff}$ are the invariant masses accepted by the detector for the respective process.*

3.1.2 Deep Inelastic scattering in the Longitudinal Phase Space Model

Non-diffractive final state may be described as a uniformly distributed particle density in rapidity, $dn/dy = const$, except near the kinematical limits y_{min} and y_{max}. In the central range y may be approximated with η, which is actually the measured variable.
The total hadronic mass W, as given in Eq. 1, can also be expressed in this description as $W^2 = c \cdot \exp(y_{max} - y_{min})$, with c being a constant.
If the calorimetric detector provides good hermeticity in the backward direction but has an acceptance limit in forward direction at $y_{CAL} \approx 3.8 < y_{max}$ the observed invariant mass is $M^2_{nondiff} = c \cdot \exp(y_{CAL} - y_{min})$, where CAL denotes the total calorimetric detector. So the observed mass is smaller than W by the amount lost within the forward beam pipe, corresponding to the factor $\exp[(y_{max} - y_{CAL})/2]$, cf. Fig. 8 (non-diffractive case).

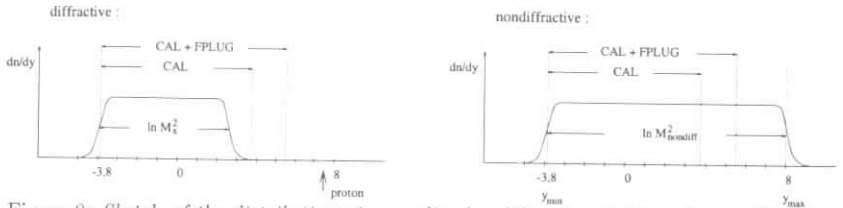

Figure 8: *Sketch of the distributions in rapidity for diffractive (left) and non-diffractive DIS (right) for the detector configurations with/without FPLUG calorimeter.*

If the acceptance in the forward direction is improved by the insertion of a FPLUG by ≈ 1.5 units in rapidity the observed non-diffractive mass distribution is shifted by the amount of

$$\Delta \ln M^2_{nondiff} = y_{CAL+FPLUG} - y_{CAL} = 1.5, \qquad (2)$$

where $y_{CAL+FPLUG}$ means the maximum accepted rapidity of the combined system CAL and FPLUG. In other terms $M^{CAL+FPLUG}_{nondiff}/M^{CAL}_{nondiff} = 2.12$. This way the invariant mass spectrum of non-diffractive events is shifted. As will be shown below, the diffractive events having a rapidity gap between the particles of the diffractively produced system and the scattered proton system will not be affected by the increase of the acceptance [11], resulting in a considerably better separation of these two processes.

3.1.3 Deep Inelastic Diffractive Scattering

Diffractive inelastic scattering is described by the subprocess $\gamma^* p \to Xp$. The relevant variables are Q^2, x and M_X. The events are characterised by the exchange of a colorless object between the system X and the proton. Its signature is a large rapidity gap between the hadrons of X and the proton which is scattered with small momentum transfer, see Fig. 7a.
The rapidity gap is the essential feature of the diffractive scattering process, see Ref. [12]. Due to the rapidity gap the M_X is virtually independent of the acceptance of the calorimeter in the forward direction y_{CAL} or $y_{CAL+FPLUG}$, see Fig. 8 (diffractive case). In contrast to the Eq. 2 one expects $M^{CAL+FPLUG}_X/M^{CAL}_X \approx 1$. Therefore the separation between diffractive and non-diffractive processes is the better the closer the acceptance of the detector approaches the proton system.
Due to fluctuations, rapidity gap events do occur also in non-diffractive events, but they are, with increasing rapidity gap, exponentially suppressed. The signature of diffractive events is

that they are not suppressed with increasing rapidity gap. This results in a plateau-like behaviour of the M_X-distribution in terms of $\ln M^2_X$ for low values of M_X for diffractive events [13]. The plateau is followed, for higher masses M_X, by a peak which is due to non-diffractive DIS. In the overlap region the non-diffractive DIS may be described as an exponential fall off with decreasing M_X.

3.1.4 Energy Dependence of Diffractive DIS

The differential cross section of diffractive events, extracted by subtraction of the exponential fall off the non-diffractive DIS events, shows an almost linear rise with W. The W dependence can be formulated in terms of Regge exchange

$$\frac{d\sigma_{\gamma^* p \to XN}(M_X, W, Q^2)}{dM_X} \propto (W^2)^{(2\alpha_{I\!P}-2)},$$

where $\alpha_{I\!P}$ is the t-averaged pomeron trajectory. Experimentally it is found that $\alpha_{I\!P} = 1.23 \pm 0.02(stat.) \pm 0.04(syst.)$ [11], which is substantially larger than expected from soft hadron-hadron scattering.
In view of various models describing the energy dependence, see for instance Ref. [14], it is of great importance to increase the mass range of M_X to higher accessible values, in order to explore whether there is a transition from hard to soft exchange as M_X increases.

3.1.5 Jet Structure of Diffractive DIS

The structure of the system X produced by the process

$$\gamma^* I\!P \to X$$

might be used to distinguish between different reaction mechanisms.
For instance in the aligned jet model [12], as well as in the LO process of POMPYT [6], a two-jet final state is expected. On the other hand a hard gluon emission will result in a final state of three partons. A clear distinction of a three–jet final state from a two–jet final state can be achieved only if the mass of the diffractive system M_X is sufficiently large.

3.2 Diffractive and Non-diffractive Event Simulation

As shown above in Sec. 3.1.3 the separation of the diffractive from non-diffractive events can be accomplished by the size of the invariant mass accepted by the detector. The peak position of the non-diffractive invariant mass spectrum depends crucially on the upper bound of the η-acceptance. The applied cuts follow the evaluation of the ZEUS data from reference [11]. Especially the noise cut-off results in a correction of the detected mass. In the following a correction factor of 1/0.68 was applied to the mass scale M_X. The improvement of separation due to the insertion of the FPLUG can be seen in Fig. 9. The vertical line indicates M_X, where the signal to background ratio is near one. The improvement due to the insertion of the FPLUG is a factor of two. This way, masses of 22 GeV for $W = 150$ GeV and 36 GeV for $W = 245$ GeV are accessible. It should be mentioned that in this plot the events at $W \neq 150$ GeV are rescaled in M_X with the relation $M_X/W = const$.
In order to demonstrate that these high masses are efficiently accepted for diffractive DIS by the improved detector the maximum η of the most forward going hadron at the hadron level is

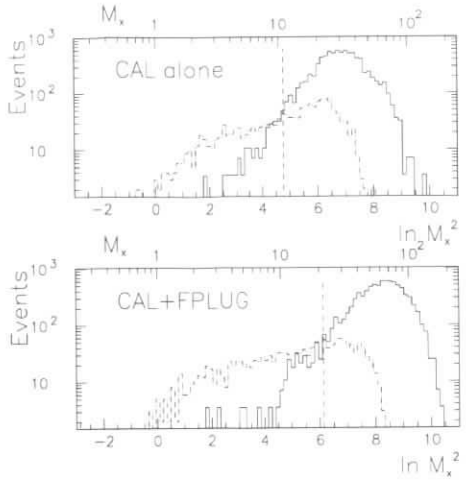

Figure 9: *The distribution of* $\ln(M_X^2)$ *for diffractive (dashed) and non-diffractive events (solid line) for an average* $\bar{W} = 150$ GeV. M_X *is corrected to the hadron level. Top: for the ZEUS detector with full calorimetry. Bottom: for the ZEUS detector with the addition of the FPLUG calorimeter. The gain for detection of diffractive events is a factor 2.0 in* M_X.

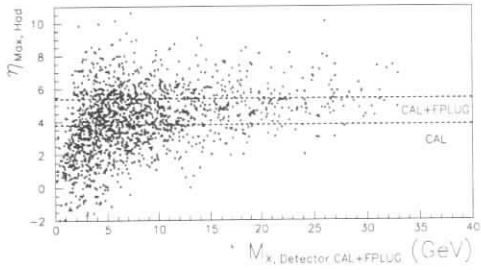

Figure 10: *The distribution of pseudorapidity* η_{max} *of the most forward going particle produced at hadron level versus reconstructed* M_X *on detector level (CAL+FPLUG) in diffractive DIS. See Sec. 2.5 for details on the event generation.*

plotted as a function of the reconstructed M_X at the detector level, see Fig. 10. The distribution shows that the most forward going hadron of a diffractive DIS event is accepted by the CAL alone in 42% of the calculated events, but it is accepted in 75% of the calculated events if the FPLUG is added and the acceptance limit is raised to $\eta = 5.4$.
It should be noted that the use of the FPLUG as an anticounter, establishing a rapidity gap between $\eta = 3.8$ and $\eta = 5.4$, accepts only $M_X < 18$ GeV for $W = 150$ GeV. The cut used for vetoing minimum ionizing particles is 400 MeV. This is an important fact showing that different selection criteria for diffractive events accept different topology.
Concerning the simulation of a "cascaded" version of the plug calorimeter, which also has been performed, the following facts have been observed. Dead material as being present with the collimator in front change also the vetoing efficiency. This in turn means a high sensitivity to

the detailed description of the dead material in the simulation.

3.3 Conclusion

There are a number of reasons to have an extended acceptance of the calorimetric measurement of the final state for diffractive events. A FPLUG calorimeter inserted into the existing forward calorimeter of ZEUS increases the separation of diffractive from non-diffractive events dramatically. It therefore would allow for the exploration of the W dependence and its interpretation in terms of pomeron exchange within the frame of Regge model and it would allow for the investigation of the final states of the system X through jet analysis.
The geometrical increase of the acceptance is 1.6 units in η for this simulation. The effective increase in $\ln M_x^2$ amounts to 1.35 units, somewhat smaller than expected from the geometrical acceptance. Remember that the situation "without a plug" has an inert collimator in place of the plug. The effects are absorption and rescattering changing the energy flow in this rapidity intervall by as much as a factor 2. The main result is that masses M_X up to 36 GeV are obtainable in diffractively produced events with the capability of the investigation of their topology. It should be mentioned that the investigation of excitation of the diffractively scattered proton is an additional subject of interest.

4 Jets in Deep Inelastic Scattering

In this section the influence of a FPLUG Calorimeter on forward jet physics in deep inelastic scattering is investigated using the *JADE algorithm* [15] and the *extended JADE algorithm* [16]. In the following the JADE algorithm is applied in the reference frame of the ZEUS detector. The extended JADE algorithm is Lorentz invariant, contrary to the JADE algorithm which is applied in the reference frame of the ZEUS detector. The jet resolution parameter is set to $y_{\rm cut} = 0.02$.
The jets of an event are ordered with respect to their distance $d_{i,\rm prot}$ to the momentum of the proton beam. The jet with the smallest distance $d_{i,\rm prot}$ is called *remnant jet*. The *forward jet* is defined to be the non-remnant jet with the smallest distance to the proton beam. The forward jet is also called *first current jet*.
At the hadron level the JADE algorithm and the extended JADE algorithm are applied to the momenta of the particles of the hadronic final state (apart from the scattered lepton). At the detector level they are applied to the momenta of the calorimeter cells not assigned to the scattered lepton and to the momentum of the pseudoparticle which is given by the momentum of the hadronic activity lost in the beam pipes.
Forward jets are expected to be of importance, to find signatures of the BFKL evolution [17] and "Hot Spots" [18].
The FPLUG improves the acceptance of the ZEUS detector with respect to the forward jet of (2+1) jets. To show this, we study at the detector level the extension of the forward jet with respect to the pseudorapidity η using the JADE algorithm. In Fig. 11 a Monte Carlo scatter plot of the pseudorapidity $\eta_{\rm jet}$ of the forward jet versus $\Delta\eta = \eta_{\rm cell} - \eta_{\rm jet}$ is shown, where $\eta_{\rm cell}$ are the pseudorapidities of the detector cells which are recombined to the forward jet. As can be seen, the forward jets are reconstructed in the forward direction around $\eta_{\rm jet} = 4$ and a considerable part of cells of the forward jets belong to the FPLUG.
However, the improvement of the FPLUG on forward jet physics may be quite small. Consider the transverse momentum of the forward jet determined by the JADE algorithm. In Fig. 12 a

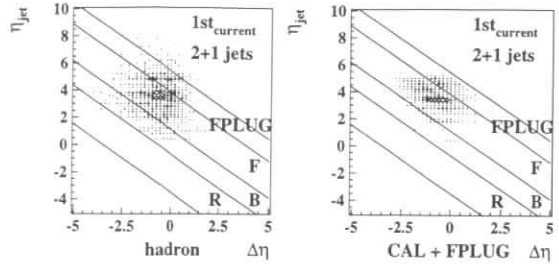

Figure 11: *Scatter plot of the pseudorapidity η_{jet} of the forward jet versus $\Delta\eta = \eta_{cell} - \eta_{jet}$ where η_{cell} are the pseudorapidities of the detector cells which are recombined to the forward jet. On the left hand side the hadron level is shown, on right hand side the detector level, using the Monte Carlo program DJANGO6 (version 2.1). Also indicated are the acceptance limits of the Rear Calorimeter (R), the Barrel Calorimeter (B), the Forward Calorimeter (F) and the FPLUG Calorimeter (FPLUG). The kinematic range is restricted to $Q^2 > 7$ GeV^2.*

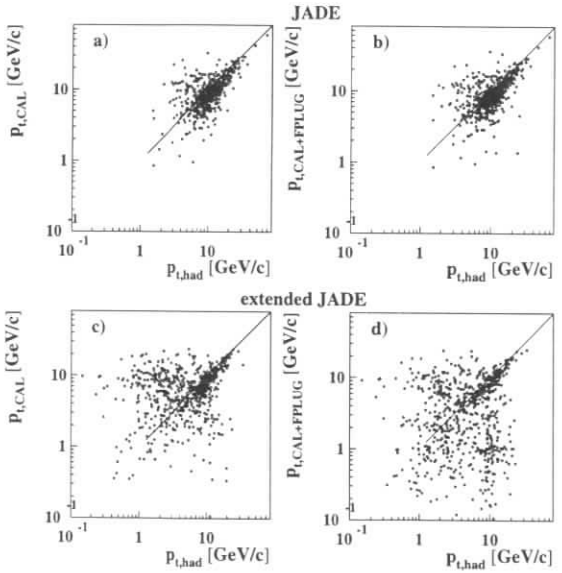

Figure 12: *Scatter plot of the transverse momentum of the forward jet: detector level versus hadron level without (a, c) and with (b, d) a FPLUG, using the Monte Carlo program DJANGO6 (version 2.2). For the scatter plots on the top the JADE algorithm is used, on the bottom the extended JADE algorithm. The kinematic range is restricted to $Q^2 > 100$ GeV^2.*

Monte Carlo scatter plot of the detector level versus the hadron level is shown without (a) and with (b) the FPLUG. By comparing Fig. 12a with Fig. 12b it can be seen that the transverse momentum is only very weakly influenced by the FPLUG.

An influence of the FPLUG on the transverse momentum of the forward jet is clearly observable, if the JADE algorithm is replaced by the extended JADE algorithm. Fig. 12c shows the Monte Carlo scatter plot (detector level versus hadron level) of the transverse momentum of the forward jet. A correlation is visible, but there are also many off-diagonal events in the left upper part around $p_{t,had} = 1$ GeV and $p_{t,CAL} = 10$ GeV. They originate in events which are identified as (2+1) jets at the hadron level but as (1+1) jets at the detector level. The forward jet of a (2+1) jet is mainly propagating into the forward direction, and it may happen that most of its energy is lost in the beampipe. In this case the energy depositions in the inner FCAL cells are too small to be identified as a jet and are recombined with the calorimeter cells in the central part of the detector to the current jet. This causes a jump in the transverse momentum of the forward jet between the hadron level and the detector level. Note that the transverse momentum of the current jet of a (1+1) jet is balanced by the transverse momentum of the scattered lepton and thus is of the order of Q.
The purity of the scatter plot of the transverse momentum of the forward jet is improved by a FPLUG calorimeter: Fig. 12d shows that the density of the off-diagonal events in the left upper part is reduced compared to Fig. 12c. On the other hand, an increase of off-diagonal events in the right lower part is observed stemming from events which are generated as (1+1) jets but reconstructed as (2+1) jets. Contrary to the off-diagonal events in the left upper part, the off-diagonal events in the right lower part can be removed by a cut on the transverse momentum.
The JADE algorithm seems to have a tendency to recombine a lot of the forward directed hadronic activity into the remnant jet. If the extended JADE algorithm is used, the forward activity is more likely resolved as a current jet.
In summary, an FPLUG Calorimeter improves forward jet physics, if the jets are determined with a jet algorithm which is sufficiently sensitive to the hadronic activity in the forward direction.

5 Summary

The investigation of improvement for physics detection by a FPLUG at the ZEUS detector yields:

- The accepted invariant masses of the diffractively produced system increases by a factor 2.0. This way masses as high as 36 GeV become accessible for the investigation of event topology in terms of jet analysis.

- Improved reconstruction of jets in the forward region using the JADE and the extended JADE algorithm. The sensitivity of hadronic activity in the η-range between 3.8 and 5.4 seems to be larger for the extended JADE algorithm. In this region additional hadronic activity by BFKL-processes and Hot Spots are expected.

There are a number of interesting topics not explicitly covered here, of which we mention: forward energy flow, double diffaction, multiple scattering in hard photo production, accepting events in hard photo production with larger rapidity gap than without FPLUG and separation of remnant jets from current jets.
In conclusion, the FPLUG will be very fruitfull for the understanding of various aspects of forward physics.

Acknowledgement

We thank the organizers of the workshop "Future at HERA" and the convenors of the working groups "Diffractive Hard Scattering" and "Jets and High E_T Phenomena" for their strong support.

References

[1] R. Brun and F. Carminati, *GEANT Detector Description and Simulation Tool*, CERN Program Library Long Writeup W5013 (1994).

[2] C. Zeitnitz and T.A. Gabriel, *The GEANT–CALOR Interface User's Guide*, 1994, unpublished.

[3] A. Fasso et al., *FLUKA 92*, Proceedings of the Workshop on Simulating Accelerator Radiation Experiments, Santa Fe (1993).

[4] C. Zeitnitz and T.A. Gabriel, *The GEANT–CALOR interface and benchmark calculations of ZEUS test calorimeters*, NIM **A349** (1994) 106.

[5] A. Bamberger et al., ZEUS Note in preparation (1996).

[6] POMPYT 1.0: P. Bruni and G. Ingelman, Proc. Europhysics Conf. on HEP, Marseilles 1993, 595.

[7] K. Charchuła, G.A. Schuler and H. Spiesberger, *DJANGO6*, version 1.1, Comp. Phys. Commun. **81** (1994) 381.

[8] G. Ingelman, *LEPTO*, version 6.1, in: Proceedings '*Physics at HERA*', vol. 3, W. Buchmüller, G. Ingelman (eds.), DESY Hamburg 1992.

[9] H. Spiesberger, *HERACLES*, version 4.4, unpublished program manual (1993); version 4.0 as described in A. Kwiatkowski, H.–J. Möhring and H. Spiesberger, Comp. Phys. Commun. **69** (1992) 155.

[10] ZEUS Collaboration, M. Derrick et al., Phys. Lett. **B315** (1993) 481;
ZEUS Collaboration, M. Derrick et al., Phys. Lett. **B338** (1994) 483;
H1 Collaboration, T. Ahmed et al., Nucl. Phys. **B429** (1994) 477.

[11] ZEUS Collaboration, M. Derrick et al., Z. Phys. **C70** (1996) 391.

[12] J.D. Bjorken, 1971 Int. Symp. Electron and Photon Interactions at High Energies, Cornell, 1971.

[13] ZEUS Collaboration, M. Derrick et al., Z. Phys. **C68** (1995) 569.

[14] J. Bartels, H. Lotter, M. Wüsthoff, DESY 96-026;
S.J. Brodsky et al., Phys. Rev. **D50** (1994) 3134.

[15] G. Kramer, DESY 82–029 (1982), published in Proc. of the 13th Spring Symp. on High Energy Physics, Bad Schwandau/GDR (1982);
JADE Collab., W. Bartel et al., Phys. Lett. **B119** (1982) 239;
JADE Collab., W. Bartel et al., Z. Phys. **C33** (1986) 22;
JADE Collab., S. Bethke et al., Phys. Lett. **B213** (1988) 235.

[16] H. Heßling, preprint DESY 95–069 (1995).

[17] L.N. Lipatov, Sov. J. Nucl. Phys. **23** (1976) 338;
E.A. Kuraev, L.N. Lipatov, V.S. Fadin, Sov. Phys. JETP **45** (1977) 199;
Y.Y. Balitskii, L.N. Lipatov, Sov. J. Nucl. Phys. **28** (1978) 822.

[18] A.H. Mueller and H. Navelet, Nucl. Phys. **B282** (1987) 727;
A.H. Mueller, Nucl. Phys. B (Proc. Suppl.) **18C** (1991) 125.

Working Group on

Polarised Protons and Electrons

Conveners:

Joel Feltesse (Saclay), Marek Karliner (Tel Aviv), Gerhard Mallot (Mainz)
Richard Milner (MIT), Andreas Schäfer (Frankfurt)

Participants:

M. Anselmino (Torino), L. Andreeva (Moscow), R. Ball (Edingburg), D. Barber (DESY), J. Bartels (DESY), Ch. Berger (DESY), J. Blümlein (DESY), C. Boros (FU-Berlin), H. Böttcher (DESY-Zeuthen), A. Borissov (DESY), M. Botje (DESY), V. Breton (LPC Clermont-Ferrand), S. Brodsky (SLAC), J. Collins (Penn State), J.B. Dainton (DESY), A. Deshpande (Yale), M. Düren (Erlangen-Nuernberg), J. Ellis (CERN), P. Gambino (MPI München), E. Gardi (Tel Aviv), T.K. Gehrmann (Durham), M. Glück (Dortmund), S. Goloskokov (Dubna), D. von Harrach (Mainz), G. Hoffstätter (DESY and Technical Univ., Darmstadt), R. Horsley (Humboldt University, Berlin), V. Hughes (Yale), G. Igo (UCLA), H. Ihssen (DESY), E. Kabuss (Mainz), J. Kalinowski (Warsaw), A. Kataev (DESY), N. Kochelev (Dubna), V. Korotkov (Protvino, DESY-Zeuthen), A. Kotikov (IN2P3, Paris), F. Kunne (Saclay), J. Kwiecinski (Krakow), Z. Liang (FU-Berlin), J. Lichtenstadt (Tel Aviv University and CERN), K.-F. Liu (Kentucky), L. Mankiewicz (TU München), M. Maul (Frankfurt), T. Meng (FU-Berlin), R. Mertig (Leiden), M. Meyer-Hermann (Frankfurt), E. Mirkes (Karlsruhe), P. Mulders (Nikhef), F. Murgia (Cagliari), A. Nagajcev (DESY), W.-D. Nowak (DESY-Zeuthen), S. Nurushev (Protvino), G. Piller (TU München), G.Ridolfi (INFN Genova, Italy), G. Raedel (CERN), K. Rith (Erlangen), A. De Roeck (DESY), A. Saalfeld (TU München), P. Schuler (DESY), S. Schramm (GSI), A. Sidorov (Dubna), T. Sloan (Lancaster), E. Stein (Frankfurt), J. Stirling (Durham), M. Stratmann (Dortmund), M. Strikman (PennState), O. Teryaev (Dubna), A. Tkabladze (Dubna), M. Tokarev (Dubna), W. van Neerven (Leiden), A. Vogt (DESY, Würzburg), W. Vogelsang (Rutherford Appleton Lab), T. Weigl (TU München), C.-Y. Wu (Frankfurt), T. Yamanishi (Osaka), H. Zohrabian (DESY)

Polarised Protons and Electrons — Working Group Reports:

Physics with a polarized proton beam - a summary

J. Feltesse[a], A. Schäfer[b]

[a] DAPNIA, CE Saclay, F-91191 Gif/Yvette, France
[b] Institut für Theoretische Physik, Universität Frankfurt, D-60054 Frankfurt, Germany

Abstract: The precise study of the nucleon spin structure has evolved over the last years into a broad field allowing to test many different aspects of QCD, some of them with outstanding precision, and most of them being unaccessible by other means. With a polarized proton beam at HERA several of the crucial questions in this field could be answered: the polarized gluon distribution $\Delta G(x, Q^2)$ could be deduced, primarily from jet production, spin asymmetries of charged current events would clarify the quark spin decomposition, measurements of the polarized structure function $g_1(x, Q^2)$ in a previously unaccesible kinematic domain would further constrain $\Delta G(x, Q^2)$ and could detect deviations from DGLAP evolution, polarized proton-proton collisions could open a completely new field of physics, and a large number of relevant details could be clarified by other measurements. HERA would be complementary to all presently planned lower energy experiments. To exploit the full potential of this option requires, however, 200 pb^{-1} of luminosity with electron and proton polarizations of order 70 percent. For 1000 pb^{-1} the physics potential would increase substantially, for luminosities below 100 pb^{-1} it becomes marginal. The availability of polarized deuteron and/or ^{3}He beams is also crucial to allow for a broad physics program. The charged current experiments would profit greatly from the availability of electron and positron beams.

1 Introduction

The understanding of spin-effects in QCD has improved dramatically since the first surprising data of EMC became available in 1988 [1]. On the experimental side the available data became much more precise and on the theoretical side many quite complicated questions could be fully analysed. Most of this work focussed on the first spin structure function $g_1(x, Q^2)$, which is, however, only one of several structure functions, namely the one most easily accessible in deep inelastic lepton-nucleon scattering. As a result of this work we have nowadays a generally accepted range of models for the polarized quark distribution functions entering $g_1(x, Q^2)$. These parametrisations imply that the quarks carry only about 30 percent of the nucleon spin. While being consistent with the data, as well as with the results of lattice gauge studies [2], these interpretations have not really been experimentally tested. Nearly all models predict a substantial polarization for both the gluons and the strange quarks (the distinction between these two contributions is scheme dependent, the polarization of the strange quarks is primarily due

to the gluon polarization), which has to be confirmed by direct experimental tests before the present standard interpretation of the data can be regarded as established. The polarized gluon distribution is of especial interest, because it could be surprisingly large. As $\alpha_s(Q^2)\Delta G(Q^2)$ with $\Delta G(Q^2) = \int_0^1 \Delta G(x,Q^2)dx$ is a renormalization group invariant, the reduction of α_s when Q^2 is evolved from a hadronic scale to a perturbative scale has to be counter balanced by a strong increase in ΔG. Typical parametrizations predict e.g. that for $Q^2 = 4$ GeV^2 the total gluon spin could be of order 1 to 2 although the nucleon as a whole has only the spin $\frac{1}{2}$. This astonishing prediction clearly has to be tested by dedicated direct experiments. Also, under NLO-evolution the parton distributions mix, such that the polarized gluons contribute also to $g_1(x,Q^2)$. This general feature of NLO-calculations has attracted great attention due to the fact, that the relevant graph involves the axial anomaly, which is probably the most important graph in all of quantum field theory. Spin experiments can thus test our understanding of its properties. In the unpolarized case the gluon distribution was determined by fits to DGLAP-evolution, from jet production, from prompt photons, and from vector meson production. All of these methods could be applied for $\Delta G(x,Q^2)$ at a polarized HERA, as will be discussed in detail in the next sections.
One crucially important point in spin physics is that the ratio of polarized to unpolarized distribution functions varies substantially with Bjorken-x, leading for the different observables in some kinematic domains to unmeasurably small asymmetries (sometimes as small as 10^{-4}) and in other kinematical domains to very large ones (up to 60 percent). This alone requires different experiments, sensitive to various x-ranges and makes most of the discussed projects rather complementary. In section 2 recent theoretical progress is reviewed. In section 3 we discuss the most favourable observables for HERA, primarily jet and charged current asymmetries. Section 4 will be devoted to the possibility of investigating fixed target polarized proton-nucleon collisions at HERA. In section 5 we try to put a polarized HERA in perspective to the various other planned or already running spin experiments.

2 Recent theoretical progress

Let us start our review with the structure function $g_1(x,Q^2)$. It is measured in inclusive collisions of longitudinally polarized nucleons and longitudinally polarized leptons. The latter have always to be polarized longitudinally. For transverse lepton polarization one cannot extract any additional information, but all asymmetries are reduced by the factor $\gamma = E_e/m_e$. However, transverse nucleon polarization gives accesss to new and even especially interesting information. It tests various well defined higher twist effects. To get an impression of the richness of structure functions and correlators involved we refer to [3]. Here we shall only discuss the twist-2 part of $g_1(x,Q^2)$ which can be written as

$$g_1(x,Q^2) = \sum_f Q_f^2[q_f^\uparrow(x,Q^2) - q_f^\downarrow(x,Q^2)] \qquad , \quad f = u,\bar{u},d,\bar{d},s,\bar{s},... \tag{1}$$

with $q_f^\uparrow(x,Q^2)$ describing the probability that the virtual photon hits a quark of flavour f polarized in the direction of the nucleon spin and carrying momentum fraction x at a given resolution Q^2. Under Q^2-evolution the singlet part of $\Delta q(x,Q^2) = q^\uparrow(x,Q^2) - q^\downarrow(x,Q^2)$ mixes with the polarized gluon distribution $\Delta G(x,Q^2)$ and in the limit $Q^2 \to \infty$ the relevant graph becomes the well known triangle anomaly. It was realized early on, that this mixing could be strong enough to play a crucial role in the interpretation of the data, so this specific NLO-graph was

added to the otherwise LO-analyses, creating quite a bit of confusion [4]. Over the last year this situation was clarified by the derivation of complete NLO evolution equations by Mertig and van Neerven [5], which were rederived independently by Vogelsang [6]. This work constitutes a major advance in our understanding of spin physics. Now the leading box-graph contribution to the anomaly is contained just as one contribution among others in the NLO-evolution equations. In principle it could still be that higher order, possibly completely non-perturbative graphs change the mixing significantly, but presently there is no indication for this. However, to know for certain that this is not the case one has to measure $\Delta G(x,Q^2)$ directly and confirm that the result is in agreement with the expectation from NLO-evolution fits to existing data. To do this would be one of the major aims of the experiments with a polarized HERA. We will discuss in the next section to which extent such HERA data would improve the NLO-fits and how $\Delta G(x,Q^2)$ could be measured directly from jet-asymmetries.

One of the main aims of the unpolarized QCD program at HERA is to detect deviations from DGLAP evolution at small x. So far no unambiguous results were obtained. The present data seem to be compatible with DGLAP- as well as BFKL- and multi-reggon-behaviour. It is natural to ask, whether the phenomenological differences between these three approximations would be larger for the polarized structure functions in the HERA x-range. In fact in an analyses by Bartels, Ryskin and Ermolaev [7] in the multi-reggon kinematics and using a fixed, Q^2-independent coupling constant the authors reached the rather drastic asymptotic ($x \to 0$) prediction

$$g_1(x,Q^2)^{NS} \sim x^{-0.41}\left(\frac{Q^2}{\mu^2}\right)^{0.2}$$
$$g_1(x,Q^2)^{S} \sim x^{-1.02}\left(\frac{Q^2}{\mu^2}\right)^{0.52} \tag{2}$$

suggesting a large deviation from NLO-behaviour at asymptoticaly small x. However, within this approach it is unclear how small x has to be to reach this behaviour and also everybody agrees that using a running coupling constant could change the situation substantially. We would like to stress that besides the test of small-x asymptotics, data points at very small x are very important to reduce the systematic error on the Bjorken- and Ellis-Jaffe sum rules. Let us remind that the Bjorken sum rule ist one of the most interesting firm predictions of QCD which should be tested with the utmost accuracy.
Blümlein and Vogt [8] implemented the additonal terms into the evolution equations and found that for the non-singlet part the deviation from NLO-DGLAP is unmeasurably small within the HERA range, but that it is very large for the singlet part, see figure 1. There is some discussion about the probable size of non-leading contributions, which presently cannot be calculated, but at least it is safe to say that the deviations could be dramatic.
Let us add that for the third twist-2 distribution function h_1, which is only accessible in nucleon-nucleon collisions or semi-inclusive lepton-nucleon collisions, the differences are even larger. It was shown by Kirschner et al. [9] that the leading double-logarithmic term of DGLAP is in this case non-leading when compared to the multi-reggon result, which is a constant as function of x (for $x \to 0$). The same caveats as for the case of $g_1(x,Q^2)$ apply also here, but with all due caution it seems clear that this would be a most interesting quantity to measure. Whether a measurement of h_1 at small x would be feasible at a polarized HERA depends on the size of a yet unknown parameter linking fragmentation properties to the transverse polarization of the

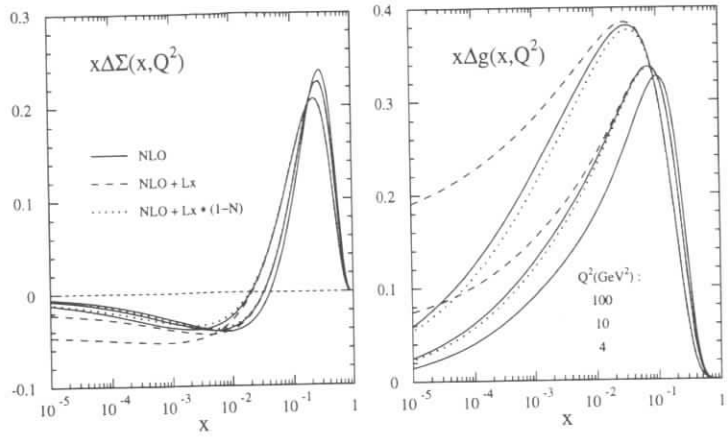

Fig. 1

Figure 1: *Predicted deviation for the singlet and gluon spin distribution function between NLO-evolution with and without the leading* $\log x$ *contributions.*

leading quark (this parameter characterizes the so called Collins effect [10]). If this parameter were sufficently large, this could open a field of investigation in addition to the measurements described below.

Let us stress that the singlet and non-singlet part of the distribution functions have widely different properties which have to be disentangled by measuring both the proton and neutron polarized structure functions. This requires to have polarized proton, deuteron and/or ^{3}He-beams. If eq. (2) holds both $g_1^p(x)$ and $g_1^n(x)$ are dominated by the singlet part at very small x. However, in the present SMC data the non-singlet part dominates. This makes it so very interesting to follow both structure functions down to lower x values.

As is pointed out by Düren in his contribution, a polarized deuteron beam with the possibility to tag both the spectator proton or the spectator neutron would practically double the effective luminosity and at the same time reduce systematic errors. However, the machine problems encountered for this option are substantial.

3 The most promising experiments with polarized electron-nucleon collisions

We shall discuss three main experiments to be performed at a polarized HERA, namely the measurement inclusive DIS, jet spin asymmetries and spin asymmetries for charged current events.

The outstanding advantage of HERA is that it can measure structure functions for very small x. For polarized reactions one has to know, however, that the probability for the exchanged

photon to be polarized, if the electron is polarized depends on $y = q \cdot P/p \cdot P$ with the photon momentum q_μ, the incoming electron momentum p_μ and the Proton momentum P_μ. For small values of y the measurable asymmetry simply scales with y. Knowledge of this fact, together with the general smallness of the asymmetries for very small x, is crucial to understand why a polarized HERA would do well in some cases and not so well in others and why in general a much higher luminosity is needed than for the current meassurements of the unpolarised structure function. There is, however, also an advantage going along with this. At medium and large x the values for Q^2 become large resulting in large values of y. Therefore one can obtain more precise results in this domain.
However, it is very difficult to make use of this for polarized DIS reactions because the spin asymmetry for small x is very small e.g for $x = 2 \cdot 10^{-4}$ it is only of the order 10^{-3} unless there are strong deviations from the predictions of present day NLO-fits, which is, however, possible for such small x values as discussed in the previous section. (Measuring such small asymmetries requires polarimeters of a quality of order 10^{-2}, a problem which is not yet solved, but for which several methods have been proposed.) The low x behaviour is predicted to be highly Q^2 dependent. Lichtenstadt et al. have analysed the situation in great detail and some of their results are combined in figure 2. Here the expected asymmetry for various x and Q^2 bins is shown, however, for the somewhat optimistic luminosity of 1000 pb^{-1}. The central curve in each plot shows the prediction from the best present NLO fit, while the dashed and dotted curve represent the expected signal for a very small respectively large (but not excluded) ΔG. The unusual feature that the statistical precision increases with Q^2 for a given x is due to the spin-dilution factor $\approx y$. Obviously with this luminosity one would just have the sensitivity to distinguish between the three cases, by combining all $x - Q^2$-bins. In judging the quality of these results one has, however, to realize that the NLO-fits which were used predict that the asymmetry goes through zero close to $x = 10^{-3}$ and this spoils the signal just in the region of highest statistical sensitivity, see figure 3. If this would not be the case the signal would be far more significant. This statement can be inverted. The increase in precision of typical NLO-fits due to the anticipated data is in fact quite significant [11]:

predicted total gluon spin from present day NLO-fit : 1.52 ± 0.74
predicted total gluon spin including the data from figure 2 : 1.29 ± 0.22
predicted total gluon spin including HERA data for 200 pb^{-1} : 1.29 ± 0.28

Such an experiment would be outstanding to check at high Q^2 and very small x that such a fit is justified.
Let us add here that as usually an important systematic uncertainty comes from QED radiative corrections, which are in principle well known, but for which the accuracy of the employed codes has recently become a topic of discussion. We refer to the working group report on unpolarized structure functions for details. For spin asymmetries the radiative corrections are much smaller than for the cross-sections themselves.
The statistical sensitivity would be substantially improved if the HERA proton energy could be reduced, keeping the same luminosity. This might interfere, however, with the two very promising experiments to be discussed next.
We conclude that the measurement of $g_1(x, Q^2)$ at HERA energies would provide an important complement to high precision experiments at lower energy, proposed e.g. for CERN (COMPASS) and SLAC.

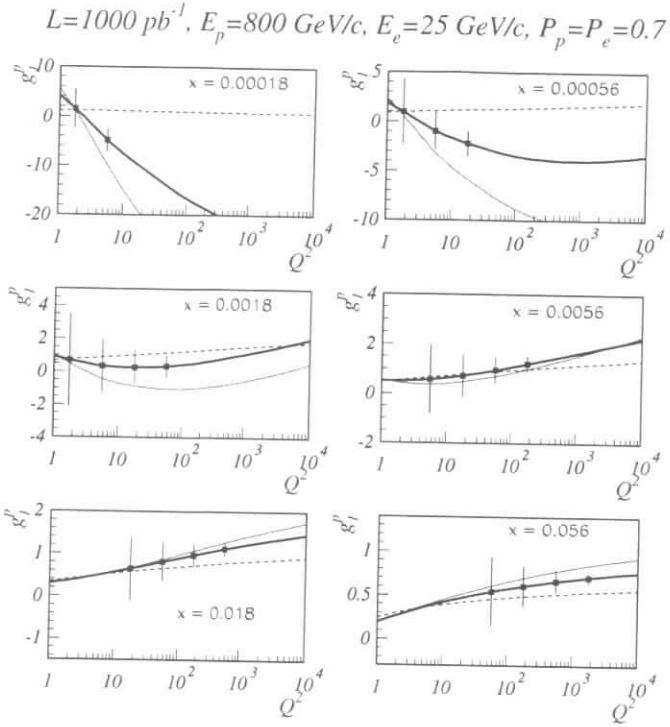

Figure 2: *Anticipated results of a 1000 pb^{-1} run for various $x - Q^2$-bins. The errors are statistical only. The solid line represents the prediction from the best NLO-fit to present data. The dashed and dotted curves show the predictions for an especially small respectively large gluon polarisation.*

One domain in which the high HERA energies really pay off is the study of jets. (This was already discussed at the last workshop [12].) Jets can in principle also be studied at lower energy and in proton-proton collisions, however, the main problem of all such studies is the control of higher order corrections. Thus the main emphasis for the determination of $\Delta G(x, Q^2)$ (respectively $G(x, Q^2)$) lies on the control of the theoretical systematic errors. In this respect jet spin asymmetries at HERA are a very favorable case [13]. The studies of Mirkes et al. [14] show that systematic uncertainties in the cross sections cancel to a large degree for the spin asymmetries and in addition the large HERA energies allow to impose cuts (most notably on the invariant jet-jet mass squared s_{jj}) which further reduce these uncertainties.
The processes leading to two-jet events (we do not count the proton remanent jet) are shown in figure 4. Luckily it turns out that for the standard sets of NLO polarized parton distributions the annihilation graph, which is proportional to $\Delta G(x)$ dominates over the Compton graph, which is proportional to $\Delta q(x)$. Therefore the 2-jet event rates are highly sensitive to the

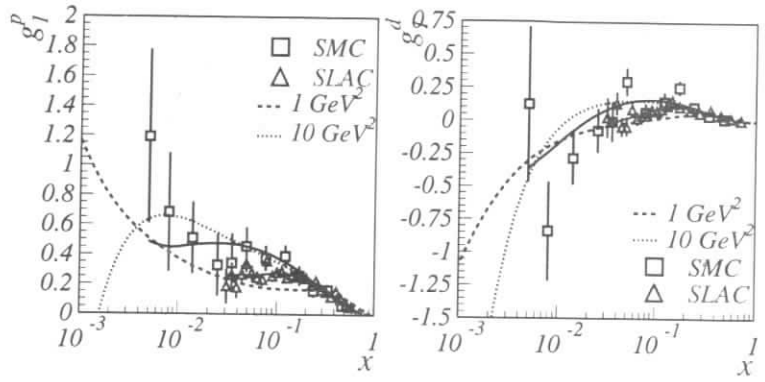

Figure 3: *Expected x-dependence for $g_1^p(x)$ and $g_1^d(x, Q^2)$ for two values of Q^2, showing the strong evolution effects for small x.*

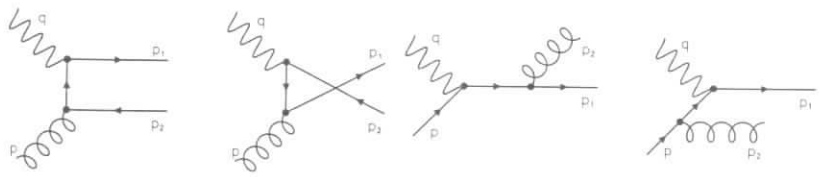

Figure 4:

polarized gluon distribution and already a relatively crude measurement would allow to decide between scenarios with large and small ΔG in the best accessible x_g-range between a few times 10^{-3} and several times 10^{-2}. Note that for 2-jet events the momentum fraction x_g and the Bjorken variable x differ strongly. With the total invariant mass squared of the outgoing jets $s_{jj} = (q + x_g P)^2 = -Q^2 + 2x_g\nu$ they are related by $x_g = x(1 + s_{jj}/Q^2)$. Typically x_g is about an order of magnitude larger than x.
We have studied the expected 2-jet events with the help of two computer codes called MEPJET and PEPSI2. MEPJET [14] was developed to describe unpolarized jet-production. It does not yet contain hadronization and describes the physics only at the parton level, but in its unpolarized version it uses either LO or NLO matrix elements and distribution functions, allowing thus to estimate the size of higher order corrections and to select the most suitable kinematic range to minimize systematic errors. PEPSI2 [15] is a polarized version of LEPTO 6.2 and as

such a general multi-purpose code. It contains hadronization and is altogether constructed in a completely different manner than MEPJET. Comparing the results of both codes one should therefore get a rather reliable feeling for the theoretical uncertainties involved. It turns out that the results for the asymmetries agree quite nicely. The predictions we can presently make and which will be discussed in the following might still have a quite substantial theoretical uncertainty (of the order 10 percent or so) but we expect that by the time experiments at a polarized HERA would start, these uncertainties will be substantially reduced, allowing to make full use of the good expected statistical accuracy.

Figure 5 shows the theoretical prediction for the spin asymmetry for three different scenarios, the standard one, one with an extremely small $\Delta G(x)$ and one with a very large $\Delta G(x)$. The cross section for photon-gluon fusion contains a factor $(2x_g - 1)$, which is responsible for the fact that in the accessible x_g-range the resulting asymmetry is negative and cancels partly with the much smaller positive contribution from the Compton graph.

Figure 6 shows the expected results for a run with 200 pb^{-1} respectively 100 pb^{-1} and

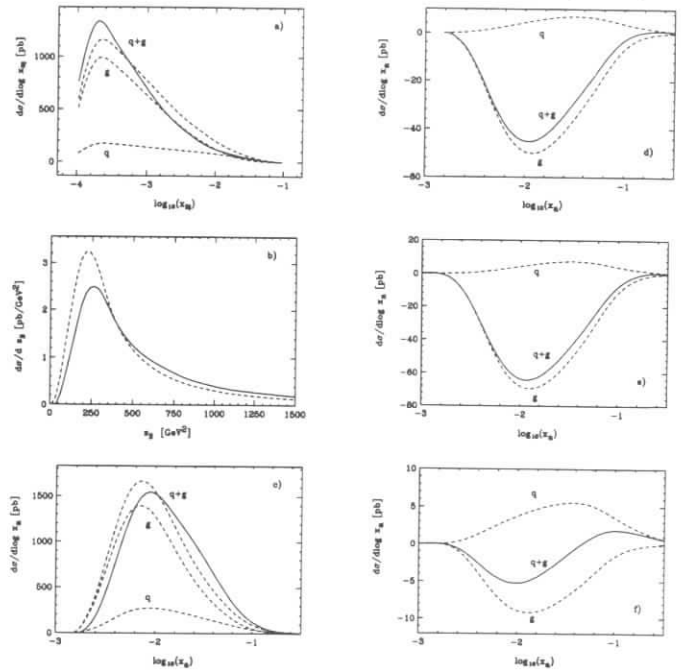

Figure 5: *a) Dependence of the* **unpolarized** *two-jet cross section on Bjorken x_{Bj} for the quark and gluon initiated subprocesses and for the sum. Both LO (dashed) and NLO (solid) results are shown; b) Dijet invariant mass distribution in LO (dashed) and in NLO (solid) for unpolarized dijet production; c) Same as a) for the x_a distribution, x_a representing the momentum fraction of the incident parton at LO; d,e,f) Results for the LO* **polarized** *two-jet cross sections. Three different scenarios were used, the standard scenario (d), a scenario with a very small polarized gluon distribution function (f) and with a larger one (e).*

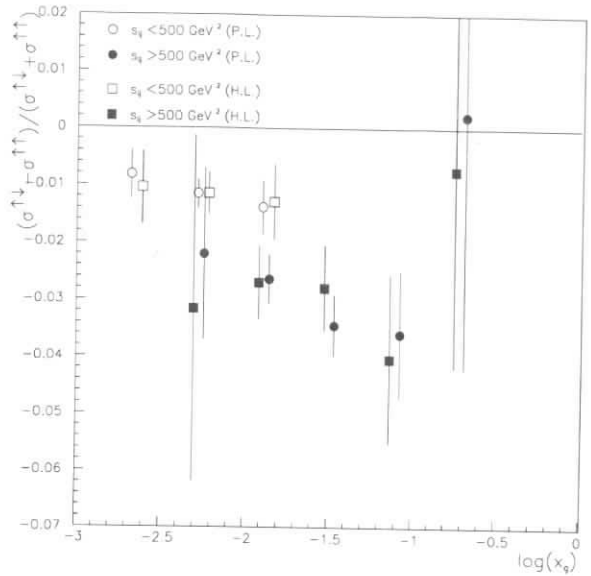

Figure 6: *Expected statistical accuracy for a standard HERA run where P.L. stands for a parton level simulation using MEPJET with a luminosity of 200 pb^{-1} ($P_e = P_p = 0.7$), and H.L. stands for a hadron level simulation using PEPSI and the realistic acceptances of the H1 detector with a luminosity of 100 pb^{-1}.*

$P_e \cdot P_p = 0.5$, and compares MEPJET and PEPSI2 predictions. Both agree reasonably well. Most important are the expected statistival errors which clearly demonstrate that the polarized 2-jet asymmetry would in fact determine $\Delta G(x)$ with quite good accuracy and would thus answer the most important open question regarding the intenal spin structure of the nucleon. For the second graph in figure 6 a $s_{jj} > 500$ GeV^{-2} cut was implemented to reduce the uncertainties due to higher orders. Obviously such a cut does not increase the relevant error, mainly because it gives more weight to the larger x_g events which have a larger spin asymmetry. The fact that such cuts are unproblematic supports our hope that one will be able to reduce the systematic errors to a very small level such that one could even make full use of a further luminosity increase, possibly up to 1000 pb^{-1}.

Since in the unpolarized case many processes at HERA have first and most accurately been studied in photoproduction, Stratmann and Vogelsang [16] have examined the photoproduction

of jets and heavy flavors for the situation with longitudinally polarized beams with regard to their sensitivity to ΔG. While open-charm production turns out to be less useful to pin down ΔG unless one can achieve very large luminosities (1000 pb^{-1}), the asymmetry for the rapidity distribution of the single-inclusive jet cross section shows a particularly strong dependence on ΔG and is measurable even for 100 pb^{-1} (see fig. 7). Furthermore, polarized photoproduction experiments may in principle allow to not only determine the polarized parton distributions of the proton, but also to get a glimpse at those of the circularly polarized *photon* which are completely unknown so far. For example, at larger rapidities the single-inclusive jet cross section shown in fig. 7 becomes also sensitive to the hadronic structure of the photon. Definitely photoproduction would be one of the most interesting processes to be studied at a polarized HERA.

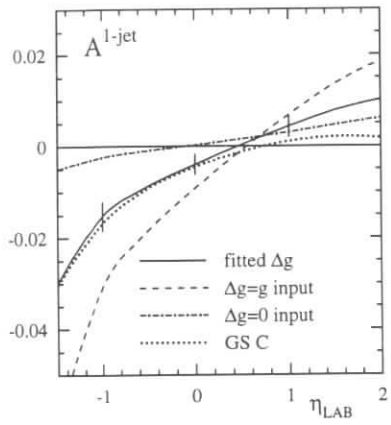

Figure 7: *Expected accuracy for photoproduction of large $P_\perp$ jets for a standard, small and large polarized gluon distribution, for the luminosity 100 pb^{-1}. For large values of the rapidity the result becomes sensitive to the resolved photon structure.*

Its large energy allows HERA to study also charged current events through e.g. the reaction

$$e + p \to \nu_e(\text{missing momentum}) + X \quad .$$

This requires high luminosity and was investigated in detail by the working group on 'Electroweak Physics'. The great advantage of charged current reactions is that here the spin asymmetries are large because W's couple only to left-handed currents. Thus the luminosity required to study spin asymmetries is not much larger than for the rest of the charged current program [17]. Also due to parity violation the charged current spin asymmetries couple primarily to a different structure function called $g_5(x, Q^2)$.

$$\begin{aligned} g_5^{W^-}(x,Q^2) &= -\left(\Delta u - \Delta\bar{d} + \Delta c - \Delta\bar{s} \ + \ ...\right)(x,Q^2) \\ g_5^{W^+}(x,Q^2) &= -\left(\Delta d - \Delta\bar{u} + \Delta s - \Delta\bar{c} \ + \ ...\right)(x,Q^2) \end{aligned} \tag{3}$$

More precisely the inclusive CC cross section asymmetry is given by

$$A_{CC} = \frac{d\sigma^{\uparrow\downarrow} - d\sigma^{\uparrow\uparrow}}{d\sigma^{\uparrow\downarrow} + d\sigma^{\uparrow\uparrow}} = \frac{a g_5^{W^\pm} + b g_1^{W^\pm}}{a F_1^{W^\pm} + b F_3^{W^\pm}} \tag{4}$$

with $a = 2(2 - 2y + y^2)$ and $b = y(2 - y)$. Obviously g_5 has no singlet part and is therefore not at all sensitive to ΔG. g_1 has a singlet part, but its contribution is strongly suppressed (y is much smaller than one for most reactions). Therefore CC spin asymmetries would serve primarily to extract information on the valence quark spin decomposition. Knowing the valence quark distributions and the combined valence and sea contributions to g_1 from usual DIS fixes, however, also the sea distribution functions and the associated anomalous gluon contribution. Note that at HERA the valence quark distributions would be measured at very large Q^2, whereas HERMES measures them at small Q^2. This would open the very exciting possibility to follow the Q^2-evolution of the quark spin decompostion in detail. The expected statistical accuracy is shown in figure 8 for various Q^2 bins as a function of x. Especially the W$^-$ asymmetries, obtained for an electron beam look very good, because the polarized valence up-quark distribution is much larger than the down-quark one. The imposed Q^2-cut depends on the experimental requirements to detect unambigously the missing momentum carried by the neutrino. Recent unpolarized experiments at ZEUS suggest that this cut could be chosen as small as 200 GeV^2 which would improve the statistics still further.

A possibility to obtain results for the singlet spin distribution in CC events is to detect D mesons in the final state. The resulting spin asymmetries are proportional to $-(\Delta\bar{s} + \tan^2(\theta_c)\Delta\bar{d})/(\bar{s} + \tan^2(\theta_c)\bar{d})$ respectively $(\Delta s + \tan^2(\theta_c)\Delta d)/(s + \tan^2(\theta_c)d)$. Here θ_c is the Cabbibo mixing angle. A sensitive determination of these quantities requires, however, a luminosity of 1000 pb^{-1} [17]. Let us finally add that by comparing semi-inclusive CC pion-asymmetries and inclusive CC asymmetries one can investigate in a very clean manner the possible spin-dependence of fragmentation, which is probably the principle theoretical uncertainty in all semi-inclusive spin experiments.

There are many more interesting quantities one could investigate in principle. However, for many of them the advantages of HERA with respect to planned lower energy experiments is not obvious, so that we do not want to discuss them here in detail. However, they would be part of the extensive spin program once a polarized HERA would be available. Such experiments include the measurement of new, up to now basically unstudied structure and fragmentation functions of leading and higher twist, an improved determination of the low-x contribution to Bjorken sum rule, which will probably in the end serve to get a more precise measurement of α_s (see the contribution by Gardi et al.), studies of spin dependent nuclear effects for deuterium and ^{3}He which would allow to test current ideas on shadowing (Strikman), and the search for T-violating effect (Gehrmann). As an example let us mention that at a polarized HERA it would be possible to study the spin dependence of diffractive processes, or loosly speaking the spin-flip coupling of the pomeron. Existing models and expert opinions differ substantially when it comes to the question how large the spin dependence could be for various observables. This topic obviously needs much further study, see the contribution of Goloskokov.

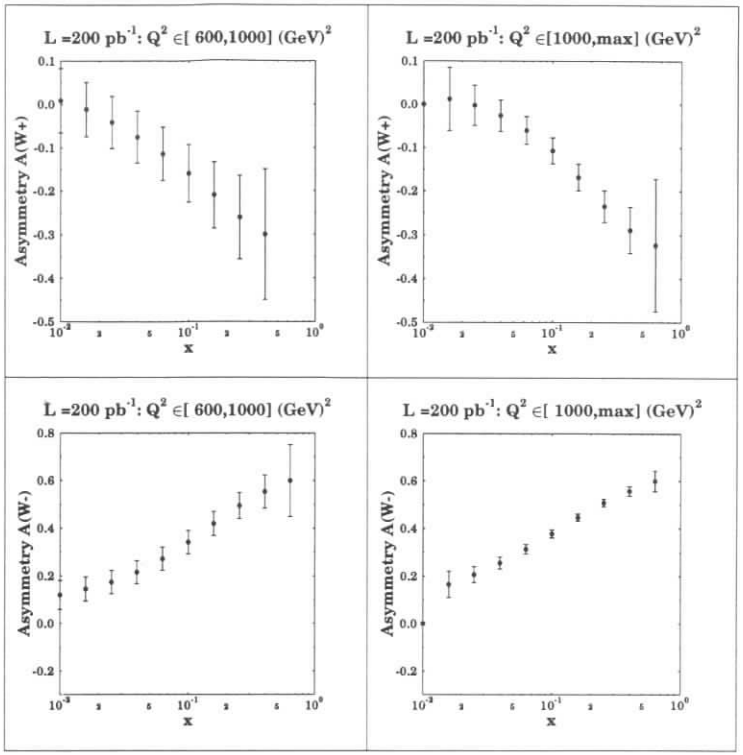

Figure 8: *Expected statistical accuracy for a standard HERA run (luminosity 200 pb^{-1}, i.e. 100 pb^{-1} per relative polarization, and and fully polarized beams) for the CC spin asymmetries for a positron and electron beam.*

4 Polarized proton-proton collisions - HERA-$\vec{N}$

One idea entering the construction of the presently running spin experiment HERMES at HERA was the option to eventually rotate it by 180 degrees and to use it as spectrometer for fixed target proton-proton physics, either double-polarized (target plus beam polarization) or single-polarized (only target polarization) [18]. The Hermes detector could not, however, handle the counting rates expected for a high-luminosity run and its angular acceptance would be too small. For this purpose one rather needed a detector of the HERA-B type. High luminosities are in fact indispensible for such an experiment to be competitive with the RHIC spin program which investigates very similar physics at comparable energies, see next section.
Polarised proton-nucleon collisions open a still wider field of phenomena than polarized lepton-nucleon reactions. Even with an unpolarized proton beam one can investigate a quite large number of single-spin asymmetries, the sizes of which are proportional to well defined twist-3 correlators. Knowledge of such correlators constraints strongly the internal nucleon wave function and thus can lead to a much better understanding of the nucleon structure. However, presently one cannot make optimal use of this possibility because those higher-twist asymmetries which can be calculated rigorously from QCD turn out to be small, typically of the order percent [19], and those which are found experimentally to be large, like single spin pion production [20], see figure 9, involve complicated fragmentation effects and are not yet understood theoretically. HERA would measure this latter effect up to much higher transverse momentum. The asymmetry which is for the present data still growing with $p_\perp$ should finally bend over and go to zero. How and where this happens is crucial to understand this fascinating effect.

In the following we shall only comment on the twist-2 observables which are less difficult to

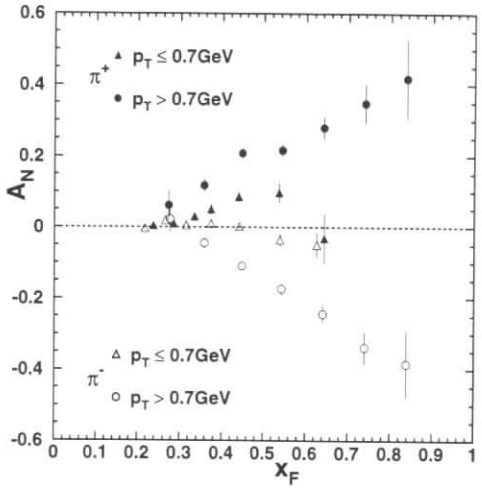

Figure 9: *The large observed single-spin pion asymmetry [20]*

measure and interpret, which require, however, both a polarized target and a polarized beam. The main aim of such experiments is to extract information on the polarized gluon distribution $\Delta G(x, Q^2)$ just as for the jet-spin asymmetries in polarized lepton-proton reactions. The sensitive x-range lies in this case between 0.1 and 0.4, such that these experiments would complement the jet-experiments in an ideal manner. Together they would cover all of the interesting x-range. In principle there are quite a number of spin dependent observables, but most of them are theoretically not very clean, more precisely the quality of the result is not only a question of statistics but also of the theoretical uncertainties. One has to rely to a large extent on the Monte-Carlo codes which are used and one can only compare the predictions for different parametrizations of the spin dependent structure functions rather than extracting the quantities of interest directly from the data. For the envisaged fixed target HERA experiment we confined our studies to reactions like $\vec{p} + \vec{p} \to \gamma + X$ and $\vec{p} + \vec{p} \to \gamma + \text{jet} + X$.

The physical origin of all discussed asymmetries is very similar. In each case the dominant contribution comes from the Compton processes $q^\uparrow + G^\downarrow \to q + \gamma$ and $q^\uparrow + G^\downarrow \to q + G$. In both cases the polarized quark cannot absorb a gluon which is polarized in the same direction

and this results in a spin-asymmetry. For direct photons the cross section reads e.g.

$$E_\gamma \frac{d^3\Delta\sigma(pp \to \gamma X)}{d^3p_\gamma} \approx \sum_q \int dx_a dx_b \left\{ \Delta q(x_a)\Delta G(x_b) E_\gamma \frac{d^3\Delta\sigma(qG \to \gamma X)}{d^3p_\gamma} + (x_a \leftrightarrow x_b) \right\} + ... \tag{5}$$

If also the jet of the outgoing quark in the Compton graph is detected one obtains a signal which is not only proportional to a convolution of $\Delta G(x)$, but to $\Delta G(x)$ directly. The corrections due to misidentifications of the quark-jet have to be calculated reliably enough with Monte-Carlo to keep the systematic error smaller than the statistical one. The resulting signal is shown in figure 10, together with the expectation for RHIC. Obviously the anticipated accuracy is impressive for the asumed luminosity of 320 pb^{-1}. The limiting factor for the luminosity is in this case the degradation of the beam. Thus the scope of experiments which could be done

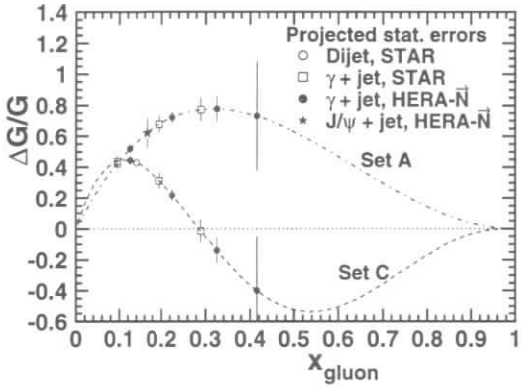

Figure 10: *Expected statistical accuracy for the determination of $\Delta G(x)$ from $\vec{p}+\vec{p} \to \gamma$+jet+$X$, assuming a luminosity of 320 pb^{-1} and an optimized detector.*

with polarized proton-nucleon collisions at HERA is large and the expected results are quite impressive. However, such experiments would require an additional dedicated detector rather similar to HERA-B. Alternatively such experiments could be done in some far future, after the original program of HERA-B is finished, using that detector, but by then most interesting questions will possibly have already been answered by RHIC.

5 Comparison with other projects in spin physics

Hadronic spin physics is presently one of the most active fields of QCD which is also reflected by the fact that nearly all great laboratories have running experiments and discuss improved ones for the future. At DESY the HERMES fixed target experiment is running and should provide very interesting results on the quark spin decomposition by analysing semi-inclusive reactions. Measuring spin asymmetries in $\pi^\pm$ production will provide information of the valence quarks and the difference between inclusive asymmetries and semi-inclusive pion asymmetries

is sensitive to the sea quark polarisation. Thus these experiments should provide combinations of polarised distribution functions, which are linearly independent from both $g_1(x)$ measured so far and $g_5(x)$, which could be measured in CC spin asymetries. This possibility, especially open charm production, is one of the major aims of the COMPASS project at CERN, which is planned to be an improved version of SMC combined with a hyperon experiment. Such an experiment would also improve the data on $g_1(x, Q^2)$ and thus the precision with which $\Delta G(x, Q^2)$ can be predicted from NLO-fits, it could analyse Λ-polarisation as a signal for Δs, it could improve substantially the accuracy of $g_2(x, Q^2)$, look for semi-inclusive asymmetries, and could possibly determine h_1. A similar project is discussed for SLAC. If realized these projects will provide partial answers to the questions addressed by a polarized HERA. Depending on their outcome these experiments might lead to a still further increased interest in the HERA experiments under discussion. It should be kept in mind that our present understanding of the nucleon spin structure is based on a consistent model but not on unambigous facts. The detailed studies planned for the future could very well lead to surprising results. Also these projects are not yet funded. In any case, due to its high energy the HERA experiments are complementary to these fixed target experiments.

This is also true for the RHIC spin program. Again the interest is concentrated on $\Delta G(x)$, however RHIC is rather sensitive in the x-range of the fixed target lepton-experiments (see figure 10) than in the low-x range covered by the HERA jet experiments. One should also note that RHIC can investigate the production of W$^\pm$ via the Compton-graph, a process which is theoretically much cleaner. We would like to stress, however, that it is a vital check to show that both, DIS experiments and proton-proton experiments can be described by the same distribution functions. Only this would prove that one really understands the physics. Therefore, one definitely needs both types of experiments. According to theoretical predictions and Monte Carlo studies and in view of the fact that it is already funded RHIC will eventually measure $\Delta G(x)$ at large x, the main open question is when it will happen. This is hard to predict because it depends, in additon to all the usual imponderabilities, on the relative priority given to the heavy ion experiments and the spin experiments. It seems realistic to assume that the time scales of the RHIC spin physics experiments and experiments with a polarized HERA would be rather similar.

Thus we conclude that in spite of the many other ongoing activities HERA would provide most relevant results, especially if polarization would be realized in the not too far future.

6 Conclusions

Spin physics provides possibly the best testing ground for QCD, especially if one is interested in effects beyond standard leading twist perturbation theory. This is mainly due to the large number of observables and the possibility to extract well defined quantities by constructing specific ratios or differences of ratios. To the extent that HERA aims at a better understanding of QCD the many options opened by a polarized nucleon beam are certainly most attractive. Some of the informations which could be deduced from HERA experiments cannot be obtained by any other existing or planned experiment and for many others HERA would be competitive or complementary to experiments at lower energy.

To make full use of these possibilities requires, however, very substantial machine upgrades. One needs about 200 pb^{-1} of luminosity with electron and proton polarization fulfilling $P_e \cdot P_p = 0.5$. To use the full potential of a polarized HERA one needs furthermore polarized proton, ^{3}He and

(best of all but also most difficult) polarized deuteron beams. In addition the charged current experiments would profit from having an electron as well as a positron beam.

References

[1] J. Ashman et al., EMC, Phys. Lett. **206B** (1988) 364, Nucl. Phys. **B328** (1989) 1

For references on the ensuing extensive discussion see the report:
M. Anselmino, A. Efremov, and E. Leader, Phys. Rep. **261** (1995) 1

[2] K. F. Liu (university of Kentucky) has written a very nice report on the status of lattice calculations concerning the nucleon spin structure for our working group. It is available under **hep-lat/9510046** and has the title 'Comments on Lattice Calculations of Proton Spin Components'.

[3] P.J. Mulders, Nucl. Phys. B461 (1996) 197
hep-ph/9510317: 'Transverse spin and transverse momenta in hard scattering processes'
nucl-th/9510035: 'Opportunities in (semi)inclusive deep inelastic scattering'

[4] G. Altarelli and G.G. Ross, Phys. Lett. **B212** (1988) 391
R.D. Carlitz, J.C. Collins and A.H. Mueller, Phys. Lett. **B214** (1988) 229
L. Mankiewicz and A. Schäfer, Phys. Lett. **B242** (1990) 455

[5] R. Mertig and W.L. van Neerven, Z. Phys. **C70** (1996) 637

[6] W. Vogelsang, Phys. Rev. **D54** (1996) 2023
W. Vogelsang, **hep-ph/9603366**: 'The spin dependent two loop splitting functions', to be published in Nucl. Phys. **B**

[7] J. Bartels, B.I. Ermolaev, M.G. Ryskin, **hep-ph/9603204** : 'Flavour singlet contribution to the structure function g_1 at small x'
J. Bartels, B.I. Ermolaev, M.G. Ryskin, Z. Phys. **C70** (1996) 273

[8] J. Blümlein and A. Vogt, Phys. Lett. **B370** (1996) 149
J. Blümlein and A. Vogt, **hep-ph/9606254** : The singlet contribution to the structure function $g_1(x, Q^2)$ at small x.
J. Blümlein, S. Riemersma, and A. Vogt, **hep-ph/9607329** : 'On small x resummations for the evolution of unpolarized and polarized nonsinglet and singlet structure fucntions.' and contribution to these proceedings

[9] R. Kirschner et al., **hep-ph/9606267**: 'Small x behaviour of the chirally-odd parton distribution $h_1(x, Q^2)$'

[10] J. Collins, Nucl. Phys. **B396** (1993) 161

[11] R.D. Ball, A. Deshpande, S. Forte, V.W. Hughes, J. Lichtenstadt, and G. Ridolfi, contribution to these proceedings

[12] See the contribution by W. Vogelsang, 'Physics at HERA', 1991, page 389

[13] A. De Roeck, J. Feltesse, F. Kunne, M. Maul, E. Mirkes, G. Rädel, A. Schäfer, and C.Y. Wu, contribution to these proceedings

[14] E. Mirkes and D. Zeppenfeld, **hep-ph/9511448** : 'Dijet production at HERA in next-to-leading order', to be published in Phys. Lett. B

[15] PEPSI2 is an updated version of PEPSI, described in : M. Veltri, L. Mankiewicz, and A. Schäfer, Comp- Phys. Comm. **71** (1992) 305

[16] M. Stratmann and W. Vogelsang, **hep-ph/9605330** : 'Photoproduction of jets and heavy flavors at future polarized e p colliders', to be published in Z. Phys. **C**
and contribution to these proceedings

[17] M. Anselmino, J. Blümlein, P. Gambino, J. Kalinowski, N. Kochelev, M. Maul, A. Schäfer, and T. Yamanishi, contribution to these proceedings

[18] M. Anselmino, E. Andreeva, V. Korotkov, F. Murgia, W.-D. Nowak, S. Nurushev, O. Teryaev, A. Tkabladze, contribution to these proceedings

[19] B. Ehrnsperger et al., Phys. Lett. **B321** (1994) 121

[20] D.L. Adams et al., FNAL E704, Phys. Lett. **B264** (1991) 462

Measurement of the Spin Dependent Structure Function $g_1^p(x, Q^2)$ at HERA

R. Ball[a], A. Deshpande[b], S. Forte[c], V. W. Hughes[b], J. Lichtenstadt[d,e], G. Ridolfi[f]

[a] Department of Physics and Astronomy, Edinburgh EH9 3JZ, Scotland
[b] Department of Physics, Yale University, New Haven, CT 06511, USA [1]
[c] INFN , Sezione di Torino, I-10125 Torino, Italy
[d] CERN, CH-1211 Geneva 23, Switzerland
[e] School of Physics and Astronomy, The Raymond and Beverly Sackler Faculty of Exact Sciences, Tel Aviv University, Tel Aviv 69978, Israel [2]
[f] INFN, Sezione di Genova, I-16146, Genova, Italy

Abstract: We present estimates of possible data on spin-dependent asymmetries in inclusive scattering of high energy polarized electrons by high energy polarized protons at HERA, including statistical errors, and discuss systematic uncertainties. We show that these data would shed light on the small x behaviour of the polarized structure function g_1, and would reduce substantially the uncertainty on the determination of the polarized gluon distribution.

1 Introduction

Nucleon structure, particularly as defined by its structure functions determined from lepton-nucleon inclusive electromagnetic scattering, is of fundamental importance and has provided crucial information for the development of perturbative QCD. The history of such experiments over the past forty years has shown that important new information has been obtained when measurements were extended to new kinematic regions. In the mid-1950's at Stanford, Hofstadter [1] extended measurements of elastic electron-proton scattering to a higher Q^2 range of 1 $(\mathrm{GeV/c})^2$ and first observed that the proton has a finite size. In the late 1960's at SLAC Friedman, Kendall and Taylor [2] extended measurements of inelastic inclusive electron scattering to the deep inelastic region of $Q^2 > 1$ $(\mathrm{GeV/c})^2$ and discovered the parton substructure of the proton.

The subfield of polarized lepton-proton scattering was initiated with the Yale-SLAC E80 and E130 experiments [3] which measured the spin-dependent structure function of the proton in the mid-1980's. These experiments were then followed up at CERN by the EM Collaboration

[1] Supported by the Department of Energy.
[2] Supported by the Israel Science Foundation of the Israeli Academy of Sciences.

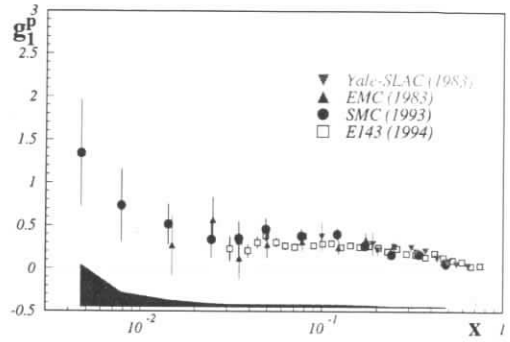

Figure 1: *The current status of the measurement of the spin structure function g_1^p. The statistical errors are shown with the data points, while the size of the systematic errors for SMC measurement is shown by the shaded area.*

which extended the kinematic range of the original measurements at SLAC to lower the x range from $x = 0.1$ to 0.01 [4]. These data allowed a determination of the singlet component of the first moment of g_1, which in the naive parton model is the fraction of the proton spin carried by quarks: this was found to be compatible with zero, thereby violating the parton model Ellis-Jaffe sum rule at the three standard deviation level. This surprising result has stimulated a large amount of experimental and theoretical work on polarized structure functions [5]. New measurements of the spin dependent structure functions of the proton and the deuteron were made by the SM collaboration [6] at CERN and by E143 [7] at SLAC which extended the kinematic range to lower x and also reduced the statistical and systematic uncertainties significantly. Figure 1 shows all published measurements of the structure function g_1^p. These measurements, along with those made for the deuteron, allowed a better determination of the first moment of the spin structure functions and verified the Bjorken sum rule. Furthermore, they made a next-to leading order QCD analysis of the x and Q^2 dependence of g_1 possible, thereby allowing a determination of the first moment of the polarized gluon distribution [8].

In view of this history it is important to consider in detail what measurements and accuracies may be obtained at HERA. The primary goal and motivation for HERA is to extend the kinematic range of electron-proton scattering. Thus far HERA research and its discoveries were the results of the new and vastly extended kinematic range in x and Q^2 , both by a factor of about 100, provided by the collider [9, 10, 11, 12]. At present the 800 GeV proton beam at HERA is unpolarized (although the 25 GeV electron/positron beam has a natural polarization). If the proton beam were to be polarized, it would be possible to measure polarization asymmetries and thus explore spin dependent structure functions along with the spin-independent structure functions in the HERA kinematic range. In this paper we discuss what might be achieved from such a programme. We show that the data HERA could provide are clearly unique and cannot be obtained by present day experiments.

In section 2 we estimate the data that could be obtained, including the statistical errors, from inclusive polarized e-p scattering with HERA in the collider mode. We also discuss systematic errors and argue that they can be controlled within adequate limits. In section 3 we

briefly review the relation of the structure function g_1 to polarized parton distributions and the perturbative evolution equations satisfied by the latter, and summarize the status of polarized parton distributions extracted from presently available fixed target data. In section 4 we show that new data from polarized colliding beam experiments at HERA would shed light on the small x behaviour of g_1 and would substantially improve the determination of the polarized gluon distribution.

2 Measurement of $g_1^p(x, Q^2)$ at HERA

2.1 Kinematic range and statistical errors for HERA data

Presently all measurements of polarized structure functions are made using fixed target deep inelastic lepton-nucleon scattering. Figure 2 shows the kinematic ranges in which polarized lepton-proton data have been obtained at SLAC and CERN as well as the possible measurements in the kinematic domain available at HERA with 800 and 25 GeV proton and electron beams, respectively. Note the large extension in $x - Q^2$ range compared to the present data. Table 1 lists the $x - Q^2$ values at which measurements can be made at HERA, the number of events that would be measured and the associated statistical errors in the measured asymmetry δA_m assuming an integrated luminosity of $L = 1000$ pb^{-1} and electron and proton polarizations of 0.7 each[3]. Kinematic cuts [11] on y and the scattered electron angle θ_e' used for data analysis by the H1 and ZEUS collaborations were applied for the evaluation of the counting rates in each $x - Q^2$ bin. Standard deep inelastic scattering formulae were used to calculate of the kinematics and asymmetries. They are given in the Appendix.

2.2 Systematic errors for HERA data

The systematic errors associated with spin dependent asymmetry measurements are of two types: 1) normalization errors and 2) false asymmetries.

The normalization errors include principally uncertainties in the electron polarization P_e and in the proton polarization P_p . These lead to a change in the magnitude of the measured asymmetry but in practice by an amount which is small compared to the statistical error, and hence they are important primarily when evaluating the first moment of $g_1^p(x)$.

Recently the HERMES collaboration has reported a measurement of P_e by Compton scattering, which yielded a relative accuracy of 5.5% [13]. It is expected that an improved accuracy will be achieved eventually.

Absolute measurement of the polarization of the high energy (800 GeV) proton beam presents a new challenge and is presently under investigation. Several methods are being considered:

1. $p - p$ elastic scattering in the Coulomb-nuclear interference region[14],

[3]Accelerator parameters that were suggested by R. Klanner and F. Willeke for this workshop.

x	Q^2 GeV^2	y	D	N_{total}	δA_m
5.6×10^{-5}	1.8	0.40	0.47	5.0×10^6	4.5×10^{-4}
1.8×10^{-4}	1.8	0.13	0.13	8.0×10^6	3.5×10^{-4}
	5.6	0.40	0.46	3.5×10^6	5.3×10^{-4}
5.6×10^{-4}	1.8	0.04	0.04	1.2×10^7	2.9×10^{-4}
	5.6	0.13	0.13	6.5×10^6	3.9×10^{-4}
	1.8×10^1	0.40	0.47	2.0×10^6	7.1×10^{-4}
1.8×10^{-3}	1.8	0.01	0.01	1.6×10^7	2.5×10^{-4}
	5.6	0.04	0.04	9.0×10^6	3.3×10^{-4}
	1.8×10^1	0.13	0.13	3.4×10^6	5.4×10^{-4}
	5.6×10^1	0.40	0.47	1.1×10^6	9.5×10^{-4}
5.6×10^{-3}	5.6	0.01	0.01	1.2×10^7	2.8×10^{-4}
	1.8×10^1	0.04	0.04	5.5×10^6	4.3×10^{-4}
	5.6×10^1	0.13	0.13	1.7×10^6	7.7×10^{-4}
	1.8×10^2	0.40	0.47	5.5×10^5	1.3×10^{-3}
1.8×10^{-2}	1.8×10^1	0.01	0.01	6.5×10^6	3.9×10^{-4}
	5.6×10^1	0.04	0.04	2.6×10^6	6.2×10^{-4}
	1.8×10^2	0.12	0.13	8.0×10^5	1.1×10^{-3}
	5.6×10^2	0.40	0.47	2.3×10^5	2.1×10^{-3}
5.6×10^{-2}	5.6×10^1	0.01	0.01	2.2×10^6	6.7×10^{-4}
	1.8×10^2	0.04	0.04	8.0×10^5	1.1×10^{-3}
	5.6×10^2	0.12	0.13	2.6×10^5	2.0×10^{-3}
	1.8×10^3	0.40	0.47	6.5×10^4	3.9×10^{-3}
1.8×10^{-1}	1.8×10^2	0.01	0.01	5.9×10^5	1.3×10^{-3}
	5.6×10^2	0.04	0.04	1.9×10^5	2.3×10^{-3}
	1.8×10^3	0.13	0.13	5.4×10^4	4.3×10^{-3}
	5.6×10^3	0.40	0.47	1.3×10^4	8.6×10^{-3}
5.6×10^{-1}	5.6×10^2	0.01	0.01	2.9×10^4	5.9×10^{-3}
	1.8×10^3	0.04	0.04	8.3×10^3	1.1×10^{-2}
	5.6×10^3	0.13	0.13	1.9×10^3	2.3×10^{-2}
	1.8×10^4	0.40	0.47	4.2×10^2	4.8×10^{-2}

Table 1: *The kinematic variables x, Q^2, y, and D, along with the number of events expected N_{total}, and the statistical uncertainty in the measured asymmetry δA_m in the kinematical region assuming an integrated luminosity $L = 1000$ pb^{-1} and proton and electron beam polarizations $P_p = P_e = 0.7$.*

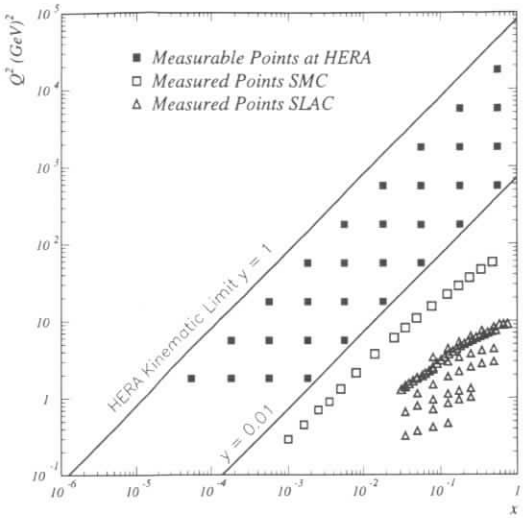

Figure 2: *Measurable $x - Q^2$ region at HERA shown with the presently explored regions by SMC(CERN) and E143(SLAC) experiments, and the kinematic limit of measurability at HERA.*

2. $p - \vec{\mathrm{p}}$ scattering using a stationary polarized proton jet target and comparing the asymmetries $A_{\mathrm{beam}} = A_{\mathrm{jet}}$, where A_{beam} is the asymmetry in the scattering of the polarized beam from an *unpolarized* jet and A_{jet} is the asymmetry measured with an *unpolarized* beam and a polarized jet target with a known polarization P_{jet}. Adjusting the jet polarization to obtain the same asymmetry, one obtains the beam polarization $P_{\mathrm{beam}} = P_{\mathrm{jet}}$ [15].
3. polarized $e - p$ scattering in which a low energy polarized electron beam collides with the polarized 800 GeV proton beam, with kinematics corresponding to the polarized $e-p$ elastic scattering measurements at SLAC [16]. The theoretical values for the asymmetry in elastic scattering are given in terms of the polarizations and the measured electric and magnetic form factors of the proton. Hence the measured asymmetry at HERA using a known polarized electron beam would determine P_p.

We comment briefly on these possible methods. For method 1 the nuclear matrix element may not be known well enough to provide a significant absolute determination of P_p. Method 2 appears quite attractive because only the invariance principle is needed from theory, and it may be possible to use the stationary polarized target of the HERMES experiment for this measurement. Method 3 is theoretically sound and simple, but may not be attractive experimentally. These methods have still to be fully developed and tested experimentally. It is reasonable to expect that a 5% accuracy will be achieved.

Inclusive π^+ or π^- production in collisions of 800 GeV protons with a fixed proton target appears to be a simple method for a relative measurement of the polarization [17].

Methods to measure P_p are presently considered and studied also for polarized protons at RHIC. The method of measuring P_p at 1 TeV has been discussed in some detail in a design report entitled "Acceleration of Polarized Protons to 120 GeV and 1 TeV at Fermilab" [18] as well as in the BNL proposal for RHIC SPIN [19].

The other type of systematic error comes from false asymmetries. These arise from variations in counting rate due to time variations in detector efficiencies, beam intensities, or crossing angles between the conditions of spins parallel and antiparallel. In view of the expected small values of the true asymmetries expected in the HERA kinematic region, (Table 1), the false asymmetries must be controlled at the level of 10^{-4}. We note that medium and high energy experiments which have measured parity violation have controlled false asymmetries to less than 10^{-5} to 10^{-8} [20].

False asymmetries can be avoided by frequent reversals of spin orientations. In the HERA collider the electron(positron) spin reversal is difficult and time consuming (several hours) and would lead to changes in beam intensity and beam emittance. Hence asymmetry data must be obtained with a fixed helicity for the electron beam by varying the proton helicity. Both the electron and proton rings are filled with about 200 particle bunches. The proton ring can be filled with bunches of protons with individually predetermined polarizations. Parallel and antiparallel spin data would be obtained at successive beam crossings occurring at time intervals of about 100 ns. Such alternations eliminate many errors in an asymmetry measurement. However, differences in the intensities and the crossing angles at successive proton bunches could still lead to false asymmetries and will have to be minimized.

The most important approach to avoid false asymmetries will be to use a spin rotator to reverse the helicity of all proton bunches at adequately frequent intervals (perhaps once per 8 hours). The design of such rotators has been studied and appears practical without appreciable change in the orbits, or in the magnitude of proton polarization [21]. Studies at the IUCF at 370 MeV have confirmed these conclusions [22]. With such approach the false asymmetries could be controlled to less than 10^{-4}.

3 Current status of $g_1(x, Q^2)$

3.1 Perturbative evolution of $g_1(x, Q^2)$

The definition and properties of the polarized structure function g_1 in perturbative QCD closely parallel that of its unpolarized counterpart F_2 (see ref. [23] for a review). The structure function g_1 is related to the polarized quark and gluon distributions through

$$\begin{aligned} g_1(x,t) &= \tfrac{1}{2}\langle e^2\rangle \int_x^1 \frac{\mathrm{d}y}{y}\Big[C_q^{\mathrm{S}}(\tfrac{x}{y},\alpha_s(t))\Delta\Sigma(y,t) \\ &+ 2n_f C_g(\tfrac{x}{y},\alpha_s(t))\Delta g(y,t) + C_q^{\mathrm{NS}}(\tfrac{x}{y},\alpha_s(t))\Delta q^{\mathrm{NS}}(y,t)\Big], \end{aligned} \tag{1}$$

where $\langle e^2\rangle = n_f^{-1}\sum_{k=1}^{n_f} e_k^2$, $t = \ln(Q^2/\Lambda^2)$, $\Delta\Sigma$ and Δq^{NS} are the singlet and non-singlet polarized quark distributions

$$\Delta\Sigma(x,t) = \sum_{i=1}^{n_f}\Delta q_i(x,t), \qquad \Delta q^{\mathrm{NS}}(x,t) = \sum_{i=1}^{n_f}(e_i^2/\langle e^2\rangle - 1)\Delta q_i(x,t),$$

and $C_q^{S,NS}(\alpha_s(Q^2))$ and $C_g(\alpha_s(Q^2))$ are the quark and gluon coefficient functions.

The x and Q^2 dependence of the polarized quark and gluon distributions is given by Altarelli-Parisi equations [24]:

$$\frac{\mathrm{d}}{\mathrm{d}t}\Delta\Sigma(x,t) = \frac{\alpha_s(t)}{2\pi}\int_x^1 \frac{\mathrm{d}y}{y}\left[P_{qq}^{\mathrm{S}}(\tfrac{x}{y},\alpha_s(t))\Delta\Sigma(y,t) + 2n_f P_{qg}(\tfrac{x}{y},\alpha_s(t))\Delta g(y,t)\right], \quad (2)$$

$$\frac{\mathrm{d}}{\mathrm{d}t}\Delta g(x,t) = \frac{\alpha_s(t)}{2\pi}\int_x^1 \frac{\mathrm{d}y}{y}\left[P_{gq}(\tfrac{x}{y},\alpha_s(t))\Delta\Sigma(y,t) + P_{gg}(\tfrac{x}{y},\alpha_s(t))\Delta g(y,t)\right], \quad (3)$$

$$\frac{\mathrm{d}}{\mathrm{d}t}\Delta q^{\mathrm{NS}}(x,t) = \frac{\alpha_s(t)}{2\pi}\int_x^1 \frac{\mathrm{d}y}{y} P_{qq}^{\mathrm{NS}}(\tfrac{x}{y},\alpha_s(t))\Delta q^{\mathrm{NS}}(y,t), \quad (4)$$

where P_{ij} are polarized splitting functions.

The full set of coefficient functions [25] and splitting functions [26] has been computed up to next-to-leading order in α_s. As in any perturbative calculation, at next-to-leading order splitting functions, coefficient functions and parton distributions depend on renormalization and factorization scheme, while of course physical observables, such as g_1 itself, remain scheme-independent up to terms of order α_s^2. The scheme choice is arbitrary, and in particular parton distributions in different factorization schemes are related to each other by well-defined linear transformations.

The factorization scheme dependence is particularly subtle in the polarized case because of the extra ambiguity related to the definition of the γ_5 matrix, i.e. to the way chiral symmetry is broken by the regularization procedure. This is reflected in an ambiguity in the size of the first moment of the gluon coefficient function C_g (which starts at order α_s). Two widely adopted choices [8, 27, 28], both compatible with the choice of $\overline{\mathrm{MS}}$ renormalization and factorization, correspond to either requiring the first moment of the gluon coefficient function to be $C_g^1 = 0$, or imposing that the first moment of the polarized quark distribution be scale independent, which implies $C_g^1 = -\frac{\alpha_s}{4\pi}$. The first moment Δg^1 of the gluon distribution can be chosen to be the same in the two schemes, whereas the first moments of the quark distribution in the two schemes differ by an amount proportional to $\alpha_s\Delta g^1$. Because the evolution equations 2-4 imply that at leading order the first moment of the polarized gluon scales as $\frac{1}{\alpha_s}$ this scheme dependence persists asymptotically and is potentially large if the first moment of the gluon distribution is large [29].

3.2 Current status of polarized parton distributions.

Parton distributions can be extracted from experimental structure function data by parametrizing them at a starting value of Q^2, evolving this initial condition up to any desired value of x and Q^2 using Eqs. 2-4, determining g_1 there by means of Eq. 1, and determining the initial parametrization which gives the best fit of $g_1(x,Q^2)$ to the data [8, 27, 28]. Here we follow the procedure used in refs. [8, 30]: we give the initial conditions at $Q^2 = 1$ GeV^2 in the form

$$\Delta f(x,Q^2) = N(\alpha_f,\beta_f,a_f)\ \eta_f\ x^{\alpha_f}(1-x)^{\beta_f}(1+a_f\ x), \quad (5)$$

where $N(\alpha,\beta,a)$ is fixed by the normalization condition, $N(\alpha,\beta,a)\int_0^1 dx x^\alpha(1-x)^\beta(1+ax) = 1$, and Δf denotes $\Delta\Sigma$, Δq_{NS}, or Δg. With this normalization the parameters η_g, η_{NS}, and η_S are respectively the first moments of the gluon, the non-singlet quark and the singlet quark

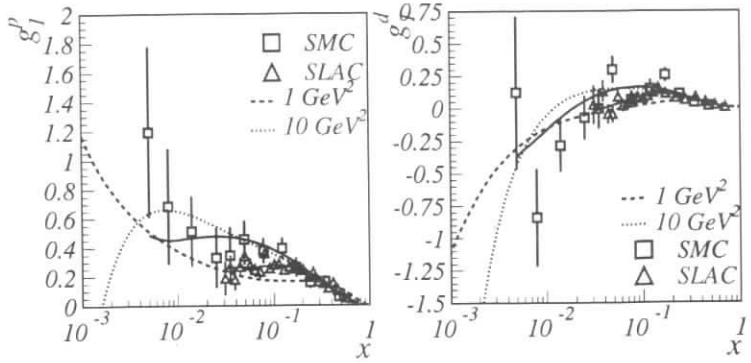

Figure 3: *The NLO fit to proton g_1^p and deuteron g_1^d data. The solid lines are fits to data at the measured Q^2 values, and the dashed and the dotted lines are fits evolved to $Q^2 = 1$ and 10 GeV^2 respectively.*

distributions at the starting scale. Evolution is performed within the AB factorization scheme (which has $C_g^1 = -\frac{\alpha_s}{4\pi}$). Further details of the fits and analysis are given in ref. [8, 30].

Using the published data on proton and deuteron structure functions by SMC [6], and E143 [7] the best fit results obtained for such analysis [8] are given in column 1 of Table 2. The data used for the analysis and the results of the NLO fit are shown in Fig. 3. Interestingly, the data require the first moment of the gluon distribution to differ significantly from zero: $\eta_g = 1.52 \pm 0.74$. This result follows mostly from the observed scaling violations in the intermediate and small x region. However, the statistical uncertainty on the size of the polarized gluon distribution is still rather large. Moreover, existing data only partially constrain the small x behaviour of the various parton distributions (values of α_S, α_g, and α_{NS}), and do not allow a precise determination of their asymptotic form for small x. Such information, besides its intrinsic theoretical interest, is required in order to obtain a precise determination of the moments of g_1 [8, 30]. New data with an extended kinematic coverage in x and Q^2 provided by HERA could reduce these uncertainties.

Since the publication of ref. [8], new data on the Q^2 dependence of g_1 have been published by the E143 collaboration. The inclusion of these data in the NLO fits results in reduction of up to 20% in the errors on the fitted parameters, all the values of the parameters being consistent with the published values. The value of the first moment of the gluon distribution at $Q^2 = 1$ GeV^2 for example becomes $\eta_g = 1.29 \pm 0.56$. In the next two years both SMC (CERN) and E143 (SLAC) plan to present new data on proton and deuteron spin structure functions and using these data as well a more accurate determination of the parameters in the fit can be expected. It can thus be anticipated that eventually the dominant uncertainty in the determination of the first moments of g_1 and the polarized gluon distribution will be due to lack of experimental information in the HERA region.

4 The impact of polarized HERA data

4.1 The small x behaviour of g_1

As shown in Fig. 2, measurements of g_1 at HERA will extend the x region down to $x = 5.6\times10^{-5}$. Knowledge of the small x behaviour of g_1 is obviously necessary in order to compute moments of g_1, and indeed in the determination of the singlet component of the first moment of g_1 the uncertainty related to the lack of knowledge of this behaviour is already comparable to the statistical uncertainty [8, 30].

The extrapolation of g_1 from the measured region down to $x = 0$ is traditionally done by assuming Regge behaviour of the structure function, which implies [31] $g_1 \sim x^a$ as $x \to 0$ with $0 \leq \alpha \leq 0.5$, i.e. a valence-like behaviour of g_1. This behaviour seems to disagree with the data (see Table 2 and Fig. 3) which suggest instead that both the singlet and nonsinglet components of g_1 rise at small x.

In fact, a valence-like behaviour of g_1 is incompatible with perturbative QCD, which at leading order predicts instead that g_1 should rise at least as $g_1(x,Q^2) \sim \frac{1}{\sqrt{\sigma}} e^{2\gamma\sigma}$, where $\sigma \equiv \sqrt{\xi\zeta}$, $\rho \equiv \sqrt{\xi/\zeta}$, $\xi \equiv \ln\frac{x_0}{x}$, $\zeta \equiv \ln\frac{\alpha_s(Q_0^2)}{\alpha_s(Q^2)}$, and Q_0 and x_0 are reference values of x and Q^2. This rise is present both in the singlet and nonsinglet components of g_1, but with different slopes γ, calculable in perturbative QCD. The sign of this rise depends on the specific form of the quark and gluon distributions, but for most reasonable forms of Δq and Δg, and in particular if Δg at moderately small x is positive definite, then g_1 will be negative. The onset of this behaviour as Q^2 is raised is clearly shown in Fig. 3. Higher order corrections lead to an even stronger drop: at k-th perturbative order the rise of $-g_1$ is enhanced by a factor of $\alpha_s^k \rho^{2k+1}$. It has been suggested [32] that these terms to all orders in α_s may exponentiate, thus leading to a rise of g_1 as a power of x; the sign of this rise is still predicted to be negative.

A non-Regge behaviour of the unpolarized structure function F_2 has been observed and accurately measured at HERA, in spectacular agreement with the perturbative QCD prediction [11, 12]. The behaviour correspondingly predicted in the polarized case is even more interesting due to the fact that higher order corrections are stronger, and also the polarized singlet and nonsinglet quark and gluon distributions all display qualitatively the same behaviour, whereas in the unpolarized case only the gluon dominates at small x.

An experimental measurement of the small x behaviour of g_1 would thus lead to significant insight on the structure of QCD both within and beyond perturbation theory. In Fig. 4 we show the expected accuracy of the determination of g_1 at HERA within the maximal extent of variation in the small x behaviour compatible with the requirement of integrability of g_1 (which implies that at small x g_1 can rise at most as $1/(x\ln^\alpha x)$ with $\alpha > 1$).

The full coverage of HERA experiments is shown in Figs. 5, 6, 7, and 8, where projected data with their estimated errors are given on the basis of the NLO fit of Table 2. The errors are estimated assuming integrated luminosities $L = 1000\ pb^{-1}$ and beam polarizations $P_p = P_e = 0.7$. In Fig. 5 g_1 at the starting scale $Q^2 = 1$ GeV^2 is shown using the best fit values of the parameters. This is then evolved up with different choices for the normalization of the polarized gluon distribution, to give a feeling for the possible range of variation. In particular, we consider two cases: a) the first moment of the gluon distributions is fixed to be 0 at $Q^2 = 1$ GeV^2 (minimal gluon: dashed lines in Fig.6) and b) the first moment of the singlet quark density was fixed to $\eta_q = a_8$ at the same reference scale (maximal gluon: dotted lines in Fig.6).

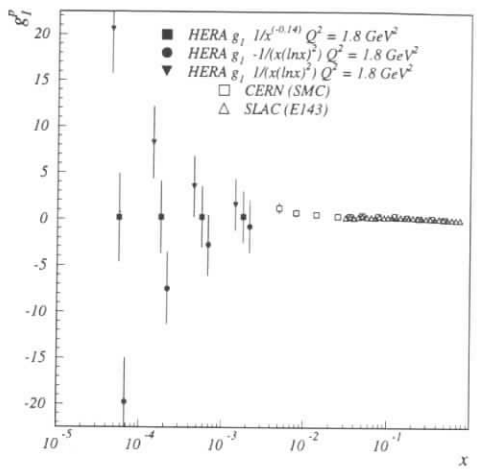

Figure 4: *The structure function g_1^p measurable at HERA for $Q^2 = 1.8$ GeV^2 with integrated luminosity $L = 1000\ pb^{-1}$ are shown. The SMC and E143 measurements are shown for comparison. Starting from the measured values of g_1^p by SMC, the measurable values for HERA at low-x are shown in two extreme cases: valence-like behaviour $g_1(x) \sim x^{-\alpha}$ with $\alpha = 0.14$ or strong powerlike positive or negative rises $g_1(x) \sim \pm 1/(x \cdot (lnx)^2)$*

Even though the current best fit value of η_g (Table 2) is very close to the maximal case, the minimal gluon is at present only excluded at 2 σ level. Of course yet wider deviations from these fits are foreseeable since the small x behaviour of the current best fit is only very loosely constrained due to the lack of direct experimental information at small x; also, as discussed above, higher order corrections beyond NLO may turn out to be important at very small x.

In Fig. 6 we show the statistical errors for each measurable data point in the complete $x - Q^2$ grid indicated in Fig. 2 and in Table 1. The bold solid lines are the predictions of g_1 values in the HERA kinematic range using the best fit values of the NLO parameters for the presently published data [6, 7]. In Fig. 7 the projected values of g_1 obtained from the NLO fit to the data are calculated for the lowest Q^2 data point reached at that x bin, which in turn has the lowest statistical error. The Q^2 values are indicated in the figure. The measured asymmetries A_m and the corresponding statistical errors on the projected measurements at HERA at different Q^2 are shown in Fig. 8.

4.2 The determination of the gluon distribution

The measurement of scaling violations in inclusive structure functions provides a theoretically clean determination of the polarized gluon distribution. Because the gluon distribution is only determined by the scale dependence of the moments of g_1 a reasonably wide kinematic coverage is required in order to achieve such a determination with satisfactory accuracy: in particular, since the gluon distribution is peaked at small x, data in this region for several values of Q^2 such as those obtainable at HERA would substantially improve the determination of $\Delta g(x,Q^2)$.

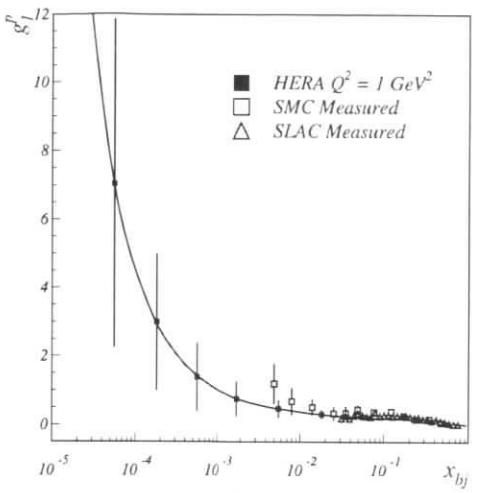

Figure 5: *The starting parametrization of g_1^p at $Q^2 = 1$ GeV^2 which gives best-fit to present-day data is shown in the x range covered at HERA. Statistical errors on g_1 after combining all measurements for each x are shown for an integrated luminosity $L = 1000$ pb^{-1}.*

To assess the impact of these data we have repeated the fit described in sect. 3.2 with the addition of the projected HERA data discussed in sect. 2.1. The values of the best-fit parameters of course do not change, but using the estimated errors from acceptance considerations on measurable g_1, we get an estimate of the extent of reduction in the measured uncertainties of various parameters. In column 3 of Table 2 we show the results of a fits with HERA data for integrated luminosity $L = 1000$ pb^{-1} and in column 4 we show the results for $L = 200$ pb^{-1}. Note in particular the sizable improvement in the determination of the first moment of Δg, which is of greatest theoretical interest due to its role in the understanding of the proton spin structure [5]: from $\delta(\Delta g^1) = \pm 0.74$ (the present value) to ± 0.22 or ± 0.28 depending on the luminosity available at HERA.

We have also performed fits with an additional parameter in the distribution functions of Eq. 5

$$\Delta f(x, Q^2) = N(\alpha_f, \beta_f, a_f)\ \eta_f\ x^{\alpha_f}(1-x)^{\beta_f}(1 + a_f\ x + b_f\ \sqrt{x}), \qquad (6)$$

(i.e. a 14 parameter fit), in order to test the sensitivity of our results to the functional form used for the parton distributions. The fits yielded a result for $\eta_g = 1.0 \pm 0.3$ consistent with the 10 parameter fit.

5 Conclusions

Inclusive DIS measurements at HERA with high integrated luminosity with high energy polarized electrons and polarized protons would yield significant and unique new information on

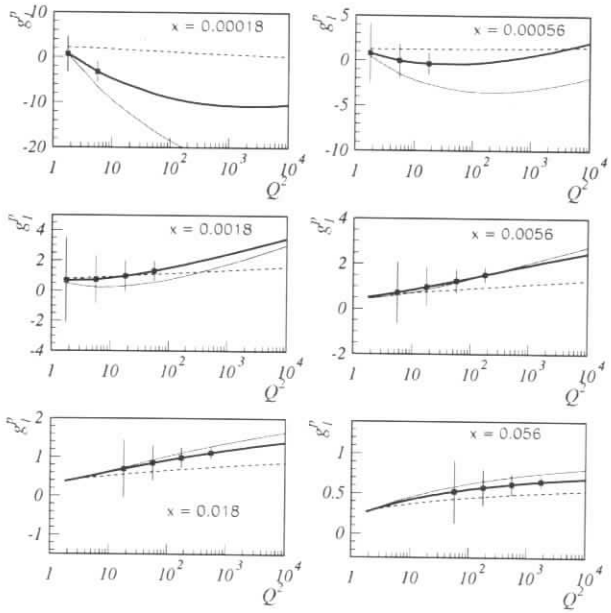

Figure 6: *Predicted values for g_p^1 from NLO fits together with estimated statistical uncertainties for a future polarized DIS experiment with an integrated luminosity L=1000 pb^{-1}. The solid bold lines are predictions based on fits to SMC and SLAC data extended in to the HERA kinematic range while the dotted and dashed lines are the maximal and minimal gluon predictions (see text).*

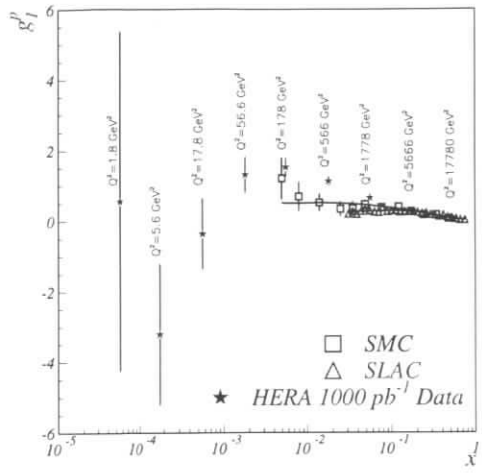

Figure 7: *The structure function g_1^p measurable at HERA shown in comparison to the SMC/E143 measurements. The values of $g_1^p(x, Q^2)$ for each measurable HERA point are taken from the NLO fit and evolved to the Q^2 value indicated in the figure. Statistical errors on $g_1(x)$ averaged over all Q^2 for measurements at HERA with integrated luminosity L = 1000 pb^{-1} are shown for each x.*

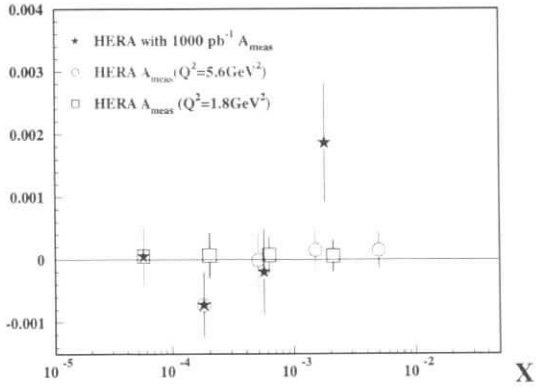

Figure 8: *The measured asymmetry A_m for different Q^2 at HERA for the projected data points shown in previous figures.*

Parameter	Published Best Fit	HERA $L = 1000\ pb^{-1}$	HERA $L = 200\ pb^{-1}$
η_g	1.52±0.74	1.29±0.22	1.29±0.28
η_q	0.48±0.09	0.45±0.04	0.45±0.05
η_{NS}	Fixed	Fixed	Fixed
α_g	-0.47±0.30	-0.64±0.11	-0.64±0.16
α_q	0.41±0.38	0.42±0.26	0.42±0.30
α_{NS}	-0.68±0.15	-0.73±0.10	-0.73±0.12
β_g	2.6±4.8	4.0 (fixed)	4.0 (fixed)
β_q	3.3±1.4	3.50±0.81	3.50±1.13
β_{NS}	2.2±0.3	2.10±0.14	2.10±0.27
$a_q = a_g$	0.1±3.0	1.2±2.5	1.2±2.10
a_{NS}	16.0±17.0	19.5±14.0	19.5±16.4

Table 2: *Results of NLO fits: Column 2 for the published results for data available in 1995, Column 3: estimated results for the available data in 1996 and data at HERA with integrated luminosity L = 1000 pb^{-1}, and Column 4: estimated results using available data in 1996 and the data at HERA with L = 200 pb^{-1}. The parameter η_{NS} is not fitted, its value is taken from hyperon β decay measurements.*

$g_1^p(x, Q^2)$ over a much extended range in x and Q^2. For such measurements the false asymmetries should be considerably smaller than the true asymmetries to be measured, and normalization systematic errors should be controlled to be less than 10%. Statistical errors on the points will dominate.

There is a strong and broad current interest in the spin structure of the nucleon. Proposals have been made and experiments are planned to study this problem at several accelerator facilities. These include COMPASS at CERN, a possible experiment at SLAC, and RHIC SPIN at BNL. A principal goal of all of these proposed experiments is to measure the polarized gluon content in the nucleon from a study of semi-inclusive processes. Another experiment involving a semi-inclusive process is discussed in this volume where the determination of Δg from a study of dijets from polarized e-p collisions at HERA is described. A measurement of Δg from inclusive process has the advantage of being theoretically clean, but requires a wide kinematic coverage in x and Q^2, and could thus only be performed at HERA.

The inclusive measurements with HERA discussed in this chapter will also provide unique information on the behaviour $g_1^p(x, Q^2)$ over an unexplored kinematic range, which is of great theoretical interest.

The fact that HERA is an operating facility with a plan for substantial increase in luminosity and with two major operating detectors, as well as a polarized electron beam, means that only the high energy polarized proton beam needs to be developed. The efforts to achieve that seem well justified and data from such experiments at HERA would provide unique and complementary information to that from other presently proposed experiments.

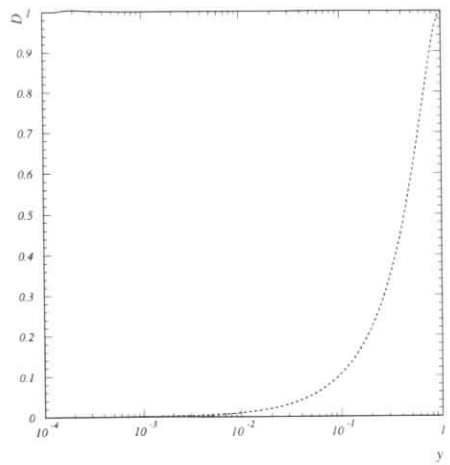

Figure 9: *The dependence of depolarization factor D on y.*

6 Appendix: Kinematics of polarized DIS at HERA

The polarized structure function g_1^p of the proton is related to the virtual photon asymmetry A_1^p by the relation [33],

$$g_1 = \frac{F_2}{2x(1+R)} A_1 \tag{7}$$

in terms of the unpolarized structure function F_2 and the ratio of longitudinal to transverse photoabsorption cross sections R.[4]. The measured longitudinal asymmetry A_m is related to A_1 by,

$$A_m = \frac{N^{\uparrow\uparrow} - N^{\uparrow\downarrow}}{N^{\uparrow\uparrow} + N^{\uparrow\downarrow}} = P_p P_e D A_1 \tag{8}$$

where $P_p(P_e)$ is the proton (electron) polarization, and D is the depolarization factor. The arrows indicate the relative direction of the spins of the electrons and protons. D is calculable from QED and is given by

$$D = \frac{y(2-y)}{y^2 + 2(1-y)(1+R),} \tag{9}$$

where

$$y = \frac{Q^2}{xs} \tag{10}$$

and s is the Mandelstam invariant of the electron-proton collision. The dependence of D on y is shown in Fig. 9. The statistical uncertainty δA_m in the measurement of A_m is given by,

$$\delta A_m = \frac{1}{\sqrt{N^{\uparrow\uparrow} + N^{\downarrow\uparrow}}} = \frac{1}{\sqrt{N_{total}}} \tag{11}$$

[4]This result holds at leading twist.

where $N^{\uparrow\uparrow}$ $^{(\uparrow\downarrow)}$ represent the number of DIS events observed with parallel (anti parallel) proton and electron polarizations, respectively. The sum in the denominator is then the square root of the total number of events observed in the experiment at selected $x - Q^2$ bins.

We estimate the yield and the associated statistical error to be observed in a future HERA experiment. The cross section for DIS is given by

$$\frac{d^2\sigma}{dxdQ^2} = \frac{4\pi\alpha^2}{xQ^4}\left[1 - y + \frac{y^2}{2(1+R)}\right] F_2 \tag{12}$$

The depolarization factor D for each of the bins was calculated and used to estimate the statistical uncertainty in the measurement of g_1^p from Eqs. 9 and 11.

Acknowledgements: We thank G. Altarelli and P. Schuler for interesting discussions and helpful comments.

References

[1] R. Hofstadter, Rev. Mod. Phys. **28** (1956) 214.

[2] J. Friedman et al., Ann. Rev. Nucl. Science **22**, (1972), 203.

[3] SLAC E80, M. J. Alguard et al., Phys. Rev. Lett. **37** (1976) 1261; ibid **41** (1978) 70;
SLAC E130, G. Baum et al., Phys. Rev. Lett. **51** (1983) 1135.

[4] EMC, J. Ashman et al., Nucl. Phys. **B328** (1989) 1.

[5] See e.g. G. Altarelli and G. Ridolfi, Nucl. Phys. B Proc. Suppl. **39B** (1995) 106;
R. D. Ball, `hep-ph/9511330`, in the proceedings of the Erice school on nucleon spin structure;
S. Forte, `hep-ph/9511345`, in the proceedings of the 7th Rencontres de Blois.

[6] SMC, B. Adeva et al., Phys. Lett. **B302** (1993) 533;
SMC, D. Adams et al., Phys. Lett. **B329** (1994) 399;
SMC, D. Adams et al., Phys. Lett. **B357** (1995) 248.

[7] E-143, K. Abe et al., Phys. Rev. Lett. **74** (1995) 346;
E-143, K. Abe et al., Phys. Rev. Lett **75** (1995) 25.

[8] R. D. Ball, S. Forte and G. Ridolfi, Phys. Lett. **B378** (1996) 255.

[9] M. Klein, H1 Collaboration, in "DIS 96" (World Scientific, 1996).

[10] R. Yoshida, ZEUS Collaboration, in "DIS 96" (World Scientific, 1996).

[11] A. De Roeck, lectures at the 1994 Cargèse school, preprint DESY-95-025.

[12] R.D. Ball and A. De Roeck, in "DIS96" (World Scientific, 1996).

[13] HERMES Collaboration, in "DIS96" (World Scientific, 1996).

[14] N. Akchurin et al., Phys. Rev. **D48** (1993) 3026.

[15] L. Wolfenstein, Ann. Rev. Nuclear Science **6** (1956) 43.

[16] M. J. Alguard et al., Phys. Rev. Lett. **37** (1976) 1258.

[17] D. Adams et al., Phys. Lett. **B246** (1991) 14.

[18] "Acceleration of Polarized Protons to 120 GeV and 1 TeV at Fermilab", Univ. of Michigan, HE 95-09, (July 1995).

[19] RHICSPIN proposal

[20] C. Y. Prescott et al., Phys. Lett. **B77** (1978) 347; Phys. Lett. **B84** (1979) 524.
V. Yuan et al., Phys. Rev. Lett. **57** (1986) 320 (and references therein);
P. A. Souder et al., Phys. Rev. Lett. **65** (1990) 694.

[21] T. Roser, Nucl. Instr. Meth. **A342** (1994) 343.

[22] R. A. Phelps et al., Phys. Rev. Lett. **72** (1994) 1479.

[23] G. Altarelli, Phys. Rep. **81** (1982) 1.

[24] G. Altarelli and G. Parisi Nucl. Phys. **B126** (1977) 298.

[25] J. Kodaira et al., Phys. Rev. **D20** (1979) 627.

[26] R. Mertig and W.L. van Neerven, Z. Phys. **C70** (1996) 637;
W. Vogelsang, preprint RAL-TR-96-020, hep-ph/9603366 (1996).

[27] W. J. Stirling and T. Gehrmann, Z. Phys. **C65** (1995) 461; Phys. Rev. **D53** (1996) 6100.

[28] M.Glück, E. Reya, M. Stratmann and W. Vogelsang, Phys. Rev. **D53** (1996) 4775 .

[29] G. Altarelli and G. G. Ross, Phys. Lett. **B212** (1988) 391;

[30] R. D. Ball, S. Forte and G. Ridolfi, Nucl. Phys. **B444** (1995) 287.

[31] R. L. Heimann, Nucl. Phys. **B64** (1973) 429.

[32] R. Kirschner and L. Lipatov, Nucl. Phys. **B213** (1983) 122;
J. Bartels, B. I. Ermolaev and M. G. Ryskin, Z. Phys. **C70** (1996) 273; preprint DESY-96-025, `hep-ph/9603204`

[33] T. Pussieux and R. Windmolders, "A Collection of Formulas for Spin Dependent Deep Inelastic Scattering", DAPNIA-SPHN-95-10, also in "Internal Spin Structure of the Nucleon", Edited by V. W. Hughes, C. Cavata, p212, (World Scientific, Singapore 1995).

Errors in the Extraction of α_s from the Bjorken Sum Rule

Einan Gardi[a], John Ellis[b] and Marek Karliner[a]

[a] School of Physics and Astronomy, Raymond and Beverly Sackler Faculty of Exact Sciences, Tel-Aviv University, Tel-Aviv, Israel
[b] Theory Division, CERN, CH-1211, Geneva 23, Switzerland

Abstract: We discuss the contributions of experimental and theoretical errors to the determination of α_s using data on the Bjorken sum rule at different values of Q^2. The experimental contribution to the error in α_s generally decreases as Q^2 decreases, whereas the theoretical errors increase. Padé summation reduces the theoretical contribution to the error to such an extent that the optimal value of Q^2 for measuring α_s may be quite low.

1 Introduction

We have described previously [1, 2] a method of extracting α_s from the Bjorken sum rule which uses Padé Summation (PS) to estimate the QCD perturbation series.[†] In this note, we analyze the error in $\alpha_s(M_Z)$ that may be obtained from the Bjorken sum rule, as a function of the experimental error and various sources of theoretical error, including the summation prescription, renormalization scale and scheme dependence, and higher-twist effects. Our prime aim is to estimate the dependence of combined theoretical and experimental errors in $\alpha_s(M_Z)$ on the momentum transfer Q^2 at which the analysis is made. This information may be of use in the planning of future polarized electron-nucleon scattering experiments, as it may enable the beam energy to be optimized for the extraction of $\alpha_s(M_Z)$.

2 Propagation of the Experimental Error

The way in which a given experimental error in measuring the Bjorken integral $\Gamma_1^p - \Gamma_1^n$ propagates into a derived error in α_s depends on Q^2. In experiments done at high Q^2 (Q_h^2) where α_s is small, the error in $\alpha_s(Q_h^2)$ is given directly by the error in the measured value of $\Gamma_1^p - \Gamma_1^n$:

$$\Delta(\Gamma_1^p - \Gamma_1^n)(Q_h^2) = \frac{1}{6} g_A \Delta f(x) \sim \frac{g_A}{6\pi} \Delta\alpha_s(Q_h^2) \tag{1}$$

[†] For a more complete list of references, see [3].

since the QCD correction factor $f(x) \sim 1 - x$ for small $x \equiv \alpha_s/\pi$. On the other hand, for experiments done at low Q^2 (Q_l^2) where α_s is large,

$$\Delta(\Gamma_1^p - \Gamma_1^n)(Q_l^2) = \frac{1}{6} g_A \Delta f(x) = \frac{g_A}{6\pi}(1 + Corr(x))\Delta\alpha_s(Q_l^2) \tag{2}$$

where, in $\overline{\rm MS}$ with $\mu = Q$, $Corr(x)$ is a *positive* correction function that results from the higher-order terms in the perturbative series for the Bjorken sum rule (see, for example, Fig. 2 in [1]), so that

$$\Delta\alpha_s(Q_l^2) \sim \frac{6\pi}{g_A}\left(\frac{1}{1 + Corr(x)}\right)\Delta(\Gamma_1^p - \Gamma_1^n)(Q_l^2) \tag{3}$$

Thus, in an experiment done at a lower momentum transfer, the same experimental error in $\Gamma_1^p - \Gamma_1^n$ would propagate to a smaller error in α_s. Although this is the most important effect on the comparison between the errors in α_s obtainable from experiments at different Q^2, it is not the whole story, since they must be evolved to the same reference value of Q^2, e.g., M_Z^2. As is well known, this evolution renders large uncertainties in α_s at low Q^2 equivalent to smaller uncertainties in α_s at higher Q^2, reinforcing the previous effect.

To evaluate these effects in more detail, we recall that to leading non-trivial order in the $\overline{\rm MS}$ renormalization scheme:

$$\Delta(\Gamma_1^p - \Gamma_1^n)(Q_l^2) = \frac{g_A}{6\pi}\frac{d}{dx}\left(x + (\frac{23}{12}C_a - \frac{7}{8}C_f - \frac{1}{3}N_f)x^2\right)\Delta\alpha_s$$

Specializing to three colours, we obtain

$$\Delta(\Gamma_1^p - \Gamma_1^n)(Q_l^2) = \frac{g_A}{6\pi}\left(1 + \frac{2}{\pi}(4.5833 - \frac{1}{3}N_f)\alpha_s(Q_l^2)\right)\Delta\alpha_s \tag{4}$$

which we may invert to yield

$$\Delta\alpha_s(Q_l^2) \sim \frac{6\pi}{g_A}\left(\frac{1}{1 + \frac{2}{\pi}\left(4.5833 - \frac{1}{3}N_f\right)\alpha_s(Q_l^2)}\right)\Delta(\Gamma_1^p - \Gamma_1^n)(Q_l^2) \tag{5}$$

In order to compare the error in an experiment at Q_l^2 to that in an experiment at Q_h^2, we use renormalization-group evolution to evaluate the error in $\alpha_s(Q_h^2)$ obtained from an experiment at Q_l^2. At leading order, we have:

$$\alpha_s(Q_h^2) = \alpha_s(Q_l^2) - \frac{\pi}{4}\left(11 - \frac{2}{3}N_f\right)t\frac{\alpha_s^2(Q_l^2)}{\pi^2} \tag{6}$$

where $t = ln\left(\frac{Q_h^2}{Q_l^2}\right)$ is positive, and therefore

$$\Delta\alpha_s(Q_h^2) = \left(1 - \frac{1}{2\pi}\left(11 - \frac{2}{3}N_f\right)t\alpha_s(Q_l^2)\right)\Delta\alpha_s(Q_l^2) \tag{7}$$

Thus, an experiment at low momentum transfer Q_l^2 yields an uncertainty

$$\Delta\alpha_s(Q_h^2) \sim \frac{6\pi}{g_A}\left(\frac{1 - \frac{1}{2\pi}\left(11 - \frac{2}{3}N_f\right)t\alpha_s(Q_l^2)}{1 + \frac{2}{\pi}\left(4.5833 - \frac{1}{3}N_f\right)\alpha_s(Q_l^2)}\right)\Delta(\Gamma_1^p - \Gamma_1^n)(Q_l^2) \tag{8}$$

This demonstrates explicitly the two reasons why the slope of $\Delta\alpha_s$ as a function of $\Delta(\Gamma_1^p - \Gamma_1^n)$ decreases with decreasing Q^2: the positivity of the higher-order perturbative corrections to the Bjorken sum rule makes the denominator larger than 1, and the running of α_s makes the numerator smaller than 1.

3 Theoretical Errors

The above discussion ignored uncertainties in the theoretical formula used to interpret the data, and we now turn to discuss how the various theoretical errors due to these uncertainties contribute to the error in the extraction of α_s from the Bjorken sum rule. The main source of uncertainty is simply that the perturbative QCD series for the Bjorken sum rule is known only up to next-to-next-to-leading-order in α_s. Moreover, this series is expected to be asymptotic, so the higher-order terms are significant. In [1, 2] we examined the utility of Padé Summation (PS) methods for the resummation of the series. We showed that using PS to extract α_s yields a result that is much less scale [1] and scheme [2] dependent than if the naive partial sum is used.

One method of evaluating the theoretical uncertainty in α_s due to higher-order terms in the series is to compare different summation prescriptions. In [1], we estimated this from the difference between the values of α_s extracted using the [2/2] PS (our preferred value) and using the [2/1] and [1/2] PS's.

Another method of evaluation is to consider the scale dependence of the value of α_s that is extracted. As we have demonstrated in [1], this is reduced significantly by using the PS method. We estimate the scale-dependence error from the differences between the values of α_s that we find when setting the scale μ^2 in the [2/2] PS of the $\overline{\rm MS}$ series to be Q^2 (our preferred value), and when we set the scale of the same function to be $(2Q)^2$ or $(\frac{1}{2}Q)^2$, taking for definiteness the average of these two. A similar result is obtained when one considers the two-parameter renormalization-scheme dependence of the PS [2].

A third theoretical uncertainty is in the size of the higher-twist effect, whose contribution to the Bjorken sum rule is currently estimated to be

$$-\frac{0.02}{Q^2} \pm \frac{0.01}{Q^2} \tag{9}$$

We note in passing that this magnitude is similar [1] to the estimated ambiguity in the Borel resummation of the perturbative QCD series.

All these three types of theoretical uncertainty are reduced at higher momentum transfer, for the simple reason that they are all associated with the unknown higher-order corrections, which become smaller at higher Q^2.

4 Combined Error

We see that the propagated experimental error in α_s tends to increase with increasing momentum transfer, while the theoretical errors have the opposite effect - they tend to decrease with

increasing momentum transfer. The interplay between these different behaviours is such that one must examine the combined experimental and theoretical error as a function of both the experimental error in $\Gamma_1^p - \Gamma_1^n$ and the momentum transfer.

We define the total theoretical error as the sum in quadrature of the three theoretical errors defined above, namely the prescription error, the scale- and scheme-dependence error, and the higher-twist error. This cannot be exactly correct, but it is the best we can offer, until the correlations between the different errors become clearer. Finally, we define the combined error as the sum in quadrature of the total theoretical error and the experimental error. This treatment may also be questioned, but again we do not have a better procedure.

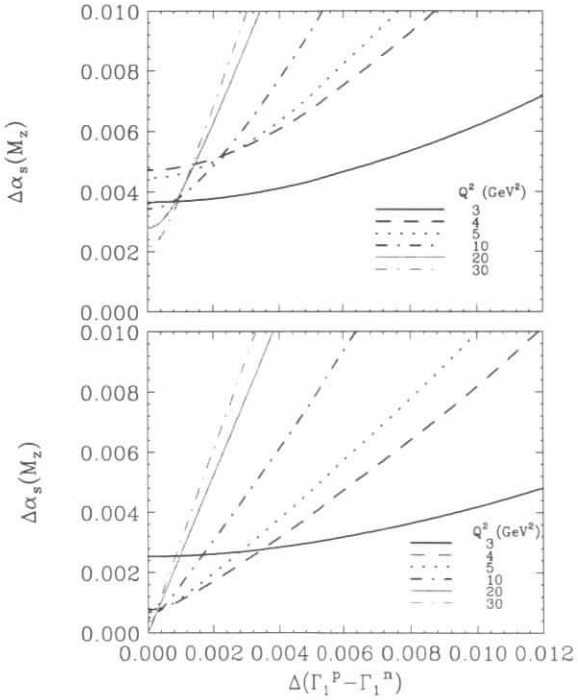

(a) with higher twist

(b) without higher twist

Figure 1: *(a) The error in $\alpha_s(M_Z)$ as a function of the experimental error in $\Delta[\Gamma_1^{(p-n)}(Q^2)]$, for $Q^2 = 3, 4, 5, 10, 30$ GeV^2. (b) The same as (a), but without the higher-twist correction.*

We now present a figure that shows the dependence of the combined error in $\alpha_s(M_Z)$ on the measurement error $\Delta(\Gamma_1^p - \Gamma_1^n)$. Fig. 1(a) shows the combined error as a function of the experimental error. We see that the slopes of the different Q^2 lines become steeper at higher Q^2.

This is due to the propagation of the experimental error described in Section 2. The values of $\Delta\alpha_s$ at which the lines for different Q^2 cross the $\Delta(\Gamma_1^p - \Gamma_1^n) = 0$ axis are the theoretical errors. We see the expected general trend that at higher Q^2 the theoretical error is lower. However, we also note that this general rule does not hold when there is a change in the number of contributing quark flavors, specifically as we go from $Q^2 = 3$ GeV^2 to $Q^2 = 4$ GeV^2.

In Fig. 1(b), both the magnitude and the error in the higher-twist effect are set to zero. For two reasons, this leads to a much smaller combined error. In the absence of the higher-twist shift, the central value of α_s and hence its experimental error is reduced, and the absence of the higher-twist error reduces the theoretical error. We see that, if there is no higher-twist effect, the higher Q^2 lines intersect the $Q^2 = 3$ GeV^2 line at much higher values of $\Delta(\Gamma_1^p - \Gamma_1^n)$.

5 Conclusions

This analysis indicates that, for a given error in $\Gamma_1^p - \Gamma_1^n$, experiments at high momentum transfer Q^2 generally yield larger errors in $\alpha_s(M_Z)$ than experiments of similar precision at low momentum transfer. This conclusion is dependent on our claim to understand the theoretical errors at the stated level, and will be true as long as the measurement error in $\Delta(\Gamma_1^p - \Gamma_1^n)$ is not reduced, down to the level where the theoretical error lurks. Our analysis indicates that the higher-twist effect is crucial for determining the optimal momentum transfer for this particular measurement. However, we emphasize that other values of the momentum transfer may be better for other measurements.

Acknowledgements

This work was supported in part by the Israel Science Foundation administered by the Israel Academy of Sciences and Humanities, and by a Grant from the G.I.F., the German-Israeli Foundation for Scientific Research and Development.

References

[1] J. Ellis, E. Gardi, M. Karliner and M.A. Samuel, *Pade Approximants, Borel Transforms and renormalons: the Bjorken Sum Rule as a case study*, hep-ph/9509312, *Phys. Lett.* **B366**(1996)268.

[2] J. Ellis, E. Gardi, M. Karliner and M.A. Samuel, *Renormalization-Scheme Dependence of Padé Summation in QCD*, hep-ph/9607404.

[3] J. Ellis and M. Karliner, *The Strange Spin of the Nucleon*, hep-ph/9601280, invited lectures at the International School of Nucleon Spin Structure, Erice, August 1995.

The Effect of Small-x Resummations on the Evolution of Polarized Structure Functions

Johannes Blümlein[a] and Andreas Vogt[b,c]

[a] DESY–Zeuthen, Platanenallee 6, D–15735 Zeuthen, Germany
[b] Deutsches Elektronen–Synchrotron DESY, Notkestraße 85, D–22603 Hamburg, Germany
[c] Institut für Theoretische Physik, Universität Würzburg, D–97074 Würzburg, Germany

Abstract: The impact of the resummation of leading small-x terms in the anomalous dimensions is briefly summarized for the evolution of non–singlet and singlet polarized structure functions.

1 Introduction

The evolution kernels of both non–singlet and singlet polarized parton densities contain large logarithmic contributions for small fractional momenta x. The leading terms in this limit are of the form $\alpha_s^k \ln^{2k-2} x$ for both cases [1, 2]. The resummation of these contributions to all orders in the strong coupling constant α_s can be completely derived by means of perturbative QCD. The appropriate framework for investigating the resummation effects is provided by the renormalization group equations.

The impact of the resulting all–order anomalous dimensions on the behaviour of the deep–inelastic scattering (DIS) structure functions at small x thus depends as well on the non–perturbative input parton densities at an initial scale Q_0^2. Hence the resummation effects can only be studied via the evolution over some range in Q^2. This evolution moreover probes the anomalous dimensions also at medium and large values of x by the Mellin convolution with the parton densities. Therefore the small-x dominance of the leading terms over less singular contributions in the anomalous dimensions does not necessarily imply the same situation for observable quantities, such as the structure functions.

In the following we present a brief survey of quantitative results which shed light on the importance of these aspects. For full accounts, including the discussion of theoretical aspects, the reader is referred to refs. [3, 4] and [5] for the non–singlet and singlet evolutions, respectively. A recent review covering also the unpolarized cases can be found in ref. [6].

2 Quantitative Results

In leading (LO) and next–to–leading order (NLO) perturbative QCD, the complete anomalous dimensions are known. Hence the effect of the all–order resummation of the most singular parts of the splitting functions as $x \to 0$ concerns only orders higher than α_s^2. Due to the Mellin convolution terms less singular as $x \to 0$ may contribute substantially at these higher orders

also. Since such contributions and further corrections are not yet known to all orders, it is reasonable to estimate their possible impact by corresponding modifications of the resummed anomalous dimensions $\Gamma(N, \alpha_s)$, where N denotes the Mellin variable. Plausible examples inspired by the behaviour of the full NLO results have been studied in refs. [3, 4, 5], including

$$\begin{aligned} &\text{A}: \ \Gamma(N,\alpha_s) \to \Gamma(N,\alpha_s) - \Gamma(1,\alpha_s) \qquad \text{B}: \ \Gamma(N,\alpha_s) \to \Gamma(N,\alpha_s)(1-N) \\ &\text{D}: \ \Gamma(N,\alpha_s) \to \Gamma(N,\alpha_s)(1-2N+N^3)\,. \end{aligned} \tag{1}$$

Clearly the presently known resummed terms are only sufficient for understanding the small-x evolution, if the difference of the results obtained by these prescriptions are small.

2.1 Polarized non–singlet structure functions

This case has been investigated in refs. [3, 4] for the structure function combination $g_1^{ep} - g_1^{en}$ for two parametrizations of the non–perturbative initial distributions, see Figure 1. Results on the interference structure function $g_{5,\gamma Z}^{eF}(x, Q^2)$ can be found in ref. [6]. For the relatively flat CW input [7], the resummation effect on $g_1^{ep} - g_1^{en}$ reaches about 15% at $x = 10^{-5}$. However, in the restricted kinematical range accessible in possible future polarized electron–polarized proton collider experiments at HERA [9], it amounts to only 1% or less. For the steeper GRSV initial distributions [8], the effect is of order 1% or smaller in the whole x range. Hence the results do not at all come up to previous expectations of huge corrections up to factors of 10 or larger as anticipated in ref. [10].

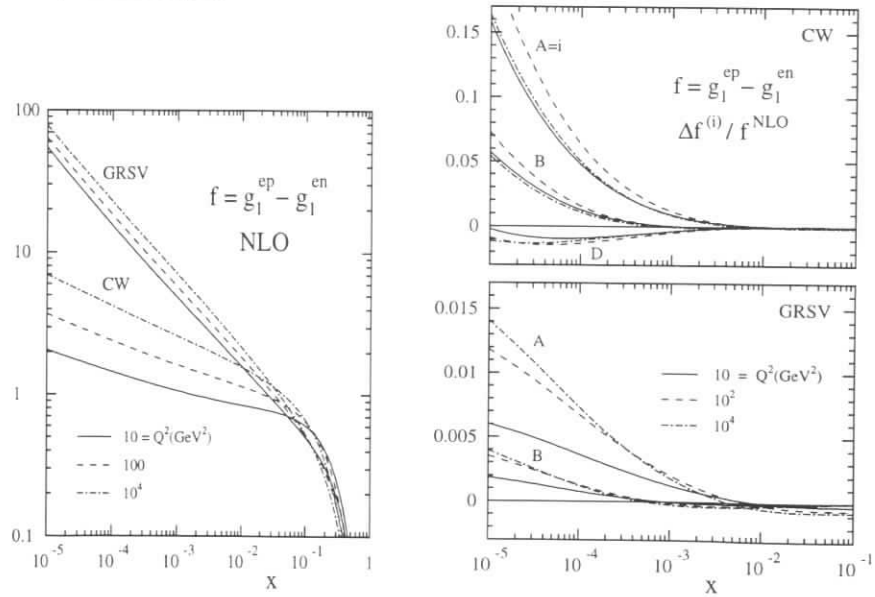

Figure 1: The NLO small-x evolution of the polarized non–singlet structure function combination $g_1^{ep} - g_1^{en}$, and the relative corrections due to the resummed kernels, for the initial distributions of refs. [7] and [8]. The dependence on possible less singular terms is illustrated by the prescriptions 'A', 'B', and 'D' of eq. (1). The figure has been adapted from ref. [6].

2.2 Polarized singlet structure functions

The numerical consequences of the small-x resummation for the evolution of $g_1^{ep,en}(x,Q^2)$ and the parton densities have been given for different input distributions in ref. [5]. Figure 2 shows an example. The effects are much larger here than for the non–singlet structure functions. Also illustrated in these figures [by the results for the prescription '(B)' in eq. (1)] is the possible impact of the yet uncalculated terms in the higher–order anomalous dimensions which are down by one power of N with respect to the resummed leading pieces as $N \to 0$. As in the non–singlet case considered before, the effect of these additional terms can be very large, even the sign of the deviation from the NLO evolution cannot be taken for granted.

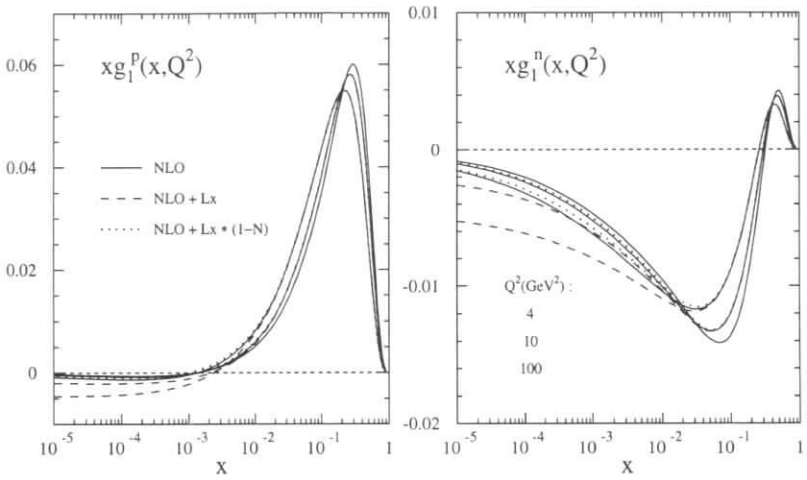

Figure 2: The x and Q^2 behaviour of the polarized proton and neutron structure functions $g_1^{p,n}(x,Q^2)$ as obtained from the GRSV standard distribution [8] at $Q_0^2 = 4\,\mathrm{GeV}^2$. The results are shown for the NLO kernels (full), the leading small-x resummed kernels (dashed), and the modification 'B' of eq. (1) of the latter by possible less singular terms (dotted). The figure has been taken from ref. [5].

3 Conclusions

The effects of the resummation of the leading small-x terms in the polarized non–singlet and singlet anomalous dimensions have been summarized. For non–singlet structure functions the corrections due to those $\alpha_s(\alpha_s \ln^2 x)^l$ contributions are about 1% or smaller, in the kinematical ranges probed so far as well as the regime accessible at a polarized version of HERA [3, 4]. In the singlet case very large corrections are obtained. As in the non–singlet cases, however, possible less singular terms in higher order anomalous dimensions, are hardly suppressed against the presently resummed leading terms in the evolution: even a full compensation of the resummation effects cannot be excluded [5]. To draw firm conclusions on the small-x evolution of also the singlet structure functions, the next less singular terms as well as the complete three–loop anomalous dimensions are needed.

Acknowledgements : This work was supported in part by the EC Network 'Human Capital and Mobility' under contract No. CHRX–CT923–0004 and by the German Federal Ministry for Research and Technology (BMBF) under contract No. 05 7WZ91P (0).

References

[1] R. Kirschner and L. Lipatov, Nucl. Phys. **B213** (1983) 122.

[2] J. Bartels, B. Ermolaev, and M. Ryskin, DESY 96–025.

[3] J. Blümlein and A. Vogt, Phys. Lett. **B370** (1996) 149.

[4] J. Blümlein and A. Vogt, Acta Phys. Polonica **B27** (1996) 1309.

[5] J. Blümlein and A. Vogt, DESY 96–050, `hep-ph/9606254`, Phys. Lett. **B**, in press.

[6] J. Blümlein, S. Riemersma, and A. Vogt, DESY 96–131, `hep-ph/9609217`, Proceedings of the Workshop 'QCD and QED in Higher Orders', Rheinsberg, Germany, April 1996, eds. J. Blümlein, F. Jegerlehner and T. Riemann (Nucl. Phys. **B** (Proc. Suppl.) **51C**, 1996), p. 30.

[7] Hai–Yang Cheng and C. Wai, Phys. Rev. **D46** (1992) 125.

[8] M. Glück, E. Reya, M. Stratmann, and W. Vogelsang, Phys. Rev. **D53** (1996) 4775.

[9] J. Blümlein, DESY 95–164, `hep-ph/9508387`, Proceedings of the Workshop 'Prospects of Spin Physics at HERA', eds. J. Blümlein and W. Nowak (DESY, Hamburg, 1995), p. 179.

[10] J. Bartels, B. Ermolaev, and M. Ryskin, Z. Physik **C70** (1996) 273.

Prospects for Measuring ΔG from Jets at HERA with Polarized Protons and Electrons

A. De Roeck[a], J. Feltesse[b], F. Kunne[b], M. Maul[c],
E. Mirkes[d], G. Rädel[e], A. Schäfer[c], and C. Y. Wu[c]

[a] Deutsches Elektronen-Synchrotron DESY, Notkestrasse 85, D-22603 Hamburg, Germany
[b] DAPNIA, CE Saclay, F-91191 Gif/Yvette, France
[c] Inst. f. Theor. Phys., Johann Wolfgang Goethe-Universität, D-60054 Frankfurt am Main, Germany
[d] Inst. f. Theor. Teilchenphysik, Universität Karlsruhe, D-76128 Karlsruhe, Germany
[e] CERN, Div. PPE, CH-1211 Genève 23, Switzerland

Abstract: The measurement of the polarized gluon distribution function $\Delta G(x)$ from photon-gluon fusion processes in electron-proton deep inelastic scattering producing two jets has been investigated. The study is based on the MEPJET and PEPSI simulation programs. The size of the expected spin asymmetry and corresponding statistical uncertainties for a possible measurement with polarized beams of electrons and protons at HERA have been estimated. The results show that the asymmetry can reach a few percent, and is not washed out by hadronization and higher order processes.

1 Introduction

After confirmation of the surprising EMC result, that quarks carry only a small fraction of the nucleon spin, this subject is being actively studied by several fixed target experiments at CERN, DESY and SLAC [1]. So far only the polarized structure functions $g_1(x, Q^2)$ and $g_2(x, Q^2)$ have been measured. These structure functions measure predominately the polarized quark distribution functions, which, as usual, contain a scheme dependent gluon admixture. A specific property of polarized structure functions is that this admixture can be rather large, due to a rather large polarized gluon distribution function $\Delta G(x_g)$, as suggested by the fact that $\alpha_S(Q^2) \int dx_g \Delta G(x_g, Q^2)$ is renormalization group invariant.

The direct measurement of the polarized gluon distribution $\Delta G(x_g, Q^2)$ has become the key experiment in order to understand the QCD properties of the spin of the nucleon. For a collider with polarized electrons and protons with beam energies such as for HERA the measurement of dijet events offers such a possibility[2].

The gluon distribution enters at leading order (LO) in the two-jets production cross section[1] in deep inelastic scattering (DIS) (see Fig. 1), and the unpolarized gluon distribution $G(x_g, Q^2)$

[1] In the following the jet due to the beam remnant is not included in the number of jets.

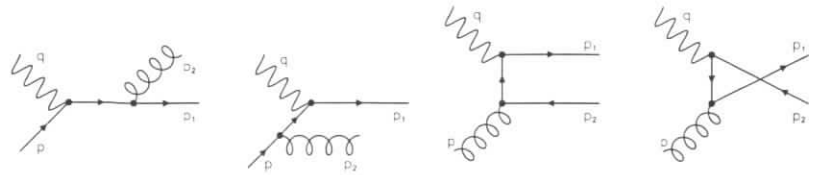

Figure 1: Feynman diagrams for the dijet cross section at LO.

has indeed already been extracted from two-jets events by the H1 collaboration at HERA. With a modest integrated luminosity of 0.24 pb^{-1} collected in 1993, first data on $x_g G(x_g)$ were extracted from dijets events [3] at LO, in a wide x_g range $0.002 < x_g < 0.2$, at a mean Q^2 of 30 GeV^2. These results were found to be in good agreement with the gluon distribution extracted at LO from scaling violations of the structure function F_2. Presently this method is being extended to NLO, and first preliminary results were shown in [4, 5]. An initial study of the feasibility of this measurement for ΔG at HERA (mainly for a polarized fixed target experiment) was presented in [6].

2 Jet cross sections in DIS

Deep inelastic electron-proton scattering with several partons in the final state,

$$e^-(l) + p(P) \rightarrow e^-(l') + \text{remnant}(p_r) + \text{parton } 1(p_1) + \ldots + \text{parton } n(p_n) \qquad (1)$$

proceeds via the exchange of an intermediate vector boson $V = \gamma^*, Z$. Z-exchange and γ^*/Z interference become only important at large Q^2 (> 1000 GeV^2) and are neglected in the following. We denote the momentum of the virtual photon, γ^*, by $q = l - l'$, (minus) its absolute square by Q^2, and use the standard scaling variables Bjorken-x $x_{Bj} = Q^2/(2P \cdot q)$ and inelasticity $y = P \cdot q / P \cdot l$. The general structure of the *unpolarized* n-jet cross section in DIS is given by

$$d\sigma^{had}[n\text{-jet}] = \sum_a \int dx_a \; f_a(x_a, \mu_F^2) \; d\hat{\sigma}^a(p = x_a P, \alpha_s(\mu_R^2), \mu_R^2, \mu_F^2) \qquad (2)$$

where the sum runs over incident partons $a = q, \bar{q}, g$ which carry a fraction x_a of the proton momentum. $\hat{\sigma}^a$ denotes the partonic cross section from which collinear initial state singularities have been factorized out (in next-to-leading order (NLO)) at a scale μ_F and implicitly included in the scale dependent parton densities $f_a(x_a, \mu_F^2)$. For *longitudinally polarized* lepton-hadron scattering, the hadronic (n-jet) cross section is obtained from Eq. (2) by replacing $(\sigma^{had}, f_a, \hat{\sigma}^a) \rightarrow (\Delta\sigma^{had}, \Delta f_a, \Delta\hat{\sigma}^a)$. The polarized hadronic cross section is defined by $\Delta\sigma^{had} \equiv \sigma^{had}_{\uparrow\downarrow} - \sigma^{had}_{\uparrow\uparrow}$, where the left arrow in the subscript denotes the polarization of the incoming lepton with respect to the direction of its momentum. The right arrow stands for the polarization of the proton parallel or anti-parallel to the polarization of the incoming lepton. The polarized parton distributions are defined by $\Delta f_a(x_a, \mu_F^2) \equiv f_{a\uparrow}(x_a, \mu_F^2) - f_{a\downarrow}(x_a, \mu_F^2)$. Here, $f_{a\uparrow}(f_{a\downarrow})$ denotes the probability to find a parton a in the longitudinally polarized proton whose spin is aligned (anti-aligned) to the proton's spin. $\Delta\hat{\sigma}^a$ is the corresponding polarized partonic cross section.

In the Born approximation, the subprocesses $\gamma^* + q \to q + g$, $\gamma^* + \bar{q} \to \bar{q} + g$, $\gamma^* + g \to q + \bar{q}$ contribute to the two-jet cross section (Fig. 1). The boson-gluon fusion subprocess $\gamma^* + g \to q + \bar{q}$ dominates the two-jet cross section at low x_{Bj} for unpolarized protons (see below) and allows for a direct measurement of the gluon density in the proton. The full NLO corrections for two-jet production in unpolarized lepton-hadron scattering are now available [7] and implemented in the $ep \to n-$jets event generator MEPJET, which allows to analyze arbitrary jet definition schemes and general cuts in terms of parton 4-momenta.

First discussions about jet production in polarized lepton-hadron scattering can be found in Ref. [8], where the jets were defined in a modified "JADE" scheme. However, it was found [7, 9] that the theoretical uncertainties of the two-jet cross section for the "JADE" scheme can be very large due to higher order effects. These uncertainties are small for the cone scheme and the following results are therefore based on the cone algorithm, which is defined in the laboratory frame. In this algorithm the distance $\Delta R = \sqrt{(\Delta\eta)^2 + (\Delta\phi)^2}$ between two partons decides whether they should be recombined into a single jet. Here the variables are the pseudo-rapidity η and the azimuthal angle ϕ. We recombine partons with $\Delta R < 1$. Furthermore, a cut on the jet transverse momenta of $p_T > 5$ GeV in the laboratory frame and in the Breit frame is imposed. We employ the one loop (two loop) formula for the strong coupling constant in a LO (NLO) analyses with a value for $\Lambda^{(4)}_{\overline{MS}}$ consistent with the value from the parton distribution functions. In addition a minimal set of general kinematical cuts is imposed on the virtual photon and on the final state electron and jets. If not stated otherwise, we require 5 GeV$^2 < Q^2 <$ 2500 GeV^2, $0.3 < y < 1$, an energy cut of $E(e') > 5$ GeV on the scattered electron, and a cut on the pseudo-rapidity $\eta = -\ln\tan(\theta/2)$ of the scattered lepton (jets) of $|\eta| < 3.5$ ($|\eta| < 2.8$). These cuts are compatible with the existing detectors H1 and ZEUS, and slightly extend the cuts of the H1 gluon analysis from jets.

Let us briefly discuss the choice of the renormalization and factorization scales μ_R and μ_F in Eq. (2). Both the renormalization and the factorization scales are tied to the sum of parton k_T's in the Breit frame,

$$\mu_R = \mu_F = \frac{1}{2}\sum_i k_T^B(i)\,. \tag{3}$$

Here $(k_T^B(i))^2 = 2E_i^2(1-\cos\theta_{ip})$, and θ_{ip} is the angle between the parton and proton direction in the Breit frame. $\sum_i k_T^B(i)$ interpolates between Q, the photon virtuality, in the naive parton model limit and the sum of jet transverse momenta when Q becomes negligible, and thus it constitutes a natural scale for jet production in DIS [9].

Let us first discuss some results for unpolarized dijet cross sections. If not stated otherwise, the lepton and hadron beam energies are 27.5 and 820 GeV, respectively. With the previous parameters and GRV parton densities [10] one obtains a LO (NLO) two-jet cross section σ^{had}(2-jet) of 1515 pb (1470 pb). Thus the higher order corrections are small. This is essentially due to the relatively large cuts on the transverse momenta of the jets. As mentioned before, the boson-gluon fusion subprocess dominates the cross section and contributes 80% to the LO cross section.

In order to investigate the feasibility of the parton density determination, Fig. 2a shows the Bjorken x_{Bj} distribution of the unpolarized two-jet exclusive cross section. The gluon initiated subprocess clearly dominates the Compton process for small x_{Bj} in the LO predictions. The effective K-factor is close to unity for the total exclusive dijet cross section which is the result of compensating effects in the low x ($K > 1$) and high x ($K < 1$) regime.

For the isolation of parton distributions we are interested in the fractional momentum x_a of the incoming parton a ($a = q, g$, denoted p in Fig. 1). For events with dijet production x_{Bj} and x_a differ substantially. For two-jet exclusive events the two are related by $x_a = x_{Bj}\left(1 + \frac{s_{ij}}{Q^2}\right)$. where s_{ij} is the invariant mass squared of the produced dijet system. The s_{ij} distribution for the kinematical region under study is shown in Fig. 2b. It is found to exhibit rather large NLO corrections as well. The invariant mass squared of the two jets is larger at NLO than at LO (the mean value of s_{ij} rises to 620 GeV^2 at NLO from 500 GeV^2 at LO).

The NLO corrections to the x_{Bj} and s_{ij} distributions have a compensating effect on the x_a distribution shown in Fig. 2c: the NLO and LO predictions have a similar shape. At LO a direct determination of the gluon density is possible from this distribution, after subtraction of the calculated Compton subprocess. This simple picture is modified in NLO, however, and the effects of Altarelli-Parisi splitting and low p_T partons need to be taken into account more carefully to determine the structure functions at a well defined factorization scale μ_F in NLO.

In the following we discuss some results for polarized dijet production. Our standard set of polarized parton distributions is "gluon, set A" of Gehrmann and Stirling [11], for which $\int_0^1 \Delta G(x)dx = 1.8$ at $Q^2 = 4$ GeV^2. Using the same kinematical cuts as before, the LO polarized dijet cross sections $\Delta\sigma$(2-jet) are shown in the first column of table 1. The negative value for the polarized dijet cross section (-45 pb) is entirely due to the cross section of the boson-gluon fusion process (-53 pb), which is negative for $x_{Bj} \lesssim 0.025$ whereas the contribution from the quark initiated subprocess is positive over the whole kinematical range. Note, however, that the shape of the x_g distribution in the polarized gluon density is hardly (or even not at all) constrained by currently available DIS data, in particular for small x_g. Alternative parametrizations of the polarized gluon distributions in the small x_g region, which are still consistent with all present data [12], can lead to very different polarized cross-sections. The polarized two-jet cross sections for such parton distributions [2] with $\int_0^1 \Delta G(x)dx = 2.7$ and $\int_0^1 \Delta G(x)dx = 0.3$ and at $Q^2 = 4$ GeV^2 are shown in column 2 and 3 in table 1, respectively.

Table 1: LO polarized dijet cross sections for different polarized parton distributions (column 1-3). The contributions from the gluon and quark initiated subprocesses are shown in the last two lines. See text for the details on the kinematics.

	$\int_0^1 \Delta G(x)dx = 1.8$	$\int_0^1 \Delta G(x)dx = 2.7$	$\int_0^1 \Delta G(x)dx = 0.3$
$\Delta\sigma$2-jet	-45 pb	-67.5 pb	-3 pb
$\Delta\sigma^g$2-jet	-53 pb	-76 pb	-10 pb
$\Delta\sigma^q$2-jet	8 pb	8.5 pb	7 pb

The fractional momentum distributions x_a of the incident parton ($a = q, g$), shown in Figs. 2d-f for the three sets of polarized parton densities, demonstrate the sensitivity of the dijet events to the choice of these parametrizations, particularly in the lower x_a range. Note, that the fractional momentum distributions are again related to x_{Bj} by $x_a = x_{Bj}\left(1 + \frac{s_{ij}}{Q^2}\right)$. The corresponding x_{Bj} and s_{ij} distributions are not shown here.

[2] We thank T. Gehrmann for providing us with these parametrizations

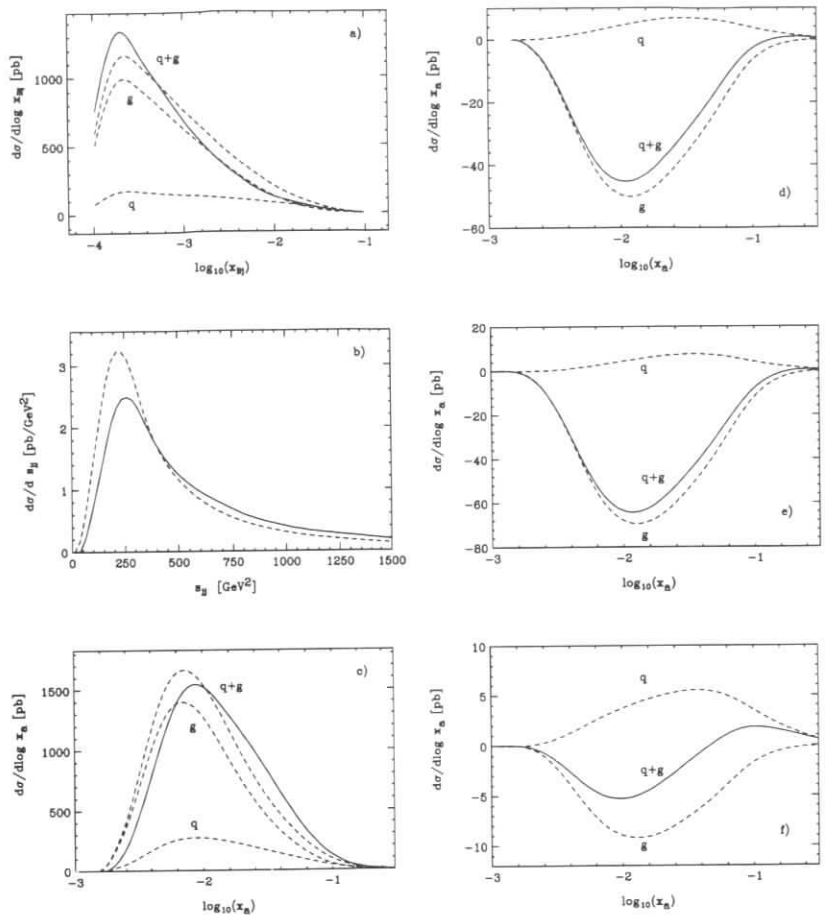

Figure 2: a) Dependence of the *unpolarized* two-jet cross section on Bjorken x_{Bj} for the quark and gluon initiated subprocesses and for the sum. Both LO (dashed) and NLO (solid) results are shown; b) Dijet invariant mass distribution in LO (dashed) and in NLO (solid) for unpolarized dijet production; c) Same as a) for the x_a distribution, x_a representing the momentum fraction of the incident parton at LO; d) Dependence of the LO *polarized* two-jet cross section on x_a for the quark and gluon initiated subprocesses (dashed) and for the sum (solid). Results are shown for the polarized parton distributions "gluon, set A" of Gehrmann and Stirling [11], for which $\int_0^1 \Delta G(x)dx = 1.8$ at $Q^2 = 4$ GeV^2; e) same as d) for $\int_0^1 \Delta G(x)dx = 2.7$ at $Q^2 = 4$ GeV^2; f) same as d) for $\int_0^1 \Delta G(x)dx = 0.3$ at $Q^2 = 4$ GeV^2.

3 Experimental asymmetries

3.1 Parton level studies

In order to study the feasibility and the sensitivity of the measurement of the spin asymmetry at HERA, we have assumed polarizations of 70% for both the electron and the proton beams and statistical errors were calculated for a total luminosity of 200 pb^{-1} (100 pb^{-1} for each polarization).

The expected experimental asymmetry $< A >= \frac{\Delta\sigma^{had}(2\text{-jet})}{\sigma^{had}(2\text{-jet})}$ under these conditions is shown in Fig. 3a, as a function of x_{Bj} and in Fig. 3b-d as a function of x_g. Figures a) and b) correspond to the nominal kinematical cuts defined previously, except for the Q^2 range which was extended to lower values $2 < Q^2 < 2500$ GeV^2 and $10^{-5} < x_{Bj} < 1$. The cross section integrated over all variables is 2140 pb, where 82% of the contribution comes from gluon-initiated events. The asymmetry averaged over all variables is $< A >= -0.015 \pm 0.0015$. It is negative at low x_{Bj} and becomes positive at $x_{Bj} > 0.01$ as expected from Fig. 2.

In Figs. 3c,d a further cut was made: $Q^2 < 100$ GeV^2. This cut permits to reject the positive contributions to the asymmetry coming from high Q^2 (equivalent to high x_{Bj}) events, where the contribution of quark-initiated events is higher. All the remaining events were separated in two bins in s_{ij} –the invariant mass of the dijet– and two bins in y, as the asymmetry and expected NLO corrections are very sensitive to these two variables. Fig.3c corresponds to low invariant masses ($s_{ij} < 500$ GeV^2), and Fig. 3d to high ones ($s_{ij} > 500$ GeV^2). Open points show low y values ($y < 0.6$), and closed points, high y values ($y > 0.6$). In the best case, the asymmetry reaches values as high as 12% (Fig. 3d).

Reducing the beam energy to 410 GeV, instead of the nominal 820 GeV, does not improve the signal in average, although the mean value of y is higher. The asymmetry signal increases only for a few points around $x_g > 0.1$, since a higher incident energy probes slightly higher values of x_g.

3.2 Hadronization and detector effects

So far we discussed cross sections only on the parton level and to lowest order. While, on the level of matrix elements, one can only calculate leading order and next to leading order corrections, in real experiments one always encounters a coherent superposition of contributions of all orders. It is therefore important to investigate next how the picture changes when one takes the effects of higher orders, the fragmentation of the jets into hadrons and detector smearing into account. These effects have been studied in two ways: i) a different program called PEPSI (see below) was used, which is a full LO lepton-nucleon scattering Monte Carlo program for unpolarized and polarized interactions, including fragmentation; ii) parton showers, to emulate the higher orders, and parton fragmentation have been added to the LO matrix elements of MEPJET. PEPSI was further used to study effects of detector smearing.

The PEPSI program is the polarized extension to the unpolarized lepton-nucleon Monte Carlo program LEPTO 6.2 [13]. It adds to the unpolarized cross section, which is a convolution of the partonic cross section σ_p and the unpolarized structure functions $q(x, Q^2)$, the respective

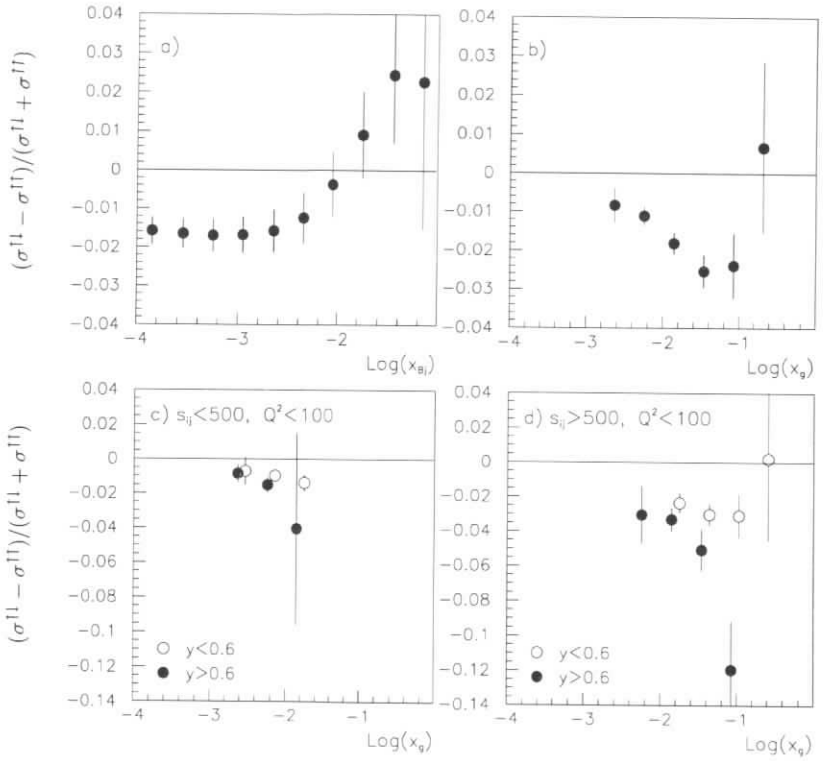

Figure 3: Expected asymmetries as a function of x_{Bj} (a) and x_g (b-d) for a luminosity of 200 pb^{-1} and beam polarizations $P_e = P_p = 70\%$; Fig.a) and b):nominal cuts; Fig.c) and d): $Q^2 < 100$ GeV^2; In Fig.c) and d) data are separated in bins of s_{ij} and y.

polarized cross section as a convolution of the polarized partonic cross section $\Delta\sigma_p$ and the polarized parton densities $x\Delta q(x)$:

$$d\sigma \sim \int_{x_{p,min}}^{x_{p,max}} \frac{dx_p}{x_p} q(x_p/x) d\sigma(x_p, y) + POL \int_{x_{p,min}}^{x_{p,max}} \frac{dx_p}{x_p} \Delta q(x_p/x) d\Delta\sigma(x_p, y) \qquad (4)$$

Here x is the Bjorken x_{Bj}, while x_p is defined via $x_p = x_{Bj}/x_a$, with x_a the fraction of the target momentum carried by the initial parton, as defined before. POL is a parameter which is $+1$ for lepton and nucleon spin being antiparallel to each other and -1 in the case where the electron and nucleon spins are parallel to each other. The unpolarized leading order (LO) partonic cross section used already in LEPTO is described in [14], the longitudinally polarized LO cross section is given in [15]. The leading order polarized cross section contains two subprocesses: the gluon bremsstrahlung and the photon-gluon fusion, see Fig. 1. The partons fragment into hadrons via string fragmentation as implemented in JETSET[16]. For the polarized parton density functions there are two different sets [11, 17] implemented which both appertain to the unpolarized parton density functions given in set [10].

Event samples corresponding to 200 pb^{-1} are generated with a similar event selection as for the partonic analysis in Section 3.1. The beam polarizations were taken to be $P_e = P_p = 70\%$. The kinematic region $5 < Q^2 < 2500$ GeV^2, $0.3 < y < 0.8$ was selected (the cut in y corresponds roughly to $E(e') > 5$ GeV). Jets are searched for with the cone algorithm (radius 1) with $p_T > 5$ GeV in the pseudorapidity region $-2.8 < \eta < 2.8$, conform with for example the present H1 detector. The LO 2-jet cross section thus calculated with PEPSI is 1511 pb, 82% of which is contributed by the boson-gluon fusion process. These numbers compare well with those of MEPJET, given in section 2.

To increase statistics we further study jets with $p_T > 4$ GeV, and repeat the studies of section 3.1. This does not change the asymmetries significantly. In Figs. 4a,b the results for the asymmetry are shown as function of x_{Bj} and x_g for similar cuts as in Fig. 3, using the "gluon set A". For Fig. 4b the Q^2 range has been limited to 100 GeV^2. The calculations are shown at the parton level (dashed and dotted lines) and at the detector level (open and closed points). A calorimetric energy resolution of $\sigma_E/E = 0.5/\sqrt{E(\mathrm{GeV})}$ is used to simulate the detector response.

The first observation is that the asymmetries produced by PEPSI are very similar to the ones from MEPJET. Secondly the asymmetry at the detector level is well correlated with the asymmetry at the parton level. This means that present detectors at HERA are well prepared to make this measurement. It was verified that this conclusion still holds with a calorimetric energy resolution which is twice worse. Also a miscalibration of the energy scale of 2%, a number within reach at the time of this measurement, does not disturb the correlation significantly.

The average asymmetry $< A >$ amounts to -0.016 ± 0.002 at the parton level and -0.015 ± 0.002 at the detector level. For the selected kinematic region 40% of the events accepted on the parton level do not enter the detector event sample, and 15% of the final selected events have a parton kinematics outside of the measured region. When the region is restricted to $s_{ij} > 500$ GeV^2 these migrations are reduced to 25% and 12% respectively.

In Fig. 4c,d the results are shown for the asymmetry for a different set of polarized parton distributions: "gluon set C"[11]. These exhibit a smaller asymmetry around $x_g \sim 0.1$ than the "gluon set A", as can be seen from the parton level curves. This difference survives after the detector smearing, and thus measurements of this quantity can help to discriminate between different sets of parton distributions.

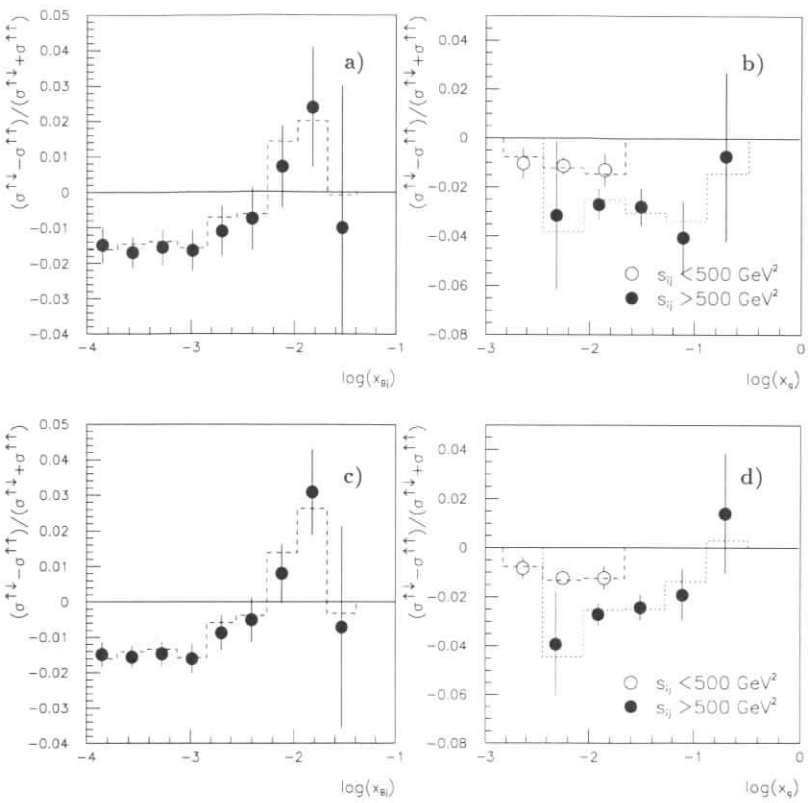

Figure 4: Expected asymmetries as a function of x_{Bj} (a,c) and x_g (b,d) for a luminosity of 200 pb^{-1} and beam polarizations $P_e = P_p = 70\%$. The figures (b,d) have an additional cut $Q^2 < 100$ GeV^2 on top of the nominal cuts, explained in the text. Figs. (a,b) are for the polarized parton set GS-A, Figs. (c,d) for GS-C [11].

3.3 Higher order effects

The studies above were based on a program that includes the LO matrix elements and fragmentation, but no higher order QCD effects. The effect of the latter, and the comparison with the effect of fragmentation, was studied in a dedicated analysis whereby the leading order MEPJET program used in section 2 and 3.1 was supplemented by two packages. The first one is the program PYTHIA57 [18] which simulates higher order effects in the framework or initial and final state parton showering and the second one is the program JETSET74 [16] for hadronization, as used in the PEPSI Monte Carlo.

Following a previous publication[7], the following cuts are used for the kinematic variables: $40 < Q^2 < 2500$ GeV^2, $1 < W^2 < 90000$ GeV^2, $0.001 < x_{Bj} < 1$, and $0.04 < y < 1$. We further impose for the outgoing lepton a cut on the minimal energy of 10 GeV and on the rapidity range $|y| < 3.5$.

Jets are generated via leading order matrix elements with the MEPJET program and then fed into PYHTIA as an external process, which adds initial and final state parton showering. Thus all QCD processes are included except for four-gluon vertices. A more detailed description of parton showering can be found in [19, 20]. For the showering scale, initial and final we used both times Q^2. We will investigate scale dependence in a forthcoming publication. The parton density functions set MRS D–' [21] was taken. For the final hadrons and partons we also choose the rapidity cut $|y| < 3.5$. The jet scheme for detecting hadron and parton jets is the cone scheme as described before with the maximal cone distance one. A sharp cut off of 5 GeV for the jet transverse momentum was taken.

In the showering process jets with small p_T can branch into jets with $p_T > 5$ GeV. The string fragmentation mechanism contributes in a similar way thus enhancing the magnitude of the total cross section within the imposed detector cuts.

Fig. 5 shows the unpolarized inclusive two-jets cross section for the sum of gluon and quark initiated events. The solid histogram shows the differential cross section versus the maximum of p_T for the analyzed two-jet events after parton showering and hadronization. It is in magnitude and shape comparable to the NLO order matrix element calculation by the MEPJET program, represented by the open triangles. A small shift in the direction of small $p_{T,\max}$ is observed, caused by the fragmentation process. The dashed histogram shows the cross section for parton showering without fragmentation. The absolute cross section is smaller than the NLO cross section, but the shapes agree well, without any significant shift. Hence we do not expect that the results calculated with PEPSI, as shown above, will be strongly affected by higher order processes. In comparison, the dotted histogram gives the leading order result from the MEPJET program.

The figure shows that the deviations are significant only for $p_{T,\max}$ smaller than 15 GeV, i.e for soft jets where also next to leading order effects are expected to be large. For larger $p_{T,\max}$ the calculations are in good agreement. The differences between the various curves can serve as a measure for the systematic errors. It has to be noted that the effects of showering and fragmentation are large if and only if the NLO effects are large, too. First studies with higher order effects included in PEPSI confirm that the the asymmetry survives in the presence of parton showers. With the present analysis the asymmetry however reduces to $< A >= 0.009 \pm 0.002$ (parton level) and the shape of the asymmetry distribution as function of x_g changes somewhat with x_g. Improved methods to determine x_g may restore the original distributions and are subject of a future study.

4 Concluding Remarks

The results show that if the assumed luminosity and beam polarizations can be delivered at HERA, the present detectors H1 and ZEUS will be in a comfortable position to measure a spin asymmetry of a few per cent in average, with a few per mile statistical precision, using two-jet events. The asymmetries survive at the hadron and detector level. In order to minimize the experimental systematic uncertainties, it is desirable to have in the HERA ring bunch

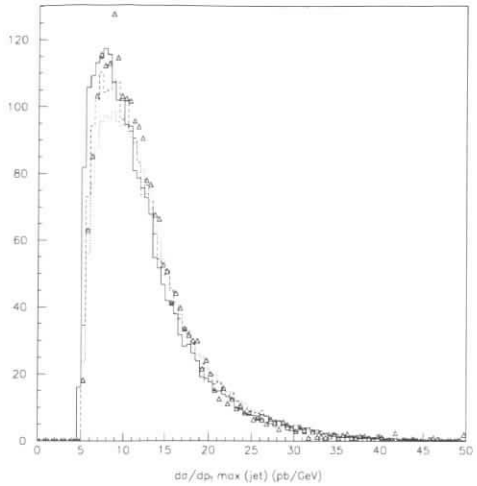

Figure 5: Simulation of higher order and fragmentation effects: triangles: NLO cross section, solid histogram: LO + parton shower + fragmentation, dashed histogram: LO + parton shower, dotted histogram: only LO matrix elements.

trains of protons with alternating helicity. On the theoretical side, NLO QCD corrections are needed. The NLO corrections reduce the renormalization μ_R and factorization scale μ_F dependence (due to the initial state collinear factorization) in the LO calculations and thus reliable predictions in terms of a well defined strong coupling constant and scale dependent parton distributions become possible. At the moment, these corrections are only available for unpolarized jet production [7, 22]. One expects for the asymmetry $< A >= \frac{\Delta\sigma^{had}(2\text{-jet})}{\sigma^{had}(2\text{-jet})}$ that the scale dependence in the individual cross sections partly cancels in the ratio. In fact, varying the renormalization and factorization scales between $\mu_R^2 = \mu_F^2 = 1/16\ (\sum_j k_T^B(j))^2$ and $\mu_R^2 = \mu_F^2 = 4\ (\sum_j k_T^B(j))^2$ in the LO cross sections introduces an uncertainty for the ratio A of less than 2 %, whereas the uncertainty in the individual cross sections is much larger.

In conclusion, the dijets events from polarized electron proton collisions at HERA can provide a good measurement of the gluon polarization distribution for $0.002 < x_g < 0.2$, the region where $x_g \Delta G(x_g)$ is expected to have a maximum.

References

[1] A. Magnon, Contribution to the Workshop DIS96, Rome, 1996.

[2] J.Feltesse, F.Kunne, E.Mirkes, hep-ph/9607336, to appear in Phys. Lett. B.

[3] H1 Collaboration, *Nucl. Phys.* B **449**, 183 (1995).

[4] J. Repond, Contribution to the DIS96 Workshop, Rome (1996).

[5] K. Rosenbauer, Contribution to the DIS96 Workshop, Rome (1996).

[6] W. Vogelsang, in Proceedings of the Workshop 'Physics at HERA', Eds. W. Buchmüller, G. Ingelman, DESY Hamburg (1992), Vol 1, p. 389.

[7] E. Mirkes and D. Zeppenfeld, hep-ph/9511448, Phys. Lett. B **380** (1996) 205; see also these proceedings.

[8] C. Ziegler and E. Mirkes, *Nucl. Phys.* B **429** (1994) 93.

[9] E. Mirkes and D. Zeppenfeld, hep-ph/9606332, in Proceedings of the "QCD and QED in Higher Orders" 1996 Zeuthen Workshop on Elementary Particle Theory, April 22-26, 1996.

[10] M. Glück, E. Reya and A. Vogt, *Z. Phys.* C **67** (1995) 443.

[11] T. Gehrmann and J. Stirling, hep-ph/9512406, *Phys. Rev.* D **53** (1996) 6100.

[12] T. Gehrmann and J. Stirling, private communication.

[13] G. Ingelman, Uppsala internal report TSL/ISV-92-0065 and Proceedings of the Workshop 'Physics at HERA', Eds. W. Buchmüller, G. Ingelman, DESY Hamburg (1992), Vol 3, p. 1366 and references therein.

[14] R. D. Peccei, and R. Rückl, *Nucl. Phys.* B **162** (1980) 125.

[15] L. Mankiewicz, A. Schäfer and M. Veltri, *Comp. Phys. Comm.* **71** (1992) 305.

[16] T. Sjöstrand, *Comp. Phys. Comm.* **39** (1986) 347;
T. Sjöstrand and M. Bengtsson, *Comp. Phys. Comm.* **43** (1987) 367;
see also T. Sjöstrand, CERN-TH 6488/92.

[17] M. Glück, E. Reya, M. Stratmann, W. Vogelsang, *Phys. Rev.* D **53** (1996) 4775.

[18] H. -U. Bengtsson and T. Sjöstrand, *Comp. Phys. Comm.* **46** (1987) 43: see also T. Sjöstrand, CERN-TH 6488/92.

[19] M. Bengtsson, T. Sjöstrand *Z. Phys.* C **37** (1988) 465.

[20] T. Sjöstrand, *Phys. Lett.* B **157** (1985) 321.

[21] A. D. Martin, R. G. Roberts, W. J. Stirling, *Phys. Lett.* B **306** (1993) 145.

[22] E. Mirkes and D. Zeppenfeld, contribution to the Workshop DIS96, Rome, 1996.

Photoproduction of Jets and Heavy Flavors in Polarized ep - Collisions at HERA

M. Stratmann[a], W. Vogelsang[b]

[a] Universität Dortmund, Institut für Physik, D-44221 Dortmund, Germany
[b] Rutherford Appleton Laboratory, Chilton, Didcot, Oxon OX11 0QX, England

Abstract: We study photoproduction of jets and heavy flavors in a polarized ep collider mode of HERA at $\sqrt{s} = 298$ GeV. We examine the sensitivity of the cross sections and their asymmetries to the proton's polarized gluon distribution and to the completely unknown parton distributions of longitudinally polarized photons.

1 Introduction

HERA has already been very successful in pinning down the proton's unpolarized gluon distribution $g(x, Q^2)$. Several processes have been studied which have contributions from $g(x, Q^2)$ already in the lowest order, such as (di)jet and heavy flavor production. Since events at HERA are concentrated in the region $Q^2 \to 0$, the processes have first and most accurately been studied in photoproduction [1-6]. As is well-known, in this case the (quasi-real) photon will not only interact in a direct ('point-like') way, but can also be resolved into its hadronic structure. HERA photoproduction experiments like [1-4] have not merely established evidence for the existence of such a resolved contribution, but have also been precise enough to improve our knowledge about the parton distributions, f^γ, of the photon.

Given the success of such unpolarized photoproduction experiments at HERA, it seems most promising [7] to closely examine the same processes for the situation with longitudinally polarized beams with regard to their sensitivity to the proton's polarized gluon distribution Δg, which is still one of the most interesting, but least known, quantities in 'spin-physics'. Recent next-to-leading (NLO) studies of polarized DIS [8, 9] show that the x-shape of Δg seems to be hardly constrained at all by the present DIS data [10], even though a tendency towards a sizeable positive *total* gluon polarization, $\int_0^1 \Delta g(x, Q^2 = 4\ \mathrm{GeV}^2)dx \gtrsim 1$, was found [8, 11, 9]. Furthermore, polarized photoproduction experiments may in principle allow to not only determine the parton, in particular gluon, content of the polarized *proton*, but also that of the longitudinally polarized *photon* which is completely unknown so far. Since, e.g., a measurement of the photon's spin-dependent structure function g_1^γ in polarized e^+e^- collisions is not planned in the near future, HERA could play a unique role here, even if it should only succeed in establishing the very *existence* of a resolved contribution to polarized photon-proton reactions.

Our contribution is organized as follows: In section 2 we collect the necessary ingredients for our calculations. Section 3 is devoted to open-charm photoproduction. In section 4 we examine polarized photoproduction of (di)jets. Section 5 contains the conclusions.

2 Polarized Parton Distributions of the Proton and the Photon

Even though NLO analyses of polarized DIS which take into account all or most data sets [10] have been published recently [8, 11, 9], we have to stick to LO calculations throughout this work since the NLO corrections to polarized charm or jet production are not yet known. This implies use of LO parton distributions, which have also been provided in the studies [8, 9]. Both papers give various LO sets which mainly differ in the x-shape of the polarized gluon distribution. We will choose the LO 'valence' set of the 'radiative parton model analysis' [8], which corresponds to the best-fit result of that paper, along with two other sets of [8] which are based on either assuming $\Delta g(x, \mu^2) = g(x, \mu^2)$ or $\Delta g(x, \mu^2) = 0$ at the low input scale μ of [8], where $g(x, \mu^2)$ is the unpolarized LO GRV [12] input gluon distribution. These two sets will be called '$\Delta g = g$ input' and '$\Delta g = 0$ input' scenarios, respectively. The gluon of set C of [9] is qualitatively different since it has a substantial negative polarization at large x. We will therefore also use this set in our calculations. For illustration, we show in Fig. 1 the gluon distributions of the four different sets of parton distributions we will use, taking a typical scale $Q^2 = 10\ \mathrm{GeV}^2$. Keeping in mind that all four LO sets provide very good descriptions of all present polarized DIS data [10], it becomes obvious that the data indeed do not seem to be able to significantly constrain the x-shape of $\Delta g(x, Q^2)$.

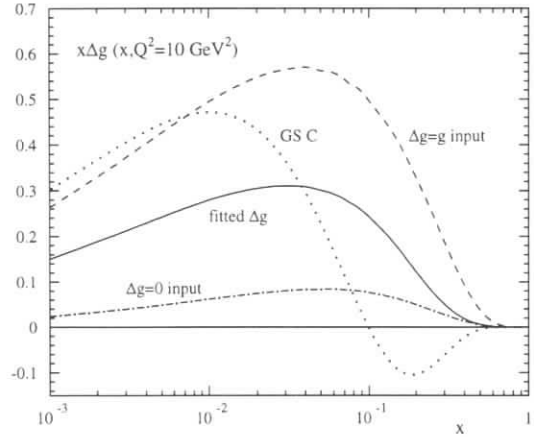

Figure 1: *Gluon distributions at $Q^2 = 10\ GeV^2$ of the four LO sets of polarized parton distributions used in this paper. The dotted line refers to set C of [9], whereas the other distributions are taken from [8] as described in the text.*

In the case of photoproduction the electron just serves as a source of quasi-real photons which are radiated according to the Weizsäcker-Williams spectrum [13]. The photons can then interact either directly or via their partonic structure ('resolved' contribution). In the case of longitudinally polarized electrons, the resulting photon will be longitudinally (more precisely, circularly) polarized and, in the resolved case, the *polarized* parton distributions of the photon, $\Delta f^\gamma(x, Q^2)$, enter the calculations. Thus one can define the effective polarized parton densities

at the scale M in the longitudinally polarized electron via[1]

$$\Delta f^e(x_e, M^2) = \int_{x_e}^1 \frac{dy}{y} \Delta P_{\gamma/e}(y) \Delta f^\gamma(x_\gamma = \frac{x_e}{y}, M^2) \tag{1}$$

($f = q, g$) where $\Delta P_{\gamma/e}$ is the polarized Weizsäcker-Williams spectrum for which we will use

$$\Delta P_{\gamma/e}(y) = \frac{\alpha_{em}}{2\pi} \left[\frac{1-(1-y)^2}{y} \right] \ln \frac{Q^2_{max}(1-y)}{m_e^2 y^2} , \tag{2}$$

with the electron mass m_e. For the time being, it seems most sensible to follow as closely as possible the analyses successfully performed in the unpolarized case, which implies to introduce the same kinematical cuts. As in [2, 4, 5, 14] we will use an upper cut[2] $Q^2_{max} = 4$ GeV^2, and the y-cuts $0.2 \leq y \leq 0.85$ (for charm and single-jet [2] production) and $0.2 \leq y \leq 0.8$ (for dijet production, [4]) will be imposed. We note that a larger value for the lower limit, y_{min}, of the allowed y-interval would enhance the yield of polarized photons relative to that of unpolarized ones since $\Delta P_{\gamma/e}(y)/P_{\gamma/e}(y)$, where $P_{\gamma/e}$ is the unpolarized Weizsäcker-Williams spectrum obtained by using $[(1+(1-y)^2)/y]$ instead of the square bracket in (2), is suppressed for small y. On the other hand, increasing y_{min} would be at the expense of reducing the individual polarized and unpolarized rates.

The polarized photon structure functions $\Delta f^\gamma(x_\gamma, M^2)$ in (1) are completely unmeasured so far, such that models for them have to be invoked. To obtain a realistic estimate for the theoretical uncertainties in the polarized photonic parton densities two very different scenarios were considered in [15, 16] assuming 'maximal' ($\Delta f^\gamma(x,\mu^2) = f^\gamma(x,\mu^2)$) or 'minimal' ($\Delta f^\gamma(x,\mu^2) = 0$) saturation of the fundamental positivity constraints $|\Delta f^\gamma(x,\mu^2)| \leq f^\gamma(x,\mu^2)$ at the input scale μ for the QCD evolution. Here μ and the unpolarized photon structure functions $f^\gamma(x,\mu^2)$ were adopted from the phenomenologically successful radiative parton model predictions in [17]. The results of these two extreme approaches are presented in Fig. 2 in terms of the photonic parton asymmetries $A_f^\gamma \equiv \Delta f^\gamma / f^\gamma$, evolved to $Q^2 = 30$ GeV^2 in LO. An ideal aim of measurements in a polarized collider mode of HERA would of course be to determine the Δf^γ and to see which ansatz is more realistic. The sets presented in Fig. 2, which we will use in what follows, should in any case be sufficient to study the sensitivity of the various cross sections to the Δf^γ, but also to see in how far they influence a determination of Δg.

We finally note that in what follows a polarized cross section will always be defined as

$$\Delta\sigma \equiv \frac{1}{2}\left(\sigma(++) - \sigma(+-)\right) , \tag{3}$$

the signs denoting the helicities of the scattering particles. The corresponding unpolarized cross section is given by taking the sum instead, and the cross section asymmetry is $A \equiv \Delta\sigma/\sigma$. Whenever calculating an asymmetry A, we will use the LO GRV parton distributions for the proton [12] and the photon [17] to calculate the unpolarized cross section. For consistency, we will employ the LO expression for the strong coupling α_s with [8, 9, 15, 16] $\Lambda^{(f=4)}_{QCD} = 200$ MeV for four active flavors.

[1] We include here the additional definition $\Delta f^\gamma(x_\gamma, M^2) \equiv \delta(1-x_\gamma)$ for the direct ('unresolved') case.

[2] In H1 analyses of HERA photoproduction data [1, 3, 6] the cut $Q^2_{max} = 0.01$ GeV^2 is used along with slightly different y-cuts as compared to the corresponding ZEUS measurements [2, 4, 5], which leads to smaller rates.

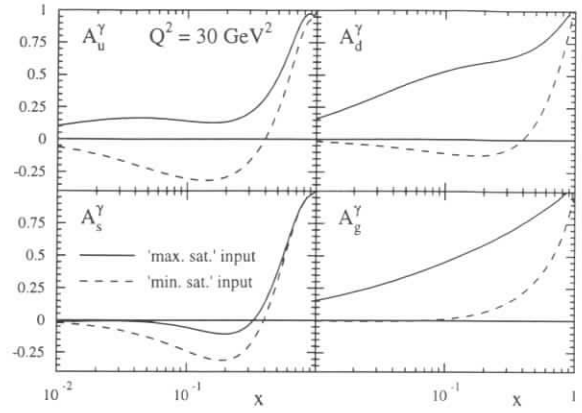

Figure 2: *Photonic LO parton asymmetries $A_f^\gamma \equiv \Delta f^\gamma / f^\gamma$ at $Q^2 = 30\,GeV^2$ for the two scenarios considered in [15, 16] (see text). The unpolarized LO photonic parton distributions were taken from [17].*

3 Charm Photoproduction at HERA

For illustration, we first briefly consider the total cross section. In the unpolarized case it has been possible to extract the total cross section for $\gamma p \to c\bar{c}$ from the fixed target [18] and HERA [5, 6] lepton-nucleon data, i.e., the open-charm cross section for a fixed photon energy without the smearing from the Weizsäcker-Williams spectrum. To LO, the corresponding polarized cross section is given by

$$\Delta\sigma^c(S_{\gamma p}) = \sum_{f^\gamma, f^p} \int_{4m_c^2/S_{\gamma p}}^1 dx_\gamma \int_{4m_c^2/x_\gamma S_{\gamma p}}^1 dx_p \Delta f^\gamma(x_\gamma, M^2) \Delta f^p(x_p, M^2) \Delta\hat{\sigma}^c(\hat{s}, M^2) . \tag{4}$$

where M is some mass scale and $\hat{s} \equiv x_\gamma x_p S_{\gamma p}$. The Δf^p stand for the polarized parton distributions of the proton. In the direct case, the contributing subprocess is photon-gluon fusion (PGF), $\gamma g \to c\bar{c}$, whose spin-dependent total LO subprocess cross section $\Delta\hat{\sigma}^c(\hat{s})$ can be found in [19, 20]. In the resolved case, the processes $gg \to c\bar{c}$ and $q\bar{q} \to c\bar{c}$ contribute; their cross sections have been calculated in [21]. Needless to say that we can obtain the corresponding unpolarized LO charm cross section $\sigma^c(S_{\gamma p})$ by using LO unpolarized parton distributions and subprocess cross sections (as calculated in [22]) in (4).

Tab. 1 shows our results [7] for the polarized cross sections and the asymmetries $\Delta\sigma^c/\sigma^c$ for the four different sets of polarized parton distributions, where we have used the scale $M = 2m_c$ with the charm mass $m_c = 1.5$ GeV. The resolved contribution to the cross section is rather small in the unpolarized case. For the polarized case, we have calculated it using the 'maximally' saturated set for the polarized photon structure functions, which should roughly provide the maximally possible background from resolved photons. The corresponding results are shown individually in Tab. 1. The resolved contribution turns out to be non-negligible only for large $\sqrt{S_{\gamma p}}$, where it can be as large as about 1/3 the direct contribution but with opposite sign. As becomes obvious from Tab. 1 (see also [23] and Fig. 4 of [7]), the asymmetry becomes very small towards the HERA region at larger $\sqrt{S_{\gamma p}} \sim 200$ GeV. One reason for this is the oscillation of

the polarized subprocess cross section for the direct part, combined with cancellations between the direct and the resolved parts. More importantly, as seen from (4), the larger $S_{\gamma p}$ becomes, the smaller are the $x_{p,\gamma}$ - values probed, such that the rapid rise of the unpolarized parton distributions strongly suppresses the asymmetry. The smallness of the asymmetries and the possibly significant influence of the resolved contribution on them will make their measurement and a distinction between the different Δg elusive[3]. The measurement of the *total* charm cross section asymmetry in $\gamma p \to c\bar{c}$ seems rather more feasible at smaller energies, $\sqrt{S_{\gamma p}} \lesssim 20$ GeV, i.e., in the region accessible by the future COMPASS experiment [24] where also the unknown resolved contribution to the cross section is negligible.

	fitted Δg			$\Delta g = g$ input			$\Delta g = 0$ input			GS C		
$\sqrt{S_{\gamma p}}$ [GeV]	dir. [nb]	res. [nb]	A [%]	dir. [nb]	res. [nb]	A [%]	dir. [nb]	res. [nb]	A [%]	dir. [nb]	res. [nb]	A [%]
20	13.9	-0.29	2.6	23.2	0.33	4.5	3.26	-0.56	0.52	19.6	-0.70	3.6
50	2.07	1.30	0.18	1.15	2.94	0.21	-0.53	0.18	-0.019	17.4	0.61	0.94
200	-7.00	2.06	-0.06	-12.8	3.60	-0.11	-1.96	0.44	-0.018	-8.79	3.23	-0.067

Table 1: *Total cross sections and asymmetries A for charm photoproduction in polarized γp collisions.*

From our observations for HERA-energies it follows that it could be more promising to study distributions of the cross section in the transverse momentum or the rapidity of the charm quark in order to cut out the contributions from very small $x_{p,\gamma}$. We will now include the Weizsäcker-Williams spectrum since tagging of the electron, needed for the extraction of the cross section at fixed photon energy, will probably reduce the cross section too strongly. The polarized LO cross section for producing a charm quark with transverse momentum p_T and cms-rapidity η then reads

$$\frac{d^2\Delta\sigma^c}{dp_T d\eta} = 2p_T \sum_{f^e,f^p} \int_{\frac{\rho e^{-\eta}}{1-\rho e^{\eta}}}^{1} dx_e x_e \Delta f^e(x_e, M^2) x_p \Delta f^p(x_p, M^2) \frac{1}{x_e - \rho e^{-\eta}} \frac{d\Delta\hat{\sigma}}{d\hat{t}} , \qquad (5)$$

where $\rho \equiv m_T/\sqrt{S}$ with $m_T \equiv \sqrt{p_T^2 + m_c^2}$, and $x_p \equiv x_e \rho e^{\eta}/(x_e - \rho e^{-\eta})$. The cross section can be transformed to the more relevant HERA laboratory frame by a simple boost which implies $\eta \equiv \eta_{cms} = \eta_{LAB} - \frac{1}{2}\ln(E_p/E_e)$, where we have, as usual, counted positive rapidity in the proton forward direction. The spin-dependent differential LO subprocess cross sections $d\Delta\hat{\sigma}/d\hat{t}$ for the resolved processes $gg \to c\bar{c}$ and $q\bar{q} \to c\bar{c}$ with $m_c \neq 0$ can again be found in [21]. For the factorization/renormalization scale in (5) we choose $M = m_T/2$; we will comment on the scale dependence of the results at the end of this section.

Fig. 3 shows our results [7] obtained for the four different sets of polarized parton distributions for $E_p = 820$ GeV and $E_e = 27$ GeV. Fig. 3a displays the p_T-dependence of the cross section, where we have integrated over $-1 \leq \eta_{LAB} \leq 2$. The resolved contribution to the cross section has been included, calculated with the 'maximally' saturated set of polarized photon structure functions. It is shown individually for the 'fitted Δg'-set of polarized proton distributions by the lower solid line in Fig. 3a. Comparison of the two solid lines in Fig. 3a shows that

[3] As was shown in [23], the situation at HERA energies somewhat improves if cuts on the produced charm quark's transverse momentum and rapidity are imposed. However, the polarized resolved contribution to the asymmetry was neglected in [23].

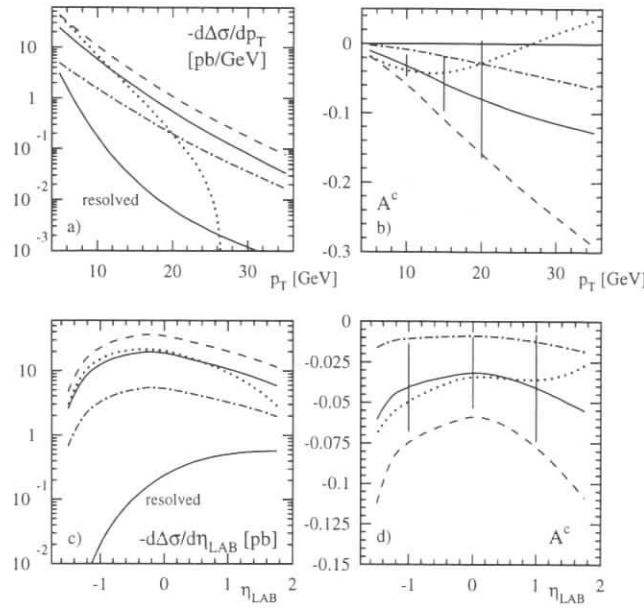

Figure 3: **a:** *p_T-dependence of the (negative) polarized charm-photoproduction cross section in ep-collisions at HERA, calculated according to (5) (using $M = m_T/2$ and $m_c = 1.5$ GeV) and integrated over $-1 \leq \eta_{LAB} \leq 2$. The line drawings are as in Fig. 1. For comparison the resolved contribution to the cross section, calculated with the 'fitted Δg' gluon distribution of [8] and the 'maximally' saturated set of polarized photonic parton distributions is shown by the lower solid line.* **b:** *Asymmetry corresponding to* **a**. *The expected statistical errors indicated by the bars have been calculated according to (6) and as explained in the text.* **c,d:** *Same as* **a,b**, *but for the η_{LAB}-dependence, integrated over $p_T > 8$ GeV.*

the resolved contribution is negligibly small in this case unless p_T becomes very small. Fig. 3b shows the asymmetries corresponding to Fig. 3a. It becomes obvious that they are much larger than for the total cross section if one goes to p_T of about 10-20 GeV, which is in agreement with the corresponding findings of [23]. Furthermore, one sees that the asymmetries are strongly sensitive to the size *and* shape of the polarized gluon distribution used. Similar statements are true for the η_{LAB}-distributions shown in Figs. 3c,d, where p_T has been integrated over $p_T > 8$ GeV in order to increase the number of events. Even here the resolved contribution remains small, although it becomes more important towards large positive values of η_{LAB}. We have included in the asymmetry plots in Figs. 3b,d the expected statistical errors δA at HERA which can be estimated from

$$\delta A = \frac{1}{P_e P_p \sqrt{\mathcal{L}\sigma\epsilon}} , \qquad (6)$$

where P_e, P_p are the beam polarizations, $\mathcal{L}$ is the integrated luminosity and ϵ the charm detection efficiency, for which we assume $P_e * P_p = 0.5$, $\mathcal{L} = 100/\text{pb}$ and $\epsilon = 0.15$. The error bars in Fig. 3b,d have been obtained by integrating the unpolarized LO cross sections $d\sigma/dp_T$

or $d\sigma/d\eta_{LAB}$ over bins of $\Delta p_T = 5$ GeV or $\Delta\eta_{LAB} = 1$, respectively, and have been plotted at the centers of the bins. It becomes obvious that it will be quite difficult to distinguish between different gluon distributions in our proposed charm experiments. The situation would, however, become much better for a higher luminosity of, say, $\mathcal{L} = 1000/\text{pb}$ in which case the error bars would decrease by a factor 3.

We now briefly address the theoretical uncertainties of our results in Fig. 3 related to the dependence of the cross sections and asymmetries on the renormalization/factorization scale M. Since all our calculations could be performed in LO only, this is a particularly important issue. When using the scale $M = m_T$ it turns out that the cross sections in Fig. 3a are subject to changes of about 10% at $p_T < 15$ GeV, and of as much as $20 - 25\%$ at larger p_T. Changes of in most cases below 10% are found for the η_{LAB}-curves in Fig. 3c. In contrast to this (not unexpected) fairly strong scale dependence of the polarized cross sections, the *asymmetries*, which will be the quantities actually measured, are very insensitive to scale changes, deviating usually by not more than a few percent from the values shown in Fig. 3b,d for all relevant p_T and η_{LAB}. This finding seems important in two respects: Firstly, it warrants the genuine sensitivity of the asymmetry to Δg, implying that despite the sizeable scale dependence of the cross section it still seems a reasonable and safe procedure to compare LO theoretical predictions for the asymmetry with future data and to extract Δg from such a comparison. Secondly, it sheds light on the possible role of NLO corrections to our results, suggesting that such corrections might be sizeable for the cross sections, but less important for the asymmetry.

4 Photoproduction of Jets

The generic cross section formula for the production of a single jet with transverse momentum p_T and rapidity η is similar to that in (5), the sum now running over all properly symmetrized $2 \to 2$ subprocesses for the direct ($\gamma b \to cd$) and resolved ($ab \to cd$) cases. When only light flavors are involved, the corresponding differential helicity-dependent LO subprocess cross sections can be found in [25]. In all following predictions we will deal with the charm contribution to the cross section by including charm only as a *final* state particle produced via the subprocesses $\gamma g \to c\bar{c}$ (for the direct part) and $gg \to c\bar{c}$, $q\bar{q} \to c\bar{c}$ (for the resolved part). For the values of p_T considered it turns out that the finite charm mass can be safely neglected. In all following applications we will use the renormalization/factorization scale $M = p_T$. We have again found that the scale dependence of the asymmetries is rather weak as compared to that of the cross sections.

It appears very promising [7] to study the η_{LAB}-distribution of the cross section and the asymmetry. The reason for this is that for negative η_{LAB} the main contributions are expected to come from the region $x_\gamma \to 1$ and thus mostly from the direct piece at $x_\gamma = 1$. To investigate this, Fig. 4 shows our results for the single-inclusive jet cross section and its asymmetry vs. η_{LAB} and integrated over $p_T > 8$ GeV for the four sets of the polarized proton's parton distributions. For Figs. 4a,b we have used the 'maximally' saturated set of polarized photonic parton densities, whereas Figs. 4c,d correspond to the 'minimally' saturated one. Comparison of Figs. 4a,c or 4b,d shows that indeed the direct contribution clearly dominates for $\eta_{LAB} \leq -0.5$, where also differences between the polarized gluon distributions of the proton show up clearly. Furthermore, the cross sections are generally large in this region with asymmetries of a few percents. At positive η_{LAB}, we find that the cross section is dominated by the resolved contribution

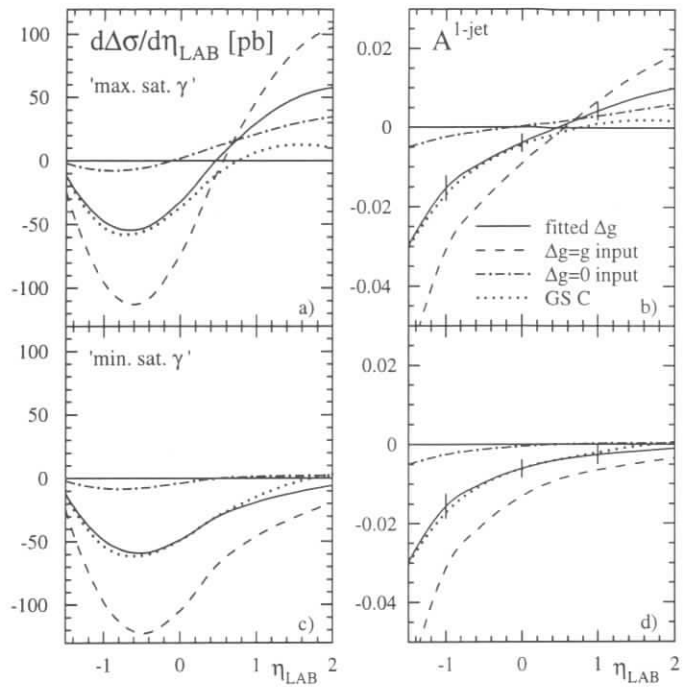

Figure 4: **a:** *η_{LAB}-dependence of the polarized single-jet inclusive photoproduction cross section in ep-collisions at HERA, integrated over $p_T > 6$ GeV. The renormalization/factorization scale was chosen to be $M = p_T$. The resolved contribution to the cross section has been calculated with the 'maximally' saturated set of polarized photonic parton distributions.* **b:** *Asymmetry corresponding to* **a**. *The expected statistical errors have been calculated according to (6) and as described in the text.* **c,d:** *Same as* **a,b**, *but for the 'minimally' saturated set of polarized photonic parton distributions.*

and is therefore sensitive to both the parton content of the polarized proton *and* the photon. This means that one can only learn something about the polarized photon structure functions if the polarized parton distributions of the proton are already known to some accuracy or if an experimental distinction between resolved and direct contributions can be achieved. We note that the dominant contributions to the resolved part at large η_{LAB} are driven by the polarized photonic *gluon* distribution Δg^γ. Again we include in Figs. 4b,d the expected statistical errors which we have estimated according to (6) with $P_e * P_p = 0.5$, $\mathcal{L} = 100/\text{pb}$, $\epsilon = 1$ for bins of $\Delta\eta_{LAB} = 1$. From the results it appears that a measurement of the proton's Δg should be possible from single-jet events at negative rapidities where the contamination from the resolved contribution is minimal.

In the unpolarized case, an experimental criterion for a distinction between direct and resolved contributions has been introduced [26] and used [4] in the case of dijet photoproduction

at HERA. We will now adopt this criterion for the polarized case to see whether it would enable a further access to Δg and/or the polarized photon structure functions. The generic expression for the polarized cross section for the photoproduction of two jets with laboratory system rapidities η_1, η_2 is to LO

$$\frac{d^3\Delta\sigma}{dp_T d\eta_1 d\eta_2} = 2p_T \sum_{f^e, f^p} x_e \Delta f^e(x_e, M^2) x_p \Delta f^p(x_p, M^2) \frac{d\Delta\hat{\sigma}}{d\hat{t}} \ , \tag{7}$$

where p_T is the transverse momentum of one of the two jets (which balance each other in LO) and

$$x_e \equiv \frac{p_T}{2E_e}\left(e^{-\eta_1} + e^{-\eta_2}\right) \ , \ x_p \equiv \frac{p_T}{2E_p}\left(e^{\eta_1} + e^{\eta_2}\right) \ . \tag{8}$$

Following [4], we will integrate over the cross section to obtain $d\Delta\sigma/d\bar{\eta}$, where $\bar{\eta} \equiv (\eta_1 + \eta_2)/2$. Furthermore, we will apply the cuts [4] $|\Delta\eta| \equiv |\eta_1 - \eta_2| \leq 0.5$, $p_T > 6$ GeV. The important point is that measurement of the jet rapidities allows for fully reconstructing the kinematics of the underlying hard subprocess and thus for determining the variable [4]

$$x_\gamma^{OBS} = \frac{\sum_{jets} p_T^{jet} e^{-\eta^{jet}}}{2yE_e} \ , \tag{9}$$

which in LO equals $x_\gamma = x_e/y$ with y as before being the fraction of the electron's energy taken by the photon. Thus it becomes possible to experimentally select events at large x_γ, $x_\gamma > 0.75$ [26, 4], hereby extracting the *direct* contribution to the cross section with just a rather small contamination from resolved processes. Conversely, the events with $x_\gamma \leq 0.75$ will represent the resolved part of the cross section. This procedure should therefore be ideal to extract Δg on the one hand, and examine the polarized photon structure functions on the other.

Fig. 5 shows the results [7] for the direct part of the cross section according to the above selection criteria. The contributions from the resolved subprocesses have been included, using the 'maximally' saturated set of polarized photonic parton densities. They turn out to be non-negligible but, as expected, subdominant. More importantly, due to the constraint $x_\gamma > 0.75$ they are determined by the polarized quark, in particular the u-quark, distributions in the photon, which at large x_γ are equal to their unpolarized counterparts as a result of the Q^2-evolution (see Fig. 2), rather *independent* of the hadronic input chosen. Thus the uncertainty coming from the polarized photon structure is minimal here and under control. As becomes obvious from Fig. 5, the cross sections are fairly large over the whole range of $\bar{\eta}$ displayed and very sensitive to the shape *and* the size of Δg with, unfortunately, not too sizeable asymmetries as compared to the statistical errors for $\mathcal{L} = 100/\text{pb}$. A measurement of Δg thus appears to be possible under the imposed conditions only if luminosities clearly exceeding 100/pb can be reached. Fig. 6 displays the same results, but now for the resolved contribution with $x_\gamma \leq 0.75$ for the 'maximally' saturated set (Figs. 6a,b) and the 'minimally' saturated one (Figs. 6c,d). As expected, the results depend on both the parton content of the polarized photon and the proton, which implies that the latter has to be known to some accuracy to extract some information on the polarized photon structure. It turns out that again mostly the polarized *gluon* distribution of the photon would be probed in this case, in particular at $\bar{\eta} > 0.75$. Contributions from the Δq^γ are more affected by the x_γ-cut; still they amount to about 50% of the cross section at $\bar{\eta} = 0$. We finally emphasize that the experimental finding of a non-vanishing asymmetry here would establish at least the definite existence of a resolved contribution to the polarized cross section.

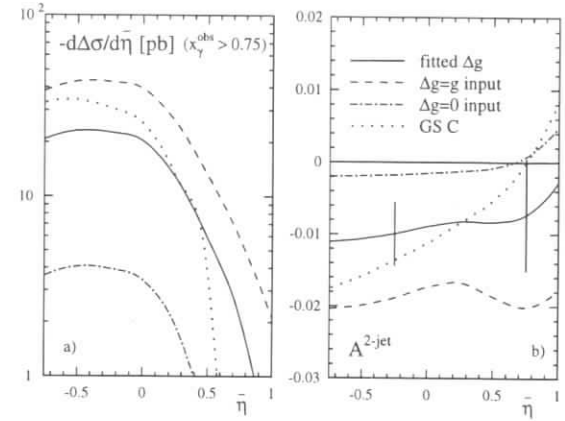

Figure 5: **a:** *$\bar{\eta}$-dependence of the 'direct' part of the polarized two-jet photoproduction cross section in ep-collisions at HERA for the four different sets of polarized parton distributions of the proton. The experimental criterion $x_\gamma^{OBS} > 0.75$ has been applied to define the 'direct' contribution (see text). The resolved contribution with $x_\gamma^{OBS} > 0.75$ has been included using the 'maximally' saturated set of polarized photonic parton distributions.* **b:** *Asymmetry corresponding to* **a**. *The expected statistical errors indicated by the bars have been calculated according to (6) and as explained in the text.*

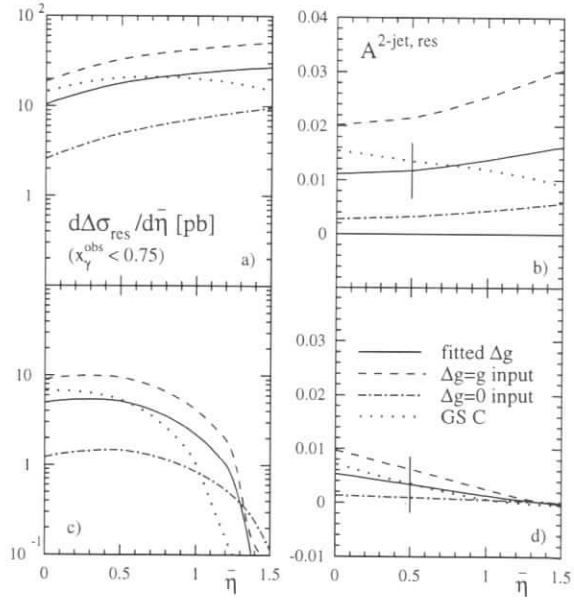

Figure 6: *Same as Fig. 5, but for the resolved part of the cross section, defined by $x_\gamma^{OBS} \leq 0.75$ (see text). For* **a,b:** *the 'maximally' saturated set of polarized photonic parton distributions has been used and for* **c,d** *the 'minimally' saturated one.*

5 Summary and Conclusions

We have analyzed various photoproduction experiments in the context of a polarized ep-collider mode of HERA. All of these have already been successfully performed in the unpolarized case at HERA. All processes we have considered have in common that they get contributions from incoming gluons already in the lowest order and thus look promising tools to measure the polarized gluon distribution of the proton. In addition, they derive their importance from their sensitivity not only to Δg, but also to the completely unknown parton content of the polarized photon entering via the resolved contributions to the polarized cross sections. As far as a 'clear' determination of Δg is concerned, this resolved piece, if non-negligible, might potentially act as an obstructing background, and it is therefore crucial to assess its possible size which we have done by employing two very different sets for the polarized photonic parton distributions. Conversely, and keeping in mind that HERA has been able to provide much new information on the unpolarized hadronic structure of the photon, it is also conceivable that photoproduction experiments at a polarized version of HERA could be *the* place to actually look for effects of the polarized photon structure and to prove the existence of resolved contributions to the polarized cross sections and asymmetries.

In the case of open-charm photoproduction we found that the resolved contribution is generally negligible except for the *total* charm cross section at HERA energies. Furthermore, the cross sections and their asymmetries are very sensitive to shape and size of Δg. We found, however, that very high luminosities, $\mathcal{L} = 1000/\text{pb}$, would be needed to measure the asymmetries with sufficient accuracy to decide between the various possible scenarios for Δg. Concerning photoproduction of jets, we find a generally much larger size of the resolved contribution. It turns out that the rapidity-distribution of the single-inclusive jet cross section separates out the direct part of the cross section at negative rapidities. In this region again a strong dependence on Δg is found with larger cross sections than for the case of charm production. The corresponding asymmetries clearly appear to be measurable here even for $\mathcal{L} = 100/\text{pb}$. At larger rapidities the cross section becomes sensitive to both the parton content of the polarized proton *and* photon, and an extraction of either of them does not seem straightforward. The situation improves when considering dijet production and adopting an analysis successfully performed in the unpolarized case [26, 4] which is based on reconstructing the kinematics of the underlying subprocess and thus effectively separating direct from resolved contributions. We find that in this case the (experimentally defined) direct contribution should provide access to Δg whereas the resolved part, if giving rise to a non-vanishing asymmetry, would establish existence of a polarized parton content of the photon. Again the corresponding measurements would require high luminosities since the involved asymmetries are rather small. The measurements we have proposed seem a very interesting challenge for a future polarized ep mode of HERA.

Acknowledgements

We are thankful to the members of the working group, in particular to J. Feltesse and M. Glück, for helpful discussions. The work of M.S. has been supported in part by the 'Bundesministerium für Bildung, Wissenschaft, Forschung und Technologie', Bonn.

References

[1] I. Abt et al., H1 collab., Phys. Lett. **B314**, 436 (1993).

[2] M. Derrick et al., ZEUS collab., Phys. Lett. **B342**, 417 (1995).

[3] T. Ahmed et al., H1 collab., Nucl. Phys. **B445**, 195 (1995).

[4] M. Derrick et al., ZEUS collab., Phys. Lett. **B348**, 665 (1995).

[5] M. Derrick et al., ZEUS collab, Phys. Lett. **B349**, 225 (1995).

[6] S. Aid et al., H1 collab., DESY 96-055.

[7] M. Stratmann and W. Vogelsang, Univ. Dortmund report DO-TH 96/10 and Rutherford report RAL-TR-96-033, to appear in Z. Phys. **C**.

[8] M. Glück, E. Reya, M. Stratmann and W. Vogelsang, Phys. Rev. **D53**, 4775 (1996).

[9] T. Gehrmann and W.J. Stirling, Phys. Rev. **D53**, 6100 (1996).

[10] A recent overview on the experimental status can be found, e.g., in R. Voss, in proceedings of the workshop on 'Deep Inelastic Scattering and QCD (DIS '95)', Paris, 1995, eds. J.F. Laporte and Y. Sirois.

[11] R.D. Ball, S. Forte, and G. Ridolfi, Phys. Lett. **B378**, 255 (1996).

[12] M. Glück, E. Reya, and A. Vogt, Z. Phys. **C67**, 433 (1995).

[13] C.F. von Weizsäcker, Z. Phys. **88**, 612 (1934);
E.J. Williams, Phys. Rev. **45**, 729 (1934).

[14] M. Klasen, G. Kramer and S.G. Salesch, Z. Phys. **C68**, 113 (1995);
M. Klasen and G. Kramer, Phys. Lett. **B366**, 385 (1996) and DESY 95-226.

[15] M. Glück and W. Vogelsang, Z. Phys. **C55**, 353 (1992), Z. Phys. **C57**, 309 (1993).

[16] M. Glück, M. Stratmann and W. Vogelsang, Phys. Lett. **B337**, 373 (1994).

[17] M. Glück, E. Reya, and A. Vogt, Phys. Rev. **D46**, 1973 (1992).

[18] see M. Arneodo et al., EMC, Z. Phys. **C35**, 1 (1987), and references therein.

[19] M. Glück and E. Reya, Z. Phys. **C39**, 569 (1988).

[20] M. Glück, E. Reya and W. Vogelsang, Nucl. Phys. **B351**, 579 (1991).

[21] A.P. Contogouris, S. Papadopoulos and B. Kamal, Phys. Lett. **246**, 523 (1990);
M. Karliner and R.W. Robinett, Phys. Lett. **B324**, 209 (1994).

[22] L.M. Jones and H.W. Wyld, Phys. Rev. **D17**, 759 (1978);
M. Glück, J.F. Owens and E. Reya, Phys. Rev. **D17**, 2324 (1978);
J. Babcock, D. Sivers and S. Wolfram, Phys. Rev. **D18**, 162 (1978);
B. Combridge, Nucl. Phys. **B151**, 429 (1979).

[23] S. Frixione and G. Ridolfi, INFN-Genova report GEF-TH-4/1996, hep-ph 9605209.

[24] G. Baum et al., COMPASS Collab., CERN/SPSLC 96-14.

[25] J. Babcock, E. Monsay and D. Sivers, Phys. Rev. **D19**, 1483 (1979).

[26] J.R. Forshaw and R.G. Roberts, Phys. Lett. **B319**, 539 (1993).

Spin asymmetries from charged current events

M. Anselmino[a], J. Blümlein[b] P. Gambino[c], J. Kalinowski[d], N. Kochelev[e], M. Maul[f], A. Schäfer[f], and T. Yamanishi[g]

[a] Università di Torino and INFN, Sezione di Torino, Via P. Giuria 1, I-10125 Torino, Italy
[b] DESY-Zeuthen, Platanenallee 6, D–15735 Zeuthen, Germany
[c] MPI für Physik, Föhringer Ring 6, D-80805 München, Germany
[d] Warsaw University, Institute of Theoretical Physics, Ul. Hoza 69, Pl-00681 Warsaw, Poland
[e] Bogoliubov Laboratory for Theoretical Physics, JINR, ul. Joliot–Curie 6, RU–141980 Dubna, Russia
[f] Institut für Theoretische Physik, Universität Frankfurt, D-60054 Frankfurt, Germany
[g] Research Center for Nuclear Physics, Osaka University, Ibaraki, Osaka, 567, Japan

Abstract: Charged currents reactions offer the possibility to measure combinations of polarized distribution functions which are linearly independent from those appearing in $g_1^{p,n}(x,Q^2)$. It turns out that the expected accuracy for an effective luminosity of 100 pb^{-1} is quite good. Also neutral current interactions offer in principle new information on the internal nucleon spin structure, however it is very difficult to extract such information due to the dominance of electromagnetic contributions. Also semi-inclusive D-production, which is a direct signal for the polarized s-quark distribution is investigated. For practical measurements one needs for this observable, however, a very high luminosity, of the order 1000 pb^{-1}. To make full use of the possibilities offered by CC reactions requires electron as well as positron beams.

A polarized proton beam at DESY would allow for the investigation of spin effects in charged current (CC) reactions (and less favourably neutral current (NC) reactions), where the outgoing neutrino is detected by its missing momentum. CC events probe a different combination of spin-dependent quark-distribution functions than electromagnetic processes, thus allowing to extract new information on the flavor decomposition of the polarized quark distribution functions. These experiments would yield results similar to those expected from semi-inclusive fixed target experiments [1, 2]. The most important property of CC reactions is that they distinguish quark and antiquark flavours, allowing to extract the polarized valence quark distributions Δu_V, Δd_V as well as the strange ones $\Delta s, \Delta\bar{s}$. The latter two are usually assumed to be identical. If a difference between them were observed this could be related to the fact that the virtual coupling of p to e.g. (K^+ + baryon) is stronger than to (K^-+baryon). Including deep inelastic weak interaction processes, but neglecting lepton and quark masses the hadronic scattering tensor can be decomposed into eight structure functions [3]:

$$\begin{aligned}\frac{1}{2m_N}W_{\mu\nu} &= -\frac{g_{\mu\nu}}{m_N}F_1(x,Q^2)+\frac{p_\mu p_\nu}{m_N p\cdot q}F_2(x,Q^2)\\ &+\frac{i\epsilon_{\mu\nu\alpha\beta}}{2p\cdot q}\left[\frac{p^\alpha q^\beta}{m_N}F_3(x,Q^2)+2q^\alpha S^\beta g_1(x,Q^2)-4xp^\alpha S^\beta g_2(x,Q^2)\right]\\ &-\frac{p_\mu S_\nu+S_\mu p_\nu}{2p\cdot q}g_3(x,Q^2)+\frac{S\cdot q}{(p\cdot q)^2}p_\mu p_\nu g_4(x,Q^2)+\frac{S\cdot q}{p\cdot q}g_{\mu\nu}g_5(x,Q^2) \quad . \quad (1)\end{aligned}$$

Here the twist–2 contributions to g_2 and g_3 are related to the structure functions g_1 and g_5, respectively. The former relation is due to Wandzura and Wilczek [4]

$$g_2(x) = -g_1(x) + \int_x^1 \frac{dy}{y} g_1(y), \quad (2)$$

whereas the latter was only found recently in ref. [5]

$$g_3(x) = 4x\int_x^1 \frac{dy}{y} g_5(y). \quad (3)$$

Furthermore, in the definition of polarized structure functions introduced in eq. (1) Dicus' relation [6] reads

$$g_4(x) = 4x\int_x^1 \frac{dy}{y} g_5(y) - 2xg_5(x), \quad (4)$$

i.e. both $g_3(x)$ and $g_4(x)$ do not vanish in general. The structure functions g_1 to g_5 are compared numerically in figure 1 [7] for the case of charged current interactions.

Clearly the structure functions $\hat{g}_3(x,Q^2) = -g_3(x,Q^2)$ and $\hat{g}_4(x,Q^2) = g_4(x,Q^2) - g_3(x,Q^2)$ are small quantities if compared to g_1 and g_5. They vanish at small x and do not exhibit strong (LO) scaling violations being non–singlet structure functions. In the present analysis their contribution to the asymmetries is suppressed due to kinematical reasons. However, they yield equally important contributions in transverse polarization asymmetries. Particularly the structure function $\hat{g}_3$ would be interesting to measure since it contains aside of its twist 2 contribution given in eq. (3) a twist–3 contribution [7].

To a good approximation one may assume $g_4 \approx 0$ (in the parton model $g_4 = 0$), for which eq. (4) results into $2xg_5(x) = g_3(x)$ [5, 6, 9, 10, 11] in the subsequent treatment. Contracted with the leptonic scattering tensor the differential cross section reads for the CC reactions with longitudinally polarized targets [12, 13]

$$\frac{d^2\sigma}{dxdQ^2} = \frac{G_F^2 M_W^4}{4\pi}\left([aF_1 - \lambda bF_3] + [-\lambda 2bg_1 + ag_5]\delta\right)\frac{1}{(Q^2+M_W^2)^2} \quad , \quad (5)$$

where G_F is Fermi's constant and M_W the W-Boson mass. λ is -1 for e^- and $+1$ for e^+, and δ denotes the longitudinal polarization of the nucleon antiparallel $(+1)$ or parallel (-1) to the polarization of the lepton. The y dependence is absorbed in the two constants $a = 2(y^2-2y+2)$ and $b = y(2-y)$.

The asymmetry is defined by

$$A := \frac{d\sigma_{\uparrow\downarrow} - d\sigma_{\uparrow\uparrow}}{d\sigma_{\uparrow\downarrow} + d\sigma_{\uparrow\uparrow}} \quad , \quad (6)$$

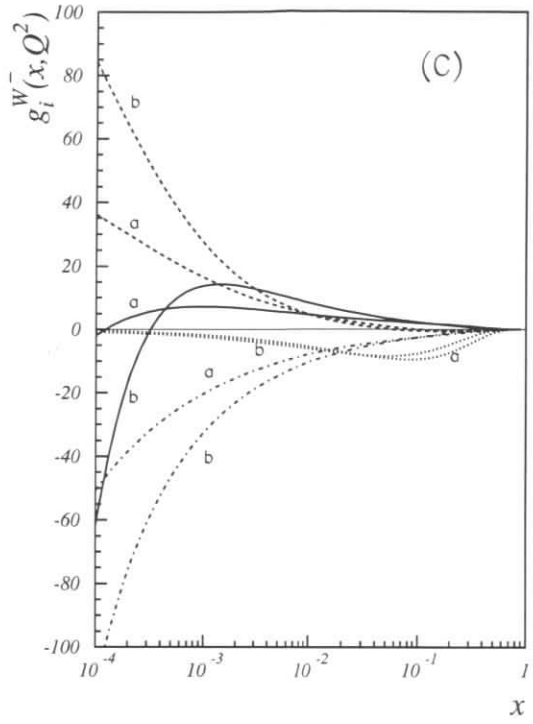

Figure 1: *x and Q^2 dependence of the charged current structure functions $g_i^{W^-}|_{i=1}^5(x)$. The lines correspond to: (a) $Q^2 = 10$ GeV^2 and (b) $Q^2 = 10^4$ GeV^2. Full lines: g_1; dashed lines: g_2; dotted lines: $-10 \cdot g_3$; dash–dotted lines: $-g_5$. The structure function g_4 obeys the relation $g_4 = g_3 - 2xg_5$. The structure functions $g_{1,5}(x,Q^2)$ were parametrized using the parton densities of ref. [8].*

which leads to

$$A^{W^-} = \frac{2bg_1 + ag_5}{aF_1 + bF_3}\,; \qquad A^{W^+} = \frac{-2bg_1 + ag_5}{aF_1 - bF_3} \quad . \tag{7}$$

It is interesting to note that for relatively low Q^2 ($\approx 10^3$ GeV^2) and in the kinematically allowed region, $a \gg b$, so that the asymmetries are dominated by the parity violating form factor g_5. This hints to the possibility of a direct extraction of this interesting quantity from the asymmetry. In the framework of the quark parton model the eight combinations of distribution

functions tested by CC asymmetries read:

$$\begin{aligned}
F_1^{W-} &= u + c + \overline{d} + \overline{s} \quad , \quad & F_1^{W+} &= d + s + \overline{u} + \overline{c} \quad , \\
F_3^{W-} &= 2(u + c - \overline{d} - \overline{s}) \quad , \quad & F_3^{W+} &= 2(d + s - \overline{u} - \overline{c}) \quad , \\
g_1^{W-} &= \Delta u + \Delta c + \Delta\overline{d} + \Delta\overline{s} \quad , \quad & g_1^{W+} &= \Delta d + \Delta s + \Delta\overline{u} + \Delta\overline{c} \quad , \\
g_5^{W-} &= \Delta u + \Delta c - \Delta\overline{d} - \Delta\overline{s} \quad , \quad & g_5^{W+} &= \Delta d + \Delta s - \Delta\overline{u} - \Delta\overline{c} \quad .
\end{aligned} \tag{8}$$

Rewriting (4) in terms of the parton distributions we get for the inclusive asymmetries:

$$\begin{aligned}
A^{W^-} &= \frac{\Delta u + \Delta c - [(y-1)^2][\Delta\overline{s} + \Delta\overline{d}]}{u + c + [(y-1)^2][\overline{s} + \overline{d}]} \quad , \\
A^{W^+} &= \frac{[(y-1)^2][\Delta s + \Delta d] - \Delta\overline{u} - \Delta\overline{c}}{[(y-1)^2][s + d] + \overline{u} + \overline{c}} \quad .
\end{aligned} \tag{9}$$

In figure 2 [13] we show the expected asymmetries for HERA energies ($E_l = 27.6$ GeV, $E_n = 820$ GeV) with integrated cross sections in the Q^2 range $600 - 1000$ (GeV)^2 and 1000 (GeV)^2 – maximum. We split the data into these two Q^2 ranges, because it might not be obvious, that the detection of missing momentum in the range $\sqrt{600}$ GeV – $\sqrt{1000}$ GeV is absolutely reliable. (Usually already $Q^2 \geq 600$ (GeV)^2 is regarded as safe). Fig. 2 shows that the low-Q^2 data do not dominate the statistics. So even if one would be very restrictive on the criteria for identifying CC events our conclusions would be hardly affected. Probably one can safely combine all data down to $Q^2 \approx 400$ GeV^2 to improve the statistics. For the polarized parton distributions we use the set "standard scenario, LO" given in [8], for the unpolarized ones those of [14]. The error bars are calculated according to

$$\Delta A = \sqrt{\frac{1 - A^2}{2\mathcal{L}\Delta x \Delta Q^2 d^2\sigma/dxdQ^2}} \quad , \tag{10}$$

where $\mathcal{L}$ denotes the effective luminosity. $d\sigma$ is the unpolarized cross section. We assumed $\mathcal{L}$ = 200 pb^{-1} (100 pb^{-1} per relative polarization) and fully polarized beams. We notice that the CC asymmetry is proportional to the degree of polarization of the proton only, while the statistical error scales as $1/\sqrt{1/2(1 - P_e)}$. The remarkable features of our results are that the asymmetries are sizable in the range $x \in [0.01, 1]$ and that even for 100 pb^{-1} the expected statistical accuracy for W^- exchange is rather good.

In figure 3 [13] we compare the contribution of the sea quarks and valence quarks to the asymmetries using two different parton distribution sets. One is again the LO standard scenario [8] the other one is LO Gluon C [15]. The main distinction between the two sets is the fact that the polarized valence quark distribution given in [8] is nearly proportional to the unpolarized valence quark contribution, whereas in [15] the fit shows larger deviations. For the parametrization of [15] the spin asymmetry is even larger than for that of [8]. Obviously the expected accuracy should allow to distinguish the two scenarios. Besides these single W boson asymmetries one can form four combinations which are determined by pure valence contributions and by valence + sea contributions:

$$A_{(\pm)_1(\pm)_2} := \frac{(d\sigma_{\uparrow\downarrow}^{W^-} - d\sigma_{\uparrow\uparrow}^{W^-})(\pm)_1(d\sigma_{\uparrow\downarrow}^{W^+} - d\sigma_{\uparrow\uparrow}^{W^+})}{(d\sigma_{\uparrow\downarrow}^{W^-} + d\sigma_{\uparrow\uparrow}^{W^-})(\pm)_2(d\sigma_{\uparrow\downarrow}^{W^+} + d\sigma_{\uparrow\uparrow}^{W^+})} \quad . \tag{11}$$

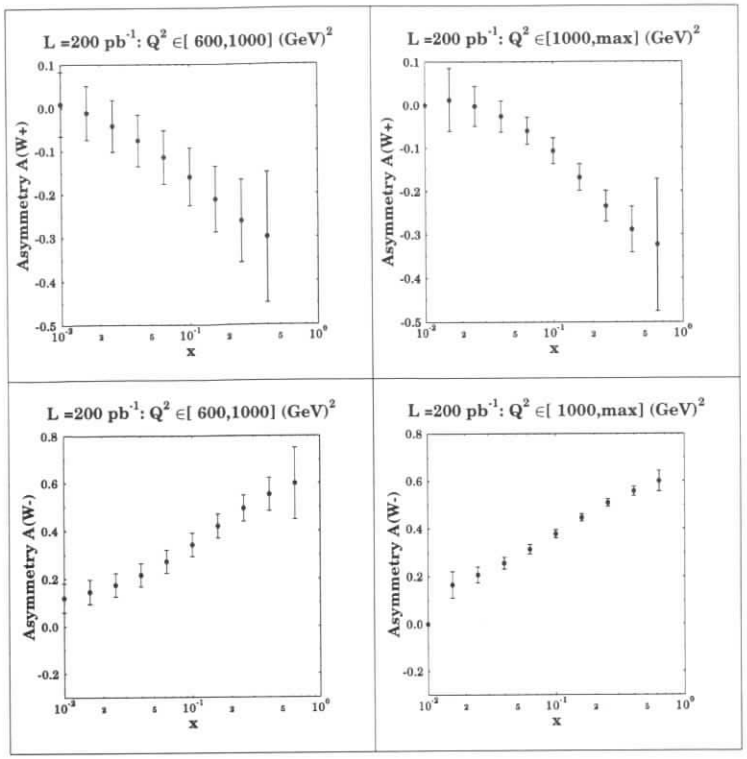

Figure 2: *Asymmetries A^{W^+} and A^{W^-} in the Q^2 range 600-1000* $(\mathrm{GeV})^2$ *and 1000- max* $(\mathrm{GeV})^2$ *for the luminosity of 200 pb^{-1}, i.e. 100 pb^{-1} per relative polarization and fully polarized beams using the parton distributions of [8].*

Here the first $\pm$ accounts for the numerator and the second for the denominator. With this definition we write:

$$
\begin{aligned}
A_{++} &= \frac{\Delta u_V + [(y-1)^2]\Delta d_V}{u_T + c_T + [(y-1)^2][s_T + d_T]} \quad , \\
A_{--} &= \frac{\Delta u_T + \Delta c_T - [(y-1)^2][\Delta s_T + \Delta d_T]}{u_V - [(y-1)^2] d_V} \quad , \\
A_{-+} &= \frac{\Delta u_T + \Delta c_T - [(y-1)^2][\Delta s_T + \Delta d_T]}{u_T + c_T + [(y-1)^2][s_T + d_T]} \quad , \\
A_{+-} &= \frac{\Delta u_V + [(y-1)^2]\Delta d_V}{u_V - [(y-1)^2] d_V} \quad . \qquad (12)
\end{aligned}
$$

Here we defined for the quark distribution functions q_f

$$
\Delta q_f = q_{f,\uparrow\downarrow} - q_{f,\uparrow\uparrow} \quad ,
$$

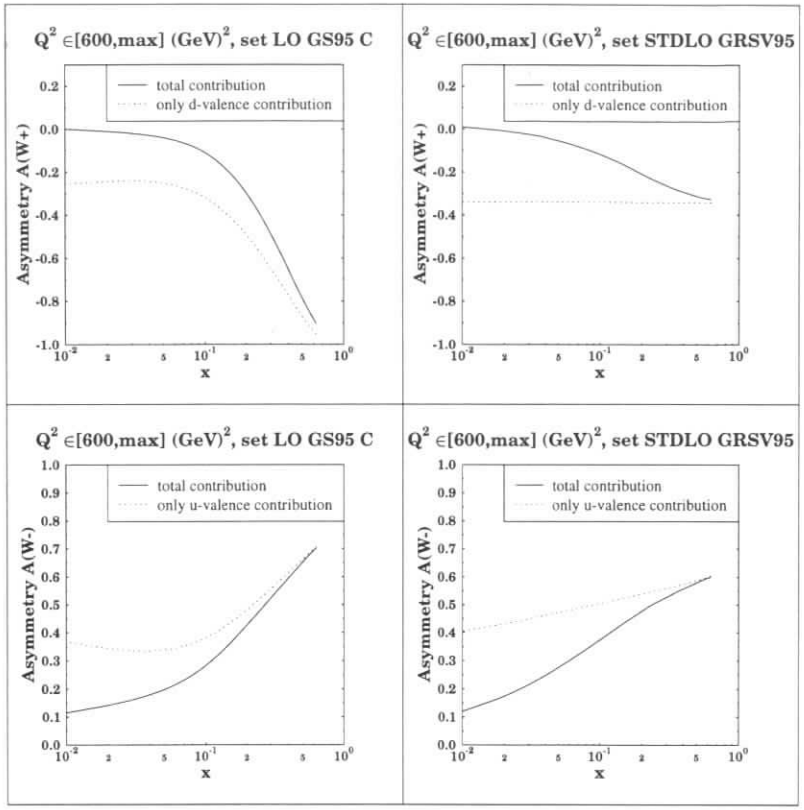

Figure 3: *Asymmetries A^{W^+} and A^{W^-} in the Q^2 range 600-max* $(\mathrm{GeV})^2$*, comparison between valence and sea quark contributions using set "Gluon C, leading order "[15], and "standard scenario, leading order " [8].*

$$
\begin{aligned}
q_{f,V} &= q_f - \overline{q}_f \quad , \\
q_{f,T} &= q_f + \overline{q}_f \quad . \qquad (13)
\end{aligned}
$$

While the inclusive asymmetries are mainly sensitive to the u- and d- quark flavour it is possible to extract direct information on the strange and antistrange sea by semi-inclusive CC current measurements. As usual, we define the fragmentation function $D_f^H(z)$, which describes the probability that a quark with flavor f fragments into a hadron H which carries the fraction z of the whole energy transferred to the nucleon. The most interesting process turns out to be D-meson production. In this case the relevant fragmentation functions are

$$
D_1^D(z) \equiv D_c^D(z) \equiv D_{\overline{c}}^D(z) \quad . \qquad (14)
$$

The fragmentation of any other flavour into a D meson is strongly suppressed. The only relevant

contributions come from $s + W^+ \to D^+$, or D^0. Also we set

$$\int_{0.2}^{1} D_1^D(z)dz \approx 1 \tag{15}$$

because each c-quark fragments in at least one charmed hadron. Furthermore the fragmentation functions are assumed to be spin independent. The resulting formulas read [13]

$$A_{W^-}^D := \frac{d\sigma_{W^-,D}^{\uparrow\downarrow} - d\sigma_{W^-,D}^{\uparrow\uparrow}}{d\sigma_{W^-,D}^{\uparrow\downarrow} + d\sigma_{W^-,D}^{\uparrow\uparrow}} = -\frac{\Delta\bar{s} + t^2\Delta\bar{d}}{\bar{s} + t^2\bar{d}} \quad ,$$
$$A_{W^+}^D := \frac{d\sigma_{W^+,D}^{\uparrow\downarrow} - d\sigma_{W^+,D}^{\uparrow\uparrow}}{d\sigma_{W^+,D}^{\uparrow\downarrow} + d\sigma_{W^+,D}^{\uparrow\uparrow}} = \frac{\Delta s + t^2\Delta d}{s + t^2 d} \quad , \tag{16}$$

where $t = \tan^2\theta_C$ contains the Cabbibo-angle. These asymmetries are obviously a direct signal for the strange and antistrange polarization and figure 4 [13] shows that the anticipated statistical accuracy for $\mathcal{L} = 1000\,\mathrm{pb}^{-1}$ should allow at least for an approximate experimental determination.

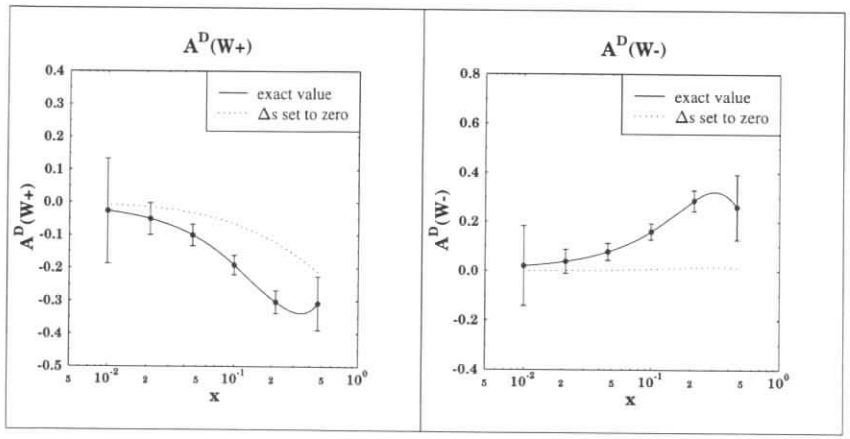

Figure 4: *Charmed asymmetries A_{W+}^D, and A_{W-}^D in the Q^2 range 600-max $(\mathrm{GeV})^2$ using "standard scenario, leading order" [8]. The error bars are given for the luminosity of 1000 pb^{-1}.*

In principle, one might easily extract information on parity violating polarized structure functions also by considering a single spin asymmetry in neutral current (NC) processes with longitudinally polarized protons and unpolarized leptons [10, 16]. The spin asymmetry for unpolarized electrons reads [10]

$$A_{NC}^{e^-p} = \eta^{\gamma Z}\,\frac{a\left[(2s_w^2 - \frac{1}{2})g_5^{\gamma Z} + \eta^{\gamma Z}(4s_w^4 - 2s_w^2 + \frac{1}{2})g_5^Z)\right] - b\left[g_1^{\gamma Z} + \eta^{\gamma Z}(4s_w^2 - 1)g_1^Z\right]}{a\left[F_1^\gamma + \eta^{\gamma Z}(2s_w^2 - \frac{1}{2})F_1^{\gamma Z}\right] - \frac{1}{2}b\,\eta^{\gamma Z}\,F_3^{\gamma Z} + \mathcal{O}[(\eta^{\gamma Z})^2]}\,, \tag{17}$$

where

$$\eta^{\gamma Z} = \frac{GM_Z^2}{2\sqrt{2}\pi\alpha}\frac{Q^2}{Q^2 + M_Z^2}\,, \tag{18}$$

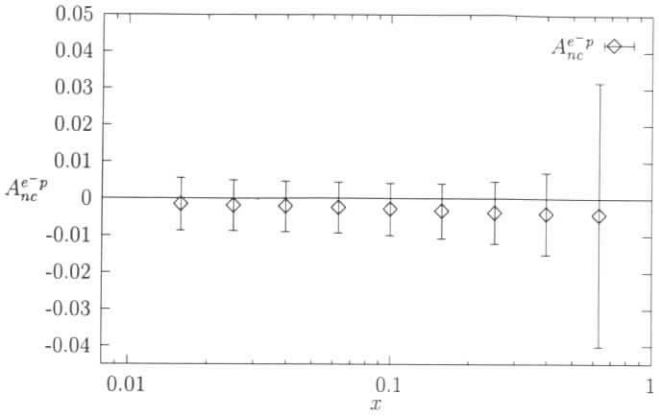

Figure 5: *Neutral current e^-p single spin asymmetry, Eq.(17) of text, for $Q^2 = 1000\ GeV^2$ at HERA energies with fully polarized proton beams. The statistical errors calculated for $\mathcal{L} = 500\,pb^{-1}$ for each polarization and $\Delta Q^2 = 500\ GeV^2$ are shown.*

s_w is the sine of the Weinberg angle, and we have neglected in the denominator the purely weak contributions, of $\mathcal{O}[(\eta^{\gamma Z})^2]$ and negligible in most of HERA Q^2 range where $\eta^{\gamma Z}$ is still rather small. The expression for the structure functions $g^{\gamma Z}$ and g^Z in terms of quark distributions can be found in Ref. [10].

For the numerical analysis of NC events we impose the following kinematical cuts: $0.01 < y < 0.9$, $x < 0.7$. In addition, we demand $Q^2 > 500\ \mathrm{GeV}^2$. The leading order polarized parton distributions are taken from Ref. [8] (here we use the set "standard scenario", eventually extrapolated to Q^2 values greater than $10^4\ \mathrm{GeV}^2$; the "valence" set yields very similar results); the unpolarized ones are taken from Ref. [14]. We have assumed fully polarized beams, and we emphasize again that $A^{W^\mp}$ are independent of the degree of polarization of the lepton beam, and proportional to the polarization of the proton: $P_e < 1$ would only marginally decrease the available statistical precision, while $P_p < 1$ would simply reduce the asymmetries by the corresponding factor. A high degree of polarization of the proton beam, more than that of the leptons, would be a most welcome feature.

In figures 5 and 6 [12] we show the expected asymmetries as functions of x both at fixed $Q^2 = 1000\ \mathrm{GeV}^2$ and averaging over all the kinematically allowed Q^2 region, that is summing all detectable events in a given x-bin. The statistical errors shown in the figures have been calculated from Eq. (7) assuming that for each longitudinal proton polarization an integrated luminosity $\mathcal{L} = 500\ \mathrm{pb}^{-1}$ can be collected. [To calculate the errors at fixed Q^2 we take $\Delta Q^2 = Q^2/2$.] For NC events the spin asymmetry is probably too small to be meaningfully measured at HERA, as an effect of the dominant parity conserving electromagnetic contribution.

In summary, we have clearly shown that measurements of charged current processes in deep inelastic scattering of longitudinally polarized or unpolarized leptons off longitudinally polarized

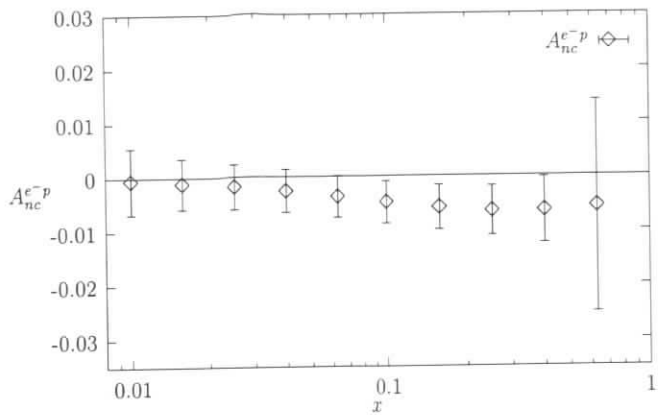

Figure 6: *Neutral current e^-p single spin asymmetry, Eq.(17) of text, averaged over the allowed Q^2 region at HERA energies with fully polarized proton beams. The statistical errors calculated for $\mathcal{L} = 500\,pb^{-1}$ for each polarization are shown.*

protons at HERA energies offer a unique and viable way of reaching more information on the quark spin content of protons.

This work has been supported by DESY, the Polish Committee for Scientific Research (J.K.), DFG, BMBF and MPI für Kernphysik (A.S.).

References

[1] M. Veltri, M. Düren, K. Rith, L. Mankiewicz, A. Schäfer, Proceedings, Physics at HERA, **vol. 1*** 447-457 (1991)

[2] L. L. Frankfurt, M. I. Strikman, L. Mankiewicz, A. Schäfer, E. Rondio, A. Sandacz, and V. Papavassiliou, Phys. Lett. **B230** 141 (1989)

[3] J. A. Bartelski, Acta Phys. Pol. **B10** 923 (1979)

[4] S. Wandzura and F. Wilczek, Phys. Lett. **B72** (1977) 195

[5] J. Blümlein and N. Kochelev, Phys. Lett. **B381** (1996) 296

[6] D. A. Dicus, Phys. Rev. **D5** 1367 (1972)

[7] J. Blümlein and N. Kochelev, DESY 96–175

[8] M. Glück, E. Reya, M. Stratmann, W. Vogelsang, Phys. Rev. **D53** 4775 (1996)

[9] B. Lampe, Phys. Lett. **B227** (1989) 469

[10] M. Anselmino, P. Gambino and J. Kalinowski, Z. Phys. **C64** 267 (1994)

[11] M. Maul, B. Ehrnsperger, E. Stein, A. Schäfer, hep-ph/9602377

[12] M. Anselmino, P. Gambino, and J. Kalinowski, preprint, hep-ph/9607427

[13] M. Maul and A. Schäfer, preprint, hep-ph/9607438

[14] M. Glück, E. Reya and A. Vogt, Z. Phys. **C67** (1995) 433

[15] T. Gehrmann, W. J. Stirling, Phys. Rev. **D53** 6100 (1996)

[16] S.M. Bilenky, N.A. Dadajan and E.H. Hristova, Sov. J. Nucl. Phys. **21** (1975) 657

On the Physics Potential of Polarized Nucleon–Nucleon Collisions at HERA

M. Anselmino[a], E. Andreeva[b], V. Korotkov[c], F. Murgia[d], W.–D. Nowak[e,1], S. Nurushev[c], O. Teryaev[f], A. Tkabladze[f]

[a] University of Torino, Italy; [b] MEPHI Moscow, Russia; [c] IHEP Protvino, Russia; [d] University of Cagliari, Italy; [e] DESY-IfH Zeuthen, Germany; [f] JINR Dubna, Russia

Abstract: The physics of polarized nucleon–nucleon collisions originating from an internal polarized target in the HERA proton beam is investigated. Based on 240 pb^{-1} integrated luminosity at 40 GeV c.m. energy, statistical sensitivities are given over a wide (x_F, p_T)–range for a variety of inclusive and exclusive final states. By measuring single spin asymmetries unique information can be obtained on higher twist contributions and their p_T-dependence. From double spin asymmetries in both photon and J/ψ production it appears possible to measure the polarized gluon distribution in the range $0.1 \leq x_{gluon} \leq 0.4$ with a good statistical accuracy.

1 Introduction

There is a widespread general consensus, much grown in the last years and based both on surprising experimental results and intense theoretical activity, that the spin structure and the spin dynamical properties of nucleons and hadrons in general are far from being understood; a satisfactory knowledge of hadronic structure and dynamics and their correct description in terms of constituents cannot ignore the spin subtleties and more experimental information is badly required.

An experiment ('*HERA–$\vec{N}$*' [1]) utilising an internal polarized nucleon target in the 820 GeV HERA proton beam would constitute a natural extension of the studies of the nucleon spin structure in progress at DESY with the *HERMES* experiment [2]. Conceivably, this would be the only place where to study high energy nucleon–nucleon spin physics besides the dedicated RHIC spin program at BNL [3] supposed to start early in the next decade.

An internal polarized nucleon target offering unique features such as polarization above 80% and no or small dilution, can be safely operated in a proton ring at high densities up to 10^{14} atoms/cm^2 [4]. As long as the polarized target is used in conjunction with an unpolarized proton beam, the physics scope of *HERA–$\vec{N}$* would be focused to 'phase I', i.e. measurements of single spin asymmetries. Once later polarized protons should become available, the same set-up would be readily available to measure a variety of double spin asymmetries. These 'phase II' measurements would constitute an alternative – fixed target – approach to similar physics which will be accessible to the collider experiments *STAR* and *PHENIX* at the low end of the RHIC energy scale ($\sqrt{s} \simeq 50$ GeV) [6].

We shall briefly discuss here the physics motivations to measure single and double spin asymmetries in several $p\vec{N}$ inclusive and exclusive processes; more details and further discussions, together with a complete list of references, which we cannot give here for lack of space, can be found in Ref. [5]. We recall that the integrated luminosity calculation is based upon realistic

[1] e-mail: nowakw@ifh.de

figures. For the average beam and target polarisation $P_B = 0.6$ and $P_T = 0.8$ are assumed, respectively. A combined trigger and reconstruction efficiency of $C \simeq 50\%$ is anticipated. Using $\bar{I}_B = 80$ mA $= 0.5 \cdot 10^{18}\ s^{-1}$ for the average HERA proton beam current (50% of the design value) and a rather conservative polarized target density of $n_T = 3 \cdot 10^{13}$ atoms/cm^2 the projected integrated luminosity becomes $\mathcal{L} \cdot T = 240\ pb^{-1}$ when for the total running time T an equivalent of $T = 1.6 \cdot 10^7\ s$ at 100 % efficiency is assumed. This corresponds to about 3 real years under present HERA conditions. However, proton currents much higher than the original HERA design value of 160 mA are envisaged in the HERA luminosity upgrade program. In addition, experience from UA6 running at CERN shows that after having gained some practical running experience it presumably becomes feasible to operate the polarized gas target at about 3 times higher density without seriously affecting the proton beam lifetime. Hence in a few years 500 pb^{-1} *per year* will presumably become a realistic figure.

We note that, except in the case of single spin asymmetries, we took into account major acceptance limitations and jet detection efficiencies. Hence it can be anticipated that the sensitivities shown in the rest of the paper are realistic for an about one year's running of a future polarized nucleon–nucleon scattering experiment at HERA. Any better estimate requires considerably intensified efforts to be invested along many different directions, like machine and target limitations, detector capabilities versus rate, acceptance, costs etc.

2 Single Spin Asymmetries

Single spin asymmetries in large p_T inclusive production, both in proton-nucleon and lepton-nucleon interactions, have recently received much attention (for references see [5]). The naive expectation that they should be zero in perturbative QCD has been proven to be false, both experimentally and theoretically. It is now clear that higher twist effects are responsible for these asymmetries, which should be zero only in leading twist-2 perturbative QCD.

Several models and theoretical analyses suggest possible higher twist effects: there might be twist-3 dynamical contributions, which we shall denote as hard scattering higher twists; there might also be intrinsic $k_\perp$ effects, both in the quark fragmentation process and in the quark distribution functions. The latter are not by themselves higher twist contributions - they are rather non-perturbative universal nucleon properties - but give rise to twist-3 contributions when convoluted with the hard scattering cross sections. The dynamical contributions result from a short distance part calculable in perturbative QCD with slightly modified Feynman rules, combined with a long distance part related to quark-gluon correlations.

An intrinsic $k_\perp$ effect in the quark fragmentation is known as Collins or sheared jet effect; it simply amounts to say that the number of hadrons h (say, pions) resulting from the fragmentation of a transversely polarized quark, with longitudinal momentum fraction z and transverse momentum $\boldsymbol{k}_\perp$, depends on the quark spin orientation. That is, one expects the *quark fragmentation analysing power* $A_q(\boldsymbol{k}_\perp)$ to be different from zero:

$$A_q(\boldsymbol{k}_\perp) \equiv \frac{D_{h/q^\uparrow}(z, \boldsymbol{k}_\perp) - D_{h/q^\downarrow}(z, \boldsymbol{k}_\perp)}{D_{h/q^\uparrow}(z, \boldsymbol{k}_\perp) + D_{h/q^\downarrow}(z, \boldsymbol{k}_\perp)} \neq 0 \qquad (1)$$

where, by parity invariance, the quark spin should be orthogonal to the $q - h$ plane. Notice also that time reversal invariance does not forbid such quantity to be $\neq 0$ because of the (necessary) soft interactions of the fragmenting quark with external strong fields, i.e. because of final state interactions. This idea has been applied to the computation of the single spin asymmetries observed in $pp^\uparrow \to \pi X$ [7].

A similar idea applies to the distribution functions, provided soft gluon interactions between initial state partons are present and taken into account, which most certainly is the case for

hadron-hadron interactions. That is, one can expect that the number of quarks with longitudinal momentum fraction x and transverse intrinsic motion $\boldsymbol{k}_\perp$ depends on the transerve spin direction of the parent nucleon, so that the *quark distribution analysing power* $N_q(\boldsymbol{k}_\perp)$ can be different from zero:

$$N_q(\boldsymbol{k}_\perp) \equiv \frac{f_{q/N^\uparrow}(x,\boldsymbol{k}_\perp) - f_{q/N^\downarrow}(x,\boldsymbol{k}_\perp)}{f_{q/N^\uparrow}(x,\boldsymbol{k}_\perp) + f_{q/N^\downarrow}(x,\boldsymbol{k}_\perp)} \neq 0 \qquad (2)$$

This effect also has been used to explain the single spin asymmetries observed in $pp^\uparrow \to \pi X$ [8].

Note that both $A_q(\boldsymbol{k}_\perp)$ and $N_q(\boldsymbol{k}_\perp)$ are leading twist quantities which, when convoluted with the elementary cross-sections and integrated over $\boldsymbol{k}_\perp$, give twist-3 contributions to the single spin asymmetries.

Each of the above mechanisms might be present and might be important in understanding twist-3 contributions; in particular the quark fragmentation or distribution analysing powers look like new non-perturbative universal quantities, crucial in clarifying the spin structure of nucleons. It is then of great importance to study possible ways of disentangling these different contributions in order to be able to assess the importance of each of them. We propose here to measure the single spin asymmetry

$$\frac{d\sigma^{AB^\uparrow \to CX} - d\sigma^{AB^\downarrow \to CX}}{d\sigma^{AB^\uparrow \to CX} + d\sigma^{AB^\downarrow \to CX}} \qquad (3)$$

in several different processes $AB^\uparrow \to CX$ which should allow to fulfil such a task. To obtain a complete picture we need to consider nucleon-nucleon interactions together with other processes, like lepton-nucleon scattering, which might add valuable information. For each of them we discuss the possible sources of higher twist contributions, distinguishing, according to the above discussion, between those originating from the hard scattering and those originating either from the quark fragmentation or distribution analysing power.

- $pN^\uparrow \to hX$. In this process all kinds of higher twist contributions may be present; this asymmetry *alone* could not help in evaluating the relative importance of the different terms.
- $pN^\uparrow \to \gamma X$, $pN^\uparrow \to \mu^+\mu^- X$, $pN^\uparrow \to jets + X$. Here there is no fragmentation process, and we remain with possible sources of non-zero single spin asymmetries in the hard scattering or the quark distribution analysing power.
- $lN^\uparrow \to hX$. In such a process the single spin asymmetry can originate either from hard scattering or from $k_\perp$ effects in the fragmentation function, but not in the distribution functions, as soft initial state interactions are suppressed by powers of α_{em}. Moreover, this process allows, in principle, a direct measurement of the Collins effect, i.e. of the quark fragmentation analysing power, via a measurement of the leading-twist difference of cross sections for the production of two identical particles inside the same jet, with opposite $\boldsymbol{k}_\perp$.
- $lN^\uparrow \to \gamma X$, $\gamma N^\uparrow \to \gamma X$, $lN^\uparrow \to \mu^+\mu^- X$, $lN^\uparrow \to jets + X$. Each of these processes yields a single spin asymmetry which cannot originate from distribution or fragmentation $k_\perp$ effects; it may only be due to higher-twist hard scattering effects, which would thus be isolated.

It is clear from the above discussion that a careful and complete study of single spin asymmetries in several processes might be a unique way of understanding the origin and importance of higher twist contributions in inclusive hadronic interactions; not only, but it might also allow a determination of fundamental non-perturbative properties of quarks inside polarized nucleons and of polarized quark fragmentations. Such properties should be of universal value and applicability and their knowledge might be as important as the knowledge of unpolarized distribution and fragmentation functions.
In the following we discuss the capability of HERA-$\vec{N}$ to investigate some of these processes.

Inclusive pion production $p^\uparrow p \to \pi^{0\pm} X$ at 200 GeV exhibits surprisingly large single spin asymmetries, as it was measured a few years ago by the E704 Collaboration using a transversely polarized beam [9]. For any kind of pions the asymmetry A_N shows a considerable rise above

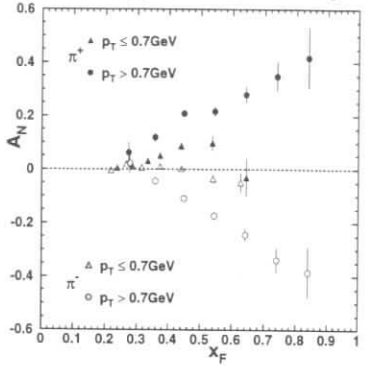

Figure 1: *Single spin asymmetry in inclusive pion production* $p^\uparrow + p \to \pi^{0\pm} + X$ *measured by the E704 Collaboration [9] and shown for two subregions of* p_T.

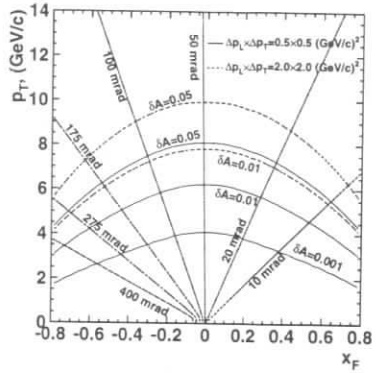

Figure 2: *Contours of the asymmetry sensitivity levels for* π^+ *production in the* $(p_T,\ x_F)$ *plane. Lines of constant laboratory angles of the pion are shown.*

$x_F > 0.3$, i.e. in the fragmentation region of the polarized nucleon. It is positive for both π^+ and π^0 mesons, while it has the opposite sign for π^- mesons. The charged pion data taken in the $0.2 < p_T < 2$ GeV range were split into two samples at $p_T = 0.7$ GeV/c; the observed rise is stronger for the high p_T sample, as can be seen from fig. 1. Contours characterizing different HERA-$\vec{N}$ sensitivity levels ($\delta A_N = 0.001$, 0.01 and 0.05) for an asymmetry measurements in the reaction $pp^\uparrow \to \pi^+ X$ are shown in fig. 2. Note that in the large p_T region the contours calculated with big $\Delta p_L \times \Delta p_T$ bins are appropriate, since usually a larger bin size is chosen where the statistics starts to decrease. We can conclude that the accessible p_T values are significantly larger than those E704 had; the combined p_T dependence of all involved higher-twist effects can be measured with good accuracy ($\delta A_N \leq 0.05$) up to transverse momenta of about 10 GeV/c in the central region $|x_F| < 0.2$ and up to 6 GeV/c in the target fragmentation region. This corresponds to an almost one order of magnitude extension in the p_T range in comparison to E704. The capability of HERA-$\vec{N}$ to really prove a predicted p_T dependence is shown in fig. 3, where the curve was obtained assuming a non–zero quark distribution analysing power (cf. eq. 2) according to Ref. [8].

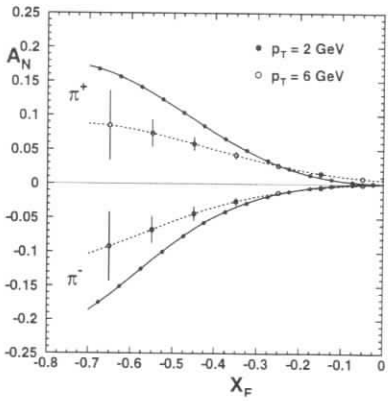

Figure 3: *Capability of HERA-*$\vec{N}$ *to discriminate predictions for different* p_T.

Inclusive direct photon production, $pp^\uparrow \to \gamma X$, proceeds without fragmentation, i.e. the photon carries directly the information from the hard scattering process. Hence this process

measures a combination of initial $k_\perp$ effects and hard scattering twist–3 processes. The first and only results up to now were obtained by E704 Collaboration [10] showing an asymmetry compatible with zero within large errors for $2.5 < p_T < 3.1$ GeV/c in the central region $|x_F| \lesssim 0.15$. The experimental sensitivity of HERA-$\vec{N}$ was determined using PYTHIA 5.7 by simultaneous simulation of the two dominant hard subprocesses contributing to direct photon production, i.e. gluon–Compton scattering ($qg \to \gamma q$) and quark–antiquark annihilation ($q\bar{q} \to \gamma g$), and of background photons that originate mainly from π^0 and η decays. It turns out that a good sensitivity (about 0.05) can be maintained up to $p_T \leq 8$ GeV/c. For increasing transverse momentum the annihilation subprocess and the background photons are becoming less essential; we expect to be able to detect a clear dependence on p_T, of the direct photon single spin asymmetry.

Inclusive J/ψ production was calculated in the framework of the colour singlet model [11]. Our calculations at HERA-$\vec{N}$ energies [5] show an asymmetry less than 0.01 in the region $|x_F| < 0.6$, i.e. the effect is practically unobservable.

3 Double Spin Asymmetries

Perturbative QCD allows sizeable lowest order double spin asymmetries for various 2→2 partonic subprocesses. Relying on the factorization theorem a rich spectrum of asymmetries at the hadronic level can be predicted which constitute the backbone of the RHIC spin physics program. When both incoming particles are longitudinally polarized, the insufficient knowledge of the polarized gluon distribution makes the predictions for double spin asymmetries A_{LL} to some extent uncertain. Conversely, the measurement of A_{LL} in certain final states seems to be one of the most valuable tools to measure the polarized gluon distribution function in the nucleon. The presently most accurate way to do so is the study of those processes which can be calculated in the framework of perturbative QCD, i.e. for which the involved production cross sections and subprocess asymmetries can be predicted. Both *direct photon (plus jet)* and *J/ψ (plus jet)* production are most suited because there are only small uncertainties due to fragmentation.

In the following we discuss the corresponding capabilities of HERA–$\vec{N}$, operated in doubly polarized mode ('Phase II'), to perform such measurements.

Inclusive photon production with HERA–$\vec{N}$ was the subject of a very recent study [12]. Basing on a NLO calculation rather firm predictions were obtained including an assessment of their theoretical uncertainties; the latter turned out to be of rather moderate size. In fig. 4 three different predictions for the asymmetry are shown in dependence on p_T and pseudorapidity η, in conjunction with the attainable statistical uncertainty of HERA–$\vec{N}$. We note that the dashed line is rather close to the prediction of Ref. [14], set A. As can be seen, there is sufficient statistical accuracy up to transverse momenta of about 8 GeV/c to discriminate between different polarized gluon distribution functions (cf. fig 4a). At $p_T = 6$ GeV/c there is sufficient accuracy to check the asymmetry prediction for photon pseudorapidities between -1.5 and 1.5 (cf. fig 4b).

In **photon plus jet production** the away-side jet is measured as well and the complete kinematics of the 2→2 subprocess can be reconstructed. In this case the asymmetry A_{LL} can be directly related to the polarized gluon distribution if a certain subprocess can be selected. Using this approach *photon plus jet* production was discussed in Ref. [5] as a tool to directly measure $\Delta G/G$. The quark–antiquark annihilation subprocess is suppressed relatively to quark-gluon Compton scattering because of the lower density of antiquarks (of the polarized sea) compared to gluons (polarized gluons). The absolute statistical error of $\Delta G(x_g)/G(x_g)$ was obtained as

$$\delta[\frac{\Delta G(x_g)}{G(x_g)}] = \frac{\delta A_{LL}}{A_{DIS} \cdot \hat{a}_{LL}}. \qquad (4)$$

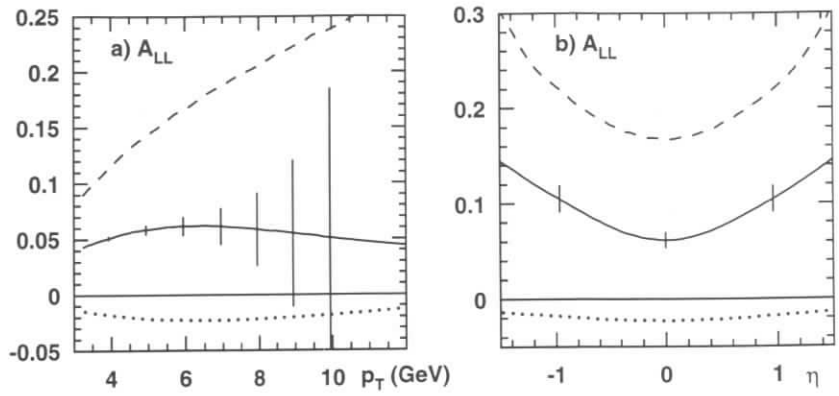

Figure 4: *Inclusive photon production: Double spin asymmetry vs. a) p_T and b) η for the NLO 'valence set' of Ref. [12] (full line), shown in conjunction with the HERA–$\vec{N}$ statistical sensitivity. The dotted line corresponds to set C of Ref. [13] and the dashed line is close to set A of Ref. [14]*

Here A_{DIS} and $\hat{a}_{LL}$ are to be taken at the appropriate values of x_F and x_g, respectively. In calculating the r.h.s. of eq. 4 we had to take into account the influence of the acceptance, as described in [5].

In fig. 5 the calculated HERA–$\vec{N}$ statistical sensitivity, on the present level of understanding, is shown vs. x_{gluon} in conjunction with predicted errors for *STAR* running at RHIC at 200 GeV c.m. energy [15]. The errors demonstrate clearly that in the region $0.1 \leq x_g \leq 0.4$ a significant result can be expected. This statement will very probably remain valid if once the systematic errors will have been estimated. As can be seen, the measurement of $\Delta G/G$ from *photon plus jet* production in doubly polarized nucleon-nucleon collisions at HERA can be presumably performed with an accuracy being about competitive to that predicted for RHIC.

At this point we note that the HERA–$\vec{N}$ fixed target kinematics causes additional problems for the jet reconstruction when compared to a collider experiment. As obtained from rather preliminary investigations [5], the number of photon events accompanied by a successfully reconstructed jet decreases considerably when approaching lower values of p_T and, correspondingly, of x_{gluon}. To have a more realistic statistical significance than that shown in Ref. [5] we now include these preliminary jet reconstruction efficiencies. As a result, the statistical error bars became somewhat larger for smaller transverse momenta.

J/ψ Production. Compared to direct photon production the production of quarkonium states below the open charm threshold is a similarly clean tool to measure the polarized gluon distribution. Hence many statements made in the previous section apply here, as well, and the principle of analysis is very similar. Because of the relatively large quark mass the $c\bar{c}$ production cross section and the expected asymmetry are supposed to be calculable perturbatively.

Quarkonium production has traditionally been calculated in the color-singlet model (CSM) [16] where the quark-antiquark pair is produced in a color-singlet state with the quantum numbers

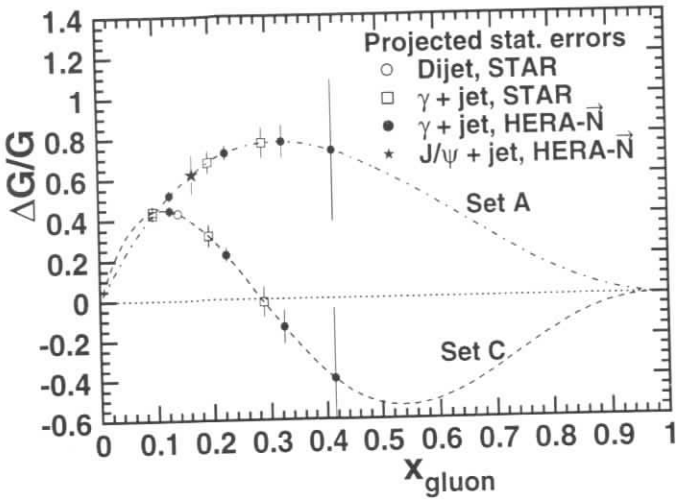

Figure 5: *Typical predictions for the polarized gluon distribution confronted with the projected statistical errors expected for HERA-$\vec{N}$ and RHIC experiments.*

of the corresponding hadron. This heavy mass pair then creates the hadronic state with a probability determined by the appropriate quarkonium wave function at the origin. It is assumed that for heavy quarks soft gluon emission is negligible, as also other non-perturbative effects like higher twist contributions. While this model gives a reasonable description of J/ψ production cross section shapes over p_T and x_F, it completely fails in the explanation of the integrated cross section; a K factor of $7 \div 10$ is needed to explain the data. The anomalously large cross section [17] for J/ψ production at large transverse momenta found at the Tevatron reveals another bad feature of the CSM; it is not able to explain the large ψ' and direct J/ψ production rates at CDF. All these observations led to the understanding that fragmentation and hadronization of color-octet [18] $q\bar{q}$ pairs are essential in the heavy quarkonium production process.
Within the framework of the color-octet mechanism the quarkonium production process can be separated, according to the factorization hypothesis, into a short and a long distance part. The former describes the quark-antiquark pair production at small distances and can be computed perturbatively. The latter is responsible for the creation of a particular hadronic state from the quark-antiquark pair; its matrix elements can not be calculated perturbatively.
The shapes of the p_T distribution of short distance matrix elements calculated within the color-octet model indicate that the new mechanism seems to be able to explain the Tevatron data for direct J/ψ and ψ' production at large p_T [19]. We note that unlike color-singlet matrix elements being connected to the subsequent hadronic non-relativistic wave functions at the origin, color-octet long distance matrix elements are unknown and have to be extracted from the experiment. As it was shown recently [20, 21] the color-octet mechanism gives the dominant contribution in J/ψ-production at HERA-$\vec{N}$ energies. This concerns not only the total cross section [20], but also J/ψ production at non-zero p_T, i.e. at those values of transverse momenta which are not due to internal motion of partons inside the colliding hadrons, $p_T \gtrsim 1.5$ GeV/c [21].

For inclusive J/ψ production we calculated the double spin-asymmetry within the framework of the color-octet model using the value of the color-octet matrix elements from [21]. It is interesting to note that the magnitude of the asymmetry does almost not depend on the choice of the color-octet matrix elements, if one assumes that the transition matrix elements of octet ${}^3P_J$-states into J/ψ are negligible compared to those of the ${}^1S_0$ state. This is the most likely scenario since only in this case it is possible to establish a consistence between different combinations of the above two matrix elements, as extracted from CDF data [19] and photo- [22] or hadroproduction [20] data. We underline that the measurement of the double spin asymmetry in J/ψ production would allow to extract information about the color-octet matrix elements *separately*, whereas from unpolarized experiments it is only possible to extract combinations of them. In fig. 6a we present the expected asymmetry versus p_T for two different sets of polarized gluon

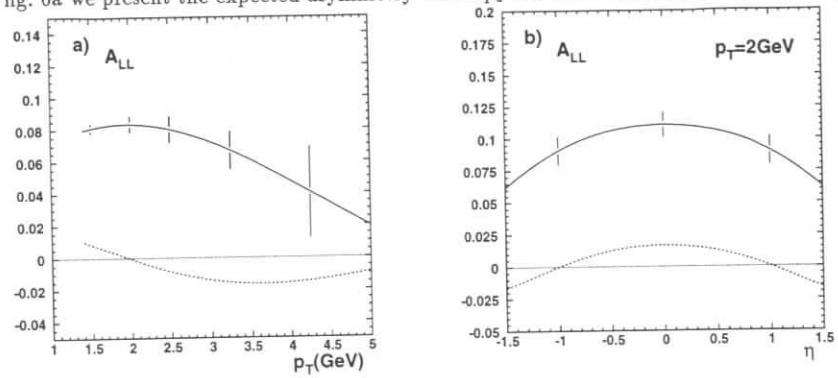

Figure 6: *Inclusive J/ψ production: Double spin asymmetry vs. a) p_T and b) η for the LO set A (full line) and the set C (dotted line) of Ref. [14], shown in conjunction with the HERA-$\vec{N}$ statistical sensitivity.*

distributions taken from [14]; the solid curve corresponds to set A and the dashed one to set C. For set A the asymmetry appears sufficiently large to be observed and its measurement would allow to extract information about the polarized gluon distribution function in the nucleon. As can be seen from fig. 6b, a very good discrimination between set A and set C is possible over the whole HERA-$\vec{N}$ pseudorapidity interval. For the mass of the charm quark we chose $m_c = 1.5$ GeV/c^2, as it was used for extraction of the color-octet matrix elements from experimental data [19, 20]. We found that unlike the J/ψ production cross section the asymmetry does practically not depend on the charm quark mass; if we vary the charm quark mass from 1.35 to 1.7 GeV/c^2 the magnitude of the asymmetry changes by about $3 \div 5\%$ over the whole considered p_T region.
In J/ψ plus jet production the study of the double spin asymmetry would allow to access directly the polarized gluon distribution function, similar to the case of *photon plus jet* production. For the absolute statistical error of $\Delta G(x_g)/G(x_g)$ an expression similar to eq. 4 is obtained:

$$\delta[\frac{\Delta G(x_g)}{G(x_g)}] = \frac{\delta A_{LL}}{[\Delta G/G] \cdot \hat{a}_{LL}} \tag{5}$$

with

$$\hat{a}_{LL} = \frac{\Delta\hat{\sigma}(gg \to J/\psi\ g)}{\hat{\sigma}(gg \to J/\psi\ g) + [q(x)/G(x)] \cdot \hat{\sigma}(gq \to J/\psi\ q)}. \tag{6}$$

Here the quark-gluon subprocess was neglected, since its contribution to $\hat{a}_{LL}$ amounts only to about 10% compared to the gluon-gluon fusion subprocess.

Unfortunately, taking into account the acceptance limitations as it was done for *photon plus jet* production, the J/ψ production cross section for HERA-$\vec{N}$ decreases significantly. Following the same principle of analysis as in Ref. [5], it turns out that the measurement of $\Delta G(x)/G(x)$ in *J/ψ plus jet* production is feasible only for $x_g = 0.1 \div 0.2$, i.e. for J/ψ transverse momenta of about 2.5 GeV/c. This prediction is shown as an additional entry in fig. 5. Although being a single point only, we underline that this is a very important measurement, because the lowest lying point from *photon plus jet* production is obtained for rather small values of p_T where perturbative QCD is not expected to give reliable predictions. We note that the nature of the gluon-gluon subprocess has rather similar consequences for *jet plus jet* production at RHIC; the prediction [15] consists of only one single point at a similar value of x_g, as well (cf. fig. 5).

4 Elastic Scattering

Large unexpected spin effects in singly polarized proton-proton elastic scattering $p + p^{\uparrow} \rightarrow p + p$ have been discovered many years ago and remain unexplained up to now. The single spin asymmetry A_N was found significantly different from zero in the region $1 \lesssim p_T^2 \lesssim 7\ (\mathrm{GeV/c})^2$ as it is shown in fig. 7 in conjunction with the HERA-$\vec{N}$ statistical errors.

At HERA-$\vec{N}$ energies the detection of the recoil proton for p_T^2 values in the range $5 \div 12\ (\mathrm{GeV/c})^2$ requires a very large angular acceptance (up to 40 degrees) [5]. The forward protons for the same interval in p_T^2 have laboratory angles of the order of a few milliradians and require a dedicated detector very close to the beam pipe. Note that although the accessible p_T^2 range would be similar to the range explored at low energies the c.m. scattering angle detected amounts to a few degrees at HERA–$\vec{N}$ energies, only.

The transverse single-spin asymmetry A_N in elastic pp scattering at HERA-$\vec{N}$ and RHIC energies has been calculated in a dynamical model that leads to spin-dependent pomeron couplings [23]. The predicted asymmetry is about 0.1 for $p_T^2 = 4 \div 5\ (\mathrm{GeV/c})^2$ with an expected statistical error of $0.01 \div 0.02$ for HERA-$\vec{N}$, i.e. a significant measurement of the asymmetry A_N can be performed to test the spin dependence of elastic pp scattering at high energies.

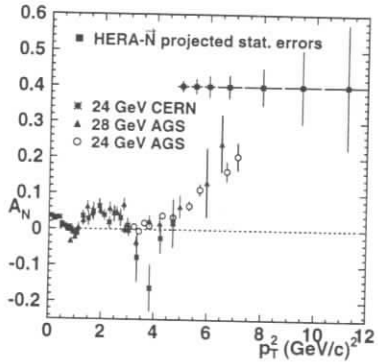

Figure 7: *Compilation of experimental data on the asymmetry in elastic proton-proton scattering as a function of p_T^2. In addition the projected statistical errors attainable with HERA-$\vec{N}$ are shown.*

5 Conclusions

The physics potential of polarized nucleon-nucleon collisions originating from an internal target in the 820 GeV HERA proton beam has been investigated. Single spin asymmetries, accessible already with the existing unpolarized beam, are found to be an almost unique and powerful tool to study the nature and physical origin of twist-3 effects; even more so when taken in conjunction with results of other experiments at HERA. When measuring the polarized gluon distribution through double spin asymmetries in *photon (plus jet)* and *J/ψ (plus jet)* production – requiring a polarized HERA proton beam – the projected statistical accuracies are found to be comparable to those predicted for the spin physics program at RHIC. In addition, significant results can be obtained on the long-standing unexplained spin asymmetries in elastic scattering.

Acknowledgements

The results presented above were obtained during a several weeks workshop in Zeuthen which was made possible thanks to the generous support of DESY-IfH Zeuthen. We are indebted to S. Brodsky and W. Vogelsang for useful discussions and helpful comments.

References

[1] W.-D. Nowak, DESY 96-095, hep-ph/9605411, to be publ. in the Proc. of the Adriatico Research Conference *"Trends in Collider Spin Physics"*, ICTP Trieste, Dec. 4–8, 1995.

[2] HERMES Coll., P. Green et al., HERMES Technical Design Report, *DESY-PRC 93/06*, July 1993.

[3] RSC Coll., *Proposal on Spin Physics using the RHIC Polarized Collider*, August 1992.

[4] E. Steffens, K. Zapfe–Düren, Proceedings of the *Workshop on the Prospects of Spin Physics at HERA*, Zeuthen, August 28-31, 1995, DESY 95–200, ed. by J.Blümlein and W.–D. Nowak, p.57.

[5] M. Anselmino et al., On Possible Future Polarized Nucleon–Nucleon Collisions at HERA, Internal Report, *DESY–Zeuthen 96–04*, May 1996.

[6] G. Bunce et al., *Particle World 3*, 1 (1992).

[7] X. Artru, J. Czyzewski and H. Yabuki, preprint LYCEN/9423 and TPJU 12/94, May 1994, hep-ph/9405426.

[8] M. Anselmino, M. Boglione and F. Murgia, Proceedings of the *XI International Symposium on High Energy Spin Physics*, Bloomington, Indiana, September 1994, ed. by K.J. Heller and S.L. Smith, p. 446.
M. Anselmino, M. Boglione, F. Murgia, *Phys. Lett. B 362*, 164 (1995).

[9] E704 Coll., D.L. Adams et al., *Phys. Lett. B 264*, 462 (1991).

[10] E704 Coll., D.L. Adams et al., *Phys. Lett. B 345*, 569 (1995).

[11] D. Kazakov et al., Proceedings of the 2nd Meeting on *Possible Measurements of Singly Polarized $p\vec{p}$ and $p\vec{n}$ Collisions at HERA*, Zeuthen, Aug.31–Sept.2, 1995, Desy Zeuthen Internal Report 95-05, ed. by H. Böttcher and W.–D. Nowak, p.43.

[12] L.E. Gordon, W. Vogelsang, preprint ANL-HEP-PR-96-15/RAL-TR-96-057, hep-ph 9607442, July 1996.

[13] T.K. Gehrmann and W.J. Stirling, *Phys. Rev. D53*, 6100 (1996).

[14] T.K. Gehrmann and W.J. Stirling, *Z.Phys. C65*, 461 (1994).

[15] A. Yokosawa, ANL-HEP-CP-96-22, to be published in the Proc. of the Adriatico Research Conference *"Trends in Collider Spin Physics"*, ICTP Trieste, Dec. 4–8, 1995.

[16] E.L. Berger and D. Jones, *Phys. Rev. D23*, 1521 (1981).
R. Baier and R. Ruckl,*Phys. Lett. B 102*, 364 (1981).

[17] F. Abe et al., *Phys. Rev. Lett. 69*, 3704 (1992)
F. Abe et al., *Phys. Rev. Lett. 71*, 2537 (1993).

[18] G.T. Bodwin, E. Braaten, and G.P. Lepage, *Phys. Rev. D51*, 1125 (1995).
G.P. Lepage et al., *Phys. Rev. D46*, 4052 (1992).

[19] P. Cho and A.K. Leibovich, *Phys. Rev. D53*, 6203 (1996).

[20] S. Gupta and K. Sridhar, TIFR/TH/96-04, hep-ph/9601349,
M. Beneke and I.Z. Rothstein, SLAC-PUB-7129, UCSD-96-05, hep-ph/9603400.

[21] L. Slepchenko and A.Tkabladze, hep-ph/9608296.

[22] N. Cacciari and M. Kramer, DESY 96-005, hep-ph/9601276,
J. Amundson, S. Fleming and I. Maksymyk, UTTG-10-95, hep-ph/9601298.

[23] S.V.Goloskokov and O.V. Selyugin,*Phys. Atom. Nucl. 58*, 1894 (1995).

Drell–Yan asymmetries at HERA-$\vec{\mathrm{N}}$

T. Gehrmann[a], W.J. Stirling[a,b]

[a] Department of Physics, University of Durham, South Road, Durham, UK
[b] Department of Mathematical Sciences, University of Durham, South Road, Durham, UK

Abstract: The production of Drell–Yan pairs in the double polarized mode of HERA-$\vec{\mathrm{N}}$ is studied at next–to–leading order in QCD. It is found that a measurement of this observable could yield vital information on the polarization of the light quark sea in the nucleon.

1 Introduction

Structure functions measured in deep inelastic lepton–nucleon scattering probe a particular combination of quark distributions in the nucleon. The mere knowledge of these structure functions is therefore insufficient for a distinction between valence and sea quarks and for a further decomposition of the light quark sea into different flavours. These are only possible if additional information from other experimental observables is taken into account.

Fits of unpolarized parton distributions (see for example [1]) obtain this information from two sources. The weak structure functions measured in neutrino–nucleon scattering probe different combinations of parton distributions than their electromagnetic counterparts. The inclusion of these structure functions in a global fit can therefore constrain the flavour structure of the unpolarized sea. A direct probe of the antiquark distributions in the nucleon is given by the production of lepton pairs in hadron–hadron collisions [2], the Drell–Yan process. It is in fact the inclusion of data from *both* processes in the global fits that leads to a precise determination of the distribution of antiquarks and its flavour decomposition.

Recent fits of polarized parton distributions [3, 4] have to rely entirely on the available data on the polarized structure function $g_1^{p,d,n}(x,Q^2)$. The distinction of valence and sea quark contributions to this structure function is possible to a certain extent if additional information from sum rules is taken into account. The flavour structure of the polarized sea is, however, completely unknown at present. It seems rather doubtful that more precise measurements of this structure function will be able to provide more information on these two issues.

Polarized neutrino–nucleon scattering experiments will not be feasible in the foreseeable future, although a measurement of polarized weak structure functions may be possible from charged current interactions at HERA [5] if polarization in the collider mode can be achieved.

An experimental study of the polarized Drell–Yan cross section would be possible with the HERA-$\vec{\mathrm{N}}$ experiment [6], operated with a polarized proton beam on a polarized nucleon target. We will examine the prospects of such a measurement in this article.

2 The polarized Drell–Yan process

The production of lepton pairs in hadronic collisions can be understood as annihilation of a quark–antiquark pair to a virtual photon, which decays into a lepton pair of invariant mass M^2. The polarized and unpolarized cross sections for this process are conventionally defined to be [7]

$$\mathrm{d}\Delta\sigma \equiv \frac{1}{2}\left(\mathrm{d}\sigma^{++} - \mathrm{d}\sigma^{+-}\right), \qquad \mathrm{d}\sigma \equiv \frac{1}{2}\left(\mathrm{d}\sigma^{++} + \mathrm{d}\sigma^{+-}\right),$$

where $(++)$ and $(+-)$ denote the configurations of aligned and antialigned hadron spins.

In the QCD–corrected parton model, these hadronic cross sections can be expressed as a convolution of parton–level coefficient functions with the appropriate parton distributions:

$$\begin{aligned}\frac{\mathrm{d}[\Delta]\sigma}{\mathrm{d}M^2} = \frac{4\pi\alpha}{9sM^2}\int_0^1 \mathrm{d}x_1\mathrm{d}x_2\mathrm{d}z\;\delta(x_1x_2z-\tau)\sum_q e_q^2 \\ \left\{\left\{[\Delta]q_1(x_1,M^2)\,[\Delta]\bar{q}_2(x_2,M^2)+(1\leftrightarrow 2)\right\}\left([-]\delta(1-z)+\frac{\alpha_s(M^2)}{2\pi}[\Delta]c_q^{DY}(z)\right)\right. \\ \left.+\left\{\left([\Delta]q_1(x_1,M^2)+[\Delta]\bar{q}_1(x_1,M^2)\right)\,[\Delta]G_2(x_2,M^2)+(1\leftrightarrow 2)\right\}\frac{\alpha_s(M^2)}{2\pi}[\Delta]c_G^{DY}(z)\right\}, \quad (1)\end{aligned}$$

with the scaling variable $\tau = M^2/s$. The parton distributions in the (not necessarily identical) hadrons are denoted by $f_{1,2}(x_i,M^2)$.

The next–to–leading order corrections to the unpolarized coefficient functions have been calculated in [8], and the polarized corrections are given in [7, 9]. It turns out that inclusion of these corrections is crucial at fixed–target energies, as they contribute about 30% of the total cross section. A fully consistent study of the Drell–Yan process at next–to–leading order was until now only possible in the unpolarized case, as the polarized parton distributions could only be determined to leading accuracy. With the recently calculated polarized two–loop splitting functions [10], the polarized distributions can now be determined to next–to–leading order from fits to structure function data [3, 4].

Using these distributions in combination with the unpolarized distributions (set A′) from [1], we have calculated the total Drell–Yan cross section $\mathrm{d}\sigma/\mathrm{d}M$ and the expected asymmetry

$$A(M) \equiv \frac{\mathrm{d}\Delta\sigma/\mathrm{d}M}{\mathrm{d}\sigma/\mathrm{d}M}$$

for proton and (idealized) neutron targets at centre–of–mass energies $\sqrt{s} = 40$ GeV (HERA–$\vec{\mathrm{N}}$) and $\sqrt{s} = 25$ GeV. The latter could be achieved by operating HERA-$\vec{\mathrm{N}}$ with a proton beam energy of about 330 GeV. Figure 1 shows the unpolarized Drell–Yan production cross section as a function of the invariant mass of the lepton pair. It should be noted that invariant masses $M \leq 4$ GeV and 9 GeV $\leq M \leq 11$ GeV must be excluded from the experimental measurement, as lepton pair production in these mass regions is dominated by the decay of quarkonium resonances. An experiment with $\sqrt{s} = 25$ GeV will clearly be restricted to the invariant mass range 4 GeV $< M <$ 9 GeV; depending on the available luminosity, a measurement for $M > 11$ GeV could be possible at $\sqrt{s} = 40$ GeV.

The Drell–Yan cross section at HERA–$\vec{\mathrm{N}}$ ($\sqrt{s} = 40$ GeV) is about two orders of magnitude larger than at RHIC–SPIN ($\sqrt{s} = 200$ GeV) when evaluated at fixed τ.

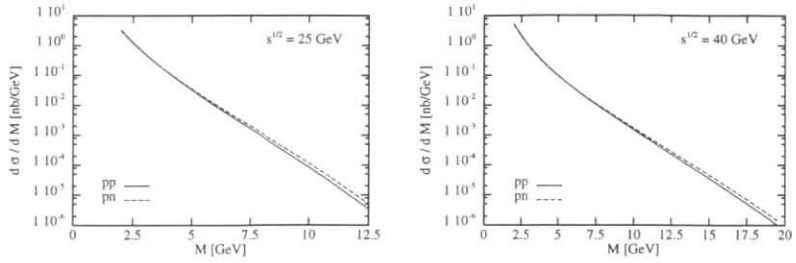

Figure 1: *Unpolarized Drell–Yan cross sections in proton–proton and proton–neutron collisions.*

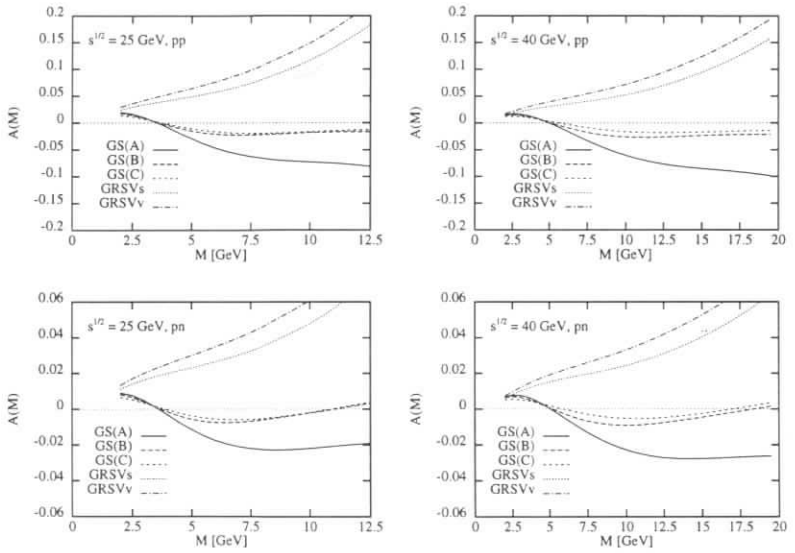

Figure 2: *Expected asymmetries in the polarized Drell–Yan process.*

Figure 2 shows the asymmetries obtained with the polarized NLO parton distributions of [3] (GS(A,B,C)) and [4] (GRSVs,v). The spread in these predictions reflects the present lack of knowledge on the behaviour of polarized sea quark distributions in the region $x > 0.1$. Not even the sign of the asymmetry at large M is predicted. A sizable asymmetry of more than $\pm 10\%$ can be expected in proton–proton collisions; the asymmetry in proton–neutron collisions is considerably smaller.

We have checked the perturbative stability of these results by varying the mass factorization scale; we find that the absolute value of the asymmetry is decreased (increased) by a maximum of 1.5% if we take $\mu_F = 2M$ ($\mu_F = M/2$). This variation is significantly smaller than the

difference between the different parton distribution functions.

3 Conclusions and Outlook

A measurement of the polarized Drell–Yan cross section in the double polarized mode of HERA-$\vec{\text{N}}$ appears feasible, given the anticipated luminosity of 240 pb^{-1} [6]. Such a measurement would provide important information on the polarization of the light quark sea at large x, a region which cannot be probed with measurements of polarized weak structure functions. Such a measurement would be unique to HERA-$\vec{\text{N}}$, as the polarized Drell–Yan process cannot be studied at the RHIC. Furthermore, HERA-$\vec{\text{N}}$ could measure Drell–Yan asymmetries off different targets, which could in principle be used to infer the flavour structure of the polarized sea. Such a measurement would however require much higher luminosity due to the small asymmetries on the (idealized) neutron target.

In this study we have only examined the invariant mass distribution of the Drell–Yan pairs, which is already able to discriminate different parametrizations for the polarized sea quark distributions. Even more information can be gained from more differential distributions (e.g. in the lepton–pair rapidity), which could be obtained with higher luminosity.

References

[1] A.D. Martin, R.G. Roberts and W.J. Stirling, Phys. Lett. **B354** (1995) 155.

[2] S.D. Drell and T.M. Yan, Phys. Rev. Lett. **25** (1970) 316; Ann. Phys. **66** (1971) 578.

[3] T. Gehrmann and W.J. Stirling, Phys. Rev. **D53** (1996) 6100.

[4] M. Glück, E. Reya, M. Stratmann and W. Vogelsang, Phys. Rev. **D53** (1996) 4775.

[5] M. Anselmino, J. Blümlein, P. Gambino, J. Kalinowski, N. Kochelev, M. Maul, A. Schäfer and T. Yamanishi, these proceedings.

[6] M. Anselmino, E. Andreeva, V. Korotkov, F. Murgia, W.-D. Nowak, S. Nurushev, O. Teryaev, and A. Tkabladze, these proceedings.

[7] P. Ratcliffe, Nucl. Phys. **B223** (1983) 45.

[8] G. Altarelli, R.K. Ellis and G. Martinelli, Nucl. Phys. **B143** (1978) 521; **B146** (1978) 544(E); **B157** (1979) 461.
J. Kubar-André and F.E. Paige, Phys. Rev. **D19** (1979) 221.
J. Kubar, M. le Bellac, J.L. Meunier and G. Plaut, Nucl. Phys. **B175** (1980) 251.

[9] B. Kamal, Phys. Rev. **D53** (1996) 1142.

[10] R. Mertig and W.L. van Neerven, Z. Phys. **C70** (1996) 637.
W. Vogelsang, Phys. Rev. **D54** (1996) 2023.

Study of the Pomeron Couplings in Diffractive Reactions at HERA

S.V.Goloskokov
BLTP, JINR, Dubna, Russia

The study of diffractive reactions has attracted considerable interest due to the observation of high p_t jets in diffractive collisions [1]. The diffractive high p_t jet production can be used as a test of the Pomeron structure. The question about the spin structure of the Pomeron arises for the reactions with polarized particles.

The Pomeron is a vacuum t-channel exchange that contributes to high-energy diffractive reactions. The Pomeron contribution to the quark-proton amplitude can be written in the form

$$T(s,t)^{A,B} = I\!P(s,t) V^{\mu}_{A I\!P} \otimes V^{B I\!P}_{\mu},$$

where $I\!P$ is a "bare" Pomeron contribution, $V_{A I\!P}$ and $V^{B I\!P}$ are the Pomeron vertices for particles A and B, respectively.

It has been shown that in models (see e.g. [2]) the Pomeron–proton vertex is of the form

$$V^{\mu}_{pp I\!P}(p,r) = mp^{\mu} A(r) + \gamma^{\mu} B(r), \tag{1}$$

where m is the proton mass.

The quark-Pomeron vertex has been calculated perturbatively [3]:

$$V^{\mu}_{qq I\!P}(r) = \gamma_{\mu} u_0 + 2m_q k_{\mu} u_1 + 2k_{\mu} \not{k} u_2 + i u_3 \epsilon^{\mu\alpha\beta\rho} k_{\alpha} r_{\beta} \gamma_{\rho} \gamma_5 + i m_q u_4 \sigma^{\mu\alpha} r_{\alpha}. \tag{2}$$

Here k is the quark momentum, r is the momentum transfer, m_q is the quark mass.

Note that in the cases (1,2) the spin-flip effects do not vanish as $s \to \infty$ in contrast to the standard Pomeron couplings in the models [4]

$$V^{\mu}_{hh I\!P} = \beta_{hh I\!P} \gamma^{\mu}. \tag{3}$$

The new form of the Pomeron couplings (2) should modify various spin asymmetries in high–energy diffractive reactions. The magnitude of the spin effects is connected with the ratio $m^2|A|/|B|$ for (1) or $m^2|u_3|/|u_0|$ for (2) found to be of the order $0.2-0.3$ for $|t|$ about few GeV^2. Thus, the spin effects may be not small. We shall discuss the effects which can be used in the future polarized diffractive experiments at HERA to study the spin structure of the Pomeron.

The transverse single spin asymmetry in polarized diffractive $Q\bar{Q}$ production in proton-proton scattering has been calculated in [5]. It was shown that the asymmetry is different for the standard and spin-dependent Pomeron vertex at the HERA-$\vec{N}$ energy $\sqrt{s} = 40GeV$ [6]. In

the first case it is about 5% and approximately constant; in the second case the asymmetry is larger than 7% and depends on the transverse momenta of the produced jet.

It was shown that the asymmetry obtained from the cross sections of diffractive $Q\bar{Q}$ production integrated over transverse momenta of the produced jet depends mainly on the Pomeron-proton coupling structure. It can be used for studying the spin structure of the proton-Pomeron coupling. The single-spin transverse A_N asymmetry in elastic pp scattering can be studied at HERA-$\vec{N}$ as a test of the spin dependence of the proton-Pomeron coupling too. The predicted asymmetry is about 10% for $p_T^2 = 4 - 5(GeV)^2$ [7]. Thus, the single-spin asymmetries can be very useful in the determination of the structure of Pomeron couplings.

The effects in diffractive deep inelastic scattering connected with the spin–dependent quark–Pomeron coupling have been studied. It was shown that the double longitudinal spin asymmetry in diffractive $Q\bar{Q}$ production for the standard quark–Pomeron vertex is very simple in form [8]

$$A_{ll} = \frac{y x_p (2-y)}{2 - 2y + y^2}. \tag{4}$$

This asymmetry is about 8% for $y = 0.7$ and $x_p = 0.1$. For the spin–dependent Pomeron coupling the asymmetry is dependent on $k_{\perp}^2$ of jets and smaller than for the standard Pomeron vertex, by about 5%.

The spin effects in diffractive reactions for the quark-Pomeron coupling in the form (1) have been studied in [9]. Strong sensitivity of asymmetries was found in diffractive meson production to the form of the Pomeron vertex at HERA energies.

We can conclude that the discussed single and double spin asymmetries depend strongly on the spin structure of the Pomeron coupling. However, to obtain the information about the Pomeron–coupling structure, the relevant asymmetries should be measured with an accuracy less than 1%. The values of cross sections in diffractive $Q\bar{Q}$ production are larger than $1000pb$, which permits one to perform these investigations at the integrated luminosity about $200(pb)^{-1}$. So, the diffractive polarization experiments at HERA allow one to study spin properties of quark-Pomeron and proton-Pomeron vertices. This gives an important test of the spin properties of QCD at large distances.

References

[1] ZEUS Collaboration, M.Derrick et al. Z.Phys. **C68** (1995) 569; H1 Collaboration, T.Ahmed et al, Phys.Lett. **B348** (1995)

[2] C.Bourrely, J.Soffer, T.T.Wu, Phys.Rev. **D19** (1979) 3249; S.V.Goloskokov, S.P.Kuleshov, O.V.Selyugin, Z.Phys. **C50** (1991) 455.

[3] S.V.Goloskokov, Phys.Lett. **B315** (1993) 459.

[4] E.A.Kuraev, L.N.Lipatov, V.S.Fadin, Sov.Phys. JETP **44** (1976) 443; P.V.Landshoff, O. Nachtmann, Z.Phys. **C35** (1987) 405.

[5] S.V.Goloskokov, Phys. Rev. **D53** (1996) 5995.

[6] W.-D.Nowak, in AIP conference proceedings 343 on High Energy Spin Physics, eds. K. J. Heller and S. L. Smith, Woodbury, NY (1995), p.412.

[7] S.V.Goloskokov, O.V. Selyugin, Phys. Atom. Nucl. **58** (1995) 1894.

[8] S.V.Goloskokov, E-prints: hep-ph 9604261.

[9] J.Klenner, A.Schäfer, W.Greiner, Z. Phys **A352** (1995)203

Spectator tagging in electron deuteron scattering and the measurement of the Bjorken Sum Rule

Michael Düren
Phys. Inst. der Univ. Erlangen-Nürnberg,
Erwin-Rommel-Str. 1, D-91058 Erlangen, Germany
E-Mail: DUEREN@VXDESY.DESY.DE

Abstract: The tagging of spectator nucleons in polarised and unpolarised electron deuteron scattering offers the possibility to measure proton and neutron structure functions separately in the same nuclear environment. In contrast to fixed target experiments, the spectator in collider mode has large momentum and is therefore rather easy to measure. In a polarised deuteron beam proton and neutron are both polarised. Tagging offers the ideal figure of merit, superior to any subtraction method of H, D and ^{3}He beams. As the proton and neutron asymmetries are measured simultaneously in one experiment many systematic uncertainties cancel and provide optimal conditions to measure the Bjorken Sum Rule. From the machine point of view, the acceleration of polarised deuterons compared to protons has both advantages and difficulties. It is not clear if deuteron polarisation can be handled at high beam energies. It might turn out that a common solution to the luminosity and polarisation problems is to significantly reduce the HERA deuteron energy.

1 Physics Motivation

HERA is a tool to investigate the structure of the nucleon. For a complete picture of the nucleon the scattering off protons alone is not sufficient, a neutron target is required. In unpolarised fixed target experiments, the neutron structure functions are derived from the difference of deuterium and hydrogen scattering processes. Nuclear effects in the deuteron are small. For nuclei with higher atomic mass nuclear effects become larger. They are known as the nuclear EMC effect.

In polarised DIS in a similar fashion the difference of the deuterium and hydrogen spin asymmetries are used to derive the neutron spin structure functions. The spins of proton and neutron in a vector polarised deuteron are aligned parallel. However, there is an approximately 5% D-state probability in the deuteron wave function which has to be taken into account in the derivation of the neutron spin structure function. In polarised DIS there is an alternative possibility to derive the neutron spin structure by using a ^{3}He target. The ^{3}He nucleus contains two anti-aligned proton spins. The ^{3}He spin asymmetry is directly related to the neutron spin. This is strictly true only for the S-state of the ^{3}He wave function. With about 10% probability the nucleus is in the S'- or D-state. In these states the spin asymmetry is dominated by

the proton spin. In principle a 'spin-nuclear' EMC effect, i.e. the modification of the spin distributions of quarks in nuclear matter, may add some uncertainty to the measurement.

Spectator tagging in deuteron scattering offers a unique experimental approach to measure differences of the proton and neutron scattering, i.e. to measure non-singlet distribution functions. Spectator tagging means that the nucleon which is not involved in the DIS scattering process is identified in the detector, so that for every DIS event on deuteron it is experimentally known if it happened in the proton or the neutron. This method cannot or can only very poorly be applied to fixed target experiments as the momentum of the spectator in the rest frame of the deuteron is defined by its nuclear Fermi momentum, i.e. it is in the 100 MeV range.

The situation is completely different in a collider experiment. The spectator is boosted to half of the beam energy and can in principle be easily detected. For an 820 GeV deuteron beam the spectator proton has a momentum of 410 GeV and is separated from the electron and deuteron beams by the first dipole field as shown in figure 1. The 410 GeV neutron spectator is not bent and can be detected in a neutron calorimeter downstream the interaction point.

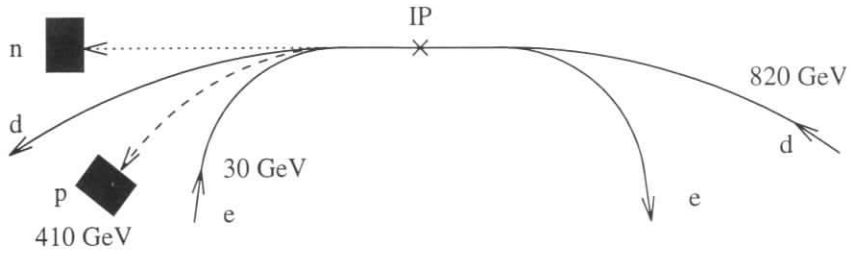

Figure 1: *The spectator nucleon in electron deuteron scattering at HERA can be detected in coincidence with the deep inelastic event. The proton and neutron tagging offers the possibility to measure proton and neutron spin structure functions simultaneously without switching targets.*

Tagging a polarised deuteron beam allows the measurement of the fundamental Bjorken Sum Rule in one nuclear environment and in one single experiment without switching targets. It has been pointed out that a precision measurement of the QCD corrections involved in the Bjorken Sum Rule allows a determination of the QCD coupling constant $\alpha_s(Q^2)$ [1]. The verification of the running of α_s with Q^2 and the comparison with results from jet physics would be fundamental tests of the standard model.

The spectator tagging method can be extended by measuring the angle and momentum of the spectator and correlating it to the kinematics of the DIS process. This way semi-inclusive (spin-)structure functions can be obtained which contain information about the nuclear structure of the deuteron. By comparing the results with the known structure functions of the free proton, nuclear corrections can be tested and possible new nuclear effects can be measured.

2 Experimental Aspects

The most striking advantage of the spectator tagging in polarised deuteron scattering is the high figure of merit which can be obtained. Assuming the Ellis-Jaffe Sum Rule for proton

and neutron and the Bjorken Sum Rule should be measured in the experiment. The precision which can be obtained is compared for the following three scenarios: deuteron tagging (I), p/d subtraction (II) and p/^{3}He subtraction (III). The maximal achievable polarisation and luminosity may be different for the different beams but due to lack of better knowledge it is assumed that the polarisation is identical and that the luminosity $\mathcal{L}_c$ (in units of charge/cm^2/s) is (1 : 0.5 : 0.5) for the proton compared to the deuteron and ^{3}He beam. The nucleonic luminosity $\mathcal{L}_n$ (in units of nucleons/cm^2/s) which is relevant for the number of DIS events is then (1 : 1 : 0.67). In order to have the same statistical error on the neutron as on the proton asymmetry the following data taking times are required approximately:

deuteron tagging (I): 2 time units deuteron beam with half of the data protons and neutrons.

p/d subtraction (II): 3 time units proton beam, 6 units deuteron beam. The error on the neutron asymmetry is derived according to $\delta A_1^n \approx \sqrt{(2\delta A_1^d)^2 + (\delta A_1^p)^2}$.

p/^{3}He subtraction (III): 1 time unit proton beam and $3^2/0.67 = 13.5$ time units on ^{3}He. The factor 3^2 comes from the dilution of the neutron asymmetry by the two unpolarised protons in ^{3}He.

To conclude: the time required for the same statistical precision on the spin asymmetries for proton and neutron is (1 : 4.5 : 7.25) for the scenario (I : II : III). Statistically, the deuteron tagging method is clearly favoured.

Assuming 100% tagging efficiency the advantages of deuteron tagging in systematics are obvious:

- proton and neutron are measured in one experiment, without changing targets, with identical luminosity, with identical beam polarisations, with identical acceptance and efficiency for the registration of the DIS event.
- the CMS energy of the electron nucleon system are the same for proton and neutron in case of deuteron tagging. It is important to mention that that is not the case for the p/d or p/^{3}He subtraction methods if the beam energies are the same for the p, d and ^{3}He beams. Each nucleon carries only a fraction of the beam energy, i.e. the nucleon in ^{3}He carries only a third of the energy compared to the nucleon in the proton beam. This leads to completely different energies and angles of the DIS event in the lab frame for a given x and Q^2. On the other hand, if one wants to keep the lab kinematics identical, the beam energies of the p, d and ^{3}He beams have to be different and therefore the polarisation, the luminosity and the luminosity measurement will be very different, leading possibly to large systematic errors in the subtraction methods (II) and (III).
- The nuclear environment of proton and neutron are identical in the tagging method (III). Therefore some of the nuclear effects will cancel in the ratio of the proton and neutron cross sections and asymmetries. The remaining nuclear effect can be determined by the comparison with the results from the free proton. If the tagging detectors have the possibility to measure the momentum and angle of the spectator, nuclear effects can be checked by selecting special kinematics, e.g. spectators at rest in the deuteron rest system or spectators at the tails of the nuclear momentum distributions.

All the above considerations assume that the DIS scattering occurs incoherently on one of the two nucleons of the deuteron and that the tagging efficiency is 100%. Both assumptions are certainly not strictly true. The incoherent scattering on nucleons does not necessarily apply at very low x and to diffractive events. This is however a generic feature of the scattering process and is also present in the subtraction methods (II) and (III). It is not necessary a limitation but can be regarded as a possibility to learn about nuclear structure especially if the momentum of the spectator is measured. Additionally, diffractive events can be identified by a rapidity gap in the hadronic final state.

The tagging efficiency has physics and technical limitations. In first order, tagging inefficiencies cancel when the spin asymmetry is formed, as long as the tagging efficiency is spin independent. However the asymmetry may be diluted by other processes. The physics limitations come from the fact that charge exchange and diffractive processes may dilute a clean DIS tagging. Detailed Monte-Carlo corrections are needed to take these processes into account. Technical limitations come from the restrictions in space due to machine elements, from particle background and from the beam divergence. The scattering angle of the spectator is below 0.2 mrad for a typical Fermi-momentum of 100 MeV/c. Due to the divergence of the beam at the interaction point the angular distribution is smeared. This limits the possibility to precisely determine the transverse Fermi momentum of the spectator. The longitudinal momentum of the Fermi motion is boosted with the γ factor of the beam. This makes is rather easy to measure. A ± 100 MeV/c longitudinal motion translates to a spectator energy of 410 ± 41 GeV. The precision with which the spectator momentum can be determined depends on the energy spread of the machine ($\sim 1\%$) and the resolution of the spectator detector.

The design of the neutron spectator detector is rather simple, it just requires a neutron calorimeter downstream the interaction point with the possibility to identify neutrons compared to charged particles and photons. The calorimeter has to be able to handle background from photoproduction. The design of the proton detector is more complicated. The protons are bent by the first separation fields of the off-axis HERA quadrupoles. In the current beam lattice the spectators with large transverse Fermi momentum are bent by the quadrupole components and cannot be properly separated. The existing proton detectors of ZEUS and H1 have an insufficient acceptance for the spectators. A clean separation of the proton spectators from the deuteron beam requires a special design of the interaction region. The optimal solution would be a dipole separation without quadrupole components. This dipole field could be part of the spin rotator and would be used as spectrometer magnet for the momentum measurement of the proton spectator at the same time.

3 Machine Aspects

The injection and acceleration of polarised protons and the maintenance of polarisation at HERA energies is regarded as a very difficult task which is currently being studied in detail. The task to produce longitudinally polarised deuterons at HERA is certainly very different. If it is easier or more difficult is hard to predict as there is not much experimental and theoretical experience with polarised deuterons. The reason why it is so different is due to the small gyromagnetic anomaly of the deuteron $(g_d - 2)/2 = -0.14$ compared to the proton $(g_p - 2)/2 = 1.79$. This leads to the effect that the number of depolarising resonances, which are the main difficulty in the proton polarisation, is reduced by a factor of 25. The deuteron spin tune at 820 GeV

is only $\nu_s = 62$ for the deuteron compared to $\nu_s = 1600$ for the proton. The spin tune of the deuteron beam is similar to the spin tune of electrons at 27.5 GeV ($\nu_s = 62.5$) which have been successfully polarised at HERA.

The main difficulty of a polarised deuteron beam is the manipulation of the spin. A spin rotator or a Siberian snake requires much stronger magnetic fields for deuterons than for protons, again due to the small gyro-magnetic anomaly. As the spin tune of the deuteron and the electron beam are similar, the geometry of the rotator bump could be similar too as it is only determined by the spin tune of the beam and not by its energy. Therefore a design like the HERA-e mini-spin rotators would allow to rotate the deuteron spins by 90° if the warm coils would be replaced by strong superconducting magnets.

Due to the smallness of the spin tune, it might be that a deuteron beam would not require Siberian snakes, however this has to be studied in detail.

4 Conclusions

The tagging of proton and neutron spectators in unpolarised and polarised electron deuteron scattering offers unique possibilities to study the difference of DIS cross sections and asymmetries in proton and neutron. The tagging offers a statistical figure of merit which is superior by a factor of about 5...7 for the measurement of the proton and neutron Ellis-Jaffe and Bjorken Sum Rules. The experimental conditions are ideal in the sense that proton and neutron can be measured in the same nuclear environment with identical experimental conditions. The main concern is the question how efficient the tagging is and whether it is possible to maintain high deuteron polarisation at HERA. First experiences were obtained at the KEK-PS where polarised deuteron beams have been successfully accelerated in a storage ring up to an energy of 10.2 GeV.

Concerning the aim to measure the Bjorken Sum Rule and the spin structure functions at small x ($x < 0.01$) with high precision, in principle the high energies at HERA are not needed. If it would be possible to collide the polarised HERA electrons at 27.5 GeV with polarised deuterons at 10...40 GeV, the center of mass energy would be large enough to cover the relevant kinematic range ($s = 1100...4400$ GeV^2). The energy would also be still high enough for gluon spin studies using jet and charm production. At these energies also deuteron polarisation is a much smaller problem and electron cooling of the stored deuterons and/or continuous injection of deuterons into the storage ring would possibly allow for low emittance and high luminosity. As the DIS cross section increases at lower energy, a much higher statistical precision could be obtained.

Acknowledgments

I would like to thank D. Barber, M. Karliner, M. Krasny, K. Rith, A. Schäfer and T. Sloan for their comments.

References

[1] J. Ellis and M. Karliner, Phys. Lett. **B341** (1995) 397;
J. Ellis, E. Gardi, M. Karliner, Phys. Lett. **B366** (1996) 268.

Nuclear effects in extraction of $g_{1n}(x, Q^2)$ at small x

M. Strikman

Pennsylvania State University, University Park, PA, USA

Abstract: We consider nuclear structure uncertainties in extraction of $g_{1n}(x, Q^2)$ from inclusive $\vec{l}$-$\vec{D}(^3\vec{H}e)$ data at small x. Theoretical uncertainties in extraction of g_{1n} from $\vec{l}\vec{D}$ data are small as far as $g_{1n}(x, Q^2) \approx -g_{1p}(x, Q^2)$ at small x. In case of ^3He combination of effects of the spin depolarization, interaction with nonnucleonic degrees of freedom, and nuclear shadowing is likely to reduce $g_{1^3\mathrm{He}}(x \leq 0.05)$ by $\sim 15\%$ and significantly enhance $g_{1^3\mathrm{He}}$ at $x \sim 0.1$.

1 Introduction

Knowledge of g_{1n} at small x is crucial for learning whether currently observed experimentally regime of dominance of nonsinglet contribution to $g_{1N}(x, Q^2)$ would be followed by dominance of singlet contribution at $x \leq 10^{-3}$. Measurement of $g_{1n}(x, Q^2)$ involves use of polarized deuterium and ^{3}He targets. Hence one has to address two question: How large are nuclear effects for $g_{1A}(x, Q^2)$? What is theoretical uncertainty in evaluation of these effects? We focus here on the region of small x which is relevant for this workshop. In this kinematics three major effects are present: (i) spin depolarization due to presence of higher orbital states in nuclei, (ii) nonnucleonic degrees of freedom in nuclei, (iii) nuclear shadowing.

2 Spin depolarization and Fermi motion

In the many-nucleon approximation where non-nucleonic degrees of freedom in nuclei and nuclear shadowing are neglected the Fermi motion, and the relativistic spin rotation effects are small at $x \leq 0.5$ [1]. As a result, the static approximation expression for the deuteron

$$g_{1^2H}(x, Q^2) = (1 - \frac{3}{2}P_D)(g_{1p}(x, Q^2) + g_{1n}(x, Q^2)) \tag{1}$$

provides very good approximation for $x \leq 0.5$. Here $P_D = 6 \pm 1\%$ is the probability of the D-wave in the deuteron. Similarly, in the case of $A = 3$ target approximately 8% depolarization effect is present. It is due to depolarization of the neutron (which in the case of S-wave ^{3}He would be 100% polarized), and from a small proton polarization [2, 3, 4, 5].

3 Nonnucleonic degrees of freedom

The EMC effect has unambiguously demonstrated that nonnucleonic degrees of freedom are present in nuclei, though this effect does not allow to identify what particular nonnucleonic degrees of freedom are responsible for the effect. However the EMC effect is small for $0.05 < x < 0.3$, so naively one would expect that such effects are not important in extraction of g_{1n} at medium and small x. It is possible to check the relevance of nonnucleonic degrees of freedom by considering the ratio of the Bjorken sum rules for the $A = 3$ and $A = 1$ systems. The QCD corrections to the sum rule which are proportional to $\alpha_s^n(Q^2)$ cancel out and one obtains:

$$R = \frac{\int_0^1 [g_1^{^3He}(x, Q^2) - g_1^{^3H}(x, Q^2)]dx}{\int_0^1 [g_1^n(x, Q^2) - g_1^p(x, Q^2)]dx} = \frac{G_A(^3\mathrm{H})}{G_A(n)}, \tag{2}$$

independent of Q^2, where we have ignored the higher twist effects. Nonrelativistic expression for $R = P_S - \frac{1}{3}P_{S'} + \frac{1}{3}P_D = 1 - (0.0785 \pm 0.0060)$ is perfectly consistent with the standard nonrelativistic expression for $G_A(^3\mathrm{H})$. However both these relations contradict the data: $\frac{G_A(^3\mathrm{H})}{G_A(n)} = 1 - (0.0366 \pm 0.0030)$.

Hence we conclude that *the use of the convolution model, combined with the 3-nucleon description of $A = 3$ nucleon system, leads to a $\sim 4\%$ violation of the Bjorken sum rule for the scattering of the $A = 3$ systems.* This is consistent with the general expectation that noticeable nonnucleonic degrees of freedom should be present in the $A = 3$ systems. Inconsistency of the convolution models and three nucleon description of $A = 3$ system with the Bjorken sum rule was first pointed out in Ref.[6].

We observe that consistency of nonrelativistic results for the Bjorken sum rule and the G_A ratio can be used as a guide to identify what nonnucleonic effects are responsible for the discrepancy in eq.2 [7]. Current analyses of $G_A(^3H)$ indicate that the major nuclear correction to the impulse approximation calculation of $G_A(A = 3)$ is due to $\Delta \to N$ transitions. Thus a natural mechanism for resolving the discrepancy between the Bjorken sum rule for $A = 3$ and for $A = 1$ targets which is present in the impulse approximation, is the necessity to account for the nondiagonal transitions $\gamma^* N \to \gamma^* \Delta$. No theoretical investigations of this structure function have been done as yet. For the simple case of $g_{1n}^{n.s.}$ one can expect the same low x behavior for this structure function as for the diagonal transitions since Regge trajectories with rather close value of intercept couple in this case. Based on $SU(6)$ symmetry, for average $x \sim 0.2 \div 0.3$ we can expect a behavior similar to the diagonal nonsinglet matrix elements. Consequently, we estimate that the contribution of the $\gamma^* N \to \gamma^* \Delta$ transition to $g_{1,A=3}^{n.s.}$ leads to a change in the ratio $\frac{g_{1,A=3}^{n.s.}(x,Q^2)}{g_{1N}^{n.s.}(x,Q^2)}$ for $x \leq 0.5$ from 1-(0.0785 ± 0.0060) to $G_A(^3\mathrm{H})/G_A(n) = 1 - (0.0366 \pm 0.0030)$. Moreover, treating the Δ-admixture as a perturbation we observe that main contribution to g_1 should originate in the ^{3}He case from the $n \to \Delta^0$ nondiagonal transition and in the ^{3}H case from the $p \to \Delta^+$ nondiagonal transition. In the $SU(6)$ limit, which seems reasonable at least for the valence quark contribution [1] $g_{1\ n\to\Delta^0}(x, Q^2)/g_{1n}(x, Q^2) = g_{1\ p\to\Delta^+}(x, Q^2)/g_{1p}(x, Q^2)$. Thus up to a small correction due to contribution of $g_{1p}(x, Q^2)$ combined effect of nucleon depolarization and nondiagonal contributions is approximately the same for $g_{1,^3He}(x, Q^2)/g_{1n}(x, Q^2)$ and for $g_{1,A=3}^{n.s.}(x, Q^2)/g_{1N}^{n.s.}(x, Q^2)$. We can write in this approximation

$$g_{1^3He}(x, Q^2) = \frac{G_A(^3H)}{G_A(n)} g_{1n}(x, Q^2) + 2p_p(g_{1p}(x, Q^2) + g_{1n}(x, Q^2)), \tag{3}$$

where $p_p \approx -2.8\%$ is polarization of a proton in ^{3}He. We neglect here contribution of $\Delta^+ \to p$ nondiagonal terms since they effectively result merely in the renormalization of p_p by a factor $\sim \frac{G_A(^3H)}{G_A(n)}$. Experimentally, $|g_{1p}(x, Q^2) + g_{1n}(x, Q^2)| \ll |g_{1n}(x, Q^2)|$, $|g_{1n}(x, Q^2)|$ for $x \leq 0.1$ and hence the last term for these x is a very small correction. In the sea region g_{1N} and $g_{1N\to\Delta}$ may have different x dependence. This leads to $\leq 4\%$ theoretical uncertainty in extraction of $g_{1n}(x \leq 0.05)$

Overall, the uncertainties in extraction of g_{1n} from this source due to poor knowledge of x dependence of nondiagonal matrix elements is likely to be of the order 4% for small x. For the deuteron case this effect is much smaller since nonnucleonic degrees of freedom are significantly smaller and also ΔN admixture is forbidden. 860

[1] Note that the SMC semi-inclusive data indicate that the sea contribution to g_1 is small down to $x \sim 0.01$.

4 Nuclear shadowing effects

At small x, when the coherence length $l = \frac{1}{2m_N x}$ far exceeds the nucleus radius, the virtual photon converts to a quark-gluon configuration h well before the target. In the case of nucleon targets this leads to diffraction in deep inelastic scattering which has recently been observed at HERA. For the nuclear targets this leads to the shadowing phenomenon which is well established experimentally, for review and references see report of Group 8.

The phenomenon of shadowing reflects the presence of quark-gluon configurations in γ^* which can interact with cross sections comparable to that of hadrons. A quantitative description of nuclear shadowing phenomenon in deep inelastic scattering was developed in the color screening models, where γ^* converts to a quark-gluon state h which interacts with the nuclear target via multiple color singlet exchanges. The effect of shadowing is determined in these models primarily by the value of the ratio $\sigma_{eff} = \frac{\langle\sigma^2\rangle}{\langle\sigma\rangle}$, where averaging is taken over different strengths of interaction, that is, over different quark-gluon configurations involved in the transition $\gamma^* \to$ "*hadron state*". Numerical analyses of nuclear shadowing for $A \geq 12$ give $\sigma_{eff} \sim 17\ mb$. Similar number follows from the estimate based on the generalization of the optical theorem to the diffractive processes $\sigma_{eff} = \frac{16\pi \frac{d\sigma(\gamma^*+p\to X+p)}{dt}|_{t=0}}{\sigma_{tot}(\gamma^*+p)}$. As soon as this parameter is fixed all color singlet models give very similar results for $x \ll \frac{1}{4m_N R_A}$ especially for light nuclei.

It follows from the formulae of the eikonal-type approximation that for the case of cross sections which constitute a small fraction of the total cross section, the shadowing effects should be larger. Several examples include shadowing in the parity violating $\vec{p}A$ scattering [8] and shadowing for valence quarks [9]. The same is true for shadowing of g_{1A} [7]. For light nuclei like ^{2}H and ^{3}He the screening effect for g_{1A} is ≈ 2 larger than for F_{2A}. Numerically, we find the reduction effect due to shadowing is $g_{1^3He}(x,Q^2)/g_{1n}(x,Q^2) \sim 0.90$, and $g_{1^2H}(x,Q^2)/(g_{1p}(x,Q^2)+g_{1n}(x,Q^2)) \sim 0.96$, with spin depolarization effects and nonnucleonic degrees of freedom effects entering multiplicatively. This estimate probably has 50% uncertainty due to due to uncertainties in the value of the real part of the spin dependent amplitude, and spin dependent diffraction, etc. The Bjorken sum rule indicates that shadowing effects generate an enhancement of $g_{1A}(x,Q^2)$ at $x \sim 0.1$. Overall one expects significant modifications of $g_{1,A=3}$ for $x \leq 0.15$, see Fig.1.

To summarize, at small x nuclear corrections lead to

$$\frac{g_{1^3He}(x,Q^2)}{g_{1n}(x,Q^2)} \sim 0.87 \pm 0.07; \quad \frac{g_{1^2H}(x,Q^2)}{g_{1p}(x,Q^2)+g_{1n}(x,Q^2)} \sim 0.86 \pm 0.04, \tag{4}$$

with errors reflecting our guess of the theoretical uncertainties involved in calculating discussed nuclear effects. Smaller error in the deuteron case reflects smaller shadowing effects and suppression of nonnucleonic degrees of freedom due to smaller energy binding and zero isospin which forbids $N\Delta$ states. Hence in the discussed x-range ^{2}H targets may have certain advantages in terms of theoretical uncertainties. Besides, in the first approximation, experimentally $g_{1p}(x,Q^2) \approx -g_{1n}(x,Q^2)$ for $x \sim 10^{-2}$ in which case shadowing does not affect the extraction of g_{1n} from the g_{1d} data and does not lead to noticeable enhancement effects at $x \sim 0.1$. If, on the other hand, at very small $x \sim 10^{-3}$ g_{1n} and g_{1p} become comparable, theoretical uncertainty in extraction of g_{1n} would be $\sim 8\%$. Experimental error is usually larger in the deuteron case since one has to combine experimental measurements of g_{1d} and g_{1p}.

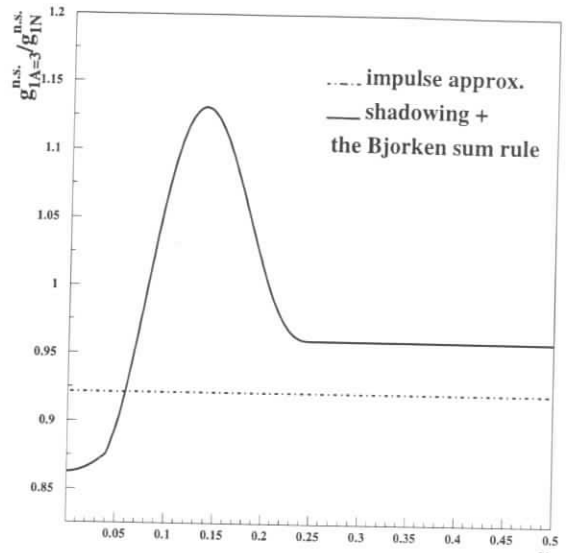

Figure 1: $g^{n.s.}_{1A=3}/g^{n.s.}_{1N}$ as a function of x. Dash-dotted curve is nonrelativistic calculation of Refs.[2-5]. The solid curve is result of calculation [7] which includes nuclear shadowing, spin depolarization, $\Delta \to N$ nondiagonal contributions, and the Bjorken sum rule constraint.

Note also existence of specific nuclear effect for the scattering off the polarized deuteron, which is analog of the Germond and Wilkin effect [10] for $\pi\vec{d}$ total cross sections: due to the presence of D-wave in the deuteron, the cross section of shadowing for scattering off deuteron with helicities $\lambda_d = \pm 1$ and $\lambda_d = 0$ differs leading to approximately 1% difference of the cross sections of unpolarized electron scattering off the deuteron in different helicity states for $x \leq 10^{-2}$ [11]. Experimental study of this effect would check the basic ideas about mechanism of nuclear shadowing. Unfortunately, the effect is quite small making its measurement nearly impossible.

References

[1] L. Frankfurt and M. Strikman, Nucl.Phys. A405, 557 (1983).
[2] R.Blankleider and R.M.Woloshin, Phys.Rev. **C29** 538 (1984).
[3] J.L.Friar et al, Phys. Rev. **C42**,2310 (1990).
[4] C. Ciofi degli Atti, S. Scopetta, E. Pace, and G. Salme, Phys.Rev. **C48**, 968 (1993).
[5] R.W.Schultze and P.U.Sauer, Phys.Rev. **C48** 38 (1993).
[6] L.P. Kaptari, A.Yu. Umnikov, Phys.Lett. **B240** 203 (1990).
[7] L.Frankfurt, V.Guzey and M.Strikman, Phys.Lett.**B381** 379 (1996).
[8] L.L.Frankfurt, M.I.Strikman, Phys.Lett.**107B**,99 (1981); Progr.Part.Nucl.Phys,**27**, 135 (1991).
[9] L. L. Frankfurt, M. Strikman, Phys.Rep.**160**, 235 (1988); Nucl.Phys.**B316**, 340 (1989).
[10] J.F.Germond and C.Wilkin, Phys.Lett. **B59B**,317 (1975).
[11] M.Strikman, in Proceedings of Symposium "Internal Spin structure of the nucleon",Jan. 1994, Eds, V.H.Hughes, C.Cavata, p.153, World Scientific,1995.

An Absolute Polarimeter for the Measurement of the Proton Beam Polarization at HERA

N. Akchurin[a], W.-D. Nowak[b], S.B. Nurushev[c,1], A. Penzo[d], A.G. Ufimtsev[c]

[a] *University of Iowa, Iowa City, USA;* [b] *DESY-IfH, 15738 Zeuthen, Germany;*
[c] *IHEP, 142284 Protvino, Russia;* [d] *INFN and University of Triest, Trieste, Italy.*

Abstract: It is proposed to build an absolute Coulomb-Nuclear Interference (CNI) polarimeter for measuring the proton beam polarization at HERA. An alternative use of a polarized (unpolarized) proton beam with an unpolarized (polarized) jet target would allow to determine the beam polarization with about 5% accuracy free of theoretical uncertainties. Consistency checks of polarization measurements would be done by using different combinations of beam and target polarization. Several realization schemes of such a polarimeter are discussed.

The beam polarization in a polarized HERA proton ring should be measured and monitored either continuously or frequently during the experimental runs. There are three stages to be considered during acceleration [1]:
- Filling the HERA ring by polarized protons of 38 GeV
- Acceleration from injection energy of 38 GeV up to the final energy of E_{fin} = 820 GeV
- Colliding regime. This is the main regime for running experiments.

The proton beam filling time is about 120' including 30' for accumulation at 38 GeV. We have to be able to check the beam polarization at this stage before ramping up the energy. The acceleration from 38 GeV to 820 GeV passes several steps and takes about 40'÷50'. This stage is crucial for initial tuning of the beam polarization, since the strongest depolarization resonances are to be crossed. From the polarimetry point of view it is desirable to maintain the intermediate plateau in the magnetic field during about 30' or more to reach the necessary precision in beam polarization measurements. A point of interest is at 200 GeV, where the E704 experiment discovered a large analyzing power in inclusive pion production [2 ÷ 4]. A relative pion polarimeter might be used for rapidly checking the polarization of the internal beam at this specific point (or at 820 GeV, if a dedicated nucleon-nucleon polarization experiment, like HERA-$\overrightarrow{N}$ [5], would have delivered calibration data, already). Another important feature desirable to be implemented at HERA is the possibility to decelerate the beam, say from 820 GeV to 200 GeV, in order to check the consistency of the spin depolarization theory. For example, the correct siberian snake function presumes the conservation of beam polarization in acceleration and deceleration processes, which might be checked directly by this method.

Possible polarimeters, both absolute and relative ones, and their figures of merit have been discussed elsewhere [6 ÷ 8]. As concerns HERA, we discuss in the following several scenarios for an absolute CNI polarimeter [9]:

Scenario 1: CNI polarimeter with detection of only recoil protons.

Scenario 2: CNI polarimeter with detection of only forward particles. It appears to be very attractive since this approach may allow to gain one or even two orders of magnitude in the azimuthal acceptance, $\Delta\ \phi\ /(2\ \pi)$, compared to the previous case.

Scenario 3: CNI polarimeter with detection of both protons. Evidently, in this case the time of polarization measurements will be of the same order as for scenario 1, but the events will be cleaner due to smaller background.

[1] *e-mail: nurushev@mz.ihep.su*

In fact, all three scenarios might be operated in parallel if three separate triggers were realized. In order to avoid any theoretical uncertainty we intend to perform the polarization measurement in two steps: In the first step we measure (calibrate) the analyzing power by using the unpolarized beam and a polarized target. In the second step, knowing the analyzing power from the previous experiment, we determine the beam polarization by measuring the left-right asymmetry with the polarized beam and an unpolarized target.

If, instead, both beam *and* target are polarized such a measurement constitutes an independent way of measuring the beam polarization gaining an additional factor 2 in running time. Simultaneously the observable A_{NN} may be measured in this case, too.

Scenario 1 has several advantages:
- It is simple and occupies little space around the polarimeter target, only. Several solid state detectors would be used for measuring the coordinate and energy of the recoil particle
- It is a fast and reliable detector as it was demonstrated in an experiment [10]
- It is not sensitive to the initial energy
- No severe constraints are imposed on the beam parameters

To calculate the statistical accuracy for scenario 1 we consider two versions: i) *Realistic version* [5]: Unpolarized beam of I = 80 mA, polarized jet target of density $n = 3 \cdot 10^{13}\ atoms/cm^2$. The luminosity is $L = 1.5 \cdot 10^{31}\ cm^{-2} \cdot s^{-1}$. In the region of interest $t = 10^{-3} \div 10^{-2}\ GeV^2$, the average differential cross-section is $d\sigma/dt = 80\ mb/GeV^2$ and the mean value of the analyzing power is $A_N = 3\%$. The geometrical acceptance for a one arm apparatus is $\Delta\ t = 10^{-2}(GeV/c)^2$, $\Delta\ \phi\ /(2\pi) = 4.5 \cdot 10^{-3}$. The anticipated combined trigger and reconstruction efficiency is assumed to be 50%. Then the counting rate is expected to be N = 27 ev/s and the CNI analyzing power of $\Delta A_N/A_N = \pm 5\%$ precision may be reached during 7 hours of data taking assuming $P_T = 0.8$ as target polarization. ii) *Optimistic version*: Unpolarized proton beam of I=160 mA (which is one goal of the HERA upgrade program), polarized jet target of density $n = 10^{14}\ atoms/cm^2$ (which is acceptable according to [11]), and addition of a second recoil arm. Finally we gain a factor $\kappa = 2 \cdot 3 \cdot 2 = 12$. With all above parameters the counting rate is expected to be N = 324 ev/s leading to $\Delta\ A_N/A_N = \pm\ 5\%$ precision after a T = 0.6 hour measurement.

The second step consists in measuring the beam polarization by using the polarized proton beam and an unpolarized target. The beam polarization, P_B, is defined through the relation $\epsilon = P_B \cdot A_N$, where A_N is taken from the previous measurement. The factor ϵ is measured in this second step. Then $\Delta\ P_B/P_B = \sqrt{(\Delta\epsilon/\epsilon)^2 + (\Delta\ A_N/A_N)^2}$ is the precision of the beam polarization P_B. Assuming for simplicity the same error bars in both steps we get: $\Delta P_B/P_B \approx \sqrt{2} \cdot \Delta A_N/A_N$. The ideal case will occur when the luminosity of the polarized beam with an unpolarized target is the same as above or better (since we can use the unpolarized target with higher density). If the beam polarization is also $P_B = 0.8$ the 5% precision might be reached in the same time as above, i.e. for T= 0.6 h. Then the final precision of the beam polarization will be $\Delta\ P_B/P_B = \sqrt{2} \cdot 5 = \simeq 7\%$.

The technique of **Scenario 2** (forward arm polarimeter) was demonstrated to work reliably in colliders [12]. This polarimeter detects the forward scattered particles moving very close (several *mm*) to the main internal circulating proton beam. The detectors sit in Roman Pots. The measured particle position transforms directly to the scattering angle if one puts some restrictions on the lattice function (see below). The accelerator lattice serves as a powerful magnetic spectrometer suppressing strongly the background. The synchrotron radiation from the nearby electron ring has to be taken into account. The following features of internal beam dynamics are to be fully exploited:
- The jet target must be positioned in a region of a large β-function (target position "TP"); the

beam particles are essentially parallel to each other in this region
- The parallel particles coming from the TP region should be focused in the focal plane. The Roman Pots with strip or pixel detectors will be installed at this position (detector position "DP")
- The difference between advanced phases at these two positions, ψ_{TP} and ψ_{DP}, must be $\Delta\,\psi\,=\,(2k+1)\,\cdot\,\pi/2$, where k is any integer number
- the betatron parameter $\alpha\,=\,-1/2\,\cdot\,d\beta/ds$ should be zero in the TP region.
In general, if the proton was scattered at the TP region under the angle $\theta\,=\,\sqrt{t}/E_{fin}$, it will be detected in the DP region at the position $d\,=\,L_{eff}\,\cdot\,\theta$, where L_{eff} is the effective length in the lattice. For the following calculations we selected the $s\,\simeq\,1500$ m region in HERA and interpolated into the TP region to get the condition $\alpha\,\simeq 0$. In order to fix the detector position we looked for phase advance differences $\Delta\,\psi$ under the above condition. For $k\,=\,0$ the calculated parameters at TP and DP show a small difference between X- and Y-planes, preferring slightly X. In order to calculate the size and the angular divergence of the beam at both positions we used the standard formulae assuming the normalized emittance $\epsilon_N = 4\pi$ mm $\cdot$ mrad. The calculations show that to reach the point $t\,=\,10^{-3}\,GeV^2$ the detector should be positioned at 4.0 mm from the beam axis in the X-plane. This is about 20 times bigger than the beam dimension. Background problems must be carefully studied together with the radiation level. If no spin rotator will be foreseen for polarimetry, we must stick to the horizontal plane. For the forward detector alone, the azimuthal acceptance might be 10 or 100 times bigger (for a 4x4 cm^2 detector), compared to the recoil detector. Hence one can expect counting rates of $10^3\,\div\,10^4$ ev/s. Therefore a 5% precision might be reached in several minutes.
We conclude that the CNI polarimeter may become a useful tool in the process of acceleration and storage of a polarized proton beam at HERA. It was shown that a recoil polarimeter or a forward polarimeter, or a combination of both of them may fit to the requirements: fast and absolute measurements of beam polarization of HERA . Additionally, new information can be obtained from such measurements (e.g. A_{NN}).

References

[1] D.P.Barber "Possibilities for polarized protons at HERA". Proc. of 6-th Workshop on High Energy Spin Physics, Protvino, September 18 - 23, 1995, p.141.
[2] D.L.Adams et al., Phys.Lett. **B264** (1991) 462.
[3] D.L.Adams et al., Phys.Lett. **B261** (1991) 191.
[4] D.L.Adams et al., Zeit.Phys. **C56** (1992) 181.
[5] W.-D.Nowak, DESY 96-095, hep–ph 9605411. To be published in Proc. of " TREND IN COLLIDER SPIN PHYSICS " Conference, ICTP Trieste, Italy, Dec. 4-8, 1995.
[6] K.Kuroda, AIP Conf. Proc. No.**25** (1983) 388.
[7] S.B.Nurushev, Proc. of the 1-st Intern.Workshop on Spin Phenomena in High Energy Physics, Protvino, September 14 $\div$ 17, 1983, p.5.
[8] Progress Report "Acceleration of polarized protons to 1 TeV in Fermilab Proton Synchrotron". SPIN Collaboration (Michigan, Indiana, Fermilab, IHEP-Protvino, JINR-Dubna, Moscow, INR-Moscow, KEK, TRIUMF), August 1, 1994.
[9] N.Akchurin et al., Phys.Rev. **D48** (1993), 3026.
[10] G.G.Beznogikh et al., Phys.Lett. **B39** (1972) 275.
[11] E. Steffens, K. Zapfe-Duren, Proceedings of the *Workshop on the Prospects of Spin Physics* at HERA, Zeuthen, August 28-31, 1995, DESY 95-200, ed. by J. Blumlein and W.-D. Nowak, p.57.
[12] U. Amaldi et al., Phys.Lett. **B44** (1973) 112.

Absolute Polarimetry for the Proton Beams of the RHIC Spin Collider and HERA

G. Igo

Department of Physics, UCLA, Los Angeles, CA 90024, USA

Abstract

Measurements of spin dependent structure functions in a colliding beam environment will require absolute beam polarimeters.

There is considerable interest in the spin physics community to develop polarimetry methods for beams in the multi-100 GeV/c range. In the beginning of the next century, polarized proton beams in the range, 100-250 GeV, will become available at RHIC used in the p-p collider mode. A workshop at DESY this year studied the option of polarizing the 820 GeV proton beam of Hera to support programs on deep inelastic spin and di-jet physics. Polarized proton beams might become available after the year 2000. Both facilities, RHIC and HERA, would require polarimeters to measure the absolute value of the beam polarization with high accuracy (5 percent at RHIC). Inclusive production of pions exhibits large analyzing power and high count rate at 200 GeV/c^2, an excellent option for measuring relative values of the beam polarization. A polarimeter for measuring the absolute value of the beam polarization should satisfy the criteria: 1. Large analyzing power; 2. Extraction of the beam polarization from the measured asymmetry should not depend on knowledge of hadronic amplitudes subject to theoretical uncertainty. 3. High count rate capability is a desirable but not necessary property since use would be limited to occasional (but essential) periods to calibrate the inclusive pion polarimeter. With these conditions in mind, two types of polarimeters suggest themselves. The first is based on the longitudinal asymmetry in electron-proton (e-p) polarized deep inelastic scattering (PDIS) and elastic scattering. In the case of the former, PDIS asymmetry data[1] at 9.7 GeV provide the analyzing power. For example, the kinematics to produce the same center of mass energy requires the collision of a 250 GeV (RHIC energy) beam with a 19.7 MeV electron beam. The 9.7 Gev data taken at SLAC exhibits a virtual photon asymmetry in the range of 0.05-0.31. The second option of polarimetry is based on the equality of analyzing power and polarization in elastic p-p scattering. The method involves the measurement of the analyzing power (using a polarized target) and the asymmetry at -t = 1.7 (GeV/c)^2, the second maximum in the analyzing power.

[1] K. Abe et al., Phys.Lett.B364(1995)61

Tracing the origin of the left-right asymmetries observed in inclusive single-spin hadron-hadron collisions

C. Boros, Z. Liang, T. Meng and R. Rittel (presented by Z. L.)

Institut für theoretische Physik der FU Berlin, Arnimallee 14, 14195 Berlin, Germany

Abstract: It is shown that the origin of the striking left-right asymmetries observed in single-spin inclusive hadron production processes in high energy hadron-hadron collisions can be traced by performing suitable experiments at HERA. The possible outcomes of these experiments are summarized. It is pointed out that the results of such a set of experiments will not only be able to differentiate between existing theoretical models, but also be helpful in locating the source(s) of the observed asymmetries.

Striking left-right asymmetries (A_N) have been observed [1-3] for hadron production in single-spin high energy hadron-hadron collisions. A number of mechanisms [4-11] have been proposed recently which can lead to non-zero A_N's in the framework of quantum chromodynamics (QCD) and/or quark or quark-parton models. Among the competing theoretical models the following two classes of models enjoy the privilege of being simple — so simple that the basic ingredients of these models can be directly tested by performing suitable experiments: (1) perturbative QCD based hard scattering models [4-9] and (2) non-perturbative quark-fusion models [11].

In the pQCD based hard scattering models [4-9], the cross section for inclusively produced hadrons in hadron-hadron collisions is expressed as convolution of (i) the cross section for the relevant elementary hard scattering (ii) the momentum distribution functions of the constituents of the colliding hadrons; and (iii) the fragmentation function of the scattered constituent which describes its hadronization process. The asymmetry can originate from any one or more of these three factors.

In the second type of models [11], the basic elementary process is quark-antiquark fusion — which is a process that *cannot* be calculated by using perturbative QCD. The asymmetry originates from the orbital motion of the valence quarks in transversely polarized nucleons and the hadronic surface effect in single-spin hadron-hadron collisions.

Both kinds of model can give significant left-right asymmetry for inclusive hadron production in single-spin hadron-hadron collisions. It is impossible to tell which one is more appriciate to describe the abovementioned data[1-3]. In particular, it is impossible to tell which factor in the type one model is asymmetric since one observes always the convolution of all the three factors. In a recent paper [12], we proposed several new experiments and pointed out that the results of such experiments together with those of others [7,11] will not only be able to differentiate between the abovementioned models, but also be helpful in locating the source(s)

of the observed asymmetries. The experiments we have proposed and/or chosen for this purpose are the following:

(A) Perform $l + p(\uparrow) \to l + \pi + X$ for large x_B (> 0.1, say) and large Q^2 (> 10 GeV^2, say) and measure the left-right asymmetry in the current fragmentation region *with respect to the jet axis*. Here, l stands for charged lepton e^- or μ^-; $x_B \equiv Q^2/(2P \cdot q)$ is the usual Bjorken-x, $Q^2 \equiv -q^2$, and $P, k, k', q \equiv k - k'$ are the four momenta of the proton, incoming lepton, outgoing lepton and the exchanged virtual photon respectively. The transverse momenta of the produced hadrons with respect to this axis come solely from the fragmentation of the quark. Hence, by measuring this transverse momentum distribution, we can directly find out whether the fragmentation function of this polarized quark is asymmetric.

(B) Perform the same kind of experiments as that mentioned in (A) and measure the left-right asymmetry of the produced pions in the current fragmentation region *with respect to the photon direction* in the rest frame of the proton, and examine those events where the lepton plane is perpendicular to the polarization axis of the proton. In such events, the obtained asymmetry should contain the contributions from the intrinsic transverse motion of quarks in the polarized proton and those from the fragmentation of polarized quarks, provided that they indeed exist.

(C) Perform the same kind of experiments as that in (A), but measure the left-right asymmetry *in the target fragmentation region* with respect to the moving direction of the proton in the collider (e.g. HERA) laboratory frame. By doing so, we are looking at the fragmentation products of "the rest of the proton" complementary to the struck quark (from the proton). Since there is no contribution from the elementary hard scattering processes and there is no hadronic surface effect, A_N should be zero if the existence of left-right asymmetries is due to such effects. But, if such asymmetries originate from the fragmentation and/or from the intrinsic transverse motion of the quarks in the polarized proton, we should also be able to see them here.

(D) Measure the left-right asymmetry A_N for $l\bar{l}$ and/or that for $W^\pm$ in $p(\uparrow) + p(0) \to l\bar{l}$ or $W^\pm + X$. Here, there is no contribution from the quark fragmentation. Hence, non-zero values for A_N in such processes can only originate from asymmetric quark distributions — including those due to orbital motion of valence quarks and surface effect.

The results of different models for these experiments are summarized in the table.

References

[1] S. Saroff et al., Phys. Rev. Lett. **64**, 995 (1990); and the references cited therein.

[2] V.D. Apokin et al., Phys. Lett. **B243**, 461 (1990); and "x_F-dependence of the asymmetry in inclusive π^0 and η^0 production in beam fragmentation region", Serpuhkov-Preprint (1991).

[3] FNAL E581/704 Collab., D.L. Adams et al., Phys. Lett. **B261**, 201 (1991); FNAL E704 Collab., D.L. Adams et al., Phys. Lett. **B264**, 462 (1991); and **B276**, 531 (1992); Z. Phys. **C56**,181 (1992); A. Yokosawa, in *Frontiers of High Energy Spin Physics*, Proceedings of the 10th International Symposium, Nagoya, Japan 1992, edited by T. Hasegawa *et al.* (Universal Academy, Tokyo, 1993); A.Bravar et al., Phys. Rev.

Lett. **75**, 3073 (1995); A. Bravar, *"Transverse spin effects in hadron-hadron inclusive reactions"*, talk at the "Adriatico Research Conference: Trends in Collider Spin Physics", Trieste, Italy, December 5-8, 1995. (Proceedings in press).

[4] G. Kane, J. Pumplin and W. Repko, Phys. Rev. Lett. **41**, 1689 (1978).

[5] D. Sivers, Phys. Rev. **D41**,83 (1990) and **D41**, 261 (1991).

[6] J. Qiu and G. Sterman, Phys. Rev. Lett. **67**, 2264 (1991); A. Schäfer, L. Mankiewicz, P. Gornicki and S. Güllenstern, Phys. Rev. **D47**, 1 (1993).

[7] J. Collins, Nucl. Phys. **B394**, 169 (1993); and **396**, 161 (1993); J. Collins, S.F. Heppelmann and G.A. Ladinsky, Nucl. Phys. **B420**, 565 (1994).

[8] A.V. Efremov, V.M. Korotkiyan, and O.V. Teryaev, Phys. Lett. **B 348**, 577 (1995).

[9] M. Anselmino, M. Boglione, and F. Murgia, Phys. Lett. **B362**, 164 (1995).

[10] S.M. Troshin and N.E. Tyurin, Phys. Rev. **D52**, 3862 (1995).

[11] Z. Liang and T. Meng, Z. Phys. **A344**, 171 (1992), Phys. Rev. **D49**, 3759 (1994); C. Boros, Z. Liang and T. Meng, Phys. Rev. Lett. **70**, 1751 (1993), Phys. Rev. **D51**, 4867 (1995), Phys. Rev. **D**, (in press) (1996); C. Boros and Z. Liang, Phys. Rev. **D53**, R2279 (1996).

[12] C. Boros, Z. Liang, T. Meng and R. Rittel, FU-Berlin preprint, FUB-HEP/96-4(1996).

Table: Predictions for left-right asymmetries in the discussed experiments if the asymmetries observed in inclusive hadron production in hadron-hadron collisions originate from the different kinds of effects mentioned in the text.

process	If the A_N observed in $p(\uparrow)+p(0)\to\pi+X$ originates from ...			
	quark distribution function	elementary scattering process	quark fragmentation function	orbital motion of valence quarks & surface effect
$l+p(\uparrow)\to l+\begin{pmatrix}\pi^\pm\\K^+\end{pmatrix}+X$	$A_N=0$ wrt jet axis	$A_N=0$ wrt jet axis	$A_N\neq 0$ wrt jet axis	$A_N=0$ wrt jet axis
in the current fragmentation region for large Q^2 and large x_B	$A_N\neq 0$ wrt $\gamma^\star$ axis	$A_N=0$ wrt $\gamma^\star$ axis	$A_N\neq 0$ wrt $\gamma^\star$ axis	$A_N=0$ wrt $\gamma^\star$ axis
$l+p(\uparrow)\to l+\begin{pmatrix}\pi^\pm\\K^+\end{pmatrix}+X$ in the target fragmentation region for large Q^2 and large x_B	$A_N\neq 0$	$A_N=0$	$A_N\neq 0$	$A_N=0$
$p+p(\uparrow)\to\begin{pmatrix}l\bar{l}\\W^\pm\end{pmatrix}+X$ in the fragmentation region of $p(\uparrow)$	$A_N\neq 0$	$A_N\approx 0$	$A_N=0$	$A_N\neq 0$

Time-reversal-odd asymmetries at HERA

T. Gehrmann[a]

[a] Department of Physics, University of Durham, South Road, Durham, UK

Abstract: Longitudinal polarization of the HERA electron beam allows the study of spatial asymmetries in the final state of single inclusive hadron production in $\vec{e}p$-collisions. We estimate the size of a particular production asymmetry which is related to the time reversal properties of the underlying parton level subprocess.

Despite the experimental success of QCD, some of its basic interaction properties are yet undetermined. In particular, only little is known about the behaviour of QCD interactions under discrete symmetry operations. It was shown in [1] that time-reversal properties of a particular interaction can be tested by measuring experimental observables which are odd under the time-reversal operation. Assuming invariance under T, these T-odd observables vanish at tree level but receive contributions from the absorptive part of higher order loop corrections, yielding in general a non-zero effect. The first measurement of a T-odd QCD observable was carried out in hadronic Z^0 decays by the SLD collaboration [2]. Due to the presence of T-odd contributions from QCD and electroweak interactions [3] at $\sqrt{s}=M_Z$, this measurement fails to provide a clean probe of the T-properties of QCD. A complimentary measurement of a T-odd observable in deep inelastic scattering at moderate Q^2 would on the contrary be insensitive to electroweak effects. Such an observable is suggested in [4, 5]: the azimuthal angle between the momenta of the outgoing electron and an outgoing hadron in the plane transverse to the current direction in the target rest frame. This angle can be expressed as a triple product

$$\sin\phi=\frac{\vec{s}\times\vec{k}'\cdot\vec{P}_T{}'}{|\vec{s}\times\vec{k}'||\vec{P}_T{}'|},$$

where $\vec{s}$ denotes the incoming electron spin, $\vec{k}'$ the momentum of the outgoing electron and $\vec{P}_T{}'$ the transverse momentum of the outgoing hadron relative to the current direction. The leading non-zero contribution inducing a $\sin\phi$-dependence into the single hadron inclusive cross section arises from the absorptive part of the one-loop corrections to the $\gamma^\star q\to qg$ and $\gamma^\star g\to q\bar{q}$ subprocesses and was calculated in [4]. The average angle $\langle\sin\phi\rangle$ is

$$\langle\sin\phi\rangle(z)=\int \mathrm{d}x\mathrm{d}y\mathrm{d}\phi\,\sin\phi\,\frac{\mathrm{d}\sigma}{\mathrm{d}x\mathrm{d}y\mathrm{d}\phi\mathrm{d}z}\Big/\int \mathrm{d}x\mathrm{d}y\mathrm{d}\phi\,\frac{\mathrm{d}\sigma}{\mathrm{d}x\mathrm{d}y\mathrm{d}\phi\mathrm{d}z}. \qquad (1)$$

As the numerator is $\mathcal{O}(\alpha_s^2)$ while the denominator is $\mathcal{O}(1)$, one should expect $\langle\sin\phi\rangle$ to be rather small. The non-vanishing of $\langle\sin\phi\rangle$ is manifest as asymmetry between the left and right event hemispheres in a frame defined by the current direction and divided by the lepton scattering plane. It has to be kept in mind that this asymmetry is subleading to the up–down asymmetry

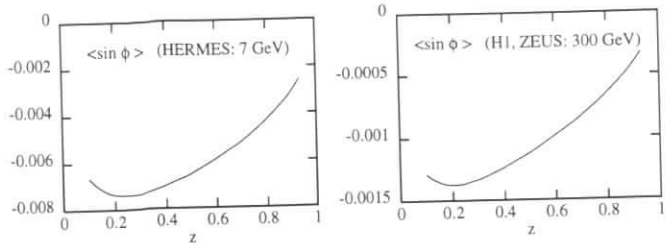

Figure 1: *Expected angular asymmetry in single inclusive hadron production with a beam of left-handed electrons.*

in the same frame, which arises from a $\cos\phi$ dependence of the cross section at $\mathcal{O}(\alpha_s)$ [6]. In order to estimate the expected asymmetries at HERA and at HERMES, we have evaluated the average angle $\langle \sin\phi \rangle$ in the single inclusive production of charged pions and kaons, using the LO parton distribution functions of [7] and the LO hadron fragmentation functions of [8]. To suppress higher twist contributions which can yield sizable T-odd asymmetries [5], we have restricted the final state to $Q^2 > 5$ GeV^2 and $W^2 > 5$ GeV^2. The resulting average angle $\langle \sin\phi \rangle$ for left-handed electrons is shown in Fig. 1 as a function of the longitudinal hadron momentum $z = (P \cdot P')/(P \cdot q)$. The asymmetry for right-handed electrons would be equal in magnitude but opposite in sign. Although the asymmetry appears small at first sight, a measurement might still be possible. The denominator of (1) can be suppressed to $\mathcal{O}(\alpha_s)$ by including only hadrons above a minimal transverse momentum in the measurement. A realistic estimate with a transverse momentum cut has to take effects due to detector resolution and geometry into account and is beyond the scope of the present study.

References

[1] A. De Rújula, J. M. Kaplan and E. de Rafael, Nucl. Phys. **B35** (1971) 365.

[2] SLD collaboration: K. Abe et al., Phys. Rev. Lett. **75** (1995) 4173.

[3] A. Brandenburg, L. Dixon and Y. Shadmi, Phys. Rev. **D53** (1996) 1264.

[4] K. Hagiwara, K. Hikasa and N. Kai, Phys. Rev. **D27** (1983) 84.

[5] J. Levelt and P. Mulders, Phys. Lett. **B338** (1994) 357.

[6] J. Chay, S.D. Ellis and W.J. Stirling, Phys. Rev. **D45** (1992) 46.

[7] M. Glück, E. Reya and A. Vogt, Z. Phys. **C67** (1995) 433.

[8] J. Binnewies, B.A. Kniehl and G. Kramer, Phys. Rev. **D52** (1995) 4947.

Cosmological Spin-offs †

John Ellis[a] and Marek Karliner[b]

[a] Theory Division, CERN, CH-1211, Geneva 23, Switzerland
[b] School of Physics and Astronomy, Raymond and Beverly Sackler Faculty of Exact Sciences, Tel-Aviv University, Tel-Aviv, Israel

Abstract: We review the implications of polarized structure function measurements for experiments to search for cold dark matter particles, such as the the neutralino and the axion.

1 Cold Dark Matter Particles

Many astrophysical observations suggest that the visible baryonic matter is accompanied by larger amounts of invisible dark matter. Mainstream theories of cosmological inflation suggest that the total density of matter in the Universe should be close to the critical density required for its future collapse in a Big Crunch. The upper limits on the baryon density coming from Big Bang Nucleosynthesis calculations suggest in this case that at least 90% of the matter is dark. Models of structure formation based on inflation suggest that most of this dark matter was non-relativistic at the epoch when galaxies and clusters began to form. There are many candidates for this Cold Dark Matter, of which the two particles that are most prominent are the lightest supersymmetric particle, presumably a combination of the supersymmetric partners of the photon, Z and neutral Higgses called a neutralino, and the axion, which is invoked to explain the fact that the strong interactions conserve CP to a very good approximation. Measurements of the quark contributions Δq to the proton spin are relevant to experimental searches for both of these Cold Dark Matter candidates, as we now discuss.

2 Searches for Neutralinos

Several strategies to search for cosmological relic neutralinos have been proposed. One is to look for the products of their annihilations in our galactic halo [2]. Limits on models from the present experimental measurements of the cosmic-ray $\bar{p}$, e^+ and γ fluxes are not yet very constraining.

A second LSP detection strategy is to look for $\chi\chi$ annihilation inside the Sun or Earth. Here the idea is that a relic LSP wandering through the halo may pass through the Sun or Earth [3], collide with some nucleus inside it, and thereby lose recoil energy. This could

†Based on chapter 3 of Ref. [1].

convert it from a hyperbolic orbit into an elliptic one, with a perihelion or perigee below the solar or terrestrial radius. If so, the initial capture would be followed by repeated scattering and energy loss, resulting in a quasi-isothermal distribution within the Sun or Earth. The resulting LSP population would grow indefinitely, à la Malthus, unless it were controlled either by emigration, namely evacuation from the surface, or by civil war, namely annihilation within the Sun or Earth. Evaporation is negligible for χ particles weighing more than a few GeV [4], so the only hope is annihilation. The neutrinos produced by any such annihilation events would escape from the core, leading to a high-energy solar neutrino flux ($E_\nu \gtrsim 1$ GeV). This could be detected either directly in an underground experiment, or indirectly via a flux of upward-going muons produced by neutrino collisions in the rock.

The polarized structure function measurements enter in the estimate of the χ capture rate, which enters in the following general formula [5] for the neutrino flux:

$$R_\nu = 2.7 \times 10^{-2} f\,(m_\chi/m_p) \left(\frac{\sigma(\chi p \to \chi p)}{10^{-40}\,\mathrm{cm}^2}\right) \left(\frac{\rho_\chi}{0.3\,\mathrm{GeV\,cm}^{-3}}\right) \left(\frac{300\ \mathrm{km\,s}^{-1}}{\bar{v}_\chi}\right) \times F_\nu \qquad (1)$$

where we have simplified to the case of capture by the Sun, where proton targets predominate. Here f is a kinematic function, ρ_χ and $\bar{v}_\chi$ are the local density and mean velocity of the halo LSPs, and F_ν represents factors associated with the neutrino interaction rate in the apparatus. The factor which interests us here is the elastic LSP-proton scattering cross section $\sigma(\chi p \to \chi p)$.

To see how the polarized structure functions enter into the estimation of the elastic scattering cross section [5], first note that the LSP interacts with hadrons via an effective four-fermion interaction of the general form $\chi\chi\bar{q}q$, which is mediated by the exchanges of massive particles such as the Z^0, Higgs bosons and squarks $\tilde{q}$, as seen in Fig. 1. This four-fermion interaction

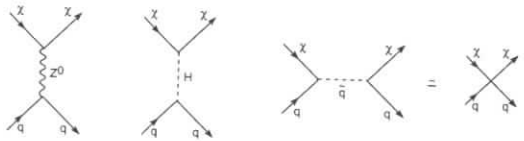

Figure 1: *The exchanges of massive particle such as the Z^0, Higgs boson and squarks give rise to an effective four-fermion interaction between the neutralinos χ and quarks inside a proton target.*

is similar in many ways to the original Fermi four-fermion weak interaction mediated by $W^\pm$ exchange. The matrix elements of the latter interaction between nucleon states are governed by the familiar β-decay constant g_A, which may be written in the form

$$|g_A| = \Delta u - \Delta d \qquad (2)$$

Analogous expressions in terms of the Δq exist for the spin-dependent part of the χ-nucleon scattering matrix element. For example, if the χ were to be a pure photino state, we would have

$$a_p = \frac{4}{9}\Delta u + \frac{1}{9}\Delta d + \frac{1}{9}\Delta s \qquad (3)$$

It is amusing to note that this is exactly the same combination of the Δq that appears in charged-lepton scattering off a proton target [5]. In a sense, the EMC and its successors have been measuring $\tilde{\gamma}$-nucleon scattering!

The EMC and subsequent measurements indicate values of the Δq that are rather different from those predicted by the naïve quark model, which means that the dark matter scattering matrix elements are also rather different, and hence also the upper limits on the halo dark matter density that can be deduced from a given search for high-energy neutrinos from the core of the Sun or the Earth. By now, as discussed in the first lecture, the determination of the Δq is quite precise, and, as discussed earlier in this lecture, we no longer believe that the LSP χ can be a pure $\tilde{\gamma}$. Consider, for example, the plausible case of an essentially pure $U(1)$ gaugino LSP $\tilde{B}$: its scattering matrix elements on protons and neutrons are given by [6]

$$a_p \simeq \frac{17}{36}\Delta u + \frac{5}{36}(\Delta d + \Delta s) \qquad a_n \simeq \quad (\Delta u \leftrightarrow \Delta d) \qquad (4)$$

We see that, in this case, the uncertainties [6] from polarized structure measurements are likely to be much smaller than those from other components in equation (1). In the long run, it seems that a search for upward-going neutrino-induced muons with a 1 km^2 detector could almost certainly detect LSP annihilation [7], if most of the cold dark matter is indeed composed of LSPs.

The third LSP search strategy is to look directly for LSP scattering off nuclei in the laboratory [8]. It is easy to see that the typical recoil energy

$$\Delta E < m_\chi v^2 \simeq 10 \left(\frac{m_\chi}{10\,\mathrm{GeV}}\right)\ \mathrm{keV} \qquad (5)$$

deposited by elastic χ-nucleus scattering would probably lie in the range of 10 to 100 keV. The type of spin-dependent interaction, mediated by Z^0 or $\tilde{q}$ exchange, that we discussed in previous paragraphs is likely to dominate for light nuclei [9], whereas coherent spin-dependent interactions mediated by H and $\tilde{q}$ exchange are likely to dominate scattering off heavy nuclei [10]. As we have already discussed, the spin-dependent interactions on individual nucleons are controlled by the Δq: translating these into matrix elements for interactions on nuclei depends on the decomposition of the nuclear spin, which must be studied using the shell model [9] or some other theory of nuclear structure [11]. The spin-independent interactions on individual nucleons are related to the different quark and gluon contributions to the nucleon mass, which is also an interesting phenomenological issue related to the π-nucleon σ-term. Again, the issue of nuclear structure arises when one goes from the nucleon level to coherent scattering off a nuclear target.

We will not discuss here the details of such nuclear calculations, but we see in Fig. 2 that the spin-independent contribution tends to dominate over the spin-dependent one in the case of Germanium, though this would not be the case for scattering off Fluorine [9].

3 Couplings of Axions

The axion [13] is another favoured candidate for the cold dark matter, whose mass and couplings to matter are scaled inversely by the axion decay constant f_a:

$$m_a \sim \frac{\Lambda_{QCD}\, m_q}{f_a}, \quad g_{a\bar{f}f} \sim \frac{m_f}{f_a}, \qquad g_{a\gamma\gamma} \sim \frac{1}{f_a} \qquad (6)$$

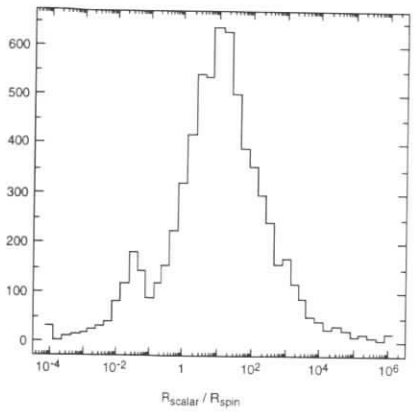

Figure 2: *A comparison of the spin-dependent and spin-independent interaction rates of relic neutralinos χ with Germanium in a sampling of supersymmetric models [12].*

The fact that no axion has been seen in any accelerator experiment tells us that

$$f_a \gtrsim 1\,\mathrm{TeV} \tag{7}$$

and hence that any axion must be associated with physics beyond the scale of the Standard Model.

Axions would have been produced in the early Universe in the form of slow-moving coherent waves that could constitute cold dark matter. The relic density of these waves has been estimated as [14]

$$\Omega_a \simeq \left(\frac{0.6\times 10^{-5}\,\mathrm{eV}}{m_a}\right)^{7/6}\left(\frac{200\,\mathrm{MeV}}{\Lambda_{QCD}}\right)^{3/4}\left(\frac{75}{H_0}\right)^2 \tag{8}$$

which is less than unity if

$$f_a \lesssim 10^{12}\,\mathrm{GeV} \tag{9}$$

In addition to these coherent waves, there may also be axions radiated from cosmic strings [15], which would also be non-relativistic by now, and hence contribute to the relic axion density and strengthen the limit in equation (9).

The fact that the Sun shines photons rather than axions, or, more accurately but less picturesquely, that the standard solar model describes most data, implies the lower limit [16]

$$f_a \gtrsim 10^{7}\,\mathrm{GeV} \tag{10}$$

This has been strengthened somewhat by unsuccessful searches for the axio-electric effect, in which an axion ionizes an atom. More stringent lower bounds on f_a are provided by the agreements between theories of Red Giant and White Dwarf stars with the observations [17] :

$$f_a \gtrsim 10^{9}\,\mathrm{GeV} \tag{11}$$

Between equations (9) and (11) there is an open window in which the axion could provide a relic density of interest to astrophysicists and cosmologists.

Part of this window may be closed by the observations of the supernova SN1987a, which is where the polarized structure function measurements come into play. According to the standard theory of supernova collapse to form a neutron star, 99% of the binding energy released in the collapse to the neutron star escapes as neutrinos. This theory agrees [18] with the observations of SN1987a made by the Kamiokande [19] and IMB experiments [20], which means that most of the energy could not have been carried off by other invisible particles such as axions.

Since the axion is a light pseudoscalar boson, its couplings to nuclear matter are related by a generalized Goldberger-Treiman relation to the corresponding axial-current matrix elements, and these are in turn determined by the corresponding Δq [21]. Specifically, we find for the axion couplings to individual nucleons that

$$\begin{aligned} C_{ap} &= 2[-2.76\,\Delta u - 1.13\,\Delta d + 0.89\,\Delta s - \cos 2\beta\,(\Delta u - \Delta d - \Delta s)]\,, \\ C_{an} &= 2[-2.76\,\Delta d - 1.13\,\Delta u + 0.89\,\Delta s - \cos 2\beta\,(\Delta d - \Delta u - \Delta s)] \end{aligned} \tag{12}$$

Evaluating the Δq at a momentum scale around 1 GeV, as is appropriate in the core of a neutron star, we estimate [6] that

$$\begin{aligned} C_{ap} &= (-3.9 \pm 0.4) - (2.68 \pm 0.06)\cos 2\beta \\ C_{an} &= (0.19 \pm 0.4) + (2.35 \pm 0.06)\cos 2\beta \end{aligned} \tag{13}$$

which are plotted in Fig. 3(a). As in the case of LSP scattering, the uncertainties associated with polarized structure function measurements are by now considerably smaller than other uncertainties, in this case particularly those associated with the nuclear equation of state. The total axion emission rate from the core of a neutron star is approximately proportional to the combination

$$C_{an}{}^2 + 0.8\,(C_{an} + C_{ap})^2 + 0.5\,C_{ap}{}^2 \tag{14}$$

which is plotted in Fig. 3(b), together with the associated with the errors in the Δq. Estimating axion emission rates in this way [22], it seems that part of the previous axion window is still open, and an experiment [23] is underway which should be able to detect halo axions if they occupy part of this window.

4 Polarized Scattering and Cosmology

The above examples show how measurements of the spin decomposition may not only deepen our understanding of nucleon structure, but may also help resolve important issues in cosmology. They are essential if one is to make reliable calculations of the nuclear interaction and detection rates for cold dark matter particles, which would be needed to confirm directly the emerging picture of structure formation in the Universe.

Acknowledgements

This work was supported in part by the Israel Science Foundation administered by the Israel Academy of Sciences and Humanities, and by a Grant from the G.I.F., the German-Israeli Foundation for Scientific Research and Development.

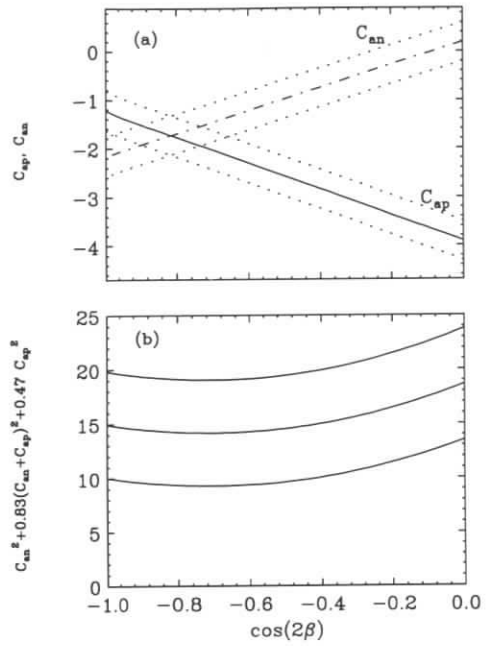

Figure 3: *(a) Axion couplings to the nucleon, as determined in Ref. [6] using polarized structure function data. (b) The total axion emission rate from the core of a neutron star, proportional to the combination* $C_{an}{}^2 + 0.8\,(C_{an} + C_{ap})^2 + 0.5\,C_{ap}{}^2$*, as determined in Ref. [6].*

References

[1] J. Ellis and M. Karliner, *The Strange Spin of the Nucleon*, hep-ph/9601280, invited lectures at the International School of Nucleon Spin Structure, Erice, August 1995.

[2] J. Silk and M. Srednicki, *Phys. Rev. Lett.* **53** (1984) 624.

[3] J. Silk, K.A. Olive and M. Srednicki, *Nucl. Phys.* **279** (1987) 804.

[4] A. Gould, *Ap. J* **321** (1987) 560.

[5] J. Ellis, R.A. Flores and S. Ritz, *Phys. Lett.* **B198** (1987) 493.

[6] J. Ellis and M. Karliner, *Phys. Lett.* **B341**(1995)397.

[7] F. Halzen, astro-ph/9508020.

[8] M. Goodman and E. Witten, *Phys. Rev.* **D30** (1985) 3059.

[9] J. Ellis and R.A. Flores, *Nucl. Phys.* **307** (1988) 883, **B400** (1993) 25 and *Phys. Lett.* **B263** (1991) 259.

[10] K. Griest, *Phys. Rev.* **D38** (1988) 2357.

[11] J. Engel and P. Vogel, *Phys. Rev.* **D40** (1989) 3132; A.F. Pacheco and D. Strottman, *Phys. Rev.* **D40** (1989) 2131; F. Iachello, L. Krauss and G. Maino, *Phys. Lett.* **B254** (1991) 220.

[12] G. Jungman, M. Kamionkowski and K. Griest, Syracuse preprint SU-4240-605 (1995).

[13] R. Peccei and H.R. Quinn, *Phys. Rev. lett.* **38** (1977) 1440 and *Phys. Rev.* **D16** (1977) 1791; S. Weinberg, *Phys. Rev. Lett.* **40** (1978) 223; F. Wilczek, *Phys. Rev. Lett.* **40** (1978) 279.

[14] L. Abbott and P. Sikivie, *Phys. Lett.* **120B** (1983) 133; J. Preskill, M. Wise and F. Wilczek, *Phys. Lett.* **120B** (1983) 127; M. Dine and W. Fischler, *Phys. Lett.* **120B** (1983) 137.

[15] R. Davis, *Phys. Rev.* **D32** (1985) 3172 and *Phys. Lett.* **180B** 225; D. Harari and P. Sikivie, *Phys. Lett.* **B195** (1987) 361; C. Hagmann and P. Sikivie, *Nucl. Phys.* **B363** (1991) 247.

[16] F.T. Avignone *et al.*, *Phys. Rev.* **D35** (1987) 2752.

[17] For a review, see G. Raffelt, *Phys. Rep.* **198** (1990) 1.

[18] J. Ellis and K.A. Olive, *Phys. Lett.* **B193** (1987) 525; D.N. Schramm, *Comm. Nucl. and Part. Phys.* **A17** (1987) 239.

[19] K. Hirata *et al.*, *Phys. Rev. Lett.* **58** (1987) 1490.

[20] R.M. Bionta *et al.*, *Phys. Rev. Lett.* **58** (1987) 1494.

[21] R. Mayle *et al.*, *Phys. Lett.* **B203** (1988) 188 and **B219** (1989) 515.

[22] J. Ellis, D.N. Schramm, G. Sigl, M.S. Turner *et al.*, in preparation (1995).

[23] P. Sikivie, *Phys. Rev. Lett.* **51** (1983) 1415; P. Sikivie *et al.*, Proposal to NSF for Research in Dark-Matter Axion Physics (1993).

Probing dissociation of space-like photons at HERA

C. Boros, Z. Liang and T. Meng (presented by T. M.)

Institut für theoretische Physik, Freie Universität Berlin, Arnimallee 14, 14195 Berlin, Germany

In this talk, I briefly summarize some of the experiments my collaborators and myself proposed in a recent paper [1]. We show: By using the characteristic spin-effects observed in high-energy hadron-hadron collisions as indicators, hadronic dissociation of space-like photons can be directly probed by performing measurements in the fragmentation region of transversely polarized and unpolarized proton beams at HERA.

It is known already for a long time that hadronic dissociation of space-like photons may play a significant role in deep-inelastic lepton-hadron scattering — especially in diffractive processes [2,3]. People seem to agree that, viewed from the hadron- or nucleus-target, not only real, but also space-like photons ($Q^2 \equiv -q^2 > 0$, where q is the four-momentum of such a photon) may exhibit hadronic structure. But, as far as the following question is concerned, different theoretical models (see e.g. Refs. 2-5 and the papers cited therein) seem to give different answers. How do such hadronic dissociation processes depend on the standard kinematic variables of deep-inelastic lepton-nucleon scattering, Q^2 and $x_B \equiv -q^2/(2pq)$, where p is the four-momentum of the struck nucleon? In particular, do virtual photons indeed behave like hadrons in the small x_B and large Q^2 region ?

Viewed from the rest frame of the struck nucleon mentioned above, the lifetime τ_γ of the virtual hadronic system is of the order $2\nu/Q^2 = 1/(Mx_B)$, where ν is the photon-energy and M is the proton-mass. This means, the corresponding formation/coherence length is of the order 100 Fermis for $x_B = 10^{-2}$. Furthermore, we note that τ_γ is function of x_B, independent of Q^2. Does it imply that the hadronic dissociation of a photon always takes place — independent of its virtuality Q^2? Is it true that we are practically *always* dealing with hadron-hadron collisions, when x_B is sufficiently small ($x_B \sim 10^{-2}$, say)?

Some of the dynamical models based on such a photon-dissociation picture (See e.g.[4]) have been used to describe the proton structure function $F_2^p(x_B, Q^2)$ in the small x_B region and the obtained results are in reasonable agreement with the existing data [6,7]. Can we, on the basis of this agreement, say: "Experiments show that space-like photons $\gamma^*(Q^2)$ always dissociate into hadronic systems — independent of their virtualities (Q^2-values)" ? Is it correct and/or appropriate to say that the question whether space-like photons dissociate hadronically depends entirely on the choice of reference frames ?

A large number of inelastic lepton-nucleus experiments have been performed in which the hadronic properties of the space-like photons have been studied. But, probably due to the complicated nucleon structure which has to be taken into account, the data can be reproduced by different models based on different physical pictures [4,5]. Can hadronic dissociation of space-like photons be probed without using nuclear targets ?

Having the present and the future experimental possibilities at HERA in mind, we think it would be useful to consider the characteristic spin-effects observed — and only observed — in the fragmentation regions of hadron-hadron collisions at comparable energies and use them as indicators to probe space-like photon $\gamma^*(Q^2, x_B)$ at given values of Q^2 and x_B. To be more precise, we propose to measure the left-right asymmetry A_N of produced charged mesons in the fragmentation region of the transversely polarized proton $p(\uparrow)$, to measure Λ-polarization P_Λ of the unpolarized protons p at HERA in the small-x_B region for different Q^2-values, and to compare the obtained results with those obtained in the corresponding hadron-hadron collisions.

In order to demonstrate in a quantitative manner how the Q^2-dependence of such dissociation processes may manifest itself, we examine the $F_2^p(x_B, Q^2)$-data [6,7] in the small-x_B region. In Fig.1, we separate the well-known vector-dominance contribution (See e.g. [4,5]) from "the rest" which may be identified as "the part due to quark-antiquark continuum" or "the rest of the contributions due to the generalized vector-dominance model", and we consider the following two extreme possibilities which correspond to two very much different physical pictures: (i) The hadronic dissociation of virtual space-like ($Q^2 > 0$) photons take place for all possible Q^2-values. In other words, in this picture $\gamma^*(Q^2)$ should always be considered as a hadronic system — independent of Q^2. (ii) The hadronic dissociation of such photons depends very much on Q^2. In terms of a two-component picture (See e.g.[2-5]) the virtual photon $\gamma^*(Q^2)$ is considered to be either in the "bare photon" state or in a hadronically dissociated state ("hadronic cloud") described by the vector-dominance model. In other words, only the latter can be considered hadronic; and the probability for $\gamma^*(Q^2)$to be in this state is the ratio between the values shown by the dashed and the full lines.

Let us first look at the left-right asymmetry data [8] for $\pi^\pm$-production in $p(\uparrow) + p$ and see what we may obtain by replacing the unpolarized proton-target p by a photon with given Q^2, $\gamma^*(Q^2)$. It is clear that the corresponding asymmetry which we denote by $A_N(x_F|Q^2)$ will have the following properties: If scenario (i) is correct, we shall see no change in $A_N(x_F|Q^2)$ by varying Q^2. If scenario (ii) is true, there will be a significant Q^2-dependence. The results are shown in Fig.2a. Similar effects are expected also for K^+-mesons. In order to emphasize the model-independence of this test the curve which goes through the existing proton-proton data points [8] should be considered as an empirical fit, although such an asymmetry-data can be described by a relativistic quark model [9].

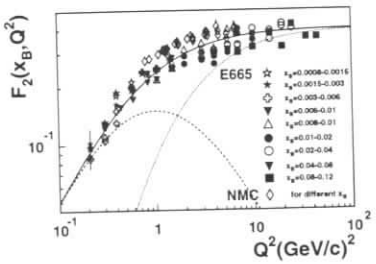

Fig.1: *Structure function $F_2^p(x_B, Q^2)$ as a function of Q^2. The data-points are taken from [6,7]; and they are parametrized (shown as solid line) in order to carry out the quantitative calculation mentioned in the text. The dashed line is the contribution from the vector meson dominance. The difference, which is called "the rest", is shown as dotted line.*

We next consider the Λ-polarization $P_\Lambda(x_F, Q^2)$ in the process $p + \gamma^*(Q^2) \to \Lambda + X$ in which unpolarized proton beam is used [10]. Also here, we expect to see *no Q^2-dependence for scenario (i) but a significant Q^2-dependence for scenario (ii).* This is shown in Fig.2b.

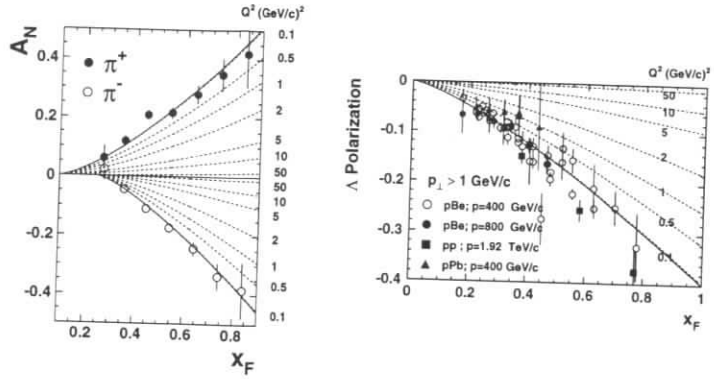

Fig.2: *(a) Left-right asymmetry for pion-production in* $p(\uparrow)+\gamma^* \to \pi^\pm + X$ *as function of* x_F *at different values of* Q^2*. The data are for* $p(\uparrow)+p \to \pi^\pm + X$ *and are from [8]. (b) Polarization for* Λ*-production in* $p+\gamma^* \to \Lambda + X$ *as function of* x_F *at different* Q^2*. The data are from [10].*

References

[1] C. Boros, Z. Liang and T. Meng, preprint FUB-HEP/95-21 (revised version).

[2] H.T. Nieh, Phys. Rev. D1, 3161 (1970); Phys. Rev. D7, 3401 (1973).

[3] T.H. Bauer, R.D. Spital, D.R. Yennie and F.M. Pipkin, Rev. Mod. Phys. **50**, 261 (1978).

[4] See e.g. G. Piller, W. Ratzka and W. Weise, Z. f. Phys. **A352**, 427 (1995).

[5] See e.g. M. Arneodo, Phys. Rep. **240**, 301 (1994).

[6] NMC Collaboration, P. Amaudruz et al., Phys. Lett. **295B**, 3 (1992).

[7] Fermilab E665 Collaboration, Ashutosh V. Kotwal, in Proc. of the Eighth Meeting of the Division of Particles and Fields of the American Physical Society (DPF'94), Albuquerque, NM, August 2-6, 1994; Fermilab Conf-94/251-E (1994).

[8] FNAL E581/704 Collaboration, D.L. Adams et al., Phys. Lett. **B261**, 201 (1991); FNAL E704 Collaboration, D.L. Adams et al., Phys. Lett. **B264**, 461 (1991); and **B276**, 531 (1992); Z. Phys. **C56**, 181 (1992); A. Yokosawa, In Frontiers of High Energy Spin Physics, Proc. of the 10th Int. Symp., Nagoya, Japan 1992, edited by T. Hasegawa et al. (Universal Academy, Tokyo, 1993); A. Bravar et al., Phys. Rev. Lett. **75**, 3073 (1995).

[9] C. Boros, Z. Liang and T. Meng, Phys. Rev. Lett. **70**, 1751 (1993), Z. Liang and T. Meng, Phys. Rev. **D49**, 3759 (1994); C. Boros, Z. Liang and T. Meng, (to appear in Phys.Rev.D).

[10] K. Heller, in High Energy Spin Physics, Proceedings of the 9th International Symposium, Bonn, Germany, 1990, edited by K.H. Althoff, W. Meyer (Springer-Verlag, 1991); and the references given therein; A.M. Smith et al., Phys. Lett. **185B**, 209 (1987); B. Lundberg et al, Phys. Rev. **D40**, 3557 (1989); E.J. Ramberg et al., Phys. Lett. **338B**, 403 (1994).

Working Group on

Light and Heavy Nuclei in HERA

Conveners:

M. Arneodo (Univ. Torino), A. Bialas (Jagellonian Univ.,Crakow),
M.W. Krasny (Univ. Paris VI and VII), T. Sloan (Univ. Lancaster),
G. van der Steenhoven (Nikhef), M. Strikman (Pennsylvania State Univ.)

Participants:

A. Airapetian (Yerevan), I. Akushevich (Minsk), J. Arvieux (Saclay), A.L. Ayala (Porto Alegre), B. Badelek (Warsaw, Uppsala), R. Baier (Bielefeld), E. Barone (Torino), J. Bjorken (SLAC), V. Breton (Paris), S. Brodsky (SLAC), J. Chwastowski (Crakow), J. Crittenden (Bonn), J. Czyzewski (Crakow), L. Dieperink (Groningen), Yu.L. Dokshitzer (CERN), K. Egiyan (Yerevan), J.M. Eisenberg (Tel Aviv), K.J. Eskola (Helsinki), A. Eskreys (Crakow), A. Febel (DESY), J. Figiel (Crakow), S. Forte (Torino, CERN), L. Frankfurt (Tel Aviv), S. Gavin (Brookhaven), M.B. Gay Ducati (Porto Alegre), M. Genovese (Grenoble), Y. Golubkov (Moscow), T. Gousset (Heidelberg), H. Gutbrod (Darmstadt), M. Gyulassy (Columbia), U. Heinz (Regensburg), P. Hoyer (Nordita), D. Indumathi (Dortmund), L. Jenkovsky (Kiev), A. Kaidalov (Moscow), K. Kinder-Geiger (CERN), B. Kopeliovich (Dubna, Heidelberg), W. Koepf (Tel Aviv), M. Krawczyk (Warsaw), S. Kumano (Saga), K. Kurek (Bialystok), A. Kurepin (Moscow), J. Kwiecinski (Cracow), J.M. Laget (Saclay), K. Lassila (Iowa), F. Lev (Moscow), G. Levin (Petersburg and Rio de Janeiro), G. Levman (Toronto), B. Levtchenko (Moscow), N. Magnussen (Wuppertal), T. Massam (Bologna), L. McLerran (Minnesota), W. Melnitchouk (Maryland and Munich), V. Metag (Darmstadt), G. Miller (Seattle), Y. Mizuno (Osaka), M. Miyama (Saga), A. Mueller (Columbia), P. Mulders (Nikhef), O. Nachtmann (Heidelberg), G. Niesler (Munich), N.N. Nikolaev (Bonn, Moscow), T. O'Neill (Argonne), N. Pavel (Hamburg), B. Pawlik (Crakow), S. Peigné (Orsay) G. Piller (Munich), J. Pirner (Heidelberg), E. Predazzi (Torino), M. Rohde (DESY), M. Ryskin (Petersburg), M. Sargsyan (Tel Aviv), H. Satz (Bielefeld), H. Schellman (Northwestern), D. Schiff (Orsay), D. Schildknecht (Bielefeld), J. Schukraft (CERN), Y. Shabelski (Santiago de Compostela), G. Shaw (Manchester), S. Simula (Rome), G. Smirnov (Dubna), W. Schaefer (Bonn), H. Schroeder (DESY), A. Schwartz (DESY), H. Spiesberger (Munich), A.W. Thomas (Adelaide), R. Venugopalan (Washington), G. Violini (Cosenza), W. Weise (Munich), F. Willeke (DESY), W. Wittek (Munich), B. Zakharov (Moscow), W. Zhu (Bejing), V. Zoller (Moscow), N. Zotov (Moscow)

Light and Heavy Nuclei in HERA — Working Group Reports:

- **Collider mode:**

Nuclear beams in HERA

M.Arneodo[a], A.Bialas[b], M.W.Krasny[c], T.Sloan[d] and M. Strikman[e]

[a] Università di Torino, I-10125 and INFN Cosenza, Italy
[b] Institute of Physics, Jagellonian University, Cracow, Poland
[c] LPNHE, Universités Paris VI and VII, IN2P3-CNRS, Paris, France
[d] School of Physics and Chemistry, University of Lancaster, Lancaster LA1 4YB, UK
[e] Pennsylvania State University, University Park, PA 16802, USA

Abstract: A study has been made of the physics interest and feasibility of experiments with nuclear beams in HERA. It is shown that such experiments widen considerably the horizon for probing QCD compared to that from free nucleon targets. In addition there is some sensitivity to physics beyond the standard model. Hence the option to include circulating nuclear beams in HERA allows a wide range of physics processes to be studied and understood.

1 Introduction

The successes of QCD in describing *inclusive* perturbative phenomena have moved the focus of investigations to new frontiers. Three fundamental questions to be resolved are the space-time structure of high-energy strong interactions, the QCD dynamics in the nonlinear, small coupling domain and the QCD dynamics of interactions of fast, compact colour singlet systems.

The study of electron-nucleus scattering at HERA allows a new regime to be probed experimentally for the first time. This is the regime in which the virtual photon interacts coherently with all the nucleons at a given impact parameter. In the rest frame of the nucleus this can be visualized in terms of the propagation of a small $q\bar{q}$ pair in high density gluon fields over much larger distances than is possible with free nucleons. In the Breit frame it corresponds to the fact that small x partons cannot be localized longitudinally to better than the size of the nucleus. Thus low x partons from different nucleons overlap spatially creating much larger parton densities than in the free nucleon case. This leads to **a large amplification of the nonlinear effects expected in QCD at small x.** The HERA ep data have confirmed the rapid increase of the parton densities in the small x limit predicted by perturbative QCD. However the limited x range available at HERA makes it difficult to distinguish between the predictions of the DGLAP evolution equations and the BFKL-type dynamics. Moreover, the nonlinear effects expected at small x are relatively small in ep scattering in the HERA kinematic domain and it may be necessary to reduce x by at least one order of magnitude to observe unambiguously such effects. However, the amplification obtained with heavy nuclear targets **allows an effective reduction of about two orders of magnitude in x** making it feasible to explore such nonlinear effects at the energies available at HERA. The question of nonlinear effects is one

of the most fundamental in QCD. It is crucial for understanding the kind of dynamics which would slow down and eventually stop the rapid growth of the cross section (or the structure function, F_2) at small x. It is also essential in order to understand down to what values of x the decomposition of the cross section into terms with different powers of $\frac{1}{Q^2}$ remains effective. It is important for the understanding of the relationship between hard and soft physics. One can also study the dynamics of QCD at high densities and at zero temperatures raising questions complementary to those addressed in the search for a quark-gluon plasma in high-energy heavy ion collisions.

Deep inelastic scattering from nuclei provides also a number of ways to probe **the dynamics of high-energy interactions of small colour singlet systems**. This issue started from the work of Gribov [1] who demonstrated the following paradox. If one makes the natural (in soft physics) assumption that at high energies any hadron interacts with a heavy nucleus with cross section $2\pi R_A^2$ (corresponding to interaction with a black body), Bjorken scaling at small x is grossly violated – $\sigma_{\gamma^* A} \propto \ln Q^2$ instead of $\frac{1}{Q^2}$. To preserve scaling, Bjorken suggested, using parton model arguments, that only configurations with small $p_t \leq p_{t0}$ are involved in the interaction (the Aligned Jet Model) [2]. However, in perturbative QCD Bjorken's assumption does not hold – large p_t configurations interact with finite though small cross sections (colour screening), which however increase rapidly with incident energy due to the increase of the gluon density with decreasing x. Hence again one is faced with a fundamental question which can only be answered experimentally: *Can* **small** *colour singlets interact with hadrons with cross sections comparable to that of normal hadrons?* At HERA one can both establish the x, Q^2 range where the cross section of small colour singlets is small – *colour transparency*, and look for the onset of the new regime of large cross sections, *perturbative colour opacity*.

Another fundamental question to be addressed is **the propagation of quarks through nuclear matter.** At large energies perturbative QCD leads to the analogue of the Landau-Migdal-Pomeranchuk effect in quantum electrodynamics. In particular Baier et al. [3] find a highly nontrivial dependence of the energy loss on the distance, L, travelled by a parton in a nuclear medium: the loss instead of being $\propto L$ is $\propto L^2$. Several manifestations of this phenomenon can be studied at HERA.

There is also an *important connection to heavy ion physics.* Study of eA scattering at HERA would be important for the analysis of heavy ion collisions at the LHC and RHIC. Measurements of gluon shadowing at small x are necessary for a reliable interpretation of the high p_t jet rates at the LHC. In addition, the study of parton propagation in nuclear media is important for the analysis of jet quenching phenomena, which may be one of the most direct global signals of the formation of a quark-gluon plasma.

Current fixed target data on lepton-nucleus scattering only touch the surface of all these effects due to the limited Q^2 range of the data at small x. Indeed the Q^2 range of these data is too small to distinguish the contribution of the vector meson dominance behaviour of the photon from its hard QCD behaviour at small x. The range of x and Q^2 in experiments with nuclei at HERA compared to the fixed target experiments is shown in Fig. 1. It can be seen that at HERA the kinematic range will be extended well into the deep inelastic scattering region.

To address the questions discussed above we identify the primary experimental programme for nuclei in HERA as:

• **Study of the x and Q^2 dependence of nuclear shadowing over a wide Q^2 range.** This will allow the processes limiting the growth of F_2 as x tends to zero to be studied in detail.

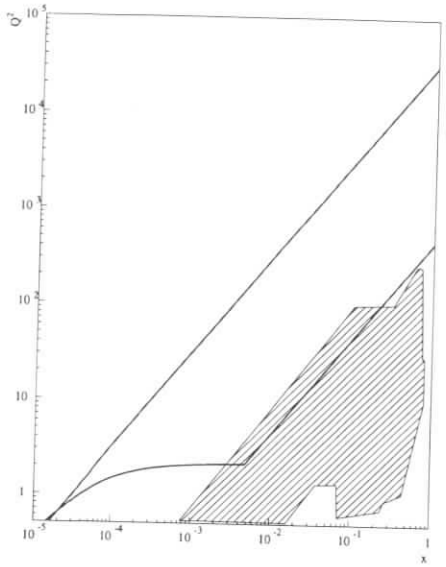

Figure 1: The kinematic region covered by experiments at HERA compared to fixed target data (shaded region).

• **To establish the difference between the gluon distributions of bound and free nucleons.** This will allow the part played by gluon fusion in the shadowing process to be studied directly.

• **Study of diffractive processes:** to see if the pomeron generated by nuclei shows any difference from that generated by free nucleons. Processes such as vector meson production can also be used to search for colour transparency.

• **Study of hadronic final states.** This allows the propagation of partons in the nuclear medium to be studied as well as the multiplicity fluctuations discussed later.

The proceedings of Working Group 8 are organised as follows. First we give an experimental overview in which we demonstrate the feasibility of carrying out this experimental programme. Then we give a theoretical overview in which we explain the relevance of the programme to QCD. Finally, we give the detailed contributions on different topics which demonstrate the depth of the physics interest. The proposed measurements in the main will be possible with the existing detectors H1 and ZEUS measuring down to low Q^2 and with luminosities at the level of 1-10 pb^{-1} per nucleon. The contribution of Chwastowski and Krasny [4] shows that if the detectors could extend their rapidity coverages various experiments of interest to nuclear structure physicists become feasible.

2 Experimental Overview

2.1 Introduction

In the following subsections the feasibility of the measurements defined above as the primary experimental programme is investigated. The nuclear targets should each have Z/A of 1/2. Hence the energy of each nucleon in a deep inelastic collision will be half that of the HERA proton energy of 820 GeV i.e. 410 GeV. The electron energy is assumed to have the standard value of 27.6 GeV. We show that most studies can be carried out with the existing detectors requiring luminosities between 1-10 pb^{-1} per nucleon. While the possibility of storing heavy nuclei up to Sn and Pb is very attractive, a program covering the light isoscalar nuclei (D, ^{4}He, C, S) would by itself have a major discovery potential. The necessary radiative corrections are described in the contributions of Kurek [5] and of Akushevich and Spiesberger [6] who show that such corrections can be kept under control using suitable cuts on the data. In most of the experiments it is proposed to measure ratios of yields. Hence, in order to minimise systematic errors, it is desirable to store different nuclei in HERA simultaneously. Otherwise frequent changes of the stored nucleus in the beam will be necessary.

2.2 Shadowing Measurements Using Nuclei in HERA

The accuracy of shadowing measurements for an experiment in which nuclear targets are stored in HERA is calculated. It is shown that for luminosities of 2 pb^{-1} per nucleon the measurements would extend considerably the accuracy and range of the existing data.

The x dependence of the differences in the nucleon structure function between bound and free nucleons has been well measured in recent years in fixed target experiments [7, 8, 9, 10, 11] following the discovery of the differences in the 1980s [12, 13, 14, 15, 16]. The present experimental situation on this x dependence is briefly summarised in Fig. 2. However, the Q^2 dependence is not well measured. In the shadowing region the data are at such low Q^2 values that they are arguably not even in the deep inelastic regime.

There are many different models [17] for the effects in the different regions shown in Fig. 2 which are all compatible with the existing data. In the shadowing region the Q^2 range of the data is insufficient to separate the different contributions from the vector dominance behaviour of the photon and QCD effects such as parton fusion. Measurements over the extended x and Q^2 ranges, which would become possible at HERA, will give more information to help separate the models and help us understand the phenomena which limit the rise of the nucleon structure function F_2 at small x; e.g. see references [18, 19].

Is it feasible to study shadowing in HERA?

To answer this question we assume that nuclear beams can be stored in HERA and luminosities of 2 pb^{-1} per nucleon, shared between 2 nuclear targets, can be achieved (i.e. $2/A$ pb^{-1} per nucleus, where A is the atomic weight). With this definition of luminosity, rate computations should use cross sections per nucleon. The counting rates in bins of Q^2 and x are then estimated to assess the statistical errors on the measurements of the ratios of F_2^A/F_2^D where the nuclear targets are assumed to be He, C or S. The cross sections are calculated from the one photon exchange formula

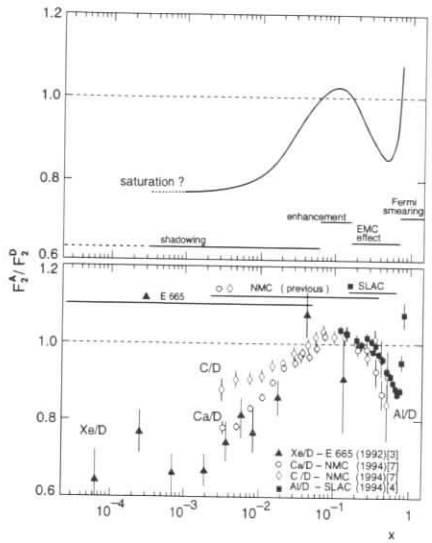

Figure 2: Partial compilation of results for F_2^A/F_2^D (from [8]). Note that below $x \approx 0.01$, the average Q^2 value of the data is smaller than 2 GeV^2.

$$\frac{d^2\sigma}{dxdQ^2} = \frac{4\pi\alpha^2}{xQ^4}\left[1 - y + \frac{y^2}{2(1+R)}\right] F_2(x,Q^2). \qquad (1)$$

The nucleon structure functions, F_2 and R, are computed from the MRS(A) set [20]. Deep inelastic scattering events are assumed to be detectable with 100% efficiency if the scattered electron energy $E' > 5$ GeV and its scattering angle is more than 3 degrees to the electron beam. Alternatively events are assumed to be detectable with 100% efficiency if a quark is scattered out by an angle of more than 10 degrees to the proton beam and with an energy more than 5 GeV. Nuclear effects on the structure functions are neglected. Such effects, which are at the 10% level, will have little effect on the statistical accuracy of measurements of ratios of structure functions, F_2^A/F_2^D.

Fig. 3 shows the estimated statistical errors on the ratios (averaged over Q^2), with these assumptions, together with the measurements of the NMC [8]. In many cases the statistical errors are $< 1\%$ i.e. smaller than the sizes of the points. It can be seen from Fig. 3 that this statistical precision will allow high accuracy measurements of the shadowing ratios down to lower x values than in fixed target experiments and over a much wider range of Q^2.

Fig. 4 shows the statistical precision of the slopes $d(F_2^A/F_2^D)/d\ln Q^2$ estimated at HERA compared to the NMC data. Impressive precision is possible at HERA, presumably due to the much larger Q^2 range covered. Measurements over such a large Q^2 range will allow the precise predictions of the parton fusion model to be tested.

If at least two different nuclear targets can be stored in different bunches in HERA during experimental running the systematic errors should be similar in magnitude to those in fixed

target experiments [7]. Radiative corrections for deep inelastic scattering from heavy nuclear targets will be necessary and these will be applied with the appropriate cuts on the data as discussed in these preceedings [5, 6].

In conclusion, measurements of the ratios (F_2^A/F_2^D) at HERA will extend the data to smaller values of x and much larger values of Q^2 than in fixed target experiments. Impressive precision on the Q^2 dependence will be possible from which the mechanism which leads to the limitation in the rise of F_2 at small x and large Q^2 can be studied.

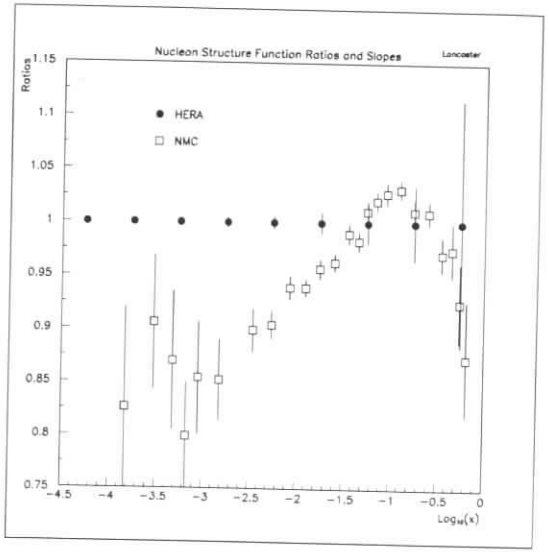

Figure 3: Ratio of the nucleon structure function in carbon to that in deuterium as a function of x. The NMC data [8] (open squares) are shown in comparison to data with the estimated statistical accuracy of an experiment of luminosity 1 pb^{-1} per nucleon at HERA.

2.3 The Accuracy of The Gluon Density Measurements Using Nuclei in HERA

2.3.1 Introduction

The major contribution to shadowing from nonlinear QCD effects is thought to arise from multigluon interactions such as gluon fusion effects. Such effects are amplified at higher x in nuclei due to the larger target size so that they should become visible in the HERA kinematic range. Similar effects are expected to limit the growth of the nucleon structure function F_2 at high Q^2 and low x. Hence it is interesting to look for such effects directly on the gluon distribution by looking for differences between the gluon density in bound and free nucleons. Different ways of doing this are studied below.

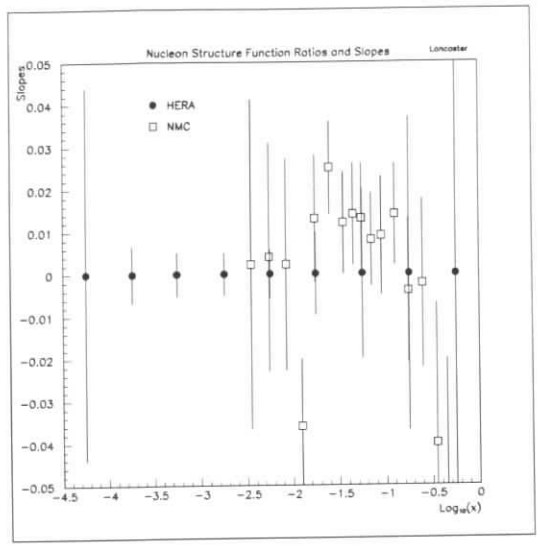

Figure 4: The slopes $d(F_2^A/F_2^D)/d\ln Q^2$ as function of x showing the NMC data [7] (open squares) and the statistical accuracy of an experiment with 1 pb^{-1} per nucleon at HERA.

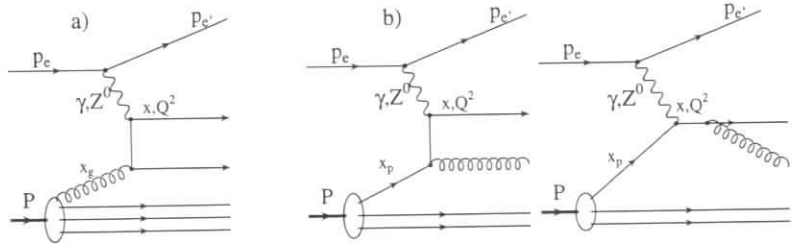

Figure 5: The processes giving rise to $2+1$ jet topology. P denotes here the projectile particle, a proton or a nucleus, Q^2 is the four-momentum transfer and x is the Bjorken variable.

2.3.2 Determination of the Gluon Density in the Nucleus from the Jet Rates

In the majority of large Q^2 deep inelastic electron-nucleus scattering events, at HERA, the scattered quark and the remnant of the nucleus will hadronize to form two jets. Such a topology is often called the $1+1$ jet configuration. Occasionally, however, more jets will be produced. In Fig. 5 the partonic processes giving rise to the $2+1$ jet topology are shown. These processes are called "boson-gluon fusion" (process a) and "the QCD Compton scattering" (processes b).

The $2+1$ jet events can be related to the partonic processes shown in Fig. 5 if the invariant

mass of the system of two jets $\overline{s} = (p_{jet1} + p_{jet2})^2$ is significantly larger than the typical scale of the strong interactions, so that perturbative QCD can be used. The contribution of these processes to the total cross section depends upon the value of the coupling constant α_s defining the strength of quark-gluon coupling and upon the momentum distribution of the incoming gluon (quark). The fractions of the parent bound nucleon momentum carried by the incoming partons, $x_{p,g}$, are constrained by the value of x, the total hadronic mass, W, and the invariant mass of the two jet system $\overline{s}$:

$$x_{p,g} = x + \overline{s}/W^2. \tag{2}$$

For values of $\overline{s}/W^2 \geq 0.01$, the values of $x_{p,g}$ must be large. In this kinematic domain the partonic distributions in bound nucleons have been well measured in fixed target experiments [17]. Thus, the coupling constant, α_s, can be derived from the measured rate of $2+1$ jet events. In turn, we shall be able to use this α_s value to determine the gluon momentum distribution at smaller x_g, corresponding to small values of both x and $\overline{s}/W^2$ (note that at small x the contribution of the QCD Compton processes (Fig. 5b,c) to the total "2+1" jet cross section is expected to be small). Such an analysis has been recently carried out by the H1 collaboration [21] using deep inelastic electron-proton scattering data collected at HERA. The systematic errors of the resulting gluon density are large and to some extent uncertain. They are dominated by the uncertainties in relating the measured rate of observed jet topologies to the basic QCD processes involving quarks and gluons. Unfolding the gluon densities involves modelling the hadronisation of the quarks which is necessary for simulating the detector effects but is only weakly constrained by the data. In addition several jet algorithms can be used leading to differences in jet counting. There exist as well ambiguities in the QCD calculation of the processes shown in Fig. 5. The amplitudes of the processes $\gamma^* g \to jet_1 + jet_2$ and $\gamma^* q \to jet_1 + jet_2$ have poles corresponding to the collinear emission of jets with respect to the direction of the incoming gluon (γ^*) and to the emission of jets of small invariant mass. Since one must use fixed order perturbative QCD, jets reconstructed in phase space close to the poles must be avoided to diminish the sensitivity to higher order terms which have so far not been calculated. This can be achieved by using only jets of high invariant mass ($\overline{s} \geq 100$ GeV^2) and by rejecting events in which one of the jets is emitted at a small angle with respect to the incoming proton direction. In the region of small $\overline{s}$ the jet rates calculated using leading order and next to leading order approximations are significantly different [22] indicating that higher order corrections are necessary for an unambigous determination of the gluon density.

Will it be possible to use the jet method to determine the gluon density in nuclei given the uncertainties described above and at the same time adding the extra ambiguity related to jet formation in the nuclear medium? Most likely it will be difficult to obtain satisfactory precision in measuring the absolute gluon distributions in the nuclei. However, we expect that good precision can be achieved in measuring the ratios of gluon distributions for various nuclei. The uncertainties due to the jet finding algorithms and to the modelling of the hadronisation processes will largely cancel in the ratios if high energy jets are used. High energy jets are expected to be formed outside the nucleus. In addition we shall be able to select jets in the restricted phase space region where the effects of rescattering of slow particles belonging to the jet but formed inside the nucleus are small. The energy loss of quarks and gluons traversing the nuclear medium prior to hadronisation is expected to be below 350 MeV/fm according to the estimation of [3] and should not give rise to large errors on the gluon density ratio. The expected statistical precision of the measurements of the ratio of the gluon densities for two nuclei of atomic numbers A1 and A2 is shown in Fig. 6. It corresponds to a luminosity of 10

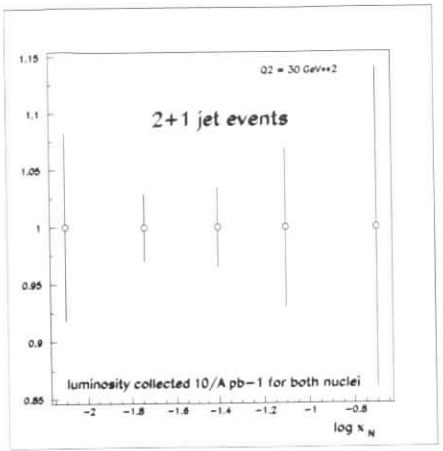

Figure 6: Statistical precision of the ratio of gluon densities in two nuclei $x_N G(x_N, A_1)/xG(x_N, A_2)$ at $Q^2 = 30$ GeV^2 determined from the "2 + 1" jet sample.

pb$^{-1}/A$ for each nucleus. In estimating this statistical precision we have followed the jet and kinematic region selection of [21] and neglected all nuclear effects. We also assume that the contribution of the QCD Compton process can be unambigously subtracted. The x_N variable is the fraction of the bound nucleon momentum carried by the gluon. It is clear that good statistical precision on the measurement of the ratio of the gluon densities can be achieved at modest luminosities.

2.3.3 The Gluon Distribution in Nuclei from Scaling Violations

The gluon distribution can also be determined from the deviations from scaling of the structure function F_2. We estimate the accuracy of such a determination of the gluon density for bound nucleons in an experiment with nuclear beams in HERA. The scaling violations of F_2 are strongly related to the gluon distribution of the target nucleon at small x values. The quantity

$$\psi = \frac{\frac{dF_2^A}{d\ln Q^2} - \frac{dF_2^D}{d\ln Q^2}}{\frac{dF_2^p}{d\ln Q^2}} \tag{3}$$

is sensitive to the differences of the gluon distribution in bound and free nucleons and is roughly proportional to $\delta G/G$ where G is the gluon density at a particular x value and δG is the difference in gluon densities between bound and free nucleons. Hence it would be interesting to measure this quantity in an experiment with nuclear beams stored in HERA.

To estimate the feasibility of such a measurement the accuracies of the determinations of the slopes $dF_2/d\ln Q^2$ have been estimated from the expected counting rates for a 2 pb^{-1} per nucleon run using the MRS(A) set of structure functions [20]. The slopes were obtained from a linear least squares fit to values of F_2 using the statistical errors calculated for such an experiment with the assumptions described in section 2.2. The error in the quantity ψ was then obtained assuming equal statistical errors for the nuclear and deuteron targets with a 1 pb^{-1} per nucleon run for each. The error on the slope $dF_2^p/d\ln Q^2$ for the proton was neglected since this should be well determined from high luminosity proton running.

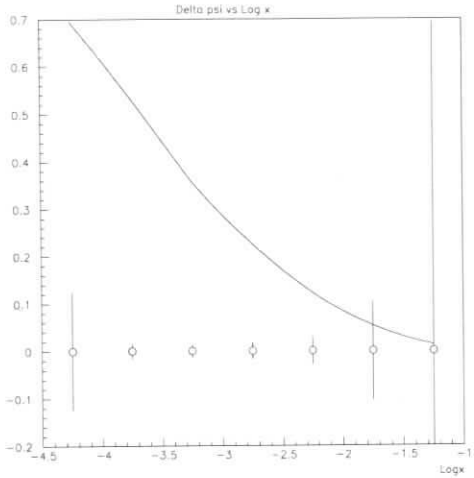

Figure 7: Accuracy of the difference between the slopes of F_2 between nuclei and deuterium as a function of x. The smooth curve shows the calculated slope for the free proton.

The results are shown in Fig. 7. For the purpose of this figure we assume that the gluon densities for bound and free nucleons are the same so that ψ=0. The estimated statistical errors are then superimposed on these values and the smooth curve shows $dF_2^p/d\ln Q^2$ for comparison computed from the MRS(A) set. Comparison of the errors on ψ with the values of the slope for the proton shows that this method will be sensitive to differences in the gluon densities between bound and free nucleons of the order of 5 per cent of the total gluon density at x in the vicinity of 10^{-3}. Hence the measurement will be quite sensitive to nuclear effects on the gluon density.

2.3.4 Determination of the Gluon Density in the Nucleus from Inelastic J/ψ production

The expected accuracy of the determination of the bound to free nucleon gluon density ratio $xG|_A/xG|_D$ using nuclei in HERA is estimated for inelastic photoproduction of J/ψ mesons at $Q^2 < 4$ GeV^2 ($eA \to eXJ/\psi$).

Inelastic production of J/ψ mesons has been used for a long time to extract or constrain the gluon distribution in the nucleon (see e.g. [23]-[28]), assuming that the dominant mechanism is the photon-gluon fusion [29]-[32]. Within this framework, the cross section is directly proportional to the gluon density. These calculations have been affected in the past by large normalisation uncertainties (up to factors of 2-5), which however have been greatly reduced recently [33]. Inelastic J/ψ production dominates at values of z, the fraction of the photon energy carried by the meson in the nucleon rest frame, smaller than ≈ 0.9. In the framework of the colour singlet model [32], the gluon distribution is probed at a value of x, the fraction of the proton's momentum carried by the gluon, $x = [m_{J/\psi}^2/z + p_t^2/z(1-z)]/W^2$, where p_t is the J/ψ transverse momentum with respect to the virtual photon direction and W is the photon-nucleon centre-of-mass energy. The scale probed by this process is approximately $m_{J/\psi}^2 \approx 10$ GeV^2.

Fig. 8 shows the expected statistical accuracy as a function of $\log_{10} x$ for an integrated luminosity of 10 pb$^{-1}/A$. Decays into e^+e^- or $\mu^+\mu^-$ pairs have been assumed. The plot refers to the kinematic region $Q^2 < 4$ GeV^2, $z < 0.9$. Nuclear effects have been neglected in the evaluation of statistical accuracies.

Possible sources of systematic uncertainties are the luminosity, the branching ratio, the global acceptance (including trigger and reconstruction efficiency, muon or electron identification etc.), the feed-in from ψ' production and the contamination from resolved photon events. In the recent H1 [26] and ZEUS [27] analyses, the total systematic uncertainty is approximately 10-20%. By and large all the above contributions would cancel in a ratio for simultaneously stored nuclei, with the partial exception of the luminosity. In practice, for an integrated luminosity of 10 pb^{-1}, the statistical uncertainty dominates.

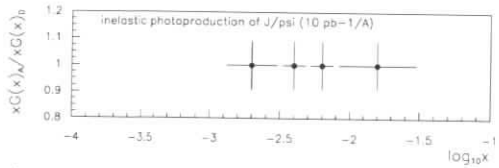

Figure 8: Expected statistical accuracy (vertical error bars) on the ratio $xG|_A/xG|_D$ as a function of $\log_{10} x$ using inelastic photoproduction ($Q^2 < 4$ GeV^2) of J/ψ mesons. An integrated luminosity of 10 pb$^{-1}/A$ for each nucleus has been assumed. The horizontal bars indicate the size of the bins.

2.4 Diffraction from Nuclei in HERA

2.4.1 Introduction

The measurements of the ZEUS and H1 collaborations [34, 35] of deep-inelastic electron-proton scattering have revealed the existence of a distinct class of events in which there is no hadronic energy flow in an interval of pseudo-rapidity, η, adjacent to the proton beam direction i.e. events with a large rapidity gap. Such events are interpreted as deep inelastic scattering from the pomeron, $I\!P$. Studies of events with a large rapidity gap from nuclear targets will allow the structure of the pomeron from a different source than the free nucleon to be determined. It will be interesting to see if these structures differ. In addition, the study of diffractive vector meson production will be interesting to search for the phenomenon of colour transparency. Such a phenomenon has not yet been convincingly seen although it is predicted in QCD.

2.4.2 Expected Accuracy of the Measurements of the Pomeron Structure

We commence by describing the terminology surrounding measurements of the Pomeron structure. In our studies we shall use the four variables β_A, Q^2, x_A and t_A, or equivalently β_A, Q^2, $x_{I\!P,A}$ and t_A, which are defined as follows:

$$x_A = \frac{-q^2}{2P\cdot q}; \quad x_{I\!P,A} = \frac{q\cdot(P-P')}{q\cdot P}; \quad Q^2 = -q^2; \quad \beta_A = \frac{-q^2}{2q\cdot(P-P')}; \quad t_A = (P-P')^2. \quad (4)$$

Here q, P and P' are, as indicated in Fig. 9, the 4-momenta of the virtual boson, incident nucleus and the final state colourless remnant Y respectively. The latter can be either a coherently recoiling nucleus or any incoherent excitation of the nucleus carrying its quantum numbers. The variables in equation (4) are related to each other via the expression:

$$x_A = \beta_A x_{I\!P,A}. \quad (5)$$

We also introduce, in order to allow the comparison of measurements with nuclei of different atomic number A, the variables:

$$x = x_A \cdot A \qquad x_{I\!P} = x_{I\!P,A}\cdot A \qquad \beta = \beta_A \qquad t = t_A. \quad (6)$$

Note that relation (5) rewritten in terms of the above variables still holds i.e.

$$x = \beta x_{I\!P}. \quad (7)$$

The A-rescaled variables can be directly related to the variables defined in [36, 37] retaining their interpretation, as was given there, for processes in which only one nucleon of the nucleus interacts with the electron and the nucleon's Fermi momentum can be neglected.

The variables $x_{I\!P,A}$, $x_{I\!P}$ and β can be expressed in terms of the invariant mass of the hadronic system X, M_X, the nucleus mass, M_A, and the total hadronic invariant mass W as

$$x_{I\!P,A} = \frac{Q^2+M_X^2-t}{Q^2+W^2-M_A^2} \approx \frac{Q^2+M_X^2}{Q^2}\cdot x_A, \quad (8)$$

$$x_{I\!P} \approx \frac{Q^2+M_X^2}{Q^2}\cdot x, \quad (9)$$

$$\beta = \beta_A = \frac{Q^2}{Q^2+M_X^2-t} \approx \frac{Q^2}{Q^2+M_X^2}. \quad (10)$$

In the kinematic domain which we shall consider here ($M_A^2 \ll W^2$ and $|t| \ll Q^2$, $|t| \ll M_X^2$) $x_{I\!P,A}$ may be interpreted as the fraction of the 4-momentum of the nucleus carried by the $I\!P$ and β as the fraction of the 4-momentum of the $I\!P$ carried by the quark interacting with the virtual boson. Note that in the interactions in which only one nucleon takes part, $x_{I\!P}$ can be interpreted as the fraction of the 4-momentum of this nucleon carried by the $I\!P$.

We shall follow in our analysis the formalism defined in [36, 37] and introduce the diffractive structure function $F_{2,A}^{D(3)}$ as a function of three kinematic variables, derived from the structure function $F_{2,A}^{D(4)}$. This latter structure function depends upon four kinematic variables chosen here as: x, Q^2, $x_{I\!P}$ and t and is defined by analogy with the decomposition of the unpolarised total eA cross section. The total cross section can be expressed in terms of two structure functions $F_{2,A}^{D(4)}$ and $\frac{F_{2,A}^{D(4)}}{2x(1+R_A^{D(4)})}$ in the form

$$\frac{\mathrm{d}^4\sigma_{eA\to eXY}}{\mathrm{d}x\mathrm{d}Q^2\mathrm{d}x_{I\!P}\mathrm{d}t} = A\cdot\frac{4\pi\alpha^2}{xQ^4}\left\{1-y+\frac{y^2}{2[1+R_A^{D(4)}(\beta,Q^2,x_{I\!P},t)]}\right\}F_{2,A}^{D(4)}(\beta,Q^2,x_{I\!P},t), \quad (11)$$

in which $y = Q^2/sx_A$ and s is the eA collision centre of mass (CM) energy squared. We shall discuss here the low y region and neglect the term containing $R_A^{D(4)}$.

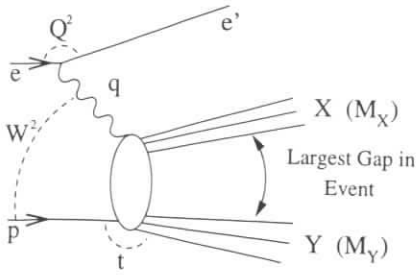

Figure 9: The diagram of the process with a rapidity gap between the system X and Y. The projectile nucleus is denoted here as p.

We shall consider in the following measurements of $\frac{d^3\sigma(eA\to eXY)}{dxdQ^2dx_{I\!P}}$, from which the structure function $F_{2,A}^{D(3)}(\beta,Q^2,x_{I\!P}) = \int F_{2,A}^{D(4)}(\beta,Q^2,x_{I\!P},t)\,dt$ can be derived. The integration is over the range $|t_{min}|<|t|<|t|_{lim}$ where t_{min} is a function of Q^2, W^2, β and the mass of the the system Y, and $|t|_{lim}$ is specified by the requirement that all particles belonging to the system Y remain undetected. The structure function $F_{2,A}^{D(3)}$ will thus be derived from

$$\frac{\mathrm{d}^3\sigma_{eA\to eXY}}{\mathrm{d}x\mathrm{d}Q^2\mathrm{d}x_{I\!P}} = A\cdot\frac{4\pi\alpha^2}{xQ^4}\left\{1-y+\frac{y^2}{2}\right\}F_{2,A}^{D(3)}(\beta,Q^2,x_{I\!P}). \tag{12}$$

The structure function $F_{2,A}^{D(3)}(\beta,Q^2,x_{I\!P})$ can be measured at HERA using a sample of "rapidity gap" events i.e. events in which there is no hadronic energy flow over a large η interval. These events originate from coherent diffractive scattering ($eA\to eA+X_{diff}$) and from incoherent diffractive scattering ($eA\to e(A-N)+N+X_{diff}$). N denotes here the nucleons ejected from the incoming nucleus. The measurement of $F_{2,A}^{D(3)}(\beta,Q^2,x_{I\!P})$ for several nuclei, separately for coherent and incoherent processes [4], will provide an important test of the quark parton interpretation of diffractive processes and a unique means to find out how universal is the concept of the pomeron.

We propose to measure the ratio of the structure functions

$$R_{A1,A2}(\beta,Q^2,x_{I\!P}) = F_{2,A1}^{D(3)}(\beta,Q^2,x_{I\!P})/F_{2,A2}^{D(3)}(\beta,Q^2,x_{I\!P}), \tag{13}$$

where A1 and A2 denote the atomic numbers of the two nuclei. This ratio can be measured at HERA with a very high systematic accuracy. The statistical precision of such a measurement will be of the order of 5 %, if luminosities of $10/A1$ and $10/A2$ pb^{-1} are collected for each nucleus. This is illustrated in Fig. 10 where we show, as an example, $R_{A1,A2}$ at $Q^2 = 12$ GeV^2 as a function of β and $x_{I\!P}$. In order to estimate the statistical precision of the measurement we have used the RAPGAP [38] Monte-Carlo and have assumed the event selection procedure of [36, 37]. We have not tried to model the nuclear dependence of the $F_{2,A2}^{D(3)}(x,Q^2,x_{I\!P})$ resulting in the ratio shown in Fig. 10 to be equal 1.

Several distinct hypotheses concerning the deep inelastic structure of the diffractive processes can be verified (rejected) by measuring the $R_{A1,A2}$:

- universal (independent of the source) pomeron structure and an A-independent pomeron flux leading to

$$R_{A1,A2}(\beta,Q^2,x_{I\!P}) = 1; \tag{14}$$

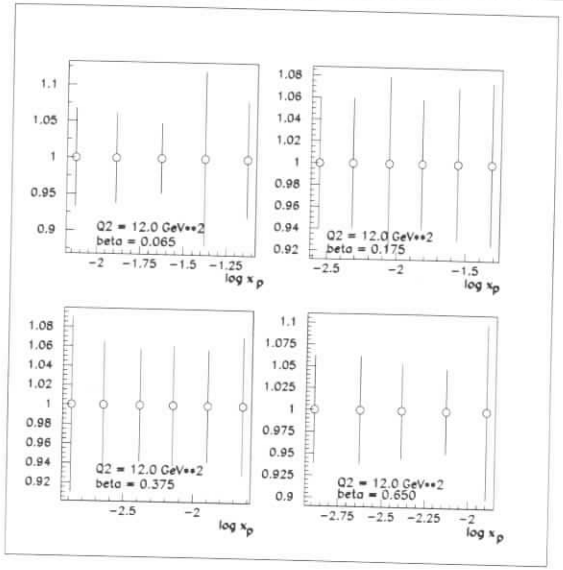

Figure 10: The ratio $R_{A1,A2}(\beta,Q^2,x_{I\!P})$ plotted as a function of $x_{I\!P}$ for fixed values of β and Q^2. The error bars correspond to a luminosity of $10/A1$ and $10/A2$ pb^{-1} for each nucleus.

- universal pomeron structure and an A-dependent pomeron flux leading to

$$R_{A1,A2}(\beta,Q^2,x_{I\!P}) = f(A1,A2); \tag{15}$$

- A-independent pomeron flux and a parent nucleus dependent pomeron structure. In a model of this type [39] the ratio $R_{A1,A2}$ can be expressed using the nuclear structure functions $F_{2,A}(x,Q^2)$ measured in inclusive electron nucleus scattering

$$R_{A1,A2}(\beta,Q^2,x_{I\!P}) = F_{2,A1}(\beta\cdot x_{I\!P},Q^2)/F_{2,A2}(\beta\cdot x_{I\!P},Q^2). \tag{16}$$

2.4.3 Measurement of the A-dependence of the Fraction of Rapidity Gap Events

One of the simplest measurements which could discriminate between the two pictures of pomeron formation proposed in [39, 40] and unresolved by the diffractive ep scattering data, is the measurement of the A-dependence of the fraction of the number of rapidity gap events with respect to the total number of deep inelastic scattering events:

$$R_{gap}(A1,A2) = \frac{N_{gap}(A1)/N_{tot}(A1)}{N_{gap}(A2)/N_{tot}(A2)}. \tag{17}$$

In the model of [39] the pomeron is replaced by multiple soft colour exchanges between the quark-antiquark pair into which the virtual photon has fluctuated and the target nucleus. In this model the ratio $R_{gap}(A1,A2)$ is expected to be 1. This is in contrast to the prediction of the colour singlet exchange model [40] in which the ratio $R_{gap}(A1,A2)$ can reach a value of 3 between nuclei with atomic numbers A1 and A2 differing by 200. In order to illustrate the

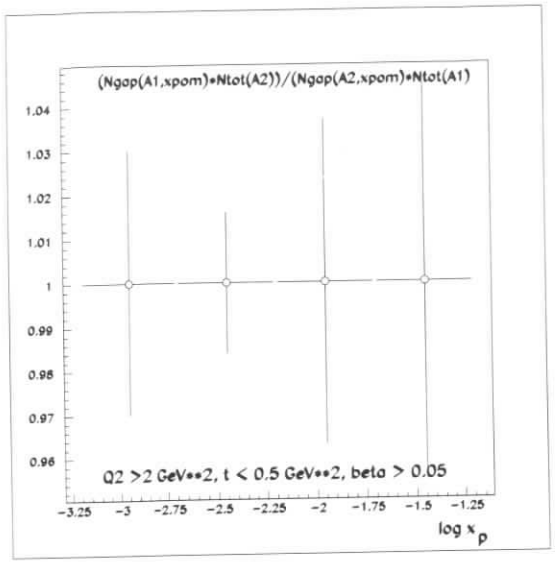

Figure 11: The integrated ratio $R_{gap}(A1, A2)$ plotted as a function of $x_{I\!P}$. The error bars correspond to a luminosity of $1/A1$ and $1/A2$ pb^{-1} for each nucleus.

statistical precision of such a measurement we show in Fig. 11 the values of $R_{gap}(A1, A2)$ and their statistical errors.

The statistical precision of $R_{gap}(A1, A2)$ is dominated by the statistical precision of $N_{gap}(A1)$ and $N_{gap}(A2)$ and was determined with help of the RAPGAP [38] Monte Carlo by counting events generated within the kinematic domain defined by the following boundaries: $Q^2 \geq 2$ GeV^2, $|t| \leq 0.5$ GeV^2 and $\beta \geq 0.05$. The ratio shown in Fig. 11 was set to unity as we have not tried to model the nuclear dependence of the $R_{gap}(A1, A2)$. We observe that statistical precisions of $\simeq 2$ % can be reached by collecting integrated luminosity of $1/A$ pb^{-1} for each nucleus. The systematic errors, as for the measurement of $F_{2,A}^{D(3)}(\beta, Q^2, x_{I\!P})$ are expected to be smaller than the statistical errors if two nuclei are stored simultaneously at HERA. This measurement, even if carried out for two light nuclei, can easily rule out one of the two models of pomeron formation.

2.4.4 Elastic Vector Meson Production

We present the accuracy expected for exclusive photoproduction of J/ψ mesons at $Q^2 < 4$ GeV^2 ($eA \to eAJ/\psi$) and exclusive production of ρ^0 mesons at $Q^2 > 4$ GeV^2 ($eA \to eA\rho^0$).

As discussed in detail later, elastic (or exclusive) production of vector mesons in the reaction $ep \to epV$, where V is a vector meson (ρ^0, ω, ϕ, J/ψ...), is thought to be of a diffractive nature. Recent calculations (cf. e.g. [41, 42, 43, 44, 45]) indicate that the cross section for these processes may depend on the gluon momentum distribution $\bar{x}G(\bar{x})$ probed at a value of $\bar{x}$, the fraction of the nucleon's momentum carried by the gluon, $\bar{x} \simeq (Q^2 + m_V^2)/W^2$, where m_V is the vector meson mass and W is the photon-nucleon centre-of-mass energy.

We have determined the statistical accuracy with which the ratios

$$R_V = \frac{1}{A^2} \frac{d\sigma^A/dt|_{t=0}}{d\sigma^D/dt|_{t=0}} \tag{18}$$

can be determined for ^{4}He, ^{12}C, ^{32}S and ^{208}Pb. Fig. 12 shows the results for J/ψ production.

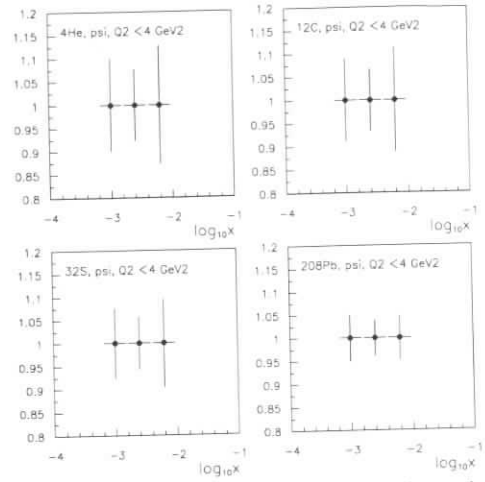

Figure 12: Expected statistical accuracy (vertical error bars) on the ratio $R_V^{1/2}$ for elastic photoproduction ($Q^2 < 4$ GeV^2) of J/ψ mesons. In all cases a luminosity of 1 pb$^{-1}/A$ for each nucleus was assumed. The horizontal bars indicate the size of the bins.

We used DIPSI [46], a Monte Carlo generator based on [41] that describes the available ZEUS data on J/ψ photoproduction. Events were generated in the range $Q^2 < 4$ GeV^2 and $30 < W < 300$ GeV; the J/ψ was assumed to decay into e^+e^- or $\mu^+\mu^-$ pairs. Events in which the decay leptons were outside the coverage of the barrel and rear tracking detectors of H1 and ZEUS (approximately $34° < \vartheta < 164°$) were rejected. A further reduction in the number of accepted events by a factor 0.2 was applied to account for efficiency and acceptance effects; this factor was taken to be independent of $\bar{x}$.

Only statistical uncertainties are shown. Possible sources of systematic uncertainties are the luminosity, the branching ratio, the global acceptance (including trigger and reconstruction efficiency, muon or electron identification etc.), the contamination from incoherent events, the feed-in from inelastic J/ψ production (à la photon-gluon fusion) and the feed-in from ψ' production. All the above contributions would largely cancel in a ratio for simultaneously stored nuclei, with the partial exception of the luminosity. In practice, for an integrated luminosity of 1 pb^{-1}, the statistical uncertainty is expected to dominate.

Fig. 13 shows the expected statistical uncertainty for ρ^0 production at $Q^2 > 4$ GeV^2. Here as well we used DIPSI, and the parameters were chosen so that the generator describes the ZEUS data [47]. Events were generated in the range $4 < Q^2 < 100$ GeV^2 and $30 < W < 300$ GeV. The ρ^0 was assumed to decay into $\pi^+\pi^-$ pairs; pairs with masses between 0.3 and 1.4 GeV were considered. Events in which the decay pions were outside the coverage of the tracking detectors of H1 and ZEUS (approximately $15° < \vartheta < 164°$) were rejected. A further reduction in the

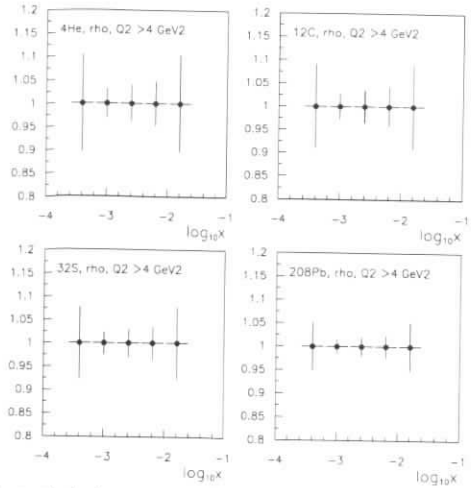

Figure 13: Expected statistical accuracy (vertical error bars) on the ratio $R_V^{1/2}$ for elastic production ($Q^2 > 4$ GeV^2) of ρ mesons. In all cases a luminosity of 1 pb$^{-1}/A$ for each nucleus was assumed. The horizontal bars indicate the size of the bins.

number of accepted events by a factor 0.6 was applied to account for efficiency and acceptance effects; this factor was independent of $\bar{x}$.

One can see from the figures that the accuracy of the measurements would be sufficient to discriminate between the colour transparency expectation of a ratio close to unity and the vector meson dominance expectation of the ratio $R_V \approx A^{-2/3}$; cf. also the discussion in section 3.6.

2.5 Parton Propagation in Nuclei

This has been studied in various fixed target experiments in the past [48, 49]. It is investigated by measuring the final state hadrons in the deep inelastic scattering. Since there will be many more than one hadron per event in experiments at HERA the statistical errors are not expected to be a limitation and high accuracy should be possible. This subject is considered in more detail in section 3.7 and in [50].

2.6 Other Physics

In addition to the primary programme for nuclear beams in HERA outlined above there will be additional experiments which have not been explored in these studies. For example, there is physics interest in studying photoproduction from nuclear targets in the HERA energy range as well as sensitivity to physics beyond the standard model. Such sensitivity arises in e-nucleus collisions via coherent two photon interactions allowing production of positive C parity states which will be inhibited at LEP. This is discussed by Krawczyk and Levtchenko [51].

3 Theoretical Overview

3.1 Introduction

In this overview we describe those aspects of the phenomenology of QCD which lead to the nonlinear effects referred to earlier. These effects are thought to be related to the mechanisms which will eventually limit the growth of the nucleon structure function as x decreases at finite Q^2.

3.2 Space-time Picture of DIS off Nuclei at Small x

3.2.1 The Rest Frame

In the rest frame of the target nucleus the life-time of a fluctuation is given by the formula

$$\tau = \frac{\beta}{m_N x_{Bj}}, \tag{19}$$

where $\beta = Q^2/(Q^2 + M^2) < 1$. M is the mass of the $q\bar{q}$ system

$$M^2 = \frac{k_t^2 + m_q^2}{z(1-z)}, \tag{20}$$

where z is the light-cone momentum fraction, k_t the transverse momentum and m_q the mass of the quark. Perturbative QCD studies show that the most probable configurations are those for which $M^2 \approx Q^2$. In the case of transversely polarised photons both configurations with small k_t and highly asymmetric fractions z and configurations with comparable z and $1-z$ contribute to the cross section. For the case of the longitudinal photons the asymmetric contribution is strongly suppressed.

In the language of noncovariant diagrams this corresponds to the virtual photon fluctuating into a quark-antiquark pair at a longitudinal distance $l_c = \frac{\beta}{m_N x}$ from the nucleus which far exceeds the nuclear radius. The distance l_c is referred to as the "coherence length". The pair propagates essentially without transverse expansion until it reaches the target. QCD evolution leads to a logarithmic decrease of β with increasing Q^2. At HERA coherence lengths of up to 1000 fm are possible, so that the interaction of the $q\bar{q}$ pair with nuclear matter can be studied in detail - notably its transparency to small size pairs - *colour transparency*.

At HERA new features of colour transparency should emerge: the incident small size $q\bar{q}$ pair resolves small x gluon fields with virtualities $\sim Q^2$. If the transverse size of the $q\bar{q}$ pair is $r_t = b_q - b_{\bar{q}}$, the cross section for interaction with a nucleon is [52]

$$\sigma_{q\bar{q},N}(E_{inc}) = \frac{\pi^2}{3} r_t^2 \alpha_s(Q^2) x g_N(x, Q^2), \tag{21}$$

where $Q^2 \approx \frac{\lambda(x)}{r_t^2}, \lambda(x \approx 10^{-3}) \approx 9, x = \frac{Q^2}{2m_N E_{inc}}$. Since the gluon density increases rapidly with decreasing x, even small size pairs may interact strongly, leading to some sort of *perturbative colour opacity* – the interaction of a small object with a large object with a cross section comparable to the geometric size of the larger object (Fig. 14).

Unitarity considerations for the scattering of a small size system [44] – i.e. the requirement that $\sigma_{inel}(q\bar{q}, target) \leq \pi R^2_{target}$ – indicate that nonlinear effects (i.e. effects not accounted for by the standard evolution equations) should become significant at much larger values of x in eA scattering than in ep scattering.

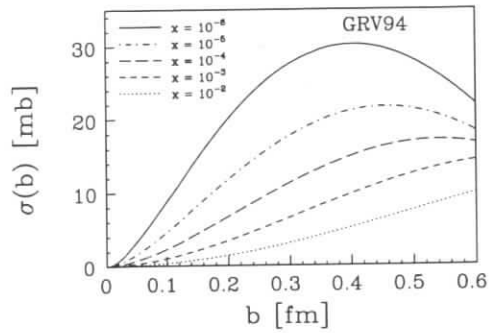

Figure 14: Colour-dipole cross section, $\sigma_{q\bar{q}N}(x,b)$ of Eq. (21), as a function of the transverse size of the $q\bar{q}$ pair for various values of x and for the GRV94 parametrization of the nucleon's gluon density.

3.2.2 The Breit Frame

In the Breit frame, small x partons in a nucleon are localized within a longitudinal distance $\sim 1/xp_N$, while the distance between two nucleons is $\sim r_{NN}m_N/p_N$ (r_{NN} is the distance between nucleons in the rest frame and p_N is the nucleon momentum). Therefore partons with $x < 1/(2m_N r_A)$, where $r_A \approx r_0 A^{1/3}$ fm is the nuclear radius and $r_0 = 1.1$ fm cannot be localized to better than the whole nuclear longitudinal size. Hence low x partons emitted by different nucleons in a nucleus can overlap spatially and fuse, provided the density is high enough, leading to shadowing of the partonic distributions in bound nucleons with respect to the free nucleon ones and to nonlinear effects already at values of $x \sim 10^{-4} \div 10^{-3}$. For example, in the simplest model of nonlinear effects corresponding to the fan diagrams of Fig. 15, the additional contribution $\delta g_A(x,Q^2)$ to $g_A(x,Q^2)$ due to the nonlinear term in the equation for the Q^2, x evolution of the gluon density is [19]:

$$Q^2 \frac{\partial}{\partial Q^2} \frac{\delta x g_A(x,Q^2)}{A} = -\frac{81}{16} \frac{A^{1/3}}{Q^2 r_0^2} \alpha_s^2(Q^2) \int_x^1 \frac{du}{u} \left[u g_N(u,Q^2) \right]^2 . \qquad (22)$$

The analogous equation for the gluon density in the nucleon has a much smaller coefficient – approximately by a factor $r_0^2/r_N^2 A^{1/3}$, where $r_N \sim 0.8$ fm is the nucleon radius. Once again one can see then that the x-range where nonlinear effects become significant differs for a heavy nucleus and for a nucleon by more than two orders of magnitude, assuming $x g_N(x,Q^2) \propto x^n$ with $n \sim -0.2$.

Thus electron-nucleus collisions at HERA can be seen as efficient amplifiers of nonlinear QCD effects.

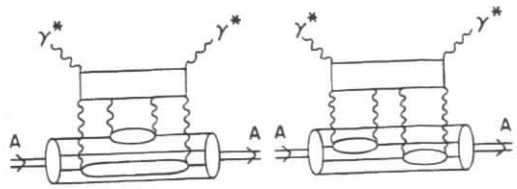

Figure 15: Typical fan diagrams leading to nonlinear evolution of $g_A(x,Q^2)$.

3.3 Theoretical Framework for Small x Phenomena in eA Collisions

3.3.1 Perturbative and Nonperturbative Shadowing

At small x the DIS cross section per nucleon in a nucleus is smaller for a bound nucleon than for a free one, the so called shadowing phenomenon. Shadowing is determined by a combination of non-perturbative and perturbative effects. In the DGLAP evolution equations one can express shadowing at large Q^2 through the shadowing at the normalization point Q_0^2. This type of shadowing is connected to the soft physics. It can be visualized e.g. in the aligned jet model of Bjorken [2], extended to account for QCD evolution effects [53]. A virtual photon converts to a $q\bar{q}$ pair with small transverse momenta (large transverse size) which interacts with the nucleus with a hadronic cross section, leading to shadowing. The effective small phase volume of these configurations ($\propto \frac{\lambda}{Q^2}$) leads to Bjorken scaling and it is due to colour transparency [53].

At large Q^2, these $q\bar{q}$ pairs evolve into systems with gluons, leading to a shift of shadowing to smaller x, which is equivalent to the standard Q^2 evolution of parton distributions. These $q\bar{q}$ pairs, which interact with the target nonperturbatively, seem to be responsible for most of the shadowing at intermediate Q^2 and $x \sim 10^{-2}$ which has been studied at fixed target energies. This mechanism of shadowing is effective for σ_T only since for σ_L the aligned jet contribution is strongly suppressed. For σ_L (as well as for the production of heavy quarks) one is more sensitive to the shadowing due to the interaction of small size $q\bar{q}$ pairs with the nuclear gluon field which can be shadowed.

At smaller x the situation may change rather dramatically because, as the recent HERA data indicate, already for $Q^2 \sim 1.5$ GeV^2 at $x \sim 10^{-4}$ perturbative contributions to $F_{2p}(x,Q^2)$ appear to become important, leading to a rapid increase of the structure functions with decreasing x. Hence contributions of various perturbative mechanisms which may generate shadowing for configurations of a size smaller than the hadronic size may become important. Perturbative QCD may be applicable to those small size pairs. Typical contributions involve diagrams of the eikonal type, various enhanced diagrams, etc. (Fig. 15,16).

3.3.2 Shadowing and Diffraction

In practically all models it is assumed that nuclei are built of nucleons. So the condition that the matrix element $< A|T[J_\mu(y)J_\nu(0)]|A >$ involves only nucleonic initial and final states is

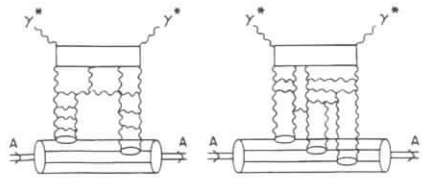

Figure 16: Examples of typical perturbative QCD diagrams contributing to nuclear shadowing.

implemented[1]. Under these natural assumptions one is essentially not sensitive to any details of the nuclear structure, such as short-range correlations etc.

In the case of scattering off the deuteron and light nuclei the same diagrams contribute to the cross section for diffraction in ep scattering and the cross section for shadowing – hence similar nonlinear phenomena like those described by eq.(22) are involved in each case. For example for the deuteron [1]:

$$\sigma_{shad} = \frac{\sigma_{tot}(eD) - 2\sigma_{tot}(eN)}{\sigma(eN)} = \frac{\frac{d\sigma_{diff}(ep)}{dt}|_{t=0}}{\sigma_{tot}(ep)} \frac{1}{8\pi R_D^2} R, \qquad (23)$$

where $R = \frac{(1-\lambda^2)}{(1+\lambda^2)}$, $\lambda = ReA/ImA \approx \frac{\pi}{2}\frac{\partial \ln A}{\partial \ln s}$ for the amplitude A of $\gamma^* p$ scattering and R_D is the deuteron radius. For small x, λ may be as large as 0.5, leading to $R \sim 0.5$ especially for the case of the longitudinal cross section. So already for light nuclei the study of the total cross sections of scattering from nuclei would allow *to establish a fundamental connection between the two seemingly unrelated phenomena of diffraction at small t in ep scattering and nuclear shadowing.* With the increase of A more complicated nonlinear interactions with several nucleons become important, see e.g. Fig. 16b.

Nuclear shadowing for the total cross sections has a simple physical meaning - it corresponds to a reduction of cross section due to screening of one nucleon by another (as well as by several nucleons for $A > 2$). If one treats the deuteron as a two nucleon system it is possible to apply the Abramovskii, Gribov, Kancheli (AGK) cutting rules [55] to elucidate **the connection between nuclear shadowing, diffraction and fluctuations of multiplicity.** One observes that the simultaneous interaction of the γ^* with the two nucleons of the deuteron modifies not only the total cross section but also the composition of the produced final states. It increases the cross section for diffractive scattering off the deuteron due to diffractive scattering off both nucleons by $\delta\sigma_{diff} = \sigma_{shad}$. At the same time the probability to interact inelastically with one nucleon only is reduced since the second nucleon screens the first one: $\delta\sigma_{single} = -4\sigma_{shad}$. In addition, a new process emerges in the case of the deuteron which was absent in the case of the free nucleon - *simultaneous* inelastic interaction with both nucleons which leads to a factor of two larger multiplicity densities for rapidities away from the current fragmentation region: $\sigma_{double} = 2\sigma_{shad}$. Altogether these contributions constitute $-\sigma_{shad}$, the amount by which the total cross section is reduced [2].

[1]The condition that nuclei are built of nucleons is not so obvious in the fast frame picture. However it is implemented in most of the models [19, 54].

[2]For simplicity we give here relations for the case of purely imaginary $\gamma^* N$ amplitude $\frac{ReA}{ImA} = 0$.

To summarize, *there is a deep connection between the phenomena of diffraction observed at HERA in ep scattering and nuclear shadowing as well as the A-dependence of diffraction and the distribution of the multiplicities in DIS.*

It follows from the above discussion that it is possible to get information about the dynamics of nuclear shadowing and hence about nonlinear effects by studying several **key DIS phenomena** such as: nuclear shadowing for inclusive cross sections F_2^A, $\frac{\sigma_L}{\sigma_T}$, F_2^{Acharm}; the cross section for nuclear diffraction; the multiplicity distribution for particle production in the central rapidity range; diffractive production of vector mesons. The advantage of the latter process is that one gets a rather direct access to the interaction of a small colour dipole with matter. It is in a sense an exclusive analogue of σ_L which is easier to measure.

3.4 The A-Dependence of Parton Distributions at Small x

As discussed above, the nucleus serves as an amplifier for nonlinear phenomena expected in QCD at small x. The simplest example of such effects is given by equation (22) where the nonlinear term is proportional to the square of the nucleon gluon density. If shadowing were absent the parton densities per unit transverse area would be enhanced by a factor $A^{1/3}$ as compared to the free nucleon case. Hence even just an upper limit on the parton densities based on unitarity – that the cross section for the inelastic interaction of a small dipole with a nucleus may not exceed $\sigma_{inel} = \pi R_A^2$ – leads to the expectation of nonlinear phenomena – shadowing of an observable magnitude – already at $x \sim 10^{-3} \div 10^{-4}$ [44].

Hence, from detailed studies of the A-dependence of the parton densities it would be possible both to check the dominance of the two-nucleon screening mechanism for $x \sim 10^{-2}$ [56, 57] and to extract information about the coherent interaction of the virtual photon with three (four) nucleons at $x \leq 10^{-3}$.

For $x \geq 10^{-2}$ for any nucleus and for all x for light nuclei, the main contribution to shadowing is given by the interaction with two nucleons of the target. Hence in this regime there is a relatively simple connection with the diffraction of a virtual photon off a proton – which is the simplest nonlinear effect in the perturbative domain in QCD. For smaller x and heavy nuclei, when essential longitudinal distances become comparable and ultimately exceed the diameter of the nucleus, several nucleons at the same impact parameter contribute to the screening. It is worth emphasizing that these multi-vacuum exchange processes cannot be singled out unambiguously using a nucleon target. The relevant QCD diagrams for the total cross section of $\gamma^* A$ interaction are rather similar to higher-order nonlinear diagrams for the proton target – except that in the nuclear case one has to impose the condition that couplings to the individual nucleons are colour singlets, see e.g. Fig. 15,16.

In a sense, the studies of nuclear shadowing at small x and large Q^2 can be considered as a simpler model of nonlinear effects which occur in the case of a nucleon target. In the latter case it is not easy to relate the coupling of say two vacuum exchanges (or a ladder with 4 gluons in the t-channel) with a nucleon to the coupling of one vacuum exchange with a nucleon. In fact the region of $10^{-3} \geq x \geq 10^{-4}$ may be optimal in this respect since nonlinearities for the nucleon case are still small though nonlinearities for the nuclear case are already quite substantial. It is worth emphasizing that experience of the studies of the total hadron-nucleus scattering indicates that interaction with bound nucleons for the total cross sections can well be

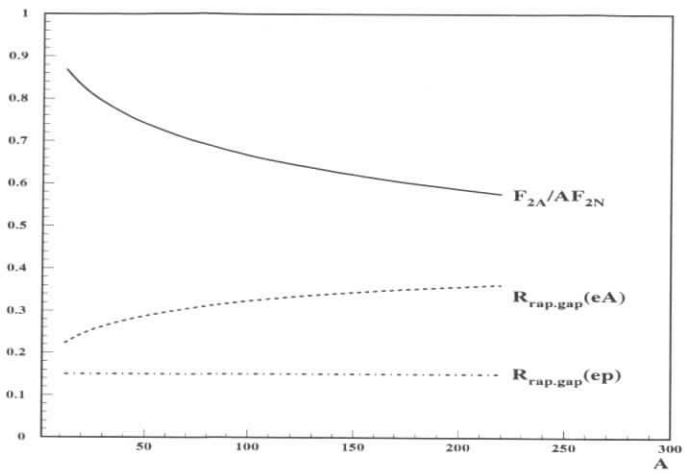

Figure 17: A-dependence of nuclear shadowing and probability of rapidity gap events in the colour screening model of shadowing; dot-dashed curve assumes A-independent probability of rapidity gap events.

approximated by the interactions with free nucleons (for a recent analysis see [58]). Therefore *nuclear structure effects do not obscure the interpretation of nuclear shadowing effects.*

Using current information from HERA on diffractive production in ep scattering it is straightforward to estimate the amount of nuclear shadowing at small x taking into account interactions with 3 or more nucleons using the eikonal approximation with an effective cross section determined from diffractive data, see eq.(24) below. The result of the calculation [40] is shown in Fig. 17 for $Re/Im = 0$; for $A \geq 12$ it weakly depends on the value of Re/Im. Since the data on diffraction indicate that the fraction of diffractive events in DIS weakly depends on x, Q^2 these considerations show that significant shadowing effects should be present for $F_2^A(x, Q^2)$ in the wide small x range of HERA. Note that the shadowing effect in DIS is expected to be much smaller than for the case of real photon scattering since the effective cross section for interaction of the hadron component of quasi-real photon at HERA is a factor of ~ 3 larger than for a highly virtual photon (we use here the HERA data on diffraction for real photons [59]).

Since the interaction of the octet colour dipole gg is a factor of 9/4 stronger than for the $q\bar{q}$ dipole, nonlinear effects are expected to be more important for gluons. So gluon shadowing would provide even more direct access to nonlinear phenomena. Note that in this case there is no simple relation of shadowing with diffraction in $\gamma^* + p$ DIS, so any information about gluon shadowing would be complementary to the information from ep DIS. There are very few data on the gluon distribution in nuclei. Among them, the enhancement of the gluon distribution at $x \sim 0.1$ indicated by the inelastic J/ψ production data [25]. Also the analysis [60] of the scaling violation for the ratio F_2^{Sn}/F_2^C [11] under the assumption that higher twist effects are not important in the Q^2, x range of the data allows to extract information about the A-

dependence of gluon distributions, indicating some nuclear shadowing for G_A for $x \leq 0.01$ and an enhancement at $x \sim 0.1$, see Figure in [60][3]. Theoretical expectations for gluon shadowing discussed in the literature are quite different – from a larger effect than for F_2^A [63], to an effect comparable to that of quarks [62, 61, 64, 65] to substantially smaller shadowing [66]; see also contributed papers to these proceedings.

Comparison of different determinations of shadowing of gluons and measurements of the scaling violation for the F_2^A/F_2^D ratios will allow to determine the range of applicability of the DGLAP evolution equations and hence provide unique clues to the role of nonlinear effects.

It is worth emphasizing also that knowledge of parton distributions in bound nucleons at these values of x will be crucial also for studies in heavy-ion physics at the LHC and RHIC.

3.4.1 BFKL Pomeron

One can envision several strategies for the study of the BFKL Pomeron in DIS. The main requirement is to enhance the contribution of scattering of small transverse size configurations in the ladder. It is natural to expect that screening for these configurations would be minimal. Hence for heavy nuclei the contribution of the BFKL Pomeron can be enhanced.

1. A procedure can be envisioned to study the A-dependence of $F_2^A(x, Q^2)$ at small x to extract the term in the structure functions $\propto A$ and then study its x dependence. Based on the above argument A.Mueller has suggested [67] that the x dependence of this term (linear in A) would be closer to BFKL type behaviour.

2. One promising direction to look for the BFKL pomeron is the Mueller-Navalet process of producing two high p_t jets with large a rapidity difference [68] to suppress the contribution from small transverse momenta (large transverse distances) in the ladder. In the case of a nuclear target large distance contributions would be screened out to a large extent.

3. Another possibility is the production of ρ mesons at large $|t|$ in inelastic diffraction. To enhance the contribution of the BFKL Pomeron it is desirable to increase the contribution of small configurations in the ρ meson, i.e. quark-antiquark pairs with small transverse separation. Large size configurations can be filtered out by exploiting the fact that they are absorbed on the nucleus surface. Once again extracting the term in the cross section $\propto A$ would allow to enhance the contribution of the BFKL Pomeron.

3.5 Diffraction off Nuclei

3.5.1 Introduction

Diffraction studies have been defined as one of the primary goals of nuclear beams in HERA. Such processes can be interpreted using two complementary languages depending on whether the rest frame of the nucleon or the Breit frame are used:

• Scattering of electrons on colourless components of the proton [36, 37]. Such scattering may be identified, for the very low x events dominated by diffraction, with the interaction with

[3]The shadowing for gluons should be accompanied by a significant enhancement at larger x since the total momentum fraction carried by gluons in nuclei is not suppressed and is probably slightly enhanced [61].

the vacuum t-channel exchange which is often referred to as the Pomeron, $I\!P$. This object is not necessarily the same as the Pomeron of the Gribov-Regge high-energy soft interactions (see report of the diffractive group). Deep inelastic electron scattering leading to the presence of a rapidity gap can thus be considered as probing the internal parton structure of the $I\!P$ originating from the proton.

One of the questions of primordial importance which may be addressed within the future electron-nucleus scattering program at HERA is then "how universal is the internal structure of the Pomeron?" or, more precisely: "Is the internal structure of the Pomeron originating from various hadronic sources (protons, neutrons, nuclei) the same?". We shall show below how nuclei may help in answering these questions.

- The diffractive interaction of different hadronic components of the virtual photon with the target via vacuum exchange. Diffraction predominantly selects the γ^* components which interact with sufficiently large cross sections such as large transverse size $q\bar{q}$, $q\bar{q}g$ colour dipoles. Therefore the study of diffraction plays a very important role in determining the relative importance of small and large size configurations and addressing the question whether small white objects interact weakly or not. Indeed if the interaction with a target becomes sufficiently strong at small impact parameters the cross section for diffraction (which includes both elastic scattering and inelastic diffractive dissociation) would reach the black body limit of 50% of the total cross section.

3.5.2 Theoretical Expectations

Diffraction off a nucleon (including dissociation of the nucleon) constitutes about 15-20% of the deep inelastic events. Therefore the interaction is definitely far from being close to the scattering off a black body. Even this number came a surprise in view of the large Q^2 value involved. Using the generalized optical theorem as formulated by Miettinen and Pumplin, one can estimate the effective total cross section for the interaction of the hadronic components of the γ^* as

$$\sigma_{eff} = 16\pi \frac{\frac{d\sigma^{\gamma^*+p\to X+p}_{diff}}{dt}|_{t=0}}{\sigma_{tot}(\gamma^* N)} \approx 12 \div 15\text{mb}. \qquad (24)$$

This cross section is significantly smaller than the ρN cross section which at the HERA energies can be estimated to be close to 40 mb using the vector dominance model and the Landshoff-Donnachie fit [69]:

$$\sigma^{\rho N}_{tot}(s) = \sigma^{\rho N}_{tot}(s_0)\left(\frac{s}{s_0}\right)^n, \qquad (25)$$

where $n \approx 0.08, s_0 = 200$ GeV^2, $\sigma^{\rho N}_{tot}(s_0) = 25$ mb. However it is sufficiently large to result in a substantial cross section of diffraction for small x - it can reach 30-40% for large A (Fig. 17)[40]. For large A the coherent diffraction dominates when the incoming wave is sufficiently absorbed at small impact parameters which, by virtue of Babinet's principle, corresponds to scattering beyond the nucleus. In such processes the nucleus remains intact and the average momentum transfer is very small ($\langle t \rangle \propto A^{-2/3}$).

One expects that hadronic configurations interacting with different strength contribute to diffraction (cf. Fig. 14). The parameter σ_{eff} characterizes just the average strength of this

interaction, while the distribution over the strengths is expected to be quite broad. The study of diffraction off nuclei allows to separate contributions to diffraction of large and small size configurations due to **the filtering phenomenon**: with the increase of A the relative contribution of more weakly interacting (smaller size) configurations should increase since they are less shadowed, leading to a relative enhancement of the colour transparent subprocesses.

Examples of promising processes are:

- Diffractive production of charm. The A-dependence of this process would be interesting already at low Q^2 since the essential transverse distances are, naively, of the order of $1/m_c$, where m_c is the charm quark mass. Since the cross section for the interaction of a colour dipole of such size is small for $x \sim 10^{-2}$, the cross section for diffractive charm production at these values of x is small and practically not shadowed, leading to a cross section $\propto A^{4/3}$. At the same time the $c\bar{c} - N$ cross section increases rapidly with decreasing x (increase of energy) for fixed Q^2. Therefore at HERA energies diffractive charm production in ep collisions may become a substantial part of the total diffractive cross section. At this point one expects the emergence of shadowing in diffractive charm production in eA collisions, leading to slowing down of the A-dependence of diffractive charm production as compared with the A dependence at $x \sim 10^{-2}$.

  One can go one step further and study the A-dependence of p_t distributions for diffractive charm production. Smaller size components will be less absorbed and so their relative contribution may increase with A.

- Diffractive production of two high p_t jets.

  Selection of large p_t jets enhances the contribution of diffraction of small size configurations. Hence, one expects broader p_t distributions in the case of nuclear targets (smaller jet alignment) with nontrivial dependences on W and Q^2. For example, if we fix the p_t of the jets, the A-dependence of dijet production should become weaker with increasing energy reflecting the increase of the absorption (which can be studied this way). If on the other hand we fix W and consider the A-dependence as a function of p_t, a stronger A-dependence is expected. Effectively, this would be another way to approach colour transparency via filtering out of the soft components.

To summarize, a study of inclusive diffraction will give better insights into the structure of the Pomeron. The interplay of soft and hard contributions will lead to a breakdown of factorization for the structure function of the Pomeron. Stated differently, the check of the degree of "universality" of the Pomeron - i.e. whether the "nuclear" Pomeron is different from the Pomeron observed in ep diffraction - will provide a very sensitive test of QCD dynamics.

An important aspect of the diffractive studies is the colour transparency phenomenon. In view of its special interest we will discuss this separately below.

3.5.3 Multiplicity Fluctuations

As we explained in section 3.3.2 diffraction off nuclei and nuclear shadowing are closely related to the simultaneous inelastic interactions of the virtual photon with several nucleons. Such interactions produce events with large multiplicity densities in the central rapidity range, leading to a much broader distribution over multiplicities in eA collisions than in the ep case. Study

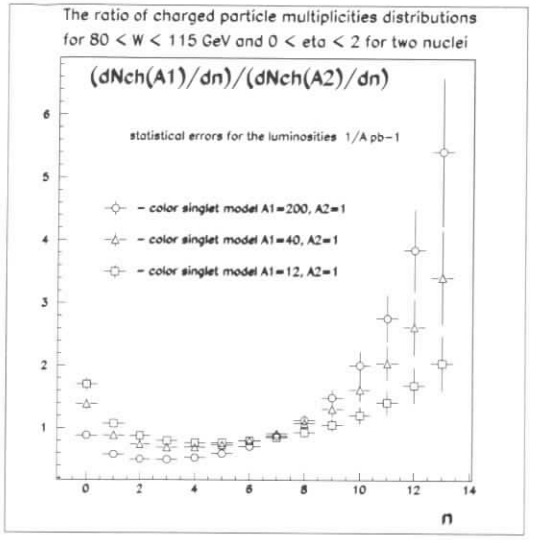

Figure 18: A-dependence of distribution over multiplicity calculated in the colour singlet model for a luminosity of 1 pb^{-1}.

of this effect will provide information complementary to that obtained from nuclear shadowing about the structure of the vacuum exchange at small x. Interesting phenomena to look for may be:

1. Local fluctuations of multiplicity in the central rapidity region, e.g. the observation of a broader distribution of the number of particles per unit rapidity, $n(\Delta\eta)$, than in ep scattering [40], see Fig. 18.

2. Long range rapidity fluctuations – i.e. positive correlation of the increase of multiplicity in one rapidity interval with the increase of multiplicity several units away.

3. Correlation of the central multiplicity with the multiplicity of neutrons in the neutron detector (most effective for heavy nuclei).

3.6 Colour Transparency Phenomena

An important property of QCD is that small objects are expected to interact with hadrons with small cross section [70]. This implies that in the processes dominated by the scattering/production of hadrons in "point-like"(small size) configurations (PLC) when embedded in the nuclei, the projectile or the outgoing hadron essentially does not interact with the nuclear environment [71, 72]. In the limit of colour transparency one expects for an incoherent cross section a linear dependence on A, for example

$$\frac{d\sigma(e+A\to e+p+(A-1)^*)}{dQ^2}=Z\frac{d\sigma(e+p\to e+p)}{dQ^2}, \qquad (26)$$

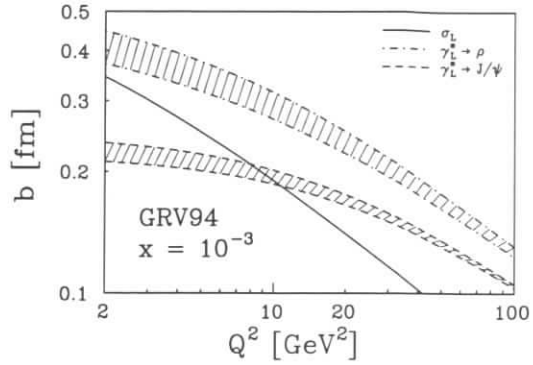

Figure 19: Average transverse size of the $q\bar{q}$ components effective in $\mathcal{A}_{\gamma_L^*N\to VN}$ for $\rho-$ and J/ψ-meson production and σ_L. The probed Q^2 scale is inversely proportional to b^2.

while for coherent processes at $t=0$ one expects

$$\frac{d\sigma(\gamma^*+A\to X+A)}{dt}=A^2\frac{d\sigma(\gamma^*+N\to X+N)}{dt}. \qquad (27)$$

No decisive experimental tests of this property of QCD were performed so far since in most of the current experiments the energies were not sufficiently high to prevent expansion of the produced small system. The high-energy E665 experiment [73] at FNAL has found some evidence for colour transparency in the ρ meson production off nuclei. However, the data have low statistics, cover a small x, Q^2 range and cannot reliably separate events without hadron production.

A quantitative formulation of colour transparency for high-energy processes can be based on eq.(21). For the case of nuclear targets it implies that for a small enough colour dipole, the cross section of its interaction with nuclei is proportional to A up to the gluon shadowing factor. As a result the colour transparency prediction for 2 jet and vector meson diffractive production is [74, 42] [4]:

$$\frac{\frac{d\sigma}{dt}(\gamma^*A\to 2jets+A)|_{t=0}}{\frac{d\sigma}{dt}(\gamma^*N\to 2jets+N)|_{t=0}}=\frac{\frac{d\sigma}{dt}(\gamma^*A\to VA)|_{t=0}}{\frac{d\sigma}{dt}(\gamma^*N\to VN)|_{t=0}}=\left[\frac{F_A^L(x,Q^2)}{F_N^L(x,Q^2)}\right]^2=\frac{G_A^2(x,Q^2)}{G_N^2(x,^2Q)}. \qquad (28)$$

Gluon shadowing constitutes a rather small effect for $x\sim 10^{-2}$ (see earlier discussion). For smaller x it increases but it is in any case much smaller than the screening effect expected in the case of lack of colour transparency if the produced system interacts with cross section comparable to $\sigma_{\rho N}\sim$ 30-40 mb. For such values of σ one expects the cross section to behave as $\propto A^{4/3}$ for $t=0$ which would be possible to test using diffractive production by quasi-real photons.

Coherent diffractive ρ,J/ψ-meson production

[4] In writing eq.(28) we neglect the difference of Q^2 scales for different processes which is reflected in a different dependence of the essential transverse size of the $q\bar{q}$ state on the process (see Fig. 19). For a discussion of the appropriate scale for dijet production see [75].

The most straightforward test of colour transparency can be made using coherent production of ρ or J/ψ-mesons at small t using nuclei with $A \geq 12$. The p_t resolution of the current detectors is good enough to single out the diffractive peak which is concentrated at $p_t \leq 0.1$ GeV. In the higher x end of the range which could be studied at HERA for vector meson production, $x \sim 10^{-2}$, one expects at large Q^2 nearly complete colour transparency since gluon shadowing effects are rather small and decrease rapidly with increase of Q^2, while the transverse separation,b, between q and $\bar{q}$ is of the order of 0.4 fm for $Q^2 \sim 10$ GeV^2 and further decreases with increase of Q^2 (Fig. 19 [44]). Study of coherent J/ψ meson production would allow to probe colour transparency for propagation of even smaller dipoles since $\langle b_{c\bar{c}}(Q^2 = 0)\rangle \sim 0.2$ fm.

On the other hand as discussed earlier at the smallest values of x of the HERA range, screening effects should start to play a role even at large Q^2 so a gradual disappearance of colour transparency is expected – the emergence of colour opacity. Noticeable screening is expected already on the basis of unitarity constraints. Qualitatively one may expect that the rise of the cross section for vector meson production with increasing energy at fixed Q^2 will slow down at significantly lower energies than for the case of the $\gamma^* + p$ reaction. Currently theoretical calculations of vector meson production by transversely polarised photons are difficult because the nonperturbative large distance contribution is not as strongly suppressed in this case as in the longitudinal case. If contribution of pairs with large transverse size is indeed important for σ_T, it would be filtered out with increasing A leading to larger values of σ_L/σ_T for large A.

Let us enumerate several other effects of Colour Transparency (CT) in diffractive production.

1. Production of excited vector meson states ρ', ϕ'.

   In the CT limit, QCD predicts a universal A-dependence of the yields of the lowest mass and excited states (this includes the effect of gluon shadowing in eq.(28)). This is highly nontrivial since the sizes of the excited states are much larger, so one might expect larger absorption. On the other hand, for lower Q^2 average transverse distances, b, are not small. At these distances the wave functions of ground and excited states differ. So in this Q^2 range the relative yields of various mesons may depend on A.

2. Production of high p_t dijets.

   The uncertainty relation indicates that coherent production of dijets with large p_t, carrying all the momentum of the diffractively produced system is dominated by distances $r_t \propto \frac{1}{p_t}$. Hence filtering out of soft jets is expected, leading to a broadening of the p_t and thrust distributions. At the same time the study of the A-dependence of low p_t jets would allow to address the question of colour opacity. Another feature to look for would be the distribution over the electron-two jet plane angle as suggested in [76].

3. Coherent diffractive production at $-t \geq 0.1$ GeV^2 for $A = 2, 4$.

   An important question here is the possibility to observe the "disappearance" of colour transparency for ρ-meson production and the emergence of "colour opacity" – due to nonlinear screening effects at $x \sim 10^{-4}$. Manifestations of CT would be the increase of the differential cross section $\frac{d\sigma}{dt}$ below the diffractive minimum ($|t_{min}(^4He)| \approx 0.2$ GeV^2 and suppression of the cross section in the region of the secondary maximum. A gradual disappearance of CT in this region with increasing energy would appear as a very fast increase with energy of the secondary maximum of the t distribution. Remarkably, in this region the cross section for the process is proportional to $[G_N(x, Q^2)]^4$, where G_N is the gluon density in the nucleon [77, 78]. The present beam optics would allow measurements of quasielastic processes with ^{4}He in the region of the secondary maximum ($|t(^4\text{He})| \approx 0.4$ GeV^2). For a luminosity of 10 pb^{-1} it would be possible to measure the ρ-meson production cross section up to $Q^2 \sim 10$ GeV^2.

4. A-dependence of rapidity gaps between jets in photoproduction.

   Recently photoproduction events which have two or more jets have been observed in the range $135 < W_{\gamma p} < 280$ GeV with the ZEUS detector at HERA [79]. A fraction of the events has little hadronic activity between the jets. The fraction of these events, $f(\Delta\eta)$, reaches a constant value of about 0.1 for large pseudorapidity intervals $\Delta\eta \geq 3$.The observed number of events with a gap is larger than that expected on the basis of multiplicity fluctuations assuming the exchange of a colour singlet. This value is rather close to estimates in perturbative QCD [80, 81, 82] neglecting absorptive effects due to interactions of spectator partons. It is much larger than the values reported by D0 [83] and CDF [84]. Small effects of absorption are by no means trivial in view of the large interaction cross section for many components of the hadronic wave function of the real photon. They may indicate that colour transparency is at work here as the ZEUS trigger may select point-like configurations in the photon wave function [85]. To check this idea it would be natural to study the A-dependence of rapidity gap survival. It is demonstrated in [85] that this probability strongly depends on the effective cross section of the interaction of the photon with the quark-gluon configurations involved in producing rapidity gap events. One would be sensitive to cross sections as small as ~ 5 mb.

3.7 Parton Propagation in Nuclear Matter

3.7.1 Introduction

Measurements of final state hadrons allow to investigate the effects of partons propagating through nuclear matter. In the present section we discuss some of these possibilities. The discussion is restricted to *incoherent* phenomena (coherent nuclear interactions were discussed in previous sections).

There are essentially two types of measurements which can be useful: (a) energy loss of high-energy particles and (b) increase of their transverse momentum, both studied as a function of the nuclear number A and/or number of nucleons emitted from the target nucleus. They are sensitive to different aspects of the interactions. Energy loss reflects the properties of inelastic collisions: the value of the inelastic parton-nucleon cross section and of the inelasticity. The increase of transverse momentum and emission of the nucleons from the target can be induced by elastic as well as by inelastic collisions and thus can provide information on both.

At this point we emphasize the importance of the measurement of the distribution of the nucleons (protons and neutrons) emitted from the target nucleus during or after the interaction. Such measurements give direct access to the number of secondary interactions inside the target [86], as was already realized (and used) in numerous emulsion experiments where protons with momenta $250 \leq p_N \leq 700$ MeV/c were measured [87]. Related information can be inferred from the measurement of the production of soft neutrons ($E_n \leq 10$ MeV) which was studied recently by the E665 collaboration [88]. Measurements of the emitted nucleons and of their energy spectrum should thus be considered a high priority. They allow to improve greatly the

analysis of the data in three respects: (a) by studies of the distribution of nucleons themselves one obtains information of the strength of the secondary interactions and - more essentially- on the fluctuations which are expected to be large and would otherwise hamper the interpretation of the data; (b) By studying the interactions as a function of the number of the emitted nucleons one can obtain not only a larger lever arm in terms of the number of secondary interactions but also, at a *fixed* nuclear number, a clean sample, free of possible biases related to the use of different targets; (c) a really exciting possibility is to develop a trigger for events with a large number of emitted nucleons (or highly reduced charge of the nuclear remnant). This would allow to study in detail the rare events with particularly strong secondary interactions. Further quantitative studies (both theoretical and experimental) of this problem are necessary to clarify the relation between the emitted nucleons and number of secondary interactions. Some work on these lines was already presented during this workshop [89, 4, 90]. The detection of such nucleons at HERA will be simpler than in fixed target experiments since they will be boosted by the motion of the target nucleus [4].

As we discussed previously there should be a substantial difference between the nuclear effects observed in the region of "finite" x (x greater than, say, 0.05) and the region of very small x (x smaller than, say, 0.001). The reason is the different nature of the photon-nucleon interactions in these two regions caused by the difference in life times of the relevant photon fluctuations into a $q\bar{q}$ pair.

One sees from eq.(19) that at finite x the life time of a fluctuation is rather short (smaller than 2 fm). This has two consequences: (a) the interaction of the photon must take place inside one of the nucleons of the target (nuclear coherence suppressed) and (b) the high-energy part of the interacting photon fluctuation can be well approximated by a simple "bare" quark. This can be seen as follows. The time necessary to produce a high-energy gluon from a quark is given by

$$\tau_g = \frac{2E_g}{q_t^2} \tag{29}$$

where E_g is the gluon energy and q_t its transverse momentum (with respect to the quark). From the obvious condition $\tau_g < \tau$ we then obtain

$$E_g < \frac{\beta k_t^2}{2m_N x}. \tag{30}$$

We conclude that at finite x there is simply no time to produce the energetic gluon cloud.

For DIS nuclear collisions this picture implies that after the first interaction of the virtual photon the nucleus is penetrated by one bare quark (following approximately the direction of the virtual photon). Alternatively one can consider the process of production of two high p_t jets in *photon-gluon fusion*. In this case one studies propagation through the nucleus of a colour octet state. Thus the observed nuclear effects measure interactions of a *bare* parton (or a system of *bare* partons) in nuclear matter.

The situation is rather different in the region of small x. In this case there is enough time for the $q\bar{q}$ system coupled to the virtual photon to "dress" itself into a cloud of energetic gluons and $q\bar{q}$ pairs (in the limit $x_{Bj} \to 0$ the condition (30) is not restrictive). Consequently, the system traversing the nucleus is a complex multiparton system resembling in some respects an "ordinary" hadron. The observed nuclear effects measure interactions of this multiparton system (*dressed* quark or $q\bar{q}$ dipole) in nuclear matter. It should thus not be surprising that the expectations for the region of small x are rather different from those at finite x.

3.7.2 Current Experimental Situation

Two major manifestations of the interaction of a parton propagating through the nuclear medium which were studied experimentally so far are the parton energy loss and the broadening of its transverse momentum distribution.

The measurements of the leading hadron spectrum in deep inelastic lepton-nucleus scattering have the biggest sensitivity to the energy loss. Measurements at incident energies below 50-100 GeV find a depletion of the leading particle spectrum which may be interpreted as due to the energy loss. At higher energies the effect nearly disappears [49], indicating that energy losses for partons propagating through nuclear matter are definitely smaller than $\Delta E/dz \leq 1$ GeV/fm. This is in agreement with the observed low multiplicity of low energy neutrons in μPb interactions at high energies [88], which is consistent with knockout of one nucleon from lead [90]. This makes it impossible to address directly the question of energy losses at high energies.

The phenomenological situation with transverse momentum broadening is somewhat confusing at the moment. The μ-pair production experiments [91] which measure the broadening of the *incident* quark find rather small broadening: $\Delta p_t^2 \sim 0.1$ GeV^2 for the distance, $L \sim 5$ fm. At the same time the transverse momentum broadening for the jets produced by *outgoing* partons in photon-nucleus interactions seems to be much larger [92]. Theoretically this difference is not understood [93].

3.7.3 Perturbative QCD Expectations for Finite x

All estimates of nuclear effects in this region of x accept that the interaction of a *bare* quark in nuclear matter is dominated by colour-exchange processes which lead to break-up of the "wounded" nucleon in the target but do not slow down significantly the energetic quark. This is based on the argument that the quark in question can only emit gluons satisfying the condition $\tau_g < \Delta l$ where Δl is the distance between the subsequent collisions. From eq.(29) we deduce that the energy loss in one secondary collision is limited by

$$\Delta E < 2q_t^2 \Delta l, \tag{31}$$

i.e., by a value which is independent of the energy of the quark. Consequently, a high energy quark can lose only a small fraction of its energy. A precise evaluation of the energy loss in a collision with one target nucleon is not possible at the present stage of the theory.

However recently a significant progress was obtained in the analysis of the propagation of a virtual parton through the nuclear medium [3]. It was demonstrated that the Landau-Pomeranchuk-Migdal effect in QCD is qualitatively different from the case of QED. It was argued that for sufficiently large distances, L, traversed by a parton the process is dominated by perturbative QCD though the momentum transfers in the individual collisions are small.

A simple relation was found between the p_t broadening and the energy loss

$$-\frac{dE}{dL} = \frac{\alpha_s N_c}{8} \Delta p_t^2(L), \tag{32}$$

which corresponds to substantially smaller energy losses than those implied by the inequality in eq.(31).

Probably the most striking prediction is the quadratic dependence of the energy loss on the traversed distance, L, as compared to the nonperturbative models where it is approximately proportional to L. Numerically the authors find for a quark

$$-\Delta E \simeq 2GeV \left(\frac{L}{10\ \mathrm{fm}}\right)^2, \tag{33}$$

neglecting the x dependence of the nucleon gluon density (and a factor of ~ 2 larger energy loss for gluons). If this effect is included the L-dependence is even steeper. The numerical coefficient is estimated here from the information on the nucleon gluon densities and consistent with eq.(32) if one uses experimental data on p_t broadening of the μ-pair spectrum [91]. Alternatively, if one uses the p_t information from γA data a much larger energy loss is predicted. However even in this case the expected energy loss is too small to be observed *directly* in DIS at collider energies.

The energy loss occurs (for realistic nuclei) via the emission of one or two gluons with energies $\sim \Delta E$. So it would be the best to look for the energy loss effects by studying the production of hadrons in the nucleus fragmentation region. Quadratic dependence on L will be manifest in the A-dependence of the number of knocked out nucleons, as well as in the fluctuations of the number of emitted soft protons and neutrons in the case of heavy nuclei. Current HERA detectors have good acceptance for such nucleons.

Broadening of the transverse momentum spectrum may be more easy to access. The transverse momentum of a parton increases as a result of multiple collisions. Since the momentum transfers in the subsequent collisions are independent, the increase of the (average) transverse momentum squared is proportional to L and hence to the number of secondary collisions. One expects for the quark

$$\Delta p_t^2 \simeq 0.2\mathrm{GeV}^2 \frac{L}{10\mathrm{fm}}, \tag{34}$$

while for gluons broadening is about a factor of 2 larger.

A word of caution is necessary here. For distances typical even for heavy nuclei the average momentum transfer is rather small so application of perturbative QCD may be difficult to justify. Also it is not clear whether it is safe to interpolate from fixed target energies to collider energies assuming that the momentum transfer in individual collisions is energy independent.

To study these effects at HERA in a clean way one needs to consider processes dominated by relatively large $x \geq 0.1$. They include processes of dijet production similar to those studied at FNAL [92]. An advantage of HERA is that it would be possible to use information about the decay of the nucleus to check the correlation between transverse momentum broadening and the number of struck nucleons.

3.7.4 Parton Propagation at Small x

This region is more relevant for HERA but, unfortunately, theoretical estimates are difficult and uncertain because the system traversing the nucleus is fairly complicated. Hence its interaction with nuclear matter not easy to evaluate. Perturbative QCD leads to the simple prediction that at large Q^2 and large incident energies, due to QCD factorization, the spectrum of leading hadrons [72] is given by,

$$\frac{1}{\sigma^{\gamma^* A}(x,Q^2)} \frac{d\sigma^{\gamma^*+A\to h+X}(x,Q^2,z)}{dz} = f(z, \ln Q^2), \tag{35}$$

which does not depend on A. (Energy losses we discussed above do not change the z spectrum in this limit). However, it is far from clear if perturbative methods are applicable at all - even at large Q^2 [94]. The incoming system can experience several soft interactions with the nucleons of the target nucleus. However, the AGK technique which can be used to relate nuclear shadowing with the A dependence of diffraction and the fluctuations of hadron production in the central region, does not allow any predictions for the A dependence of the spectrum of leading hadrons in the current fragentation region since these effects depend on the details of the virtual photon wave function. In view of these difficulties it is not possible to give unbiased quantitative predictions and we restrict ourselves to a discussion of qualitative expectations and possible interpretations of the future measurements.

As we have already mentioned, at small x the virtual photon fluctuates into a $q\bar{q}$ pair a long time before it enters the nucleus. This has several consequences. First, it opens the possibility of *coherent* phenomena in which the nucleus participates as a whole which were discussed in a previous section. They should be carefully separated from the incoherent interactions we are concerned with. Second, there is enough time for this fluctuation to emit a large number of gluons and new $q\bar{q}$ pairs *before* it enters the nucleus. The cross-section of such a "dressed" fluctuation is generally fairly large, leading to substantial "shadowing" effects, as already discussed. Finally, the system produced in the first collision is by no means a single bare quark but rather a multiparton conglomerate - result of a quark-gluon cascade of length equal to the available rapidity, i.e. very long at small values of x. Studies of interactions in nuclear matter provide an opportunity to obtain information about this object.

The cascade origin of the system travelling through the nucleus implies strong correlations between partons. Consequently, large fluctuations are expected in its physical properties and thus also in the observable nuclear effects. For example, the cross section for secondary interactions is expected to vary widely from event to event. This variation may or may not be correlated with the fluctuations of the parton multiplicity and energy distributions. For a clean interpretation of the results it is therefore crucial to obtain information on the number of secondary interactions inside the nucleus which is the most important parameter determining the strength of the interaction. Fortunately, as we have already explained, this information is accessible through measurements of the distribution of nucleons (protons and neutrons) emitted by the colliding nucleus. They seem thus crucial for the success of this investigation.

The distribution of the number of collisions gives straightforward information on the fluctuations of the cross section for secondary interactions inside the nucleus. Its change as Q^2 increases from 0 to the deep inelastic region should give information on the extent to which the structure of parton bound states (i.e. hadrons) differs from that of the "dressed" $q\bar{q}$ pair.

Similar remarks apply to measurements of the energy loss (which measures the energy distribution inside the parton system in question). Correlation between the observed energy loss and the number of collisions gives information on clustering phenomena inside the parton system. It will be interesting to look for possible effects of constituent quarks at low Q^2 and to see when they disappear as Q^2 increases. Fig. 20 illustrates the possibility of such an investigation. It shows the ratio of the total energy loss of the incident virtual photon in the nucleus to that in collision with one nucleon, assuming that the photon fluctuates into K constituents which interact independently (losing energy) with the target. One sees that the curves corresponding to different values of K are substantially different. This seems to give a chance to see possible effects of constituent quarks ($K = 2$) at low Q^2 which should gradually disappear ($K \to \infty$) as Q^2 increases. It should be remembered, however, that variations in

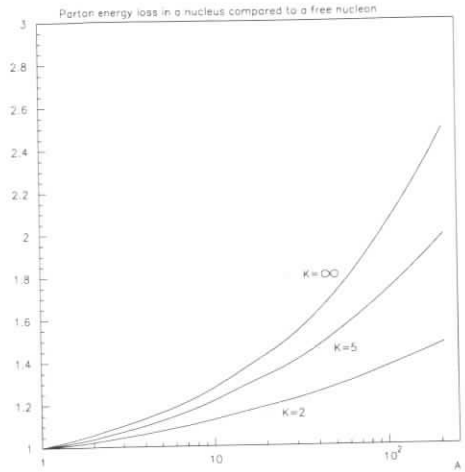

Figure 20: Energy loss of the incident virtual photon in nuclei assuming that the photon fluctuates into K constituents interacting independently in nuclear matter with an interaction cross section of 20 mb.

the cross-section of the photon fluctuation in question will smear out this clean effect. It is therefore necessary to rely on an independent estimate of the number of collisions as we already emphasized at the beginning of this section. In this case the ratio in question is given by

$$\frac{\Delta E_A}{\Delta E_1} = K(1-(1-1/K)^N) \tag{36}$$

(N is the number of collisions) and one can easily see that this is indeed a much better way to analyze the data, particularly at high N.

It should be noted at this point that, in contrast to the situation at finite x, in the present case the energy loss is expected to be a finite fraction of total available energy, as explained above. Consequently, there seem to be no particular difficulties in this measurement.

To summarize, one expects a dramatic increase of the energy loss in nuclear matter when one goes from finite to small values of x. If confirmed by future data this should allow to study details of the parton structure of the QCD cascade. Investigation of the transition region of $x \approx 0.01$ is also of great interest. HERA is very well suited for this task.

3.8 Connection to Heavy-ion Collisions at High Energies

The interplay between the physics which can be studied in high-energy eA collisions at HERA and that to be studied in the heavy ion physics was discussed at the dedicated workshop "Nuclei at HERA and Heavy Ion Physics" which was held at Brookhaven National Laboratory in 1995. It was concluded that the measurements of eA collisions at HERA can provide crucial

information necessary for unambigous interpretation of the heavy ion colllisions at RHIC and LHC for establishing whether a quark-gluon plasma is formed in these collisions.

Three major links are

- *Nuclear gluon shadowing*

One needs $xg_A(x,Q^2)$ for $x \sim 10^{-2}$, $Q^2 \sim 1-10\mathrm{GeV}^2$ and $x \sim 10^{-3}$, $Q^2 \sim 10\mathrm{GeV}^2$ to fix the initial conditions at RHIC and LHC respectively. This is especially important for the LHC since mini-jet production determines the initial conditions for $\sqrt{s} \geq 100\mathrm{GeV}$ A. The bulk of the particles produced at central rapidities in AA collisions at the LHC is expected to be generated due to this mechanism [95]. Currently uncertainties in nuclear shadowing transform into at least a factor 2-4 differences in the final transverse energy flow [96].

- *Jet quenching*

Recent QCD studies [97] have demonstrated that the medium induced energy losses and p_t broadening of a high energy parton traversing a hot QCD medium are much larger than in the case of a cold medium. This provides a unique new set of global probes of the properties of the state formed during AA collisions [96]. To interpret unambiguously this effect it is necessary both to measure the nuclear gluon shadowing and to study the parton propagation in cold matter in DIS to confirm that the energy losses (p_t-broadening) remain small at energies comparable to those to be studied at RHIC and LHC.

- *Testing of soft dynamics of interactions with nuclei*

Study of eA interactions at HERA in **the same energy range** as that to be studied in pA and AA collisions at RHIC ($\sqrt{s} \sim 200$ GeV) will provide a unique testing ground for the modern models of interactions with nuclei which aim at describing on the same footing ep, eA, pp, pA, AA collisions [89]. It would allow to be established whether or not the same dynamics determines hadroproduction in eA collisions and in central AA collisions.

4 Acknowledgements

We thank all our colleagues in working group 8 for their invaluable assistance and for numerous discussions. AB acknowledges support by the KBN grant No 2 P03B 083 08 and by a PECO grant from the EEC Programme "Human Capital and Mobility", Network "Physics at High Eneregy Colliders", Contract No ERBICIPDCT940613. MS thanks the U.S. Department of Energy for financial support under grant number DE-FG02-93ER-40771.

References

[1] V. N. Gribov, Sov. Phys. JETP **30** 709 (1969).

[2] J. D. Bjorken in Proceedings of the International Symposium on Electron and Photon Interactions at High Energies, p. 281–297, Cornell (1971).

[3] R. Baier, Yu.L. Dokshitzer, A.H. Mueller, S. Peigné and D. Schiff, hep-ph 9608322 and these proceedings.

[4] J. Chwastowski and M.W. Krasny, "What can we gain by detecting nuclear fragments in electron-nucleus collisions at HERA?", these proceedings.

[5] K. Kurek, "QED Radiative Processes in Electron-Heavy Ion Collisions at HERA", these proceedings.

[6] I. Akushevich and H. Spiesberger, "Radiative Corrections to Deep Inelastic Scattering on Heavy Nuclei at HERA", these proceedings.

[7] NMC, M. Arneodo et al., Nucl. Phys. **B 441** (1995) 3.

[8] NMC, M. Arneodo et al., Nucl. Phys. **B 441** (1995) 12.

[9] E665, M.R. Adams et al., Z. Phys. **C 67** (1995) 403.

[10] NMC, M. Arneodo et al., "The A dependence of the nuclear structure function ratios", submitted to Nucl. Phys. B.

[11] NMC, M. Arneodo et al., "The Q^2 dependence of the structure function ratio F_2^{Sn}/F_2^C and the difference $R^{Sn} - R^C$ in deep inelastic muon scattering", submitted to Nucl. Phys. B.

[12] EMC, J.J. Aubert et al., Phys. Lett. **B 123** (1983) 275.

[13] EMC, J. Ashman et al., Phys. Lett. **B 202** (1988) 603 and Z. Phys. **C 57** (1993) 211.

[14] EMC, M. Arneodo et al., Phys Lett **B 211** (1988) 493 and Nucl. Phys. **B 333** (1990) 1.

[15] SLAC, A. Bodek et al., Phys. Rev. Lett. **50** (1983) 1431, ibid. **51** (1983) 534 and R. G . Arnold et al., ibid. **52** (1984) 727.

[16] BCDMS, G. Bari et al., Phys. Lett. **B 163** (1985) 282 and A.C. Benvenuti et al., ibid. **B 189** (1987) 483.

[17] For a review of the experimental and theoretical situation of nuclear effects in DIS see e.g.
L.L. Frankfurt and M.I. Strikman, Phys. Rep. **160** (1988) 235;
T. Sloan, G. Smadja and R. Voss, Phys. Rep. **162** (1988) 45;
R.J.M. Covolan and E. Predazzi, in "Problems of Fundamental Modern Physics", Editors R. Cherubini, P. Dalpiaz and B. Minetti, World Scientific, Singapore (1991) p. 85;
M. Arneodo, Phys. Rep. **240** (1994) 301.

[18] J. Kwiecinski,A.D. Martin and P.J. Sutton, Phys. Rev. **D52** (1995).

[19] A.H.Mueller and J-W.Qiu, Nucl. Phys. **B268** (1986) 427.

[20] A.D. Martin, R.G. Roberts and W.J. Stirling RAL Report TR 96-037 and Int. J. of Mod Phys **A10** (1995) 2885.

[21] H1, S. Aid et al., Nucl. Phys. **B449** (1995) 3.

[22] D. Graudenz, CERN-TH-95-121, April 1995. Talk given at Workshop on Deep Inelastic Scattering and QCD (DIS 95), Paris, France, 24-28 April 1995.

[23] EMC, J.J. Aubert et al., Nucl. Phys. **B 213** (1983) 1 and J. Ashman et al., Z. Phys. **C 56** (1992) 21.

[24] NMC, D. Allasia et al., Phys. Lett. **B 258** (1991) 493.

[25] NMC, P. Amaudruz et al., Nucl. Phys. **B 371** (1992) 553.

[26] H1, S. Aid et al., Nucl. Phys. **B 472** (1996) 3.

[27] ZEUS, M. Derrick et al., paper pa-02 47 submitted to the XXVIII International Conference on High Energy Physics Warsaw, July 25-31, 1996.

[28] H1, S. Aid et al., paper pa-02 73 submitted to the XXVIII International Conference on High Energy Physics Warsaw, July 25-31, 1996.

[29] T. Weiler, Phys. Rev. Lett. **44** (1980) 304.

[30] E.L. Berger and D. Jones, Phys. Rev. **D 23** (1981) 1521.

[31] R. Baier and R. Rückl, Nucl. Phys. **B 201** (1981).

[32] A.D. Martin, C.-K. Ng and W.J. Stirling, Phys. Lett. **B 191** (1987) 200.

[33] M. Krämer et al., Phys. Lett. **B 348** (1995) 657 and Nucl. Phys. **B 459** (1996) 3.

[34] ZEUS,M. Derrick et al. Phys. Lett. **B315** (1993) 481.

[35] H1, T. Ahmed et al. Nucl. Phys. **B429** (1994) 477.

[36] H1, T.Ahmed et al., Phys.Lett. **B348** (1995) 681.

[37] ZEUS, M. Derrick et al. Z. Phys. **C68** (1995) 569.

[38] H. Jung, "Hard Diffractive Scattering in High Energy ep Collisions and the Monte Carlo Generator RAPGAP", DESY preprint DESY 93-182 (1993), to appear in Comput. Phys. Commun.

[39] W. Buchmuller and A. Hebecker, Phys.Lett. **B355** (1995) 573.

[40] L.Frankfurt and M.Strikman, Phys.Lett. **B382** (1996) 6.

[41] M.G. Ryskin, Z. Phys. **C 57** (1993) 89.

[42] S.J.Brodsky, L.Frankfurt, J.F.Gunion, A.H.Mueller and M.Strikman, Phys.Rev. **D50** (1994) 3134.

[43] J. Nemchik et al., Phys.Lett. **B341** (1994) 228.

[44] L. Frankfurt, W. Koepf and M. Strikman, Tel-Aviv University preprint TAUP-2290-95 (1995); Phys.Rev. **D54** (1996) 3194.

[45] M.G. Ryskin et al., "Diffractive J/ψ photoproduction as a probe of the gluon density", Rutherford Lab. preprint RAL-TR-95-065, hep-ph/9511228 (1995).

[46] M. Arneodo, L. Lamberti and M. G. Ryskin, DESY report DESY 96-149, to appear in Comp. Phys. Comm.

[47] ZEUS Collab., M. Derrick et al., Phys. Lett. **B 356** (1995) 601.

[48] EMC, J. Ashman et al., Z.Phys. **C52** (1991) 1.

[49] E665, M.R.Adams et al., Z.Phys. **C61** (1994) 179.

[50] N.Pavel, these proceedings.

[51] M. Krawczyk and B. B. Levtchenko, these proceedings.

[52] B. Blättel, G. Baym, L.L. Frankfurt and M. Strikman, Phys. Rev. Lett. **71** (1993) 896.

[53] L. L. Frankfurt and M. Strikman, Phys. Rep. **160** (1988) 235.

[54] L.M Lerran and R.Venugopalan, Phys.Rev. **D50** (1994) 225.

[55] V.Abramovskiĭ, V. N. Gribov and O. V. Kancheli, Sov. J. Nucl. Phys. **18**, 308 (1974).

[56] L. L. Frankfurt and M. I. Strikman, Nucl. Phys. **B316** (1989) 340.

[57] B.Z.Kopeliovich and B.Povh, Phys.Lett. **B367** (1996) 329 and contribution to these proceedings.

[58] B.K. Jennings and G.A. Miller Phys. Rev. **C49** (1994) 2637.

[59] H1, S.Aid et al., Z. Phys. **C69** (1995) 27.

[60] T.Gousset and H.J. Pirner, Phys.Lett.**B375** (1996) 354 and contribution to these proceedings.

[61] L.Frankfurt, M.Strikman and S. Liuti, Phys. Rev. Lett. **65** (1990) 1725.

[62] J.W.Qiu Nucl.Phys. **B291** (1987) 746.

[63] L. Frankfurt, M. Strikman and S. Liuti, Proceedings of the Conference on Particles and Nuclei XIII, Perugia, Italy (1993) page 342, edited by A. Pascolini (published by World Scientific).

[64] K.J. Eskola, Nucl.Phys.**B400** (1993) 240.

[65] K.J. Eskola, Jian-wei Qiu, Xin-Nian Wang, Phys.Rev.Lett.**72** (1994) 36.

[66] N.N.Nikolaev and V.G.Zakharov, Z.Phys. **C49** (1991) 607.

[67] A.H.Mueller, In the proceedings of the BNL workshop on Nuclei at HERA and Heavy Ion Physics, BNL-62634 (1995).

[68] A.H.Mueller and H.Navelet, Nucl.Phys. **B282** (1987) 727.

[69] A.Donnachie and P.Landshoff, Phys.Lett **B296** (1992) 227.

[70] F. E. Low, Phys. Rev. **D12** (1975) 163.

[71] S.J. Brodsky in Proceedings of the Thirteenth International Symposium on Multiparticle Dynamics, ed. W. Kittel, W. Metzger and A. Stergiou (World Scientific, Singapore, 1982) page 963.

[72] A.H. Mueller in Proceedings of the Seventeenth Rencontre de Moriond, Moriond, 1982 ed. J. Tran Thanh Van (Editions Frontieres, Gif-sur-Yvette, France, 1982) Vol. I, page 13.

[73] E665,M.R. Adams et al., Phys.Rev.Lett. **74** (1995) 1525.

[74] L. Frankfurt, G.A. Miller and M. Strikman, Phys. Lett. **B304** (1993) 1.

[75] J.Bartels,H.Lotter and M. Wusthoff, Phys.Lett. **B379** (1996) 239.

[76] J.Bartels, C.Ewerz, H.Lotter, M.Musthoff, DESY 96-085.

[77] H.Abramowicz, L.Frankfurt and M.Strikman, DESY-95-047; SLAC Summer Inst.1994:539-574.

[78] L. Frankfurt, W.Koepf, M.Sagrsyan, M.Strikman, contribution to these proceedings.

[79] ZEUS, M.Derrick et al., Phys.Lett. **B369** (1996) 55.

[80] J.D.Bjorken, Phys.Rev. **D47** (1992) 101.

[81] A.H.Mueller and W.-K.Tang, Phys.Lett. **B284** (1992) 123.

[82] V.Del Duca and W.-K.Tang, Phys.Lett. **B312** (1993) 225.

[83] D0, S.Abachi et al., Phys.Rev.Lett. **72** (1994) 2332; FERMILAB-PUB-95-302-E(1995).

[84] CDF, S.Abe et al,Phys.Rev.Lett. **74** (1995) 85.

[85] L.Frankfurt and M.Strikman, contribution to these proceedings.

[86] B.Andersson, I.Otterlund and E.Stenlund, Phys.Lett. **B73** (1978) 343.
J.Babecki and G.Nowak, Acta Phys. Polonica **B9** (1978) 401.

[87] see e.g. J.Babecki et al., Acta Phys.Polonica **B9** (1978) 495.

[88] E665, M.R.Adams et al Phys.Rev.Lett. **74** (1995)5198.

[89] K. Geiger, Contribution to these proceedings; J.Ellis, K. Geiger and H. Kowalski, to be published in Phys.Rev.D, e-Print Archive: hep-ph/9605425.

[90] M.Strikman, M.Tverskoy, M.Zhalov, these proceedings.

[91] D.M. Alde et al., Phys.Rev.Lett. **66** (1991) 2285 and references therein.

[92] T. Fields and M.D. Corcoran, in the EPS Conference proceedings, Marseille, France, July 22-28, 1993; Phys.Rev.Lett. **70**,143,1993;
R.C. Moore, et al., Phys.Lett. **B244** (1990) 347 ;
M.D. Corcoran, et al., Phys.Lett. **B259** (1991) 209.

[93] M. Luo, J. Qiu and G. Sterman, Phys.Rev.**D49**(1994) 4493.

[94] J.Bjorken, SLAC-PUB-7096, January 1996.

[95] X-N.Wang and M.Gyulassy, Phys.Rev.Lett. **68** (1992) 1480.

[96] M.Gyulassy, Proc. 'Nuclei at HERA and Heavy Ion Physics', BNL-62634, 1995.

[97] R. Baier, Yu.L. Dokshitzer, A.H. Mueller, S. Peigné and D. Schiff hep-ph 9607355.

NUCLEAR GLUON DISTRIBUTION IN QCD

A. L. Ayala F[a] [a)b)*] M. B. Gay Ducati [a)**] and E. M. Levin [† c)d)]

[a)] *Instituto de Física, Univ. Federal do Rio Grande do Sul Caixa Postal 15051, 91501-970 Porto Alegre, RS, BRAZIL*

[b)] *Instituto de Física e Matemática, Univ. Federal de Pelotas, Campus Universitário, Caixa Postal 354, 96010-900, Pelotas, RS, BRAZIL*

[c)] *Physics Division, Argonne National Laboratory Argonne, IL 60439, USA*

[d)] *Theory Department, Petersburg Nuclear Physics Institute 188350, Gatchina, St. Petersburg, RUSSIA*

Abstract: This letter is a digest of the result of Ref.[1], prepared for the DESY Workshop. The Glauber (Mueller) approach has been developed to calculate the gluon distributions in a nucleus. This approach includes shadowing corrections due to gluons rescatterings inside the nucleus. It is shown that the shadowing corrections are essential in the region of small x. As the second order corrections to the Glauber formula are sizable, we improve this description deriving a nonlinear evolution equation, and solving it in the semiclassical approach. The results are shown and discussed.

1 Introduction.

The gluon structure function is the observable that governs the physics of the high energy processes in QCD [2]. In this letter, we will show how the space-time picture [3] can be used to describe the interaction of a probe with the nucleus and obtain a nuclear gluon distribution function from Glauber (Mueller) approach. This approach was first suggested in Ref.[4] and extensively developed in Ref.[1]. In Glauber (Mueller) approach [5], a high energy virtual probe creates a GG pair with momentum Q^2, which penetrates the nucleus and suffers multiple interactions with the nucleons. These rescatterings of the gluon pair generate the shadowing corrections which could be taken into account in a closed formula, based on the GLAP evolution[7] at low x (high energy). We show that these corrections are relevant and modify the gluon distribution and the anomalous dimension in the region of small gluon x. We discuss also the kinematic region where this approach is valid and a possible improvement.

2 The Glauber approach to high energy in QCD

The main features and the kinematics of the Glauber approach to high energy processes have been discussed in Fig.1. The virtual probe with virtuality Q^2 decays in a GG pair with transverse separation $r_\perp$ and transverse momentum $\vec{k}_\perp$. This pair interacts with a nucleon due to exchange of a gluon ladder diagram. $l_\perp$ denotes the transverse moment of the gluon in the ladder attached to the GG pair. The Bjorken x is defined as $x_{Bj} \equiv \frac{Q^2}{s}$, where $\sqrt{s} = W$ is the

* E-mail: ayala@if.ufrgs.br

** E-mail:gay@if.ufrgs.br

† E-mail: levin@lafex.cbpf.br;levin@ccsg.tau.ac.il

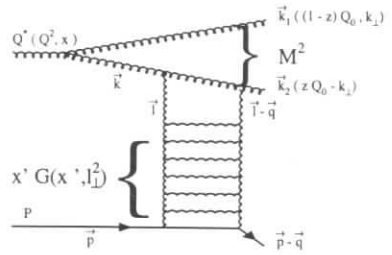

Figure 1: *Kinematics of the Glauber approach.*

c.m. energy of the incoming gluon. In DLA , the change in $r_\perp$ during the passage of the GG pair through the nucleus may be neglected. Indeed, $r_\perp$ can vary by an amount $\Delta r_\perp \propto R\frac{k_\perp}{E}$ where E denotes the energy of the pair in the target rest frame and R is the size of the target. The transverse momentum is $k_\perp \propto 1/r_\perp$. Therefore

$$\Delta r_\perp \propto R\,\frac{k_\perp}{E} \ll r_\perp, \tag{1}$$

which in terms of Bjorken x has the form:

$$x \ll \frac{1}{2\,m\,R}. \tag{2}$$

In Glauber (Mueller) approach, the nuclear gluon distribution is given by

$$xG_A(x,Q^2) = \frac{4}{\pi^2}\int_x^1 \frac{dx'}{x'}\int_{\frac{4}{Q^2}}^\infty \frac{d^2r_\perp}{\pi r_\perp^4}\int_0^\infty \frac{d^2b_\perp}{\pi} 2\left\{1 - e^{-\frac{1}{2}\sigma_N^{GG}(x',r_\perp^2)S(b_\perp^2)}\right\} \tag{3}$$

The term in curly brackets is the total cross section of the interaction of the gluon pair with nucleus in the eikonal approach. This term is the solution of the s-channel unitarity constraint [6] if the elastic amplitude of the gluon nuclei scattering is purely imaginary at high energy and the structure of the final state is mostly the uniform distribution of the produced gluons.

In DLA perturbative QCD, the GG pair cross section with the nucleon $\sigma_{GG}(r_\perp^2)$ can be written (for $N_c = 3$)

$$\sigma_{GG}(r_\perp^2) = \frac{3\alpha_S(\frac{4}{r_\perp^2})}{4}\pi^2 {r_\perp}^2\left(xG_N^{GLAP}(x,\frac{4}{r_\perp^2})\right). \tag{4}$$

This expression is valid in DLA since it was obtained considering $l_{i\perp} \ll k_\perp$ and neglecting the longitudinal part of the momentum l_i. The factor $1/r_\perp^4$ comes from the wave function of

the two gluons in the high energy probe, after the integration over the fraction of energy of the probe carried by the gluon. Using the Gaussian parameterization for the nucleon profile function $S(b_\perp)$, we can take the integral over $b_\perp$ and obtain the answer ($N_c = N_f = 3$)

$$xG_A(x,Q^2) = \frac{2R_A^2}{\pi^2}\int_x^1 \frac{dx'}{x'}\int_{\frac{1}{Q^2}}^{\frac{1}{Q_0^2}} \frac{dr_\perp^2}{r_\perp^4}\left\{C + ln(\kappa_G(x',r_\perp^2)) + E_1(\kappa_G(x',r_\perp^2))\right\} \tag{5}$$

where C is the Euler constant and E_1 is the exponential integral (see Ref.[9] Eq. **5.1.11**) and

$$\kappa_G(x',r_\perp^2) = \frac{3\alpha_S A\pi r_\perp^2}{2R_A^2} x' G_N^{GLAP}(x',\frac{1}{r_\perp^2}) \tag{6}$$

where A is the number of the nucleons in a nucleus and R_A^2 is the mean nuclear radius. If eq. (5) is expanded for small κ, the first term will correspond to the usual GLAP equations in the small x region (Born approximation of Mueller formula), while the other terms will take into account the shadowing corrections (SC).

3 pQCD calculations from Mueller approach.

To calculate the nuclear gluon distribution $xG_A(x,Q^2)$ we use the GRV parameterization [10] for the nucleon gluon distribution. The GRV distribution is suited for our calculation because its initial virtuality is small and we can estimate the SC for large distance ($r_\perp^2 \propto 1/0.25\ GeV^{-2}$). In this distribution, the most essential contribution comes from the region where $\alpha_S ln(1/x) \approx 1$ and $\alpha_S ln Q^2 \approx 1$, which allows the use of DLA, where the Mueller formula is proven.

As the DLA does not work quite well in the accessible kinematic region ($Q^2 > 1$ GeV^2 and $x > 10^{-4}$) and the Mueller Formula is proven in DLA, we develop a more realistic approach subtracting the Born term of the Mueller formula and adding the GRV gluon distribution. This procedure gives

$$\begin{aligned} xG_A(x,Q^2) &= xG_A(x,Q^2)(eq.\ (3)) + AxG_N^{GRV}(x,Q^2) \\ &- A\frac{\alpha_S N_c}{\pi}\int_x^1 \int_{Q_0^2}^{Q^2} \frac{dx'}{x'}\frac{dQ'^2}{Q'^2} x' G_N^{GRV}(x',Q'^2)\ . \end{aligned} \tag{7}$$

The above equation includes also $AxG_N^{GRV}(x,Q_0^2)$ as the initial condition for the gluon distribution and gives $AxG_N^{GRV}(x,Q^2)$ as the first term of the expansion with respect to κ_G. Therefore, this equation is an attempt to include the full expression for the anomalous dimension for the scattering off each nucleon, while we use the DLA to take into account all SC

In order to investigate the general features of the nuclear gluon distribution given by eq. (7), we calculate the ratio

$$R_1 = \frac{xG_A(x,Q^2)(eq.\ (7))}{AxG_N^{GRV}(x,Q^2)}\ , \tag{8}$$

which is shown in Fig.2. From this ratio we can see the general behavior of the SC as a function of $ln(1/x)$ and Q^2. The suppression due to the SC increases with $ln(1/x)$. For $A = 40$ (Ca) and $Q^2 = 10\,GeV^2$, the suppression varies from 4 % for $ln(1/x) = 3$ to 25 % for $ln(1/x) = 10$. For $A = 197$ (Au) the suppression is still bigger, going from 6% to 35% in the same kinematic region.

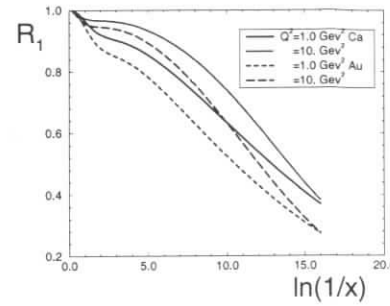

Figure 2: R_1 *as a function of* $ln(1/x)$ *and* Q^2

In the semiclassical approach (see [2]), the nucleon structure function is supposed to have Q^2 and x dependence as

$$xG_N(x,Q^2) \propto \{Q^2\}^{<\gamma>}\{\frac{1}{x}\}^{<\omega>}\ . \tag{9}$$

where $<\omega>$ is the average value of effective power of xG_A for $x \to 0$ and $<\gamma>$ is the average value of the anomalous dimension . We can calculate both exponents using the definitions

$$<\omega> = \frac{\partial \ln(xG_A(x,Q^2))}{\partial \ln(1/x)}\ . \tag{10}$$

$$<\gamma> = \frac{\partial \ln(xG_A(x,Q^2))}{\partial \ln(Q^2/Q_0^2)}\ ; \tag{11}$$

Fig.3 shows the calculation of $<\omega>$ as a function of x and Q^2 for GRV distribution and for Au. We can see that the SC give rise to a flattening of the nuclear distribution as A grows in small x region.

Fig.4 shows the results for $<\gamma>$ as a function of $ln(1/x)$ and Q^2 for GRV distribution and Au. As x decreases, the anomalous dimension presents a sizeable reduction and goes to zero for $ln(1/x) > 15$, unlike the GLAP evolution.

We can estimate what distances work in the SC calculation from the average value of the anomalous dimension. Let us consider the expansion of eq. (5) in respect to κ (see eq. (6)). From semiclassical approach, κ may be written $\kappa \propto (Q^2)^\gamma/Q^2$ and if $\gamma \leq 1$, the integral over $r_\perp$ in eq. (5) becomes divergent. If $1 \leq \gamma \leq 1/2$ only the second term of the expansion (first SC term) is concentrated at small distances. From Fig.4, we see that $1 \leq \gamma \leq 1/2$ for $Q^2 > 1GeV^2$ and even for $Q^2 = 1GeV^2$ at very small values of x.

4 The generalization of Glauber Approach.

The Mueller formula (5) is not an evolution equation but an analogue of the Glauber formula which gives the possibility to calculate $xG_A(x,Q^2)$ and the SC for nucleus from the solution of

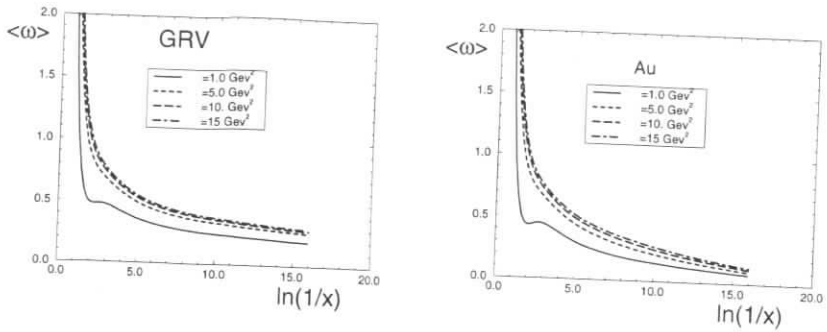

Figure 3: $< \omega >$ *as a function of* x *and* Q^2 *for GRV distribution a) and Au b)*

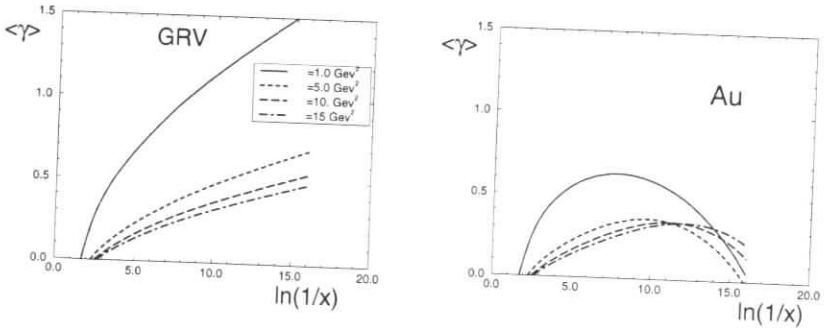

Figure 4: $< \gamma >$ *as a function of* x *and* Q^2 *for a) GRV distribution and b) Au*

GLAP equations. In order to investigate the corrections to this approach the second iteration of the Mueller formula must be calculated. The second iteration takes into account the rescattering of the next to the fastest gluon in the gluon-nucleon process. This task was done in ref [1] and the main conclusion is that the second iteration gives a sizable contribution for $x < 10^{-2}$ and becomes of the order of the first iteration for $x < 10^{-3}$. It occurs because the second iteration gives correction of the order of $\alpha_S ln(Q^2/Q_0^2) ln(1/x) \approx 1$ for the DLA.

In order to improve the calculation of the nuclear distribution $xG_A(x,Q^2)$ we suggest to derive the Mueller formula in respect to $y = ln(1/x)$ and $\xi = ln(Q^2)$, and write it as an equation for κ. The result reads

$$\frac{\partial^2 \kappa(y,\xi)}{\partial y \partial \xi} + \frac{\partial \kappa(y,\xi)}{\partial y} = \frac{N_c \alpha_S}{\pi} \{ C + \ln \kappa(y,\xi) + E_1(\kappa(y,\xi)) \} \equiv F(\kappa) . \tag{12}$$

where κ is given by

$$\kappa = \frac{N_c \alpha_S \pi}{2 Q^2 R_A^2} x G_A(x,Q^2) \tag{13}$$

This is a generalized nonlinear evolution equation for nuclear gluon distribution. This equation sums all contributions of the order $(\alpha_S y \xi)^n$ absorbing them in $xG_A(y,\xi)$, as well as all contributions of the order of κ^n. This equation provides the correct matching both with the GLR equation and with the Glauber (Mueller) formula in the kinematic region where $\alpha_S y \xi \leq 1$.

We solve eq. (12) in semiclassical approach for α_S constant using the method of characteristics (see ref [1] for a detailed discussion). In semiclassical approach, we write κ in the form

$$\kappa = e^S \tag{14}$$

where the partial derivatives $\partial S/\partial y = \omega$ and $\partial S/\partial \xi = \gamma$ are supposed to be smooth functions of y and ξ. The initial condition for the characteristics is given by

$$\begin{aligned} S_0 &= ln\, \kappa_{in}(y_0,\xi_0) \\ \gamma_0 &= \left. \frac{\partial ln \kappa_{in}(y_0,\xi)}{\partial \xi} \right|_{\xi=\xi_0} = < \gamma >_{Glauber} - 1 . \end{aligned} \tag{15}$$

where κ_{in} is

$$\kappa \rightarrow \kappa_{in} = \frac{N_c \alpha_S \pi}{2 Q^2 R_A^2} x G_A(x,Q^2) , \tag{16}$$

and xG_A is given by the Mueller formula. The GLAP equation for κ is obtained taking the term in the curly in r.h.s of eq. (12) equal to κ.

Fig.5 shows the general features of the solution, calculated for $x_0 = 10^{-2}$ and several values of Q^2 close to $1\, GeV^2$; Fig.5a shows the characteristic curves in the y v.s. ξ plane; Fig.5b shows the evolution of the γ values with y. When the value of γ goes to zero, the nonlinear effects play an important role and the solution goes to an asymptotic solution $(\kappa_{asymp}(y))$ which is ξ independent and satisfies the equation: $\frac{d\kappa_{asymp}(y)}{dy} = F(\kappa)$ (see [1] for details). When γ goes to a constant value, the nonlinear effects disappear, and the solution tends to the usual GLAP evolution. This figure also shows the lines with definite value of the ratio $R = \frac{xG(x,Q^2)(generalized\ equation)}{xG(x,Q^2)(GLAP)}$ (horizontal lines). These lines give a way to estimate how big are the SC, which are rather big.

References

[1] A.L.Ayala Fº, M.B. Gay Ducati and E.Levin: *QCD Evolution of the Gluon Density in a Nucleus*, CBPF - FN - 020/96, hep-ph 9604383, April 1996.

[2] L. V. Gribov, E. M. Levin and M. G. Ryskin: *Phys.Rep.* **100** (1983) 1.

[3] V. Del Duca, S. T. Brodski and P. Hoyer: *Phys. Rev.* **D46** (1992) 931

[4] A.L. Ayala Fº, M.B. Gay Ducati, and E. Levin: *Proceedings of Workshop on Deep Inelastic Scattering and QCD*, pg 493, Paris, April 1995, World Scientific, 1995.

[5] A.H. Mueller: *Nucl. Phys.* **B335** (1990) 115;

[6] E. Levin: *Phys. Rev.* **D49** (1994) 4469

[7] V.N. Gribov and L.N. Lipatov: *Sov. J. Nucl. Phys.* **15** (1972) 438; L.N. Lipatov: *Yad. Fiz.* **20** (1974) 181; G. Altarelli and G. Parisi:*Nucl. Phys.* **B 126** (1977) 298; Yu.L.Dokshitzer: *Sov.Phys. JETP* **46** (1977) 641.

[8] A.H. Mueller: *Nucl. Phys.* **B415** (1994) 373.

[9] M. Abramowitz and I.A. Stegun: *"Handbook of Mathematical Functions"*, Dover Publication, INC, NY 1970.

[10] M. Gluck, E. Reya and A. Vogt: *Z. Phys.* **C53** (1992) 127.

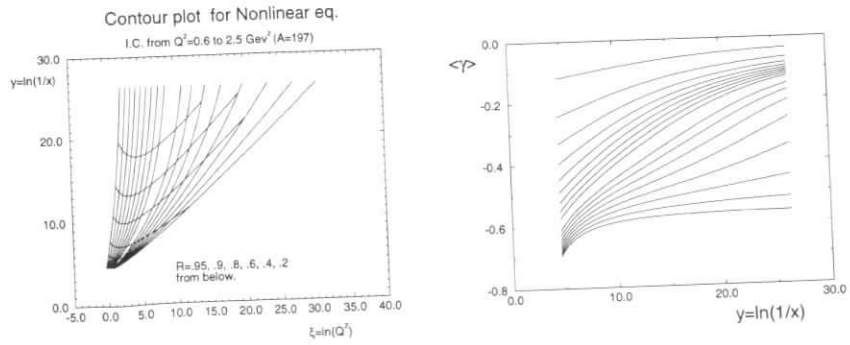

Figure 5: *a) The characteristics curves for solution of eq. (12); b) the γ evolution.* $R = \frac{xG(x,Q^2)(generalized\ equation)}{xG(x,Q^2)(GLAP)}$.

Shadowing in the deuteron

B. Badełek[ab] and J. Kwieciński[c]

[a] Institute of Experimental Physics, Warsaw University, ul.Hoża 69, PL-00 681 Warsaw, Poland
[b] Department of Physics, Uppsala University, Box 530, S-751 21 Uppsala, Sweden
[c] Institute of Nuclear Physics, ul.Radzikowskiego 152, PL-31 342 Cracow, Poland

Abstract: Shadowing correction to the deuteron structure function is calculated in the HERA kinematic region. The double interaction formalism relating the shadowing to inclusive diffractive processes is used. Both the vector meson and parton contributions are considered for low and high Q^2 values. The QCD corrections with parton recombination are included for high Q^2.

Accelerating deuterons at HERA will give an opportunity to rise a precision of the QCD analysis of the structure functions (F_2^d contains almost completely a flavour singlet quark distributions) and to measure the neutron structure function, F_2^n (and thus the flavour non-singlet $F_2^p - F_2^n$). To these aims, shadowing in the deuteron has to be quantified in a wide interval of kinematic variables. Shadowing in the deuteron, *per se* a very interesting low x phenomenon, is well established experimentally, observed in the low Q^2 (including the photoproduction) and in the large Q^2 region and apparently only weekly dependent on Q^2 [1]. In this paper we summarise the results of our earlier studies of the deuteron shadowing [2], updated and adapted to the HERA kinematics.

The deuteron structure function F_2^d is related in the following way to F_2^p, F_2^n and to the shadowing term δF_2^d, which is non-negligible for x less than, say, 0.1:

$$2F_2^d(x,Q^2) = F_2^p(x,Q^2) + F_2^n(x,Q^2) - 2\delta F_2^d(x,Q^2). \tag{1}$$

(F_2^d and δF_2^d are normalised per nucleon).

The shadowing term $\delta F_2^d(x,Q^2)$ is related through the (double) pomeron exchange to the diffractive structure function, $\partial^2 F_2^{diff}/\partial\xi\partial t$

$$\delta F_2^d(x,Q^2) = \int d^2\mathbf{k}_\perp \int_{\xi_0}^1 d\xi S(k^2) \frac{\partial^2 F_2^{diff}}{\partial\xi\partial t} \tag{2}$$

where $S(k^2)$ is the deuteron form factor. We define $\xi = 2kq/p_dq$ where k, q and p_d are the four momenta of the pomeron, virtual photon and of the deuteron respectively; $\xi_0 = x(1 + M_{\pi 0}^2/Q^2)$ where $M_{\pi 0}^2$ is the lowest mass squared of the diffractively produced hadronic system. We also have $t \cong -k_\perp^2 - k_\parallel^2$ where $k_\parallel^2 = M^2\xi^2$ with M being equal to the nucleon mass. The integration over ξ corresponds to the integration over M_x^2 where M_x is the mass of the diffractively produced system. The region of low M_x^2 is dominated by the diffractive production of low mass vector

mesons which is assumed to be described by the vector meson dominance mechanism. In this model the contribution of the vector mesons to the nuclear shadowing is

$$\delta F_{2v}^d = \frac{Q^2}{4\pi} \sum_v \frac{M_v^4 \delta\sigma_v^d}{\gamma_v^2 (Q^2 + M_v^2)^2} \tag{3}$$

where the sum extends over the low mass vector mesons ρ, ω and ϕ. M_v are the masses of the vector mesons v and γ_v can be obtained from the leptonic widths of the vector mesons. The double scattering cross section $\delta\sigma_v^d$ is obtained from the Glauber model, with the energy–dependent vector meson–nucleon cross sections. The contribution of large M_x^2 corresponds to the partonic mechanism of shadowing, δF_{2p}^d, which is related to the partonic content of the pomeron. We used the parametrization of parton distributions in a pomeron from ref. [3] which was constrained to describe the data on deep inelastic diffraction from HERA [4].

Results of the calculations of $\delta F_2^d(x, Q^2)$ are shown in fig.1.

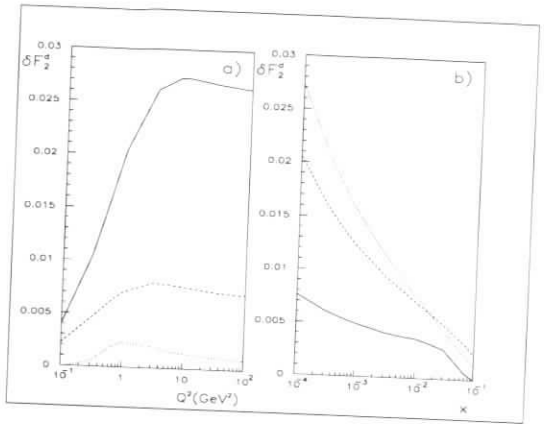

Figure 1: *Shadowing contribution, $\delta F_2^d(x, Q^2)$, to the deuteron structure function; a) continuous line: x=0.0001, broken line: x=0.01, dotted line: x=0.1; b) continuous line: Q^2=0.2 GeV^2, broken line: Q^2=1 GeV^2, dotted line: Q^2=10 GeV^2.*

In fig.2 plotted is the quantity $2F_2^d(x, Q^2)/F_2^p(x, Q^2) - 1$ which in the absence of shadowing would be just equal to $F_2^n(x, Q^2)/F_2^p(x, Q^2)$ and is often referred to as a ratio of neutron and proton structure functions. The F_2^d has been calculated according to eqs (1) and (2) where the structure functions for the proton and the neutron were calculated according to a model [5]. In this model the contributions from both the parton model with QCD corrections suitably extended to the low Q^2 region and from the low mass vector mesons were taken into account.

The model describes the data fairly well. Thus a quantitative method to obtain the shadowing contribution to the deuteron structure function is available. It should be used in extracting the neutron structure function from the F_2^d and F_2^p measurements as well as in the QCD analysis including, in particular, measurements of F_2^d. A shadowing model of ours, extended to encompass the meson exchange effects, [9], gives the same results for the δF_2^d. Other approaches, generally similar to ours, [10], predict larger values of the effect.

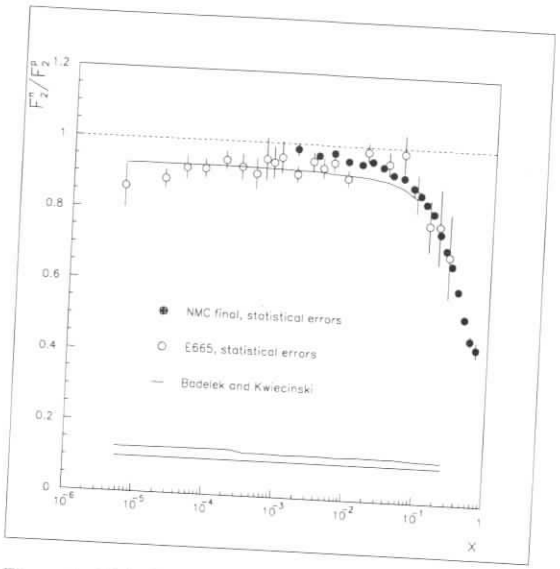

Figure 2: $F_2^n/F_2^p = 2F_2^d/F_2^p - 1$ *as a function of x. The line shows a result of our calculations, [2], with MRS(A), [6], as asymptotic function. Data come from the E665, [7] and from the NMC, [8]. Errors are statistical, band at the bottom shows the magnitude of the E665 systematic uncertainty.*

The curve in fig.2 has been calculated for the (x, Q^2) points corresponding to the E665 experiment results, i.e. at lowest values of x, $x \sim 10^{-5}$, $Q^2 \sim 0.005$ GeV^2. It would be desirable to measure the shadowing in the region of similarly low values of x but at higher scales in order to check its possible Q^2 dependence (anticipated to be weak). This would be possible uniquely at HERA.

HERA might also permit detection of the shadowing modifications due to the QCD effects: (mild) logarithmic scaling violations induced by the QCD evolution and recombination of partons from *different* nucleons in the deuteron [2]. Influence of these effects on δF_2^d is shown in fig.3.

Fortran codes to calculate $\delta F_2^d(x, Q^2)$ and $F_2^d/F_2^p(x, Q^2)$ are available upon request from *badelek@fuw.edu.pl*.

This research has been supported in part by the Polish Committee for Scientific Research, grant number 2 P03B 184 10.

References

[1] B. Badełek and J. Kwieciński, Rev. Mod. Phys. (in print).

[2] B. Badełek and J. Kwieciński, Nucl. Phys. **B370** (1992) 278; Phys. Rev. **D50** (1994) R4.

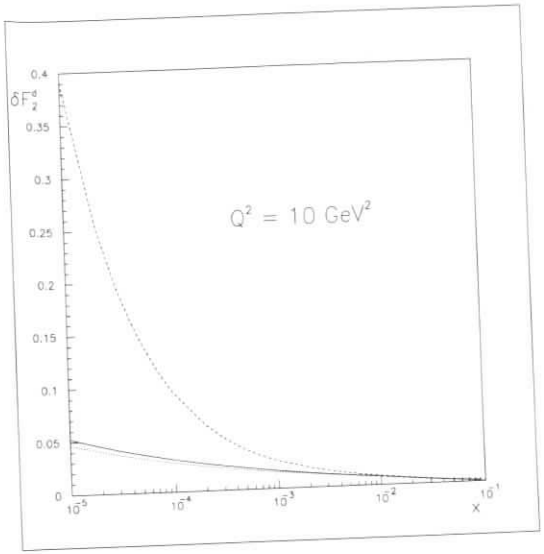

Figure 3: *QCD effects in the δF_2^d for Q^2=10 GeV^2. Dotted curve marks the results without- and continuous one – with the QCD evolution starting from Q_0^2=4 GeV^2. The dotted line shows the effect of the QCD evolution with the recombination terms in the evolution equations. Gluon distribution was assumed as given by the parametrization of Glück, Reya and Vogt, [11].*

[3] K. Golec-Biernat and J. Kwieciński Phys. Lett. **B353** (1995) 329.

[4] ZEUS Collaboration, M. Derrick et al., Phys. Lett. **B315** (1994) 228; **B338** (1994) 483. H1 Collaboration, T. Ahmed et al., Nucl. Phys. **B429** (1994) 477; Phys.Lett. **B348** (1995) 681.

[5] J. Kwieciński and B. Badelek, Z. Phys. **C43** (1989) 251; B. Badelek and J. Kwieciński, Phys. Lett. **B295** (1992) 263.

[6] A.D. Martin, W.J. Stirling and R.G. Roberts, Phys. Rev. **D50** (1995) 6734.

[7] E665 Collaboration, M.R. Adams et al., Phys. Rev. Lett. **75** (1995) 1466.

[8] NMC, E.M. Kabuss, presented at DIS96, Rome, Italy.

[9] W. Melnitchouk and A.W. Thomas, Phys. Rev. **D47** (1993) 3783.

[10] See e.g. N.N. Nikolaev and B.G. Zakharov, Z. Phys. **C49** (1991) 607; V. Barone et al., Phys. Lett. **B321** (1994) 137; V.R. Zoller, Phys. Lett. **B279** (1992) 145.

[11] M. Glück, E. Reya and A. Vogt, Z. Phys. **C67** (1995) 433.

Longitudinal and Transverse Nuclear Shadowing

V. Barone[a] and M. Genovese[b,1]

[a] Università di Torino and INFN, 10125 Torino, Italy
[b] Université Joseph Fourier and IN2P3-CNRS, 38026 Grenoble, France

Abstract: Nuclear shadowing arises from multiple scattering of the hadronic fluctuations ($|q\bar{q}\rangle, |q\bar{q}g...\rangle$) of the virtual photon in a nucleus. We predict different longitudinal and transverse shadowing and an A–dependence of $R \equiv \sigma_L/\sigma_T$ which can be up to a 50% effect. The possibility of detecting nuclear effects on R at HERA is discussed.

While there are very different ideas on the nature of the EMC effect at intermediate and large values of x, the situation seems to be less controversial at small x, the region of nuclear shadowing (NS). There is a general consensus that NS is due to the recombination of partons belonging to different nucleons. A concrete and quantitative realization of this old idea has been offered in [1] where NS is attributed to the multiple scattering of the hadronic fluctuations of the virtual photon in nuclei. One can thus speak of parton recombination in that the multiple scattering diagrams involve quarks and gluons which do not belong to a single nucleon. This approach leads rather naturally to the prediction of different shadowing effects in the longitudinal and transverse channels and consequently to an enhancement of $R \equiv \sigma_L/\sigma_T$ in nuclei [2]. In the following we shall sketch the derivation of this result and present some quantitative estimates. We shall also study the possibility of measuring nuclear effects on R at HERA.

In virtual-photon–nucleus scattering, using Glauber formalism, the nuclear cross section is given by

$$\sigma^{\gamma^* A} = A\,\sigma^{\gamma^* N} - 4\pi\,\frac{A-1}{A}\,\left.\frac{d\sigma^D}{dt}\right|_{t=0}\int d^2\vec{b}\;T^2(\vec{b}) + \ldots\,, \tag{1}$$

where $d\sigma^D/dt$ is the $\gamma^* N$ diffraction dissociation cross section integrated over the mass M^2 of the excited hadronic states

$$\left.\frac{d\sigma^D}{dt}\right|_{t=0} = \int dM^2\;\left.\frac{d^2\sigma^D}{dt\,dM^2}\right|_{t=0}\mathcal{F}(k_L^2)\,. \tag{2}$$

The longitudinal form factor of the nucleus $\mathcal{F}(k_L^2)$ appearing in (2) suppresses heavy mass excitations corresponding to non negligible longitudinal momenta of the recoil proton, $k_L = (Q^2+M^2)/2\nu = x m_N\,(1+M^2/Q^2)$.

Eq. (1) establishes a link between the leading nuclear shadowing correction and the pomeron structure function which is proportional to $d\sigma^D/dt$. This allows relating the diffractive DIS

[1]Supported by EU Contract ERBFMBICT 950427.

currently under experimental study at HERA to the small-x nuclear phenomena which will hopefully be a future chapter of the HERA program.

In the Nikolaev–Zakharov picture of small–x DIS [3, 4] the double scattering term in (1) can be calculated on the basis of the Fock structure of the virtual photon interacting with the nucleus. At small x, the hadronic states into which the γ^* fluctuates ($|q\bar{q}\rangle, |q\bar{q}g\ldots\rangle$) have a very long lifetime $\sim 1/m_N x$ and their transverse size is frozen during the scattering process. Hence one can write the virtual photoabsorption cross sections for scattering off a nucleon $\sigma_{L,T}^{\gamma^* N}$ as (focusing for the moment on the $q\bar{q}$ Fock component)

$$\begin{aligned}\sigma_{L,T}^{\gamma^* N}(x,Q^2) &= \langle\sigma(\rho,x)\rangle_{L,T} \\ &\equiv \int_0^1 d\alpha \int d^2\vec{\rho}\,|\Psi_{L,T}(Q^2,\rho,\alpha)|^2\,\sigma(\rho,x)\,,\end{aligned} \tag{3}$$

where $\Psi_{L,T}$ are the $q\bar{q}$ wave functions of the virtual photon, ρ the transverse separation of the pair, α the momentum fraction carried by one of the components, and $\sigma(\rho,x)$ is the interaction cross section of the $q\bar{q}$ color dipole with the nucleon, which does not depend on the flavor and on the photon polarization. Glauber's expansion, written in terms of the dipole cross section, reads

$$\sigma_{L,T}^{\gamma^* A}(x,Q^2) = A\,\langle\sigma(\rho,x)\rangle_{L,T} - \frac{A-1}{4\,A}\,\langle\sigma(\rho,x)^2\rangle_{L,T}\int d^2\vec{b}\,T^2(\vec{b}) + \ldots\,, \tag{4}$$

where $\langle\sigma(\rho,x)\rangle_{L,T} \equiv \sigma_{L,T}^{\gamma^* N}(x,Q^2)$. By comparing eqs. (1) and (4) one identifies the contribution to $d\sigma^D/dt$ corresponding to the $q\bar{q}$ content of the photon (or of the pomeron, from another viewpoint) as

$$\left.\frac{d\sigma_{L,T}^{D,q\bar{q}}}{dt}\right|_{t=0} = \frac{\langle\sigma(\rho,x)^2\rangle_{L,T}}{16\,\pi}\,, \tag{5}$$

For small ρ, $\sigma(\rho,x)$ has the color transparency behavior $\sigma(\rho,x) \propto \rho^2$. Because of the structure of $\Psi_{L,T}(Q^2,\rho,\alpha)$ the dominant contribution to $\sigma_{L,T}^{\gamma^* N}$ comes from pairs of transverse size $\rho^2 \sim [m_q^2 + Q^2\,\alpha(1-\alpha)]^{-1}$. Symmetric pairs, with $\alpha \sim 1/2$ and $\rho^2 \sim 1/Q^2$, have $\sigma_{L,T} \sim (1/Q^2)\log(Q^2/m_q^2)$, *i.e.* scaling cross sections. Asymmetric pairs, with $\alpha \sim 0,1$ and large size $\rho^2 \sim 1/m_q^2$, have a scaling transverse cross section $\sigma_T \sim 1/Q^2$, but a vanishing longitudinal cross section σ_L.

Because of the color transparency property of $\sigma(\rho,x)$, the second and higher terms in the series (4) contain powers of ρ^2. As a consequence, symmetric pairs with $\rho^2 \sim 1/Q^2$ give a $1/(Q^2)^2$, *i.e.* negligible, contribution to the double scattering term, whereas asymmetric pairs with $\rho^2 \sim 1/m_q^2$ lead to a scaling $1/Q^2$ screening. Since asymmetric pairs lead to a vanishing σ_L, we can conclude that shadowing in the longitudinal cross section is negligible at moderate and large values of Q^2, whereas it is significant and almost Q^2 independent in the transverse cross section. Thus, R is expected to be enhanced in nuclei for $Q^2 \gtrsim 5$ GeV^2.

So far we have considered only the lowest Fock state of γ^*, yielding the component $\propto M^2(M^2+Q^2)^{-3}$ of the mass spectrum. At large M^2 the triple pomeron component, related to the $q\bar{q}g$ Fock state of the photon, becomes dominant. Its mass spectrum is

$$\left.\frac{d\sigma_{L,T}^{D,3\mathbb{P}}}{dM^2\,dt}\right|_{t=0} = \sigma_{\rm tot}^{\gamma^* N}\,A_{3\mathbb{P}}\,\frac{M^4}{(Q^2+M^2)^3}\,. \tag{6}$$

Putting all terms together one ends up with

$$\sigma_{L,T}^{\gamma^* A}(x,Q^2) = A\,\sigma_{L,T}^{\gamma^* N}(x,Q^2) - \frac{A-1}{4\,A}\left\{\langle\sigma(\rho,x)^2\rangle_{L,T} + 16\pi\,\left.\frac{d\sigma_{DD}^{3\mathbb{P}}}{dt}\right|_{t=0}\right\}\int d^2\vec{b}\,T^2(\vec{b}) + \ldots\,, \tag{7}$$

A full calculation of the $3\mathbb{P}$ contribution has been performed [4], which has confirmed the behavior (6) both for the longitudinal and the transverse cross section and predicted a coupling $A_{3\mathbb{P}}$ substantially flavor and Q^2 independent for $Q^2 \gtrsim 2$ GeV^2.

Our estimate of $\Delta R \equiv R_A - R_N$ in [2] was based on eqs. (7) and (6), with $A_{3\mathbb{P}}$ taken phenomenologically from photoproduction data. Now, the $A_{3\mathbb{P}}$ value computed in [4] is somehow larger than the one used in [2]. This means that, since the triple pomeron contribution does not discriminate between longitudinal and transverse cross sections, the results for ΔR given in [2] slightly overestimate the nuclear effects on R. We correct them here by an educated guess, leaving a precise quantitative determination to a forthcoming paper.

Thus our prediction for $\Delta R \equiv R_A - R_N$ in the atomic mass range $A \simeq 30 - 80$ (say Cu–Pb), at $x = 10^{-3}$ and $Q^2 = 10$ GeV^2 is: $\Delta R \simeq 0.10 - 0.15$, that is a $30 - 50\%$ effect (with $R_N \simeq 0.30 - 0.35$). We found that at small $Q^2 \sim 1$ GeV^2 shadowing is similar in the longitudinal and transverse cross sections. We expect the largest nuclear effects at x around 10^{-3} and Q^2 larger than few GeV^2.

Let us address the problem of detecting nuclear effects on R at HERA. In order to extract R one has to use nucleon beams with at least two different energies. We consider the possibility of having two beams with nucleon energies $E_1 = 410$ GeV and $E_2 = 205$ GeV. The electron energy is 27.6 GeV.

We estimate now the statistical error on ΔR. By considering two targets A and B and the cross section ratios $\rho_1 \equiv \sigma_B^{(1)}/\sigma_A^{(1)}$ and $\rho_2 \equiv \sigma_B^{(2)}/\sigma_A^{(2)}$, corresponding to the two target energies, one easily finds the relation

$$\Delta R = (\rho-1)\,(1+\bar{R})\left[\frac{\rho\,(1-z_2)}{1+z_2\bar{R}} - \frac{1-z_1}{1+z_1\bar{R}}\right]^{-1}\,, \tag{8}$$

among $\Delta R \equiv R_A - R_B$, $\bar{R} \equiv (R_A + R_B)/2$, $z_{1,2} \equiv (1-y_{1,2})/(1-y_{1,2}+y_{1,2}^2/2)$, and the ratio of cross section ratios $\rho \equiv \rho_1/\rho_2$. It is clear from eq. (8) that in order to extract ΔR one needs $\bar{R}$, besides ρ. Since our purpose here is simply to evaluate the expected statistical error on ΔR, we use (8) as a constraint between $\bar{R}$ and ΔR [5]. In the following target B is assumed to be deuteron. We choose $x = 10^{-3}$, $Q^2 \simeq 20$ GeV^2, let $\bar{R}$ vary in a reasonable range around $0.3-0.4$, fix ρ so as to get a ΔR value around 0.10-0.15 (which is our estimate presented above), and calculate the error on ΔR. The statistical error on $\rho_{1,2}$, with a luminosity of 1 pb^{-1} per nucleon, is taken to be $\delta\rho_{1,2} = 0.0090$ (interpolating the values computed by Sloan [6]). We set $\rho_1 \simeq 0.80$ and, finally, assume a 30% error on $\bar{R}$. The result of our evaluation is shown in Fig. 1 where the solid line represents the central value of ΔR and the dashed and dotted lines mark the estimated statistical error with integrated luminosities of 1 pb^{-1} and 10 pb^{-1} per nucleon, respectively. The estimated statistical uncertainty on ΔR is thus $30 - 35\%$. Our conclusion is that the nuclear effects on R predicted by our model are visible at HERA and can be measured with a reasonable accuracy.

Finally we would like to comment on a different approach to parton recombination [7]. In the fusion model of [7] parton recombination is an initial state process and the shadowing of nuclear structure functions arises from the shadowing of the glue density, which is universal, not depending on the specific process or observable considered. Thus one would expect that all gluon–dominated physical quantities, such as F_2^A and F_L^A at small x, should behave similarly, at variance with our finding. However no quantitative results for R_A and ΔR have been provided so far for this class of models. It would be interesting to work out their predictions to see

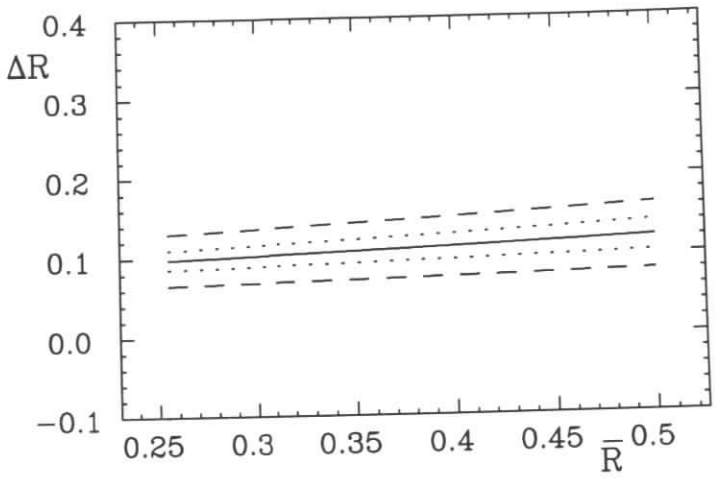

Figure 1: ΔR *vs.* $\bar{R}$ at $x = 10^{-3}$ and $Q^2 = 20$ GeV^2.

whether a possible HERA measurement of R_A and ΔR can also discriminate between different models of nuclear shadowing.

References

[1] V. Barone *et al.*, Z. Phys. C58 (1993) 541.

[2] V. Barone *et al.*, Phys. Lett. B304 (1993) 176.

[3] N.N. Nikolaev and B.G. Zakharov, Z. Phys. C49 (1991) 607; Phys. Lett. B260 (1991) 414.

[4] N.N. Nikolaev and B.G. Zakharov, Z. Phys. C64 (1994) 631. M. Genovese, N.N. Nikolaev and B.G. Zakharov, JETP 81 (1995) 633.

[5] P. Amaudruz *et al.* (NMC), Phys. Lett. B294 (1992) 120.

[6] T. Sloan, The Accuracy of Shadowing Measurements Using Nuclei in HERA, contribution to the Workshop on "Future Physics at HERA".

[7] F.E. Close, J. Qiu and R.G. Roberts, Phys. Rev. D40 (1989) 2820.
S. Kumano, Phys. Rev. C48 (1993) 2016.

Nuclear Effects at HERA

Stanley J. Brodsky

Stanford Linear Accelerator Center, Stanford University, Stanford, California 94309

Abstract: The development of a nuclear beam facility at HERA would allow the study of fundamental features of quark and gluon interactions in QCD. I briefly review the physics underlying nuclear shadowing and anti-shadowing as well as other diffractive and jet fragmentation processes that can be studies in high energy electron-nucleus collisions.

The use of nuclear targets and beams in high energy collisions provides a practical way to vary the external parameters of QCD. At HERA, one can employ nuclear beams to probe deep inelastic lepton scattering on nuclei in the small x regime where non-additive nuclear effects are large, reflecting the space-time propagation of quarks and gluons. One can also test other important nuclear effects, such as the energy loss of quarks propagating in nuclear matter, color transparency phenomena in coherent and quasielastic diffractive processes, and nuclear photoabsorption.

In the conventional infinite momentum frame parton model picture of DIS, the electron scatters on a quark constituent of the target. In the corresponding description in the nuclear rest frame, the incident transversely polarized virtual photon first splits into a pair $\gamma_T^* \to q\bar{q}$ and the anti-quark is absorbed in the target. The scattered quark then appears as a jet aligned with the incident virtual photon [1]. Thus from the laboratory frame perspective, the nuclear dependence of the transverse nuclear structure function $F^T(x,Q^2)_A$ directly reflects the nuclear dependence of the quark-nucleus cross section $\sigma_{qA}(\hat{s})$ at a corresponding CM energy squared $\hat{s} = \mathcal{O}(\bar{k}_\perp^2/x)$ [2]. Here $\bar{k}_\perp^2$ is the mean square transverse momentum of the interacting quark. At very small x the effective laboratory energies can reach 10^5 GeV, and thus the nuclear dependence of the transverse structure function reflects the Pomeron-like interactions of the quark, including its elastic and inelastic interactions within the nucleus. Thus one expects that the dominant quark interactions to occur on the front surface of the nucleus and $F^T(x,Q^2)_A < AF^T(x,Q^2)_N$ [3]. At moderate $x \sim 0.15$, the Reggeon contributions to the quark-nucleon scattering become important; because of their phase structure the multi-scattering amplitudes can lead to constructive interference, and thus to anti-shadowing; *i.e.* $F^T(x,Q^2)_A > AF^T(x,Q^2)_N$ [4]. For electron scattering on light nuclei, such as the deuteron, one can also generate non-additive contributions from the "hidden color" non-nucleon Fock components of the nucleus [5].

Examining the nuclear dependence of the final hadronic state is also illuminating. The hadronization and fragmentation of the jet which is produced aligned along the photon direction will reflect the energy loss mechanisms and multiple scattering of the quark as it propagates

through the nucleus. On general quantum mechanical grounds, the high energy outgoing jet can only lose a finite amount of energy so that the fragmentation function still factorizes in leading twist—even though the quark transits the nucleus [6]. More recently, Baier *et al.* have argued that the energy loss can scale as the square of the nuclear length because of specific non-Abelian effects [7]. Bjorken has also discussed the predictions for rapidity gaps in deep inelastic electron-nucleus collisions [1].

In contrast, the leading-twist contribution to the longitudinal structure function $F^L(x,Q^2)_A$ derives from the interaction of a approximately symmetric $q\overline{q}$ component of the virtual photon wavefunction with relative impact separation $b_\perp \sim \mathcal{O}(1/Q)$. The specific nuclear effects at low x then reflect the interactions of a small-color singlet system, thus leading to decreasing nuclear absorption with increasing Q^2. Thus the study of shadowing as a function of photon polarization and Q^2 can illuminate the basic mechanisms underlying short-distance QCD processes.

It is also interesting to measure the shadowing of the charm and bottom cross section. The basic underlying subprocess at low x is photon-gluon fusion. Thus the nuclear dependence of the heavy quark structure functions measures the shadowing of the gluon distribution in the nucleus, which in turn reflects the shadowing of the gluon-nucleus cross section.

It is also very interesting to measure the nuclear dependence of totally diffractive vector meson production $d\sigma/dt(\gamma^* A \to VA)$ [8] at HERA energies. For large photon virtualities (or for heavy vector quarkonium), the small color dipole moment of the vector system implies minimal absorption; *i.e.*, color transparency. The interacting $q\overline{q}$ system stays small over the entire nuclear length at HERA energies. Thus, remarkably, QCD predicts that the forward amplitude $\gamma^* A \to VA$ at $t \to 0$ is nearly linear in A. One also is sensitive to corrections from the nonlinear A-dependence of the nearly forward matrix element that couples two gluons to the nucleus, which in turn reflects the square of the nuclear dependence of the gluon structure function of the nucleus [9]. Because of color transparency, the integral of the diffractive cross section over the forward peak is thus predicted to scale approximately $A^2/R_A^2 \sim A^{4/3}$. A test of this striking prediction could be carried out at very small $t_{\rm min}$ at HERA and would provide a striking test of QCD in exclusive nuclear reactions. Evidence for color transparency in quasi-elastic ρ leptoproduction $\gamma^* A \to \rho^0 N(A-1)$ has recently been reported by the E665 experiment [10] at Fermilab.

In QCD, the proton is represented at a given light-cone time $\tau = t + z$ as a superposition of quark and gluon Fock states $|uud>, |uudg>, |uudgg>, |uudQ\overline{Q}>$, etc. Thus when the proton is expanded on a free quark and gluon basis, it is a fluctuating system of arbitrarily large particle number. The light-cone wavefunctions $\psi_n(x_i, k_{\perp i}, \lambda_i)$ are the probability amplitudes which describe the projections of the proton state on this Hilbert space. The structure functions measured in deep inelastic lepton scattering are directly related to the light-cone x momentum distributions of the quarks and gluons determined by the $|\psi_n|^2$. An equally interesting measure of the proton's structure is to examine the system of hadrons produced in the proton's fragmentation region when one quark is removed; *i.e.*, the proton's "fracture functions". At HERA the particles derived from the spectator $\overline{3}_C$ system which are intrinsic to the proton's structure are produced in the proton beam direction with approximately the same rapidity as that of the proton at relatively small transverse momentum. Thus in high energy ep collisions, the electron resolves the diffractively-excited proton, revealing the correlations of the spectator quarks and gluons in its light cone Fock components with invariant mass extending up to the energy of the collision.

It is of particular interest to examine the fragmentation of the proton when the electron strikes a light quark and the interacting Fock component is the $|uudc\overline{c}>$ or $|uudb\overline{b}>$ state. These Fock components correspond to intrinsic charm or intrinsic bottom quarks in the proton wavefunction. Since the heavy quarks in the proton bound state have roughly the same rapidity as the proton itself, the intrinsic heavy quarks will appear at large x_F. One expects heavy quarkonium and also heavy hadrons to be formed from the coalescence of one (or more) heavy quarks with the valence u and d quarks, since they have nearly the same rapidity[11]. Since the heavy and valence quark momenta combine, these states are preferably produced with large longitudinal momentum fractions. A recent analysis by Harris, Smith and Vogt of the excessively large charm structure function of the proton at large x as measured by the EMC collaboration at CERN implies that the probability $P_{c\overline{c}}$ that the proton contains intrinsic charm Fock states is of the order of 0.6% [12]. In the case of intrinsic bottom, PQCD scaling predicts $P_{b\overline{b}} = P_{c\overline{c}} \frac{m_\psi^2}{m_\Upsilon^2} \frac{\alpha_s^4(m_b)}{\alpha_s^4(m_c)}$, more than an order of magnitude smaller. A discussion of the physics of intrinsic heavy quark states and the dependence of the resolution of intrinsic heavy particle Fock states on photon virtuality Q^2 is presented in Ref. [13].

It is also illuminating to study the target fragmentation region at HERA with nuclear targets [13]. The spectator system evolves as $\overline{3}_C$ of color if a single quark is removed in the DIS process. One then can examine the composition and fragmentation of this system. Some of the main issues in the nuclear case are nuclear modifications of leading particle effects due to increased density of comovers [8], nuclear modifications of intrinsic sea distributions in the target fragmentation region, particularly intrinsic charm, production of heavy quarkonia at large x_F, etc.

The forward proton fragmentation regime is a challenge to instrument at HERA, but it may be feasible to tag special channels involving neutral hadrons or muons. In the case of the gas jet fixed target ep collisions at HERMES, the target fragments emerge at low velocity and large backward angles, and thus may more be accessible to precise measurement.

I thank J. D. Bjorken, P . Hoyer, A. Hebecker, A. Mueller, E. Quack, and R. Vogt for helpful discussions. Work supported by the Department of Energy, contract DE–AC03–76SF00515.

References

[1] J. D. Bjorken, SLAC-PUB-95-7096, presented at the Conference on Fundamental Interactions of Elementary Particles, Moscow, Russia, 23-26 October 1995. e-Print Archive: hep-ph/9601363.

[2] P. Landshoff, J. C. Polkinghorne, and R. Short, *Nucl. Phys.* **B28,** 225 (1971).

[3] S. J. Brodsky, F. E. Close, and J. F. Gunion, SLAC-PUB-1012, *Phys. Rev.* **D6,** 177 (1972).

[4] S. J. Brodsky and H.-J. Lu, SLAC-PUB-5098, *Phys. Rev. Lett.* **64** 1342 (1990).

[5] S. J. Brodsky, C.-R. Ji , and G. P. Lepage, *Phys. Rev. Lett.* **51** 83, (1983).

[6] S. J. Brodsky and P. Hoyer, SLAC-PUB-5935, *Phys. Lett.* **B298** 165 (1993). e-Print Archive: hep-ph/9210262.

[7] R. Baier, Yu. L. Dokshitser, A. H. Mueller, S. Peigne, and D. Schiff, BI-TP-95-40. e-Print Archive: hep-ph/9604327.

[8] S. J. Brodsky and A. H. Mueller, SLAC-PUB-4615, *Phys. Lett.* **206B** 685 (1988).

[9] S. J. Brodsky, J. F. Gunion, A, H. Mueller, L. Frankfurt, and M. Strikman, *Phys. Rev.* **D50** 3134 (1994).

[10] M. R. Adams *et al.*, *Phys. Rev. Lett.* **74** 1525 (1995).

[11] R. Vogt and S. J. Brodsky, SLAC-PUB-95-7068. e-Print Archive: hep-ph/9512300.

[12] B. W. Harris, J. Smith, and R. Vogt, LBL-37266, *Nucl. Phys.* **B461** 181 (1996). e-Print Archive: hep-ph/9508403

[13] S. J. Brodsky, P. Hoyer, A. H. Mueller, and Wai-Keung Tang, SLAC-PUB-5585, *Nucl. Phys.* **B369** 519 (1992).

Color Transparency and Color Opacity in Coherent Production of Vector Mesons off Light Nuclei at small x

L. Frankfurt[a,d], V. Guzey[b], W. Koepf[c], M. Sargsian[a,e], M. Strikman[b,d]

(a) Tel Aviv University, Tel Aviv, Israel
(b) Pennsylvania State University, University Park, PA, USA
(c) Ohio State University, Columbus, USA
(d) S.Petersburg Nuclear Physics Institute, Russia
(e) Yerevan Physics Institute, Yerevan, Armenia

Abstract: Coherent electroproduction of vector mesons off ^{2}H and ^{4}He is considered in the kinematics of deep inelastic scattering. Special emphasize is given to the $-t \sim 0.8 - 1GeV^2$ region where cross section is dominated by the interaction of $q\bar{q}$ configuration in γ^* with two nucleons. This kinematics provides unique possibilities to study quantitatively onset of Color Transparency in the vector meson production with increase of Q^2 as well as its graduate disappearance at very small x- perturbative Color Opacity.

1 Introduction

The recent theoretical analyses [1, 2, 3] have demonstrated that in the limit of large Q^2 exclusive production of vector mesons in the process $\gamma^*_L + p \to V + p$ is controlled by the calculable interplay of hard-perturbative QCD and nonperturbative QCD. Recent experimental data [4] seem to indicate that the hard mechanism starts to dominate already at $Q^2 \geq 5$ GeV^2.

In the small x region the vector meson production is essentially three stage process in the target rest frame. First, at the distance $l_c \sim \frac{1}{2m_N x}$ before the target γ^*_L transforms into a small transverse size $q\bar{q}$ pair: $b_{q\bar{q}} \equiv r_{qt} - r_{\bar{q}t} \approx 3/Q$ $b_{q\bar{q}}(Q^2 \sim 10GeV^2) \approx 0.4fm$; then the small $q\bar{q}$ pair interacts with the target with amplitude [5]:

$$A(q\bar{q}T)\mid_{t=0} = \frac{Q^2\pi^2}{3x}\left[b^2\alpha_s(Q^2)\cdot\left(i - \frac{\pi}{2}\frac{d}{ln x}\right)xG_T(x,Q^2)\right], \qquad (1)$$

where $G_T(x,Q^2)$ is the gluon density of the target. The third stage - transformation $q\bar{q} \to V$ occurs long after the target at distances $\sim 2q_0/m_V^2$. The use of the completeness over diffractively produced states allows to express the result in terms of bare parton distributions within a target and within the vector meson similar to the DIS processes[1] as: $A^{\gamma^*T\to VT} = \psi^{\gamma^*\to q\bar{q}} \otimes A(q\bar{q}T) \otimes \psi^{q\bar{q}\to V}$, where $\psi^{\gamma^*\to q\bar{q}}$ is the wave function of $\gamma^* \to q\bar{q}$ transition, $\psi^{q\bar{q}\to V}$ is the $q\bar{q}$ component of the V wave function. $A(q\bar{q}T)$ describes the $q\bar{q}$ scattering off target T with cross section given by eq.(1).

The use of the nuclei allows to check QCD prediction that cross section of interaction of small $q\bar{q}$ with a nucleon is indeed small - Color Transparency, and whether it can reach (due to increase of the gluon density at small x) values comparable to those for the interaction of light hadrons (pions) - perturbative Color Opacity. One possible strategy is to study coherent vector meson production of heavy enough nuclei at $t \sim 0$. Another possibility which we consider here is to use the process $\gamma^* + A \to V + A$ with the lightest nuclei (A=2,4), $V = \rho, \rho', \omega, \phi...$ at $x \leq 10^{-2}$ and focus on the region of comparatively large $|t|$ where **interaction with two nucleons dominate.** We restrict by the coherent channel because this case can be singled out experimentally in an unambiguous way. There is clear experimental evidence for the dominance

of the rescattering diagrams in the coherent production off the deuteron at $|t| \geq 0.6GeV^2$(see Ref.[6] and references therein). Due to the quadrupole contribution the diffractive minimum is filled up. This is the reason why our next choice is the ^4He target, which is a spherical nucleus without quadrupole form factors for which diffractive minimum occurs at $-t \sim 0.2GeV^2$ and where, as a result, one is sensitive to rescatterings at considerably smaller $|t|$.

2 Cross Section

At small x, and large Q^2 where average $b_{q\bar{q}}$ is small, nuclear effects are generated through the double rescattering of the $q\bar{q}$ pair off the target nucleons. As a result of QCD evolution parton wave function of a compact configuration can evolve to normal hadron transverse size. Such a configuration will lead to shadowing effects in the leading power of Q^2. This effect is not too small at $t = 0$ at sufficiently small x [2].Thus in QCD there is no direct relation between smallness of cross section and smallness of secondary interactions. Strict QCD prediction is that double scattering effects should decrease with Q^2 increase more fastly than single scattering amplitudes [1] but actual calculation of double scattering term is model dependent at the moment. Hence we account for double scattering of $q\bar{q}$ pair which is numerically large and neglect leading twist effects due to QCD evolution of the $q\bar{q}$ pair to normal hadron size which decrease with t more rapidly. For the deuteron we obtain (suppressing spin indices):

$$\frac{d\sigma^{\gamma^* {}^2H \to V^2H}}{dt} = \frac{1}{16\pi}\left|2f^{(1)}(t)S_d(\frac{q}{2}) + \frac{i}{2}f^{(2)}\left(\frac{t}{2}\right)\int\frac{d^2k'_\perp}{(2\pi)^2}S_d(k'_\perp)e^{-Bq'^2}\right|^2 \tag{2}$$

where $t \approx -q_\perp^2$ and $S_d(k) = F_c(q) + \left(3\frac{(Jq)^2}{q^2} - 1\right)F_Q(q)/\sqrt{2}$ and F_C and F_Q represents the charge and quadrupole deuteron form factors. Similarly for the coherent scattering off ^4He we obtain:

$$\frac{d\sigma^{\gamma^* {}^4He \to V^4He}}{dt} = \frac{1}{16\pi}\left|4f^{(1)}(t)\Phi(t) + \frac{i3f^{(2)}(\frac{t}{2})}{4\pi(\alpha+B)}e^{\frac{\alpha}{8}t}\right|^2 \tag{3}$$

where $\Phi(t)$ is the charge form factor of ^4He ($\Phi(t) \approx \exp(3\alpha t/3)$ for small t). We restrict ourselves by the calculation of double scattering amplitudes since multiscattering amplitudes violate energy-momentum conservation in respect to production of multiparticle states. So their contribution should be 0 (S.Mandelstam cancelation) within the approximation when only a $q\bar{q}$ pair is considered. In Eqs.(2) and (3) the multiple scattering amplitudes are defined as:

$$f^{(n)} \sim \int d^2b\psi^L_{\gamma^*}(b)\psi_V(b)\sigma^n_{q\bar{q}N}(b)exp(Bt/n) \tag{4}$$

where $\sigma_{q\bar{q}}$ is given by eq.(1). Because of the small size of $q\bar{q}$ the slope of the elementary amplitude, $B \approx 2.5\ GeV^{-2}$[4] is mainly determined by the two-gluon nucleon form factor

3 Onset of Color Transparency (CT)

The onset of CT leads to a rather nontrivial dependence of the coherent production cross section on x, t and Q^2. To estimate the effects we analyze the ratio $R(t) = \frac{d\sigma^{\gamma^* L}}{dt}(t)/\frac{d\sigma^{\gamma^* L}}{dt}(t=0)$. It follows from eqs.(2-4) that at $-t \geq -t_0 \sim 0.5\ GeV^2$ ($> 0.2GeV^2$ for $A = 4$) when coherent cross sections are dominated by rescatterings, the $R(|t| > |t_0|) \sim x^2G_N^2(x,Q^2)e^{Bt}/Q^4$. Therefore one should expect the strong decrease of R with increasing Q^2. At the same time for fixed Q^2 one expects a fast increase of the cross section with decrease of x. This increase

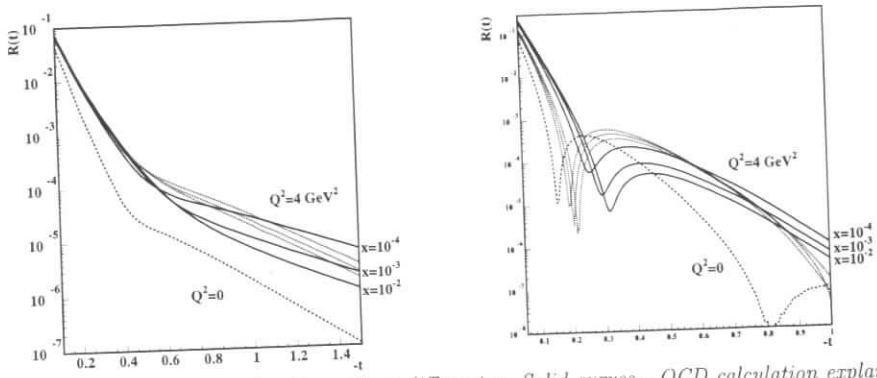

Figure 1: *The $R(t)$ as a function of t at different x. Solid curves - QCD calculation explained in text, dotted curves are VMD predictions, dased curve is for $Q^2 = 0$, which for ^4He include $n > 2$ rescattering term.*

is restricted by unitarity condition[3]. An observation of a slowing down of such an increase at small x would be a clear signature of the onset of color opacity. For $Q^2 \sim 5GeV^2$ such effect could occur already at HERA energies.

In Fig.1 we present $R(t)$ for fixed Q^2 and different x, calculated for coherent scattering off d and ^4He. We show also in this figure expectation of the Vector Dominance model (VMD) in which ρ-meson is produced in the first interaction and scatters off the nucleons with cross section similar to πN cross section. In the case of ^4He target one expects a clean minimum which is very sensitive to amount of rescattering terms in eq.(4). Investigation of the depth of diffraction minima would allow to check another prediction of QCD, namely the large value of the real part of the production amplitude $ReF/ImF \sim 0.3 - 0.4$.

3 Critical Assessments and Conclusions

In this discussion we assumed that the only mechanism that generates the nuclear effects are double rescatterings and neglected the leading twist mechanism of multiple scattering related to the leading twist nuclear shadowing. It may compete with the mechanism we discussed above in a certain x, Q^2 range. This question requires further studies and detailed experimental study of t, x Q^2 dependences at large kinematical range is necessary. However the important signature which will be held at the wide kinematical range is that relative contribution of the secondary rescatterings would be strongly suppressed as compared to the case of the real photon projectile. If such a suppression will disappear at very small x close to unitarity bound, this would establish the x, Q^2 range for onset of the Color Opacity phenomenon.

References

[1] S. J. Brodsky et al, Phys. Rev. **D50** 3134 (1994).

[2] H. Abramowicz, L. L. Frankfurt and M. I. Strikman DESY-95047; SLAC Summer Inst.1994:539-574.

[3] L. L. Frankfurt W. Koepf and M. I. Strikman, Phys. Rev. **D 54**,3194(1996).

[4] ZEUS, M. Derrick et al.,Z.Phys.Lett.bf B356, 601 (1995); Contribution to XXV11 INt.Conf. on High Energy Physics, Warsaw, July, 1996.

[5] B. Blattel, G. Baym, L.L. Frankfurt and M. I. Strikman Phys. Rev. Lett. **70**, 896 (1993).

[6] T. H. Bauer, R. D. Spital, D. R. Yennie and F. M. Pipkin, Rev. Mod. Phys. **50** 261 (1978).

Possible evidence for color transparency from dijet production with large rapidity gaps in γp scattering at HERA and how to test it in $\gamma p, \gamma A$ scattering

L.Frankfurt[a,b] and M. Strikman[c,b]

[a] School of Physics and Astronomy, Tel Aviv University, Tel Aviv 69978, Israel
[b] Institute for Nuclear Physics, St. Petersburg, Russia
[c] Department of Physics, Pennsylvania State University, University Park, PA 16802, USA

Abstract: We argue that the probability of gap survival in dijet production in γp scattering as measured by ZEUS may be due to the color transparency phenomenon and suggest ways to test this hypothesis in the future γp and γA processes.

The interaction of spatially small systems with a hadron has been the subject of discussions for a long time now (for the long and somewhat contradictory history of the theoretical and experimental investigations of this phenomenon see ref [1]). One expects that small color singlets interact weakly if energies are not extremely high - color transparency (CT). The current HERA data are in the kinematic region where the coherent length $l_c = 1/2m_N x$ significantly exceeds the nucleon radius. In this kinematic range color coherent effects should reveal themselves most clearly. Here we explain a practical idea how to search for CT in high p_t dijet production at HERA both in γp and γA collisions.

1 Gap survival for γp case

In order to study soft interactions which accompany a hard scattering, Bjorken [3] suggested to investigate the ratio of the cross sections of the high p_t dijet production with a large rapidity gap (LRG) to that of dijets without a rapidity gap:

$$f_{ac} = \frac{\sigma(a+c \to (jet(p_t)+X) + LRG + (jet(-p_t)+Y))}{\sigma(a+c \to jet(p_t) + jet(-p_t) + Z)} = \kappa P_{LRG} \tag{1}$$

Here c can be a proton or a nuclear target. To account for the difference between scales of hard and soft processes quantify the role of soft physics Bjorken evaluated f_{ac} as the product of 2 factors:

$$f_{ac} \equiv \kappa P_{RGS}. \tag{2}$$

Factor κ is the probability of producing a rapidity gap in hard subprocess, while P_{RGS} characterizes probability of gap survival due to soft interactions of constituents which do not participate in the hard collision.

Natural mechanism for the colorless hard collision is the exchange by 2 gluons. At first sight this contribution should be 0. Really it follows from the QCD factorization theorem that the exchange by an extra gluon between the partons involved in a hard collision is canceled out for the total cross section of dijet production. However for diffractive processes the presence of the LRG trigger in the final state destroys the cancelation between different terms, leading to the factorization theorem breaking[7]. In perturbative QCD κ, can be estimated as the ratio of cross sections of hard collisions of partons due to a double gluon color singlet exchange to that due to a single gluon exchange [3, 4, 5], give $\kappa \sim 0.15$ cf.discussion in [6] which depends rather weakly on p_t of the jets. Account for the leading $\alpha_s \ln x$ corrections may lead to a certain increase of κ with the length of rapidity gap. κ is different for the hard collisions of partons belonging to the different representations of $SU(3)_{color}$. This leads to a certain dependence of κ on the kinematics and to a weak dependence on a projectile.

Within the framework of conventional soft dynamics P_{RGS} should be approximately independent of the projectile. This is because of the different geometry of collisions characteristic for soft and for hard collisions. Hard collisions are concentrated at small impact parameters which are characterized by the average slope of the diffractive cross section: $a+b \to X_1 + X_2$, where X_1, X_2 are diffractive states. On the contrary, soft interactions are predominantly peripheral, at impact parameters increasing with energy. This has been established experimentally via the observation of the diffractive cone shrinkage with increase of the energy. Thus a reasonable approximation is that P_{RGS} is determined by collisions at zero impact parameters. Within the eikonal approximation used by Bjorken [3] the eikonal phase at zero impact parameters is a function of the dimensionless ratio $\sigma_{tot}(ac)/B_{ac}$, where B_{ac} is the slope of the differential cross section for the soft ac scattering. We observe that this ratio is practically the same for proton and photon projectiles. Here for a photon projectile we use as a guide the vector dominance model where $B_{\gamma c} \approx B_{\pi c}$ and $\sigma_{inel} \approx \sigma_{\pi c}$. Hence in the eikonal approximation:

$$P_{RGS}(p\bar{p}) = P_{RGS}(\gamma p). \tag{3}$$

This projectile independence is because a collision at central impact parameters is almost black.

A second possible source of filling the gap between the jets can be radiation from the two gluon exchange. This radiation should be a small effect since both gluons are located at the same parameter. In this case radiation of gluons with transverse momenta $\ll p_t$ is cancelled out because such a gluon can not resolve colorless exchange, cf.[8]. Radiation of hard gluon is suppressed by the smallness of the coupling constant. Besides, this radiation is projectile independent since it is determined by the properties of the 2 gluon exchange.

Very recently photoproduction events which have two or more jets have been observed in the $W_{\gamma p}$ range $135 < W_{\gamma p} < 280 GeV$ with the ZEUS detector at HERA [2]. A class of the events is observed with little hadronic activity between the jets. The value of $f_{\gamma p} = 0.07 \pm 0.03$ is reported based on the last bin: $\Delta\eta \geq 3$. This value is rather close to the estimates in perturbative QCD [3, 4, 5] neglecting absorptive effects due to interactions of spectator partons in colliding particles, i.e.assuming $P_{RGS} \sim 1$. It is significantly larger that the values reported by D0 [9] and CDF [10] at $\sqrt{s}$=1.8 TeV: $f_{p\bar{p}} = 0.0107 \pm 0.0010(stat.)^{+0.0025}_{-0.0013}(sys.)$ [9], and 0.0086 ± 0.0012 [10]. The difference in the gap survival probability is another manifestation of the lack of factorization in the hard processes when extra constraints are imposed on the event selection, see review in [11].

We thus conclude that the probability of gap survival seems to be an effective probe of soft interactions which accompany hard interactions. Specifics of the photon projectile is that its wave function contains a significant $q\bar{q}$ component with large transverse momenta where color is screened. For such configurations, CT would lead to significant enhancement of P_{RGS}. In the ZEUS experiment the requirement of observing two high p_t jets in the acceptance of the detector have led to an effective selection of jets carrying a fraction of more than 0.7 of the photon momentum. This component of the wave function is dominated by the small size $q\bar{q}$

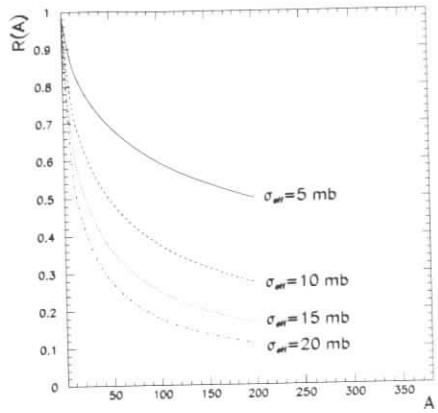

Figure 1: A dependence of the rapidity gap survival probability on σ_{eff}.

component of the photon wave function since the soft component is suppressed at least by a factor $1-z$. Hence the larger value of $f_{\gamma p}$ observed in this experiments as compared to f_{pp} maybe a manifestation of CT. In other words, kinematics of of the ZEUS experiment may **effectively suppress the soft component in the parton wave function of photon**. One of the ways to check this interpretation is to investigate the dependence of P_{RGS} as a function of the fraction of the photon momentum carried by the jet. The prediction is a significant depletion of $f_{\gamma p}$ when this fraction decreases to values below 0.5. One should also try to introduce a cut for the jet fraction larger that 0.7, but to avoid kinematics when the jet from accompanying quark would fill the gap. This may increase the color transparency effect.

2 A-dependence of gap survival

Another way to check the color transparency interpretation of the ZEUS data would be to study the A-dependence of P_{RGS}. One can address here in **a quantitative way** the key question of *how large is the effective cross section for the interaction of the photon in the configuration which leads to the production of events with rapidity gaps between jets?* Is it close to the average value of σ_{eff} ~20 mb or maybe much smaller, as the CT interpretation of the ZEUS data suggests.

Let us define

$$R(A) = \frac{f_{\gamma A}(\Delta\eta)}{f_{\gamma p}(\Delta\eta)}, \tag{4}$$

for $\Delta\eta \geq 3$ where $f_p(\Delta\eta)$ flattens out. It is easy to calculate the A-dependence of $R(A)$ using the eikonal approximation [12]:

$$R(A) = \int d^2B\tilde{T}(B)\exp(-\sigma_{eff}\tilde{T}(B)). \tag{5}$$

Here $\tilde{T}(B)$ is the standard nuclear thickness function: $\tilde{T}(B) = \int_{-\infty}^{\infty} dz\rho_A(\sqrt{B^2+z^2})$, where the nuclear density $\rho_A(r)$ is normalized according to $\int \rho_A(r)d^3r = 1$. σ_{eff} is the cross section of inelastic soft interaction of the hadronic component of the photon wave function, excluding diffractive cross section. The results of the calculation of $R(A)$ are presented in Fig.1 as a function A for several values of σ_{eff}. One can see that measurements with nuclear targets could provide a quantitative measurement of σ_{eff} and hence shed a new light on the dynamics of strongly interacting color singlet object responsible for the jet events with rapidity gaps. If one would observe $\sigma_{eff} \leq 10mb$ this would provide a clear evidence for CT in the production of dijets with LRG. It seems that the optimal range of the targets is $A \leq 40$ since for larger A, $R(A)$ depends rather weakly on A.

3 Acknowledgments

We would like to thank A.Levy for useful comments. This work was supported in part by U.S.Department of Energy and by BSF.

References

[1] L. L. Frankfurt, G. A. Miller and M. Strikman, Ann. Rev. of Nucl. and Particle Phys. 44 (1994) 501.

[2] ZEUS Collaboration, M.Derrick et al, Phys.Lett.B369(1996)55.

[3] J.D.Bjorken, Phys.Rev. D47 (1992)101.

[4] A.H.Mueller and W.-K.Tang, Phys.Lett.B284(1992)123.

[5] V.Del Duca and W.-K.Tang, Phys.Lett.B312(1993)225.

[6] D.Zeppenfeld,MADPH-95-933 (1995)

[7] J. C. Collins, L. L. Frankfurt and M. Strikman, Phys. Lett B307 (1993) 161.

[8] V.Gribov,Yad.Fiz.5(1967) 399.

[9] D0 Collaboration, S.Abachi et al, Phys.Rev.Lett.72(1994)2332; FERMILAB-PUB-95-302-E(1995).

[10] CDF Collaboration, S.Abe et al,Phys.Rev.Lett. 74(1995)855.

[11] H.Abramowicz, L.Frankfurt and M.Strikman, DESY-95-047; SLAC Summer Inst.1994:539-574.

[12] L. Bertocchi and D. Trelleani, J. Phys. **G3**, 147 (1977).

The Ratio of Gluon Distributions in Sn and C

T. Gousset[a1] and H.J. Pirner[a]

[a] Institut für Theoretische Physik, Universität Heidelberg, Philosophenweg 19, D-69120 Heidelberg, Germany

The investigation of nuclei with deep inelastic lepton scattering has produced very accurate data on nuclear structure functions $F_2^A(x)$. Especially the measurement of the ratio of tin to carbon structure functions has been carried out recently with very high statistics [1]. It shows shadowing for $x \leq 0.05$. Antishadowing ($\leq 2\%$) is visible around $x = 0.1$. In the interval $0.25 \leq x \leq 0.8$ the nuclear valence quark density is reduced. By measuring three different μ-beam energies (120, 200 and 280 GeV) NMC has also been able to determine the weak $\ln Q^2$ dependence of the structure function ratio. Using perturbative QCD evolution equations one can extract from this dependence the little known underlying gluon densities [2]. Measurements of the gluon distribution in nuclei give experimental windows viewing the partonic structure of nuclear binding. Currently there is a discussion to use nuclear beams in HERA. The study of the gluon distribution in nuclei at small x would be one of the outstanding new opportunities to investigate nuclei on the parton level. Also the forthcoming heavy ion experiments at RHIC and LHC need a good understanding of the nuclear parton distributions to calculate the cross sections for hard processes initiated by nuclear collisions.

At Leading-Log (LL), the structure function per nucleon is the sum over active flavors of quark and antiquark densities weighted by the corresponding charge squared $F_2(x,Q^2) = x\sum_i e_i^2 q_i(x,Q^2)$. As usual, we define the Bjorken variable relative to nucleon kinematics $x = Q^2/2M_N\nu$, with M_N the nucleon mass, ν the virtual photon energy in the rest-frame of the nucleon or nucleus, and $Q^2 = -q^2$ its virtuality. The LL Q^2-evolution of F_2 reads

$$\frac{\partial F_2}{\partial \ln Q^2} = \frac{\alpha_S}{2\pi} x \left(\sum_i e_i^2 P_{qG} * G + P_{qq} * \frac{F_2}{x} \right), \tag{1}$$

where G is the gluon density in the nucleon or in the nucleus. The splitting functions are denoted by P_{qq} and P_{qG}. It is understood that distributions, structure functions, as well as α_S are Q^2 dependent.

For x sufficiently small, the second term in the evolution equation of F_2 is small in comparison with the first. Furthermore, the first term can be approximated in a simple way to easily extract the gluon distribution from the evolution of F_2. One has

$$\frac{\partial F_2}{\partial \ln Q^2} \approx \frac{\alpha_S}{2\pi} \left(\frac{2}{3} \frac{\sum_i e_i^2}{2} 2xG(2x,Q^2) + \Delta(x,Q^2) \right). \tag{2}$$

[1]Supported by the Federal Ministry of Education, Science, Research and Technology (BMBF) under grant no. 06 HD 742

The second term, $\Delta(x,Q^2)$, is a certain integral over F_2 [2] which can be computed from F_2 data. Due to the steep rise of G, Δ becomes a small correction as soon as $x \leq 0.1$, so that only an approximate knowledge of F_2 is needed to estimate Δ. In the following, we shall take into account both contributions to the evolution equation.

We can now turn to the study of the new NMC data on tin to carbon ratio of structure functions. Namely, measurements of

$$f_1(x) = \frac{F_2^{\mathrm{Sn}}}{F_2^{\mathrm{C}}}, \qquad f_2(x) = \frac{\partial}{\partial \ln Q^2} \frac{F_2^{\mathrm{Sn}}}{F_2^{\mathrm{C}}}, \tag{3}$$

have been performed [1]. Using Eq. (2), it is easy to relate the tin to carbon ratio of gluon distributions

$$r(x,Q^2) = \left. \frac{G^{\mathrm{Sn}}}{G^{\mathrm{C}}} \right|_{x,Q^2},$$

to f_1 and f_2, and one finds

$$r(2x,\langle Q^2\rangle) = f_1 + \left. \frac{f_2 - \frac{\alpha_S}{2\pi} \frac{\Delta^{\mathrm{Sn}} - f_1 \Delta^{\mathrm{C}}}{F_2^{\mathrm{C}}}}{f_3 - \frac{\alpha_S}{2\pi} \frac{\Delta^{\mathrm{C}}}{F_2^{\mathrm{C}}}} \right|_{x,\langle Q^2\rangle}, \tag{4}$$

where

$$f_3 = \frac{\partial \ln F_2^{\mathrm{C}}}{\partial \ln Q^2} = \frac{\partial \ln F_2^{d}}{\partial \ln Q^2} + \frac{\partial}{\partial \ln Q^2} \ln \frac{F_2^{\mathrm{C}}}{F_2^{d}}. \tag{5}$$

In this analysis, we use the fact that the ratio of carbon to deuteron structure functions shows practically no Q^2 dependence, so that we can drop the second term in the right hand side of Eq. (5), and use for f_3 the deuteron data.

We plot the ratio $r(x)$ in Fig. 1 together with $f_1(x)$. One observes a signal for a stronger antishadowing in the gluon case ($\approx$8%) than in the quark case ($\approx$1%). In the shadowing region, there is no evidence for a difference between quarks and gluons. It is, however, presently impossible to draw a firm conclusion in this region.

There are theoretical approximations. Neglect of NLL corrections together with the use of Eq. (2) lead to an approximation presumably better than 20% for an absolute extraction of gluon density. Because the ratio $r(x)$ remains close to 1 in the whole range of x being considered, they are hopefully even far better for the ratio we are evaluating.

For the discussion of the accuracy reachable with HERA using nuclear beams there are two scenarios. If the present H1 systematic errors are added independently for each nucleus, the ratios $f_1 = F_2^{A1}/F_2^{A2}$ of nuclear structure functions would have prohibitively large errors (10%) of the same size as the EMC-effect. Drastically reduced errors, however, can be obtained if two nuclei can be stored and/or measured simultaneously. Then the leading error on the ratio of nuclear gluon densities would be the error in $f_2 = d(F_2^{A1}/F_2^{A2})/d\ln Q^2$. The situation would be similar to the NMC measurements, but with a much extended range in Q^2 and x. Note in Fig. 1 only the statistical errors have been included, a consideration of systematic errors (at small x mostly from radiative corrections) would increase our uncertainty by 50%.

The LL approximation becomes insufficient at very small x. An extension to NLL has been proposed for the proton case and can be carried out for the nuclear case as well. In the

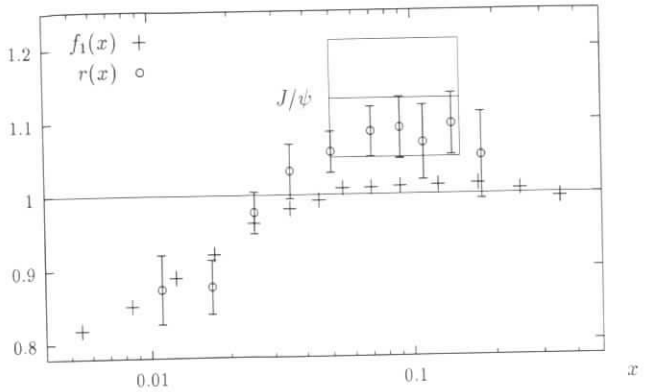

Figure 1: The ratio $r(x) = G^{Sn}(x)/G^{C}(x)$ of tin to carbon gluon density as a function of x together with the ratio of structure function, $f_1(x) = F_2^{Sn}(x)/F_2^{C}(x)$. The statistical error on f_1 is less than 1% in the whole range of x. We also show the extraction of r, $\langle r \rangle = 1.13 \pm 0.08$, from J/ψ electroproduction data as a rectangle the sides of which are the x-range of the data and the errorbar in $\langle r \rangle$.

nuclear case, additionnal merging terms are expected to play an important role in the evolution equation with the increase of the gluon density. These non-linear effects are expected to appear at very small x ($< 10^{-2}$). With such possible contributions, it is necessary to carry out the measure of the gluon density in other channels. In this respect, the ratio of longitudinal to transverse virtual photon cross sections at small x provides a direct information on $G(x)$. It is also important to extend the inclusive measurements of F_2 and F_L to jet, open charm and charmonium productions.

Apart from its own interest, the gluon density is a basic input in heavy ion collision observables. The range of x values accessible via the NMC F_2-measurements $0.01 \leq x \leq 0.2$ is sufficient to estimate the importance of shadowing for the minijet production rate at RHIC. One needs, however, much smaller x information, down to $x \approx 10^{-4}$, for heavy ion collision at LHC. To cover this range, HERA with nuclear beams would be very helpful.

References

[1] A. Mücklich, Ph.D. thesis, Universität Heidelberg, 1995; A. Mücklich, talk given at the Workshop on Deep Inelastic scattering and QCD, Paris, 1995.

[2] T. Gousset and H.J. Pirner, Phys. Lett. B 375 (1996) 349.

Binding effects and nuclear shadowing

D. Indumathi[a] and W. Zhu[b]

[a] Institut für Physik, Universität Dortmund, D-44221, Germany

[b] Department of Physics, East China Normal University, Shanghai 200 062, P.R.China

Abstract: The effects of nuclear binding on nuclear structure functions have so far been studied mainly at fixed target experiments, and there is currently much interest in obtaining a clearer understanding of this phenomenon. We use an existing dynamical model of nuclear structure functions, that gives good agreement with current data, to study this effect in a kinematical regime (low x, high Q^2) that can possibly be probed by an upgrade of HERA at DESY into a nuclear accelerator.

The ratio of the structure functions of bound and free nucleons is smaller than one at $x < 0.1$; this has been observed previously and is called nuclear shadowing [1]. Nuclear shadowing and its scaling proporties are generally regarded as the shadowing effect arising from gluon recombinations in the partonic model. A surprising fact of the HERA data is the rapid rise of the structure function F_2 of the proton as x decreases. The expected shadowing effect of gluon recombinations is not visible at least down to $x \sim 10^{-3}$ [2]. On the other hand, one of us (WZ) [3] has pointed out that the effect of shadowing due to gluon recombinations on a steep gluon distribution will be weakened by momentum conservation; in particular, gluon fusion can be neglected in the QCD nonlinear evolution equation in the small-x region where the gluon density rises like the Lipatov $x^{-1/2}$ behavior. Obviously, reconsideration of the partonic shadowing model is necessary. We have thus evolved a new approach to nuclear shadowing, which explains available data without needing Glauber rescattering [4]. On the other hand, there is a strong likelihood of HERA being upgraded to a nuclear accelerating machine [5]. We therefore apply our model and obtain predictions for the nuclear structure functions in the kinematical regime of the HERA machine.

The Model : We quickly review the model. We consider the DIS process in the Breit frame, where the exchanged virtual boson is point-like and the target consists of partons. The z-component of the momentum of the struck quark is flipped in the interaction. Hence, due to the uncertainty principle, a struck quark carrying a fraction x of the nucleon's momentum, P_N, during the interaction time $\tau_{\text{int}} = 1/\nu$, will be off-shell and localized longitudinally to within a potentially large distance $\Delta z \sim 1/(2xP_N)$, which may exceed the average two-nucleon separation D_A for a small enough $x < x_0 = 1/m_N D_A$.

The struck sea quark with its parent will return to its initial position within τ_{int} if the target is a free nucleon. However, in a bound nucleon target, it can interact with other nucleons in the nucleus and so loses its energy-momentum. Since it can be randomly distributed outside

the target nucleon, and interacts incoherently with the rest of the nucleus, we regard this effect as an additive (second) binding effect rather than as a Glauber rescattering.

A simple way of estimating the second binding effect is to connect this new effect with the traditional binding effect, which influences the parton input distributions at the starting point, $Q^2 = \mu^2$, of the QCD evolution. At such low scales, we picture the nucleon as being composed of valence quarks, gluons, and mesonic sea quarks. For example, we identify the GRV (LO) parametrisations [6] as the input parton distributions of the free nucleon at $\mu^2 = 0.23$ GeV^2.

We consider that the attractive potential describing the nuclear force arises from the exchange of scalar mesons. Hence the energy required for binding is taken away solely from the mesonic component of the nucleon, and not from its other components. We identify this with the sea quarks (and antiquarks) in the nucleon. Therefore, we assume that the nuclear binding effect only reduces the sea distributions of the nucleon at $Q^2 = \mu^2$.

For a binding energy, b, per nucleon, this corresponds to the reduction of the bound nucleon sea densities from the free-nucleon value, $S_N(x,\mu^2)$, given by GRV at $Q^2 = \mu^2$ to

$$\begin{aligned} S_A(x,\mu^2) &= K(A) S_N(x,\mu^2) \\ &= \left(1 - \frac{2b}{M_N \langle S_N(\mu^2)\rangle_2}\right) S_N(x,\mu^2) \ . \end{aligned} \tag{1}$$

Here $\langle S_N\rangle_2$ is the momentum fraction (second moment) of the sea quarks and we assume that the decrease in number of sea quarks due to the binding effect is proportional to their density.

We assume that the energy loss of sea quarks, $U_s(Q^2)$, due to the second binding effect is also proportional to the density,

$$U_s(Q^2) = \beta M_N \int_0^{x_0} x S_A(x,Q^2) \simeq \beta M_N \langle S_A(Q^2)\rangle_2 \ , \tag{2}$$

and the strength of this interaction is similar to eq. (1), viz.,

$$\beta = \frac{U_s(Q^2)}{M_N \langle S_A(Q^2)\rangle_2} = \frac{U(\mu^2)}{M_N \langle S_N(\mu^2)\rangle_2} \ , \tag{3}$$

$U(\mu^2) = a_{\rm vol}/6$ being the binding energy between each pair of nucleons. In consequence, we have, due to the second binding effect, a depletion of the sea quarks, given by

$$S_A(x,Q^2) - S'_A(x,Q^2) = \beta S_A(x,Q^2) \ . \tag{4}$$

Combining the above mentioned two kinds of binding effects and the swelling effect on a bound nucleon, which was discussed in ref. [7], we are able to explain recent data on the EMC effect in a broad kinematical region using only a few fundamental nuclear parameters [4].

Predictions for HERA : Our model predicts correctly the A-, Q^2 and x-dependences of the nuclear structure functions (and not only the ratio of cross sections) measured by the NMC in the ranges of $x < 0.8$, $Q^2 > 0.5$ GeV^2. However, being a fixed target experiment, the available Q^2 range is limited. It would therefore be interesting, as well as instructive, to obtain more results and predictions in the small-x region, and in a larger Q^2 range.

We have done this for the case of a few typical nuclei, the results for which are shown in Fig. 1. We see that the small-x shadowing is weakly dependent on Q^2 and is dominated by the

second binding effect. Due to this, there is hardly any x-dependence, as saturation has already set in by $x \sim 10^{-2}$. However, the magnitude of the shadowing is large for heavier nuclei.

We therefore conclude that it would be definitely worthwhile to make the effort to study such processes at HERA in an attempt to understand better the nature of the binding of nucleons in nuclei.

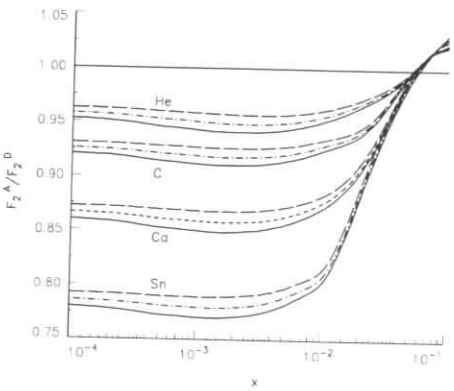

Figure 1: *The structure function ratios as functions of x and Q^2 for He/D, C/D, Ca/D, and Sn/D. The full, broken, and long-dashed curves correspond to $Q^2 = 4, 30$, and 100 GeV^2 respectively.*

References

[1] J.J. Aubert *et al.*, The EMC, Phys. Lett. B **123**, 275 (1982). For a recent review, see M. Arneodo, Phys. Rep. **240**, 301 (1994).

[2] For a recent review, see A. De Roeck, preprint DESY 95-025.

[3] W. Zhu, D. Xue, K.M. Chai and Z.X. Xu, Phys. Lett. B **317**, 200 (1993); W. Zhu, K.M. Chai and B. He, Nucl. Phys. B **427** 525 (1994); W. Zhu, K.M. Chai and B. He, Nucl. Phys. B **449** 183 (1995).

[4] D. Indumathi and W. Zhu, Dortmund University preprint, DO-TH-95/22, to appear in Z. für Physik C, 1996.

[5] The Workshop at DESY, 1995–96, on Future Physics at HERA; Working Group activity on Light and Heavy Nuclei in HERA.

[6] M. Glück, E. Reya, and A. Vogt, Z. Phys. C **48**, 471 (1990); Z. Phys. C **67** 433 (1995).

[7] W. Zhu and J.G. Shen, Phys. Lett. B **219**, 107 (1989); W. Zhu and L. Qian, Phys. Rev. C **45**, 1397 (1992).

Interplay of Soft and Hard Interactions in Nuclear Shadowing at High Q^2 and Low x

Boris Kopeliovich[ab] and Bogdan Povh[a]

[a] Max-Planck Institut für Kernphysik, Postfach 103980, 69029 Heidelberg, Germany
[b] Joint Institute for Nuclear Research, Dubna, 141980 Moscow Region, Russia

Abstract: Nuclear shadowing corrections are dominated by soft interaction and grow as function of $1/x$ more slowly than the single scattering term, which has an essential contribution from hard interaction. Therefore we predict vanishing nuclear shadowing at very low x provided that Q^2 is high and fixed. At the same time, at medium and low Q^2, nuclear shadowing grows with $1/x$ as is well known for soft hadronic interactions.

Experimental observation [1, 2] of nuclear shadowing in deep-inelastic scattering at low x was probably the first signal that this process is substantially contaminated by soft physics even at high Q^2. Since nuclear shadowing is closely related to diffraction [3], it is not surprising that recent measurements at HERA found diffraction to be a large fraction of the total cross section.

The structure function $F_2(x,Q^2)$ is proportional to the total cross section of interaction of a virtual photon with the target. This invites one to consider deep-inelastic lepton scattering in the rest frame of the target, where the virtual photon demonstrates its hadronic properties. Namely, the hadronic fluctuations of the photon interact strongly with the target [4]. Such a process looks quite different from the partonic interpretation of deep-inelastic scattering. The observables are Lorentz-invariant, but the space-time interpretation depends on the reference frame.

The observed virtual photoabsorption cross section on a nucleon is an average of total interaction cross sections σ_{tot}^{hN} of hadronic fluctuations weighted by probabilities $W_h^{\gamma^*}$,

$$\sigma_{tot}^{\gamma^* N}(x,Q^2) = \sum_h W_h^{\gamma^*}(x,Q^2)\ \sigma_{tot}^{hN} \equiv \langle \sigma_{tot}^{hN} \rangle\ . \tag{1}$$

In the case of a nuclear target the same procedure leads to [5],

$$\frac{\sigma_{tot}^{\gamma^* A}(x,Q^2)}{\sigma_{tot}^{\gamma^* N}(x,Q^2)} = 1 - \frac{1}{4}\frac{\langle (\sigma_{tot}^{hN})^2 \rangle}{\langle \sigma_{tot}^{hN} \rangle}\ \langle T \rangle\ F_A^2(q_L) + ... \tag{2}$$

Here $T(b) = \int_{-\infty}^{\infty} dz\ \rho_A(b,z)$ is the nuclear thickness at impact parameter b and $\langle T \rangle = (1/A)\ \int d^2b\ T^2(b)$ is its mean value. $\rho_A(b,z)$ is the nuclear density dependent on b and longitudinal coordinate z. The longitudinal nuclear formfactor

$$F_A^2(q_L) = \frac{1}{A\langle T \rangle}\ \int d^2b \left| \int_{-\infty}^{\infty} dz\ \rho_A(b,z)\ \exp(iq_L z) \right|^2 \tag{3}$$

takes into account the effects of the finite lifetime $t_c \approx 1/q_L$ (the coherence time) of hadronic fluctuations of the photon, where, $q_L = (m_h^2 + Q^2)/2m_N\nu$ is the longitudinal momentum transfer in $\gamma^* N \to hN$. At large $q_L > 1/R_A$, the nuclear formfactor (3) vanishes and suppresses the shadowing term (2). This is easily interpreted: for large q_L the fluctuation lifetime and its path in nuclear medium are shorter, and shadowing is reduced. For further estimations we assume that the mean mass squared of a photon fluctuation is Q^2, leading to $q_L = 2m_N x$.

Thus, all the factors in the first-order shadowing term (2) are known, except $\langle (\sigma_{tot}^{hN})^2 \rangle$. First, let us analyse the Q^2-behaviour of this factor. It is known that $\langle \sigma_{tot}^{hN} \rangle \propto 1/Q^2$ according to Bjorken scaling. In QCD this is usually interpreted as a consequence of color screening: the higher the value of Q^2, the smaller the mean transverse size squared $\langle \rho^2 \rangle \sim 1/Q^2$ of its hadronic fluctuation. Due to color screening the cross section of interaction of such a fluctuation with external gluonic fields vanishes as $\sim 1/Q^2$. However, the situation is more complicated, as a finite admixture of soft fluctuations having large size is unavoidable [6, 7, 8]. We classify in a simplified way the hard and soft mechanisms of deep-inelastic scattering in Table 1.

Table 1. Contributions of soft and hard fluctuations of a virtual photon to the DIS cross section and to nuclear shadowing

Fluctuation	$W_h^{\gamma^*}$	σ_{tot}^{hN}	$W_h^{\gamma^*}\sigma_{tot}^{hN}$	$W_h^{\gamma^*}(\sigma_{tot}^{hN})^2$
Hard	~ 1	$\sim 1/Q^2$	$\sim 1/Q^2$	$\sim 1/Q^4$
Soft	$\sim \mu^2/Q^2$	$\sim 1/\mu^2$	$\sim 1/Q^2$	$\sim 1/\mu^2 Q^2$

As previously stated, the mean fluctuation of a highly virtual photon is hard and has a small transverse size $\sim 1/Q^2$. This is why we assign to it a weight close to 1 and a small $\sim 1/Q^2$ cross section in Table 1. On the contrary, a soft fluctuation having a large size $\sim 1/\mu^2$, where μ is a soft parameter of the order of Λ_{QCD}, is expected to be quite rare in the photon, suppressed by factor $\sim \mu^2/Q^2$.[1] On the other hand, such a soft fluctuation has a large $\sim 1/\mu^2$ cross section. Therefore, the soft contribution to $\langle \sigma_{tot}^{hN} \rangle$ has the same leading twist behaviour $\sim 1/Q^2$ as the hard one. Thus, according to Table 1 one cannot say that Bjorken scaling results from the smallness of the interaction cross section of hard photon fluctuations, that also arises from the rareness of the soft components of a virtual photon.

The last column of Table 1 summarizes the Q^2-dependence of hard and soft contributions to $\langle (\sigma_{tot}^{hN})^2 \rangle$, which sets the size of nuclear shadowing and diffraction effects. In this case the hard component turns out to be a higher twist effect, and the leading contribution comes from soft interaction. This is why the applicability of pure perturbative calculations to nuclear shadowing or diffraction is questionable.

Since $\langle (\sigma_{tot}^{hN})^2 \rangle$ is dominated by soft interactions, we can parameterize it as [5],

$$\frac{\langle (\sigma_{tot}^{hN})^2 \rangle}{\langle \sigma_{tot}^{hN} \rangle} = \frac{N}{F_2^p(x,Q^2)}\ \left(\frac{1}{x}\right)^{2\Delta_P(\mu^2)} \tag{4}$$

[1] This is shown to be true for a transverse photon by perturbative calculations [8], but in a longitudinal photon soft fluctuations have an extra suppression $\sim 1/Q^4$ [8]. Therefore shadowing is a higher twist effect.

We are interested in the behaviour of this factor at very low x and assume for the numerator dominance of the soft Pomeron with intercept $\alpha_P(0) = 1 + \Delta(\mu^2)$, where $\Delta(\mu^2) \approx 0.1$ is known from Regge phenomenology of soft hadronic interactions. This explains particularly why a soft Pomeron intercept was found in diffraction at high Q^2 [9], while the intercept describing x-dependence of $F_2^p(x, Q^2)$ at high Q^2 is much larger, $\Delta_P(Q^2) \approx 0.3 \div 0.4$ [5].

The proton structure function was fixed in [5] by fitting available data. The only unknown parameter N is universal for all nuclei and is fixed by the fit at $N = 3\ GeV^{-2}$ [5].

Now we are in a position to predict nuclear shadowing down to low x. The fact that $2\Delta_P(\mu^2) < \Delta_P(Q^2)$ at high Q^2 leads to the unusual prediction of vanishing nuclear shadowing at very low x. That is, the first shadowing correction in (2) decreases with $1/x$ provided that the nuclear formfactor saturates, $F_A^2(x) \to 1$. This is demonstrated in Figs. 1-2, where we have plotted our predictions for carbon and tin versus x at fixed values of Q^2. Note that formula (2) does not include the small (a few percent) effect of nuclear antishadowing. We have renormalized all curves by factor 1.03 in order to incorporate this effect, which we assume to be A-independent for simplicity.

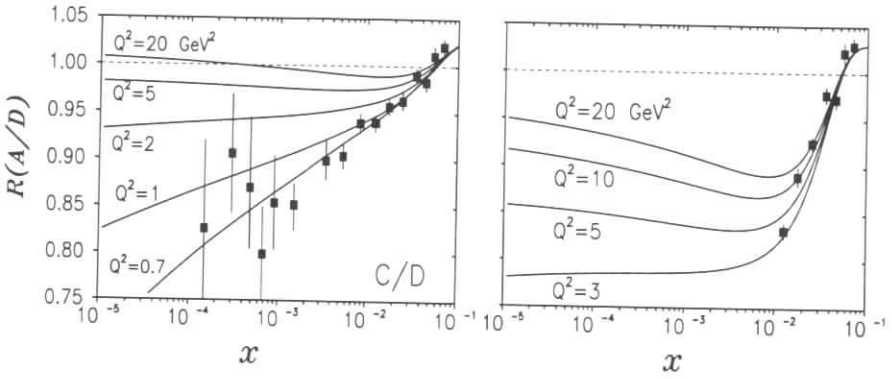

Figure 1: *Normalized ratio $F_2^A(x, Q^2)/F_2^D(x, Q^2)$ calculated for carbon using (2). The data points are from [1].*

Figure 2: *The same as in Fig. 1 but for tin. The data points are from [10].*

Note that comparison with data [1] in Fig. 1 is marginal, since Q^2 substantially varies from point to point. To make the comparison with data more sensible it was suggested in [5] to plot the data against a new variable,

$$n(x, Q^2, A) = \frac{1}{4}\frac{N}{F_2^p(x, Q^2)}\langle T(b)\rangle F_A^2(q_L)\left(\frac{1}{x}\right)^{2\Delta_P(\mu^2)} . \qquad (5)$$

One may expect according to (2) - (4) that nuclear shadowing is A-, x- and Q^2-independent at fixed $n(x, Q^2, A)$. Data from the NMC experiment plotted against $n(x, Q^2, A)$ in Fig. 3 nicely confirm such a scaling. Note that the data points for different nuclei may differ within a few percent due to the antishadowing effect, if it is A-dependent.

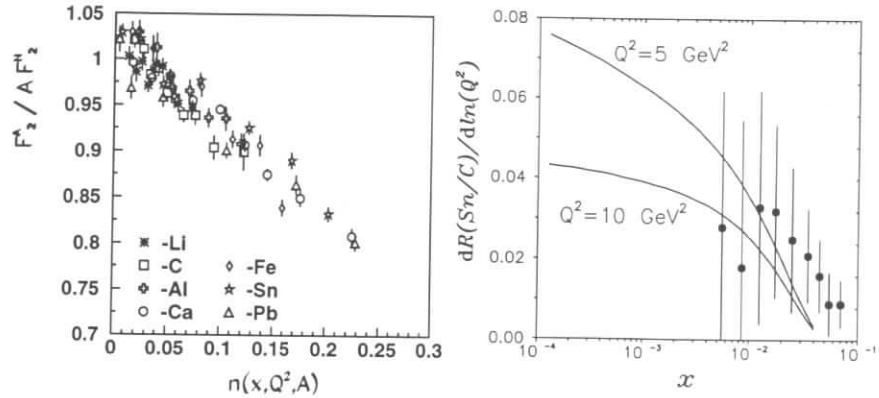

Figure 3: *Nuclear shadowing versus scaling variable $n(x, Q^2, A)$ (see text). The data for Li, C and Ca are from [1, 2], other data points are from [10].*

Figure 4: *Logarithmic Q^2-derivative of the ratio of structure functions for tin to carbon. The data are from [11].*

The results depicted in Figs. 1-2 demonstrate a substantial variation of nuclear shadowing with Q^2, especially at low x. Q^2-dependence of shadowing was observed recently by the NMC experiment [11]. Their data are plotted in Fig. 3 together with our predictions, which reproduce well the order of magnitude of the effect. We cannot claim a precise description, since the data represent the results of averaging over large interval of Q^2 down to quite low values, where our approximation may not work. It is important that all Q^2-dependence of shadowing originates in formula (2) only from the proton structure function in the denominator. Consequently, this effect in (2) has no relation to shadowing of gluons in nuclei.

To conclude, we would like to comment on the approximations used.

First of all, in saying that $\langle\sigma_{tot}^{hN}\rangle$ is dominated by soft interaction we neglected the higher twist corrections $\sim 1/Q^2$ presented in Table 1. Thus, one should be cautious using this approximation at low Q^2.

Although we use a double-leading-log type parameterization for $F_2^p(x, Q^2)$, which provides a vanishing effective Δ_P at $x \to 0$, it is almost a constant in the range of x under discussion, i.e. is compatible with the BFKL solution [12].

It is easy to show that the higher-order shadowing corrections omitted in (2) are soft as well. However, the x-dependence of the n-fold correction is governed by the power $n\Delta_P(\mu^2) - \Delta_P(Q^2)$ which may be positive for $n = 3$ or 4 and so on. A question arises, whether the growth of higher-order shadowing corrections can change our conclusion about the shadowing decreasing with $1/x$. We think it cannot. Indeed, let us consider an eikonal shadowing where the first term correspond to the hard Pomeron with a large $\Delta_P(Q^2)$, but all other terms correspond to the

soft $\Delta_P(\mu^2)$. Eikonalization of formula (2) leads to the full shadowing correction, which reads

$$1-\frac{\sigma_{tot}^{\gamma^* A}(x,Q^2)}{A\,\sigma_{tot}^{\gamma^* N}(x,Q^2)}=\frac{1}{\langle\sigma_{tot}^{hN}\rangle}\left\{\sqrt{\langle(\sigma_{tot}^{hN})^2\rangle}-\frac{2}{A}\int d^2b\left[1-\exp\left(-\frac{1}{2}\sqrt{\langle(\sigma_{tot}^{hN})^2\rangle}T(b)\right)\right]\right\}\ , \quad (6)$$

where we assume x small and fix $F_A^2=1$. The first term in curly brackets is bigger than the second one and both grow with $1/x$. For this reason, the right hand side of (6) decreases with $1/x$ more steeply than $(1/x)^{\Delta_P(\mu^2)-\Delta_P(Q^2)}$. Thus, addition of higher order shadowing corrections makes vanishing of the shadowing for $x\to 0$ even stronger.

In order to estimate q_L in (2)-(3) we assumed $\langle m_h^2\rangle\approx Q^2$. This may not be a good approximation for so called triple-Pomeron term in shadowing, which provides a mass distribution in diffractive dissociation $\propto 1/m_h^2$, not steep enough to neglect the high-mass tail. The nuclear formfactor in Gaussian form, convoluted with this mass distribution, results in a modified formfactor

$$\tilde{F}_A^2(x)=\frac{Ei\,(-q_{max}^2R_A^2/3)-Ei\,(-q_{min}^2R_A^2/3)}{2\ln(q_{max}/q_{min})}\ , \quad (7)$$

where Ei is the integral exponential function, $q_{min}=m_N(x+m_{min}^2/2m_N\nu)$ and $q_{max}=m_N(x+m_{max}^2/2m_N\nu)$. The limit of integration over m_h are m_{min} and m_{max}. In contrast to formfactor (3), the modified one (7) grows logarithmically with $1/x$. However, with a reasonable choice of the mass interval, this growth does not stop the power decrease (4) of the shadowing correction, even if the triple Pomeron contribution (i.e. gluon fusion) dominates nuclear shadowing.

Summarising, we predict the unusual phenomenon of vanishing nuclear shadowing for $x\to 0$ at fixed large Q^2.

References

[1] CERN NMC, P. Amaudruz et al., Z. Phys. **C51** (1991) 387

[2] CERN NMC, M. Arneodo et al., Nucl. Phys. **B441** (1995)

[3] V.N. Gribov, Sov. Phys. JETP **29** (1969) 483

[4] T.H. Bauer et al., Rev. Mod. Phys. **50** (1978) 261

[5] B.Z. Kopeliovich and B. Povh, Phys. Lett. **B367** (1996) 329

[6] J.D. Bjorken and J. Kogut, Phys. Rev. **D8**, (1973) 1341

[7] L.L. Frankfurt and M.I. Strikman, Phys. Rept. **160** (1988) 235

[8] N.N. Nikolaev and B.G. Zakharov, Z. Phys. **C49** (1991)

[9] DESY H1, T. Ahmed et al., Phys. Lett. **B348** (1995) 681

[10] The NM Collaboration, preliminary data, A. Witzmann, talk at the Conf. on High-Energy Physics, Brussels, 1995

[11] A. Mücklich, Ph.D. thesis, Universität Heidelberg, 1995; A. Mücklich, talk given at the Workshop on Deep Inelastic scattering and QCD, Paris, 1995.

[12] L.N. Lipatov, Sov. Phys. JETP **63** (1986) 904

Comments on Electron-Deuteron Scattering at HERA.

M.W. Krasny

L.P.N.H.E IN2P3-CNRS, 4, pl. Jussieu, T33 RdC 75252 Paris Cedex 05, France

Abstract: While storing of deuterons in the HERA ring is relatively easy, designing precision measurements for electron-deuteron scattering turns out, as discussed in this note, to be difficult.

1 Electron-Deuteron scattering at low and high x

The deuteron structure function F_2^d can be expressed (following the notation of [1]) in terms of the proton structure function F_2^p and the neutron structure function F_2^n as follows:

$$2F_2^d=F_2^p+F_2^n-2\delta_d, \quad (1)$$

where δ_d represents a correction, which includes the square of the double scattering amplitude as well as all interference terms of single and double scattering amplitudes. The structure functions F_2^d and F_2^p can be determined from the measured differential cross sections in ed and ep scattering. Their difference provides an important constraint on the nonsinglet structure function F_{NS} which describes the valence quark momentum distribution:

$$F_{NS}=F_2^p-F_2^n=2(F_2^p-F_2^d)-2\delta_d \quad (2)$$

The NMC collaboration has measured [2] the $F_2^p-F_2^d$ asymmetry in the $x\geq 10^{-2}$ region with a precision, which will be difficult to match at HERA, where, due to to the difference of the magnetic rigidities, protons and deuterons can not collide simultaneously with the same beam of electrons. In the region of $x\leq 10^{-2}$ and $Q^2\geq\ 2\ GeV^2$ such a measurement can be done only at HERA. Can we reach satisfactory precision in this "exclusively HERA" x-region?

The expected $F_2^p-F_2^d$ difference, if extrapolated to low x using the NMC data, is below 0.01 [2] i.e. below 2 % of the $F_2^p(F_2^d)$ values. This difference is thus of the size of δ_d as calculated in [1]. The estimation of δ_d is however model dependent and to a large extent uncertain. Similarly, as has been pointed out in [3], there exists significant theoretical uncertainty of the low-x behavior of the F_{NS}. By measuring the $F_2^p-F_2^d$ difference at HERA one may hope to provide only weak constraint on the (δ_d, F_{NS}) plane. We are afraid, that by repeating the NMC "fully inclusive measurement", we shall be able neither to constrain the size of nuclear effects nor to provide a constraint on the F_{NS} sufficiently strong to improve the precision of determination of the gluon density at low x. Can we do better and try to pin down the size of δ_d by measuring the spectator nucleon?

2 Tagging of the spectator nucleon in the low-x electron-deuteron scattering

The effective longitudinal momentum distribution of nucleons bound in the deuteron stored at HERA at the energy of 820 GeV is shown in Fig. 1.

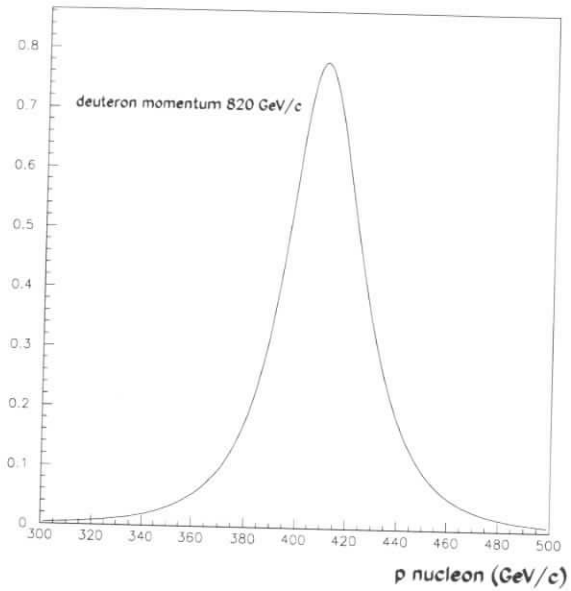

Figure 1: *Distribution of the effective longitudinal momentum of nucleons in the deuteron.*

We have used in the calculation the "Bonn wave function" of the deuteron. If an electron scatters off the proton the above distribution represents the longitudinal momentum distribution of the spectator neutron and vice versa. Can we tell, on the event by event basis, which nucleon has interacted by measuring the longitudinal momenta of the nucleons? The relative change of the longitudinal momentum of the nucleon which has interacted with an electron can be expressed by the following formula:

$$\frac{\delta p_z}{p_z} \simeq x(1+\frac{M_X^2}{Q^2}), \tag{3}$$

where x is the Bjorken variable, Q^2 is the 4-momentum transfer from the electron to the deuteron and M_X stands for the mass of the hadronic system, excluding the scattered nucleon and the spectator nucleon. In this formula we neglected the transverse momentum of the interacting nucleon. For the large x values the change of the nucleon longitudinal momentum is large and the spectator can be tagged unambigously. This is no longer the case in the low

x region (e.g. the nucleon of the effective initial momentum of 420 GeV/c gets its momentum reduced by 10 GeV in the interaction in which $x = 10^{-3}$ and $M_X^2/Q^2 = 30$). Such a change of the longitudinal momentum is significantly smaller than the momentum spread of the spectator and the interacting nucleon can not be identified unambigously in such a case.

Can we improve the efficiency of the spectator tagging by measuring not only the longitudinal momentum but, as well, the transverse momentum of the nucleons? In Fig. 2 we show the

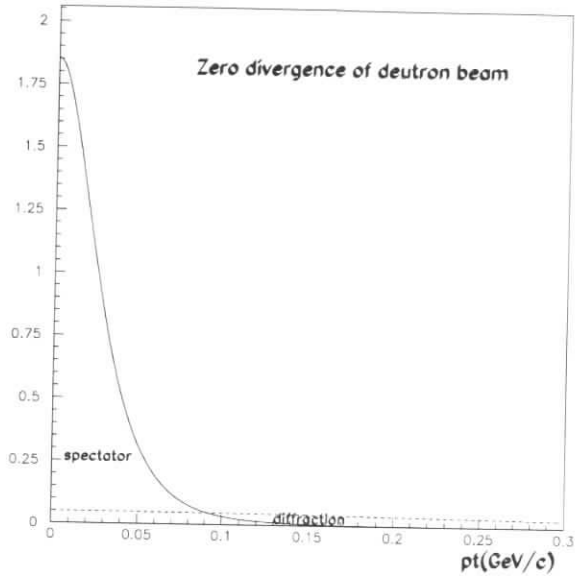

Figure 2: *The p_t spectra of the spectator and the diffractively scattered nucleon for a "pencil-like beam".*

distribution dN/dp_t^2 of the spectator nucleon ploted as a function of its transverse momentum, p_t, for a fraction of events, in which its longintudinal momentum is contained within $\pm 10\%$ of the peak value of Fig. 1. By doing this selection we choose a specific configuration of nucleons in the deuteron in which nucleons move perpendicularly to the incoming electron direction. We show, as well, for comparison, the corresponding distribution for diffractively scattered nucleon. The distributions are significantly diferent allowing for a clean identification of the spectators in the $p_t \leq 50\ MeV$ domain and diffractively scattered nucleons in the $p_t \geq 150\ MeV$ domain. If however, we include in the calculation the effect of intrinsic divergence of the deuteron beam, than the identification efficiency deteriorates significantly (both diffractive and spectator nucleons contribute to the whole p_t domain shown in Fig. 3). The plot presented in Fig. 3 corresponds to the mini β optics with the p_t spread at the interaction point of $\sqrt{60^2+170^2}$ MeV/c. It is clear that it will be difficult to achieve, in the "shape fit", 1 % precision of subtraction of the diffractive contribution. We thus conclude that within the presently considered

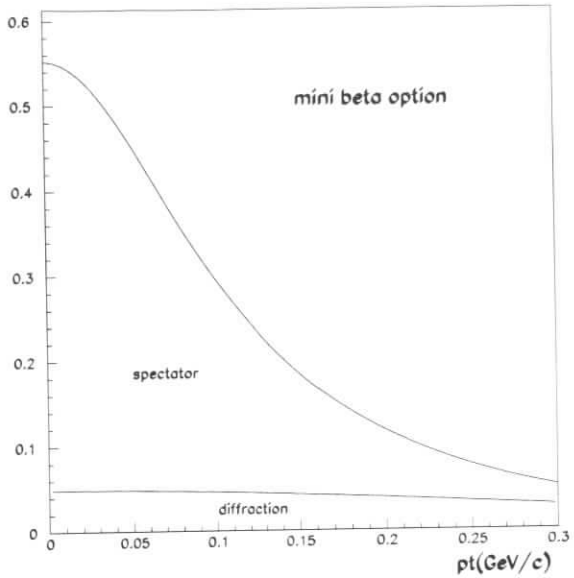

Figure 3: *The p_t spectra of the spectator and the diffractively scattered nucleon for the mini β optics.*

collision optics it will be difficult to resolve the the nuclear effects with respect to the effects of low x behavior of the nonsinglet structure function at the satisfactory level of precision.

Acknowledgements

I would like to thank to Mark Strikman and Gary Levman for their comments.

References

[1] B. Badelek, J. Kwiecinski, Phys.Rev D50 (1994) R4

[2] M. Arneodo et al., Phys.Rev. D50 (1994) R1.

[3] B. I. Ermolaev, S. I. Manayenkov, M.G. Ryskin, DESY 95-017, February 1995.

Q^2 evolution studies of nuclear structure function F_2 at HERA

S. Kumano, M. Miyama
Department of Physics, Saga University, Saga 840, Japan

Abstract: Q^2 dependence of nuclear structure functions is important for understanding perturbative QCD in nuclear environment. However, current experimental data are not sufficient for studying nuclear dependence in the Q^2 evolution because the data are limited in the small Q^2 region at small x. The future HERA program can study the evolution in the large Q^2 region, and it provides us crucial information on recombination effects and on higher-order α_s effects in the nuclear structure functions.

Nuclear modification of the structure function F_2 has been an interesting topic since the discovery of the EMC effect in 1983. Although most studies discuss x dependence of the modification, Q^2 dependence becomes increasingly interesting. It is because the NMC measured Q^2 variations of the ratio F_2^A/F_2^D [1]. Furthermore, it is found recently that there exist significant differences between tin and carbon Q^2 variations, $\partial[F_2^{Sn}/F_2^C]/\partial[\ln Q^2] \neq 0$ [1]. However, the NMC data are taken in the limited small Q^2 range at small x, so that they are not sufficient to test nuclear Q^2 evolution. The Q^2 dependence is important for understanding perturbative QCD in nuclear environment, and the future HERA nuclear program can make important contributions to this interesting topic.

The Q^2 dependence of structure functions can be calculated by using the DGLAP equations. They have been successful in describing many experimental data. However, as it becomes possible to reach the small x region by high-energy accelerators, it is necessary to investigate the details of small x physics. The longitudinal localization size of a parton exceeds the average nucleon separation in a nucleus in the small x region ($x < 0.1$). It means that partons in different nucleons could interact in the nucleus, and the interaction is called parton recombination (PR). This mechanism is used for explaining nuclear shadowing. There are a number of studies on the recombinations. Among them, we employ the evolution equations proposed by Mueller and Qiu. They investigated gluon-gluon recombination effects on the evolution. The DGLAP and PR evolution equations are given by (see Ref. [2] for the details)

$$\frac{\partial}{\partial t}\, q_i(x,t) \;=\; \int_x^1 \frac{dy}{y} \left[\sum_j P_{q_i q_j}\left(\frac{x}{y}\right)\, q_j(y,t) \;+\; P_{qg}\left(\frac{x}{y}\right)\, g(y,t) \right] + \left(recombination\ terms \;\propto\; \frac{\alpha_s A^{1/3}}{Q^2} \right) , \qquad (1a)$$

$$\frac{\partial}{\partial t}\, g\,(x,t) \;=\; \int_x^1 \frac{dy}{y}\, \left[\sum_j P_{gq_j}\left(\frac{x}{y}\right)\, q_j\,(y,t) \;+\; P_{gg}\left(\frac{x}{y}\right)\, g\,(y,t) \right] + \left(recombination\ terms \;\propto\; \frac{\alpha_s A^{1/3}}{Q^2} \right) , \qquad (1b)$$

where the variable t is defined by $t = -(2/\beta_0)\ln[\alpha_s(Q^2)/\alpha_s(Q_0^2)]$. In the PR evolution case, there is an extra evolution equation for a higher-dimensional gluon distribution. The first two terms in Eqs. (1a) and (1b) describe the process that a parton p_j with the nucleon's momentum fraction y splits into a parton p_i with the momentum fraction x and another parton. The splitting function $P_{p_i p_j}(z)$ determines the probability that such a splitting process occurs and the p_j-parton momentum is reduced by the fraction z.

Although the DGLAP equations are well tested by various experimental data, the PR equations are not well established yet. An interesting problem is possible nuclear dependence in the Q^2 evolution. There are two possible sources for the nuclear dependence in the evolution equations. One is the input parton distributions, and another is the recombination effects. The modification of the input x-distributions in a nucleus affects the Q^2 evolution through splitting functions. The recombination contributions enter into the evolution equations as additional higher-twist effects.

In studying the Q^2 evolution, it is very important to have correct input distributions. Fortunately, there are many data on the x dependence of F_2^A/F_2^D, so that we could have reasonable nuclear input distributions. We employ a hybrid parton model with recombination and Q^2 rescaling mechanisms in Ref. [3]. However, it does not matter in the Q^2 evolution studies what kind of model is used if it can explain the experimental x dependence of F_2^A/F_2^D. In the hybrid model, we first calculate Q^2 rescaled valence-quark distributions at Q_0^2. Sea-quark and gluon distributions are simply modified by a constant mount so as to satisfy the momentum conservation. Then, obtained distributions are used as input distributions for calculating the recombination effects. In this way, nuclear parton distribution with the rescaling and recombination effects are obtained at Q_0^2. Because the recombinations are higher-twist effects, final distributions are very sensitive to the choice of Q_0^2. It is fixed so that obtained shadowing agrees with the NMC ratios F_2^{Ca}/F_2^D at small x. In the following, we discuss two topics on the Q^2 evolution. The first is Q^2 variation of F_2^A/F_2^D [2, 3] and the second is $\partial[F_2^{Sn}/F_2^C]/\partial[\ln Q^2]$ [4].

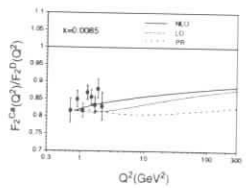

Figure 1: Q^2 variation of F_2^{Ca}/F_2^D.

We compare calculated evolution results with the NMC data in Fig. 1 at x=0.0085 [2]. The initial distributions at Q_0^2=0.8 GeV^2 in the nucleon and the calcium nucleus are taken from Ref. [3]. In Fig. 1, the dotted, solid, and dashed curves are obtained in the leading-order (LO) DGLAP, next-to-leading-order (NLO) DGLAP, and NLO evolution equations with parton-recombination contributions respectively (Λ =0.2 GeV and N_f=3). As shown in the figure, NLO and recombination contributions to the ratio are conspicuous at such a small x. If we evolve F_2 from Q_0^2=0.8 GeV^2, the recombination effects are larger than the NLO ones. It is interesting to find such large recombination contributions in Fig. 1. However, the recombination cannot be tested at this stage because we do not have the data in the wide Q^2 region at small x. The future HERA nuclear program should be able to study the large Q^2 region, so that the parton recombination mechanism could be tested.

Next, Q^2 evolution differences in various nuclei could also be investigated at HERA. There are significant differences between tin and carbon Q^2 variations according to recent NMC analysis. It is the first indication of nuclear effects on the Q^2 evolution of F_2. The phenomena are worth investigating theoretically.

The Q^2 evolution of the structure functions F_2 in tin and carbon nuclei is investigated in Ref. [4]. As the input distributions, we employ those in Ref. [3]. F_2 is evolved by using LO DGLAP, NLO DGLAP, and PR equations with the help of a computer program in Ref. [2]. Calculated results for $\partial[F_2^{Sn}/F_2^C]/\partial[\ln Q^2]$ at Q^2=5 GeV^2 are compared with the NMC data. The DGLAP evolution curves agree roughly with the experimental tendency, but the PR results are significantly different from the data. However, it does not mean that the recombination mechanism should be ruled out because there exists an unknown parameter K_{HT} associated with the higher-dimensional gluon distribution in the recombination. In order to discuss the validity of the PR evolution, the constant K_{HT} must be evaluated theoretically.

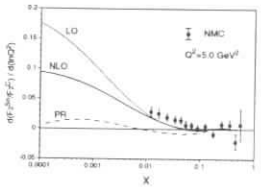

Figure 2: Nuclear dependence in Q^2 evolution of F_2.

In this way, the NMC experimental result $\partial[F_2^{Sn}/F_2^C]/\partial[\ln Q^2] \neq 0$ could be essentially understood by the difference of parton distributions in the tin and carbon nuclei together with the ordinary DGLAP evolution equations. However, we find an interesting indication that "large" higher-twist effects on the Q^2 evolution could be ruled out. As shown in Fig. 2, there are large differences among three evolution results at small x ($\approx 10^{-4}$). The future HERA program can study nuclear dependence of the Q^2 evolution ($\partial[F_2^A/F_2^D]/\partial[\ln Q^2]$) in this small x region, and it provides us crucial information on recombination effects and on higher-order α_s effects.

Acknowledgment

This research was partly supported by the Grant-in-Aid for Scientific Research from the Japanese Ministry of Education, Science, and Culture under the contract number 06640406.

References

[1] P. Amaudruz et al. (NMC collaboration), Nucl. Phys. B 441 (1995) 3. Sn/C Q^2 variation data are preliminary.

[2] M. Miyama and S. Kumano, Comput. Phys. Commun. 94 (1996) 185.

[3] S. Kumano, Phys. Rev. C48 (1993) 2016; Phys. Rev. C50 (1994) 1247; S. Kumano, M. Miyama, and K. Umekawa, research in progress.

[4] S. Kumano and M. Miyama, Phys. Lett. B 378 (1996) 267.

Diffraction and Shadowing in Deep-Inelastic Scattering from Nuclei[1]

G. Niesler, G. Piller and W. Weise

Physik Department, Technische Universität München, D-85747 Garching, Germany

Abstract: Shadowing effects in deep-inelastic photon and lepton scattering from deuterium probe the mass spectrum of diffractive photo- and leptoproduction from nucleons. For heavier nuclear targets diffractive hadron-nucleon transition amplitudes can be studied in addition. At small $Q^2 \lesssim 1\,GeV^2$, as in the recent data from the NMC and E665 collaboration, shadowing is due to the coherent interaction of low mass vector mesons. Nuclei at HERA would yield the opportunity to investigate shadowing effects at large Q^2 where the diffractive excitation and coherent multiple interaction of heavy hadronic states is important.

Diffractive photo- and leptoproduction of hadrons from nucleons and shadowing effects in high energy (virtual) photon-nucleus scattering processes are closely related [1]. Their connection is displayed most clearly if one considers the scattering of high energy (virtual) photons from deuterium. The total photon-deuteron cross section can be split into two parts. First, it receives contributions from incoherent photon scattering off single nucleons inside the deuteron. This yields twice the photon-nucleon cross section. Secondly, at high photon energies $\nu > 3\,GeV$, or for lepton scattering at small values of the Bjorken variable $x < 0.1$, the photon can interact coherently with both nucleons inside the target. This double scattering process reduces the total photon-deuteron cross section, i.e. causes shadowing. It is driven by the diffractive excitation of the photon on the first nucleon into a hadronic state X, which subsequently interacts with the second nucleon and converts into the outgoing photon. Neglecting the real part of the diffractive photon-nucleon amplitude one obtains the double scattering correction to the total photon-deuteron cross section [1]:

$$\delta\sigma_{\gamma^* d} = -4\pi \int_{4m_\pi^2}^{W^2} dM_X^2 \left.\frac{d^2\sigma_{\gamma^* N\to XN}}{dM_X^2\,dt}\right|_{t\approx 0} \mathcal{F}_d(k_L). \qquad (1)$$

Here $\frac{d^2\sigma_{\gamma^* N\to XN}}{dM_X^2\,dt}|_{t\approx 0}$ is the forward differential cross section for diffractive photoproduction of hadrons with invariant mass M_X. The latter requires a minimal momentum transfer $k_L = (Q^2 + M_X^2)/2\nu$ parallel to the momentum of the incident photon. Contributions with a momentum transfer k_L larger than the inverse of the typical target size are suppressed by the longitudinal deuteron form factor $\mathcal{F}_d(k_L)$. As a consequence, shadowing from diffractive excitation of large mass intermediate states will only be seen at sufficiently high photon energies ν.

[1]Work supported in part by grants from BMBF.

High precision data on shadowing in deep-inelastic lepton-nucleus scattering have recently become available from experiments at CERN (NMC) and Fermilab (E665) [2]. To investigate which diffractively excited hadronic states dominate the observed shadowing, one has to know the diffractive leptoproduction cross section (see Eq.(1)). However, in the kinematic regime of the NMC and E665 experiments such data are available only for the resonance region, $M_X^2 \lesssim 3\,GeV^2$. Nevertheless, since in these fixed target experiments the average momentum transfer is small ($\overline{Q^2} < 1\,GeV^2$) for small values of $x < 0.005$, we may, for a qualitative analysis, study shadowing effects for real photon beams at corresponding photon energies $50\,GeV < \nu < 300\,GeV$. Here the diffractive photoproduction cross section is measured in the region $4m_\pi^2 < M_X^2 < 18\,GeV^2$ [3]. At $M_X^2 \lesssim 3\,GeV^2$ it receives large contributions from vector mesons, while for $M_X^2 > 4\,GeV^2$ it drops like $\sim M_X^{-2}$. This is consistent with the expected Regge behaviour $\frac{d^2\sigma}{dM_X^2\,dt}|_{t\approx 0} \sim M_X^{-2} \approx M_X^{-2\alpha_P(0)}$, where $\alpha_P(0)$ is the intercept of the pomeron trajectory, $\alpha_P(t=0) \approx 1.08$. In Fig.1 we show the shadowing correction for deuterium, $\delta\sigma_{\gamma d}$, caused by the diffractive excitation of all kinematically allowed hadronic states and compare it with the contribution from low mass vector mesons. We observe that vector mesons are dominant for photon energies $\nu < 300\,GeV$. This is in agreement with results from the generalized vector meson dominance model [4], where it is found that the shadowing observed by NMC and E665 is mainly due to the coherent multiple scattering of low mass vector mesons. Also note that according to Regge phenomenology, the diffractive photoproduction cross section rises as $W^{4(\alpha_P(0)-1)}$ which leads to an increase of the shadowing correction proportional to $\nu^{2(\alpha_P(0)-1)} \approx \nu^{0.16}$.

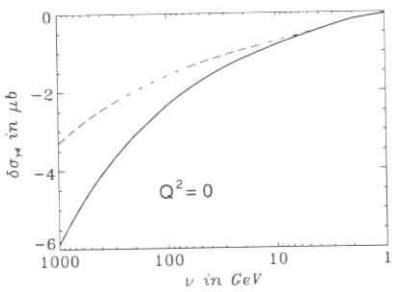

Figure 1: *Shadowing correction $\delta\sigma_{\gamma d}$ in high energy photon-deuterium scattering. The dashed line shows the contribution from low mass vector mesons.*

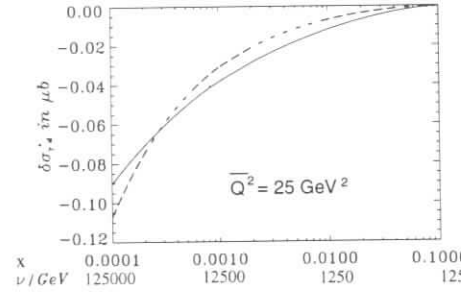

Figure 2: *Shadowing correction $\delta\sigma_{\gamma^* d}$ for deep-inelastic scattering form deuterium at $\overline{Q^2} = 25\,GeV^2$. For the full (dashed) line the diffractive leptoproduction cross section from H1 (ZEUS) was used.*

At large momentum transfers, $Q^2 \gtrsim 10\,GeV^2$, the situation is different. Here shadowing is caused by the coherent interaction of heavy hadronic states. This can be shown by using recent data on diffractive leptoproduction from nucleons measured at the HERA collider [5]. They cover the kinematic region of large $\overline{Q^2} \gtrsim 10\,GeV^2$ and very small x ($10^{-4} < x < 0.02$). However, the dependence of the production cross section on t, the momentum transfer to the

nucleon target, is not yet available. We construct the forward diffractive production cross section by assuming a t-dependence similar to diffractive hadron-hadron collisions. Vector meson contributions to the diffractive cross section are strongly suppressed, e.g. $\sigma(\gamma^* N \to \rho N) \approx 1/Q^{4.2}$ [6]. At large masses one finds $\frac{d^2\sigma}{dM_X^2 dt}|_{t\approx 0} \sim (Q^2 + M_X^2)^{-a}$, where $a \approx 1.3$ (H1) or $a \approx 1.3$–1.5 (ZEUS) respectively. In Fig.2 we show the shadowing correction $\delta\sigma_{\gamma^* d}$ calculated for $\overline{Q^2} = 25\,GeV^2$ and $a = 1.3(1.5)$. We observe that the vector meson contribution to shadowing is negligible in this kinematic regime. The main effect is caused by large mass hadronic states: $M_X^2 \sim Q^2$. The energy dependence of the calculated shadowing effect is proportional to ν^{a-1}.

To conclude: We have investigated the relation between shadowing effects in deep-inelastic scattering from nuclei and diffractive photo- and leptoproduction from free nucleons. We find that the momentum transfer Q^2 selects the diffractive states which dominate the observed shadowing effect. As a consequence shadowing as observed in recent measurements of the NMC and E665 collaboration is controlled by the coherent multiple scattering of low mass vector mesons. If nuclei would become available at the HERA collider, shadowing effects could be explored at large $Q^2 \gtrsim 10\,GeV^2$, where the high mass tail of the diffractive production cross section is relevant. Therefore the investigation of shadowing effects in deep-inelastic scattering from deuterium over a large range of Q^2 probes the M_X^2- and Q^2-dependence of the diffractive leptoproduction cross section. For heavier nuclear targets shadowing is sensitive not only to double scattering but also to the multiple interaction of diffractively excited hadronic states. This offers the possibility to study both diagonal and off-diagonal diffractive hadron-nucleon amplitudes.

References

[1] V.N. Gribov, Sov. Phys. JETP **29**, 483 (1969)

[2] NMC Collab., P. Amaudruz et al., Nucl. Phys. **B 441**, 3 (1995); A. Arneodo et al., Nucl. Phys. **B 441**, 12 (1995); E665 Collab., M.R. Adams et al., Phys. Rev. Lett. **75**, 1466 (1995); Z. Phys. **C 67**, 403 (1995)

[3] T.J. Chapin et al., Phys. Rev. **D 31**, 17 (1985)

[4] G. Piller, W. Ratzka and W. Weise, Z. Phys. **A 352**, 427 (1995)

[5] H1 Collab., T. Ahmed et al., Phys. Lett. **B 348**, 681 (1995); ZEUS Collab., M. Derrick et al., Z. Phys. **C 68**, 569 (1995); preprint DESY 96-018

[6] ZEUS Collab., M. Derrick et al., Phys. Lett **B 356**, 601 (1995)

Diffraction in DIS on nuclear targets

N.N.Nikolaev[a,b,c], W.Schäfer[b], B.G.Zakharov[c], V.R.Zoller[d]

[a] ITKP, Universität Bonn, Nußallee 14-16, Bonn D-53115, FRG
[b] Inst. f. Kernphysik, KFA Jülich, D-52425 Jülich, FRG
[c] L.D.Landau Inst. Theor. Physics, Kosygina 2, 117334 Moscow, Russia
[d] Inst. Theor. exp. Physics, B.Cheremushkinskaya 25, 117259 Moscow, Russia

Abstract: We discuss the implications of a strong enhancement of diffraction for multiproduction in DIS off nuclear targets. The predicted effects are large and observable at HERA. We present the prediction of a large tensor structure function $b_2(x)$ of the deuteron which does not vanish at small x.

Diffractive DIS on nuclei is a huge effect

At the DESY Mini School in May 1994 one of the present authors (NNN) presented a prediction of a strong nuclear enhancement of diffractive DIS (DDIS), which on a strongly absorptive nuclei must reach $f_D \sim 50\%$ of the total DIS rate [1]! The participants may remember how it has been ridiculed by fellow experimentalists as an utterly useless prediction and at the Round Table discussion some of the fellow theorists stated it must be wrong. It took slightly more than a year for a serious discussion on the electron-nucleus option at HERA to be on the floor.

The detailed evaluation of nuclear enhancement of DDIS is published in [2]. The argument for the enhancement goes as follows: The microscopic QCD mechanism of DDIS is a grazing, quasielastic scattering of multiparton Fock states of the photon on the target proton, which is best described viewing these Fock states as systems of color dipoles spanned between quarks, antiquarks and gluons [3]. The crucial finding is that for transverse photons DDIS is dominated by the contribution from soft dipoles $r \sim 1/m_f$, still the $1/Q^2$ leading twist behavior of σ_T^D is a rigorous QCD result [3]. The rest of the story is simple: DDIS on nuclei essentially amounts to an elastic (coherent DDIS) and small admixture of quasielastic (incoherent DDIS) scattering of soft dipoles off a target nucleus. For soft dipoles and strongly absorbing targets

$$\sigma^D \sim \sigma^{ND} \sim \frac{1}{2}\sigma^{tot}. \qquad (1)$$

Here ND stand for the non-diffractive and/or non-LRG DIS. In the conventional A^α parameterization of nuclear cross sections, we find $\alpha \approx 0.9$ for the total DIS at moderately small $x \sim 10^{-3}$ (or $\alpha \approx -0.1$ for the structure function per bound nucleon) and very large $\alpha_{coh}^D \approx 0.25$-$0.3$ for the coherent DDIS per bound nucleon. Finally, for the incoherent DDIS per bound nucleon we predict $\alpha_{inc}^D \approx -0.4$. For the reference, for the carbon target $\sigma_{coh}^D : \sigma_{inc}^D \approx 2.2 : 1$.

Coherent DDIS $eA \to e'XA$ is at work for $x, x_{I\!P} \lesssim 0.1 \cdot A^{-1/3}$ which is precisely the kinematical range of the eA collisions at HERA. What are the consequences of this striking nuclear enhancement of DDIS? Are they observable at HERA?

DDIS and A^α physics in multiproduction off nuclei

The multiproduction off nuclei is usually discussed in terms of the normalized Feynman z and/or (pseudo)rapidity η distributions $R(z) = [dn/dz]_A/[dn/dz]_N$ and $R(\eta) = [dn/d\eta]_A/[dn/\eta]_N$ In the hadron-nucleus collisions, the more hadronlike is a hadron, i.e., larger is σ_{tot}^{hN} the stronger is the shadowing in σ_{tot}^{hA}, the higher is the average multiplicity, the larger is $R(\eta) > 1$ at mid-rapidity, the stronger is nuclear attenuation of the projectile fragments $R(z \sim 1) < 1$, the stronger is the hadronic activity in the target nucleus region (for the review see [4]. We predicted a striking reversal of this trend when going from pointlike photons in the nonshadowing (NS) region of $x \gtrsim 0.1$ to the hadronlike photons in the shadowing (SH) region of small $x \lesssim 0.03 - 0.01$ [2].

Indeed, in coherent DDIS the target nucleus remains in the ground state, there is vanishing hadronic activity in the nucleus region and coherent DDIS falls into the LRG category. Incoherent DDIS also contributes to LRG events but the fraction of incoherent DDIS rapidly decreases with A [2]. Because the DDIS rate increases at small x, hadronic activity in the nucleus region must decrease with the decreasing x, i.e., for more hadronlike photons. The predicted [2] effect is large, $\sim 30\%$, and has been fully confirmed by the E665 μXe scattering data [5]. The very sharp t distribution permits an unambiguous selection coherent DDIS. HERA experiments can extend these measurements to a much smaller x and higher Q^2 on a broad range of nuclei.

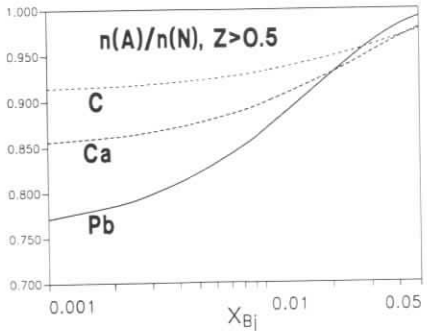

Figure 1: *Our predictions for attenuation of forward hadrons in ND DIS off nuclei as a function of x_{bj}.*

Now consider $R(z)$ for the generic, DDIS/ND unseparated, DIS off a nucleus. The very forward hadrons with $z \sim 1$ are predominantly the diffraction dissociation products [6]. It is precisely the part of the phase space usually discussed in terms of the fragmentation of the isolated struck quark and the Landau-Pomeranchuck-Migdal effect (for the quantum theory of the LPM effect see [7]). Our point is that DDIS completely invalidates this interpretation in the SH region of small x. Indeed, because of (1) for *heavy, strongly absorbing* nuclei we predict a *universality* of the z-distributions, $R(z) = 1$, which derives from the nuclear enhancement of DDIS, the Landau-Pomeranchuck effect is irrelevant for this prediction. The corrections to $R(z) = 1$ for slight nuclear distortions of the mass spectrum in DDIS must be marginal with one subtle exception: because of the M^2 dependent factorization scale [8] and related effects of color transparency [9] DDIS into small masses $M^2 \ll Q^2$ the vector mesons included will have

a much steeper A^α dependence with the exponent $\alpha \approx 1.35$-1.4. Therefore, in the narrow region of $z \to 1$ to which only the small mass excitations can contribute, we predict $R(z) > 1$!

The ND DIS is the counterpart of inelastic hadron-nucleus scattering and our principal prediction is that nuclear effects in ND events must be similar to those seen in $\pi A, pA$ collisions: $R_{ND}(z) < 1$ at $z \sim 1$ and $R(\eta) > 1$ in the mid-rapidity region. In particular, hadronic final states will be a superposition of subprocesses with the ν-fold average multiplicity (ν cut pomerons along the lines reviewed in [4]. Only the $\nu = 1$ subprocesses contribute to production of large-z particles. In Fig. 1 we show the expected x dependence of nuclear attenuation of forward hadrons with $z > 0.5$, in the parameterization $R(z) \approx A^{\alpha(z)}$ for the very forward hadrons and for a sufficiently small $x \sim 10^{-3} - 10^{-4}$ we predict $\alpha(z) \sim -0.15$. For the central, mid-rapidity region we predict $R(\eta) \sim A^{0.15}$. The mean multiplicities in the ND DIS are dominated by central production and must exhibit similar A dependence. Such a strong nuclear effects can easily be observed at HERA.

Nuclear enhancement of coherent DDIS implies enhancement of low multiplicities, whereas the enhancement of central production implies the enhancement of high multiplicities. Consequently, we predict a substantial broadening of the multiplicity distributions, although the overall nuclear increase of the average multiplicities can be relatively weak.

DDIS and the tensor spin structure functions of the deuteron

For DIS of *unpolarized* leptons off the spin-1 deuterons one can define the tensor spin structure function [10]

$$b_2(x,Q^2) = \frac{1}{2}\left[F_2^+(x,Q^2) + F_2^-(x,Q^2) - 2F_2^0(x,Q^2)\right] ,$$

where $+,-,0$ refer to the deuteron spin projection on for instance the $\gamma^* D$ collision axis. One can similarly define the longitudinal tensor structure function $b_L(x,Q^2)$.

In the usually discussed impulse approximation the tensor parton densities vanish for the S-wave bound state. The $S-D$ interference makes the nucleon momentum distributions and folding corrections to structure functions different for $\pm, 0$ polarizations, but at moderately small x the corresponding tensor asymmetry is a per mill and even smaller effect and vanishes at $x \to 0$ [11].

An interesting finding is that an order in magnitude larger tensor spin structure function is generated by DDIS via shadowing corrections [12]. Our point is that nuclear shadowing depends on the alignment of nucleons in the deuteron, which because of the $S-D$ interference is different for $\pm$ and 0 polarization states. The striking finding is that unlike all other spin asymmetries which are well known to vanish in the limit $x \to 0$, the tensor spin asymmetry is finite and even rises at small x. Besides the spin-alignment dependent shadowing for DDIS, another source of the tensor asymmetry is DIS off pions in the deuteron. The number of pions in the deuteron also depends on the deuteron spin state. Our predictions for the tensor asymmetry are shown in Fig. 2. The pion effects have a sign opposite to that of the diffractive NS effects and dominate at $x \gtrsim 10^{-2}$, diffractive NS takes over at $x \lesssim 10^{-2}$.

We predict a nonvanishing $b_L(x,Q^2)$. Typically, the ratio $R_{LT} = b_L/b_2 \sim 0.2$ and is very similar to the familiar ratio σ_L/σ_T for the nucleon target.

Acknowledgment. NNN thanks Prof. U.Meißner for the hospitality at the Inst. Theor. Kernphysik of the Univ. of Bonn. The work of NNN is supported by the DFG grant ME864/13-1.

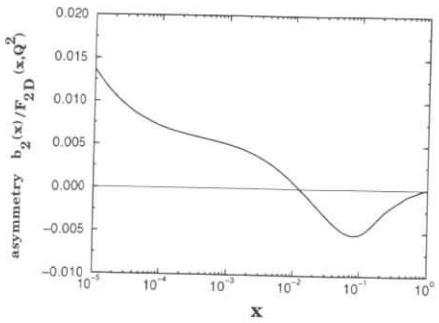

Figure 2: *Our predictions for the tensor asymmetry in DIS of unpolarized leptons off tensor polarized deuterons ($Q^2 = 10\ GeV^2$).*

References

[1] N.N.Nikolaev, Lectures at the DESY Mini-School on Diffraction at HERA, DESY, 4-7 May 1994.

[2] N.N. Nikolaev, B. G. Zakharov and V. R. Zoller, Z. Phys. **A351**, 435 (1995) .

[3] N.N. Nikolaev and B.G. Zakharov, *Z. Phys.* **C49**, 607 (1991); **C53**, 331 (1992); **C64**, 631 (1994); *J. Exp. Theor. Phys.* **78**, 598 (1994);

[4] N.N. Nikolaev, Sov. Phys. Uspekhi **24**, 531 (1981).

[5] E665 Collab., M.R.Adams et al., *Z. Phys.* **C65**, 225 (1995).

[6] V.R.Zoller, *Z. Phys. C44*, 665 (1989).

[7] B.G.Zakharov, *JETP Letters* **63**, 906 (1996).

[8] M.Genovese, N.Nikolaev and B.Zakharov, *Phys. Lett.* **B378**, 347 (1996); **B380**, 213 (1996).

[9] B.Z.Kopeliovich, J.Nemchik, N.N.Nikolaev and B.G.Zakharov, *Phys. Lett.* **B324**, 469 (1994).

[10] P.Hoodbhoy, R.L.Jaffe and A.Manohar, *Nucl. Phys.* **B312**, 571 (1989).

[11] A.Yu.Umnikov, hep-ph/9605291 (1996); H.Khan and P.Hoodbhoy, *Phys. Rev.* **C44**, 1219 (1991).

[12] N.N.Nikolaev and W.Schäfer, paper in preparation.

Two-photon mechanism production of the Higgs boson, SUSY particles, hadrons and lepton pairs in eA Collisions at HERA

Maria Krawczyk[a] and B.B. Levtchenko[b]

[a] Institute of Theoretical Physics, University of Warsaw, 00 681 Warsaw, Poland
[b] Institute of Nuclear Physics, Moscow State University, 119899 Moscow, Russia

Abstract: We present prospects for the study of a light neutral Higgs boson, SUSY-particle, hadrons and leptons production in the two-photon coherent eA collisions.

1 Introduction

Particle production in the two-photon processes in lepton-lepton, hadron-hadron and nucleus-nucleus collisions has been already discussed in the literature [1]-[5]. One of the goals of the present analysis is to study the discovery potential of electron-nucleus collisions at HERA in the case of coherent electromagnetic particle production. Preliminary results were presented in [6].

Requirement of coherency implies that the collision is quasi-elastic, the impact parameter b is larger than the nuclear radius and the nuclear charge acts as a whole. For such collisions the hadronic background from $\gamma^* q$ and $\gamma^* g$ (direct and resolved) subprocesses will be absent offering a better experimental environment for studying new particle production.

Due to the large charge Z of heavy ion and the strong contraction of the electromagnetic fields in a high-energy collision we expect in such an electron-nucleus interaction a large particle production rate by the two-photon fusion mechanism. It turns out that the cross sections, which is scaled with Z^2, are comparable or even large than the total cross sections expected in e^+e^- , ep and pp collisions of the same incident energy per particle.

An important characteristic of eA collider is its discovery range: how heavy produced particles can be and how large will be production cross sections for them. In the equivalent photon approximation the invariant mass squared of the two-photon system, denoted by W^2, is fixed by the photon energies ω_e and ω_A. As it well known [4], [5] that the time duration of the electromagnetic pulse, produced by a charge moving with a relativistic γ factor, corresponds to field frequencies of $\omega \leq \gamma/b$. In the case of a heavy-ion beam the largest photon energy is $\omega_A \simeq \gamma_A/R_A$ although for photons emerged from an electron beam the photon energy can be close to the electron energy $\omega_e \leq E_e$. Thus the discovery range of the eA HERA collider for coherent processes extends to masses:

$$W \approx (4\omega_e\omega_A)^{1/2} \leq \left(\frac{4\,E_e E_p}{m_p R_A}\right)^{1/2} . \qquad (1)$$

This means the invariant mass values accessible at HERA energies are up to 86 GeV, 71 GeV and 54 GeV for eC, eCa and ePb collisions, respectively.

The paper is organized as follows: In the next section we compare the discovery ranges of eA (HERA), e^+e^- (LEP2) and ep (HERA) colliders using the two-photon luminosity function . In Sect.3, we evaluate cross sections for coherent production of lepton and slepton pairs (e^+e^-, $\mu^+\mu^-$, $\tau^+\tau^-$, $\tilde{l}^+\tilde{l}^-$), charged pion pair, pseudoscalar ($J^C = 0^+$) resonances and 2HDM light Higgs boson. Conclusion is given in the last section.

2 Two-photon luminosity function

The equivalent photon approximation [1], [2], [7] allows to express the cross section for the production of a final state with the effective mass W in two photon collision as a product:

$$d\sigma_{eA} = \sigma_{\gamma\gamma} \cdot \frac{dL_{\gamma\gamma}}{dW} dW, \qquad (2)$$

where the cross section $\sigma_{\gamma\gamma}$ describes the $\gamma\gamma \to f$ transition for real non-polarized photon and a differential two-photon luminosity function (TPL) $dL_{\gamma\gamma}/dW$ is introduced[1]. Results presented here were obtained with use a particular form of $dL_{\gamma\gamma}/dW$ [6] derived for untagged scattered electron and nucleus

$$\frac{dL_{\gamma\gamma}}{dW} = \frac{2Z_A^2\alpha^2}{\pi} \frac{f(t^*)}{W} ln\left(\frac{s_{eA}}{4m_e^2}\right), \quad f(t^*) = (\ln t^* + \frac{\sqrt{3}}{2})^2 + (t^* - 4)^2 - 3 \qquad (3)$$

with $t^* = \frac{R_A W^2}{2\gamma_A \sqrt{s_{eA}}}$. Eq. (3) is valid in the leading logarithm approximation.

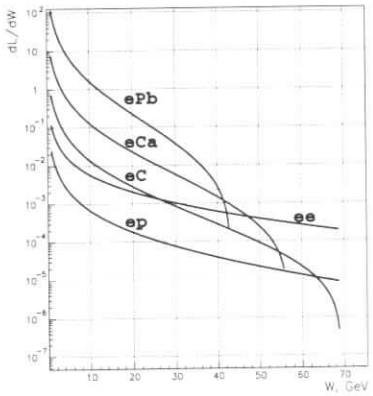

Figure 1: *Spectra of the two-photon luminosity function for e^+e^- (LEP, 200 GeV), ep(HERA, 300 GeV), and eA (HERA, 300A GeV) colliders.*

In Fig. 1 shown the dependence of TPL on the two-photon invariant mass for different colliding beams. The TPL function for e^+e^- (LEP2) was calculated with using Eq.(6) of ref. [7], as for the ep collision (HERA) the elastic part of the photon spectra from the proton was taken from [8]. Because of the used approximation the range of allowed W values in (3) is narrow (see Fig.1) as compared to (1) and defined by the condition $f(t^*) \geq 0$.

The advantage of eA collisions over e^+e^- and ep collisions lies in the Z^2 factor, which enchances the photon flux up to a factor 10^4. This allow, in the range of W below 40 GeV, the study of 'new phenomena' at HERA with large statistics.

3 Particle production processes

In this section we present a few examples of particle production in eA collisions through the two-photon mechanism. Processes with production of the 'old' particles (light hadrons and leptons) will create a background at search of 'new' particles (like Higgs bosons and sleptons). Cross sections presented here were calculated at $E_e = 27\,\text{GeV}$ and $E_A = E_p A$ with $E_p = 820\,\text{GeV}$.

[1] $L_{\gamma\gamma}$ is a dimensionless quantity. To get the production rate Eq. (2) have to be multiplied by the machine luminosity $\mathcal{L}_{eA}$ $[cm^{-2}sec^{-1}]$. For ion beams $\mathcal{L}_{eA} \sim A^{-1}\mathcal{L}_{ep}$.

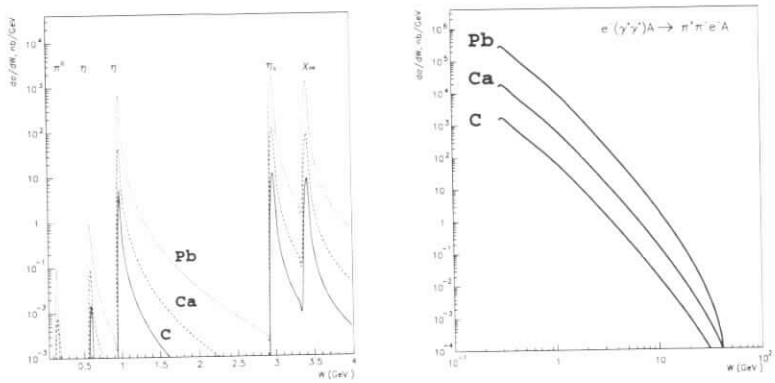

Figure 2: *Differential cross section for production of C-event pseudoscalar hadrons (a) and a $\pi^+\pi^-$ pair (b) as a function of W and a nucleus size.*

Resonances and pions

A region of the low mass in the two-photon system is the resonance region. C-even pseudoscalar hadrons - π^0, η, η', η_c, χ_{c0} - will be produced copiously at $W < 4\,\text{GeV}$. Their production cross section $\sigma_{\gamma\gamma}$ is well known [1]. Therefore, Eqs. (2) and (3) allows easily to evaluate dependence of the production rate on W. Fig. 2a shows a resonance structure of the differential cross section (2) in that region. As another example the cross section (2) for pair production of charged pions is plotted in Fig. 2b. What can be measured in the above processes and how is discussed in details in [1]. We note here only, that the study of the angular and energy correlations between pions allows, in principle, to extract components of the amplitude M_{ab} $(a, b = +, -, 0)$ for the $\gamma\gamma \to f$ transition.

Lepton pairs

The Bethe-Heitler process is a source of lepton pairs with extremely high yield (Fig. 3). Copious production of τ-leptons provide an opportunity to study QCD in τ decay [9]. However it will also to complicate the Higgs boson search in lepton decay modes because the main background above the τ threshold is due to $\gamma^*\gamma^* \to \tau^+\tau^-$ (see below and Fig. 4c). How to suppress the Bethe-Heitler background is discussed in [10] (see also [14]).

SUSY particles

Non-strongly interacting sypersymmetric particles'- sleptons and charginos- can be detected at the eA collider discussed here if their masses lies in the range $M_{sl} < 30$ GeV. Chargino couple to photons in the standard way of spin 1/2 fermions and sleptons are spin-zero particles. The two-photon cross section for production a pair of them can be found in [11], [1]. $\sigma(\gamma\gamma \to \tilde{l}^+\tilde{l}^-)$ is not logarithmically enhanced thus the production rate for sleptons is significantly lower than the chargino rate. As an example , the total cross section for slepton production versus the mass of the produced particle is shown Fig. 4a. At an integrated luminosity of $10^3/A\,\text{pb}^{-1}$ only sleptons

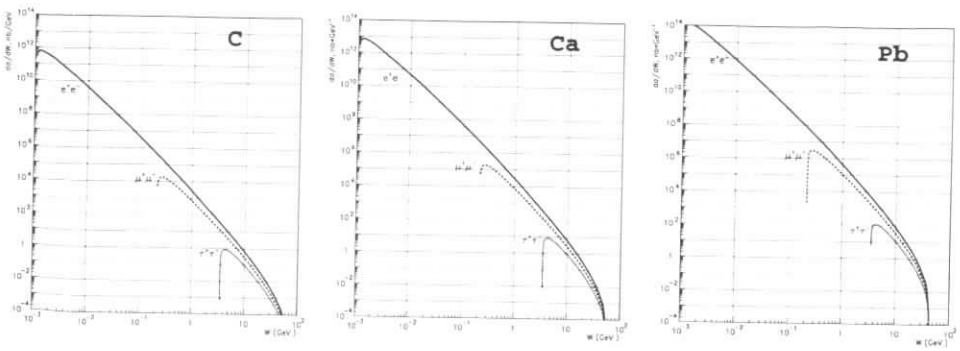

Figure 3: *Same as Fig. 2 for production of BH leptons in coherent eA collisions.*

with masses not heavier 29 GeV, 25 GeV and 20 GeV can be detected in eC, eCa, ePb collisions respectively.

Light neutral Higgs boson

The current mass limits on the Higgs particles from LEP data [12] restrict a class of models of spontaneous symmetry breaking available for analysis at HERA. The SM Higgs scalar and the MSSM scalar and pseudoscalar Higgs particles should be heavier than 66 GeV and 45 GeV, respectively. Minimal extension of the standard model like the general two doublet model (2HDM) [13] may yet have a very light ($\lesssim 40\,\mathrm{GeV}$) scalar h or pseudoscalar A[12, 14, 15]. The model parameters $tan\beta$ and α regulate coupling of Higgs particle to the "up" and "down" components of fermion doublets. We further restrict ourselves to the scenario with a large $tan\beta \sim \frac{m_t}{m_b} \gg 1$

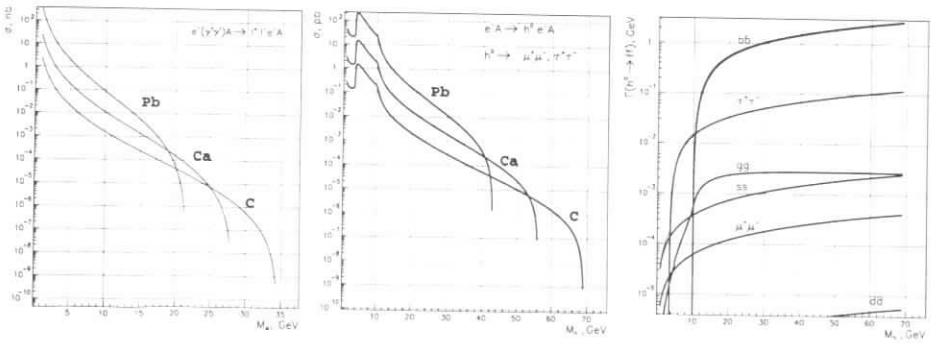

Figure 4: *Cross sections for slepton (a) and 2HDM light Higgs boson (b) production through two-photon fusion. The cross sections are plotted versus the mass of the produced particle. Also shown (c) the partial decay widths for h for $\tan\beta = 30\,(\alpha = \beta)$.*

and $\alpha = \beta$. This leads to the enhancement of the coupling to down-type fermions by factor $tan\beta^2$ for both h and A. We focus here on the resonant production of very light Higgs scalar h in the two-photon eA collisions[2].

The cross sections for the production of the h decaying into leptons versus the Higgs boson mass are presented in Fig. 4b. A specific structure of the curves is due to the variation of the h branchings (Fig.4c) with increasing the mass. Fig. 4b shows that at an integrated luminosity of $10/A\,\mathrm{pb}^{-1}$ there is a chance to observe the Higgs boson at HERA for $M_h \lesssim 5$ GeV, 8 GeV, 10 GeV in eC, eCa and ePb collisions respectively. However, at $\mathcal{L}_{eA} \sim 1/A\ \mathrm{pb}^{-1}$ only ions with $A \sim 200$ produce sufficient photon flux for h production with mass $\sim 2M_\tau$.

4 Conclusion

Analysis of the last section shows that in the two-photon coherent eA collisions a number of the traditional processes (with hadron and lepton production) can be studied at HERA with high statistics. However, at $\mathcal{L}_{eA} \sim 1/A\ \mathrm{pb}^{-1}$ only the restricted mass range $M_i < 13$ GeV can be explored in processes with SUSY particle production [6].

The general two Higgs doublet model provide a chance to study the Higgs production at HERA, since in framework of 2HDM light neutral Higgs particle is not rule out by present data. Therefore the search for the Higgs in the two-photon coherent eA interactions should be performed. Taking into account all results presented above it seems at an intergated luminosity $\sim 10/A\ \mathrm{pb}^{-1}$ and higher beams of light-to-medium size ions ($A \sim 40$) will produce photon flux sufficient for study new phenomena in eA collisions at HERA .

Acknowledgment. We are grateful to W. Krasny for stimulating discussions and help.

References

[1] V.M. Budnev, I.F. Ginzburg, G.V. Meledin, V.G. Serbo, Phys. Rep. **C15** (1975) 181
[2] P. Kessler, Acta Phys. Austriaca, 41 (1975) 141
[3] J.H. Field, in *Lecture Notes in Physics*: Photon Photon Collisions, v. 191 (1983) 270
[4] G. Baur, C.A. Bertulani, Phys. Rep. **C163** (1988) 299
[5] E. Papageorgiu, Nucl. Phys. **A498** (1989) 593c; Phys. Rev. **D40** (1989) 92
[6] B.B. Levtchenko, Preprint INP 96-71; hep-ph/9608295
[7] J.H. Field, Nucl. Phys. **B168** (1980) 477
[8] N. Arteaga-Romero, C. Carimalo, P. Kessler, Z. Phys. **C52** (1991) 289
[9] G. Altarelli, QCD at Colliders, Preprint CERN-TH-95/196
Proceedings of tau '94, Nucl. Phys. **B(Proc.Suppl.)** (1995) 1
[10] P.J. Bussey, B. Levtchenko, A. Shumilin, These Proceedings
[11] J. Ohnemus, T.F. Walsh, P.M. Zerwas, Preprint DESY 93-173, hep-ph/9402302
[12] P. Maettig, talk at ICHEP'96
[13] J.F. Gunion, H.E. Haber, G. Kane, S. Dawson, The Higgs Hunter's Guide, Addison-Wesley, Reading 1990
[14] A.C.Bawa, M. Krawczyk ,Phys.Lett. **B 357** (1995)637; M. Krawczyk, talk at Moriond'96; M. Krawczyk contr. to this proceedings
[15] J. Kalinowski, M. Krawczyk, Phys. Lett. **B361** (1995) 66; Acta phys. Polon. **B 27** (1996) 961
[16] D. Choudhury, M. Krawczyk, NLC Workshop, Hamburg, 30 August-1 September 1995; MPI-PTh/96-46, IFT-96/13(hep-ph/9607271), submitted to Phys.Lett.B

[2] A light neutral Higgs particle production at the low energy $\gamma\gamma$ collider was discussed in [16] and in the gluon-gluon fusion at the ep HERA collider in [14].

Leading Baryon Production in ed Interactions at HERA

G. Levman
University of Toronto, Toronto, Canada

Abstract: With a Forward Neutron Calorimeter and a Leading Proton Spectrometer, experiments at HERA have the possibility of detecting both the scattered and spectator baryons in *ed* collisions. The deuteron stripping channels $ed \rightarrow eX(p)(n)$, $eX(n)(n)$, $eX(p)(p)$ have been studied by modifying the HERWIG Monte Carlo program. For double tagged events most ambiguities are broken; however, an essential ambiguity remains between diffractive proton scattering with a neutron spectator, and diffractive neutron scattering with a proton spectator.

1 Introduction

Both the ZEUS and the H1 collaborations possess a Leading Proton Spectrometer (LPS)[1] and a Forward Neutron Calorimeter (FNC)[2] for the detection of energetic, low transverse momentum baryons produced in *ep* collisions. This note contains some remarks on the use of these detectors, especially the FNC, in the study of *ed* stripping channels, where one or both of the spectator/produced baryons can be detected.

The FNCs for both experiments are similar. They are compensating, transversely segmented, lead-scintillator calorimeters with excellent energy and position resolution, located approximately 100 m downstream of the main detector at a scattering angle of $\theta = 0$. The scattering angle covered, from 0 to 7 μr, is determined by the aperture of the proton machine beam line elements. The acceptance covers only a portion of the azimuth and is a complicated function of θ[3]. The transverse momentum measurement is limited by the intrinsic p_T of the beam.

2 Double Tagged Stripping Reactions

In this note it is assumed that the HERA machine will be essentially unchanged for *ed* running and that the beam energy will be 820 GeV for deuterons. The HERWIG[4] Monte Carlo program was modified to allow the generation of *ed* stripping reactions. In addition, diffractive baryon production was introduced[5][6]; non-diffractive baryon production through mechanisms such as reggeon or meson exchange, or excited baryon production and decay, was represented by one pion exchange[7][8]. The reaction types are shown in Table 1.

	Target nucleon	$ed \rightarrow$	Process	Signature
1	n	$enXp_s$	$\mathbb{P}$ exchange	fast n/fast p
2		$enXp_s$	0 exchange	slow n/fast p
3		$epXp_s$	- exchange	slow p/fast p
4	p	$epXn_s$	$\mathbb{P}$ exchange	fast p/fast n
5		$epXn_s$	0 exchange	slow p/fast n
6		$enXn_s$	+ exchange	superfast n

Table 1: Double tagged leading baryon reactions in *ed* collisions. Generic diffractive scattering is represented by $\mathbb{P}$ exchange; non-diffractive scattering, +/0/- charge exchange, by π exchange.

The distribution of momentum p of the spectator baryons was modeled with the Hulthen distribution[9]: in the rest frame of the deuteron,

$$H(p) \propto p^2 \left[\frac{1}{p^2 + a^2} - \frac{1}{p^2 + b^2} \right]^2 , \tag{1}$$

where $a = 46$ MeV and $b = 260$ MeV. In the HERA frame the energy distribution is strongly peaked at E=413 GeV with an RMS width of 23 GeV (Fig. 1). Because the average p_T of the spectator is only 63 MeV, 87% of the spectators are detected in the FNC.

Figure 1 shows that the energy spectrum of spectator neutrons is not separated from that of diffractively produced neutrons whose distribution peaks at 395 GeV with a width of 26 GeV; however because the p_T distribution is much broader only 22% of diffractive neutrons are detected. In contrast, the energy distribution for non-diffractive neutrons is clearly separated although the acceptance for these is only about 10%. Note that reactions 3 and 6 in Table 1 produce either two protons or two neutrons. In the LPS the protons will appear as two separate tracks; in the FNC the energies will add and reaction 6 will have an energy distribution like π exchange of Fig. 1, but on a 'pedestal' of 410 GeV.

3 Conclusions

The FNC and the LPS will be essential for sorting out the stripping channels in *ed* collisions at HERA; however, an important ambiguity will remain between diffractive proton and neutron production when the struck nucleon cannot be distinguished from the spectator, although the difference in their p_T spectra might be helpful.

Acknowledgments

I thank M. Arneodo, W. Krasny, and T. Massam for fruitful discussions.

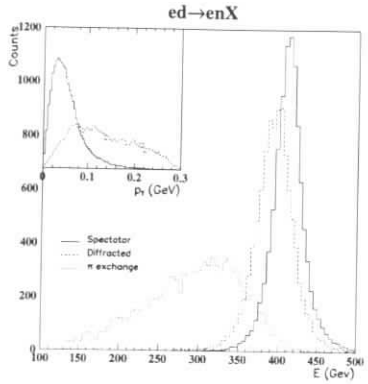

Figure 1: The energy spectrum of FNC neutrons detected in the FNC in *ed* reactions. Resolution effects have not been folded in (10k events of each type are plotted). The spectra for leading protons will be similar. The inset shows the p_T distribution for tagged spectator and diffractive neutrons.

References

[1] T. Massam, *these proceedings.*

[2] S. Bhadra et al., Nucl. Instr. and Meth. **A354** (1995) 479.

[3] ZEUS Coll., M. Derrick et al., *Observation of events with an energetic forward neutron in deep inelastic scattering at HERA*, DESY report 96-093, to be published in Phys. Lett. **B** (1996) .

[4] G. Marchesini et al., Comput. Phys. Commun. **67** (1992) 465.

[5] G. Ingelman and P. Schlein, Phys. Lett. **152B** (1985) 256.

[6] A. Donnachie and P. V. Landshoff, Phys. Lett. **191B** (1987) 309, and Nucl. Phys. **B303** (1988) 634.

[7] M. Bishari, Phys. Lett. **38B** (1972) 510.

[8] G. Levman and K. Furutani, *Virtual pion scattering at HERA*, DESY Report 95-142 (1995).

[9] Gross, Franz, *Relativistic Quantum Mechanics and Field Theory* (Wiley, 1993).

Use of the LPS in eA events at HERA A new stripping channel.

T.Massam

INFN Bologna. Via Irnerio 46, 40126 Bologna, Italy.

1 Introduction

To see the utility of a modified LPS in $e-d$ experiments, consider first the limitations without the LPS. The aim is to make measurements on (en) interactions or compare (ep) and (en) or sum them in (ed) or look at coherent (ed) interactions. Q^2 depends only on the electron variables but

$$x_{Bj} = \frac{Q^2}{2(qn)} \; or \; \frac{Q^2}{2(qp)} \tag{1}$$

so here the 4-momentum of the incident proton or neutron must be known. But, inside the deuteron, the neutron, for example, has some momentum distribution determined by the neutrons wave function[1] (Fig1).

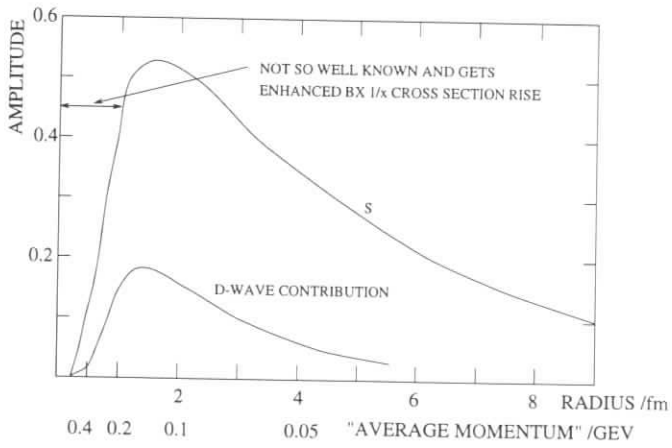

Figure 1: The deuteron wave function.

The Fermi-momentum extends up to about 30% of the nucleon mass, which implies that the incident neutron momentum has a laboratory energy ranging over $400 GeV \pm 130 GeV$.[2].

The observed cross section is averaged over the values of x_{Bj} given approximately by

$$x_{Bj} = (1 + p^*_{par}/m_n) \times \frac{Q^2}{(qd)} \qquad (2)$$

where p^*_{par} is the longitudianal momentum of the neutron in the deuteron system, m_n the neutron mass and the last term is the value of x_{Bj} if the neutron carries just half the deuteron's momentum. For constant Q^2, the relative importance of the momentum distribution is increased at the high momentum end through 2 and the $\frac{1}{x}$ term in the ep inelastic cross section.

The deuteron wave function is well determined at low momentum, but the high momentum part which depends on the repulsive core part of the nucleon-nucleon interaction is not so well known[1]

2 Stripping

Half a century ago the interactions of neutrons with nuclei was being studied, using known-energy deuteron beams, measuring the spectator protons and making various corrections for nuclear effects[3]. The aim now would be to build an efficient *stripping channel* to measure the spectrum of protons around $410GeV$, aiming at a fractional momentum resolution $\Delta p/p \sim 10^{-3}$ compared to the value $\Delta p/p \sim 10^{-4}$ for the deuteron beam. Tagging the spectator proton would be equivalent to making a neutron beam with momentum resolution 0.1% – apart from "nuclear effects", i.e. rescattering, shadowing and so on.

This however defines only the kinematics. To obtain a cross section measurment requires knowing the neutron luminosity as a function of momentum which in turn requires a good knowledge of the deutron's momentum wave function. Supplementary information on the high momentum tails of the fermi distribution might be obtained by studying the transverse momentum distribution of the spectator, but this would require high-β operation of HERA to keep the transverse momentum spread of the deuteron beam low enough. (The transverse momentum spread of the present beam is $25MeV$ horizontally and $90MeV$ vertically.)

3 A first design trial

Designing a stripping channel is essentially an accelerator design problem, with specifications requiring high acceptance for $0.35 \leq x_L \leq 0.65$ and $p_T \leq 0.3GeV$. These ranges would allow the measurement of background outside the range containing the majority of the spectator protons. The present beam optics has been used to gain some insight into the problem. The impact of the proposed HERA low-β optics is not discussed[4].

Fig.2 shows a section of the present beam line with the vacuum chamber limitations and trajectories which span most of the spectator proton phase space. After the station $S3$ particles with $x_L \sim 0.5$ diverge strongly from the beam line so that the acceptance of a typical silicon detector area becomes small. To understand the possibilities, assume that there is a detector station at S3 to measure position and that another station $S7$ is added some drift-distance after S3 to measure the track direction. This information together with the position of the

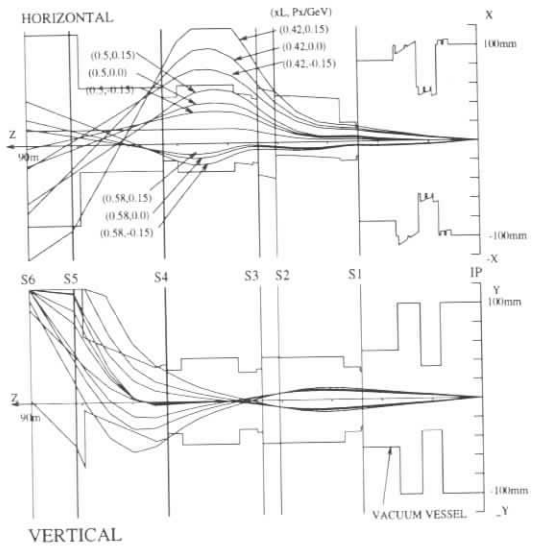

Figure 2: The present beamline showing the vacuum chamber limits and some spectator proton orbits which span the expected transverse and longitudinal momentum ranges.

interaction vertex allows the momentum of the particle to be reconstructed using the two-station reconstruction method which was developed for the LPS.

Limitations arise because of the finite size of the beam because detectors cannot be placed closer than the 10σ profile of the beam. There are also limitations because of blind-spots on the detectors where there is no momentum dispersion in both horizontal and vertical planes. Consider the vertical projection of the beam before $S3$. There are no vertical bending magnets so a particle on the horizontal plane through the quadrupole axes sees no deflecting field and so no momentum dispersion. In the horizontal projection there are bending magnets and then the combined affect is to displace the blind-spot off axis by an amount which depends on the beam energy.

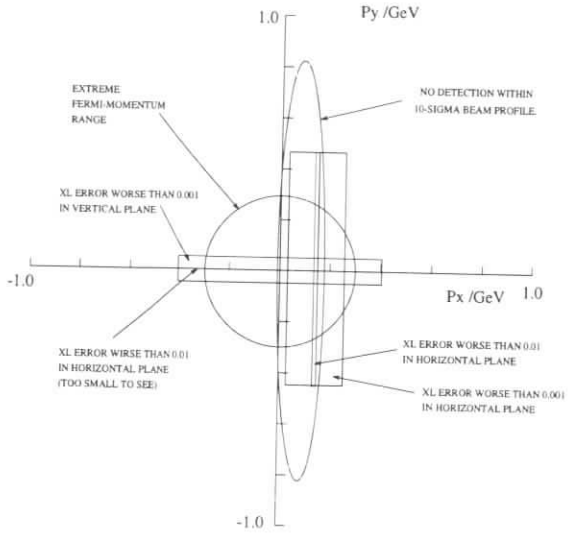

Figure 3: The transverse phase space plane at the interaction point showing the various limitaions to the acceptance.

Fig.3 gives a summary of the different factors influencing the acceptance. Everything has been mapped back onto the transverse momentum plane at the interaction point using a particle momentum of $410GeV$ to perform the tracking. The features to note are:

1. The circle containing the wanted events defined by the fermi-momentum spread. Note that the population of this area is sharply peaked at $p_x = p_y = 0.0$ so the picture gives an optimistic impression.

2. The part lost because the detector at $S3$ cannot be put in the beam.

3. The limits of 1% and 0.1% resolution for independent momentum measurements in the horizontal plane and in the vertical plane, calculated assuming $15\mu m$ position resolution

and $2\mu radian$ angular resolution. (The latter would require a much longer drift space after $S3$ than is at present available.) Where the resolution is good in both planes there are two independent momentum measurements. Only when the measurement is poor in both planes must the track be rejected with cuts which must be included in efficiency calculations. If accuracy of 1% is adequate, the loss from this cause is negligible.

4. The region with poor x_L resolution in both planes is inside the cut which is imposed by the 10σ size of the beam at $S3$.

5. Limitations by the beam's vacuum vessel. This has not been included.

4 Conclusions

It looks encouraging to study further a HERA stripping channel, but serious design problems are evident. Though the beam and the spectator protons from the deuterons are widely separated in longitudinal phase space there is not enough deflection to separate the two "beams" and at the $S3$ station position so the detectors cannot be placed at the position of maximum intensity of the spectator protons. Further station positions must be investigated to reach an optimum solution.

Ideally, to fully understand ed events, there should be high acceptance for both forward protons and forward neutrons. A comparison of the proton and neutron spectators and ambiguities which can arise is given in [2].

References

[1] The nucleon-nucleon interaction. G.E.Brown ans A.D.Jackson, North Holland, 1976.

[2] The momentum spread quoted here correspod to a level of 2% in the spectrum quoted by G. Levman, these proceedings.

[3] Nuclear stripping reactions. S.T.Butler and O.H.Hittmair, Wiley 1957.

[4] A first study of the LPS in a low-β machine has been made. T.Massam, these proceedings.

What can we gain by detecting nuclear fragments in electron-nucleus collisions at HERA?

J.Chwastowski[ab], M.W. Krasny[c]

[a] Institute of Nuclear Physics, ul. Kawiory 26A, 30-055 Krakow, Poland
[b] Deutsches Elektronen-Synchrotron DESY, Notkestrasse 85, D-22603 Hamburg, Germany
[c] L.P.N.H.E IN2P3-CNRS, 4, pl. Jussieu, T33 RdC 75252 Paris Cedex 05, France

Abstract: Detecting nuclear debris in deep inelastic electron-nucleus scattering is a challenge at HERA collider, where the energies of ions could reach 400 GeV/nucleon. If realized, it may provide a very useful tool to tag the number of nucleons which interacted with the virtual photon. In this note we point out that such a tag could be of primordial importance in searches for nonlinear QCD effects and in measuring the structure of the Pomeron in coherent electron-nucleus collisions.

1 Introduction

The nuclear option for HERA, if realized in the future, could provide new and unique possibility of studying electron-nucleus interactions in the new, so far unexplored, energy domain of $\sqrt{s} \simeq 3\ TeV$. To reach such an energy in interactions with electrons of 30 GeV the nuclei have to be accelerated to a very large energy, exceeding the binding energy of nucleons in the nucleus by 5 orders of magnitude. The nuclear debris will thus emerge at very small angles, which will be typically of the fraction of miliradians. The detection of these debris is a difficult task, especially for charged fragments with Z/A equal to that of the beam nucleus. In this paper we leave out the discussion how this can be done but rather try to point out why designing such a detection system could be of importance.

One of the challenges of the nuclear option at HERA is to discover nonlinear QCD effects which are responsible for taming the growth of the partonic distributions at low x [1]. These effects are expected to be amplified in the electron-nucleus collisions by the factor $A^{1/3}$ with respect to electron-nucleon collisions, provided that x is sufficiently small and the collisions are central. In the central collisions the virtual photon can interact with partons originating from several nucleons ejecting these nucleons from the nucleus. The number of these "wounded" nucleons may thus be a measure of an effective density of the partonic system which interacted with the virtual photon. By analyzing events in which large number of wounded nucleons is detected we expect to increase the discovery potential of the nonlinear QCD effects.

The unexpectedly large cross section for deep inelastic diffractive scattering measured at HERA allows for a precise measurement of the Pomeron structure at modest luminosities. One

of the question of primordial importance, which could be addressed within the nuclear program of HERA is: how universal is the concept of the Pomeron? In particular: is the structure of the Pomeron which originates from the nucleon the same as of the Pomeron which originates from the nucleus? Within the present HERA optics it will be difficult, if not impossible, to detect coherently recoiled nucleus in diffractive deep inelastic electron-nucleus scattering. It may turn out however, that incoherent processes give rise to large multiplicities of neutrons which are evaporated from the nucleus. If a large fraction of evaporation neutrons is detected we could use their signal as an anti-tag to select coherent processes with respect to incoherent ones.

In this note we present Monte Carlo studies which illustrate the ideas sketched above. In section 2 we describe a model of nuclear evaporation which we use in our studies. Section 3 is devoted to the discussion of merits of wounded nucleons tagging while in section 4 we show that with help of the Forward Neutron Counter [2], [3], we may be able to filter out coherent from incoherent diffractive processes.

2 A model of nucleus evaporation and its implementation in the VENUS Monte Carlo

We use, in our analysis, the Venus Monte Carlo [4] to simulate the eA interactions. We incorporated into this Monte Carlo the PDF library [5] and chose the GRV 94 HO structure function set for our studies [6]. In order to investigate the nucleus fragmentation processes we have developed a toy model of nuclear evaporation. This model is based on parametrisations of the proton-nucleus [7] and muon-nucleus [8] scattering data and includes the production of the following fragments: $p, n, t, \alpha, Li, Be, B, C$. The fragment multiplicities are fixed using the data of [9]. Their spectra are described by:

$$E\frac{d\sigma_f}{dp} \propto exp(-\frac{T_f - 125MeV}{T_{0f}})$$

were T_{0f} is the fragment dependent characteristic temperature, given in Table 1, and T_f is the fragment kinetic energy. The neutron spectra are described by a combination of three exponentials as suggested in [8]. The evaporation spectra are, in this simpleminded model, uncorrelated with the type and kinematics of the primary interaction.

Table 1: Characteristic temperatures of evaporations.

fragment	p	n	d, t, α, Li, Be, B, C
$T_{0f}(MeV)$	45	0.7, 5, 45	35

In Figure 1 we show the pseudorapidity distribution of all particles emerging from interactions of 30 GeV electrons with lead nuclei of 410 GeV/nucleon. We requested that: $Q^2 > 1GeV^2$, $0.05 < y_{Bj} < 0.5$, $0.05 < x_{Bj} < 0.01$ and the angle between the momenta of the incident and scattered electron greater than 3. We observe an abundant production of evaporation fragments in the nucleus hemisphere. These fragments are emitted at small angles. The wounded nucleons (represented on this plot as a difference of the spectra of nucleons and

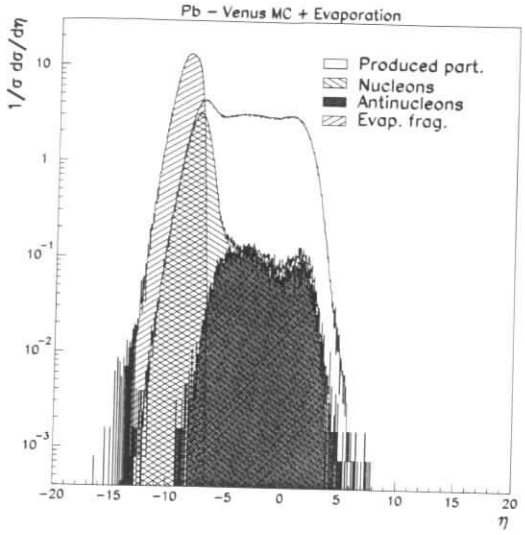

Figure 1: *Pseudorapidity distribution of all particles in ePb interactions in the HERA reference frame.*

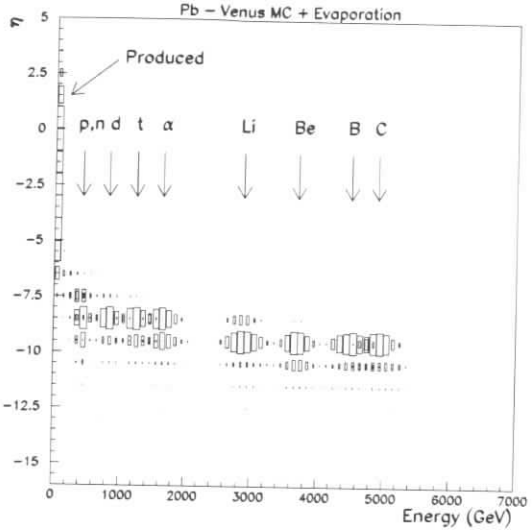

Figure 2: *Correlation between particle energy and rapidity.*

antinucleons) are emitted at larger angles (larger η). In Figure 2 we show the correlation between the particle (fragment) energy and its pseudorapidity. This plot shows a clear separation of various nuclear fragments in the (E, η) plane. It is worth pointong out that the fragments can be identified unambigously, owing to an apparent quantization of their energies in units of 410 GeV.

3 Wounded nucleon tagging of multiparton processes

The experiments at HERA [10], [11] discovered strong rise of partonic density in the low x domain. The challenge for HERA is to find a mechanism responsible for dumping the growth of partonic distributions such that the unitarity constraint is preserved. As it has been shown in [12], the HERA electron-proton scattering data will likely be insufficient to establish a presence of such mechanism because the effective partonic densities are still relatively low down to the x values of 10^{-4}.

In electron-nucleus scattering the effective partonic densities are, for the central collisions and $x \leq 1/(2R_A m_p)$, amplified by a factor $A^{1/3}$. Therefore, already in the x-domain accessible at HERA we reach the limit of saturation of partonic densities and may observe a break-down of the applicability of linear QCD evolution equations [13], [14] to the dense partonic system.

It is clear, from the above arguments that, the heaviest nuclei are the best for searches of non-linear QCD phenomena (provided that the luminosity achievable at HERA is inverse-

proportional to the atomic number and that the measurement errors of partonic densities are independent of the accelerated ion type). It may however turn out that the two above conditions can not be fulfilled and high statistical and systematic precision can be achieved only for the isoscalar nuclei. Can we produce a high partonic density fluctuations in interactions of the electrons with the heaviest of isoscalar nuclei - Calcium. In Fig. 3a we show the correlation between the "thickness of the nucleus" ($A^{1/3}$) and the number of wounded nucleons which have been ejected from the nucleus, as predicted by the VENUS model. The apparent high degree of correlation, if confirmed experimentally, would allow to use the collision dependent number of wounded nucleons as a measure of an effective density of partons in the nucleus. The multiplicity spectrum of wounded nucleons is shown in Fig. 3b for ePb and eCa scattering. It is apparent that the large multiplicity tail for eCa scattering is extended towards multiplicities which are significantly larger than the average multiplicity of wounded nucleons for ePb scattering. There are two reasons for fluctuations of wounded nucleon multiplicities. The first is related to the dispersion of the impact parameter of the virtual photon (central collisions lead to larger multiplicities). The second is related to the fluctuations in the final state rescattering processes. We propose a way to disantangle these two sources of fluctuations by looking at the multiplicities of hadrons produced in the central region. We are aware that the efficiency of relating a large multiplicity fluctuation to the a large partonic density fluctuation will remain most likely to some extent uncertain. Nevertheless, we expect to increase significantly the sensitivity to high partonic density effects already for light nuclei by using the wounded nucleon tag. We consider this approach as a back-up solution if it turns out that only light nuclei can be accelerated at HERA.

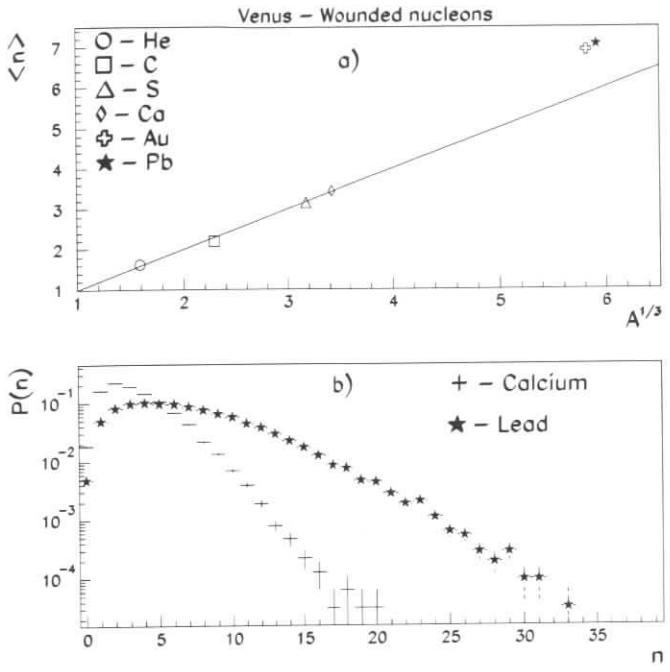

Figure 3: *a) Average multiplicity of wounded nucleons vs. $A^{1/3}$. Solid line corresponds to $< n >= A^{1/3}$. b) Wounded nucleon multiplicity distribution for Lead and Calcium.*

4 Evaporation of neutrons from wounded nucleus and selection of coherent diffractive processes

Testing universality of the Pomeron structure by using "Pomeron sources" of different partonic compositions is one of the challenges of the nuclear program for HERA. We propose a test in which the Pomeron structure function F^{3D} [15] measured in the electron-nucleus scattering is compared with the one measured in electron-proton scattering. The electron-nucleus diffractive scattering can be coherent ($eA \to eA + X_{diff}$) or incoherent ($eA \to e(A-N) + N + X_{diff}$, where N is the number of ejected nucleons from the initial nucleus) providing two distinct "classes of Pomeron sources" for universality test. Is it feasible to tag coherent diffraction events in electron-nucleus scattering at HERA? The most natural way would be to tag coherently recoiled nucleus. Unfortunately, in particular for heavy nuclei, if one uses the low β beam optics, an identification of low transverse momentum recoil is difficult to realize. The idea we present here is to tag instead the incoherent processes by detecting neutrons evaporated from the nucleus. In Fig. 4a we present the integrated number of neutrons emitted in the ePb incoherent scattering

within a circle of the radius R at the distance of 100 m from the ePb interaction point, as predicted by the evaporation model described in section 2. The distance of 100 m corresponds to the position at which both H1 and ZEUS experiments installed their Forward Neutron Counters (FNC). Owing to the Lorenz boost almost all neutrons can be detected within the acceptance region of the FNC of 10 cm. As it is shown in Fig.4b the probability of zero neutron multiplicity events in incoherent deep inelastic eCa events is below 2 % while for the ePb scattering this probability in negligible. If these probabilities turn out not to be significantly larger for a subsample of incoherent deep inelastic events with rapidity gap, we may be able to select incoherent with respect to coherent events using the neutron tag.

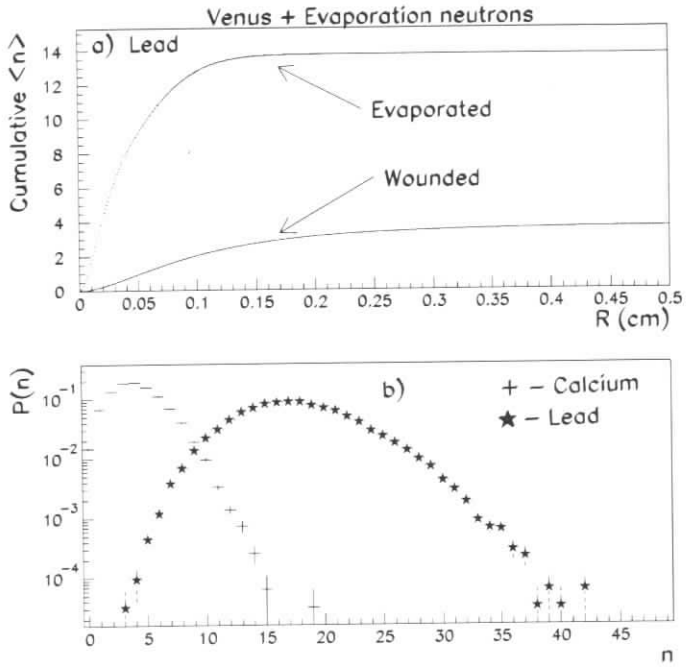

Figure 4: *a) The integrated multiplicity of wounded and evaporated neutrons within a circle of R (m) at the distance of 100 m from the ePb interaction point. b) The multiplicity distribution of evaporated and wounded neutrons for ePb and eCa scattering.*

5 Conclusions

The two examples of processes shown above illustrate what we may gain by detecting nuclear debris, in particular wounded and evaporated nucleons, in eA interactions. While detection of

evaporated neutrons can be realized using the existing H1 and ZEUS setup, the detection system of charged fragments require designing a new detection scheme and, most likely, a new beam optics for the interaction point. We hope that the qualitative preliminary studies presented in this contribution will trigger further studies on both the physics and detector issues related to detection of nuclear fragments in deep inelastic electron nucleus collisions at HERA.

Acknowledgments

We would like to thank Mark Strikman for stimulating discussions and to Andrzej Olszewski for help in understanding the emulsion data.

References

[1] L.N. Gribov, E.M. Levin and M.G. Ryskin, Phys. Rep. 100 (1983) A.H. Mueller, J.Qiu, Nucl.Phys. B 286 (1986) 427.

[2] M. Derrick et al., DESY 96-093 (May 1996).

[3] I.Abt et al., DESY Desy internal report H1-96-01 (1996).

[4] K.Werner, Phys. Rep. 232 (1993) 88.

[5] H. Plothow-Besch, PDFLIB - User's Manual, CERN Program Library W5051, 1995.

[6] M. Glück, E. Reya and A. Vogt, DO-TH 94/24.

[7] Yu.D. Bayukov et al., Leningrad Radium Institute ITEP-85-5 preprint.
Yu.D. Bayukov et al., Leningrad Radium Institute ITEP-83-172 preprint.

[8] E665 Collab., M.R. Adams et al.,Phys.Rev.Lett 74 (1995) 5198.

[9] KLMM Collab., M.L. Cherry et al., Phys. Rev. C 52 (1995) 2652.

[10] I. Abt et al., Nucl.Phys. B 407 (1993) 515.

[11] M.Derrick et al., Phys. Lett. B 316 (1993) 412.

[12] K. Golec-Biernat, M.W. Krasny and S.Riess, Phys.Lett. B 337 (1994) 367.

[13] G. Altarelli, G. Parisi, Nucl.Phys. B 126 (1977) 297.

[14] E.A. Kuraev, L.N. Lipatov, V.S. Fadin, Phys.Lett. 60B (1975) 50.

[15] T. Ahmed et al., Phys.Lett. B 348 (1995) 681.

Hadron Distributions in Deep Inelastic Electron-Nucleus Scattering at Collider Energies

Nikolaj A. Pavel
Imperial College, Blackett Laboratory, Prince Consort Road, London SW72BZ

Abstract: Electron nucleus scattering at very high energies reached in collider machines allows to search for new nuclear effects in the deep inelastic scattering process. Here some physics topics which could be investigated with future eA collider machines running at high luminosities are discussed.

Introduction

Electron-nucleus scattering experiments offer some strong advantages over other high energy physics experiments when studying nuclear effects in the hadronic final state produced. The electron is a pointlike particle and its coupling through the electro-weak forces is well described in the Standard Model. No deconvolution of projectile and target fragments is necessary. Thus, by comparing the results of scattering on nuclei with different size the influence of nuclear matter on the DIS process can be studied most directly.

In order to do high precision electron-nucleus (eA) scattering experiments, not only high luminosities are needed, but also an excellent control of all systematic errors which do not cancel when taking the ratio of distributions from scattering on different nuclei. Therefore effects of multiple scattering and external bremsstrahlung in a target, difference in the acceptance and detector efficiciency between data sets with different targets have to minimised.

At low energies this can be most easily achieved by using an intensive electron beam and an internal gas jet target, as planned by the HERMES Collaboration. In this experiment the upper limit of the energy transfer ν [1] is about $\nu = 25\,\mathrm{GeV}$ since the electron ring at HERA

variable	description
$Q^2 = -(k - k')^2$	square of the four momentum transfer
ν= (P q)/(P k)	energy of the boson exchanged
$x_{Bj} = Q^2/(2Pq) = Q^2/(2M_{nucleon}\,\nu)$	Bjorken scaling variable
$W = Q^2/x_{Bj} * (1 - x_{Bj})$	inv. mass of the hadronic final state
M_X	inv. mass of the had. final state in LRG events

Table 1: Kinematic variables in DIS used in this text; the four momenta are defined in Fig.1

[1] the kinematic variables are defined in Tab.1 and Fig.1

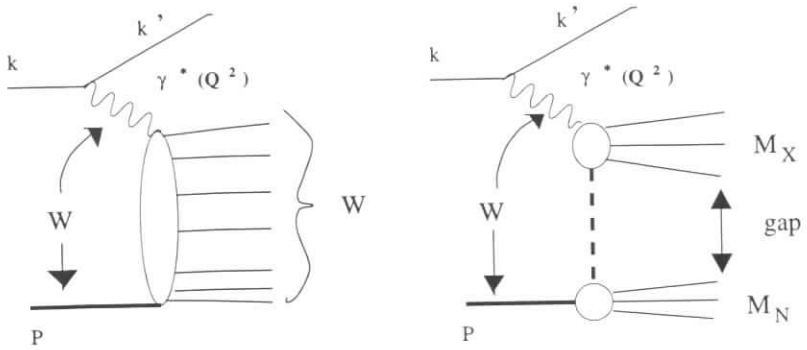

Figure 1: Schematic diagram of the particle production in DIS events without (a) and with a large rapidity gap (b) (called in text NRG and LRG events respectively). With k, k' and P the four momenta of the incoming and scattered electron and the proton beam are denoted respectively; $q = (k - k')$ is the four momentum of the virtual photon exchanged. W is the invariant mass of the $\gamma^* p$ system, M_X denotes the invariant mass of the hadronic final state observed in LRG events and M_N represents the scattered proton or a low mass nuclear state.

operates at 27.5 GeV; a cut on y ($y < 0.9$) to reduce the systematic uncertainty from coherent radiactive correction on nuclei, is here already considered.

In order to access the higher energy range one has to work with an eA collider where one also meets conditions which allow to minimise the systematic errors for measurement of ratios of cross sections as much as by using an internal gas jet targets. At the present time two options for the realisation of such an experiment are discussed: The first option is to inject light and heavy nuclei into the proton ring of HERA and to use the existing detector of the ep collision experiments for the measurements. The second option is to build two storage rings for electrons and heavy ions at the GSI, where a lower center of mass energy of the collisions is envisaged. In this article the first experiment will be labelled by 'HERA-N' and the second by 'GSI-N'.

The kinematic range covered in Q^2, x_{Bj} and ν for both options in the current phase of planning is shown in Fig.2, where cuts on the scattered electron energy and angle are imposed which are necessary to ensure a reliable identification of the neutral current DIS events and a precise determination of the event kinematic. Also the kinematic region which will be investigated by the HERMES experiment is indicated by the hatched area. One can see that the three experiments together cover a vast range in ν, Q^2 and x_{Bj}, where the GSI-N experiment fills in the gap between the HERMES and HERA-N experiment. By small variations of the beam energies of the collider experiments a partial overlap of the kinematic ranges can be achieved.

Physics Aims

The physics questions which are primarily addressed in the eA collider experiments will be somewhat different from those in past analyses of hadron distributions in eA scattering, where intranuclear hadron- and quark-reinteraction effects were studied from which one can infer information about the space-time structure of the hadronisation process. The arguments going

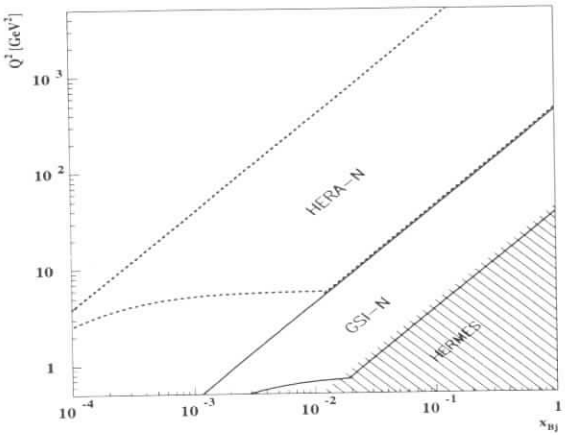

Figure 2: The comparison of the kinematic range covered by electron-nucleus collider experiments under study (HERA-N and GSI-N experiment). A cut on the scattered electron angle ($\vartheta'_e < 175°(170°)$ for HERA-N and GSI-N resp.) is considered to ensure a reliable identification of a DIS neutral current event and the precise determination of its kinematics. The region covered in the fixed target experiment HERMES is also shown.

along with these ideas are briefly sketched elsewhere in these proceedings [1] Measurements with electron [2], muon [3, 4, 5] and neutrino [6] beams had been performed in the range of ν from 10 – 200 GeV. While at very low ν ($\nu \lesssim 25$ GeV) sizeable nuclear effects have been observed, at higher ν ($\nu \gtrsim 70$ GeV) the effects were found to be very small. But the errors on the ratio of distributions were of the order of several percent and the distributions had to be integrated over large intervals in z_h as well as in Q^2 and x_{Bj} (for a more detailed review see [7, 6]).

Much more precise data are required not only in the low ν range which will be covered by HERMES but also in the higher energy range to complete the investigation of the space-time structure. This could be done best in the eA collision experiment GSI-N, where one aims for luminosities as high as $10^{32} cm^{-2} s^{-1}$.

At sufficiently high values of ν, where hadronic intranuclear rescattering effects should vanish, one can search for effects of a possible interaction of the struck quark with the nuclear matter. The energy loss or broadening of transverse momentum of a quark during its passage through nuclear matter has been estimated in many publications e.g. [8]. This question is closely related to the phenomena observed in heavy ion collisions. Experimental information on this topic is very important for a better understanding of the hadron production in such complex reactions and for the identification of the quark gluon plasma, which one wants to create in high energy heavy ion collisons. Also the investigation of more subtle relationships between the hadron distributions in eA scattering and the EMC effect, which has been initiated in [3], should be pursued. In earlier studies of this problem only weak conclusions could be drawn since the statistics were not sufficient to study the effects as a function of x_{Bj}.

With the HERA-N collider eA scattering can be investigated at even higher values of ν,

where the above questions can be futher studied. The major part of the events populate the very low-x_{Bj} region ($x_{Bj} \lesssim 10^{-3}$). It is evident that the experimental analysis will be focussed on the parton dynamics at very low x_{Bj} and high parton densities. Here, however, another topic will be briefly discussed for which the measurement of the hadronic final state is essential and where again the nucleus is used as a kind of 'tool' for the investigation.

Recently a class of DIS events has been observed at HERA which is characterised by a large rapidity gap between the observed hadronic final state and the proton beam direction [9, 10], which will be called here 'large rapidity gap (LRG)' events. The fraction of these LRG events in the total DIS event sample has been found to be independent of Q^2, which shows that the production mechanism for LRG events is a leading twist effect. The qualitative difference in the event topology for non-rapidity-gap (NRG) and LRG events is sketched in Fig.1.

One possible interpretation of these events is that there is a colourless particle, with which the photon interacts, while the proton remains unaffected like in a diffractive ep interaction. This particle could be identified with the pomeron, since diffractive scattering processes amongst hadrons have been successfully described by the pomeron exchange picture. One could further assume that the pomeron is a short lived quantum state with some partonic substructure, which is probed by the virtual photon such that the photon couples to a pointlike constituent in the pomeron [11].

On the other hand the leading twist behaviour of the cross section for the LRG events can also be explained in the model of Buchmüller [12], which is not based on the pomeron exchange model. In that model the LRG events are interpreted as being produced by the boson-gluon-fusion (BGF) process (i.e. a leading twist, non-diffractive DIS process), where the $q\bar{q}$ cluster evolves with a certain probability into a colour singlet parton cluster, which fragments independently from the rest of the nucleon into hadrons.

Since the latter model involves soft colour interaction it is to be expected that the amount of nuclear matter surrounding the vertex of the primary BGF process strongly influences the probability of the production of a LRG event and thus the fraction of LRG events observed. The relevant scale for this nuclear effect would be the size of the nucleus, i.e. the atomic number A. All other kinematic dependencies should be same as those found in ep scattering. In the Pomeron based models, nuclear effects may be induced by multi-pomeron exchange or by additional higher twist contributions due to coherent scattering on more than one nucleon in the nucleus. In this case a different x_{Bj} and Q^2 dependence of the LRG event in scattering on different nuclei is expected.

Besides the measurement of the LRG event rate, the hadron distributions themselves should be studied. Experimentally it was found that the transverse momentum spectra in LRG events in ep scattering resemble those of DIS at the an invariant mass of the hadronic final state W of $W = M_X$ [13]. This observation supports the hypothesis that the scale of the the phase space available for the particle production is given by M_X rather than by W. In that case it should be possible to investigate the space-time structure of the hadronisation in diffractive dissociation processes in a similar way to that done for DIS events without a large rapidity gap at lower energies [7]. The important question to be answered in this context would be, whether the hadrons are formed at a larger distance from the the primary hard scattering vertex or whether this process is universal as far as the space-time structure and the nature of the preconfined states are concerned. This aspect of the diffractive multiparticle production has been only poorly if at all studied in the past.

Conclusions

Electron-nucleus collider machines offer the unique possibility to measure with high precision hadron distributions in electron-nucleus scattering at energies, at which the effects of intranuclear hadron rescattering are expected to be neglibly small. In that kinematic regime one can search for the effect of quark interaction in dense nuclear matter. This information would be most valuable for the undestanding of the hadron production in high energy heavy ion collisions. Also the relationship between the hadron production in eA scattering and the EMC effect can be investigated in order scrutinize the origin of the EMC effect. Moreover it will be possible to study the mechanism of diffractive scattering at high scattering in detail using the nucleus as a kind of test medium. The information from these analysis is expected to contribute to discriminate between the various models for this kind of process.

References

[1] N.A. Pavel, 'Study of the Hadronisation Process at HERMES', this Proceedings.

[2] L.S. Osborne et al., Phys. Lett. B166 (1978) 1624.

[3] N.A. Pavel, Ph.D. thesis, Univ. of Wuppertal WUB 89-24 (1989); EMC coll., J. Ashman et al., Z. Phys. C52 (1991) 1.

[4] EMC Collab., J. Ashman et al., Z. Phys. C52 (1991) 361.

[5] A.F. Salvarani, PhD thesis, (1991) Univ. of California, San Diego.

[6] BEBC WA21/WA59 Collab., W. Burkot et al., Z. Phys. C70 (1996) 47.

[7] N.A. Pavel, Nucl. Phys. A532 (1991) 465.

[8] S.J. Brodsky, P. Hoyer, Phys. Lett. B298 (1993) 165;
R. Baier, Y.L. Dokshitzer, S. Peigne, D. Schiff, Phys. Lett. B345 (1995) 277;
X. Wang, M. Gyulassy, M. Plümer, Phys. Rev. D51 (1995) 3436;
M. Luo, J.W. Qiu, G. Sterman, Phys. Rev D50 (1994) 1951.

[9] ZEUS Collab., M. Derrick et al., Phys. Lett. B315 (1993) 481.

[10] H1 Collab., I. Abt et al., Phys. Lett. B348 (1995) 682.

[11] G. Ingelmann, P. Schlein, Phys. Lett. B152 (1985) 256.

[12] W. Buchmüller, Phys. Lett. B335 (1994) 479;
W. Buchmüller, DESY 95-065 (1995); W. Buchmüller, A. Hebecker DESY 95-077 (1995).

[13] N.A. Pavel, Habilitationsschrift (University Hamburg Oct.'94), DESY 95-147 (1995).

Energy loss of high energy partons in a finite QCD medium

R. Baier[a], Yu. L. Dokshitzer[b], A. H. Mueller[1c], S. Peigné[d] and D. Schiff[d]

[a] Fakultät für Physik, Universität Bielefeld, D-33501 Bielefeld, Germany
[b] Theory Division, CERN, 1211 Geneva 23, Switzerland[2]
[c] Physics Department, Columbia University, New York, NY 10027, USA
[d] LPTHE[3], Université Paris-Sud, Bâtiment 211, F-91405 Orsay, France

Abstract: We shortly summarize results which we have recently obtained on the radiative energy loss of high energy quarks and gluons suffering multiple collisions in a QCD medium of finite length. These results are also generalized to the case of nuclear matter.

1 Introduction

Gluon radiation induced by multiple scatterings of a very energetic incident quark or gluon propagating through QCD matter becomes coherently suppressed compared to independent emission [1, 2, 3, 4]. In the case of QED the analogous suppression of photon radiation is known as the Landau-Pomeranchuk-Migdal (LPM) effect [5, 6].

In order to calculate the soft gluon radiation intensity static and screened scattering centres are assumed [7]. This leads to a probability distribution in terms of the transverse scattering momentum $\vec{q}_\perp$,

$$V(\vec{q}_\perp^{\,2})d^2q_\perp \equiv \frac{\mu^2}{\pi(\vec{q}_\perp^{\,2}+\mu^2)^2}d^2q_\perp. \tag{1}$$

It is reasonable to assume that successive scatterings are independent. As a consequence the mean free path λ of the parton has to be large compared to the characteristic range μ^{-1} of the "Coulomb potential" (1), i.e. $\lambda \gg \mu^{-1}$.

We may actually generalize this treatment to the case of cold nuclear matter and define a probability distribution $V(\vec{q}_\perp^{\,2})$ related to the gluon distribution function [4].

[1]Supported in part by the U.S. Department of Energy under grant DE-FG02-94ER-40819
[2]Permanent address: Petersburg Nuclear Physics Institute, Gatchina, 188350 St. Petersburg, Russia
[3]Laboratoire associé au Centre National de la Recherche Scientifique

2 Gluon radiation spectrum

For a fast quark of energy E, which e.g. is produced through deep inelastic scattering and which propagates through a hot medium of length L, the induced gluon intensity (per unit length of propagation) reads in leading order of the strong coupling α_s,

$$\frac{\omega dI}{d\omega dz} \simeq \frac{3\alpha_s N_c}{\pi L}\ln\left|\frac{\sin\left(\frac{\omega_0}{\lambda}L\right)}{\frac{\omega_0}{\lambda}L}\right|, \tag{2}$$

where ω denotes the energy of the soft gluon, $\omega \ll E$, and λ is the mean free path of the quark. Here the number of colours N_c is assumed to be large (for a more detailed discussion see [1, 3]). The quantity ω_0 charcterizes the spectrum, $\omega_0 \equiv \sqrt{i\kappa\tilde{v}(1/\sqrt{\kappa})}$. The value of the dimensionless parameter $\kappa = \frac{\mu^2\lambda}{2\omega}$ determines the shape of the radiation intensity. $\tilde{v}$, related to the Fourier transform of the potential $V(\vec{q}_\perp^{\,2})$ in the impact parameter space $\vec{B}$, is given by

$$\tilde{v}(B^2) \equiv 4\frac{1-V(\vec{B}^2)}{\vec{B}^2} \simeq \begin{cases} \ln 1/B^2 \text{ for the Coulomb case (1)} \\ (\vec{q}_\perp^{\,2})/\mu^2 \text{ otherwise} \end{cases} \tag{3}$$

for $B^2 \to 0$. The parameter κ may be viewed as the typical phase difference between neighbouring scattering centres. The interesting coherent phenomena for which the medium properties are important show up for $\kappa \ll 1$, because then a group of $N_{coh} \simeq 1/\sqrt{\kappa}$ centres radiate coherently.

For large L the spectrum (2) approaches [1, 2, 3]

$$\frac{\omega dI}{d\omega dz} \simeq \frac{3\alpha_s N_c}{2\pi}\sqrt{\frac{\mu^2}{\lambda\omega}\ln(1/\sqrt{\kappa})}, \tag{4}$$

when putting $\tilde{v}(1/\sqrt{\kappa}) \simeq \ln 1/\sqrt{\kappa}$ for $\kappa \ll 1$. Modulo logarithms (4) is valid for

$$O(\lambda\mu^2) < \omega < \omega_{\rm fact} \doteq O\left(\frac{\mu^2}{\lambda}L^2\right) < E, \tag{5}$$

as long as $L \le L_{cr} \doteq O(\sqrt{E\lambda/\mu^2})$ for $E \to \infty$. For $\omega \ge \omega_{\rm fact}$ the radiation is totally suppressed. It is important to state that the spectra (2) and (4), respectively, do not depend on the parton's energy E.

We note that the matter properties enter in the spectra (2) and (4) via the ratio $\hat{q} \equiv \mu^2\tilde{v}/\lambda$. Effectively $\hat{q}$ plays the role of the transport coefficient [6],

$$\hat{q} \equiv \mu^2\tilde{v}/\lambda \doteq \frac{\langle\vec{q}_\perp^{\,2}\rangle}{\lambda} = \rho\int d^2q_\perp\vec{q}_\perp^{\,2}\frac{d\sigma}{d^2q_\perp}, \tag{6}$$

with ρ the density of the scattering centres and $d\sigma/d^2q_\perp$ the "parton-centre" cross-section, where $\lambda \equiv 1/\rho\sigma$. Within logarithmic accuracy the jet broadening is therefore given by

$$\langle\vec{q}_\perp^{\,2}\rangle_L \equiv \hat{q}L \simeq \frac{\mu^2}{\lambda}\tilde{v}(\lambda/L)L, \tag{7}$$

after the parton's passage through matter of length L, i.e. (7) is effectively a random walk result.

3 Energy loss in finite length media

In [3] the radiative energy loss in a hot medium of finite extent L, $L \leq L_{cr}$ is derived. For a quark jet the result is

$$-dE/dz \simeq \frac{\alpha_s N_c}{8}\hat{q}L, \tag{8}$$

which amounts to the total loss of $-\Delta E(L) \simeq \frac{\alpha_s N_c}{8}\hat{q}L^2$, i.e. it is increasing quadratically with the length L [8] and independent of E for $E \to \infty$. This remarkable dependence on the length L can also be heuristically obtained by integrating the spectrum given by (4) over ω and z, with $0 \leq \omega \leq \omega_{\rm fact}$ and $0 \leq z \leq L$. This result may actually be generalized to cold nuclear matter [4]: the relation (8) between the energy loss and the jet broadening (7) is shown to be valid in general and indeed does not depend on the parameters of the model.

The energy loss per unit distance (8) may be compared to the one for an infinite medium $L \to \infty$, with E large but fixed, which is obtained in [1] by

$$-dE/dz \simeq \alpha_s N_c \sqrt{\hat{q}E}, \tag{9}$$

i.e. depending on the incident quark energy.

4 Phenomenology

In order to estimate the energy loss e.g. of a very energetic quark in cold matter of finite extent [9] one has to know the coefficient $\hat{q}$ in (8). One possibility [4, 11] is to use jet broadening (7), which e.g. is measured by the momentum imbalance of jets in deep inelastic production of dijets [10]. The analysis by Luo et al. [10] determines $\hat{q} \simeq \frac{4}{3}\pi^2\alpha_s(A^{1/3}/L)\lambda^2_{LQS}$, with $L \simeq \frac{3}{4}R$ expressed in terms of the nuclear radius $R \simeq 1.2A^{1/3}fm$. With $\lambda^2_{LQS} \simeq 0.05 - 0.1\text{GeV}^2$ [10], this gives the estimate [11]

$$\hat{q} \simeq (3.7 - 7.4)\ \alpha_s\,\text{GeV}/fm^2. \tag{10}$$

According to (8) this gives $-dE/dz \simeq (1.2 - 2.5)$ GeV$/fm$ for $L \simeq 10fm$ and $\alpha_s \simeq 0.3$, which is a rather large loss per unit distance.

An independent estimate may be obtained by relating $\hat{q}$ to the proton's gluon structure function $xG(x, Q^2)$ [4, 11, 12]. This uses (6) in terms of the (transport) quark-proton cross section

$$\int_0^{\mu^2/B^2} d^2q_\perp \vec{q}_\perp{}^2 \frac{d\sigma^{q-\text{proton}}}{d^2q_\perp} \simeq \frac{\alpha_s C_F \pi^2}{2} xG(x, \mu^2/B^2 \simeq \mu^2/\sqrt{\kappa}), \tag{11}$$

where x is small and estimated to be $x \simeq O(1/(\lambda m_{\rm proton})) \simeq O(0.1)$.

Depending on $xG(x) \simeq 1 - 5$ in the region of interest of small x, and with the nuclear density $\rho \simeq 0.17fm^{-3}$, one finds [4, 11]

$$\hat{q} \simeq (0.2 - 1.0)\ \alpha_s\,\text{GeV}/fm^2, \tag{12}$$

which gives an energy loss $-dE/dz < 0.35$ GeV$/fm$, i.e. a significantly smaller value than the one quoted above!

In case of hot matter a corresponding estimate yields $-dE/dz \sim 3$ GeV$/fm$ [1].

Not only because of these uncertainties careful measurements of the energy loss of partons at HERA's future experiments using different nuclei are indeed an important challenge. It is especially crucial to look for possible differences of the parton propagation in cold versus hot matter, which are expected on the basis of the above (still crude, because asymptotic) estimates [1, 3, 4, 11].

Acknowledgement

This research is supported in part by the EEC Programme "Human Capital and Mobility", Network "Physics at High Energy Colliders", Contract CHRX-CT93-0357.

References

[1] R. Baier, Yu. L. Dokshitzer, S. Peigné and D. Schiff, Phys. Lett. 345B (1995) 277, and references therein; see also:
D. Schiff, Proceedings of Workshop on Deep Inelastic Scattering and QCD, Paris, April 1995, Eds. J.-F. Laporte and Y. Sirois, p. 481;
S. Peigné, Thése de doctorat, Université Paris-Sud, Orsay, May 1995.

[2] R. Baier, Yu. L. Dokshitzer, A. H. Mueller, S. Peigné and D. Schiff, The Landau-Pomeranchuk-Migdal effect in QED, preprint BI-TP 95-40, CERN-TH.96/14, CUTP-724, LPTHE-Orsay 95-84 (1996).

[3] R. Baier, Yu. L. Dokshitzer, A. H. Mueller, S. Peigné and D. Schiff, Radiative energy loss of high energy quarks and gluons in a finite volume quark-gluon plasma, LPTHE-Orsay 96-34 (1996).

[4] R. Baier, Yu. L. Dokshitzer, A. H. Mueller, S. Peigné and D. Schiff, Radiative energy loss and p_T - broadening of high energy partons in nuclei (in preparation).

[5] L. D. Landau and I. Ya. Pomeranchuk, Dokl. Akad. Nauk SSSR 92 (1953) 535, 735.

[6] A. B. Migdal, Phys. Rev. 103 (1956) 1811; and references therein.

[7] M. Gyulassy and X.-N. Wang, Nucl. Phys. B420 (1994) 583; M. Gyulassy, X.-N. Wang and M. Plümer, Phys. Rev. D51 (1995) 3236.

[8] A. H. Mueller, Proceedings of Workshop on Deep Inelastic Scattering and QCD, Paris, April 1995, Eds. J.-F. Laporte and Y. Sirois, p. 29.

[9] S. J. Brodsky and P. Hoyer, Phys. Lett. B298 (1993) 165.

[10] M. Luo, J. Qiu and G. Sterman, Phys. Rev. D49 (1994) 4493; and references therein.

[11] A. H. Mueller, Invited talk at Quark Matter '96, Heidelberg, May 1996.

[12] E. Levin, LPM effect for nuclear matter in QCD, preprint CBPF-NF-061/95.

Radiative Corrections to Deep Inelastic Scattering on Heavy Nuclei at HERA

I.Akushevich[a], H.Spiesberger[b]

[a] DESY-IfH Zeuthen, 15735 Zeuthen, Germany[1]
[b] Max-Planck-Institut für Physik, Werner-Heisenberg-Institut, Föhringer Ring 6, D-80805 München, FRG

Abstract: Radiative corrections to deep inelastic scattering on heavy nuclei at a possible future HERA experiment are calculated. We discuss the contributions from the elastic, quasielastic and inelastic radiative tails and their sensitivity to experimental cuts.

1 Introduction

The physical interpretation of the data of experiments on deep inelastic scattering requires the separation of the Born cross section from background contributions known as radiative corrections. Radiative corrections receive contributions from loop diagrams and from processes with the emission of additional photons. Some of the radiative events can be identified and removed from the event sample by experimental methods. However, a substantial contribution with soft or collinear photons can not be separated from non-radiative events. Thus, radiative effects have to be calculated theoretically and subtracted from measured cross sections. In this paper the FORTRAN codes HERACLES [1] and POLRAD [2] are applied for the calculation of radiative corrections to the scattering of leptons off heavy nuclei at a possible future modified HERA collider.

2 Physics of radiative corrections

There are three basic channels for the scattering of electrons on nuclei: elastic, quasielastic and inelastic processes. Their contribution depends on the kinematic region which we describe with the help of the four momentum transfer Q^2, the Bjorken scaling variable x_A and the invariant mass of the hadronic final state $W_A^2 = Q^2(1-x_A)/x_A + M_A^2$ (where M_A is the mass of the nucleus)[2]. For $W_A = M_A$, only elastic scattering is allowed. Quasielastic scattering, corresponding to direct collisions with individual nucleons inside the nucleus, occurs at fixed $x_A \sim M/M_A$ where M is the mass of the hit nucleon. Inelastic scattering sets in when the pion threshold is reached ($W_A \geq M_A + m_\pi$, m_π is the pion mass).

At the Born level, both x_A and Q^2, and consequently W_A, are fixed completely by the measured momentum of the scattered lepton. Therefore it is also fixed which of the three basic processes contributes to the cross section. Including radiative corrections, however, a radiated photon may remain unobserved and the true values of x and Q^2 depend on the unknown momentum transported away by the photon. Then all processes contribute to the measured cross section. The total radiative corrections of order $O(\alpha)$ are obtained as the sum of these radiative contributions and, in addition, loop corrections. The latter are, first of all, due to the vacuum polarization, but also vertex and box graphs contribute, in particular at large Q^2. The former can conveniently be separated into initial state and final state radiation and the so-called Compton peak. Initial (final) state radiation is dominated by events which have a photon collinear to the incoming (scattered) lepton. The Compton peak is characterized by events with small true momentum transfer reached due to the emission of a hard photon although the scattered lepton mimics large Q^2.

The radiative corrections can be large and even exceed the Born cross section in the interesting region of small x. In a realistic experimental situation, part of the events with a radiated photon can be tagged in the calorimeter or be rejected by applying cuts on kinematic variables of the hadronic final state. An important example is the hadronic transverse momentum, $p_{T,had}$. Since $p_{T,had}$ is a measure of the true momentum transfer, a cut $p_{T,had} > p_{T,min}$ will remove the Compton peak almost completely. In particular, such a cut has a large influence on the tails from the elastic and quasielastic processes since these are dominated by the Compton peak. The effect of cuts on the inelastic radiative tail is more complicated and can, most easily, be analyzed with the help of Monte Carlo methods.

The FORTRAN codes HERACLES and POLRAD are used to obtain radiative corrections for HERA kinematics with lepton and nuclear beam momenta equal to 27.6 GeV and 410 GeV, resp. We will present results for beams composed of nuclei with $A = 2Z$ (D, ^{4}He, ^{12}C, ^{32}S and ^{208}Pb) which can be stored in the HERA ring with the same energy per nucleon at the same machine setup.

POLRAD is a program for radiative correction calculations in deep inelastic scattering of polarized leptons on polarized and unpolarized nuclei of spin 0, 1/2 and 1. The explicit formulae were introduced and discussed in [2]. The contributions to the total radiative corrections at lowest order were obtained on the basis of the covariant method for radiative correction calculations, offered by Bardin and Shumeiko in [3] and developed in [4]. Soft photonic higher-order effects are taken into account by the exponentiation prescription described in [5]. POLRAD includes routines for the calculation of the elastic and quasielastic radiative tails. Since the code is based on an analytic integration of bremsstrahlung contributions, it is restricted to the evaluation of inclusive cross sections.

In contrast to this, HERACLES [1] is a Monte Carlo event generator and can therefore be used to obtain cross sections in almost arbitrary phase space regions. It includes the complete QED corrections of $O(\alpha)$ and, in addition, the complete standard model one-loop electroweak corrections. Some higher-order effects are included, but soft photon exponentiation is not performed. The program allows the use of either parton distribution functions or, for the purely leptonic QED corrections, of arbitrary structure functions. It therefore allows the inclusion of

[1] now at NC PHEP, Bogdanovich str.153, 220040 Minsk, Belarus

[2] We use kinematical variables defined in terms of both nuclear and nucleon masses and momenta. The former set (M_A, x_A, W_A) is used for elastic scattering; the latter set (M, x, W) is better suited for the description of the kinematics of quasielastic and inelastic processes.

the longitudinal structure function, which is in our calculation obtained from the standard QCD expression.

3 Numerical results

The results of HERACLES and POLRAD are shown in Figs. 1 and 2. The investigated quantities are defined as

$$\delta_{RC}(A) = \frac{d\sigma^A/dy}{d\sigma_0^A/dy} - 1, \qquad \delta(A) = \frac{1+\delta_{RC}(A)}{1+\delta_{RC}(D)} - 1,$$

where $d\sigma^A/dy$ and $d\sigma_0^A/dy$ are the observed and the Born cross sections of deep inelastic scattering on the nucleus A, resp. The first quantity δ_{RC} describes the correction of the cross section itself, whereas the second one, $\delta(A)$, describes the correction of the ratio of cross sections $d\sigma^A/d\sigma^D$ which is expected to be accessible with better accuracy by the experiments. These correction factors are obtained from the cross sections after integrating x in the region $10^{-4} \leq x \leq 10^{-3}$. Results for larger values of x are discussed in the text below. For the explicit calculation, fits or models of inelastic and quasielastic structure functions and elastic formfactors for each nucleus are needed. A traditional model for parton distributions, MRS(A) [6], modified by shadowing effects as described in [7] is used for the deep inelastic structure functions. Quasielastic suppression factors and elastic nuclear formfactors were calculated in accordance with the models of Refs. [8][3] and [9], respectively.

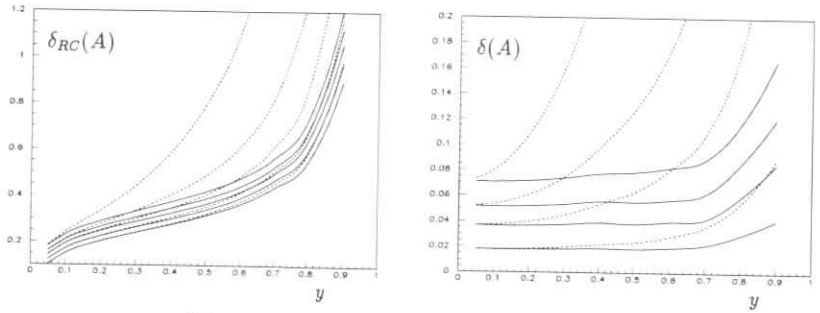

(a) (b)

Figure 1: *Radiative corrections $\delta_{RC}(A)$ and $\delta(A)$ for $10^{-4} \leq x \leq 10^{-3}$, as a function of y, with full lines showing the inelastic contribution, dashed lines showing the total inclusive radiative correction. The curves from bottom to top correspond to the nuclei D, He, C, S, Pb.*

The results for $\delta_{RC}(A)$ and $\delta(A)$ obtained from POLRAD are presented in Fig. 1. These quantities are shown with and without the contributions from the elastic and quasielastic tails. The radiative correction $\delta_{RC}(A)$ due to the inelastic tail grows rapidly with increasing y and reaches values of 100% for $y \sim 0.8$. Both the elastic and quasielastic tails give large additional contributions. The A-dependence of the inelastic cross section is contained only in the shadowing correction factor and is therefore weak. In contrast to this, the elastic tail depends much stronger on the type of the nucleus since the correpsonding squared form factor is proportional to Z^2/A. At larger values of x the corrections are slightly smaller, reaching 100 % only at values of y above 0.9 for $10^{-3} \leq x \leq 10^{-2}$. Moreover, the cross section both at the Born level and including radiative corrections has a smaller A dependence at large x because the shadowing correction factor tends to 1 for large x and becomes larger than 1 for $x \sim 0.07$.

[3]Stein's and Bernabeu's approaches for D and [4]He, and the Fermi-gas model for heavier nuclei.

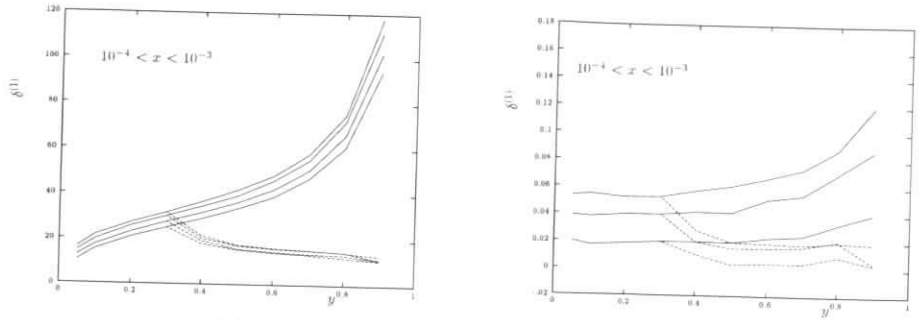

(a) (b)

Figure 2: *Inelastic contribution to the radiative corrections $\delta_{RC}(A)$ for $10^{-4} \leq x \leq 10^{-3}$, as a function of y, for the nuclei D, He, C, and S (corresponding to the lines from bottom to top) obtained from HERACLES. The full lines show the corrections without cuts, dashed lines are the results after cuts as explained in the text.*

Fig. 2 shows the results for the inelastic contribution as obtained from HERACLES. The full lines in this figure do not fully agree with the full lines of Fig. 1, since here we included the contribution from the longitudinal structure function F_L according to the standard QCD formula. The dashed lines exemplify the influence of experimental cuts on the radiative corrections. We did not attempt to apply the full set of cuts as are presently being used in the experimental analyses of H1 or ZEUS for structure function measurements since this would require a simulation and analysis of the full hadronic final state. Rather we simply rejected events which have a radiative photon of energy $E_\gamma \geq 10$GeV emitted in the cone of half-opening angle $\theta_{max} = 3°$ around the direction of the incoming electron beam. Most of these photons can not be observed directly. However, they reduce the amount of the total energy minus longitudinal momentum, $E - p_z$, which can be reconstructed from the observed final state. In addition, a cut on the transverse momentum $p_T^e + p_T^\gamma \geq 0.5$ GeV was applied which has little effect on the inelastic tail, but would remove most of the constributions from the elastic and quasielastic tails. The results in Fig. 2 demonstrate that a cut of this type reduces the corrections due to the inelastic radiative tail to the level of 15 to 30 %. In particular, the strong increase of corrections towards increasing y does not appear anymore. We also remark that the same cut eliminates the contribution from the elastic and quasielastic tails practically completely. Fig. 2b shows that the corrections of the cross section ratios are reduced as well.

In obtaining our results for the contributions of radiative tails to the measured cross section we used specific model assumptions for structure functions and form factors. In particular, we used the extrapolation of the fit from [7] for the shadowing corrections into the region of very small values of x. It is just this quantity (and parton densities, of course) whose measurement is aimed at with possible future experiments at HERA and an iterative procedure specifying

fit parameters for shadowing corrections will be used to improve the precision of predictions for radiative corrections. However, not the complete required input for radiative correction calculations can be verified by the experiment and there will remain a residual uncertainty from tails extending into kinematical regions outside of what is experimentally accessible. The elastic and quasielastic tails are basically dominated by the values of form factors in the region of very small Q^2 (the Compton peak). Different models or fits of experimental data practically coincide in this region. Also, no marked effect coming from the resonance region fit of structure functions and the Fermi-motion term in the shadowing corrections was found. It was also checked that a modification of the low-Q^2 behaviour of the inelastic structure functions as proposed in [10] changes the results for the radiative corrections by a few per mille only.

In conclusion, our calculations have shown that radiative corrections to the cross section for scattering of leptons off heavy nuclei may be large and should be properly taken into account. Simple experimental cuts will, however, allow to reduce them considerably.

Acknowledgement. I.A. is very grateful to N.Shumeiko for useful discussions and support.

References

[1] H. Spiesberger, *HERACLES, version 4.6*, unpublished;
A. Kwiatkowski, H. Spiesberger and H.-J. Möhring, *HERACLES, version 4.0*, Comp. Phys. Commun. **69** (1992) 155.

[2] I. V. Akushevich and N. M. Shumeiko, J. Phys. **G20** (1994) 513;
I. V. Akushevich, A. N. Ilyichev and N. M. Shumeiko, Yad. Fiz. **58** (1995) 2029.

[3] D. Yu. Bardin and N. M. Shumeiko, Nucl. Phys. **B127** (1977) 242.

[4] A. A. Akhundov, D. Yu. Bardin and N. M. Shumeiko, Yad. Fiz. **26** (1977) 1251;
N. M. Shumeiko, Sov. J. Nucl. Phys. **29** (1979) 807;
T. V. Kukhto and N. M. Shumeiko, Nucl. Phys. **B219** (1983) 412.

[5] N. M. Shumeiko, Sov. J. Nucl. Phys. **29** (1979) 807.

[6] A. D. Martin, R. G. Roberts and W. J. Stirling, Phys. Rev. **D50** (1994) 6734.

[7] G. Smirnov, Phys. Lett. **B364** (1995) 87.

[8] T. de Forest and J. D. Walecka, Adv. Phys. **15** (1966) 1;
E. J. Moniz, Phys. Rev. **184** (1969) 1154;
J. Bernabeu, Nucl. Phys. B**49** (1972) 186;
S. Stein et al., Phys. Rev. **D12** (1975) 1884.

[9] A. I. Akhiezer, A. G. Sitenko and V. K. Tartakovsky, Nuclear electrodynamics, Kiev, 1989;
J. Bailey et al., Nucl. Phys. **B151** (1979) 367.

[10] A. D. Martin, R. G. Roberts and W. J. Stirling, Phys. Rev. **D51** (1995) 4756.

QED RADIATIVE PROCESSES IN ELECTRON-HEAVY ION COLLISIONS AT HERA

[a] Krzysztof Kurek

[a] Institute of Physics, Warsaw University Branch, Lipowa 41, 15-424 Bialystok, Poland

Abstract: Elastic radiative tail corrections and beamstrahlung process are discussed in the context of heavy ions mode at HERA collider. The contribution of the radiative elastic tail are calculated without the use of the Born approximation and the multiphotons interactions with heavy nuclei/ions are taken into account. The numerical results for the cross sections are presented for the scattering on lead and tin for the lowest x-bins, where these contributions are important. A comment on beamstrahlung process is given. The effect is strongly machine design dependent and is found to be negligible for planned heavy ions mode at HERA.

1 Introduction.

The heavy ions mode at HERA collider which is actually considered as a one of the future possibilities will allow to study deep inelastic electron scattering on heavy targets with very high energy. The determination of the one photon cross section from the data demands excluding of a contribution from the other electroweek processes. These other contributions must be calculated theoretically and subtracted from the measured cross section. The set of theoretical calculations needed to experimental analysis is called *radiative corrections scheme*. There are many radiative corrections schemes on the market ready to use in the DIS on heavy ions at HERA (see e.g. [1, 2] and references therein).

In this paper I discuss these radiative processes which are not included (or included in Born approximation which is not correct in the case of heavy targets) in the standard radiative corrections schemes. There are two types of such procesess:

- The *radiative elastic tail*, the bremsstrahlung process from electron current in the elastic channel.
- The *beamstrahlung* process , originally considered for e^+e^- linear collider with TeV range of energy, where electron crossing a very high density positron bunch thus suffer strong acceleration and radiate a sizeable fraction of incident energy. In the case of heavy ions the electron is affected by heavy ions bunch. The heavy ions bunches (due to high electric charge) as well as dense positron bunches are a source of strong field in which electron can radiate.

The paper is organized as follows. In Section 2 the cross sections of the elastic tail for planned HERA heavy nuclei/ions mode are calculated for lead, tin and calcium in the Born one photon approximation as well as using the method in which the multiphotons interactions with heavy nuclei are taken into account. Section 3 contains a comment about beamstrahlung process. Finally, the summary is given in Section 4.

2 The contribution of the elastic radiative tail.

It is well known that the one of the more important contribution to the cross section measured in the DIS experiments in the small x bins proceeds from elastic tail. In the standard approach the only Born cross section is taken into account what means that the only one photons processes are considered (one photon emitted from lepton and one photon transmitted to target particle). To find the corresponding formulae the reader is reffered to the original papers [1, 2]. For the scattering on the heavy target the Born approximation is not correct because the effective coupling between virtual photon and heavy target particle is very strong due to the high electric charge Ze of the heavy nuclei/ions. Therefore the one photon exchange approximation is not valid and multiphotons exchange processes should be taken into account. The calculations presented in this paper are based on the method described in detail in [3] where the elastic radiative tail was calculated for NMC fixed target experiment for the muon scattering on heavy targets [4].

The basic concept of the method is to calculate the electron wave function in the presence of the "external" field generated by the heavy ion (Furry wave function). It can be done in the high energy approximation (Bethe et al., [5]). The cross section of the elastic radiative tail calculated using Furry electron wave function is given by the famous Bethe-Heitler formula [6] modified by extra factor R and multiplied by the formfactor of heavy ion [5, 3]. The calculations were done in the rest frame of the heavy ion's bunch using the potential approximation (the recoil effect of nucleus was neglected). Both used approximations (high energy and potential) are exellent approximations in the case of heavy nuclei at HERA . The one photon Born cross section in potential approximation is given exatly by Bethe-Heitler formula (R = 1) with heavy ion's formfactor.
The formulae for the elastic radiative tail cross section for the heavy targets are given in [3]. The

numerical calculations were done for scattering electrons with energy 27.6 GeV on the heavy nuclei/ions beam with energy 410 GeV per nucleon. The corresponding "fixed target" energy (energy in the heavy ion rest frame) is about 22 TeV. The cross sections for the elastic radiative tail for different x and y bins for lead and tin are presented in Fig. 1 and 2, respectively. For comparison the Born cross sections are also presented. The numbers in the brackets in Fig. 1 and 2 show how important the effect of multiphotons interactions is. The calculations were also done for the lighter nuclei (calcium) and the cross sections are very close to the cross sections calculated with Born approximation. The effect of multiphotons processes is really important only for the heaviest nuclei. The cross sections were calculated for the smallest x bins (0.0001 to 0.01) planned to reach at HERA, where the elastic tail is the important correction.

To calculate R factor which modified Bethe-Heitler formula in the case of heavy targets the pure Coulomb potential was assumed [5]. For the case of nuclei the pure Coulomb potential is modified by the nuclear charge density (which is not point-like) and therefore the square of formfactor $F(q)^2$, the Fourrier transform of charge density, appeared in front of the formula

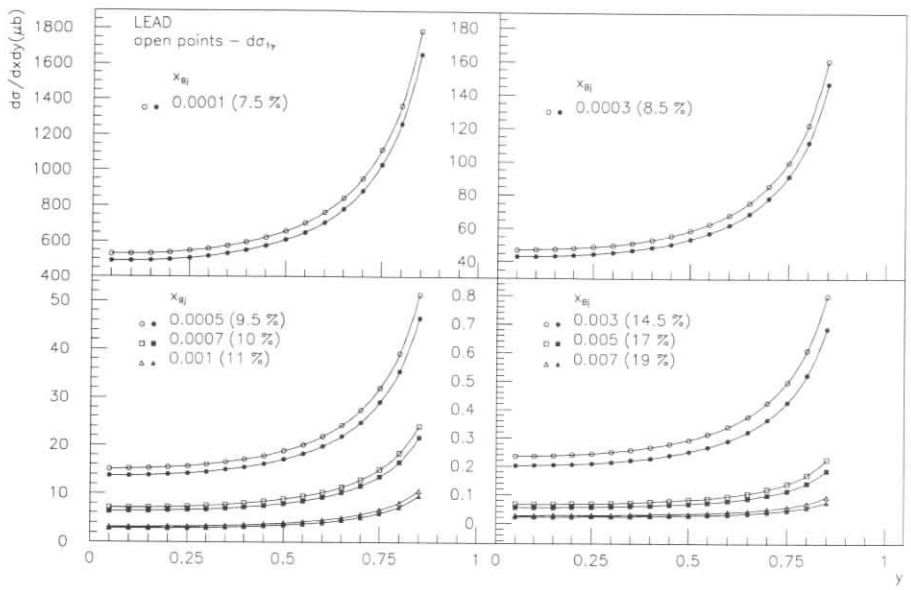

Figure 1: *The differential cross sections for the elastic radiative tail for lead nuclei/ions in Born approximation (open points) and with the multiphotons interactions taken into account according with the method proposed in [3]. Numbers in brackets show how large the differences between Born and multiphotons cross sections are.*

(12) in [3]. To take into account the nuclear charge density the Furry wave function should be calculated in the presence of *modified* Coulomb field. Unfortunately for real nucleus density it is not possible to solve the Dirac equation for the Furry wave function. The presence of F^2 in formula (12) in [3] is justified only for Born one photon cross section. When the multiphotons processes are taken into account (R factor) it is not clear how the formfactors should be put into the cross section formula. [1] However the formfactor is not taken into account correctly there are some arguments that the obtained results for the cross sections are correct [3]. To check how important for the cross section's calculations the shape of formfactor is, the different shapes of formfactor was probed in the cross section's multiphotons part (the difference between Born and the multiphotons cross section; such difference of cross sections contains also interference

[1] e.g. if it is formally considered double photons exchange Feynmann diagrams instead of F^2 the combination of three F's (interference terms) and four F's should be integrated. In the presented method all diagrams (processes) are summed up and such procedure is not possible.

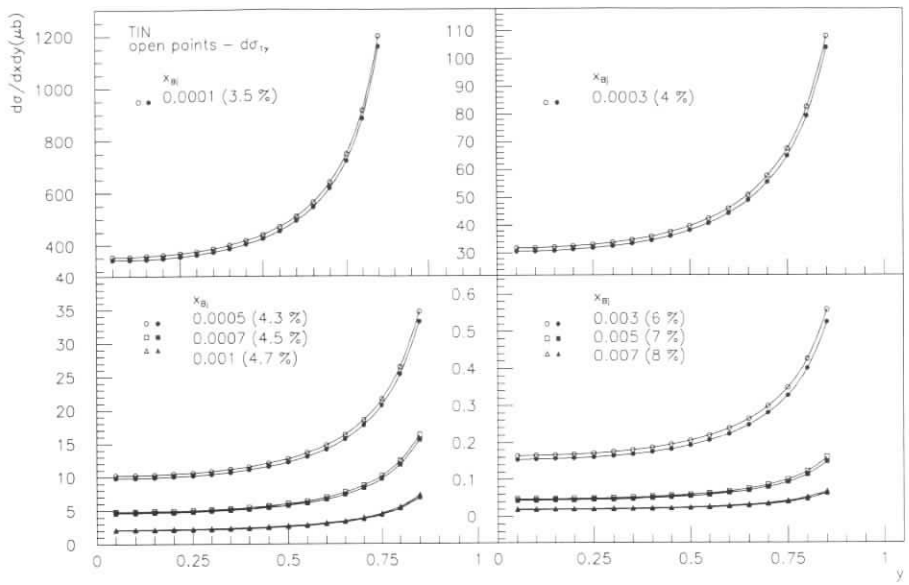

Figure 2: *The differential cross sections for the elastic radiative tail for tin nuclei/ions .*

terms) while the Born part become unchanged with true, physical formfactor, F.

Comparison of the results allowed to estimate how crucial the shape of formfactor is in the cross section calculations. The numerical results were obtained for lead and are presented in Fig. 3. The formfactor's formula used in calculations was taken from [7].

To varying shape of the formfactor the γ parameter was changed (see [7]). For two cases the shape was assumed to be only exponential factor; the sum of the oscillations were neglected (modified in Fig. 3).
From Fig. 3 it is clear that the differences (numbers in brackets) are smaller than 1% except two unphysical situations where the formfactor is nearly constant (point like charge density) and very "narrow" (flat charge density in the nucleus). In these cases the differences are a little larger for higher x bins where the contribution from elastic tail is smaller as it is seen from Fig. 1 and 2. The obtained results justify the multiphotons formula for the tail cross section with the formfactor treatment as in the Born approximation.

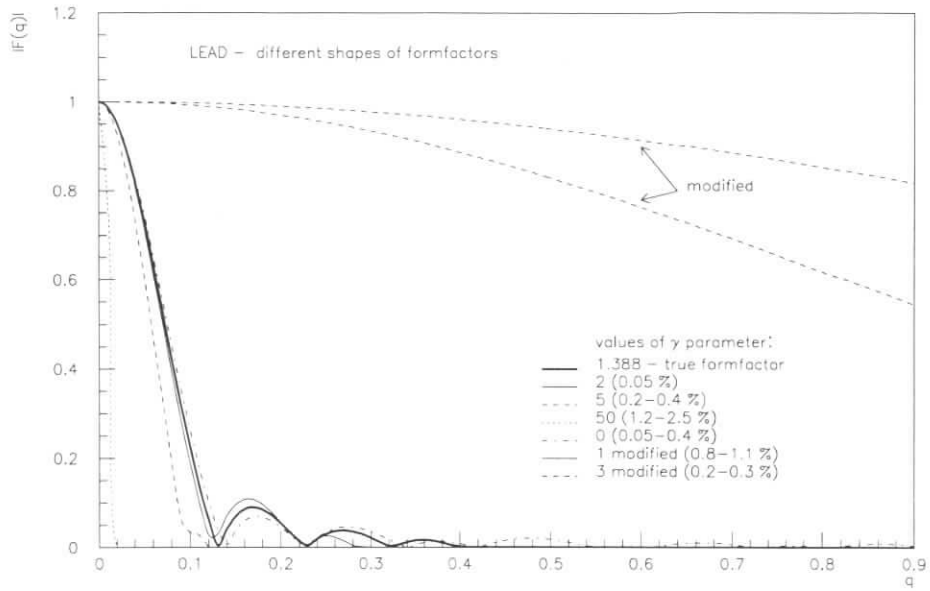

Figure 3: *The different shapes (determined by γ) of the lead formfactor used in the estimation of the uncertainties of the proposed method of calculations. The two curves with label modified are only the exponential term (see [7]). The numbers in brackets show the differences between the cross sections with different formfactor's shape taken into account in the multiphotons interactions.*

3 Comment on beamstrahlung process in the heavy ions mode at HERA.

The beamstrahlung process is a radiation of photons due to interactions between electron crossing target particles bunch. The whole bunch is a source of strong electromagnetic field which affects the electron. The effect was estimated to be quite large in the case of very dense electrons and positrons bunches which were considered in the context of the future electron-positron linear collider in TeV range of energy (see [8, 9] and references therein).
The question is if the beamstrahlung effect can be important in the case of the electron scattering on heavy ions bunch. The bunches of ions at HERA will not so dense as in planned e^+e^- linear colliders but - due to the high electric charge the heavy ions bunch maybe significant source of classical electromagnetic field.

The effect depends strongly on the machine designe: the shapes of the bunches, density and energy. The machine's parameters determin also if the classical or quantum beamstrahlung should be considered. In both cases the set of neaded formulae is known. In the quantum case the calculations were done in one photon approximation (one real photon emission) as well as the real multiphotons emissions were taken into account [9].
To distinguish which case (classical or quantum) should be considered in the case of heavy ions at HERA the parameter Υ was defined:

$$\Upsilon = \frac{\omega_c}{3p} = \frac{2Er_e\lambda_e}{\sqrt{3}m\sigma_z(\sigma_x+\sigma_y)}N. \qquad (1)$$

where p, E, r_e, λ_e and m are momentum, energy, classical radius, Compton wave length and mass of electron; σ_z, σ_x and σ_y are the parameters of the heavy ion's bunch (elliptical) and N is a number of ions inside the bunch. The ω_c is a classical so-called *critical* frequency up to which the spectrum of radiated photons is important. The meaning od the Υ is the classical average ratio of the radiated energy and electron incident energy. The Υ parameter should be much smaller than one in the classical case. If the Υ is greater than one the quantum calculations are needed. It is exactly the case in planned future e^+e^- machines.
The assumed parameters of HERA heavy ions beam for calculating Υ were the following:

energy of ions	- 410 GeV/nucleon ,
bunch spacing	- 160 bunches/ 96 ns ,
typical current	- 50 mA ,
$\sigma_z, \sigma_x, \sigma_y$	- 0.11 m, 70 μm , 300 μm

These parameters give N $\simeq 10^{10}$ ions and $\Upsilon \simeq 10^{-7}$. It is now clear that the HERA is operating in classical regime. The energy loss due to beamstrahlung process can be calculated using the following classical formula

$$\delta = \frac{4N^2Er_e^3}{3\sqrt{3}m\sigma_z(\sigma_x+\sigma_y)^2} \simeq 10^{-9}. \qquad (2)$$

This result shows that the beamstrahlung process at HERA with heavy ions beams is not important in contrast to the collisions of very dense electrons-positrons beams considered in the new generation of the linear electrons-positrons colliders.

4 Summary

In this paper the elastic radiative tail correction and the beamstrahlung process were calculated for the future DIS process with electrons and heavy ions at HERA collider. The multiphotons interactions, which are important in the heaviest nuclei, were taken into account and compared with Born standard approach. The method originally proposed by Bethe et al. [5] was modified and applied to improve the standard radiative corrections schemes in the case of heavy targets [3]. The effect is quite large in the HERA kinematics (up to 19%). The uncertainties connected with the formfactor treatment were discussed and estimated to be less than 1% .
The beamstrahlung process was also discussed. The HERA machine parameters and kinematics allow to consider this process classically. The numerical results show that the electron interactions with the whole heavy ions bunch (beamstrahlung) is negligible.

Acknowledgements

I thank Michele Arneodo for inviting me to participate in the heavy ions sessions in HERA workshop 95-96.

References

[1] D. Bardin et al., Contrib. to the Zeuthen Workshop on Elementary Particle Theory – Deep Inelastic Scattering, Teupitz, Germany, April 1992, *Nucl. Phys.* **B** (Proc. Suppl.) **29A** 1992 209; D. Bardin et al., *Z. Physik* **C42** (1989) 679; A.A. Akhundov et al.,DESY report 94-115/CERN-TH.7339/94/IC/94/154, (1994).

[2] B.Badelek at al.*Z. Physik* **C66** (1995) 591.

[3] K.Kurek, *Z. Physik* **C63** (1994) 561.

[4] NMC; P. Amaudruz et al., *Z. Physik* **C51**(1991)387;
NMC; P. Amaudruz et al., *Z. Physik* **C53** (1992)73.

[5] H.A. Bethe and L.C. Maximom, *Phys. Rev.* **93** (1954) 768;
A. Nordsieck, *Phys. Rev.* **93**(1954) 785;
H. Davies, H.A. Bethe and L.C. Maximom, *Phys. Rev.* **93** (1954) 788.

[6] J.M Jauch and F. Rohrlich, *The Theory of photons and electrons; the relativistic quantum field theory of charged particles with spin one-half*, Springer, New York (1976),
A.I. Akhiezer, V.B. Berestetskiĭ, *Quantum Electrodynamics*, Wiley, New York (1965).

[7] B. Frois et al., *Phys. Rev. Lett.* **38**(1977) 152; I. Sick et al., *Phys. Lett.* **88B**(1979) 245.
J.R. Ficenec et al.,*Phys. Lett.* **42B**(1972) 213.

[8] for references see e.g. K. Kurek, J. Skowroński, Proceedings of International Conference on High-Energy Physics, 26, Dallas, 1992, ed.: R. Schwitters, New York, 1993, vol. II. or M.Jacob, T.T.Wu,*Nucl.Phys.***B371** (1992) 59.

[9] M.Jacob, T.T.Wu and G.Zobernig *Z. Physik* **C53** (1992)479.

VNI – An Event Generator for Deep-Inelastic Final States in a Space-Time Description of Shower Development and Hadronization

Klaus Geiger

Physics Department, BNL, Upton, N.Y. 11973, U.S.A.: klaus@bnl.gov

*VNI*3.1 is a Monte Carlo implementation of a quantum kinetic approach to the description of high energy particle collisions, including e^+e^-, deep-inelastic ep and eA, hadron-hadron, hadron-nucleus and nucleus-nucleus collsions. In the case of deep-inelastic electron scattering off a proton or nucleus at HERA, the basic concept is the following [1]: The history of the triggering photon-proton (nucleus) hard scattering is traced back to the initial hadronic (nuclear) state and forward to the formation of colour-singlet pre-hadronic clusters and their decays into hadrons. The time evolution of the space-like initial-state shower and the time-like secondary partons are treated similarly, and cluster formation is treated using a spatial criterion motivated by confinement and a non-perturbative model for hadronization.

The central element in this approach is the use of QCD transport theory [2] and quantum field kinetics [3] to follow the evolution of a generally mixed multiparticle system of partons and hadrons in 7-dimensional phase-space $d^3rd^3kdk^0$. Included are both the perturbative QCD parton-cascade development [4, 5], and the phenomenological parton-hadron conversion model which has been proposed previously in Refs. [6, 7], in which a dynamical parton-cluster formation is considered as a local, statistical process that depends on the spatial separation and colour of nearest-neighbour partons, followed by the decay of clusters into hadrons. In contrast to the commonly-used momentum-space description, in the present approach the microscopic history of the dynamically-evolving particle system is traced in space-time *and* momentum space, so that the correlations of partons in space, time, and colour can be taken into account for both the perturbative cascade evolution and the non-perturbative hadronization. One strength of this approach lies in the possible extension of its applicability to the collision dynamics of complicated multi-particle systems, as in eA, pA and AA collisions, for which a causal time evolution in position space and momentum space is essential.

The model contains three main building blocks which generically embody high-energy collisions involving leptons, hadrons, or nuclei in colliders (for DIS ep collisions, the model components are illustrated in Fig. 1):

a. the *initial state* associated with the incoming collision partners (the beam particles), in particular the phenomenological construction of the hadron (nucleus) in terms of quark and gluon phase-space distributions;

b. the *parton cascade development* with mutual- and self-interactions of the system of quarks and gluons consisting of both the materialized partons from parton showers, and the spectator partons belonging to the remnants of the collided beam particles;

c. the *hadronization* of the evolving system in terms of parton coalescence to colour-neutral clusters as a local, statistical process that depends on the spatial separation and colour of nearest-neighbour partons, followed by the decay of clusters into hadrons according to the density of final hadron states.

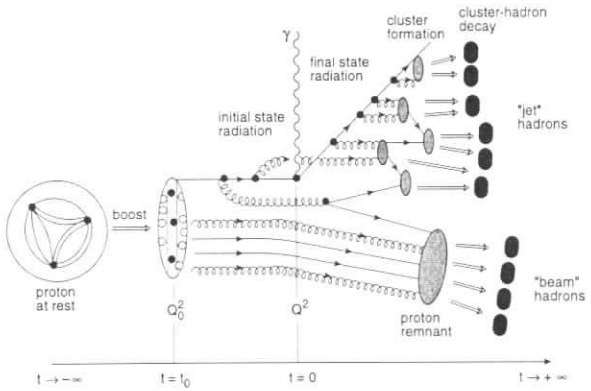

Such a pragmatical division, which assumes complex interference between the different physics regimes to be negligible, is possible if the respective dynamical scales are such that the short-range hard interaction, with its associated perturbative parton evolution, and the non-perturbative mechanism of hadron formation occur on well-separated space-time scales. For DIS, this condition of validity requires $\min(W^2, Q^2) \geq L_c^{-2} \gg \Lambda^2_{QCD}$, meaning that the characteristic mass scale for the γp hard scattering and parton shower development (W^2, Q^2, or a combination of the two) is larger than the inverse 'confinement length scale' $L_c = O(1\,fm)$ separating perturbative and non-perturbative domains. Specifically, for DIS, in the small-x regime probed at HERA ($10^{-4} \lesssim x \lesssim 10^{-3}$), one has $60 \lesssim W \lesssim 300$ GeV for $10 \leq Q^2 \leq 300$ GeV^2, so that the above requirement is well satisfied. It is important to realize however, that in this model the interplay between perturbative and non-perturbative regimes is controlled locally by the space-time evolution of the mixed parton-hadron system itself, rather than by an arbitrary global division between parton and hadron degrees of freedom.

Recently the approach discussed above has been applied [1] in detail to deep-inelastic ep scattering at HERA, and will be applied in the future to more complicated situations, in particular the extension to eA collsions at HERA energy. It allows to map the history of the particle densities and associated spectra, including the rapidity, longitudinal and transverse distributions of particles, so that these may be compared with intuitive pictures of the space-time development of hadronic final states in DIS. They will also form the basis for investigating the effects of multiple parton scattering, energy-loss phenomena, parton shadowing, and other interesting effects in eA scattering which are not present in ep.

The aforementioned application to ep shows encouraging results for, e.g., inclusive hadron spectra in x_F and p_T, and the transverse energy flow, or, distributions of the mass M_X of the observed hadronic final state in events without a large rapidity gap, which can be used to estimate the background to the cross-section for LRG events.

As already mentioned, the new features of this approach open the way to future applications of the model to eA, pp, pA and AA collisions, where the novel features associated with high parton densities will become more marked. In this respect the possible eA experiments at HERA can play a key role since these collisions provide the 'cleanest' way of probing parton- and hadron- evolution in a nuclear medium, rather than in vacuum.

References

[1] J. Ellis, K. Geiger, and H. Kowalski, preprint CERN-TH/96-105 (1996), hep-ph/9605428.

[2] K. Geiger, Phys. Rep. **258**, 237 (1995).

[3] K. Geiger, Phys. Rev. **D54**, 673 (1996).

[4] Yu. L. Dokshitzer, D. I. Dyakonov, and S. I. Troyan, Phys. Rep. **58**, 269 (1980); Yu. L. Dokshitzer, V. A. Khoze, A. H. Mueller, and S. I. Troyan, Rev. Mod. Phys. **60**, 373 (1988).

[5] K. Konishi, A. Ukawa, and G. Veneziano, Nucl. Phys. **B157**, 45 (1979).

[6] J. Ellis and K. Geiger, Phys. Rev. **D52**, 1500 (1995); Nucl. Phys. **A590**, 609 (1995).

[7] J. Ellis and K. Geiger, CERN-TH. 95-283 (1995), hep-ph/9511321.

Experiments with Light and Heavy Nuclei at HERMES

G. van der Steenhoven

Nationaal Instituut voor Kernfysica en Hoge-Energiefysica (NIKHEF),
P.O. Box 41882, NL-1009 DB Amsterdam, The Netherlands

Abstract: The physics prospects for using light and heavy nuclear targets in fixed-target experiments at HERMES are discussed. The kinematics of such experiments imply that the measurements can be used as a sensitive probe of the space-time dynamics of deep-inelastic scattering (DIS), enabling investigations of quark propagation and colour transparency. Moreover, the dilute internal gas targets used at HERMES make it possible to detect low-energy recoil products, that can be used to tag certain classes of DIS events. In this way neutron structure function data can be measured that do not suffer from ambiguities related to the structure of the deuteron. Moreover, new information on the origin of the EMC effect and the breaking of the Gottfried Sum Rule can be obtained.

1 Introduction

The HERMES experiment makes use of the HERA polarized electron (or positron) beam, which is interacting with a (fixed) polarized internal gas target flowing through a thin-walled storage cell. The deep-inelastic scattering events are observed with the HERMES (forward-angle) spectrometer, which also enables a fairly good identification of the hadronic final state. HERMES has started to produce first data on the neutron spin-structure function in 1995.

By injecting (polarized) nuclear targets into the storage cell, the HERMES set-up can be used for two new classes of experiments: (i) measurements in which the nucleus acts as a 'femtometer' detector; and (ii) measurements in which the deep-inelastic structure functions are tagged by detecting an additional hadron in the final state. The first class of experiments enables the study of quark propagation in the medium and the possible observation of colour transparency. The second type of experiments makes it possible to measure neutron structure functions without uncertainties related to nuclear corrections. Moreover, information can be obtained on the origin of the EMC effect, and the break down of the Gottfried Sum Rule. These experiments are discussed in more detail in sections 2 and 3, respectively.

The conditions for electro-nuclear fixed target experiments at HERMES are unique. The kinematics are well-matched to the length scales involved in hadron formation (see section 1.1), and the use of internal gas targets makes it possible to detect low-energy recoil products, which is impossible at other deep-inelastic scattering facilities (see section 1.2). Together these conditions are well fit for measurements that address the unknown transition from the region where perturbative QCD applies (at high Q^2) to the non-perturbative domain at lower-Q^2 values.

In this report the prospects for using nuclear targets at HERMES are summarized. The discussions are brief when dedicated contributions exist that provide all necessary detail (section 2). In other cases the summaries are longer, in particular when the specific contributions do not include any count-rate estimates (section 3). Some practical considerations concerning the realisation of such experiments at HERMES are presented in the last section of this report.

1.1 Kinematics

Three length scales enter the description of the semi-inclusive processes in deep-inelastic scattering that are at the basis of most of the physics issues addressed in this report:

- The coherence length describes the hadronic $q\bar{q}$ fluctuation of a virtual photon

$$l_C \approx \frac{2\hbar c\nu}{Q^2 + m_{q\bar{q}}^2} = \frac{\hbar c}{m_p x(1 + \frac{m_{q\bar{q}}^2}{Q^2})} \approx \frac{\hbar c}{m_p x}. \tag{1}$$

  where ν represents the energy transfer, Q^2 the four-momentum transfer, $m_{q\bar{q}}$ the mass of the hadronic fluctuation and x is the usual Bjorken-scaling parameter ($\frac{Q^2}{2m_p\nu}$). Note that the last equality sign only holds in the high-Q^2 limit. A typical value of l_C for HERMES kinematics is 3 fm, whereas l_C is much larger (10 - 30 fm) for the deep-inelastic lepton scattering experiments at CERN (NMC) and Fermilab (E665).

- The formation length describes the distance between the initial lepton interaction vertex and the hadron formation point:

$$l_F \approx \frac{2\hbar c\nu}{\delta m_V^2}, \tag{2}$$

  with δm_V^2 the characteristic squared-mass difference between low-lying vector-meson states ($\delta m_V^2 \sim 1$ GeV^2). A typical value of l_F for HERMES kinematics is 5 fm, whereas l_F is much larger (50 fm) at NMC and E665.

- The transverse size of the hadronic fluctuation is mainly relevant for colour-transparency studies:

$$r_\perp \approx \frac{5\hbar c}{Q}. \tag{3}$$

  Depending on the Q^2-range selected the values for $r_\perp$ range from about 0.3 fm to 0.7 fm, but usually considerably smaller than the radius of a nucleon.

It is seen that the sizes of l_F and l_C are commensurate with nuclear dimensions for deep-inelastic scattering at HERMES energies. Hence, experiments that want to exploit the nuclear medium, and thus want to maximize its influence, are best carried out at HERMES (as compared to E665, SMC, NMC, etc.)

1.2 Internal nuclear targets at HERMES

The advantages of using an internal target in semi-inclusive deep inelastic scattering are twofold: (i) a high level of undiluted target polarization can be obtained; and (ii) the use of a dilute gas allows the detection of low-energy recoil products.

In order to study the feasibility of electro-nuclear experiments at HERMES, the type of nuclei that can be used and the maximum luminosity that can be obtained must be determined.

The HERMES set-up has already been operated with polarized and unpolarized ^{1}H, ^{2}H, and ^{3}He targets. For heavier targets the exact species is not important as the experiments discussed only require a certain (varying) amount of nuclear matter. Hence, the only requirement is that a fairly large A-range is covered.

To avoid heating the target, considerations are restricted to the gaseous elements ^{4}He, N, O, F, Ne, Cl, Ar, Kr, Xe, and Rn. These have boiling points at atmospheric pressure of 4.2, 77, 90, 85, 27, 239, 87, 121, 166, and 211 K, respectively. The elements F and Cl have to be excluded, as they are highly reactive with steel and human lung tissue. Moreover, the elements oxygen (O) and radon (Rn) are not considered either. Compared to oxygen the nearby element nitrogen (N) is much easier to handle, while Rn is radioactive and difficult to provide.

It is worth noting that the DESY machine group will resist efforts to use a ^{4}He target because they use ^{4}He for leak checking and any ^{4}He contamination will reduce their sensitivity. The remaining elements (^{3}He, ^{14}N, ^{20}Ne, ^{40}Ar, ^{84}Kr, and ^{131}Xe) cover a large enough A-range, and their use is not expected to be opposed by the DESY machine group, provided that the beam life time is not affected.

Atomic bremsstrahlung of beam positrons in the HERMES target reduces the beam lifetime. In the absence of other beam-loss mechanisms, the lifetime would be:

$$T_{\text{targ}} \approx T_0 \left[Z(Z+1) \left(\ln \frac{183}{Z^{1/3}} \right) \left(\frac{n}{8.1 \times 10^{25}\,\text{atoms/cm}^2} \right) \right]^{-1}, \tag{4}$$

where n is the target thickness and $T_0 = 21\,\mu$s is the revolution time of HERA [1]. In order to prevent a significant reduction in the ~ 10 h beam lifetime, HERMES is required to run with $T_{\text{targ}} \geq 45$ h. Thus the maximum thickness for unpolarized targets is [4]:

$$n_{\text{max}} = \frac{1.05 \times 10^{16}\,\text{atoms/cm}^2}{Z(Z+1)\ln(183Z^{-1/3})}. \tag{5}$$

Figure 1 exhibits the corresponding luminosity L_A for a beam current of 35 mA (taken from ref. [4]). It is concluded that the *nucleon* luminosity is not decreasing steeply with A. Therefore, the luminosity that is available for nuclear targets at HERMES is not expected to be a strong limiting factor.

2 A femtometer detector in deep-inelastic scattering

The space-time evolution of hadron-formation in deep-inelastic scattering cannot be described from first principles in QCD. Hence, several models have been developed to describe this non-perturbative process. In order to calibrate and select among these models it is desirable to perform experiments in which hadron formation is actually modified by embedding it in a medium of varying density, i.e. using nuclear targets.

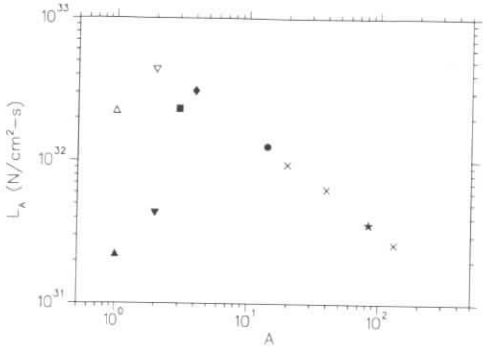

Figure 1: Maximum ($I_{\text{beam}} = 35\,\text{mA}$) obtainable luminosity in nucleons/cm^2-s for ^{1}H, ^{2}H, ^{3}He, ^{4}He, N, Ne, Ar, Kr, and Xe [4]. For ^{1}H and ^{2}H the open symbols are the beam lifetime limits for unpolarized running and the closed circles are the ABS limits for polarized running.

2.1 Quark Propagation

By comparing the production of leading hadrons (such as pions, kaons, lambda's and protons) in deep-inelastic scattering off nuclei to the production off nucleons, one can determine the attenuation of those hadrons in the nuclear medium. In the kinematic domain accessed by HERMES these attentuation ratios R_A can be measured for various nuclei and hadrons in such a way that $l_F \sim R_{nucleus}$. Consequently, the results are expected to be extremely sensitive to the model assumed for the formation process of the hadron. In fact, such data can be used to determine the hadron formation time τ_{form}. Moreover, the good particle identification capabilities offered by the HERMES spectrometer (especially if it is also equiped with a ring-imaging cherenkov (RICH)), allows a separate determination of attenuation ratios for different hadrons. As the formation time models strongly depend on the hadron mass, the results for different hadrons provide additional constraints on such models.

Few measurements of R_A exist. At high ν some data have been reported by EMC [2], which are all very close to unity. In the low energy domain ($2 \leq \nu \leq 20$ GeV), a significant hadronic attenuation has been observed in a single poor-statistics measurement taken at SLAC [3] (with hardly any particle idenfication). Hence, HERMES can make a unique contribution to this field by performing precise measurements of R_A in the energy domain which is expected to be most sensitive to the hadron formation process, and by measuring the hadron formation time. Detailed count-rate estimates for such experiments are presented in ref. [4], while Kopeliovich et al. [5] and Pavel [6] discuss various models for hadronization processes in nuclei.

Further information on the hadron formation process can be obtained by searching for slow protons and/or neutrons ($\lesssim 2$ GeV) that are produced in semi-inclusive deep-inelastic scattering events. If these nucleons are normal hadronization products the yield should be proportional to A, but if they result from secondary interactions of leading hadrons the rate will increase

faster. Hence, the measurement of slow protons and neutrons can be used to determine the number of secondary interactions in deep inelastic scattering [8].

To date only one result has been reported on the observation of slow neutrons in deep inelastic scattering. At Fermilab [7] a surprisingly low number of slow neutrons was observed, suggesting that only few reinteractions occur at high energy. At HERMES we expect a larger number of neutrons per DIS-event, because of the increased influence of the nuclear medium on the quark propagation process. A simple count rate estimate shows that one can expect about 1000 slow neutron events in 3 months of running time using a Xenon target at a luminosity of $3\ 10^{31}$ N/cm^2/s and a 100 msr time-of-flight scintillator array.

2.2 Colour Transparency

Colour transparancy (CT) represents one of the few QCD-based predictions that have not been verified experimentally (the other well-known one being the quark-gluon plasma). In the case of CT it is predicted that a hadron propagating through a medium will experience hardly any (final-state) interactions if the hadrons are produced in configurations with small transverse size $r_\perp$ and have a long enough expansion time. The kinematics at HERMES imply that $r_\perp \sim 0.3$ fm, while the coherence length is still small such that the interactions occur inside the nuclear medium. Moreover, the (missing) energy resolution ($\lesssim 0.5$ GeV) offered by the HERMES spectrometer enables the observation of (almost) exclusive reaction channels, which makes the interpretation of the data considerably less ambiguous. These unique properties of the HERMES set-up are exploited in several proposals for CT-measurements that are summarized in this section.

Traditionally, exclusive (high z) production of protons has been used for CT studies. However, Hüfner and Kopeliovich [9] have argued that it may be very difficuly to obtain unambiguous evidence for CT from such measurements. Instead they advocate the use of ρ^0 or ϕ production. It turns out that exclusive coherent or incoherent (low-t) production of vector mesons is highly sensitive to the occurrence of CT. In ref. [4] it is shown that a modest 30 fills per target could already provide significant data on colour transparency in the exclusive ρ^0 channel. Moreover, these data can be used to determine the time it takes for an initial point-like configuration to expand to its full physical size (expansion time).

Apart from the aforementioned unpolarized measurements, Frankfurt et al. [10] have argued in favour of using a tensor polarized deuterium target for CT studies. They have demonstrated large effects on the tensor analyzing power in proton production on deuterium. This effect can be attributed to the fact that at high t the relative importance of CT is larger for the d-state as compared to the s-state in deuterium.

Finally, it would be desirable to isolate the coherent ρ^0 production channel, which is theoretically easier to approach. Experimentally, one could isolate the (exclusive) coherent channel from the dominant incoherent channel by detecting a recoiling light target nucleus [11], which can only be achieved with an internal target such as is available at HERMES.

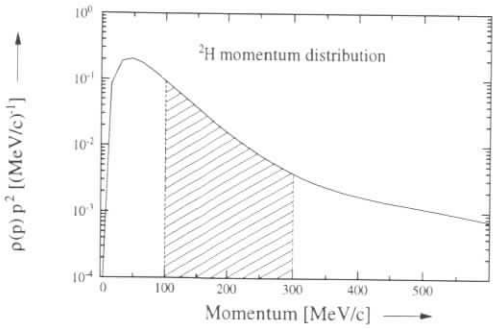

Figure 2: Deuteron wave function, $\rho(p)p^2 = |\psi(p)|^2 p^2$, as a function of the nucleon momentum. The hatched area indicates the relevant momentum range for a neutron tagging experiment.

3 Tagged Structure Functions

3.1 Neutron Structure Functions

The (spin) structure functions of the neutron are usually measured by subtracting ^{2}D and ^{1}H data. The evaluation of the neutron structure functions from such a subtracted data requires the application of nuclear corrections that account for the dynamics of the neutron inside the deuteron. These corrections are reasonably well under control for unpolarized structure functions provided that $x \lesssim 0.5$, but are less well known for the *spin* structure functions. Hence, there is interest in an unambiguous determination of the unpolarized structure function $F_2^n(x)$ for $x \to 1$ and $g_1^n(x)$ in the entire $x-$domain.

Alternatively, the neutron structure functions can be measured in deep inelastic scattering (DIS) off a deuteron target with simultaneous detection of a recoiling proton, i.e the proton acts as a spectator which tags a DIS-events off a neutron [16]. The method assumes the dominance of the spectator mechanism. Simula [17] has investigated the relative merits of various scaling variables that can be used to identify the spectator mechanism for deep-inelastic electron scattering off a deuteron target.

The cross section for the observation of a spectator proton in deep-inelastic scattering off a deuteron target reads:

$$\sigma_{\text{recoil}} \sim F_2^n\left(\frac{x}{2-\alpha}\right)|\psi(\alpha, p_\perp)|^2. \tag{6}$$

where the neutron structure function F_2^n is evaluated at a rescaled momentum fraction with α the lightcone momentum fraction carried by the spectator:

$$\alpha = \frac{\sqrt{m_p^2 + p^2} - \vec{p}\cdot\hat{q}}{m_p} \tag{7}$$

The second term in the cross-section expression, $\psi(\alpha, p_\perp)$, essentially represents the nucleon wave function of the deuteron, which is illustrated in figure 2.

The yield of a neutron-tagging experiment is determined by the lower and upper limits of the integral $\int |\psi(p)|^2 p^2 dp$. The lower limit is set by the detection threshold of the low-momentum recoil detectors that will be placed close to the storage cells in the HERMES vacuum chamber. The exact value of the lower limit will depend on the wall thickness of the storage cell. In a 100 μm aluminum wall, as is presently used at HERMES, a proton (passing under 45 degrees) of 4.2 MeV, i.e. 88 MeV/c momentum, will be stopped. Hence, it is not unrealistic to use a lower limit of 100 MeV/c. The upper limit is determined by the uncertainty in the knowledge of the deuteron wave function, for which usually 300 MeV/c is taken, i.e. the domain where the d-state starts to dominate.

Under the assumption that recoil detection equipment covers 400 msr of the non-forward acceptance of the HERMES storage cell, the count-rate of a neutron tagging experiment has been estimated. The proton kinetic-energy acceptance is assumed to range from 2 to 30 MeV. A target thickness of $1 \cdot 10^{14}$ atoms/cm^2 has been taken, and an average positron current of 30 mA. With a typical target polarization of 80% and a beam polarization of 50%, we arrive at the error bars for F_2^n and the asymmetry A_1^n listed in table 1. The uncertainties shown correspond to 400 hours (or 50 fills) of data taking for each spin direction.

$x-$bin	$< Q^2 >$	δF_2^n	$\delta A_1^n\rfloor_{tag}$	$\delta A_1^n\rfloor_{D-H}$
0.02 - 0.03	1.2	1.9 %	0.055	0.018
0.04 - 0.06	1.9	1.3 %	0.046	0.016
0.10 - 0.15	3.3	1.1 %	0.059	0.026
0.20 - 0.30	4.3	1.2 %	0.092	0.051
0.40 - 0.50	5.5	2.2 %	0.253	0.167
0.60 - 0.70	9.1	7.5 %	0.772	0.520

Table 1: *Estimated statistical uncertainties in F_2^n and A_1^n for some selected $x-$bins in a neutron-tagging experiment off a polarized ^2H target. The statistical uncertainties associated with the traditional ^2D - ^1H subtraction method (also for 800 hours of beam time) are displayed in the last column.*

From table 1 it is seen that the recoil method leads to small error bars for F_2^n, which is of particular interest at high values of x. A measurement in this domain is of particular interest in view of the existing predictions for the ratio F_2^n/F_2^p, which in the limit of $x \to 1$ should approach the value 3/7 according to pQCD, while models based on the dominance of a scalar valence di-quark component in the nucleon predict this ratio to approach the value 1/4 [18]. Because of the relatively large nuclear corrections at large values of x, the existing data cannot distinguish between these conflicting predictions. The recoil method will enable a precise measurement of F_2^n/F_2^p at high x, as it does not suffer from such uncertainties [19].

The statistical errors anticipated for $A_1^n\rfloor_{tag}$ are significantly larger than those obtained in the $D-H$-subtraction method (taken from [12]). This is to be expected from the fact that the recoil proton cannot be detected over its full 4π phase space. However, the systematic uncertainty is expected to be considerably less. This can best be seen from ref. [13], where it is shown that the difference between the asymmetry for a free neutron and one bound in deuterium can be as large as a factor of 2 (depending on x). Moreover, if a laser-driven source comes available for HERMES the (polarized) target thickness can be improved by a factor

of 4, yielding error bars for A_1^n that are similar to the ones quoted in [12] for the (^{2}D - ^{1}H) subtraction method.

It is concluded that neutron tagging, which is virtually absent of nuclear-physics complications, can provide important neutron structure function data in the nearby future.

3.2 The origin of the EMC Effect

The neutron-tagging technique can be extended to study the possible origin of the EMC effect, i.e. the unexplained observation of an A-dependence of the unpolarized structure function $F_2(x)$. The concept is based on the known importance of nucleon-nucleon correlations in nuclei. As a consequence the momentum of a recoiling backward-going proton in deep-inelastic scattering is a direct measure of the momentum of the struck neutron. The dominance of this mechanism for backward-going protons has been demonstrated in ref. [14] for deep-inelastic neutrino scattering off ^{2}H (also see ref. [16]). Using the neutron-tagging technique it is thus possible to measure the dependence of $F_2^n(x)$ on the momentum of the parent neutron in which the struck quark resided.

The nucleon-momentum dependence of $F_2(x)$ can be instrumental in discriminating among models that have been developed to explain the EMC effect in the $x-$range between 0.1 and 0.8. While models assuming an intrinsic modification of $F_2(x)$ in general predict a strong increase of the EMC-effect with nucleon momentum (or effectively the nucleon density), models based on nuclear dynamics do not predict such effects.

There are essentially two proposals for studying the origin of the EMC effect in this way. Melnitchouk, Sargsian and Strikman [19] have suggested to use a ^{2}H target. As the high-momentum tail of the nucleon wave function is expected to be roughly the same for all nuclei, it is advantageous to use a ^{2}H target for which the wave function is well known (see figure 2). Alternatively, the tagged structure functions are measured on various target nuclei, which enables the variation of the nuclear density involved. However, a word of caution is appropriate in the latter case as part of the slow protons may be due to hadronization or rescattering of fragmentation products [20]. Simula has considered some of these complications in his contribution to the workshop [21].

In order to assess the feasibility of such tagged-structure function measurements, we have evaluated the error bars to be expected for 800 hours of data taking, i.e. about 100 fills, at a luminosity of $1.25 \cdot 10^{32}$ nucleons/cm^2/s on a ^{14}N unpolarized gas target. Assuming the availability of 800 msr of recoil-detection equipment one arrives at the results displayed in figure 3 for the ratio of the semi-inclusive over the inclusive deep-inelastic cross section [23].

It is seen that precise data can be obtained in about half a year worth of data taking. Measurements of this type do not exists nor are foreseen at any other laboratory.

3.3 The break-down of the Gottfried Sum Rule

In the quark-parton model one can relate the difference between the structure functions of the proton and the neutron to the difference between the u and d sea-quark distributions:

$$S_G = \int \frac{1}{x}(F_2^p(x) - F_2^n(x))dx = \frac{1}{3} - \frac{2}{3}\int (\bar{d}(x) - \bar{u}(x))dx. \qquad (8)$$

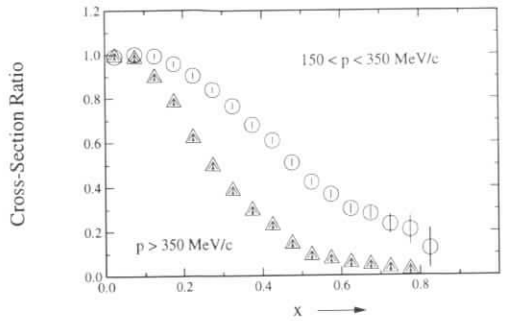

Figure 3: Ratio of cross sections for semi-inclusive and inclusive deep inelastic scattering off a ^{14}N target. The solid circles represent the data tagged by a proton of a momentum between 150 and 350 MeV/c, while the triangles correspond to events with proton momenta larger than 350 MeV/c [23].

Under the assumption that the sea is u-d flavour symmetric, the Gottfried Sum Rule is obtained [24], i.e., $S_G = \frac{1}{3}$. It came as a surprise when NMC and SLAC [25] found that $S_G = 0.240 \pm 0.016$, implying that the sea is flavour asymmetric, i.e. $\bar{d}(x) \neq \bar{u}(x)$.

Meson-cloud models [26] turned out to be able to reproduce the low value of S_G, i.e. $S_G]_{meson-cloud} \approx 0.1 - 0.2$. This result gives rise to the question whether or not the nucleon has an explicit mesonic component. In order to study the validity of these meson-cloud models, several experiments have been proposed that could be carried out at HERMES.

In deep inelastic scattering (DIS) off a ^{3}He target, for instance, the observation of recoiling ^{3}H nuclei identifies a possible DIS-event off a positive pion. As opposed to the nucleon case there can hardly be any contamination from target fragmentation as the fragmentation function of a quark leading to a ^{3}H nucleus must be vanishingly small, i.e. $D_{qq}^{^3H}(z) = 0$. The kinematics and cross section for such an experiment are discussed by Dieperink [22].

It has also been proposed to measure the polarization of a semi- inclusively produced Δ^{++} or a Λ from the angular distribution of the decay products. In simple models of di-quark fragmentation processes this polarization is very close to zero, while meson cloud models predict a very strong polarization signal [27].

For either of these measurements extensions and changes have to be made to the HERMES set-up, including – once again – the option to detect low-mass recoil products outside the acceptance of the forward spectrometer.

4 Outlook

A considerable number of different measurements have been proposed that could make use of light or heavy nuclear targets at HERMES. More details are given in the contributions to the Workshop, which are also included in the proceedings. For many of the proposed measurements count-rate estimates exist, that show the feasibility of most of the proposed experiments.

In order to fully exploit the ideas discussed in this report (with the various contributions attached to this report), several additions to the HERMES set-up need to be considered:

- Gaseous targets ^{3}He, ^{14}N, ^{20}Ne, ^{40}Ar, and ^{131}Xe need to be available and be allowed to use.
- A ring-imaging cherenkov counter should replace the existing threshold Cherenkov counter in order to improve the particle identification of the hadronic final state in HERMES. A RICH will be of particular interest for studies of quark propagation in nuclei. (Alternatively, a second threshold cherenkov counter could be used.)
- Large solid-angle recoil detection equipment is needed. As protons with extremely low proton momenta need to be detected, it would be natural to consider detectors that will be mounted inside the scattering chamber. A large neutron time-of-flight wall could be of similar interest in order to tag the proton structure functions.
- For some of the measurements -especially those of the neutron spin structure function through recoil tagging- a high-intensity polarized deuterium target needs to available, i.e. a laser-driven source or an upgraded ABS system .

A full-scale programme investigating the non-perturbative domain of QCD by exploiting light and heavy nuclear targets at HERMES, could start as early as 1999. Test experiments can be prepared during the on-going programme of spin-structure functions measurements.

References

[1] M. Düren, *Effect of the Electron Beam Tails at the HERMES Collimators*, DESY-HERMES 90-01 (1990).

[2] M. Arneodo, Phys. Rep. 240 (1994) 301.

[3] L.S. Osborne *et al.*, Phys. Rev. Lett. 40 (1978) 1624.

[4] T.G. O'Neill and G. van der Steenhoven, *Proposal for Unpolarized A > 3 Running at HERMES*, DESY-HERMES 96-16 (1996); and contribution to this workshop (working group 8) on *Color Transparency and Quark Propagation*

[5] B. Kopeliovich, J. Nemchik and E. Predazzi, contribution to this workshop (working group 8) on *Hadronization in Nuclear Environment.*

[6] N. Pavel, contribution to this workshop (working group 8) on *Study of Hadronization in Deep-Inelastic Lepton-Nucleus Scattering at HERMES*

[7] M.R. Adams *et al.*, Phys. Rev. Lett. 74 (1995) 5198.

[8] M. Strikman, M.G. Tverskoy, M. Zhalov, contribution to this workshop (working group 8) on *Soft Neutron Production - a window to the Final State Interaction in Deep-Inelastic Scattering*

[9] J. Hüfner andd B. Kopeliovich, contribution to this workshop (working group 8) on *Towards Study of Color Transparency with Medium Energy Electron Beams.*

[10] L. Frankfurt, M. Sargsian, M. Strikman, contribution to this workshop (working group 8) on *Near Threshold Large Q^2 Electroproduction off Polarized Deuterium.*

[11] L. Frankfurt, W. Koepf, J. Mutzbauer, G. Piller, M. Sargsyan, M. Strikman, contribution to this workshop (working group 8) on *Coherent ρ^0 production from polarized deuterium.*

[12] The HERMES collaboration, *HERMES Technical Design Report*, July 1993.

[13] R.M. Woloshyn, Nucl. Phys. **A496** (1989) 749.

[14] G.D. Bosveld, A.E.L. Dieperink, O. Scholten, Phys. Rev. **C 45** (1992) 2616.

[15] G.D. Bosveld, A.E.L. Dieperink, A.G. Tenner, Phys. Rev. **C 49** (1994) 2379.

[16] L.L. Frankfurt and M. Strikman, Phys. Rep. **76** (1981) 215.

[17] S. Simula, *Semi-Inclusive Deep Inelastic Scattering off the Deuteron and the Neutron to Proton Structure Function Ratio*, INFN-ISS 96/2, and contribution to this workshop (working group 8) on *Investigation of the neutron structure function via semi-inclusive deep inelastic scattering off the deuteron.*

[18] W. Melnitchouk and A.W. Thomas, Phys. Lett. **B 377** (1996) 11.

[19] W. Melnitchouk, M. Sargsian, M. Strikman, contribution to this workshop (working group 8) on *Tagged-Structure Functions of the Deuteron and the origin of the EMC effect*

[20] J. Guy et al, Phys. Lett. **B 229** (1989) 421.

[21] S. Simula, contribution to this workshop (working group 8) on *Semi-Inclusive Deep Inelastic Scattering off Nitrogen.*

[22] A.E.L. Dieperink, contribution to this workshop (working group 8) on *Pobing the nucleon meson-cloud in semi-inclusive deep inelastic scattering: tagging of ^{3}He*

[23] R.S. Hicks and G. van der Steenhoven, *The measurement of nuclear decay products in deep inelastic reactions*, NIKHEF-HERMES internal note (1991).

[24] K. Gottfried, Phys. Rev. Lett. **18** (1967) 1174.

[25] P. Amaudruz at al., Phys. Rev. Lett. **66** (1991) 2712; A. Baldit et al., Phys. Lett. **B 332** (1994) 244.

[26] A.W. Thomas, Phys. Lett. **126 B** (1983) 97.

[27] W. Melnitchouk and A.W. Thomas, contribution to this workshop (working group 8) on *Meson Cloud Signatures in Semi-Inclusive Deep-Inelastic Scattering from Polarized Nucleons.*

Color Transparency and Quark Propagation

T. G. O'Neill[a] and G. van der Steenhoven[b]

[a] Argonne National Laboratory, Argonne, Illinois 60439, United States of America
[b] NIKHEF, P.O. Box 41882, 1009 DB Amsterdam, The Netherlands

Abstract: Experiments with unpolarized nuclear targets at HERMES can be used to obtain data on exclusive ρ^0 electroproduction and semi-inclusive hadron production. The $A(e,e'\rho^0)$ data have the potential of providing evidence for the color transparency hypothesis. The semi-inclusive data can provide detailed information on the effect of the nuclear medium on quark propagation. Estimates are presented of the data quality that can be obtained for a range of nuclear targets.

1 Introduction

During its first year of operation the HERMES experiment has demonstrated its capability for measuring nucleon spin-structure functions in deep-inelastic scattering. The same apparatus can also be used for measurements on unpolarized $A > 3$ nuclear gas targets, in which the nuclear medium acts as a probe of non-perturbative QCD effects. In particular, the effect of the nuclear medium on hadron production in deep-inelastic scattering can be studied. The prospects for two such experiments at HERMES are discussed in this paper.

In semi-inclusive deep-inelastic scattering the struck quark will propagate over a certain distance (and time) before interactions with other quarks (and gluons) lead to the production of the detected hadron. When the quark propagation process is embedded in the nuclear medium, the number of hadrons produced will depend on the interaction of the propagating quark with neighboring nucleons. Experiments at SLAC [1] and CERN [2] have yielded first evidence for a modification of the quark-propagation process in the nuclear medium. Semi-inclusive measurements at HERMES on various nuclear targets will enable a systematic study of quark-propagation, thus providing the first quantitative data on the formation time $\tau_{\rm form}$.

Exclusive ρ^0 electroproduction on nuclei is expected to be a sensitive means of searching for color transparency, the proposed reduction of initial and final state interaction effects in nuclei due to the formation of a hadron of small initial transverse size. Data from the recent Fermilab deep-inelastic muon scattering experiment E665 contain a hint of color transparency in the reaction $A(\mu,\mu'\rho^0)$ [3]. Compared to E665, $A(e,e'\rho^0)$ measurements at HERMES have the advantage of higher statistical precision and considerably better missing energy resolution ($\sim 0.5\,$GeV instead of 5 GeV), which should allow improved exclusion of contamination from other reaction channels. Moreover, at HERMES the data can also be used to determine $\tau_{\rm exp}$, the time it takes for an exclusively produced ρ^0 meson to expand from an initial color-transparent

point-like configuration to its usual size. The expansion time is closely related to the hadron formation time $\tau_{\rm form}$, and is probably similar in magnitude. The proper times $\tau_{\rm form}$ and $\tau_{\rm exp}$ are fundamental properties determined by hadron internal dynamics, and should not vary with kinematics or target.

2 Color Transparency in $A(e,e'\rho^0)$

The nuclear transparency T_A is defined as the ratio of the measured exclusive cross section to the cross section in the absence of initial and final state interactions (ISI and FSI). It can be measured by taking the ratio of nuclear per-nucleon to free nucleon cross sections:

$$T_A = \frac{\sigma_A}{A\sigma_N}. \qquad (1)$$

Elastic and inelastic ISI and FSI can move flux out of the experimental acceptance or from exclusive to non-exclusive channels, resulting in $T_A \leq 1$. In 1982 Mueller and Brodsky [4] proposed the color-transparency effect: the ISI and FSI should be suppressed at high Q^2 and ν because the exclusive reaction selects or produces hadrons in a spatially small, non-interacting state (the point-like configuration or PLC). Three experiments have searched for the resulting increase in the nuclear transparency, using the reactions $A(p,2p)$ [5], $A(e,e'p)$ [6], and $A(\mu,\mu'\rho^0)$ [3]. None has yielded a consistent, unambiguous confirmation of the phenomenon.

There are three necessary conditions for color transparency: (i) the exclusive reaction mechanism must select or produce hadrons of reduced transverse size (the point-like configuration); (ii) the small hadrons must experience reduced initial and final-state interactions (color screening); and (iii) the hadrons must remain small long enough to produce a detectable enhancement of nuclear transparency. Color screening is fairly well-justified experimentally and theoretically for all three reactions [4]. Dominance of the point-like configuration in the reaction mechanism at moderate Q^2 values is on much stronger theoretical ground for the reaction $A(e,e'\rho^0)$ than for the reactions $A(p,2p)$ and $A(e,e'p)$. Qualitatively this can be understood from the mechanism that is assumed to dominate the exclusive, incoherent $A(e,e'\rho^0)$ reaction, i.e. a ρ^0 meson is produced as a fluctuation of a short-wavelength virtual photon into a small-sized quark-antiquark pair.

Count rates for exclusive, incoherent ρ^0 production were estimated on the basis of the preliminary analysis of the 1995 HERMES data for ρ^0 production on ^{3}He. The A-dependence observed in the Fermilab E665 $A(\mu,\mu'\rho^0)$ [3] experiment were used to extrapolate the rates to different nuclei. Figure 1 shows the expected precision for nuclear transparency measurements, assuming that σ_N is determined from the ^{1}H and ^{2}H data only (we expect $T_{^2\rm H} \approx 1$). A month of data taking for each target is assumed, where one month is assumed to contain 30 fills of 6.7 hours each, with an average current of 20 mA. For the target thickness the maximum number of nucleons per cm^2 commensurate with a HERA positron life time of 45 hours is taken. Expected improvements in the extraction of $A(e,e'\rho^0)$ events should lead to significantly better statistical accuracy than shown in the figure.

If color transparency is observed, the nuclear transparency $T_A(Q^2,\nu)$ at high Q^2 will exhibit a dependence on ν. At low ν the ISI and FSI correspond to those of the ρ^0-meson, while at high ν, T_A probes the much weaker interaction of the point-like configuration. The midpoint in the variation in T_A occurs at lab frame expansion time $t_{\rm exp} = \gamma\tau_{\rm exp} \approx R_A$. For typical

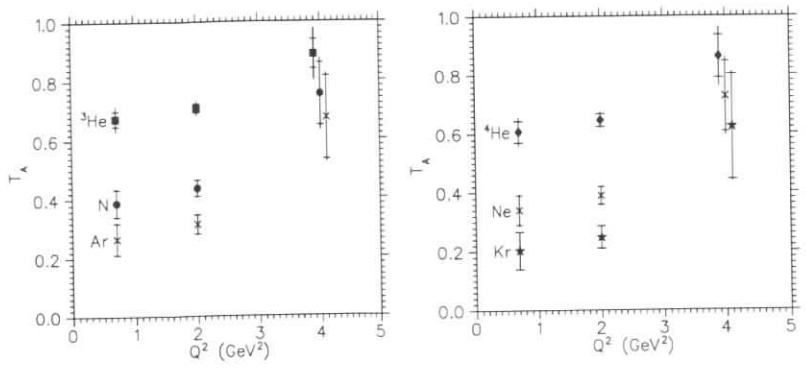

Figure 1: *Nuclear transparency T_A for the candidate $A > 3$ targets, with errors expected after 30 fills. The inner error bars show the errors expected in the limit of very large statistics on ^1H (applicable in the case of future ^1H data from a laser-driven source).*

PLC expansion models, this is approximately where $dT_A/d\nu$ is largest and sensitivity to $\tau_{\rm exp}$ is maximal:

$$\tau_{\rm exp} \approx \frac{R_A}{\gamma} \approx \frac{R_A M_p}{\nu}. \tag{2}$$

Therefore, HERMES not only has the potential of observing evidence for color transparency, but also first measurements of the expansion time τ_{exp} can be obtained.

3 Quark Propagation

The process of hadron formation in deep inelastic scattering cannot be calculated from first principles as it occurs at energy-momentum scales where pQCD is not applicable. Consequently phenomenological models have been developed to describe the process. In these models a formation time $\tau_{\rm form}$ is introduced representing the time between the primary hard interaction and the actual formation of the observed hadron. By embedding the hadron-formation process in the nuclear medium, one obtains an experimental tool to modify the formation process and thus obtain information on $\tau_{\rm form}$. In this section the prospects for such measurements at HERMES are discussed.

Experimental studies of quark-propagation inside the nuclear medium involve (among other observables) measurements of the "attenuation" ratio R_A of hadrons produced in semi-inclusive deep inelastic scattering off nuclear target A and the same yield measured on deuterium (D):

$$R_{\rm A}(z) = (\frac{1}{\sigma_A}\frac{d\sigma_A}{dz})/(\frac{1}{\sigma_D}\frac{d\sigma_D}{dz}), \tag{3}$$

where $d\sigma/dz$ is the cross section for the production of a hadron with fraction z of the energy transfer, and σ_A is the cross section for production of all hadrons. Note that R_A is the semi-inclusive analogue of the nuclear transparency in exclusive reactions such as $A(e, e'\rho^0)$. Due to reinteractions of the propagating quarks with the surrounding medium the quantity $R_{\rm A}(z)$

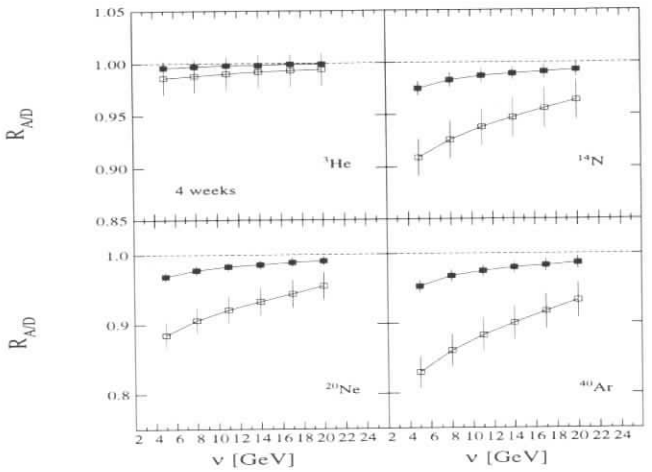

Figure 2: *Attenuation ratios for four different target nuclei. The solid (open) squares represent the results for detection of leading pions (protons). The error bars correspond to 30 fills at 20 mA average current with target thicknesses correponding to a 45 hr electron-beam lifetime.*

will be less than unity. The probability of such reinteractions is determined by the product of the quark-nucleon cross section σ_{qN} and the pathlength $l_{\rm form}$ traversed. Hence, a systematic study of $R_{\rm A}(z)$ for various nuclei should provide quantitative information on σ_{qN} and $l_{\rm form}$, or—equivalently—the time $\tau_{\rm form}$.

In the literature quite a few models have been proposed to describe quark propagation in the medium. Good overviews can be found in refs. [7], [8], and [9]. For our present purposes we will only consider the formulation proposed by Low and Gottfried [10]:

$$t_{\rm form} = \gamma\tau_{\rm form} \approx \left(\frac{E_h}{M_h}\right)\tau_{\rm form} = \frac{z\nu}{M_h}\tau_{\rm form}, \tag{4}$$

where γ is the Lorentz factor, and E_h and M_h represent the energy and mass of the detected hadron. In order to ensure that the detected hadron is a fragmentation product of the struck quark a *leading* hadron must be selected, *i.e.* $z = E_h/\nu > 0.5$. Using this expression for $t_{\rm form}$ (and assuming $\sigma_{qN} = 0$) the experimental prospects for measurements of $R_{\rm A}(z)$ have been investigated.

Monte-Carlo simulations were performed with a modified version of the PEPSI code for selected nuclear targets. The acceptance of HERMES was only crudely implemented, omitting all details incorporated in a full Monte Carlo. On the basis of these simulations we have evaluated attenuation ratios for all gaseous nuclear targets mentioned in section 2. Selected results are displayed in figure 2 for leading pions and protons. The error bars displayed are based on the equivalent of 30 fills of running time at 20 mA beam average current and the maximum target thicknesses allowed by electron beam lifetime considerations. Hence, the simulated data correspond to the same running conditions as were used in section 2. The uncertainties also

include a contribution from the ^{2}H data, *i.e.* it is assumed that the equivalent of 30 fills of unpolarized ^{2}H data at $n = 1.0 \times 10^{15}$ atoms/cm^2 is available.

In doing the simulations the following cuts were imposed: (i) $z \geq 0.5$; (ii) $Q^2 \geq 1.0$ (GeV/c)^2; and $W \geq 2$ GeV. These cuts ensured the selection of semi-inclusive deep inelastic scattering events with a leading hadron that can be associated with the current quark.

As expected from the chosen expression of $t_{\rm form}$ the results show a strong dependence on the hadron type. In particular the protons are very sensitive to the medium effects. We conclude that data of the quality displayed in figure 2 will be a sensitive tool in selecting the appropriate model for quark-propagation processes.

4 Conclusion

The quality of the data that can be obtained at HERMES under standard beam conditions for measurements of transparency factors for exclusive incoherent ρ^0 production and semi-inclusive production of leading pions and protons has been evaluated. It has been shown that the equivalent of one month of data taking will yield data that could provide evidence of color transparency. At the same time the ν-distributions of semi-inclusively produced hadrons will provide information on the influence of the nuclear medium on quark propagation. Such data can be used to determine the hadron expansion and formation times.

References

[1] L.S. Osborne *et al.*, Phys. Rev. Lett. 40 (1978) 1624.

[2] M. Arneodo, Phys. Rep. 240 (1994) 301.

[3] M.R. Adams *et al.*, Phys. Rev. Lett. 74 (1995) 1525.

[4] A. H. Mueller, in: *Proceedings of the XVII Rencontre de Moriond, 1982*, ed. J. Tran Thanh Van (Editions Frontières, Gif-sur-Yvette, France, 1982) p. 13; S. J. Brodsky, in: *Proceedings of the Thirteenth International Symposium on Multiparticle Dynamics*, eds. W. Kittel, W. Metzger, and A. Stergiou (World Scientific, Singapore, 1982) p. 963.

[5] A. S. Carroll *et al.*, Phys. Rev. Lett. 61 (1988) 1698.

[6] N. C. R. Makins *et al.*, Phys. Rev. Lett. 72 (1994) 1986; T. G. O'Neill *et al.*, Phys. Lett. B 351 (1995) 87.

[7] A. Bialas, Proc. of the Topical Conference on *Electro- nuclear Physics with Internal Targets*, SLAC, Stanford 1989, p. 65.

[8] N.A. Pavel, Nucl. Phys. A 532 (1991) 465C.

[9] G. Anton *et al.*, in *The ELFE project, an Electron Laboratory for Europe*, Conference Proceedings of the Italian Physical Society, Vol. 44, eds. J. Arvieux and E. de Sanctis, Mainz, 7-9 October 1992, p. 333.

[10] F.E. Low and K. Gottfried, Phys. Rev. D 17 (1978) 2487.

Hadronization in Nuclear Environment

Boris Kopeliovich[ab], Jan Nemchik[cd] and Enrico Predazzi[c]

[a] Max-Planck Institut für Kernphysik, Postfach 103980, 69029 Heidelberg, Germany
[b] Joint Institute for Nuclear Research, Dubna, 141980 Moscow Region, Russia
[c] Università di Torino and INFN, Sezione di Torino, I-10125, Torino, Italy
[d]Institute of Experimental Physics SAV, Solovjevova 47, CS-04353 Kosice, Slovakia

Abstract: We present a space-time description of hadronization of highly virtual quarks originating from a deep-inelastic electron scattering (DIS). Important ingredients of our approach are the time- and energy–dependence of the density of energy loss for gluon radiation, the Sudakov's suppression of no radiation, and the effect of color transparency, which suppresses final state interaction of the produced colorless wave packet. The model is in a good agreement with available data on leading hadron production off nucleons and nuclei. The optimal energy range for study of the hadronization dynamics with nuclear target is found to be a few tens of GeV, particularly energies available in the experiment HERMES.

A quark originated from a hard process, converts into colorless hadrons owing to confinement. Lorentz dilation stretches considerably the duration of this process. While hadrons carry a little information about the early stage of hadronization, a nuclear target, as a set of scattering centres, allows us to look inside the process at very short times after it starts. The quark-gluon system produced in a hard collision, interacts while passing through the nucleus. This can yield precious information about the structure of this system and the space-time pattern of hadronization.

The modification of the quark fragmentation function in nuclear matter was considered for high-p_T hadron production in [1, 2], for deep-inelastic lepton scattering in [3, 4, 5], and for hadroproduction of leading particles on nuclei in [6, 7]. The data are usually presented in the form,

$$R_{A/N} = \frac{D_{eff}(z_h, p_T)}{A\, D(z_h, p_T)}, \qquad (1)$$

where $D(x, p_T)$ and $D_{eff}(x, p_T)$ are the quark fragmentation function in vacuum and in a nucleus, respectively.

We treat hadronization of a highly virtual quark, perturbatively a gluon bremsstrahlung and the deceleration of the quark as a result of radiative energy loss. We assume that subsequent hadronization of the radiated gluons, which includes the nonperturbative stage, does not affect the energy loss of the quark.

The radiation of a gluon takes the time

$$t_r \approx \frac{2\nu}{k_T^2}\alpha(1-\alpha)\,. \qquad (2)$$

This expression follows from the form of the energy denominator corresponding to a fluctuation of a quark of energy ν into a quark and a gluon, having transverse momenta k_T and relative shares of the initial light-cone momentum α and $1-\alpha$, respectively. If one calculates radiated energy taking into account condition (2) one arrives at the density of energy loss per unit of length, which turns out to be energy and time independent [8] like in the string model.

In the case of inclusive production of leading particles at $z_h \to 1$, however, energy conservation forbids the radiation of gluons with energy greater than $(1-z_h)\nu$. Then, the time dependence of the radiative energy loss can be written as

$$\Delta E_{rad}(t) = \int_{\lambda^2}^{Q^2} dk_T^2 \int_0^1 d\alpha\ \alpha\nu \frac{dn_g}{d\alpha dk_T^2} \Theta(1-z_h-\alpha)\ \Theta(t-t_r)\,, \tag{3}$$

where $dn_g/d\alpha dk_T^2 = \epsilon/\alpha k_T^2$ represents the distribution of the number of gluons. The factor $\epsilon = 4\alpha_S(k_T^2)/3\pi$.

Although soft hadronization is usually described in terms of the string model, we model it by radiation as well, choosing the bottom limit λ^2 in (3) small. We fix the QCD running coupling $\alpha_S(k_T^2) = \alpha_S(k_0^2)$ at $k_T^2 \le k_0^2$, in the region which is supposed to be dominated by nonperturbative effects. the parameter $k_0 \approx 0.7\ GeV$ is chosen to reproduce the density of energy loss for radiation of soft gluons ($k_T^2 \le k_0^2$) corresponding to the string tension, $dE/dt =) \approx 1\ GeV/fm$. This value of k_0 is consistent with the transverse size of a string corresponding to the gluon-gluon correlation radius, $R_c \sim 1/k_0 \sim 0.3$ fm suggested by QCD lattice results.

After integrating eq. (3) in the soft radiation approximation, we get

$$\Delta E_{rad}(t) = \frac{\epsilon}{2} t(Q^2-\lambda^2)\Theta(t_1-t) + \epsilon\nu(1-z_h)\Theta(t-t_1) +$$
$$\epsilon\nu(1-z_h)\ln\left(\frac{t}{t_1}\right)\Theta(t-t_1)\Theta(t_2-t_1) + \epsilon\nu(1-z_h)\ln\left(\frac{Q^2}{\lambda^2}\right)\Theta(t-t_2) \tag{4}$$

Here we have set $t_1 = (1-z_h)/x_{Bj}m_N$ and $t_2 = t_1\ Q^2/\lambda^2$, where x_{Bj} is the Bjorken variable.

Eq. (4) shows that for $t \le t_1$, the density of energy loss is constant, $dE/dt = -\epsilon Q^2/2$, exactly as in the case with no restriction on the radiated energy [4, 5]. At longer time intervals, $t > t_1$ more energetic gluons can be radiated and the restriction $\alpha < 1-z_h$ becomes important. As a result, the density of energy loss slows down to $dE/dt = -\epsilon\nu(1-z_h)/t$ which is a new result compared to what was known in the string model. At still longer $t > t_2$, no radiation is permitted, but obviously a color charge cannot propagate a long time without radiating which must be suppressed by a Sudakov's type formfactor. Assuming a Poisson distribution for the number of emitted gluons we get the formfactor, $F(t) = \exp[-\bar{n}_g(t)]$, where $\bar{n}_g(t)$ is the number of non radiated gluons,

$$\bar{n}_g(t) = \epsilon\left[\frac{t}{t_1} - 1 - \ln\left(\frac{t}{t_1}\right)\right]\Theta(t-t_1)\,. \tag{5}$$

In order to calculate a time interval for the leading hadron production (or, better, a colorless ejectile which does not loose energy anymore), one needs a model of hadronization and of color neutralization. In the large N_c limit, each radiated gluon can be replaced by a $q\bar{q}$ pair, and the whole system can be treated as a system of color dipoles. It is natural to assume that the leading (fastest) hadron originates from a $q\bar{q}$ dipole made of the leading quark and of the antiquark coming from the last emitted gluon. This dipole is to be projected into the hadron wave function, $\Psi(\beta, l_T)$, where β and $1-\beta$ are the relative shares of the light-cone momentum

carried by the quarks, and l_T is the relative transverse momentum of the quarks. The result of this projection leads to the fragmentation function of the quark into the hadron, which reads

$$D(z_h) = \int_0^\infty dt W(t,\nu,z_h)\,, \tag{6}$$

where $W(t,\nu,z_h)$ is a distribution function of the leading hadrons over the production time t.

$$W(t,\nu,z_h) \ \propto\ \int_0^1 \frac{d\alpha}{\alpha}\,\delta\left[\alpha - 2\left(1-\frac{z_h\nu}{E_q(t)}\right)\right]\int\frac{dk_T^2}{k_T^2}\,\delta\left[k_T^2 - \frac{2\nu}{t}\alpha(1-\alpha)\right]\times$$
$$\int dl_t^2\ \delta\left[l_T^2 - \frac{9}{16}k_T^2\right]\int_0^1 d\beta\delta\left[\beta - \frac{\alpha}{2-\alpha}\right]|\Psi_h(\beta,l_T)|^2\,. \tag{7}$$

Here the quark energy $E_q(t) = \nu - \Delta E_{rad}(t)$. We have chosen a hadronic wave function in the light-cone representation which satisfies the Regge end-point behaviour, $|\Psi_h(l_T^2,\beta)|^2 \propto \sqrt{\beta}\sqrt{1-\beta}(1+l_T^2 r_h^2/6)^{-1}$, where r_h is the charge radius of the hadron.

Fig.1 shows function $W(t)$ for several values of z_h and exhibits the approximate $(1-z_h)\nu$-scaling of the mean production time, $t_{pr} = \int dt\ t\ W(t)$, which depends weakly on Q^2 and vanishes at $z_h \approx 1$.

Our predictions for the fragmentation function $D(z_h)$ depicted in Fig. 2 nicely agrees with the EMC data [9].

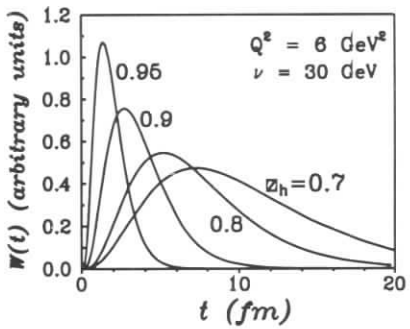

Figure 1: *Distribution of the hadron production time at $\nu = 30\ GeV$, $Q^2 = 6\ GeV^2$ and $z_h = 0.70 \div 0.95$*

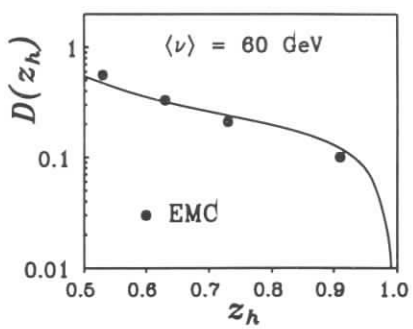

Figure 2: *Comparison of our prediction for $D(z_h)$ with data [13]*

The production of the leading colorless wave packet with the desired (detected) momentum completes the process of hadronization. Any subsequent inelastic interaction is forbidden, otherwise a new hadronization process begins and the leading hadron energy falls to lower values. Such a restriction means a nuclear suppression of the production rate.

On the other hand, soft interactions of the leading quark during the hadronization in nuclear matter cannot stop or absorb the leading quark [10]. Although rescatterings of the quark in the nucleus result in an additional induced soft radiation, [10, 11], at the same time the quark

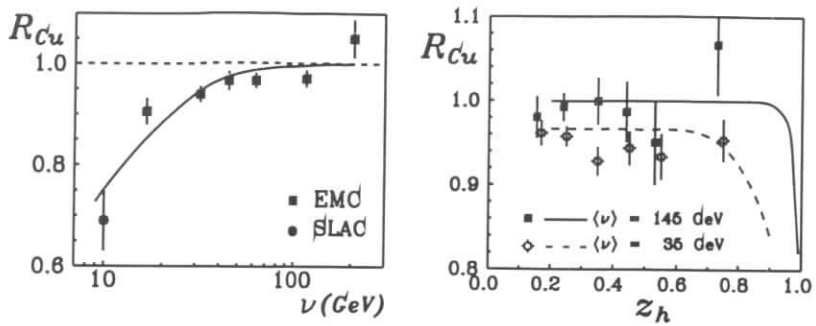

Figure 3: *Comparison of our calculations for the ν-dependence of nuclear suppression (1) integrated over z_h at $Q^2 = 6$ GeV^2 with data [13,14]*

Figure 4: *z_h-dependence of nuclear suppression.*

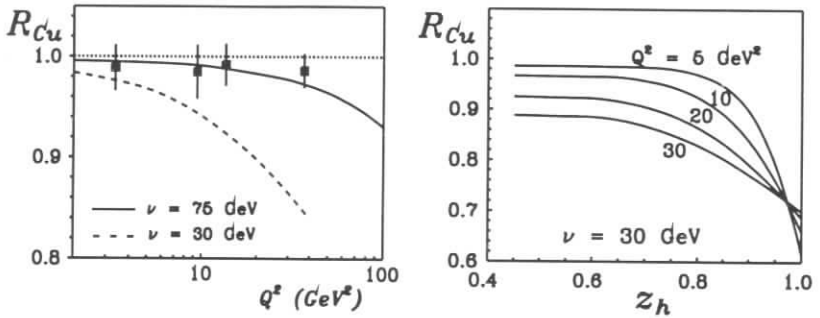

Figure 5: *Predictions for the Q^2 dependence of nuclear transparency at $\nu = 30$ and 75 GeV. Data [14] at $\nu = 75$ GeV are integrated over z_h*

Figure 6: *Predictions for the z_h dependence of nuclear transparency at $\nu = 30$ GeV vs Q^2*

looses much more energy due to the hard gluon radiation following the deep-inelastic scattering just as in vacuum. Thus, the induced soft radiation can be treated as a small correction to the energy loss and can be neglected, provided Q^2 is high enough.

The transverse size of the colorless wave packet produced in a hard reaction can be small, therefore the nuclear suppression is weaker due to color transparency. We take into account the evolution of the wave packet during its propagation through the nucleus using the path integral technique developed in [12]. Figs. 3 - 5 show quite a good agreement of our parameter-free calculations with available data [13, 9] on the ν-, z_h- and Q^2-dependence of nuclear suppression. Unfortunately, there is still no data in the region, $z_h > 0.8$.

Note that at high energies many of interesting effects go away or are difficult to observe.

Nuclear suppression integrated over z_h vanishes (see Fig. 3). The region of high z_h, where nuclear suppression is expected to be enhanced (see Fig. 4) squeezes at high ν towards $z_h = 1$, where the cross section vanishes. There is almost no Q^2-dependence at high ν and moderate values of Q^2 (see Fig. 5).

We present in Figs. 5 and 6 our predictions for the Q^2 and z_h dependence of nuclear suppression for the energy range of the HERMES experiment. We expect the onset of nuclear effects at moderate values of Q^2 (Fig. 5) as well as in the region of $z_h > 0.8$ (Fig. 6), which can be tested by the HERMES experiment.

To conclude, we have developed a phenomenology of electroproduction of leading hadrons on nuclei which is based on the perturbative QCD. Our parameter-free model is in a good agreement with available data. We stress that the energy range of the HERMES experiment is especially sensitive to the underlying dynamics of hadronization.

References

[1] B.Z. Kopeliovich, F. Niedermayer, *Yad. Fiz.* **42** (1985) 797.

[2] V.T. Kim, B.Z. Kopeliovich, *JINR preprint* **E2-89-727** (1989) Dubna.

[3] A. Bialas, J. Czyzewski, *Phys. Lett.* **B222** (1989) 132.

[4] B.Z. Kopeliovich and J. Nemchik, "Hadronization of Highly Virtual Quarks in Nuclear Matter", JINR preprint **E2-91-150**, Dubna, 1991.

[5] B.Z. Kopeliovich and J. Nemchik, "Color Transparency and Hadron Formation Length in Deep-Inelastic Scattering on Nuclei", Preprint SANITA, **INFN-ISS 91/3**, Rome, 1991.

[6] A. Bialas, M. Gyulassy, *Nucl. Phys.* **B291** (1987) 793.

[7] B.Z. Kopeliovich, L.B. Litov, J. Nemchik, *Int. J. Mod. Phys.* **E2** (1993) 767.

[8] F. Niedermayer, Phys. Rev. **D34** (1986) 3494.

[9] EMC-CERN, J. Ashman et al., Z. Phys. C **52** (1991) 1.

[10] B.Z. Kopeliovich, *Phys. Lett.* **B243** (1990) 141.

[11] M. Gyulassy and X.-J. Wang, Nucl. Phys. **B420** (1994) 583

[12] B.Z. Kopeliovich and B.G. Zakharov, Phys. Rev. **D44** (1991) 3466.

[13] L.S. Osborne et al., Phys. Rev. Lett. **40** (1978) 1624.

Study of Hadronisation in Deep Inelastic Lepton-Nucleus Scattering at HERMES

Nikolaj A. Pavel

Imperial College, Blackett Laboratory, Prince Consort Road, London SW7 2BZ

Abstract: Precise experimental data on hadron distribution from deep inelastic electron-nucleus (eA) scattering in the range of relatively low transfered energy $\nu \lesssim 25$ are needed to investigate the space-time structure of the hadronisation process and to test models concerning quark interaction in nuclear matter. An answer to theses question is of fundamental interest and would help to better understand the hadron production in more complex reactions e.g. heavy ion collisions. Here the idea and aims of such experiment at HERMES are discussed.

1 Introduction

The production of hadrons from excited quarks, which is observed in high energy collisions, is a process, which still cannot be calculated by any theory. Although QCD is well established as the theory to describe the interaction between quarks, the hadron formation process itself cannot be approached by existing techniques of pertubative QCD, since Q^2, the square of the four-momentum transfer is much smaller than the QCD-scale Λ_{QCD}. Various models have been developed to circumvent this problem. They reproduce many details of the hadron distributions measured in deep inelastic scattering (DIS) and e^+e^-annihilation. However, for a deeper understanding of this process it is necessary to answer fundamental questions such as of the space-time structure of the hadronisation and the nature of the quantum state just before the final state hadrons exist in the form, in which they are observed them in the detector.

Results from e^+e^-collision and lepton-proton deep inelastic scattering (DIS) experiments are well suited to study correlations amongst the final state hadrons and to test fine details of the models, but not to address the above quesitons. In DIS on nuclei, however, one can benefit from secondary interaction of the final state particles for the investigation. Hadrons produced instantaneously at the γ^*-parton interaction point would would undergo rescattering in the nuclear matter and the observed hadron spectra would become softer. If the hadrons are in parts produced outside the nucleus because of a finite hadron formation time τ_h, this softening becomes smaller and eventually vanishes.

The picture becomes more complicated, it one also considers a possible interaction of the constituent quarks of the hadron with the nuclear matter and a finite time τ_c, after which these constituent quarks appear (see Fig.1 for an illustration).

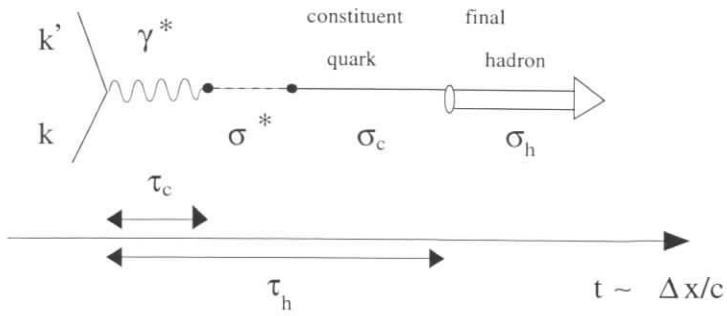

Figure 1: Illustration of the different time scales and interaction cross sections involved in space-time structure of the hadronisation. σ_h is assumed to be the π-nucleon cross section above the resonances (≈ 20 mb), σ_c and σ^* are the cross section of constituent quarks and for a possible interaction before the constituent quarks exist. k, k' are the four momenta of the incoming and scattered lepton.

variable	description
$Q^2 = -(k-k')^2 = -q^2$	square of four momentum transfer
$\nu = (Pq)/(Pk)$	energy of the boson exchanged (energy transfer in target rest frame)
$x = Q^2/(2Pq) = Q^2/(2M_{nucleuon}\,\nu)$	Bjorken scaling variable
$z_h = E_{had}/\nu$	fraction of the photon energy carried by a hadron, where E_{had} is the hadron energy in the target rest frame

Table 1: Kinematic variables in DIS used in this text; k, k' and P are the four momenta of the incoming (scattered) electron and the target nucleon respectively.

The target nucleus in DIS can be used is as a kind of passive 'detector' at the scale of some fermi to test the various models of the space-time structure and quark reinteraction. . In contrast to hadron scattering no deconvolution of the distributions of the projectile and target fragmentation particles has to be made, so that differences in the hadron distributions in DIS on different nuclei can most directly reflect nuclear effects in the hadronisation.

2 Experiments on Lepton-Nucleus Scattering in the Past

Hadron distributions in lepton-nucleus scattering have been investigated in several DIS experiments in the range of the energy transfer ν between ~ 5 and ~ 400 GeV (for a review see [1, 2]). (The kinematic variables used in this paper are explained in Tab.1.) Fig.2 shows the ν dependence of the ratio of forward charged hadron mulitiplicities ($z_h > 0.2$) on copper and deuterium. For $\nu < 25$ GeV a strong reduction of the hadron multiplicity in DIS on copper is observed which can be explained by inelastic intranuclear reaction of final state hadrons so that the z_h spectra of hadrons for lepton-nucleus scattering becomes softer as compared to DIS on free nucleons. This effect vanishes at $\nu \gtrsim 100$ GeV.

The data are compared with the several predictions for the space-time structure (see [3,

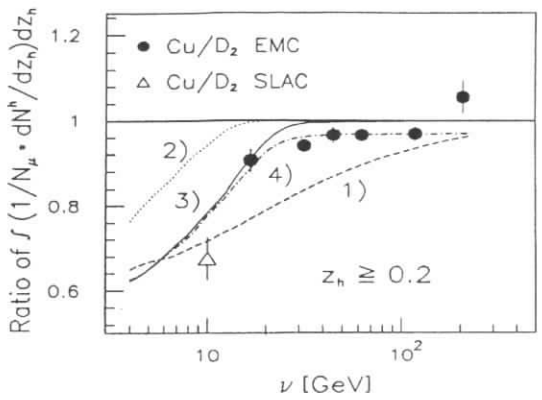

Figure 2: The ratio of the hadron multiplicity integrated over $z_h > 0.2$ for copper and deuterium as a function of ν. The data are compared with predictions of models for intranuclear reinteraction. (1): model with $\tau_h \propto E_{had}$, $\sigma_q = 0\,\mathrm{mb}$; (2-4) model with two scales τ_h, τ_c (string model [10]): (2) $\sigma_q = 0\,\mathrm{mb}$ (3) $\sigma_q = 20\,\mathrm{mb}$ in both cases $\sigma^* = 0\,\mathrm{mb}$ (4) (dashed-dotted line) $\sigma_q = 20\,\mathrm{mb}$ and $\sigma^* = 0.75\,\mathrm{mb}$.

1, 4] for details). The model with two time scales (τ_h, τ_c) as extracted from the Lund string fragmentation model [10] fits the ν dependence best. Date from ν-nucleus scattering [2] in the energy range from $8 < \nu < 64\,\mathrm{GeV}$ qualitatively confirm this result. In the mean time more elaborated models have been developed to calculate the energy loss of quarks by gluon radiation [5, 6, 7].

All experiments so far suffer from insufficient statistics, so that the distributions had to be integrated over large intervals of Q^2, x and/or z_h. In particular in the low energy range between ν $5 - 30\,\mathrm{GeV}$, where large nuclear effects have been observed, more precise data are requested to discriminate between the various theoretical concepts and ideas concerning the hadron formation time and a possible interaction during the preconfinement state.

3 HERMES as an Electron-Nucleus Scattering Experiment

It has been already pointed out earlier in time [1, 8, 9] that electron scattering experiments using a gas jet target in an intensive electron beam offers ideal conditions to measure hadron distributions in eA scattering with high statistical accuracy and minimal systematic errors. The gas jet target used in the HERMES experiment has a small longitudinal extension and the sort of gas (i.e. target nucleus) can be very easily and frequently changed so that systematic errors due to different detector acceptances for different targets are minimized. The effects of reinteraction of the final state hadrons inside the target and external Bremsstrahlung are small because of the density being much smaller in gas jet target than in any other kind of targets.

classes of models :		
models with 1 time scale : $\tau_h \propto \nu$ or $\propto z_h\nu$ free param.'s: σ_c	model with 2 time scales τ_h, τ_c from string model [10] free param.'s: σ_c,σ^*	gluon radiation from quark $\tau_h \propto \frac{\nu}{\kappa}(1 - z_h)$ κ = energy loss of quark per unit of path length κ is Q^2-dependent
experimental test:		
$r_A(z_h)\|_{\nu\ fixed}$ $z_h > 0.4$ $R_A(\nu)\|_{Q^2\ fixed}$ $z_h > 0.5, 0.7$	$R_A(\nu)\|_{Q^2\ fixed}$ $z_h > 0.5, 0.7$ determination of σ_c, σ^* (A-dependence)	$r_A(z_h)\|_{\nu,Q^2\ fixed}$ $z_h > 0.4$ $R_A(Q^2)\|_{\nu\ fixed}$ $z_h > 0.5, 0.7$

Table 2: Models for space-time structure of the hadronisation process and proposed measurements to investigate them. By $r_A(z_h)$ $(R_A(..))$ the ratio of z_h distributions $(1/N_{evt} * dN^h/dz_h)$ and the ratio of integrated z_h distributions $\int_{z_h,min}^1 1/N_{evt} * dN^h/dz_h$ are denoted respectively.

At the HERMES experiment the achievable luminosities allow to measure hadron multiplicities with $< 1\%$ statisitical errors for $z_h > 0.5$ in bins of $\Delta\nu \sim 2\,\mathrm{GeV}$ and $\Delta Q^2 \sim 2 - 3\,\mathrm{GeV}^2$ up to $Q^2 = 30\,\mathrm{GeV}^2$ in about 500 h data collecting time , which correspond to several months running time (see [11] for details). This comfortably permits to perform all the measurements outlined in Table 2. In addition valuable information about the interaction mechanism can be extracted from the measurement of the nuclear broadening of hadron transverse momentum p_t distributions (i.e. measuring $< p_t^2 >$ in eA scattering). Static forces which retard an undressed quark should lead only lead to change of the energy, whereas rescattering of either hadrons or quarks inside the nucleus would increase the value of $< p_t^2 >$.

The list of concepts concerning the space-time structure of the hadronisation and necessary measurements to test them, which is given in Table 2, is not meant to be complete but indicates the way how the data from a eA scattering experiment at HERMES would contribute to study the problems and questions rised in the introduction.

4 Conclusions

Measurements of hadron distributions from eA scattering in the HERMES experiment will provide most valuable and precise information about nuclear effects in the hadron production. The data are very much needed and important to investigate the question on the space-time structure of the hadron formation process and possible quark interaction in nuclear matter, since existing data are not precise enough or cover a higher energy range where nuclear effects are small. A better understanding of these aspects of the hadronisation is important not only on its own but also for the interpretation of the results from heavy ion collisions at high energies.

References

[1] N.A. Pavel, Nucl. Phys. A532 (1991) 465.

[2] BEBC WA21/WA59 Collab., W. Burkot et al., Z. Phys. C70 (1996) 47.

[3] N.A. Pavel, Ph.D. thesis, Univ. of Wuppertal WUB 89-24 (1989);
EMC coll., J. Ashman et al., Z. Phys. C52 (1991) 1.

[4] A. Bialas, M. Gyulassy, Nucl. Phys. B291 (1987) 793.

[5] B.Z. Kopeliovich, Phys. Lett. B243 (1990) 141.

[6] B.Z. Kopeliovich, F. Niedermayer, Yad. Fiz 42 (1985) 797.

[7] S.J. Bordsky, P. Hoyer, Phys. Lett. B298 (1993) 165.

[8] G. Anton et al., Proceedings of the Workshop on 'THE ELFE PROJECT', Mainz, 1993, ed. J. Arvieux, E. De Sanctis, page 333.

[9] N.A. Pavel, talk on the Workshop on the HERMES Project, DESY, 1993 (not published).

[10] T. Chmaj, Acta Phys. Pol. B18 (1987) 1131.

[11] T. O'Neill, G. van der Steenhoven, contribution to this workshop (working group 8).

Towards Study of Color Transparency with Medium Energy Electron Beams

Jörg Hüfner[a] and Boris Kopeliovich[bc]

[a] Inst. für Theor. Physik der Universität , Philosophenweg 19, 69120 Heidelberg, Germany
[b] Max-Planck Institut für Kernphysik, Postfach 103980, 69029 Heidelberg, Germany
[c] Joint Institute for Nuclear Research, Dubna, 141980 Moscow Region, Russia

Abstract: Interference between vector mesons electroproduced at different longitudinal coordinates leads within Glauber approximation to a Q^2-dependence of nuclear effects similar to what is expected to be an onset of color transparency (CT). We suggest such a mapping of the photon energies and virtualities, which eliminates the undesirable Q^2-variation and allows to measure a net CT effect.

We develop a multichannel evolution equation, which for the first time incorporates CT and the effects of the coherence length in the exclusive electroproduction of vector mesons.

1. Vector Meson production. Coherence length

Vector mesons electroproduced at different points separated by longitudinal distance Δz have a relative phase shift $q_c \Delta z$, where $q_c = (Q^2 + m_V^2)/2\nu$ is the longitudinal momentum transfer in $\gamma^* N \to VN$, Q^2 and ν are the virtuality and energy of the photon, respectively. Taking this into account one arrives at the well known formula for nuclear transparency, $Tr = \sigma_A/A\sigma_N$, for the coherent production of vector mesons off nuclei [1],

$$Tr_{coh} = \frac{(\sigma_{tot}^{VN})^2}{4A\sigma_{el}^{VN}} \int d^2b \left| \int_{-\infty}^{\infty} dz\ \rho(b,z)\ e^{iq_c z} \exp\left[-\frac{1}{2}\sigma_{tot}^{VN} \int_z^{\infty} dz' \rho(b,z') \right] \right|^2 \qquad (1)$$

In the low-energy limit $q_c \gg 1/R_A$ and destructive interference eliminates the coherent production. However, nuclear transparency (1) monotonically grows with energy and reaches value $Tr_{coh} = \sigma_{el}^{VA}/A\sigma_{el}^{VN}$. Numerical examples for nuclear transparency in coherent production can be found in [2, 3, 4].

Formula for nuclear transparency for incoherent quasielastic photoproduction of vector mesons in Glauber approximation derived only recently [4], reads

$$\begin{aligned} Tr_{inc} = {} & \frac{\sigma_{tot}^{VN}}{2A\sigma_{el}^{VN}} (\sigma_{in}^{VN} - \sigma_{el}^{VN}) \int d^2b \int_{-\infty}^{\infty} dz_2\ \rho(b,z_2) \int_{-\infty}^{z_2} dz_1\ \rho(b,z_1) \\ \times\ & e^{iq_L(z_2-z_1)} \exp\left[-\frac{1}{2}\sigma_{tot}^{VN} \int_{z_1}^{z_2} dz \rho(b,z) \right] \exp\left[-\sigma_{in}^{VN} \int_{z_2}^{\infty} dz\ \rho(b,z) \right] \\ + \ & \frac{1}{A\sigma_{in}^{VN}} \int d^2b \left[1 - e^{-\sigma_{in}^{VN} T(b)} \right] - Tr_{coh}\ , \end{aligned} \qquad (2)$$

In contrast to coherent production nuclear transparency (2) decreases with energy from $Tr_{inc} = \sigma_{in}^{VA}/A\sigma_{in}^{VN}$ at low energy ($q_c \gg 1/R_A$) down to value $Tr_{inc} = \sigma_{qel}^{VA}/A\sigma_{el}^{VN}$ at high energies ($q_c \ll 1/R_A$), where σ_{qel}^{VA} is the cross section of quasielastic VA scattering. Numerical examples are presented in [2, 3, 4].

Such an energy dependence is easily interpreted in terms of lifetime of the photon fluctuations, which propagate over the coherence length $l_c \sim 1/q_c$: at low energy ($l_c \ll R_A$) the vector meson appears deep inside the nucleus and covers then about a half of the nuclear thickness. At high energy the vector meson preexists as a photon fluctuation long time and propagates through the whole nuclear thickness, resulting in a more of absorption.

Variation of l_c may be caused by either its ν- or Q^2-dependence. In the latter case l_c decreases with Q^2 and the nuclear transparency grows, what is expected to be a signature of color transparency (CT) [5], a QCD phenomenon related to suppressed initial/final state interaction in a nucleus for a small-size colorless wave packet [6]. Examples for incoherent electroproduction of ρ-meson on xenon are shown in Fig. 1 (more examples are in [2, 3, 4]). The predicted Q^2-dependence is so steep that makes it quite problematic to observe an additional Q^2-dependence generated by the color transparency effects.

Note that the cross section of photoproduction of the vector mesons on nuclei is energy-dependent at low energy due to quark (Reggeon) exchanges. This is very easy to include in our calculations, but we neglect the energy-dependence for the sake of simplicity.

2. Beyond Glauber approximation. Formation length.

According to the uncertainty principle one needs (formation) time to resolve different levels, V, V'..., in the final state. Corresponding formation length $l_f \approx 2\nu/(m_{V'}^2 - m_V^2)$ is longer than the coherence length. It has a close relation to the onset of CT [7, 5], which is possible only if $l_f \geq R_A$. Note that a full CT effect at $Q^2 \gg m_V^2$ imposes a stronger condition $l_f m_V/\sqrt{Q^2} \gg R_A$. This is because a small size, $\sim 1/Q^2$, wave packet, decomposed over different V-meson states, includes all states up to $M^2 \sim Q^2$. Such a decomposition must be frozen by Lorentz time dilation up to the heaviest states, what leads to above condition within oscillatory model.

At medium energies and Q^2 one can expect only an onset of CT, i.e. a monotonic growth of $Tr(Q^2)$ with Q^2, which results mostly from interference of the two lowest states, V and V'. Inclusion of the second channel in the case of coherent production is quite simple and the results are presented in [3]. We concentrate on the incoherent electroproduction here. For the first time we present the evolution equation and its solution incorporating both the coherence and formation length effects, what is of a special importance in the intermediate energy range.

The solution of the general multichannel equation will be presented elsewhere. Here we consider the two-coupled-channel case. Since we have to sum over all final states of the nucleus, the propagation of the charmonium wave packet through the nucleus is to be described by density matrix $P_{ij} = \sum |\psi_i\rangle|\psi_j\rangle^+$. The wave function $|\psi_i\rangle$ has three components, γ^*, V and V'. The evolution equation reads,

$$i\frac{d}{dz}\hat{P} = \hat{Q}\hat{P} - \hat{P}\hat{Q}^+ - \frac{i}{2}\sigma_{tot}^{VN}\left(\hat{T}\hat{P} + \hat{P}\hat{T}^+\right) + i\sigma_{el}^{VN}\hat{T}\hat{P}\hat{T}^+. \qquad (3)$$

Here

$$\hat{Q} = \begin{pmatrix} 0 & 0 & 0 \\ 0 & q & 0 \\ 0 & 0 & q' \end{pmatrix} \; ; \quad \hat{T} = \begin{pmatrix} 0 & 0 & 0 \\ \lambda & 1 & \epsilon \\ \lambda R & \epsilon & r \end{pmatrix} \qquad (4)$$

are the longitudinal momentum transfer and scattering amplitude operators, respectively, where $q(q') = (m_{V(V')}^2 + Q^2)/2\nu$. For other parameters we use notations from [8], $r = \sigma_{tot}^{V'N}/\sigma_{tot}^{VN}$, $\epsilon = f(VN \to V'N)/f(VN \to VN)$ and $R = f(\gamma N \to V'N)/f(\gamma N \to VN)$. The value of parameter $\lambda = f(\gamma N \to V'N)/f(VN \to VN)$ is inessential, since it cancels in nuclear transparency. The boundary condition for the density matrix is $P_{ij}(z \to -\infty) = \delta_{i0}\delta_{j0}$. Note, the same eq. (3) reproduces Glauber approximation (2) when $\epsilon = 0$. It also calculates coherent production when one fixes $\sigma_{el}^{VN} = 0$.

Combination of the two effects of coherence and formation (onset of CT) lengths may provide an unusual energy behaviour of nuclear transparency. An example is shown in Fig. 2 for real photoproduction of ρ and ρ' on lead predicted by eq. (3). We try two models for the ρ and ρ' wave functions, the nonrelativistic oscillator and a relativized version: i) $r = 1.5$, $\epsilon = -0.5$, $R^2 = 0.074$ ($Q^2 = 0$) for the nonrelativistic oscillator; ii) $r = 1.25$, $\epsilon = -0.14$, $R^2 = 0.22$ for the relativized wave function [3]. We calculate the Q^2-dependence of R^2 in accordance with [3]. Our predictions for energy dependence of nuclear transparency for incoherent photoproduction of ρ and ρ' are shown in Fig. 2 for the two sets of parameters. While both variants give similar results for the ρ, we expect a nontrivial energy dependence for the ρ', which results from interplay of the effects of coherence and formation lengths. It turns out to be extremely sensitive to the form of the wave function. Thus, such kind of measurement may bring unique information about the structure of vector mesons.

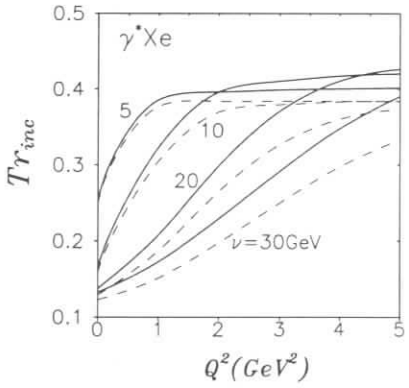

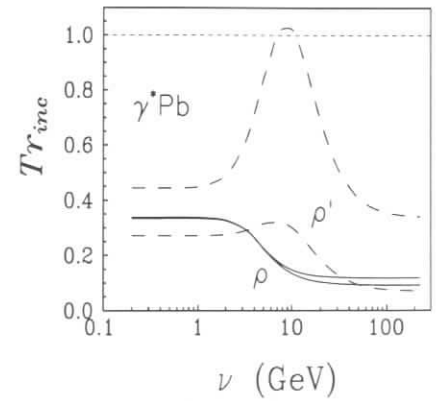

Figure 1: *Q^2-dependence of nuclear transparency for ρ-meson electroproduction on xenon at photon energies $\nu = 5$, 10, 20 and 30 GeV. Dashed curves correspond to Glauber approximation, solid curves are calculated with the evolution equation eq. (3).*

Figure 2: *Nuclear transparency versus ν for real photoproduction of ρ (solid curves) and ρ' (dashed curves) on lead. Upper curves correspond to the nonrelativistic oscillatory wave functions, while the bottom curves are calculated with relativized variant [9]*

Note that at low energy, where the eikonal approximation is exact, the nuclear transparency for the ρ' is about the same as for the ρ despite the bigger radius and stronger absorption of the ρ'. This is because the transitions $\rho \rightleftharpoons \rho'$ are possible even without interference, but their

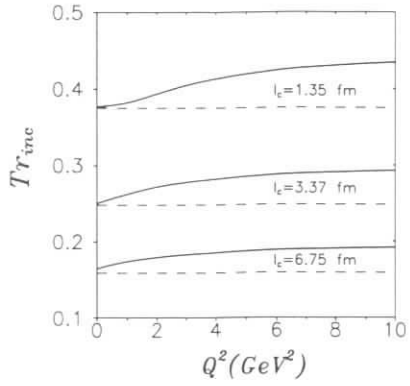

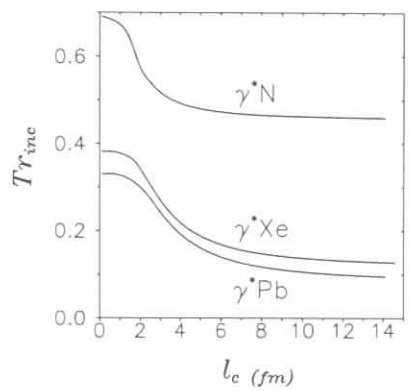

Figure 3: *Q^2-dependence of nuclear transparency at fixed $l_c = const$ for xenon. Glauber approximation predictions are shown by dashed curves. Solid curves demonstrate the effect of CT in the two coupled channel approximation*

Figure 4: *Nuclear transparency for nitrogen, xenon and lead versus the coherence length.*

probability is $\propto \sigma_{el}^{VN}$ rather than σ_{tot}^{VN}. For this reason it is very much suppressed for J/Ψ, but not for ρ.

We have arrived at the main point: how to search for a signal of CT? The two coupled channels are supposed to reproduce well the onset of CT, which is expected to manifest itself as an additional growth of nuclear transparency with Q^2. The results obtained with eq. 11 and relativized wave functions are shown in Fig. 1 by solid curves. We see that variation of the transparency with Q^2 due to the coherence length effect predicted by Glauber model is rather steep and makes it very difficult to detect a CT signal even with high-statistics measurements.

In order to single out the effect of CT one should remove the l_c-dependence of nuclear transparency. This can be done mapping values of Q^2 and ν in a way, which keeps $l_c = 2\nu/(m_V^2 + Q^2)$ constant. Our predictions for Q^2-dependence of nuclear transparency at different values of l_c are plotted in Fig. 3 both for single- (Glauber) and double-channel approaches. The former, as we expected, provides a constant nuclear transparency, while the latter results in a rising $Tr(Q^2)$. Observation of such a dependence on Q^2 should be grated as an onset of CT. We show l_c-dependence of transparency in Glauber model in Fig. 4.

3. Onset of CT in $(e, e'p)$

The principal difference of $(e, e'p)$ reactions from the above discussed photoproduction of vector mesons is a strong correlation between the values of Q^2 and the energy of the recoil proton, $E_p \approx m_p + Q^2/2m_p$. Therefore, while one wants just to increase the proton energy in order to freeze its small size, one unavoidable has to increase Q^2, i.e. to suppress the cross section. This is why no CT effect is still detected in this reaction. As was demonstrated above, in order to freeze size $\sim 1/Q^2$ of the ejectile during propagation through the nucleus, its energy must be $\nu > R_A\sqrt{Q^2}\omega$, where $\omega \approx 0.3\ GeV$ is the oscillatory parameter. This demands unreachable values of Q^2 of a few hundred GeV^2. The same problem concerns $(p, 2p)$ quasielastic proton scattering at large angles.

On the other hand, a growth of Q^2 causes an increase of the ejectile energy. It is known, however, since [10] that nuclear matter is more transparent at higher energies due to inelastic shadowing corrections. This effect is general and independent of color dynamics or whether the CT effect exists or not. The growth of nuclear transparency in $(e, e'p)$ with energy, and consequently with Q^2, was estimated in [11], assuming a simplest "anti-CT" scenario: a regular proton, rather than a small-size fluctuation, is knocked out in $(e, e'p)$ reaction. The predicted Q^2 dependence turns out to be similar to what one expects to be an onset of CT up to about $Q^2 \approx 20\ GeV^2$. Therefore, one should be very cautious interpreting the growth of $Tr(Q^2)$ as a signal of CT in this region. It can be safely done only at quite high, still unreachable Q^2.

4. Conclusion

We have developed for the first time a multichannel approach to incoherent exclusive electroproduction of vector mesons off nuclei, which incorporated effect of the coherent and formation lengths. It is based on a multichannel evolution equation for the density matrix of the produced wave packet. Variation of the coherence length with the photon energy and Q^2 causes substantial changes of the nuclear transparency even in Glauber approximation. This fact makes it very difficult to observe an onset of CT. We suggest such a mapping of ν and Q^2 values, which keeps the coherence length constant. in This case the nuclear transparency cannot change within Glauber approximation. We provide estimates of the onset of CT within two coupled channel model.

One faces even more problems searching for a signal of CT in $(e, e'p)$ quasielastic scattering, due to its specific kinematics. It is very difficult to interpret the growth of nuclear transparency with Q^2 as an onset of CT at $Q^2 < 20/GeV^2$.

References

[1] T.H. Bauer et al., Rev. Mod. Phys. **50** (1978) 261

[2] J. Hüfner, B.Z. Kopeliovich and J. Nemchik, in the Proceedings of ELFE Workshop, July 1995, ed. S.D. Bass, hep-ph/9511215

[3] B.Z. Kopeliovich and J. Nemchik, MPIH-V41-1995, nucl-th/9511018

[4] J. Hüfner, B.Z. Kopeliovich and J. Nemchik, DOE/ER/40561-260-INT96-19-13, nucl-th/9605007, to appear in Phys. Lett. B

[5] B.Z. Kopeliovich, J. Nemchik, N.N. Nikolaev and B.G. Zakharov, Phys. Lett **B324** (1994) 469; Phys. Lett. **B309** (1993) 179

[6] Al.B. Zamolodchikov, B.Z. Kopeliovich and L.I. Lapidus, Sov. Phys. JETP Lett. **33**, (1981) 612

[7] B.Z. Kopeliovich and B.G. Zakharov, Phys. Rev. **D44** (1991) 3466

[8] J. Hüfner and B.Z. Kopeliovich, Phys. Rev. Lett. **76** (1996) 192

[9] J. Nemchik, N.N. Nikolaev, E. Predazzi and B.G. Zakharov, DFTT 71/95, hep-ph/9605231, to appear in Z. Phys.C

[10] V.N. Gribov, Sov. Phys. JETP, **29** (1969) 483

[11] B.Z. Kopeliovich and J. Nemchik, Phys. Lett. **B 368** (1996) 187

TUM/T39-96-18, OSU-96-0701

Coherent ρ Production from Polarized Deuterium[1]

L. Frankfurt[ae], W. Koepf[b], J. Mutzbauer[c],
G. Piller[c], M. Sargsyan[af], M. Strikman[de]

[a] School of Physics and Astronomy, Tel Aviv University, Tel Aviv 69978, Israel
[b] Department of Physics, Ohio State University, Columbus, OH 43210, USA
[c] Physik Department, Technische Universität München, D-85747 Garching, Germany
[d] Department of Physics, Pennsylvania State University, University Park, PA 16802, USA
[e] Institute for Nuclear Physics, St. Petersburg, Russia
[f] Yerevan Physics Institute, Yerevan 375036, Armenia

Abstract: We discuss the coherent leptoproduction of vector mesons from polarized deuterium as a tool to investigate the evolution of small size quark-gluon configurations. Kinematic regions are determined where the final state interaction of the initially produced quark-gluon wave packet contributes dominantly to the production cross section. Two methods for an investigation of color coherence effects, which are appropriate for future experiments at HERMES, are suggested.

1 Scales in color coherence

High energy exclusive production processes from nucleon targets are determined by the transition of initial partonic wave functions to final hadronic states. Interesting details about such transition amplitudes can be obtained by embedding the production process into nuclei, where the formation of a particular final state hadron is probed interactively via the interaction with spectator nucleons (for a review see [1]).

In this context, we discuss the coherent photo- and leptoproduction of vector mesons from polarized deuterium at large photon energies $\nu \gtrsim 4\,GeV$:

$$\gamma^* + \vec{d} \longrightarrow V + d. \tag{1}$$

The corresponding amplitude can be split into two pieces: In the single scattering term only one nucleon participates in the interaction. This is in contrast to the double scattering contribution. Here the (virtual) photon interacts with one of the nucleons inside the target and produces an intermediate hadronic state which subsequently re-scatters from the second nucleon before forming the final state vector meson. At small $Q^2 \lesssim 1\,GeV^2$ exclusive vector meson production from deuterium is well understood in terms of vector meson dominance. In this framework the final state vector meson is formed instantaneously in the interaction of the photon with one of the nucleons from the target [2]. On the other hand, in the limit of large $Q^2 \gg 1\,GeV^2$ perturbative QCD calculations show that photon-nucleon scattering yields rather a small size, color singlet quark-gluon wave packet (ejectile) than a soft vector meson [3]. At high energies ν the final state interaction of such an ejectile with the second nucleon should differ substantially from the final state interaction of a soft vector meson. Therefore the magnitude of the final state interaction contains interesting informations about the initially produced ejectile and its evolution while penetrating through the target.

The ejectile wave packet and its propagation are characterized to a large extent by the following scales: The average **transverse size** of the ejectile wave packet, b_{ej}, which for the case of longitudinal photons is $\approx 4\ldots5/Q$ for $Q^2 \geq 5GeV^2$ for the contribution of the minimal Fock space component [4]. For these Q^2 it amounts to less than a quarter of the typical diameter of a ρ-meson ($\approx 1.4\,fm$). Furthermore the initially produced small quark-gluon wave packet does not, in general, represent an eigenstate of the strong interaction Hamiltonian. Expanding the ejectile in hadronic eigenstates one finds that inside a nuclear target all hadronic components, except the measured vector meson, are filtered out via final state interaction after a typical **formation time**: $\tau_f \approx 2\nu/\delta m_V^2$. Here δm_V^2 is a characteristic squared mass difference between low-lying vector meson states, which is related to the inverse slope of the corresponding Regge trajectory ($\delta m_V^2 \sim 1GeV^2$). If the formation time is larger than the nuclear radius, the ejectile will resemble an approximate eigenstate of the strong interaction while penetrating through the nuclear target. Therefore final state interaction should decrease with rising Q^2 at large photon energies. This phenomenon is usually called color coherence.

However the coherent vector meson production cross section, including its contribution from double scattering, is sensitive also to the **coherence length**: $\lambda \approx 2\nu/(m_V^2 + Q^2)$. The latter characterizes the minimal longitudinal momentum transfer $k_L \approx \lambda^{-1}$ required for the coherent production of the vector meson. (Here we omit the t-dependence of λ and k_L which is discussed in details in ref.[5].) Since the deuteron has to stay intact, one finds dominant contributions to the production cross section for $\lambda > R_d$, where $R_d \approx 4\,fm$ is the deuteron radius. Consequently vector meson production amplitudes from nucleons at a similar impact parameter but at different longitudinal positions will interfere and add up coherently. A decrease of the coherence length leads to a decrease of the coherent vector meson production cross section. Therefore if one investigates the double scattering contribution in different kinematic regions one should be careful in interpreting a variation of the final state interaction as a modification of the the ejectile wave function. First possible effects arising from a change in the coherence length have to be accounted for.

2 Single versus double scattering

In the single scattering contribution the vector meson is produced off one of the nucleons in the target, while the second nucleon does not participate in the interaction. The corresponding Born amplitude is determined by the vector meson production amplitude $f^{\gamma^* p(n)\to Vp(n)}$ from the proton or neutron, respectively, and the deuteron form factor S_d^j (where j indicates the dependence of the form factor on the target polarization):

$$F^{(1)} = f^{\gamma^* p\to Vp}(\boldsymbol{k}_\perp) S_d^j(-\boldsymbol{k}_\perp/2, k_-/2) + f^{\gamma^* n\to Vn}(\boldsymbol{k}_\perp) S_d^j(\boldsymbol{k}_\perp/2, -k_-/2). \tag{2}$$

[1] Work supported in part by grants from BMBF, GIF and the DoE.

The precence of $k_- = k_0 - k_L$ in the form factors accounts for the recoil of the deuteron. If the target polarization is chosen perpendicular to the momentum transfer $\boldsymbol{k}$, at large ν only the difference of the monopole and quadrupole form factor, $S_d^J = S_d^0 - S_d^2$, enters in (2). In terms of the S- and D-components of the deuteron wave function these are $S_d^0(k) = \int_0^\infty dr\, j_0(kr)[u^2(r) + w^2(r)]$ and $S_d^2(k) = \sqrt{2}\int_0^\infty dr\, j_2(kr)w(r)[u(r) - w(r)/\sqrt{8}]$. It is important to realize that the monopole and quadrupole form factor are equal at $k = |\boldsymbol{k}| \approx 0.35\,GeV$. This generates a zero in $S_d^0 - S_d^2$ and consequently a node in the single scattering contribution to the vector meson production cross section at $t = t_d \approx -\boldsymbol{k}^2 \approx -0.5\,GeV^2$ [5] (see also the discussion of elastic hadron-deuteron scattering in ref.[6]). It should be emphasized that the latter is determined solely by the deuteron wave function and does not depend on details of the nucleon production amplitude, $f^{\gamma^* p(n) \to V p(n)}$. Thus we have identified a kinematic window where the single scattering contribution vanishes and the double scattering contribution can be investigated to high accuracy. A similar behavior of the single scattering amplitude can be achieved for a deuteron polarization along either $\hat{\boldsymbol{\kappa}} = (2\boldsymbol{q} + \boldsymbol{k})/|2\boldsymbol{q} + \boldsymbol{k}|$ or $\hat{\boldsymbol{n}} = \hat{\boldsymbol{k}} \times \hat{\boldsymbol{\kappa}}$, where $\boldsymbol{q}$ stands for the photon three-momentum. On the other hand, for an unpolarized deuteron target the sum of the monopole and quadrupole form factor enters in the Born amplitude. As a consequence the single scattering contribution always dominates the vector meson production cross section at moderate $-t \lesssim 1\,GeV^2$, leaving no favorable kinematic window for an investigation of final state interaction.

The double scattering amplitude stems from the final state interaction of an initially produced hadronic state. Expanding the latter in hadronic eigenstates h yields:

$$F^{(2)} \approx \frac{i}{2}\sum_h \int \frac{d^2\boldsymbol{k}'_\perp}{(2\pi)^2} S_d^J(\boldsymbol{k}'_\perp, k_-/2) f^{\gamma^* p \to h p}(\boldsymbol{k}_\perp/2 - \boldsymbol{k}'_\perp) f^{hn \to V n}(\boldsymbol{k}_\perp/2 + \boldsymbol{k}'_\perp) + (p \leftrightarrow n). \quad (3)$$

The transfered momentum is split between both interacting nucleons. Therefore if the re-scattering amplitude of the ejectile $f^{hn(p) \to V n(p)}$ is sizable, double scattering will be important in the region of moderate and large $-t \gtrsim 0.4\,GeV^2$.

In Fig.1 we show the differential cross section for the coherent ρ-production from deuterium polarized perpendicular to the momentum transfer,

$$\frac{d\sigma_d}{dt} = \frac{1}{16\pi}\left(|F^{(1)}|^2 + 2Re\left(F^{(1)*}F^{(2)}\right) + |F^{(2)}|^2\right). \quad (4)$$

calculated within vector meson dominance [5]. In this framework the double scattering amplitude accounts for the sizable re-scattering of the soft ρ-meson. The energy and momentum transfer are taken within the kinematic domain of the HERMES experiment. Figure 1 demonstrates that the minimum of the single scattering amplitude (at $-t \approx 0.5\,GeV^2$) is completely filled by final state interaction. Furthermore double scattering exceeds the Born contribution by a factor ~ 5 at $-t > 0.5\,GeV^2$.

3 Signatures for color coherence

Of course vector meson dominance is appropriate for small $Q^2 \lesssim 1\,GeV^2$ only. However we want to study the dependence of the final state interaction on Q^2 and ν to obtain informations on the ejectile wave function and its propagation through the nucleus. For this purpose we suggest

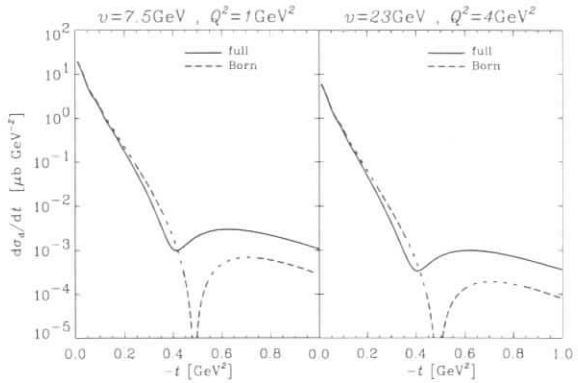

Figure 1: *The differential production cross section for coherent ρ-production from polarized deuterium for different values of Q^2 and ν. The target polarization is chosen perpendicular to the momentum transfer. The full line is the result for the production cross section within vector meson dominance. The dashed curve shows the Born contribution.*

investigations which are to a large extent independent on details of the ejectile production amplitude.

In this respect it is most promising to study coherent vector meson production from deuterium polarized perpendicular to the momentum transfer $\hat{\boldsymbol{k}}$ (or parallel to $\hat{\boldsymbol{\kappa}}$ or $\hat{\boldsymbol{n}}$) at $t \sim t_d$. Here the single scattering contribution to the cross section is very small and even vanishes at $t = t_d$ as discussed above. Exploring the production cross section in this kinematic window for different Q^2 and ν yields direct informations on the ejectile wave function. Since the transverse size of the ejectile shrinks with rising Q^2, perturbative QCD suggests that the vector meson production cross section should decrease and ultimately vanish at $t = t_d$ for $Q^2 \gg 1\,GeV^2$ and $\nu \gtrsim R_d\,\delta m_V^2/2 \approx 10\,GeV$. The latter requirement ensures that the formation time of the vector meson exceeds the deuteron size, $\tau_f > R_d$.

Furthermore Fig.1 demonstrates that in the domain of vector meson dominance ($Q^2 = Q_0^2 \lesssim 1\,GeV^2$) double scattering is by far dominant for $-t > 0.5\,GeV^2$: $\frac{(d\sigma_d(Q_0^2))/dt)_{full}}{(d\sigma_d(Q_0^2)/dt)_{Born}} \approx 5$. If final state interaction vanishes at large $Q^2 = Q_1^2 \gg 1\,GeV^2$ and large energies $\nu \gtrsim 10\,GeV$, we expect the above ratio to approach unity. Assuming that the Q^2-dependence of the initial ejectile production amplitude factorizes, and is approximately equal to the Q^2-dependence of the vector meson production cross section from free nucleons $d\sigma_N/dt$, we obtain:

$$\frac{(d\sigma_d(Q_1^2)/dt)_{full}}{(d\sigma_d(Q_0^2)/dt)_{Born}} \frac{(d\sigma_N(Q_0^2)/dt)}{(d\sigma_N(Q_1^2)/dt)} \longrightarrow 1. \quad (5)$$

In both cases it is important to keep the coherence length constant or to account for its possible modification.

4 Summary and Outlook

We discussed the coherent production of vector mesons from polarized deuterium as a tool to investigate the propagation of small size quark-gluon configurations, which are initially produced in high energy lepton-nucleon interactions at large Q^2. A kinematic window was found where the differential cross section stems only from contributions of the final state interaction of the ejectile. Two methods for an investigation of color coherence effects, which are appropriate for future experiments at HERMES, were proposed. Note that also the incoherent, diffractive production of vector mesons from polarized deuterium provides a variety of possibilities for detailed investigations of color coherence effects at HERMES [5]. Especially detecting the recoil nucleon from deuteron break-up yields a possibility to explore the evolution of small size quark-gluon configurations at different, well defined length scales.

References

[1] L.L. Frankfurt, G.A. Miller and M.I. Strikman, Ann. Rev. Nucl. Part. Sci. **45**, 501 (1994)

[2] T.H. Bauer et al., Rev. Mod. Phys. **50**, 261 (1978)

[3] S.J. Brodsky et al., Phys. Rev. D **50**, 3134 (1994)

[4] L.L. Frankfurt, W. Koepf and M. Strikman, Preprint hep-ph/9509311, in print by Phys. Rev. D

[5] L.L. Frankfurt et al., in preparation

[6] V. Franco and R.J. Glauber, Phys. Rev. Lett. **22**, 370 (1969)

Investigation of the neutron structure function via semi-inclusive deep inelastic electron scattering off the deuteron

Silvano SIMULA

INFN, Sezione Sanità, Viale Regina Elena 299, I-00161 Roma, Italy

Abstract: The production of slow nucleons in semi-inclusive deep inelastic electron scattering off the deuteron is investigated in the region $x \gtrsim 0.3$ for kinematical conditions accessible at $HERA$. Within the spectator mechanism the semi-inclusive cross section exhibits a scaling property, which can be used as a model-independent test of the dominance of the spectator mechanism itself, providing in this way an interesting tool to investigate the neutron structure function. The possibility of extracting model-independent information on the neutron to proton structure function ratio from semi-inclusive experiments is also illustrated.

Untill now, experimental information on the structure function of the neutron has been inferred from nuclear (usually deuteron) deep inelastic scattering (DIS) data [1] by unfolding the neutron contribution from the inclusive nuclear cross section. Such a procedure typically involves the subtraction of both Fermi motion effects and contributions from different nuclear constituents (i.e., nucleons, mesons, isobars, ...), leading to non-trivial ambiguities related to the choice of the model used to describe the structure of the target and the mechanism of the reaction. An interesting way to get information on the neutron structure function could be the investigation of semi-inclusive DIS reactions of leptons off the deuteron. In Ref. [2] the process $^2H(\ell,\ell' N)X$ has been investigated at moderate and large values of the Bjorken variable $x \equiv Q^2/2M\nu$ ($x \gtrsim 0.3$) within the so-called spectator mechanism, according to which, after lepton interaction with a quark of a nucleon in the deuteron, the spectator nucleon is emitted because of recoil and detected in coincidence with the scattered lepton. It has been shown [2] that the semi-inclusive cross section corresponding to such a mechanism exhibits a scaling property (the spectator scaling), which can be used as a model-independent test of the dominance of the spectator mechanism itself. In the spectator-scaling regime the neutron structure function can be investigated from semi-inclusive data and, moreover, the neutron to proton structure function ratio $R^{(n/p)}(x,Q^2) \equiv F_2^n(x,Q^2)/F_2^p(x,Q^2)$ can be obtained directly from the ratio of the semi-inclusive cross sections of the processes $^2H(e,e'p)X$ and $^2H(e,e'n)X$.

The aim of this contribution is to address the issue of the spectator scaling in case of electron kinematical conditions accessible at $HERA$. To this end, let us briefly remind that the semi-inclusive cross section of the process $^2H(e,e'N)X$ reads as follows

$$\frac{d^4\sigma}{dE_{e'}\, d\Omega_{e'}\, dE_2\, d\Omega_2} = \sigma_{Mott}\; p_2\; E_2\; \sum_i\; V_i\; W_i^D(x,Q^2;\vec{p}_2) \qquad (1)$$

where E_e ($E_{e'}$) is the initial (final) energy of the electron; $Q^2 \equiv -q^2 = |\vec{q}|^2 - \nu^2$ is the squared four-momentum transfer; $i \equiv \{L, T, LT, TT\}$ identifies the different types of semi-inclusive response functions (W_i^D) of the deuteron; $\vec{p}_2$ is the momentum of the detected nucleon; $E_2 = \sqrt{M^2 + p_2^2}$ its energy ($p_2 \equiv |\vec{p}_2|$) and V_i is a virtual photon flux factor (see [2]). Within the spectator mechanism the virtual photon is absorbed by a quark belonging to the nucleon N_1 in the deuteron and the recoiling nucleon N_2 is emitted and detected in coincidence with the scattered electron. Thus, Eq. (1) can be written in terms of the structure function $F_2^{N_1}(x^*, Q^2)$ of the struck nucleon as [2]

$$\frac{d^4\sigma}{dE_{e'}\, d\Omega_{e'}\, dE_2\, d\Omega_2} = K\; M\; p_2\; n^{(D)}(p_2)\; \frac{F_2^{N_1}(x^*, Q^2)}{x^*}\; D^{N_1}(x, Q^2; \vec{p}_2) \qquad (2)$$

where $n^{(D)}$ is the (non-relativistic) nucleon momentum distribution in the deuteron, $x^* \equiv Q^2/(Q^2 + M_1^{*2} - M^2)$ and M_1^* is the invariant mass of the struck nucleon, given through the energy and momentum conservations by: $M_1^* = \sqrt{(\nu + M_D - E_2)^2 - (\vec{q} - \vec{p}_2)^2}$, with M_D being the deuteron mass. In Eq. (2) $K \equiv (2Mx^2E_eE_{e'}/\pi Q^2)\,(4\pi\alpha^2/Q^4)\,[1 - y + (y^2/2) + (Q^2/4E_e^2)]$, with $y \equiv \nu/E_e$, and the quantity $D^{N_1}(x, Q^2; \vec{p}_2)$ depends both upon kinematical factors and the ratio $R_{L/T}^{N_1}$ of the longitudinal to transverse cross section off the nucleon (see [2]). The relevant quantity, which will be discussed hereafter, is related to the semi-inclusive cross section (1) by

$$\begin{aligned} F^{(s.i.)}(x, Q^2; \vec{p}_2) &\equiv \frac{1}{\tilde{K}}\, \frac{d^4\sigma}{dE_{e'}\, d\Omega_{e'}\, dE_2\, d\Omega_2} \\ &= M\; p_2\; n^{(D)}(p_2)\; \frac{F_2^{N_1}(x^*, Q^2)}{x^*}\; \tilde{D}^{N_1}(x, Q^2; \vec{p}_2) \end{aligned} \qquad (3)$$

where $\tilde{K}$ is a kinematical factor given by $\tilde{K} \equiv K\; [D^{N_1}(x, Q^2; \vec{p}_2)]_{R_{L/T}^{N_1}=0}$ and $\tilde{D}^{N_1}(x, Q^2; \vec{p}_2) = D^{N_1}(x, Q^2; \vec{p}_2)\; /\; [D^{N_1}(x, Q^2; \vec{p}_2)]_{R_{L/T}^{N_1}=0}$. Eq. (3) differs from the definition of $F^{(s.i.)}$ given in [2], for $\tilde{K}$, which incorporates kinematical factors depending on $\vec{p}_2$, is used instead of K, which depends only on the electron kinematical variables.

In the Bjorken limit one would expect $R_{L/T}^{N_1} \to_{Bj} 0$, so that $\tilde{D}^{N_1} \to_{Bj} 1$, which implies $F^{(s.i.)}(x, Q^2; \vec{p}_2) \to_{Bj} M\; p_2\; n^{(D)}(p_2)\; F_2^{N_1}(x^*)/x^*$, where $F_2^{N_1}(x^*)$ stands for the nucleon structure function in the Bjorken limit (apart from logarithmic QCD corrections). Therefore, in the Bjorken limit and at fixed values of p_2 the function (3) does not depend separately upon x and the nucleon detection angle θ_2, but only upon the variable $x^* \to_{Bj} x/(2 - z_2)$, with $z_2 = [E_2 - p_2 cos(\theta_2)]/M$ being the light-cone momentum fraction of the detected nucleon. In what follows, we will refer to the function $F^{(sp)}(x^*, Q^2, p_2)$ and variable x^*, given explicitly by

$$F^{(sp)}(x^*, Q^2, p_2) \equiv M\; p_2\; n^{(D)}(p_2)\; F_2^{N_1}(x^*, Q^2)\; /\; x^* \qquad (4)$$

$$x^* \equiv \frac{Q^2}{Q^2 + (\nu + M_D - E_2)^2 - (\vec{q} - \vec{p}_2)^2 - M^2} \qquad (5)$$

as the spectator-scaling function and variable, respectively. The essence of the spectator scaling relies on the fact that the variable x^* gathers different electron and nucleon kinematical conditions (in x and θ_2), corresponding to the same value of the invariant mass produced on the struck nucleon. The deuteron response will be the same only if the spectator mechanism dominates and, therefore, the experimental observation of the spectator scaling represents a test of the dominance of the spectator mechanism itself.

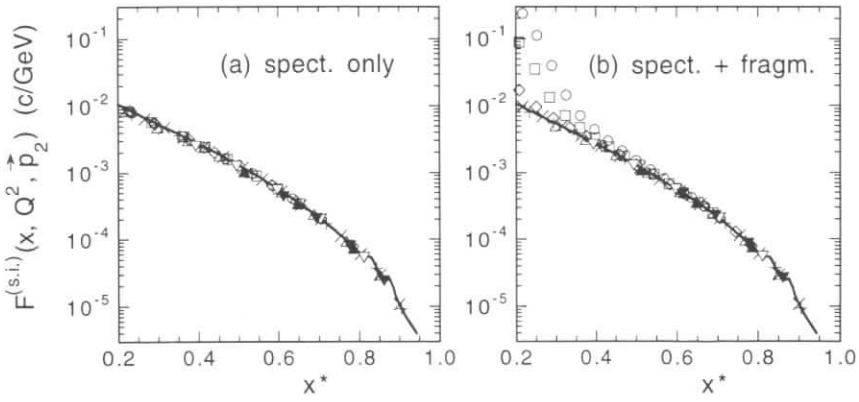

Fig. 1. (a) The function $F^{(s.i.)}(x, Q^2, \vec{p}_2)$ (Eq. (3)) for the process $^2H(e, e'p)X$ plotted versus the spectator-scaling variable x^* (Eq. (5)) at $Q^2 = 10\ (GeV/c)^2$ and $p_2 = 0.5\ GeV/c$. The values of x have been varied in the range $0.20 \div 0.95$, whereas the various markers correspond to different values of the nucleon detection angle θ_2 chosen in the range $10^\circ \div 150^\circ$. The solid line is the spectator-scaling function $F^{(sp)}(x^*, Q^2, p_2)$ (Eq. (4)) calculated using the deuteron momentum distribution corresponding to the Paris nucleon-nucleon interaction [5] and to the parametrization of the neutron structure function of Ref. [3]. (b) The same as in (a), but including the effects of the target fragmentation of the struck nucleon, evaluated as in Ref. [6], as well as the contribution of the proton emission arising from virtual photon absorption on 6q cluster configurations in the deuteron, evaluated following Ref. [9] and adopting a 6q bag probability equal to 2%. In particular, the open dots and squares, which exhibit large violations of the spectator scaling, correspond to $\theta_2 = 10^\circ$ and 30°, respectively.

Eq. (3) has been calculated considering electron kinematical conditions accessible at $HERA$ (i.e., $E_e = 30\ GeV$ and $Q^2 = 10\ (GeV/c)^2$) and $p_2 = 0.1,\ 0.3,\ 0.5\ GeV/c$. The Bjorken variable x and the nucleon detection angle θ_2 have been varied in the range $0.20 \div 0.95$ and $10^\circ \div 150^\circ$, respectively (for sake of simplicity, the polar angle ϕ_2 has been chosen equal to 0). As for the nucleon structure function, the parametrization of the $SLAC$ data of Ref. [3], containing $R_{L/T}^{N_1} \simeq 0.18$, has been adopted. The results of the calculations, performed at $p_2 = 0.5\ GeV/c$, are shown in Fig. 1(a) and compared with the spectator-scaling function (4). It can clearly be seen that at $Q^2 = 10\ (GeV/c)^2$ the spectator scaling is almost completely fulfilled (within 10%) in the whole x-range, including the region at $x^* \gtrsim 0.8$, where (small) contributions from nucleon resonances are still visible. Using the new definition (3), the spectator scaling is fulfilled not only at $p_2 \lesssim 0.3\ GeV/c$, as shown in [2], but also at higher values of p_2.

In the spectator-scaling regime the measurement of the semi-inclusive cross section both for the $^2H(e, e'p)X$ and $^2H(e, e'n)X$ processes would allow the investigation of two spectator-scaling functions, involving the same nuclear part, $Mp_2n^{(D)}(p_2)$, and the neutron and proton structure functions, respectively. Therefore, assuming $R_{L/T}^n = R_{L/T}^p$ (as it is suggested by recent $SLAC$ data analyses [4]), both the nuclear part and the factor $\tilde{D}^{N_1}(x, Q^2; \vec{p}_2)$ cancel out in the ratio $R^{(s.i.)}(x, Q^2, \vec{p}_2) \equiv d^4\sigma[^2H(e, e'p)X]/d^4\sigma[^2H(e, e'n)X]$, which provides in this way directly the neutron to proton structure function ratio $R^{(n/p)}(x^*, Q^2)$. With respect to the function $F^{(s.i.)}(x, Q^2, \vec{p}_2)$, the ratio $R^{(s.i.)}(x, Q^2, \vec{p}_2)$ exhibits a more general scaling property, for

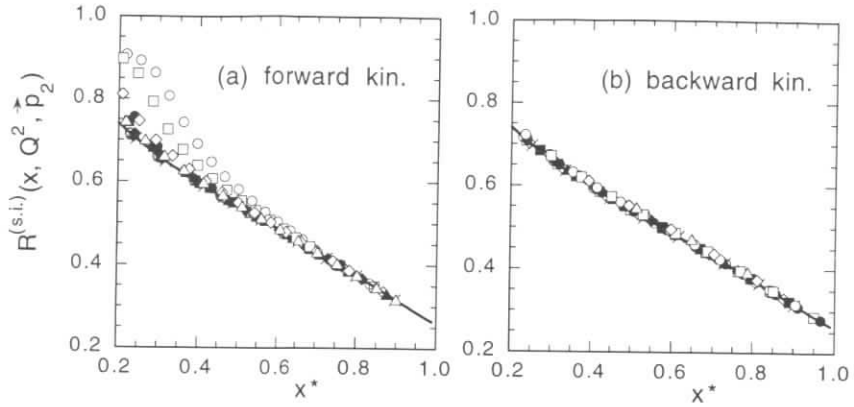

Fig. 2. The ratio $R^{(s.i.)}(x, Q^2, \vec{p}_2)$ of the semi-inclusive cross sections for the processes $^2H(e, e'p)X$ and $^2H(e, e'n)X$, calculated at $Q^2 = 10\ (GeV/c)^2$ and $p_2 = 0.1, 0.3, 0.5\ GeV/c$. The values of x have been varied in the range $0.20 \div 0.95$. Forward ($\theta_2 < 90°$) and backward ($\theta_2 > 90°$) nucleon emissions are shown in (a) and (b), respectively. The solid line is the neutron to proton structure function ratio $R^{(n/p)}(x^*, Q^2)$ calculated using the parametrization of the nucleon structure function of Ref. [3].

at fixed Q^2 it does not depend separately upon x, p_2 and θ_2, but only on x^*. This means that any p_2-dependence of the ratio $R^{(s.i.)}$ would allow to investigate off-shell deformations of the nucleon structure functions (see below).

The results presented and, in particular, the spectator-scaling properties of $F^{(s.i.)}$ and $R^{(s.i.)}$ could in principle be modified by the effects of mechanisms different from the spectator one, like, e.g., the fragmentation of the struck nucleon, or by the breakdown of the impulse approximation. In order to estimate the effects of the so-called target fragmentation of the struck nucleon (which is thought to be responsible for the production of slow hadrons in DIS processes), we adopt the approach of Ref. [6], where the hadronization mechanism has been parametrized through the use of fragmentation functions, whose explicit form has been chosen according to the prescription of Ref. [7], elaborated to describe the production of slow protons in DIS of (anti)neutrinos off hydrogen and deuterium targets. Furthermore, the effects arising from possible six-quark ($6q$) cluster configurations at short internucleon separations, are explicitly considered. According to the mechanism first proposed in Ref. [8], after lepton interaction with a quark belonging to a $6q$ cluster, nucleons can be formed out of the penta-quark residuum and emitted forward as well as backward. The details of the calculations can be easily inferred from Ref. [9], where $6q$ bag effects in semi-inclusive DIS of leptons off light and complex nuclei have been investigated. The estimate of the nucleon production, arising from the above-mentioned target fragmentation processes, is shown in Fig. 1(b) for the function $F^{(s.i.)}$ and in Fig. 2 for the ratio $R^{(s.i.)}$. It can clearly be seen that: i) only at $x^* \lesssim 0.4$ the fragmentation processes can produce relevant violations of the spectator scaling (see Figs. 1(b) and 2(a)); ii) backward kinematics (see Fig. 2(b)) appear to be the most appropriate conditions to extract the neutron to proton ratio $R^{(n/p)}$. Moreover, explicit calculations show that the relevance of the fragmentation processes drastically decreases when $p_2 < 0.5\ GeV/c$.

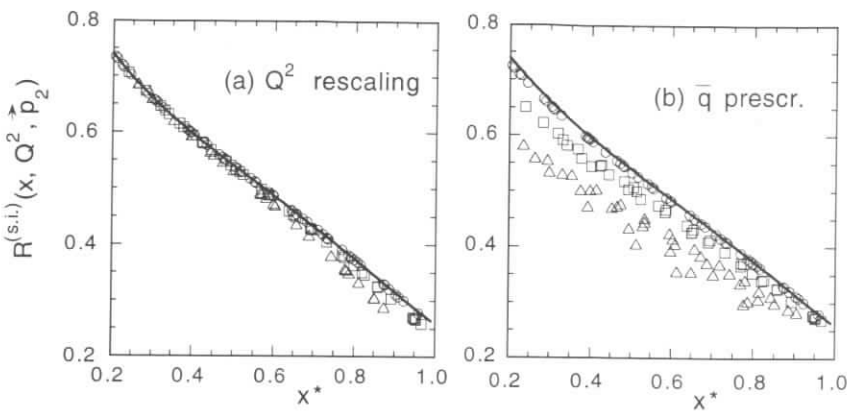

Fig. 3. The ratio $R^{(s.i.)}(x, Q^2, \vec{p}_2)$ of the semi-inclusive cross sections for the processes $^2H(e, e'p)X$ and $^2H(e, e'n)X$, calculated considering the off-shell effects proposed in Refs. [13] (a) and [14] (b), respectively. Backward nucleon kinematics only ($\theta_2 > 90°$) have been considered. The dots, squares and triangles correspond to $p_2 = 0.1$, 0.3, 0.5 GeV/c, respectively. The solid line is the same as in Fig. 2.

As far as the impulse approximation is concerned, it should be reminded that our calculations have been performed within the assumption that the debris produced by the fragmentation of the struck nucleon does not interact with the recoiling spectator nucleon. Estimates of the final state interactions of the fragments in semi-inclusive processes off the deuteron have been obtained in [10], suggesting that rescattering effects should play a minor role thanks to the finite formation time of the dressed hadrons. Moreover, backward nucleon emission is not expected to be sensitively affected by forward-produced hadrons (see [11]), and final state interaction effects are expected to cancel out (at least partially) in the cross section ratio $R^{(s.i.)}(x, Q^2, \vec{p}_2)$. Besides fragmentation processes and final state interactions, also nucleon off-shell effects [12] might produce violations of the spectator scaling, in particular at high values of p_2 ($\gtrsim 0.3\ GeV/c$). The results of the calculations of the ratio $R^{(s.i.)}(x, Q^2, \vec{p}_2)$, obtained considering the off-shell effects suggested in Refs. [13] and [14], are shown in Fig. 3(a) and 3(b), respectively. It can be seen that the measurement of the ratio $R^{(s.i.)}(x, Q^2, \vec{p}_2)$ represents an interesting tool both to investigate the ratio of free neutron to proton structure function, provided $p_2 \sim 0.1 \div 0.2\ GeV/c$, and to get information on the possible off-shell behaviour of the nucleon structure function when $p_2 \gtrsim 0.3\ GeV/c$.

In conclusion, the production of slow nucleons in semi-inclusive deep inelastic electron scattering off the deuteron has been investigated in kinematical regions accessible at $HERA$. Within the spectator mechanism the semi-inclusive cross section exhibits the spectator-scaling property, which can be used as a model-independent test of the dominance of the spectator mechanism itself. In the spectator-scaling regime both the neutron structure function and the neutron to proton structure function ratio can be obtained directly from semi-inclusive DIS data off the deuteron. Finally, the pattern of possible spectator-scaling violations could provide relevant information on the off-shell behaviour of the nucleon structure function in the medium.

References

[1] J.J. Aubert et al.: Nucl. Phys. **B293** (1987) 740. A.C. Benvenuti et al.: Phys. Lett. **237B** (1990) 599. P. Amaudruz et al.: Nucl. Phys. **B371** (1992) 3.

[2] S. Simula: preprint INFN-ISS 96/2 (nucl-th 9605024), to appear in Phys. Lett. **B**.

[3] A. Bodek and J.L. Ritchie: Phys. Rev. **D23** (1981) 1070. L.W. Whitlow et al.: Phys. Lett. **282B** (1992) 475.

[4] L.W. Whitlow et al.: Phys. Lett. **250B** (1990) 193. S. Dasu et al.: Phys. Rev. **D49** (1994) 5641.

[5] M. Lacombe et al.: Phys. Rev. **C21** (1980) 861.

[6] C. Ciofi degli Atti and S. Simula: Phys. Lett. **319B** (1993) 23. In Proc. of the 6^{th} Workshop on *Perspectives in Nuclear Physics at Intermediate Energies*, ICTP (Trieste, Italy), May 3-7, 1993, eds. S. Boffi, C. Ciofi degli Atti and M. Giannini, World Scientific (Singapore, 1994), pg. 182.

[7] G.D. Bosveld, A.E.L. Dieperink and O. Scholten: Phys. Rev. **C45** (1992) 2616.

[8] C.E. Carlson, K.E. Lassilla and P.U. Sukhatme: Phys. Lett. **263B** (1991) 277. C.E. Carlson and K.E. Lassilla: Phys. Rev. **C51** (1995) 364.

[9] C. Ciofi degli Atti and S. Simula: Few Body Systems **18** (1995) 55. S. Simula: Few Body Systems Suppl. **9** (1995) 466.

[10] A.G. Tenner and N.N. Nikolaev: Nuovo Cim. **A105** (1992) 1001.

[11] G.D. Bosveld, A.E.L. Dieperink and A.G. Tenner: Phys. Rev. **C49** (1994) 2379.

[12] U. Oelfke, P.U. Sauer and F. Coester: Nucl. Phys. **A518** (1990) 593. L.P. Kaptari and A.Yu. Umnikov: Phys. Lett. **259B** (1991) 155. M.A. Braun and M.V. Tokarev: Phys. Lett. **320B** (1994) 381. A.Yu. Umnikov and F.C. Khanna: Phys. Rev. **C49** (1994) 2311. W. Melnitchouk, A.W. Schreiber and A.W. Thomas: Phys. Rev. **D49** (1994) 1183; Phys. Lett. **335B** (1994) 11. S.A. Kulagin, G. Piller and W. Weise: Phys. Rev. **C50** (1994) 1154. Yu.A. Umnikov, F.C. Khanna and L.P. Kaptari Phys. Rev. **C53** (1996) 377. W. Melnitchouk and A.W. Thomas: preprint DOE/ER/40762-069.

[13] G.V. Dunne and A.W. Thomas: Nucl. Phys. **A455** (1986) 701.

[14] L. Heller and A.W. Thomas: Phys. Rev. **C41** (1990) 2756.

Tagged Structure Functions of the Deuteron and the Origin of the EMC Effect

W. Melnitchouk[a], M. Sargsian[b,e], M. Strikman[c,d]

[a] Department of Physics, University of Maryland, College Park, MD 20742, USA
[b] School of Physics and Astronomy, Tel Aviv University, Tel Aviv 69978, Israel,
[c] Department of Physics, Pennsylvania State University, University Park, PA 16802, USA
[d] Institute for Nuclear Physics, St. Petersburg, Russia
[e] Yerevan Physics Institute, Yerevan 375036, Armenia

Abstract: We demonstrate how measurement of tagged structure functions of the deuteron in $(e, e'N)$ semi-inclusive reactions at backward kinematics can be used to discriminate between different models of the nuclear EMC effect. A procedure for extracting the large-x neutron to proton structure function ratio from $(e, e'N)$ reactions is also outlined.

1 Objectives and Theoretical Framework

More than a decade after the discovery of the nuclear EMC effect [1] and many fine measurements of the ratios of structure functions of nuclei and deuterium, no consensus has been reached on the origin of the effect. The observed effect is approximately proportional to the nuclear density and the x dependence of the effect, while non-trivial, has the same basic shape for all nuclei, making it easy to fit in a wide range of models with very different underlying assumptions. Proportionality to nuclear density suggests that one should expect a much smaller EMC effect in the deuteron compared to that in heavy nuclei. By virtue of the uncertainty principle, however, one may try to enhance the effect by isolating the configuration where the two nucleons in the deuteron are close together. For example, it is easy to check that the main contributions to the deuteron wave function for nucleon momenta $\mathbf{p} \geq 300$ MeV/c come from distances $\lesssim 1.2$ fm. In order to encounter such a situation, new experiments, which allow control of the inter-nucleon distances in the deuteron, are necessary.

The aim of this discussion is to demonstrate that use of semi-inclusive processes off the deuteron,

$$e + D \to e + N + X, \tag{1}$$

where a nucleon is detected in the deuteron fragmentation region, could meet the above requirements, and may help to boost our understanding of the origin of the EMC effect. In particular, one may be able to distinguish between models in which the EMC effect arises from hadronic degrees of freedom (nucleons and pions), and models in which the effect is attributed to the explicit deformation of the wave function of the bound nucleon itself. Using heavier nuclei as targets in the reaction (1) may be problematic due to the contribution of secondary interactions, therefore the deuteron is a more ideal target for our purpose.

The cross section for the semi-inclusive $(e, e'N)$ reaction off the deuteron can in general be expressed through four invariant structure functions:

$$\frac{d\sigma}{dx dW^2 (d\alpha_s/\alpha_s) d^2\mathbf{p}_T} = \frac{2\alpha_{em}^2}{Q^4}\left(1 - y - \frac{x^2 y^2 M^2}{Q^2}\right)$$
$$\times \left[F_L^D + \left(\frac{Q^2}{2\mathbf{q}^2} + \tan^2(\theta/2)\right)\frac{\nu}{M} F_T^D + \left(\frac{Q^2}{\mathbf{q}^2} + \tan^2(\theta/2)\right)^{\frac{1}{2}} \cos\phi\ F_{TL}^D + \cos(2\phi)\ F_{TT}^D\right] \tag{2}$$

where the semi-inclusive structure functions $F^D_{L,T,TL,TT}(x,\alpha_s,p_T,Q^2)$ are related to the components of the deuteron electromagnetic tensor $W^{\mu\nu}_D$ by [2]:

$$\begin{aligned} F^D_L &= \nu(1+\cos\delta)^2\cdot W^{--}_D, \quad F^D_T = M(W^{xx}_D + W^{yy}_D), \\ F^D_{TL} &= 2\nu(1+\cos\delta)\cdot W^{-x}_D, \quad F^D_{TT} = \frac{\nu}{2}\sin^2\delta\cdot(W^{xx}_D - W^{yy}_D). \end{aligned} \tag{3}$$

The kinematic variables in Eqs.(2) and (3) are $x = Q^2/2M\nu$, $W^2 = -Q^2 + 2M\nu + M^2$, where ν is the energy of virtual photon in the target rest frame and M the nucleon mass (we define the photon three-momentum $\mathbf{q}$ to be in the $+z$ direction). The squared four-momentum transferred to the deuteron is $Q^2 = 4E(E-\nu)\sin^2(\theta/2)$, with E the beam energy and $y = \nu/E$. The angles θ and ϕ are the electron scattering and detected nucleon azimuthal angles, respectively, and $\sin^2\delta = Q^2/\mathbf{q}^2$. The spectator nucleon momentum is denoted by $\mathbf{p}_s = (\mathbf{p}_{sT}, p_{sz})$, and the interacting nucleon momentum by $\mathbf{p}$, so that in the deuteron rest frame $\mathbf{p}_s = -\mathbf{p}$. The variable $\alpha_s = 2\left(\sqrt{M^2+\mathbf{p}_s^2} - p_{sz}\right)/M_D$ is the deuteron's light-cone momentum fraction carried by the detected nucleon. The "$-$" components in Eq.(3) correspond to the projection in the $z-t$ direction on the light-cone.

In a microscopic description of the process (1) the tensor $W^{\mu\nu}_D$ describes both the deep inelastic scattering (DIS) from a bound nucleon in the deuteron, as well as the dynamics of the nuclear interaction, which are in general not factorizable. However, by considering specific kinematics one can obtain approximate factorization of the two subprocesses, and thus allow for a quantitative treatment of the reaction (1). The kinematics required for factorization are: (I) $Q^2/\mathbf{q}^2 \sim 4Mx/Q^2 \ll 1$, $Q^2 \ll E(E-\nu)$, and (II) $\alpha_s \geq 1-x$, $p_T \approx 0$, $|\mathbf{p}_s| \lesssim 500$ MeV/c. The requirement (I) enhances the contribution of the longitudinal structure function, F_L, which is expressed through the "good" component of the electromagnetic current, Eq.(3). This component is less influenced by effects of final state interactions (FSI), thus allowing a separation of FSI from the dynamics of DIS from a bound nucleon. The conditions (II) suppress contributions from the direct production of nucleons in the $\gamma^* N$ interaction. These restrictions allow one to write [2]: $W^{\mu\nu}_D(x,\alpha_s,p_T,Q^2) \approx \eta S(\alpha_s,p_T)\cdot W^{\mu\nu\ eff}_N(x,\alpha_s,p_T,Q^2)$, where η represents to the factored out FSI effect ($\eta \approx 1$ for the above kinematics), and $S(\alpha_s,p_T)$ is the nucleon spectral function in the deuteron. Note that $W^{\mu\nu\ eff}_N(x,\alpha_s,p_T,Q^2)$ coincidences with the free nucleon tensor $W^{\mu\nu}_N$ in the limit $\alpha_s \to 1$ and $p_T \to 0$.

Using the kinematical constraints (I) and (II) one can express the cross section in Eq.(2) as:

$$\frac{d\sigma^{eD\to epX}}{dxdW^2d(\log\alpha_s)d^2\mathbf{p}_T} \approx \frac{2\alpha^2_{em}}{Q^4}(1-y)S(\alpha_s,p_T)F^{eff}_{2N}\left(\frac{x}{2-\alpha_s},p_T,Q^2\right). \tag{4}$$

Though the factorized form in Eq.(4) is quite universal for any self-consistent relativistic approach describing nuclear dynamics and DIS from a bound nucleon, the particular form for the spectral function $S(\alpha_s,p_T)$ or the bound nucleon structure function F^{eff}_{2N} could be very different. Since the goal is primarily to study nuclear effects on F^{eff}_{2N}, one therefore needs to minimize any effects coming from uncertainties in the deuteron wave function (or spectral function) itself. This can be achieved by measuring the ratio of cross sections at large x to that at $x \sim 0.1$–0.2, where the observed EMC effect is small [2, 3, 4]. If both cross sections are measured at the same α_s and p_T, the nuclear effects parameterized by the deuteron spectral function cancel [4]:

$$G(\alpha_s,p_T,x_1,x_2,Q^2) \equiv \frac{d\sigma(x_1,\alpha_s,p_T,Q^2)/dxdW^2d(\log\alpha_s)d^2\mathbf{p}_T}{d\sigma(x_2,\alpha_s,p_T,Q^2)/dxdW^2d(\log\alpha_s)d^2\mathbf{p}_T} = \frac{F^{eff}_{2N}(x_1/(2-\alpha_s),p_T,Q^2)}{F^{eff}_{2N}(x_2/(2-\alpha_s),p_T,Q^2)}. \tag{5}$$

This ratio is therefore the ideal experimental quantity to measure since it is not biased by any theoretical normalization of the deuteron wave function.

2 Predictions for $G(\alpha_s,p_T,x_1,x_2,Q^2)$

To assess the expected EMC effect which could be identified in the measurement of G in Eq.(5) we apply several theoretical approaches to the possible modification of the bound nucleon structure functions.

2.1 Binding Models

In the so-called binding models, the bulk of the EMC effect at $x \sim 0.6$ comes from the fact that the typical value for the interacting nucleon light-cone fraction is less than unity, i.e. the average spectator light-cone momentum fraction is $\langle\alpha_s\rangle > 1$. Contributions to the EMC effect from deformation of the bound nucleon structure function in this approach is minimal — indeed, in most versions of this model the explicit dependence on the nucleon virtuality p^2 in F^{eff}_{2N} is ignored, and only recently have the first attempts [5, 6] to account for this possible dependence been made. In any generic quark-parton model, F^{eff}_{2N} can be expressed through the quark spectral function ρ as [5, 6]: $F^{eff}_{2N}(x,p^2,Q^2) = \int dp^2_q\ \rho(p^2_q,p^2,x,Q^2)$, where p_q is the quark four-momentum. A simple microscopic quark–"diquark" model of the nucleon was discussed in Ref.[5], where the quark spectral function was determined from the dynamics contained in the nucleon–quark–spectator "diquark" vertex function, $\Gamma(p,p_q)$. Within the instant-form approximation [5], taking the positive energy nucleon projection,

$$\rho(p^2_q,p^2,x,Q^2) \ \to\ \mathrm{Tr}\left[(\not{p}+M)\,\overline{\Gamma}(p,p_q)\,(\not{p}_q - m_q)^{-1}\ \not{q}\,(\not{p}_q-m_q)^{-1}\,\Gamma(p,p_q)\right], \tag{6}$$

where m_q is the quark mass. The simplest approximation is to assume that the vertex function is independent of the nucleon virtuality. The momentum dependence of the vertex function can then be parameterized as $\Gamma(p,p_q) \propto (m^2_q - p^2_q)/(\Lambda^2 - p^2_q)^n$, which allows one to account for the bound nature of the nucleon state [5]. The parameters Λ and n are then fixed by comparing with the quark distribution data, with the overall normalization fixed by baryon number conservation [5]. The result for the α_s dependence of G is shown in Fig.1 by the dot-dashed curve. The values of x_1 and x_2 are selected to fulfill the condition $x_1/(2-\alpha_s) = 0.6$ (large EMC effect in inclusive measurements) and $x_2/(2-\alpha_s) = 0.2$ (essentially no EMC effect in inclusive measurements). The relatively weak α_s dependence reflects the assumption that the vertex function Γ is independent of p^2 — including such dependence would lead to a steeper slope.

2.2 Suppression of Point-like Configurations in Bound Nucleons

A significant EMC effect in inclusive (e,e') reactions occurs for $x \sim 0.5$–0.6, which corresponds to the high-momentum component of the quark distribution in the nucleon where 3 quarks are likely to be close together [3, 4]. It is assumed in this model that for large x the dominant contribution to $F_{2N}(x,Q^2)$ is given by the weakly interacting point-like configurations (PLC) of partons. The suppression of this component in a bound nucleon is predicted to be the main source of the EMC effect. To calculate this suppression one can use a perturbation series over a small parameter, $\kappa = |\ \langle U_A\rangle/\Delta E_A\ |$, which controls corrections to the description of a nucleus as a system of undeformed nucleons. Here $\langle U_A\rangle \sim -40$ MeV is the average potential energy per nucleon, and $\Delta E_A \approx M^*\text{–}M \sim 0.6$–$0.7$ GeV is the typical energy for nucleon excitations within the nucleus. The estimation of the deformation of the bound nucleon wave

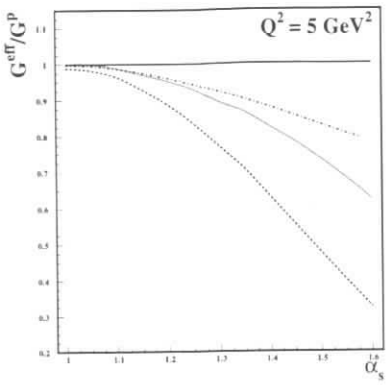

Figure 1 The α_s dependence of $G(\alpha_s, p_T, x_1, x_2, Q^2)$. G^{eff} is normalized to G calculated with the free proton structure function. Dashed, dot-dashed and doted curves represent the PLC suppression, binding and delocalization models, respectively.

function by a Schrödinger equation with a potential which explicitly takes into account the internal structure of the bound nucleon [3] gives the following suppression factor:

$$\delta_A(\mathbf{k}^2) = (1+z)^{-2}, \qquad z = (\mathbf{k}^2/M + 2\epsilon_D)/\Delta E_D, \quad |\mathbf{k}| = \sqrt{\frac{M^2+p_T^2}{\alpha_s(2-\alpha_s)} - M^2}, \tag{7}$$

where $F_{2N}^{eff}(x, Q^2, \alpha_s, p_T) \approx \delta(k) F_{2N}(x/(2-\alpha_s), Q^2)$. The x dependence of the suppression effect is based on the assumption that the PLC contribution in the nucleon wave function is negligible at $x \leq 0.3$, but gives the dominant contribution at $x \geq 0.5$ [4, 7]. The result for G is illustrated by the dashed curve in Fig.1, which in this model has a somewhat larger magnitude for the slope compared with the binding model.

2.3 QCD Radiation, Quark Delocalization

It was observed in Refs.[8, 9] that the original EMC data could be roughly fitted as: $F_{2A}(x, Q^2)/A = F_{2D}(x, Q^2 \xi_A(Q^2))/2$, with $\xi_{Fe}(Q^2) \approx 2$ for $Q^2 \approx 20$ GeV^2, the so-called dynamical rescaling. The observation has been interpreted as an indication that gluon radiation occurs more efficiently in a nucleus than in a free nucleon due to quark delocalization, either in a bound nucleon (or in two nearby nucleons), or in the nucleus as a whole. The Q^2 dependence of $\xi(Q^2)$ follows from QCD evolution equations. In the leading logarithmic approximation one has: $\xi_A(Q^2) = \xi_A(Q_0^2)^{\alpha_{QCD}(Q_0^2)/\alpha_{QCD}(Q^2)}$. If the confinement size in a nucleus, λ_A, is larger than that in a free nucleon, one may expect that the Q^2 evolution may start at $Q_0^2(A) < Q_0^2(N)$, i.e. $Q_0^2(A)/Q_0^2(N) = 1/\xi(Q_0^2(A))$. On dimensional grounds $Q_0^2(A)\lambda_A^2 = Q_0^2(N)\lambda_N^2$, thus $\lambda_A/\lambda_N \approx \sqrt{\xi(Q_0^2(A))}$.

Since in this model the delocalization is approximately proportional to the nuclear density, one can expect that the effect is also proportional to the $\mathbf{k}^2$ of a bound nucleon. Fixing the parameters of the model to fit the Fe data, and assuming $\lambda(\mathbf{k}^2)/\lambda = 1 + a\mathbf{k}^2$ we obtain $a \approx 0.4/ < \mathbf{k}^2 >_{Fe}$, where $< \mathbf{k}^2 >_{Fe} \sim 0.08$ GeV^2/c^2. Using this expression for $\lambda(\mathbf{k}^2)$ one can calculate the $\xi_D(Q^2, \mathbf{k}^2)$, and express the effective structure function of a bound nucleon as:

$$F_{2N}^{eff}(x, \alpha_s, p_T, Q^2) = F_{2N}\left(x, Q^2\xi(Q^2, \mathbf{k}^2)\right), \tag{8}$$

where $\mathbf{k}$ is defined through α_s and p_T according to Eq.(7).

In Fig.1 the predictions of the delocalization model for the α_s dependence of G are denoted by the dotted curve. The predictions are noticeably different for the various models, which suggests that measurement of this ratio for the reaction (1) will be valuable for understanding the origin of the EMC effect.

3 Extraction of the n/p Structure Function Ratio

Aside from providing insight into the origin of the nuclear EMC effect per se, the measurements of tagged events may also be useful in connection with the problem of extracting the neutron structure function from deuteron data. A large ambiguity exists in the asymptotic value of F_{2n}/F_{2p} as $x \to 1$ extracted from inclusive ep and eD data: inclusion of the EMC effect in the deuteron when extracting F_{2n} leads to significantly larger values for F_{2n}/F_{2p} than the 1/4 value obtained in analyses in which only Fermi motion is accounted for [10]. Unlike in inclusive measurements, where the nucleon structure function in the deuteron is smeared by a nucleon momentum distribution in the deuteron, semi-inclusive reactions allow one to select specific values of α_s and p_T in the spectral function $S(\alpha_s, p_T)$, thereby giving the opportunity to minimize the nuclear effects in the deuteron. By selecting backward produced nucleons with $\alpha_s \approx 1$ and $p_T \approx 0$, one can approximately determine the free neutron to proton ratio,

$$\frac{F_{2n}(x, Q^2)}{F_{2p}(x, Q^2)} \approx \left.\frac{F_{2n}^{eff}(x/(2-\alpha_s), p_T, Q^2)}{F_{2p}^{eff}(x/(2-\alpha_s), p_T, Q^2)}\right|_{\alpha_s \approx 1, p_T \approx 0}. \tag{9}$$

For non-zero p_T, deviations of this ratio from the free limit are proportional to p^2 with a good accuracy [2]. Hence, if one samples the data as a function of p^2, interpolation to the pole $p^2 - M^2 = 2M\epsilon$, where ϵ is the deuteron binding energy, should be smooth as long as the momentum of the spectator nucleon is $\lesssim$ 100–200 MeV/c.

References

[1] J. J. Aubert *et al.* (EM Collaboration), Phys. Lett. B **123**, 275 (1983).

[2] W. Melnitchouk, M. Sargsian, and M. Strikman, preprint TAUP-2360-96, UMD PP# 97-15; DOE/ER/40762-094.

[3] L. L. Frankfurt and M. I. Strikman, Phys. Rep. **160**, 235 (1988).

[4] L. L. Frankfurt and M. I. Strikman, Nucl. Phys. **B250**, 1585 (1985).

[5] W. Melnitchouk, A. W. Schreiber, and A. W. Thomas, Phys. Rev. D **49**, 1183 (1994).

[6] S. A. Kulagin, G. Piller, and W. Weise, Phys. Rev. C **50**, 1154 (1994).

[7] L. L. Frankfurt M. M. Sargsian, and M. I. Strikman, Z.Phys. A **335**, 431 (1990).

[8] F. E. Close, R. G. Roberts, and G. G. Ross, Phys. Lett. B **129**, 346 (1983).

[9] O. Nachtmann and H. J. Pirner, Z. Phys. C **21**, 277 (1984).

[10] M. I. Strikman, Nuclear Parton Distributions and Extraction of Neutron Structure Functions, in Proc. of XXVI International Conference on High Energy Physics, World Scientific, Singapore, V.1, 806-809 (1992) Dallas, TX; W. Melnitchouk and A. W. Thomas, Phys. Lett. B **377**, 11 (1996).

Tagged nuclear structure functions with *HERMES*

Silvano SIMULA

INFN, Sezione Sanità, Viale Regina Elena 299, I-00161 Roma, Italy

Abstract: The production of slow nucleons in semi-inclusive deep inelastic electron scattering off nuclei, $A(e,e'N)X$, is analyzed for kinematical conditions accessible at *HERA* with the *HERMES* detector. The sensitivity of the semi-inclusive cross section to possible medium-dependent modifications of the nucleon structure function is illustrated.

The investigation of deep inelastic scattering (DIS) of leptons off the nucleon and nuclei is a relevant part of the experimental activity proposed both at present electron facilities, like $HERA$ and $TJNAF$, and at possible future ones, like $ELFE$ and GSI. As is well known, existing inclusive DIS data [1] have provided a wealth of information on quark and gluon distributions in the nucleon and nuclei. However, important questions, concerning, e.g., the mechanism of quark and gluon confinement as well as the origin of the EMC effect, are still awaiting for more clear-cut answers. To this end, the investigation of semi-inclusive DIS processes is expected to be of great relevance. Recently, in [2]-[5] the production of slow nucleons[a] in semi-inclusive DIS processes off nuclei, $A(\ell,\ell'N)X$, has been analyzed within the so-called spectator mechanism, according to which, after lepton interaction with a quark belonging to a nucleon of a correlated nucleon-nucleon (NN) pair, the recoiling nucleon is emitted and detected in coincidence with the scattered lepton. The basic idea is that the momentum of the recoiling nucleon carries information on the momentum of the struck nucleon before lepton interaction, allowing to tag the structure function of a nucleon bound in a nucleus. In Ref. [5] the semi-inclusive reaction $^2H(\ell,\ell'N)X$ has been analyzed, showing that the experimental investigation of this process can be an effective tool to get information on the neutron structure function as well as on the neutron to proton structure function ratio. The aim of this contribution is to show that, at kinematical conditions accessible at $HERA$ with $HERMES$, the semi-inclusive cross section of the process $A(e,e'N)X$, for $A > 2$, exhibits an appreciable sensitivity to possible medium-dependent modifications of the nucleon structure function.

In case of electron scattering the semi-inclusive cross section reads as follows

$$\frac{d^4\sigma}{dE_{e'}\, d\Omega_{e'}\, dE_2\, d\Omega_2} = p_2\, E_2\, \sigma_{Mott} \sum_{i=L,T,LT,TT} V_i(x,Q^2)\; W_i^A(x,Q^2,\vec{p}_2) \qquad (1)$$

[a] By slow nucleons we mean nucleons with momentum up to $\sim 0.7\ GeV/c$ in a frame where the target is at rest (lab system).

where $x = Q^2/2M\nu$ is the Bjorken variable; $Q^2 = -q^2 = \vec{q}^2 - \nu^2 > 0$ is the squared four-momentum transfer; V_i is a kinematical factor; W_i^A is the semi-inclusive nuclear response; $\vec{p}_2$ is the momentum of the detected nucleon and $E_2 \equiv \sqrt{M^2 + p_2^2}$ its energy ($p_2 \equiv |\vec{p}_2|$).

Let us consider the process in which a virtual photon interacts with a nucleon of a correlated NN pair, and the recoiling nucleon is emitted and detected in coincidence with the scattered electron. Within the impulse approximation and in the Bjorken limit, the semi-inclusive nuclear structure function $F_2^A(x,\vec{p}_2)$ is given by the following convolution formula (cf. [2])

$$F_2^A(x,\vec{p}_2) = M \sum_{N_1=n,p} Z_{N_1} \int_x^{\frac{M_A}{M}-z_2} dz_1\; z_1\; F_2^{N_1}\left(\frac{x}{z_1}\right) \int d\vec{k}_{c.m.}\, dE^{(2)} \; P_{N_1N_2}(\vec{k}_{c.m.} - \vec{p}_2, \vec{p}_2, E^{(2)})\; \delta(M_A - M(z_1+z_2) - M^f_{A-2} z_{A-2}) \qquad (2)$$

where $Z_{p(n)}$ is the number of protons (neutrons); $\vec{k}_1$ and $\vec{k}_2$ are initial nucleon momenta in the lab system before interaction with c.m. momentum $\vec{k}_{c.m.} = \vec{k}_1 + \vec{k}_2$; $\vec{p}_1 = \vec{k}_1 + \vec{q}$ and $\vec{p}_2 = \vec{k}_2$ are nucleon momenta in the final state; F_2^N is the structure function of the struck nucleon. In Eq. (2), x/z_1 is the Bjorken variable of the struck nucleon having initial light-cone momentum $z_1 = k_1^+/M$; $z_2 = (E_2 - p_2\cos\theta_2)/M$ is the experimentally measurable light-cone momentum of the detected nucleon (θ_2 is the detection angle with respect to $\vec{q}$); $z_{A-2} = (\sqrt{(M^f_{A-2})^2 + k^2_{c.m.}} + (k_{c.m.})_{\|})/M^f_{A-2}$ is the light-cone momentum of the residual (A-2)-nucleon system with final mass $M^f_{A-2} = M_{A-2} + E^*_{A-2}$ and intrinsic excitation energy E^*_{A-2}. The relevant nuclear quantity in (2) is the two-nucleon spectral function $P_{N_1N_2}$, which represents the joint probability to find in a nucleus two nucleons with momenta $\vec{k}_1$ and $\vec{k}_2$ and removal energy $E^{(2)}$. For deuteron it simply reduces to the nucleon momentum distribution and for ^3He to the square of the wave function in momentum space, times the removal energy delta function $\delta(E^{(2)} - E^{(2)}_{thr})$, with $E^{(2)}_{thr} = 2M + M_{A-2} - M_A$ being the two-nucleon break-up threshold. In case of ^4He and heavier nuclei, the two-nucleon spectral function is not yet available in the exact form; however, realistic models taking into account those features of the two-nucleon spectral function which are relevant in the study of semi-inclusive DIS processes, have been developed [2]-[4]. In this contribution the $2NC$ model of Ref. [6], where the c.m. motion of the correlated pair is properly taken into account, is adopted, viz.

$$P_{N_1N_2}(\vec{k}_1,\vec{k}_2,E^{(2)}) = n^{rel}_{N_1N_2}(|\vec{k}_1 - \vec{k}_2|/2)\; n^{c.m.}_{N_1N_2}(|\vec{k}_1 + \vec{k}_2|)\; \delta(E^{(2)} - E^{(2)}_{thr}) \qquad (3)$$

where $n^{rel}_{N_1N_2}$ and $n^{c.m.}_{N_1N_2}$ are the momentum distribution of the relative and c.m. motion of the correlated N_1N_2 pair, respectively. We point out that the $2NC$ model reproduces the high momentum and high removal energy components of the single-nucleon spectral function of ^3He and nuclear matter, calculated using many-body approaches, as well as the high momentum part of the single-nucleon momentum distribution of light and complex nuclei (see [6]). Therefore, in the kinematical region $0.3\ GeV/c \lesssim p_2 \lesssim 0.7\ GeV/c$ for the momentum of the recoiling nucleon, the non-relativistic description (3) of the nuclear structure is expected to be well grounded. Using the $2NC$ model, the nuclear effects on the energy and angular distributions of the nucleons produced in semi-inclusive $A(e,e'N)X$ processes have been extensively investigated [2]-[4], showing that backward emission is strongly enhanced when the effects due to the c.m. motion of the correlated pair are taken into account.

Besides the spectator mechanism, there are other reaction mechanisms which could lead to forward as well as backward nucleon emission, like, e.g., the so-called target fragmentation of

the struck nucleon (see [2]) and the hadronization processes following lepton interactions with possible six-quark ($6q$) cluster configurations at short NN separations (see [3, 4]). Furthermore, it should be considered that within the spectator mechanism the virtual boson can be elastically absorbed by the struck nucleon. The contribution from this process, which involves the nucleon form factor instead of the nucleon structure function, vanishes in the Bjorken limit, but it can affect the semi-inclusive cross section at finite values of Q^2 and for $x \to 1$. In what follows, we will refer to such a process as the quasi-elastic (QE) contamination.

The semi-inclusive cross section of the process $^{12}C(e,e'p)X$ has been calculated including in (1) all the nuclear response functions and considering electron kinematical conditions accessible at *HERA* with *HERMES* (i.e., $E_e = 30\ GeV$ and Q^2 in the range $5 \div 15\ (GeV/c)^2$). The relative and c.m. momentum distributions adopted in the calculations are taken from [6]. As for the nucleon structure function, the parametrization of the *SLAC* data of Ref. [7] has been considered. In case of backward proton emission the results obtained for the contributions resulting from the spectator mechanism, the (above-mentioned) hadronization processes and the QE contamination are separately shown in Fig. 1 as a function of the kinetic energy T_2 of the detected nucleon. It can clearly be seen that for $50\ MeV \lesssim T_2 \lesssim 250\ MeV$ (corresponding to $0.3\ GeV/c \lesssim p_2 \lesssim 0.7\ GeV/c$) backward nucleon emission is mainly governed by the spectator mechanism (cf. [2]-[4]). Therefore, in what follows, we will limit ourselves to the case of backward nucleon emission.

In [2] a ratio of semi-inclusive cross sections, evaluated at different values of x but keeping fixed both Q^2 and the nucleon kinematical variables, has been introduced, viz.

$$R_1(x_0, x; Q^2, \vec{p}_2) \equiv d^4\sigma(x, Q^2, \vec{p}_2) \ / \ d^4\sigma(x_0, Q^2, \vec{p}_2) \tag{4}$$

The ratio R_1 turns out to be almost independent of the effects due to the rescattering of the recoiling nucleon with the residual $(A-2)$-nucleon system (cf. [2]); such an important feature is mainly due to the fact that the nucleon kinematical variables are the same in the numerator and denominator of the cross section ratio R_1. In order to investigate the sensitivity of R_1 to possible medium-dependent modifications of the nucleon structure function, three models available in the literature have been considered. In the first one [8] the valence-quark distributions in the nucleon are expected to be suppressed when the nucleon is bound in a nucleus, since point-like configurations (*plc*) in the nucleon should interact weaker in the medium with respect to normal-size configurations. In [8] the suppression factor is expected to be a function of the momentum of the struck nucleon. The second and third models are Q^2-rescaling models [9, 10], where the rescaling is driven by nucleon swelling [9] or by the off-shellness of the struck nucleon [10]. The results obtained are reported in Fig. 2 in terms of the ratio of the quantity R_1, evaluated using the medium-modified nucleon structure function, to the quantity R_1, calculated with the free F_2^N. It can clearly be seen that the ratio R_1 is remarkably sensitive to possible deformations of the nucleon structure function.

Another useful cross section ratio can be defined as

$$R_2(Q_0^2, Q^2; x, \vec{p}_2) \equiv d^4\sigma(x, Q^2, \vec{p}_2) \ / \ d^4\sigma(x, Q_0^2, \vec{p}_2) \tag{5}$$

where both x and the nucleon kinematical variables are kept fixed. The ratio R_2 is expected to be mainly dominated by the Q^2 behaviour of the nucleon structure function. As a matter of fact, explicit calculations show that R_2 is almost independent both of p_2 and of the mass number A, when the free nucleon structure function is adopted. Besides the three models

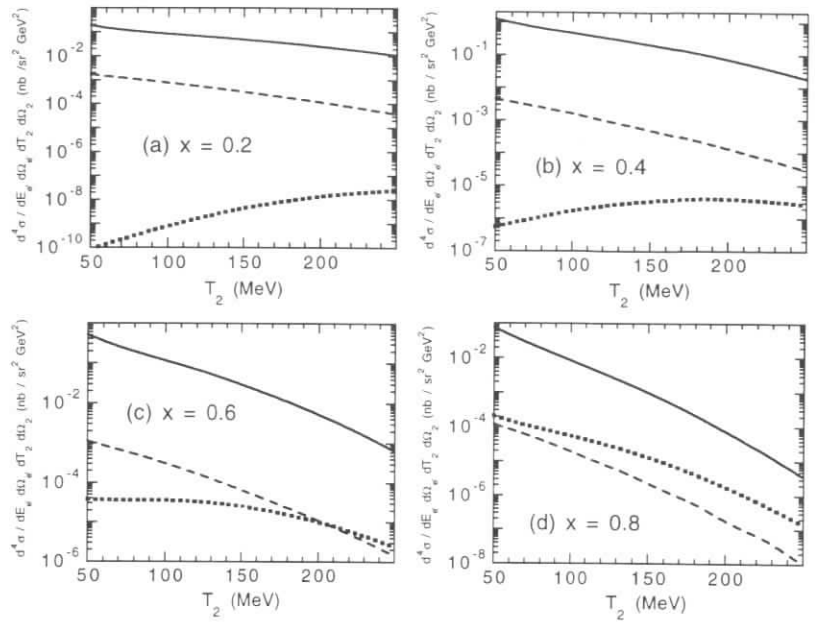

Fig. 1. The semi-inclusive cross section (1) of the process $^{12}C(e,e'p)X$, evaluated at $Q^2 = 10\ (GeV/c)^2$ and for backward proton emission at $\theta_2 = 140°$, versus the kinetic energy T_2 of the detected nucleon at various values of the Bjorken variable x. The solid lines are the results obtained within the spectator mechanism. The dashed lines correspond to the proton emission arising both from the target fragmentation of the struck nucleon, evaluated as in [2], and from virtual photon absorption on $6q$ cluster configurations, evaluated as in [3, 4]. The dotted lines are the contribution from the QE contamination (see text).

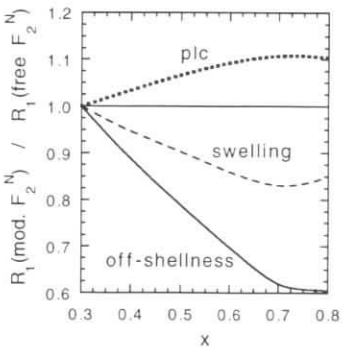

Fig. 2. The ratio of the quantity $R_1(x_0 = 0.3, x; Q^2, \vec{p}_2)$ (Eq. (4)), calculated using medium-modified and free nucleon structure functions. The calculations have been performed in case of the process $^{12}C(e,e'p)X$ at $Q^2 = 10\ (GeV/c)^2$, $p_2 = 0.4\ GeV/c$ and for backward proton kinematics ($\theta_2 = 140°$). The dotted, dashed and solid lines correspond to the models of Refs. [8], [9] and [10], respectively.

employed in the calculations shown in Fig. 2, a further model [11] has been considered. It generates both x- and Q^2-rescaling of F_2^N, driven by binding effects on the energy transferred

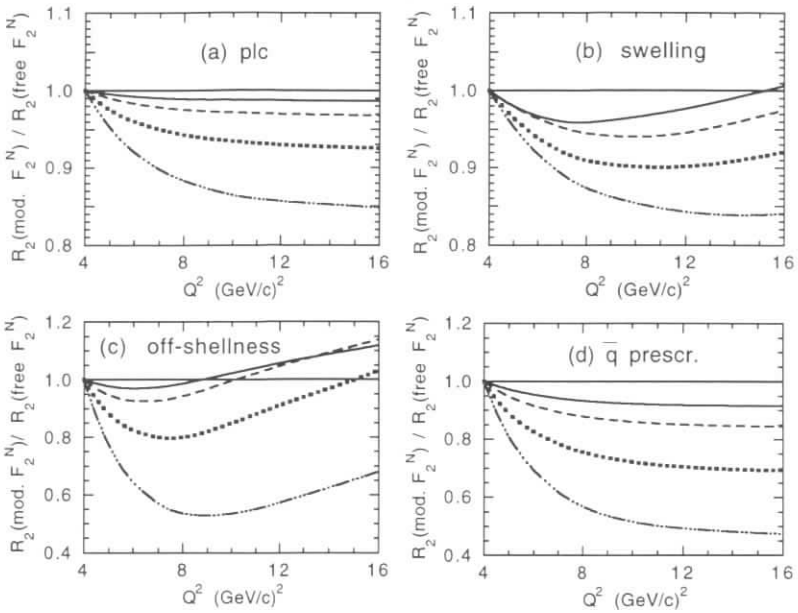

Fig. 3. The ratio of the quantity $R_2(Q_0^2 = 4\ (GeV/c)^2, Q^2; x, \vec{p}_2)$ (Eq. (5)), calculated using medium-modified and free nucleon structure functions. The calculations have been performed in case of the process $^{12}C(e, e'p)X$ at $x = 0.6$ and for backward nucleon kinematics ($\theta_2 = 140°$). The solid, dashed, dotted and dot-dashed lines correspond to $p_2 = 0.3, 0.4, 0.5$ and $0.6\ GeV/c$, respectively. The models adopted for the description of the medium-dependent modifications of F_2^N are from [8] (a), [9] (b), [10] (c) and [11] (d), respectively.

to the struck nucleon. The results are shown in Fig. 3. It can be seen that also the ratio R_2 is appreciably affected by possible deformations of the nucleon structure function and, moreover, the p_2-dependence of the deviations with respect to the predictions obtained using free F_2^N, could provide relevant information on the type of medium effects on F_2^N.

Before closing, it should be reminded that our calculations have been performed within the assumption that the debris produced by the fragmentation of the struck nucleon does not interact with the recoiling spectator nucleon. Estimates of the final state interactions of the fragments in semi-inclusive processes off the deuteron have been obtained in [12], suggesting that rescattering effects should play a minor role thanks to the finite formation time of the dressed hadrons. Moreover, backward nucleon emission is not expected to be sensitively affected by forward-produced hadrons (cf. [13]), and the effects due to the final state interactions of the fragments are expected to cancel out (at least partially) in the cross section ratios R_1 and R_2.

In conclusion, the production of slow nucleons in semi-inclusive deep inelastic electron scattering off nuclei, $A(e, e'N)X$, has been investigated in kinematical regions accessible at *HERA* with the *HERMES* detector. It has been shown that backward nucleon production is mainly governed by the spectator mechanism, provided the Bjorken variable x and the kinetic energy

of the detected nucleon are in the range $0.2 \div 0.8$ and $50 \div 250\ MeV$, respectively. The ratios (4) and (5) of the semi-inclusive cross sections, evaluated at different electron kinematics keeping fixed the nucleon ones, exhibit an appreciable sensitivity to possible medium-dependent modifications of the nucleon structure function.

References

[1] For a review see: M. Arneodo: Phys. Rep. **240** (1994) 301.

[2] C. Ciofi degli Atti and S. Simula: Phys. Lett. **B319** (1993) 23; in Proc. of the 6^{th} Workshop on *Perspectives in Nuclear Physics at Intermediate Energies*, ICTP (Trieste, Italy), May 3-7, 1993, eds. S. Boffi, C. Ciofi degli Atti and M. Giannini, World Scientific (Singapore, 1994), pg. 182.

[3] S. Simula: in Proc. of the Workshop on *CEBAF at Higher Energies*, CEBAF (USA), April 14-16, 1994, eds. N. Isgur and P. Stoler, p. 379.

[4] C. Ciofi degli Atti and S. Simula: Few Body Systems **18** (1995) 55. S. Simula: Few Body Systems Suppl. **9** (1995) 466.

[5] S. Simula: preprint INFN-ISS 96/2, nucl-th 9605024, to appear in Phys. Lett. **B** (1996); preprint INFN-ISS 96/5, nucl-th 9608053 (contribution to this workshop); contribution to the Study Group on *Long-Term Perspectives at GSI*, GSI (Germany), June 1996.

[6] C. Ciofi degli Atti, S. Simula, L.L. Frankfurt, M.I. Strikman: Phys. Rev. **C44** (1991) R7. C. Ciofi degli Atti and S. Simula: Phys. Rev. **C53** (1996) 1689.

[7] A. Bodek and J.L. Ritchie: Phys. Rev. **D23** (1981) 1070. L.W. Whitlow et al.: Phys. Lett. **282B** (1992) 475.

[8] L.L. Frankfurt, M.I. Strikman: Physics Reports **76** (1981) 216; *ib.* **160** (1988) 235.

[9] F.E. Close, R.L. Jaffe, R.G. Roberts and G.G. Ross: Phys. Rev. **D31** (1985) 1004.

[10] G.V. Dunne and A.W. Thomas: Nucl. Phys. **A455** (1986) 701.

[11] L. Heller and A.W. Thomas: Phys. Rev. **C41** (1990) 2756.

[12] A.G. Tenner and N.N. Nikolaev: Nuovo Cim. **A105** (1992) 1001.

[13] G.D. Bosveld, A.E.L. Dieperink and A.G. Tenner: Phys. Rev. **C49** (1994) 2379.

Probing the nucleon meson cloud in semi-inclusive deep inelastic scattering: Tagging of ^{3}He

A.E.L. Dieperink

Kernfysisch Versneller Instituut, Zernikelaan 25, NL-9747AA Groningen, The Netherlands

Abstract: It is proposed to study the pion cloud component in the nucleon using semi-inclusive deep inelastic scattering on light nuclear targets in which the recoiling target nucleus is detected.

1 Introduction

The meson cloud model provides a convenient phenomenological model for treating the non-perturbative sea effects. It has been applied successfully to explain both the SU(2) sea, $(\bar{d}-\bar{u})$ as well as the SU(3) flavor symmetry breaking $(2\bar{s}-\bar{u}-\bar{d})$ effects in the nucleon, observed in inclusive dis and DY experiments. More detailed tests of the pion cloud model can be addressed in exclusive scattering, as originally proposed by Lusignoli [1] to determine the pion structure function. This can be achieved in principle by detecting the slow recoiling proton (or isobar) after dis on a proton target. However, it has been pointed out [2, 3] that the semi-exclusive cross section at all but the smallest x values is dominated by background contributions from di-quark (target) fragmentation.
Several ideas to isolate the meson process from the fragmentation contribution have been suggested. First the measurement of polarization transfer using a polarized proton target [3].
In this note we discuss the semi-inclusive dis on a nuclear target [4] $A(N,Z)$

$$e + A(N,Z) \rightarrow e' + A(N',Z') + X.$$

We argue that in this case the target fragmentation process in which one nucleon is destroyed will in general lead to breakup of the A system whereas in the meson cloud in principle there is a chance to leave the recoiling nucleus A in the ground state. The deuteron has isospin $T=0$ and does not couple elastically to pions and neither does ^{4}He. Therefore it is natural to consider the process on a ^{3}He target in which either ^{3}He (corresponding to an interaction with a π^0), or ^{3}H (interaction with π^+) is detected.

2 The semi-inclusive cross section

For simplicity we neglect final state interactions between spectators and debris of hit hadron.

2.1 Kinematics

We define the variables in the target rest frame and take $\vec{q}$ along the z axis.
Kinematics is defined by the l.c. variables $x = \frac{Q^2}{2m\nu}$, $Q^2 = 4EE'\sin^2(\theta/2)$, $y = \frac{E-E'}{E}$ for the photon, and $p_T^2 = \vec{p}^2\sin^2\alpha$, $z = p^-/m_A$, for the observed nucleus $(m \equiv m_N)$.
Then the four-momentum of the hit pion $t(z,p_T) = t_{\max} - p_T^2/z$, where $t_{\max} = -m_A^2(1-z)^2/z$.
In terms of t the three-momentum of the recoiling nucleus is $|p| = \frac{1}{2m_A}\sqrt{t^2-4m_A^2 t}$.
Therefore the slowest recoil (in the trf) occurs when t is maximal $(t=0)$, i.e. if $z=1$.
Also for given z no particles with target mass (m_A) are produced beyond the kinematical limit $x > \frac{m_A}{m}(1-z)$, i.e. for $t_{\min} = t_{\max} = -mx^2/(1-\frac{m}{m_A}x)$.
In the trf the polar angle is $\cos\alpha = \frac{2m^2(1-z)-t}{\sqrt{t^2-4m^2t}}$ with a maximum value $\alpha_{\max} = \arccos\sqrt{1-z^2}$.

2.2 Cross section

The semi-inclusive cross section for the reaction $e+A \rightarrow e'+X+A$ is given by (after integrating over the azimuthal angle ϕ)

$$\frac{d\sigma}{dxdydzdp_T^2} = \frac{4\pi\alpha^2 s}{Q^4}\left(xy^2H_1 + (1-y)H_2\right),$$

where $H_i(x,z,p_T)$ are the semi-inclusive structure functions.
Using the pion cloud model for H_2, the Bjorken limit, $H_1 = H_2/2x$, and integrating over y one finds

$$\frac{d\sigma}{dxdzdp_T^2} = \frac{4\pi\alpha^2 s}{Q^4}\frac{g_{\pi AA}^2}{16\pi^2}\frac{(-t)|F_{\pi AA}(t)|^2 F_2^\pi(x_\pi)}{(t-m_\pi^2)^2},$$

where the effective pion lc momentum is $x_\pi = \frac{m}{m_A}\frac{z}{1-z}$.
The nuclear pion form factor, $F_{\pi AA}(t)$, can be related to the axial form factor $F_A^5(t)$, $F_{\pi AA}(t) = F_{\pi AA}(0)F_A^5(t)/F_A^5(0)$. We may assume that the t dependence of the axial nuclear form factor is the equal to that of the vector one.
We note that the cross section is a delicate tradeoff between the t dependence of the nuclear form factor $F_A(t)$ which favors small values of $|t|$ (and hence $z \approx 1$, p_T small) and the pion structure function $F_2^\pi(\frac{x}{3(1-z)})$ which decreases rapidly with increasing $z \rightarrow 1-\frac{m}{m_A}x$.

3 Estimates

Let us discuss the special case of a ^{3}He target. The magnetic form factor for ^{3}He is parametrized as [5] $F_A(t) = (\exp At + Bt\exp Ct)$, with $A = 0.48$ fm^2, $B = 0.18$ fm^2, and $C = 0.85$ fm^2.
For concreteness let us consider $x = 0.1$ and a kinetic energy of the recoil of $T = 10(25)$ MeV, at $\alpha = 30^o$ (in practice the smallest angle).
Then $|\vec{p}| = 237(375)$ MeV/c, $p_3 = 205(325)$ MeV/c, $p_T = 119(188)$ MeV/c, $z = 0.93(0.89)$ Then the corresponding values of t, x_π are $t = -(237$ MeV/$c)^2$ and $t = -(374$MeV/$c)^2$, $x_\pi = 0.48$ and $x_\pi = 0.30$, respectively.
As an example we show in figure 1 the differential cross section as a function of z and α for $x = 0.10$ and $x = 0.15$.

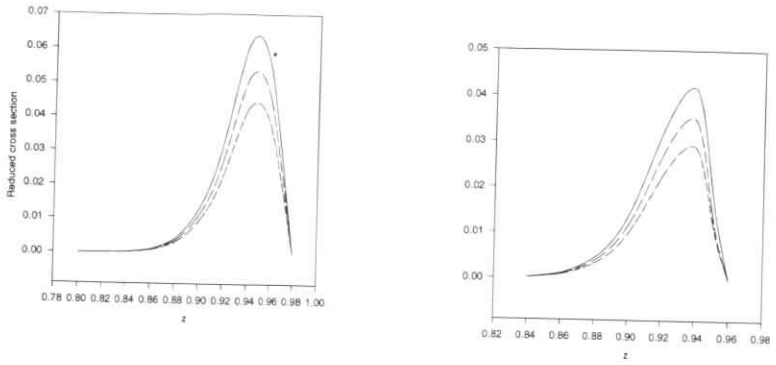

Figure 1: Semi-inclusive cross section for $x = 0.10$ (left) and $x = 0.15$ (right). The angle $\alpha = 30, 40, 50°$ (top to bottom)

4 Discussion

The reaction discussed above can be considered as one example of deep inelastic diffractive scattering on a nucleus in which the nucleus as a whole emerges intact. At smaller values of x, ($x \leq 0.1$) one would expect that heavier mesons or reggions will dominate the reaction. Of particular interest are σ meson exchange, and at very small x one could even speculate on a 'nuclear pomeron' exchange, characterized by vacuum quantum numbers. In principle one could distinguish between the various processes by detecting different iso-spin T_3 members of recoiling nuclei or by using targets with various isospin T.
For example on a $A = 3$ target the ratio of ^{3}He and ^{3}H in the final state, or ^{4}He and d targets ($T = 0$) to check pion isospin selection rule.
In addition the dependence on Q^2, the photon-target center of mass energy, $W^2 = (P + q)^2 = m_A^2 + Q^2(1/x - 1)$, or $M_X^2 = (P + q - p)^2$ is expected to be different for the various processes.

References

[1] M.Lusignoli et al., Nucl. Phys. B155(1979) 394

[2] G.D.Bosveld, A.E.L.Dieperink and O.Scholten, Phys. Rev. C45(1992) 2616

[3] W.Melnitchouk and A.W.Thomas, Z. Phys. A353(1995) 311

[4] A.E.L.Dieperink and S.Pollock, Z. Phys. A348(1994) 117

[5] C.R.Otterman et al., Nucl. Phys. A436 (1985) 688

Meson Cloud Signatures in Semi-Inclusive DIS from Polarized Nucleons

W. Melnitchouk[a], A.W. Thomas[b]

[a] Department of Physics, University of Maryland, College Park, MD 20742, USA
[b] Department of Physics and Mathematical Physics, University of Adelaide, 5005, Australia

Abstract: We investigate the possibility of identifying an explicit mesonic component of the nucleon wavefunction through measurements of polarized Δ^{++} and Λ fragments produced in deep-inelastic leptoproduction off polarized protons. The meson-exchange model predicts a high correlation between the polarizations of the produced baryon and the target proton, in marked contrast with the competing diquark fragmentation process.

1 Introduction

A number of recent experiments have suggested quite non-trivial symmetry breaking effects among the nucleon's quark distributions. The $\overline{u} - \overline{d}$ asymmetry, for example, has been established by the New Muon and NA51 Collaborations at CERN [1], an intuitive understanding of which is provided by a pionic cloud around the nucleon [2]. A non-perturbative kaon cloud, on the other hand, may also generate an asymmetry between the strange and antistrange quark distributions in the nucleon, which the CCFR Collaboration [3] has recently investigated, as well as a polarized strange quark distribution, which may contribute to the explanation of the observed violation of the Ellis-Jaffe sum rule [4].

While strongly suggesting that non-perturbative effects play an important role in nucleon DIS, the results of these experiments do not rule out mechanisms other than meson clouds as those responsible for the symmetry breaking in the quark distributions. Indeed, the evidence for the meson cloud picture is rather indirect, and it seems a formidable challenge to seek direct experimental confirmation of mesonic effects in inclusive DIS. The pertinent question to ask is whether pions or kaons leave any unique traces at all in other processes, which cannot be understood in terms of perturbative quark and gluon degrees of freedom alone.

We propose a series of experiments involving tagged structure functions in semi-inclusive DIS on polarized protons, in which the nucleon's meson cloud may in fact give rise to rather characteristic fragmentation distributions in comparison with the predictions of parton model hadronization [5]. These differences will be significantly enhanced when initial and final state polarization effects are included [6]. With the high luminosity beam, polarized internal targets and 4π detectors capable of capturing slow moving baryons, one should be able to perform this experiment at HERMES.

2 Kinematics of Target Fragmentation

We focus on semi-inclusive production of polarized Δ^{++} baryons from a polarized proton, $e\vec{p} \to e'\vec{\Delta}^{++}X^-$. Because the g_1 structure function of a pion is zero, an unpolarized electron beam will suffice for this purpose. The choice of the Δ^{++} for the final state baryon reduces the backgrounds that one would otherwise have to consider due to the decay of Δs themselves. Furthermore, the decay products of Δ^+ or Δ^0 would include neutral hadrons whose detection would be more difficult, thus increasing the overall experimental uncertainties. Studies of the spin dependence of the fragmentation process here will require the target proton polarization to be parallel to the photon direction, with the spin of the produced baryon quantized along its direction of motion. Experimentally, the polarization of the produced $\vec{\Delta}^{++}$ (for the spin projection $\pm 3/2$ and $\pm 1/2$ states) can be reconstructed from the angular distribution of its decay products (p and π^+). For the case of the K cloud, the relevant reaction to observe is $e\vec{p} \to e'\vec{\Lambda}X^+$. Determining the polarization of the Λ hyperon is considerably easier because the Λ is self-analyzing.

In order to separate cleanly the target and current fragmentation regions requires high values of Q^2. With a 30 GeV electron beam at HERMES one will probe the $0.05 \lesssim x \lesssim 0.1$ region, which is relevant for the pionic contribution, up to $Q^2 \sim 5$ GeV^2 and $W^2 = (P+q)^2 \lesssim 50$ GeV^2, where P and q are the target nucleon and photon four-momenta, respectively.

In the rest frame of the nucleon the produced baryons will typically be slow, with three-momentum given by:

$$|\mathbf{p}| \;=\; \frac{1}{2M}\sqrt{(M^2 + M_B^2 - t)^2 - 4M^2M_B^2}\;, \qquad (1)$$

where M is the nucleon mass, M_B the produced baryon mass, and $t = -p_T^2/\zeta - (M_B^2 - M^2\zeta)(1-\zeta)/\zeta$ is the four-momentum transfer squared between the proton and baryon, with $\zeta = p\cdot q/P\cdot q$ the light-cone fraction of the target proton's momentum carried by the baryon. The slowest baryons will be those for which t is maximized, which occurs when $\zeta \to 1$. As the upper limit on ζ is $1-x$, slow baryon production also corresponds to the $x \to 0$ limit, and the slowest possible particles produced at $\zeta = 1$ (at $x = 0$) will have momentum $|\mathbf{p}_{min}| = (M_B^2 - M^2)/2M \approx 340$ MeV for $B = \Delta$, and ≈ 193 MeV for $B = \Lambda$. For the pion-exchange process considered here, the peak in the differential cross section occurs at $|\mathbf{p}| \sim 600$ MeV, which, for $\zeta \sim 0.8$, corresponds to a missing mass of $p_X^2 = (P - p + q)^2 \sim 5$ GeV^2 for $Q^2 \sim 4$ GeV^2 at HERMES energies.

3 Pion Cloud Dynamics

The pion model is a dynamical model of the nucleon where the dissociation of a physical nucleon into a pion and an "undressed" nucleon or Δ is explicitly witnessed by the probing photon. In the pion-exchange model the differential cross section is:

$$\frac{d^5\sigma}{dx dQ^2 d\zeta dp_T^2} \;\propto\; \frac{\mathcal{F}_{\pi\Delta}^2(p_T^2,\zeta)\; F_2^\pi(x/(1-\zeta),Q^2)}{(t-m_\pi^2)^2} T^{S\,s}(t), \qquad (2)$$

where $\mathcal{F}_{\pi\Delta}$ is the hadronic pion–nucleon form factor, and F_2^π the pion structure function. The quantity $T^{S\,s}(t)$ is the amplitude for a nucleon of spin S to emit a pion of four-momentum squared t, leaving a Δ with spin s.

Note that Eq.(2) is correct only on the light-cone — in the instant-form approach the factorization of the γN cross section into $\gamma\,\pi$ and $\pi\,N$ cross sections holds only in the infinite momentum frame [7]. The formulation on the light-cone also allows one to use the on-mass-shell structure function of the pion in Eq.(2) [8], without the need to extrapolate the pion structure function into the (unknown) off-mass-shell region. For the $\pi N\Delta$ form factor in Eq.(2) we take the form suggested in earlier studies of the pionic content of the proton in inclusive DIS [8]:

$$\mathcal{F}_{\pi\Delta}(p_T^2,\zeta) \;=\; \left(\frac{\Lambda^2+M^2}{\Lambda^2+s_{\pi\Delta}}\right)^2, \qquad (3)$$

where $s_{\pi\Delta} = (m_\pi^2+p_T^2)/(1-\zeta)+(M_\Delta^2+p_T^2)/\zeta$. Since the form factor on the light-cone is not yet very well constrained, other forms for its shape are also possible, however the effects discussed will be largely insensitive to the form factor details, and will be dictated entirely by the proton–pion spin correlations.

Because it is emitted collinearly with the pion, production of Δ baryons with helicity $\pm 3/2$ is forbidden, which leads to the selection rule:

$$\mathcal{T}^{S\,\pm\frac{3}{2}}(t) \;=\; 0. \qquad (4)$$

The yield of spin projection $\pm 1/2$ states is finite, on the other hand, and given by:

$$\mathcal{T}^{+\frac{1}{2}\,\pm\frac{1}{2}}(t) \;=\; \frac{1}{12M_\Delta^2}\left[(M-M_\Delta)^2-t\right]\,\left[(M+M_\Delta)^2-t\right]^2\,(1\pm\cos\alpha). \qquad (5)$$

Because the production of Δ baryons is limited to forward angles in the target rest frame, the factor $(1\pm\cos\alpha)$ associated with the final state polarization will significantly suppress the $s=-1/2$ yield relative to that of $s=+1/2$ final states.

The differential cross section, $Q^2d^3\sigma/dxdQ^2d\zeta$, for the individual polarization states of the produced Δ^{++} (for DIS from a proton with $S=+1/2$) is shown in Fig.1(a) for typical HERMES kinematics, $x=0.075$, $Q^2=4$ GeV^2 and $E=30$ GeV. The pion-exchange model predictions (solid curves) use the form factor in Eq.(3) with a cut-off $\Lambda=800$ MeV, which is consistent with the earlier studies of the contribution of the pion cloud to the inclusive cross sections [8], and which gives for the average number density of the $\pi\Delta$ component $< n >_{\pi\Delta}\approx 0.02$. The spectrum shows strong correlations between the polarizations of the target proton ($S=+1/2$) and the Δ^{++}.

A potentially significant background will be that due to uncorrelated spectator fragmentation. We can estimate the importance of this process within the parton model framework, in which the differential cross section is assumed to factorize into a product of the polarized quark distribution in the nucleon with the fragmentation function for the spectator system to fragment into a baryon with polarization s. For the quark helicity distributions we can use the parametrization from Ref.[9], while for the fragmentation functions we adopt the model of Ref.[6], which combines empirical [10] information on the unpolarized diquark fragmentation functions together with SU(6) relations amongst the spin-dependent fragmentation functions.

In Fig.1(a) the parton model predictions (dashed) for the various polarization states of the Δ are plotted in comparison with the pion-exchange cross sections. In the quark-parton model the correlations are significantly weaker, with the ratio of polarized Δs being $s=+3/2:+1/2:-1/2:-3/2\approx 3:2:1:0$. The comparisons assume that there is no significant interference

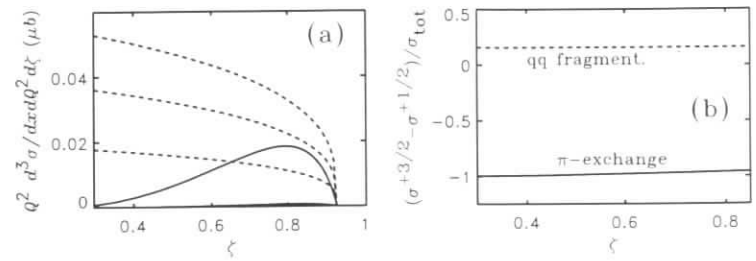

Figure 1: (a) *Differential electroproduction cross section for various polarization states of the* Δ^{++} *(for* $x=0.075$, $Q^2=4$ *GeV*^{2} *and* $E=30$ *GeV). The* π*-exchange model predictions (solid curves: top* $s=+1/2$*, bottom* $s=-1/2$*) are for a cut-off mass* $\Lambda=800$ *MeV. The quark-parton model background estimates (dashed) are for* $s=+3/2$ *(largest),* $+1/2$ *and* $-1/2$ *(smallest).* (b) *Polarization asymmetry for the* π*-exchange (solid) and diquark (qq) fragmentation (dashed) models, where* σ_{tot} *is the sum over all polarization states.*

between the parton fragmentation and pion-exchange contributions. At small values of the exchanged four-momentum squared t one may expect this to be a good approximation, since the distance scales at which the pion and diquark are formed are rather different. For larger values of t this approximation may be less justifiable, and the possibility would exist that interference effects could modify the above simple predictions. This problem would be most pronounced for hard $\pi N\Delta$ vertices, however for relatively soft form factors ($\Lambda\lesssim 800$ MeV), as we have used, the above predictions should be a reliable guide.

Although the total unpolarized parton model cross sections are larger than the pion-exchange cross sections, even at larger values of ζ where the pionic effects are strongest, the differences between the pion-exchange model and fragmentation backgrounds can be enhanced by examining polarization asymmetries. Note that from the angular distributions of the decay $\Delta^{++}\to p\pi^+$ one will be able to experimentally differentiate the $s=\pm 3/2$ and $s=\pm 1/2$ components of the Δ. In Fig.1(b) we show the difference $\sigma^{+3/2}-\sigma^{+1/2}$, where $\sigma^s\equiv Q^2d^3\sigma^{(s)}/dxdQ^2d\zeta$, as a fraction of the total unpolarized cross section. The resulting ζ distributions are almost flat, but significantly different for the two models. In particular, because of the selection rule in Eq.(1) the pion model predicts a large *negative* asymmetry, while the asymmetry in the diquark fragmentation model is small and *positive*. The ratios for t-dependent monopole and dipole form factors [8, 11], are almost indistinguishable from those in Fig.1(b). Therefore, a measurement of the polarization asymmetry appears to test only the presence of a pionic component of the nucleon wave function, independent of the details of the form factor.

Of course the two curves in Fig.1(b) represent extreme cases, in which Δs are produced entirely via pion emission or diquark fragmentation. In reality we can expect a ratio of polarization cross sections which is some average of the curves in Fig.1(b). The amount of deviation from the parton model curve will indicate the extent to which the pion-exchange process contributes. Unlike inclusive DIS, which can only be used to place upper bounds on the pion number, the semi-inclusive measurements could pin down the absolute value of $< n >_{\pi\Delta}$.

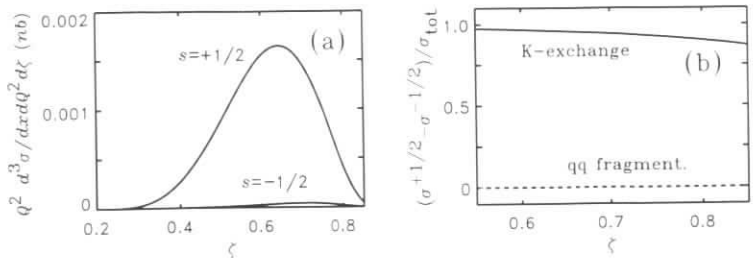

Figure 2: (a) Λ *production cross section in the* K*-exchange model, for a form factor cut-off* $\Lambda = 800$ *MeV, for* $s = +1/2$ *(upper solid curve) and* $s = -1/2$ *(lower solid) final states.* (b) *Polarization asymmetry for* K*-exchange (solid) compared with a leading fragmentation approximation estimate for the parton fragmentation process (dashed). (The kinematic conditions are as in Fig.1.)*

4 Kaon Cloud of the Nucleon

A direct test of the presence of a kaon cloud of the nucleon would be to observe also the differential Λ production cross section at large ζ, and in particular the relative polarization yields. Although some data do exist for Λ production in the target fragmentation region [12], the large errors and limited kinematical range covered do not permit one to unambiguously discern the presence of K effects.

The differential hyperon H $(= \Lambda, \Sigma^0)$ production cross section (included in the observed Λ cross section will be contributions from Σ^0 recoil states, which subsequently decay to $\Lambda\gamma$) is similar to the pion cross section in Eq.(2), with the trace factor here given by:

$$\mathcal{T}_H^{+\frac{1}{2}\,\pm\frac{1}{2}}(t) \;=\; \frac{1}{2}\left((M_H - M)^2 - t\right)(1 \pm \cos\alpha)\,, \qquad (6)$$

for a proton initially polarized in the positive-z direction.

The Λ production cross section for the two possible polarizations in the K-exchange model, with a form factor cut-off $\Lambda = 0.8$ GeV, is shown in Fig.2(a) as a function of ζ. The target and recoil polarizations are predicted to be very strongly correlated, so that the asymmetry shown in Fig.2(b) for the cross sections $(\sigma^{+1/2} - \sigma^{-1/2})/(\sigma^{+1/2} + \sigma^{-1/2})$ is almost unity. The K-exchange ratios are very similar to the π-exchange results in Fig.1(b), indicating the similar spin transfer dynamics inherent in the meson cloud picture of the nucleon.

This is in strong contrast with the expectation from the $qq \to \Lambda$ diquark fragmentation picture, in which the target–recoil spin correlation is much weaker. In fact, to a first approximation the $\Lambda^{\uparrow\downarrow}$ yields in the quark-parton model are equal [6]. Since one has equal probabilities to form a $\Lambda^\uparrow$ and $\Lambda^\downarrow$, in the leading fragmentation approximation the asymmetry will be zero. Of course, SU(6) symmetry breaking effects, as well as non-leading fragmentation contributions, will modify this result, as will contributions from the production and decay of $\Sigma^{0\uparrow\downarrow}$ hyperons. However, the qualitative result that the asymmetry is small should remain true. Therefore the observation of a large polarization asymmetry in the large-ζ region of the target fragmentation region will be evidence for a kaon-exchange fragmentation mechanism.

5 Conclusion

We have outlined a series of semi-inclusive experiments on polarized proton targets that may for the first time enable one to unambiguously establish the presence of a pion and kaon cloud of the nucleon at high energies. Instrumental in identifying the mesonic signature will be detection of the polarization of the slow fragments in the target fragmentation region, which should largely eliminate the backgrounds resulting from the competing diquark fragmentation process. While the experiments proposed here are difficult, requiring all the intensity and duty factor one can obtain at HERMES, it does seem that they will provide quite clear information on the role of the pseudoscalar mesons in the nucleon.

References

[1] P.Amaudruz et al., Phys.Rev.Lett. **66** (1991) 2712; A.Baldit et al., Phys.Lett. B **332** (1994) 244.

[2] A.W.Thomas, Phys.Lett. **126** B (1983) 97.

[3] A.O.Bazarko et al., Z.Phys. C **65** (1995) 189.

[4] J.Ashman et al., Phys.Lett. B **206** (1988) 364.

[5] W.Melnitchouk and A.W.Thomas, in: Proceedings of the Workshop on CEBAF at Higher Energies, eds. N.Isgur and P.Stoler (April 1994) p.359.

[6] W.Melnitchouk and A.W.Thomas, Z.Phys. A **353** (1995) 311.

[7] W.Melnitchouk, A.W.Schreiber and A.W.Thomas, Phys.Rev. D **49** (1994) 1183.

[8] W.Melnitchouk and A.W.Thomas, Phys.Rev. D **47** (1993) 3794; A.W.Thomas and W.Melnitchouk, in: Proceedings of the JSPS-INS Spring School (Shimoda, Japan), (World Scientific, Singapore, 1993).

[9] T.Gehrmann and W.J.Stirling, Z.Phys. C **65** (1995) 461.

[10] M.Arneodo et al., Nucl.Phys. **B264** (1986) 739.

[11] L.L.Frankfurt, L.Mankiewicz and M.I.Strikman, Z.Phys. A **334** (1989) 343; E.M.Henley and G.A.Miller, Phys.Lett. B **251** (1990) 497; A.I.Signal, A.W.Schreiber and A.W.Thomas, Mod.Phys.Lett. A **6** (1991) 271; W.Melnitchouk, A.W.Thomas and A.I.Signal, Z.Phys. A **340** (1991) 85; S.Kumano and J.T.Londergan, Phys.Rev. D **44** (1991) 717; W.-Y.P.Hwang, J.Speth and G.E.Brown, Z.Phys. A **339** (1991) 383.

[12] M.Arneodo et al., Phys.Lett. **145** B (1984) 156.

Soft Neutron Production - a window to the Final State Interactions in DIS

M. Strikman[a,b], M.G. Tverskoy[b], M.B.Zhalov[b]

[a] Pennsylvania State University, University Park, PA, USA
[d] S.Petersburg Nuclear Physics Institute, Russia

Abstract: We analyze the production of soft neutrons ($E_n \leq 10$ MeV) in deep inelastic scattering and conclude that the recent E-665 data indicate strong suppression of the final state interactions in DIS at high energies. Hence we suggest that studies of the energy dependence of the soft neutron yields would provide a sensitive probe of the dynamics of the final state interactions in DIS.

The final state interactions (FSI) in deep inelastic scattering allow us to probe the space-time evolution of strong interactions. Observing these effects is a challenging job, especially if one wants to study their energy dependence. The soft neutron yield ($E_n \leq 10MeV$) is one of the very few observables which can be studied both at fixed target energies using standard detectors of low energy neutrons and at collider using a forward neutron calorimeter [1]

The mechanism of soft neutron production is reasonably well understood - such neutrons are produced by pre-equilibrium emission and evaporation from the residual nuclear system left after the cascade stage of the fast particle-nucleus interactions. In the case of heavy nuclei these neutrons provide the major channel of "cooling" of the residual system. For intermediate A, where the Coulomb barrier is not high, neutrons take away about half of the excitation energy, with the rest carried by the charged fragments.

The total neutron multiplicity is *approximately proportional* to the number of nucleons knocked out from the nucleus at the fast stage of interaction provided the number of the number of of knocked out nucleons is sufficiently small. Therefore, the measurement of such a multiplicity should provide *a global measure of the number of wounded nucleons*. The standard Monte-Carlo cascade codes describe the neutron yields in the intermediate energy reactions ($E_{inc} \leq 1GeV$) reasonably well. We estimate the precision of current codes to be on the level $\sim 20\%$, which includes all possible reasonable variation of the input parameters such as the level density of nuclear states, etc.

Recently the E-665 collaboration [2] has reported the first data on the production of low energy neutrons with kinetic energies $E_n \leq 10$ MeV in DIS of high energy muons off a number of nuclear targets: D, C, Ca, Pb. Relatively small **average** multiplicity of such neutrons, $\langle N_n(A) \rangle$ was reported:

$$\langle N_n(Pb)(E_n \leq 10 \text{ MeV}) \rangle \simeq 5 \pm 1 \pm 0.3. \quad (1)$$

$$\langle N_n(Ca)(E_n \leq 10 \text{ MeV}) \rangle \simeq 1.8 \pm 0.5 \pm 0.3. \quad (2)$$

The second error reflects systematic errors associated with the method of background subtraction which assumed that background is the same as for scattering off the deuteron. Obviously this assumption is more important for the case of lighter targets where overall neutron multiplicity is smaller. Hence we will concentrate on the analysis of the Pb data and briefly comment on the Ca data.

It appears that the only available high-energy data on production of soft neutrons were obtained at ITEP [4] for the incident protons with $1.4 \leq p_p^{inc} \leq 9$ GeV/c. We find that in the overlapping energy range: 7.5 MeV $\leq E_n \leq$ 10 MeV the spectra measured in the two experiments using lead target have similar shapes. However, the neutron multiplicity is much higher for the high-energy proton projectiles, which reflects the much larger number of wounded nucleons in pA interactions. To compare the number of neutrons produced per wounded nucleon we calculated $\frac{1}{A\sigma_{tot}(aN)} \frac{d\sigma^3(a+A\to n+X)}{d^3p/E}$ for proton and muon projectiles, since in the Glauber type models without secondary interactions this quantity does not depend on the projectile [3]. We still found about a factor of two larger value of this quantity for the proton case, indicating that secondary interactions are more important for the proton projectile.

The DIS data were taken for small x where some nuclear shadowing is observed. Shadowing leads to increase of the fraction of diffraction events in which no neutron is produced. However at the same time shadowing leads to increase of contribution of events where γ^* inelastically interacts with $\geq$ two nucleons. It is easy to check that the overall effect is a small increase in the neutron multiplicity. So for the rough estimates we will neglect shadowing in the further analysis.

It is generally assumed that in DIS high-energy hadrons are formed beyond the nucleus and that only hadrons with energies $\leq$ few GeV are involved in FSI. The most conservative assumption seems to be that only recoiling nucleons reinteract in the nucleus. The spectrum of these nucleons can be approximated at small x and not very large energies, where the triple Pomeron contribution is still small, as

$$\frac{1}{\sigma_{\gamma^* p}} \frac{z d\sigma^{\gamma^*+p\to N+X}}{dz d^2p_t} \propto \exp(Ap_t^2)\sqrt{z}, \quad (3)$$

with $\langle p_t^2 \rangle^{1/2} \sim 0.4$ GeV/c, see discussion in [3]. Here z is Feynman x for the nucleons. Therefore the average kinetic energies of the produced nucleons in the nucleus rest frame are of the order 300-400 MeV. Hardly any time formation arguments could be applicable in this case. So production of soft nucleons through the creation of the hole due to removal of one nucleon and subsequent interactions of this nucleon with the rest of the nucleus should be considered as a *lower limit* for the rate of the soft neutron production. This limit obviously does not include production of soft neutrons in the process of absorption of slow pions produced in the elementary lepton-nucleon DIS, for which time formation arguments do not apply as well.

To estimate this *lower limit* we used a Monte Carlo code for the intermediate energy hadron -nucleus interaction for all stages of the process: cascade, which includes processes of knock-out of nucleons, production and subsequent interaction of pions, pre-equilibrium emission and evaporation of neutrons and charged particles, see e.g. [5]. The total number of simulated events in every case was 50000. We focused on the case of scattering off Pb, since the muon data are more accurate in this case. We checked our version of the code using ITEP data [4]. and found a good agreement with these data, see Fig.1, confirming that we can trust predictions of the code with stated above accuracy of about 20 %. To calculate the rate of the soft neutron production we considered the following model: (i) a nucleon was removed from any point in the nucleus with a probability proportional to the nuclear density; (ii) An energy W was assigned to

[1] Note that for collider kinematics, soft neutrons have energies $\approx E_A/A$ and very small transverse momenta. As a result the H1 and ZEUS neutron detectors have nearly 100% acceptance for these neutrons. [1]

1085

it, (iii) Nucleon propagation in the nuclear medium and subsequent production of soft neutrons was modeled using the Monte-Carlo code tested using pA data.

The multiplicity of the produced neutrons for different cutoffs in E_n is shown in Fig.2. One can see that for kinetic energies of interest: 200 MeV $\leq W \leq$ 500 MeV the soft neutron multiplicities rather weakly depend on W. We estimate

$$\langle N_n(Pb)(E_n \leq 10 \text{ MeV})\rangle_{lowerlimit} = 6 \pm 1.5, \tag{4}$$

which is reasonably close to the experimental number of 5 ± 1. Qualitatively, the shape of the energy distribution is also reproduced. However, the shape for $E_n \geq 2MeV$ is more sensitive to the energy spectrum of the knocked out nucleons. Thus a more detailed comparison with the data would require modeling of the initial spectrum of the knock out nucleons. This will be reported elsewhere. In the case of μCa scattering our limit for the same cuts is $N_n(Ca) \geq 1.2 \pm 0.2$ which is somewhat smaller than the number reported by E-665 (eq.2). However within the systematic errors the lower bound is not significantly below the data. Note also, that in the case of $A \ll 200$ one needs to perform further tests of the codes since deexcitation process is more complicated in this case: for Ca about 50% of the energy is released via emission of protons and heavier fragments, though for $A \geq 200$ neutrons carry practically away practically all excitation energy.

Let us briefly discuss how many more extra neutrons one could expect from the secondary interactions e.g. in the string models, where produced quark interacts with effective cross section $\sigma_{eff} \approx 20$ mb, for discussion of these models and references see [6]. The total number of nucleons knocked out by the quark can be easily calculated if the nucleon correlations in nuclei are neglected:

$$\Delta N(A) = \sigma_{eff} \frac{A-1}{2A^2} \int T^2(b) d^2b, \tag{5}$$

where $T(b) = \int_{-\infty}^{\infty} dz \rho_A(b,z)$, and nuclear density $\rho_A(\vec{r})$ is normalized to $\int d^3r \rho_A(\vec{r}) = A$. For $20 \leq A \leq 200$, $\Delta N(A) \propto A^{0.5}$. For $\sigma_{eff} = 20$ mb: $\Delta N(Ca) \simeq 0.7$, $\Delta N(Pb) \simeq 1.5$. Naively this would lead to increase of our lower bound estimate by a factor of 1.7 and 2.5 respectively. Clearly, this would be hard to accommodate at least in the case of scattering off Pb.

Thus we conclude that the E-665 data for neutron yield from Pb indicate substantial suppression of FSI. To reconcile this with the data at lower energies where substantial FSI effects were observed one would need to assume that FSI decrease with increase of the energy. This is consistent both with the trend of the E-665 data for $\langle N_n(Pb)(E_n \leq 10 \text{ MeV})\rangle$ to fall with increase of E_{inc} and with decrease of the probability for the produced fast hadrons to reinteract with nuclei which was also observed by E665 [7].

We conclude that a systematic study of the energy dependence of the neutron yield starting from the incident energies available at HERMES is necessary. Since the absorption of the leading hadrons is expected to decrease rather rapidly with increase of E_{inc} in the HERMES energy range, one can expect substantial decrease of the soft neutron yield in the HERMES kinematics. It would be interesting to study correlation between the soft neutron multiplicity and the spectrum of leading hadrons (z-distribution, p_t broadening, etc). It is necessary also to repeat the E665 experiment at higher energies to check the rather amazing finding of this experiment of the low rate of production of soft neutrons. If the decrease with E_{inc} and low neutron multiplicity at $E_\mu \geq 200$ GeV are confirmed, the soft neutrons would provide a perfect tool to look for relatively rare final state interactions in DIS at HERA collider at small x by

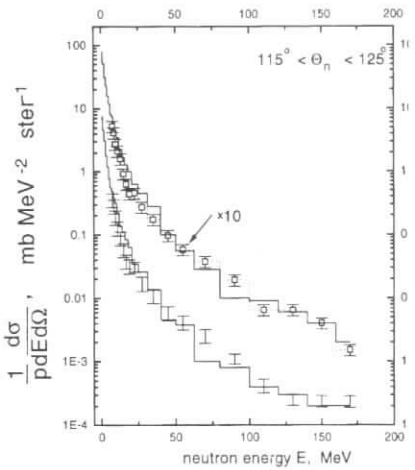

Figure 1: *Comparison of the results of the Monte Carlo cascade-evaporation calculation of the neutron spectra in $p + Pb \to n + X$ process -solid curves with the ITEP data [4] at $P_p = 1.4GeV/c$ and $P_p = 2GeV/c$ - dashed lines with open circles and squares.*

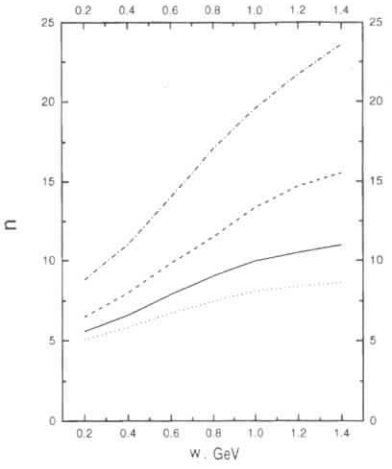

Figure 2: *Multiplicity of neutrons produced in the process where a nucleon with energy W was produced inside Pb for different energy intervals of the neutron energy. Dotted, solid, dashed curves are multiplicities of evaporated nucleons for $0 \leq T_n \leq 6$ MeV, $0 \leq T_n \leq 10$, $0 \leq T_n \leq 50$ MeV dashed-dotted curve is the total neutron multiplicity.*

selecting events with much larger than average neutron multiplicity. The study of soft neutron production at the electron machines for $x \sim 1$ and $Q^2 = 0.5 - 1GeV^2$ would be also of help to check dynamics of low-energy FSI.

We would like to thank K.Griffioen for discussions of the E-665 neutron data, G.van der Steenhoven for useful comments and B.Z.Kopeliovich for discussion of the string models. The research was supported by the DOE grant DE-FG02-93ER40771 and the ISF grant SAK 000.

References

[1] J.Chwastowski and M.W.Kransy, Contribution to this volume.
[2] E665, M.R.Adams et al Phys.Rev.Lett. 74 (1995)5198.
[3] L.Frankfurt and M.Strikman, Phys.Rep. **76**,217(1981).
[4] Yu.D. Bayukov et al., ITEP-172, 1983.
[5] V.S.Barashenkov and V.D.Toneev "Interaction of high energy particles with nuclei" Moscow, 1972.
[6] B.Z.Kopeliovich, Contribution to this volume and private communication.
[7] E665, M.R.Adams et al, Z.Phys..C61,179,1994

Nearthreshold Large Q^2 Electroproduction off Polarized Deuteron

L. Frankfurt[a,d], M. Sargsian[a,e], M. Strikman[b,d]

[a] Tel Aviv University, Tel Aviv, Israel

[b] Pennsylvania State University, University Park, PA, USA

[d] S.Petersburg Nuclear Physics Institute, Russia

[e] Yerevan Physics Institute, Yerevan, Armenia

Abstract: The exclusive and inclusive electroproduction off the polarized deuteron is considered at large Q^2 and $x \geq 0.5$. It is shown that the use of a polarized target will allow to emphasize smaller than average internucleon distances in the deuteron. As a result, we expect amplification of all the effects (color transparency, relativistic dynamics, etc.) sensitive to small internucleon distances. Numerical estimates are given for the processes $e + \vec{d} \to e + p + n$ and $e + \vec{d} \to e + X$.

1 Motivation

The theoretical analysis [1] of the intermediate energy $Q^2 \sim 1$ GeV^2 electrodisintegration of the deuteron at $x \sim 1$ indicates that there is a fast convergence of the higher (large l) partial waves of the final pn continuum wave function. As a result, we can substitute the (infinite) sum over the partial waves with the phenomenological amplitude for pn scattering. This simplification allows to implement relativistic kinematics of the final state interaction (FSI) amplitude through the analysis of the corresponding (covariant) Feynman diagrams [2]. The main theoretical conclusion [2] is that, at $Q^2 \geq 1$ GeV^2, there exists a unique scheme of legitimate calculations within the extended eikonal approximation which selfconsistently accounts for relativistic dynamics. This enhances considerably the exploration potential of the electroproduction reaction, especially off a deuteron target, whose wave function is well established at Fermi momenta ≤ 400 MeV/c.

Based on this, we discuss two alternative studies:

- Investigation of the QCD prediction that the absorption of a high momentum virtual photon by a nucleon leads to the production of a small size color singlet state, optimistically called a point-like configuration (PLC). Such a study requires selection of kinematics where small enough Fermi momenta dominate and where the transverse momenta of the spectator nucleons are large enough so that the dominant contribution is given by the reinteraction of the PLC with a spectator nucleon (see Sect. 2).

- Probing relativistic effects in deuteron electrodisintegration at moderate $Q^2 \leq 4$ GeV^2 and rather large longitudinal Fermi momenta. Such a study will provide a critical discrimination between the different approaches to high energy scattering off deeply bound nucleons.

Both these studies would greatly benefit from the use of a polarized target. The reason is that the use of a $\vec{d}$ allows to enhance the contribution of the D-state in the deuteron's ground state wave function. Due to the diminishing probability of the D-state at small Fermi momenta, these reactions would be sensitive to smaller internucleon distances in the deuteron as compared to the unpolarized case, leading to an amplification of all the effects sensitive to small internucleon distances.

2 Color Transparency Effects and Vanishing FSI

In QCD, the absorption of a high Q^2 photon by a nucleon produces a PLC, which, at very high energies, would not interact with the nucleons, thus eliminating FSI. This vanishing of

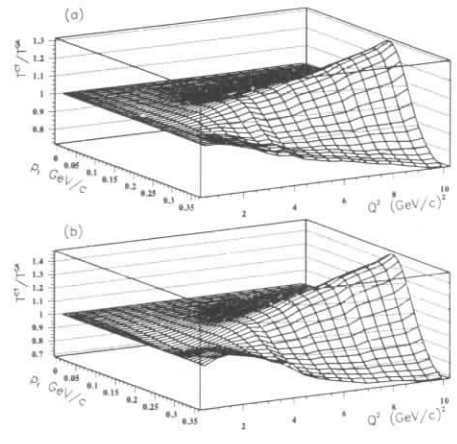

Figure 1: *p_t and Q^2 dependence of the ratio T^{GA}/T^{CT} for $\alpha \equiv (E_s - p_s^z)/m = 1$. a) quantum diffusion, b) three state model.*

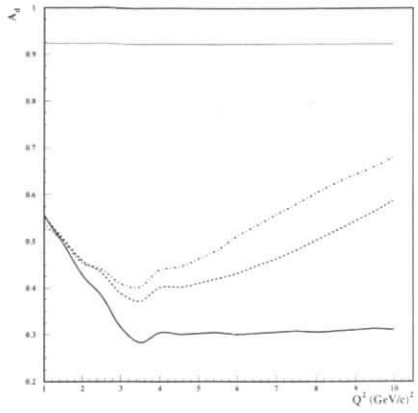

Figure 2: *Q^2 dependence of A_d for $\alpha = 1$. Solid line - elastic eikonal, dashed - QDM, dashed-dotted - three state model, dotted - PWIA.*

the FSI has been termed color transparency (CT). At high but finite energies, a PLC is actually produced, but it expands as it propagates through the nucleus [3]. To suppress the expansion effects, it is necessary to ensure that the expansion length, $l_h \sim 0.4(p/\text{GeV})$, is greater than the characteristic longitudinal distance in the reaction. In the considered $d(e, e'pn)$ and $d(e, e'pN^*)$ reactions, where one nucleon carries almost all the momentum of the photon while the second nucleon (or its resonance) is a spectator, the actual expansion distances are the distances between the nucleons in the deuteron [1]. Thus, suppressing large distance effects through the deuteron's polarization, one effectively will diminish the PLC's expansion, leading to an earlier onset of CT.

The scattering amplitude $\mathcal{M}$, including the np final state interaction, can be written as:

$$\mathcal{M} = < p_s^z, \vec{p}_t | d > - \frac{1}{4i} \int \frac{d^2 k_t}{(2\pi)^2} < \tilde{p}_s^z, \vec{p}_t - \vec{k}_t | d > \mathbf{F^{np}}(\vec{\mathbf{k}}) \, [1 - i\beta] \,, \qquad (1)$$

where $\tilde{p}_s^z = p_s^z - (E_s - m)\frac{M_d + \nu}{|\vec{q}|}$ and $E_s = \sqrt{p_s^2 + m^2}$. Here, p_s is the spectator momentum and M_d the mass of the deuteron. The difference between $\tilde{p}_s^z$ and p_z accounts for the longitudinal momentum transfer. Spin indices are suppressed to simplify the notations. The function $\mathbf{F^{np}}$ represents the FSI between the outgoing baryons and its form depends on the model describing the soft rescattering. Within the elastic eikonal (Glauber) approximation (GA), $\mathbf{F^{np}}(\vec{\mathbf{k}}) \to f^{np}(\vec{\mathbf{k}_t})$, where $f^{pn} = \sigma_{tot}^{pn}(i + a_n)e^{-b_n k_t^2/2}$. At $Q^2 > 3$ (GeV/c)^2, the quantities σ_{tot}^{pn}, a_n and b_n depend only weakly on the momentum of the knocked-out nucleon, with $\sigma_{tot}^{pn} \approx 40$ mb, $a_n \approx -0.2$ and $b_n \approx 6 - 8$ GeV^{-2} for the kinematics we use.

The reduced interaction between the PLC and the spectator nucleon can be described in terms of its transverse size and the distance z from the photon absorption point, i.e., in Eq.(1) we replace $\mathbf{F^{pn}} \to f^{PLC,N}(z, k_t, Q^2)$. For numerical estimates of the reduced FSI $f^{PLC,N}(z, k_t, Q^2)$, we use the quantum diffusion model (QDM) [4] as well as the three state

model [5]. Latter is based on the assumption that the hard scattering operator acts on a nucleon and produces a PLC, which is represented as a superposition of three baryonic states, $|PLC\rangle = \sum_{m=N,N^*,N^{**}} F_{m,N}(Q^2)|m\rangle$. In Fig.1, we compare the predictions of the elastic eikonal and the two CT models for the transparency, $T = \sigma^{FSI}_{e,e'p}/\sigma^{PWIA}_{e,e'p}$, for an unpolarized target. We consider so-called perpendicular kinematics, where the light cone momentum $\alpha = \frac{E_s - p^z_s}{m} \approx 1$ and $p_t \leq 400\ MeV/c$. It was demonstrated in Ref.[1] that these kinematics maximize the contribution from the FSI and minimizes various theoretical uncertainties. One can see from Fig.1 that, optimistically, one may expect 30% effects from CT at $Q^2 \geq 4 - 6$ GeV^2.

Using a polarized target emphasizes the role of the deuteron's D-state, allowing to probe the space-time evolution at smaller space-time intervals. For numerical estimates, we consider the asymmetry A_d measurable in electrodisintegration of a polarized deuteron with helcities of ± 1 and 0: $A_d(Q^2, \vec{p}_s) = \frac{\sigma(1)+\sigma(-1)-2\cdot\sigma(0)}{\sigma(1)+\sigma(0)+\sigma(-1)}$, where $\sigma(s_z) \equiv \frac{d\sigma^{\vec{d},s_z}}{dE_{e'}d\Omega_{e'}d^3p}$ and s_z is the deuteron's helicity. The Q^2 dependence of the asymmetry A_d for "perpendicular" kinematics, at $p_t = 300$ MeV/c, is presented in Fig.2. One can see from this figure that CT effects can change A_d by as much as factor of two for $Q^2 \sim 10$ GeV^2.

3 Study of the Relativistic Effects

Let us consider now different kinematics, namely $Q^2 \leq 4$ GeV^2. In this case we expect minimal CT effects and therefore the consequences of the FSI are well under control. The kinematics, where the light-cone momentum $\alpha > 1$ and $p_t \approx 0$, are most sensitive to relativistic effects in the deuteron. There are several techniques to treat the deeply bound nucleons as well as relativistic effects in the deuteron. One group of approaches handles the virtuality of the bound nucleon within a description of the deuteron in the lab. frame (we will call them virtual nucleon (VN) approaches) by taking the residue over the energy of the spectator nucleon. One has to deal with negative energy states which arise for non-zero virtualities (see e.g. Ref.[6]). Due to the binding, current conservation is not automatic and one has to introduce a prescription to implement e.m. gauge invariance (see e.g. Ref.[7]). Another approach is based on the observation that high energy processes evolve along the light-cone. Therefore, it is natural to describe the reaction within the light-cone non-covariant framework [8]. Negative energy states do not enter in this case, though one has to take into account so called instantaneous interactions. For this purpose one employs e.m. gauge invariance to express the "bad" electromagnetic current component (containing instantaneous terms) through the "good" component $J^A_+ = -q_+/q_- J^A_-$ [8]. In the approximation when non-nucleonic degrees of freedom in the deuteron wave function can be neglected, one can unambiguously relate the light-cone wave functions to those calculated in the lab. frame by introducing the LC pn relative three momentum $k = \sqrt{\frac{m^2+p_t^2}{\alpha(2-\alpha)} - m^2}$.

Turning to numerical estimates, it is worth noting that it is well established that, by using a polarized deuteron target in $(e, e'p)$ reactions, one can decisively disentangle the VN and LC prescriptions (see e.g. [8]). Now using the recent advances in the FSI calculation, one can repeat a similar comparison for the tensor asymmetry, $T^{20} = \frac{1}{3}(\sigma^{1,1} + \sigma^{1,-1} - 2\sigma^{1,0})$, accounting also for the FSI diagrams. The result of such a comparison is presented in Fig.3 for backward kinematics ($\theta_s = 180^\circ$). One can see that account of the FSI further increases the difference between the predictions of the VN and LC approaches, thus making their experimental investigation more feasible.

The advantage of using a $\vec{d}$ target to enhance the contribution of small internucleon distances

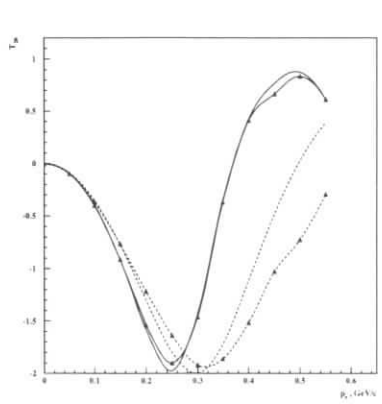

Figure 3: *p_s dependence of the $(e, e'p)$ tensor polarization at $\theta_s = 180^0$. Solid and dashed lines are PWIA predictions of the LC and VN methods, respective marked curves include FSI.*

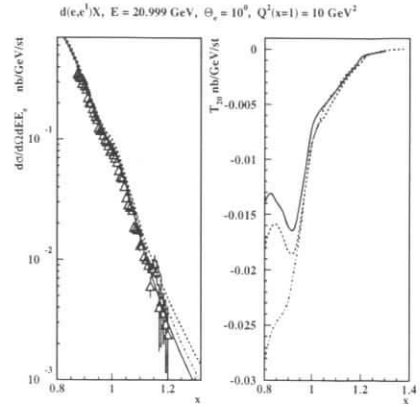

Figure 4: *Q^2 dependence of the unpolarized and tensor polarized cross sections. Solid line - LC approach with PLC suppression, dashed - LC, and dashed-dotted - VN. Experimental data from Ref.[9].*

holds even for inclusive $\vec{d}(e, e')$ scattering. In Fig.4, we compare the predictions of the VN and CT approaches for $d(e, e')$ reactions with unpolarized and polarized deuteron targets. Yielding practically the same predictions for a unpolarized target at $x < 1$, the two approaches differ by as much as a factor of two in the tensor polarization cross section.

3 Conclusions

We demonstrated that the use of a polarized deuteron target allows to probe effectively smaller internucleon distances in the deuteron ground state wave function for semiexclusive $(e, e'N)$ and inclusive (e, e') reactions. This opportunity can be successfully used to gain a better understanding of the structure of (moderate) high energy, large Q^2 eA interactions. In particular, we demonstrated that the use of a $\vec{d}$ target would allow to observe the onset of Color Transparency at intermediate energies as well as to confront different descriptions of relativistic effects in the deuteron and electromagnetic interactions with deeply bound nucleons.

References

[1] L. L. Frankfurt, W. R. Greenberg, G. A. Miller, M. M. Sargsian, M. I. Strikman, Z. Phys. **A352**, 97 (1995); Phys. Lett. **B369**, 201 (1996).

[2] L. L. Frankfurt, M. M. Sargsian, M. I. Strikman, TAUP-2328-96 & nucl-th/9603018 (1996).

[3] L. L. Frankfurt, G. A. Miller and M. I. Strikman, Ann. Rev. Nucl. Part. Phys. **44**, 501 (1994).

[4] G. R. Farrar, L. L. Frankfurt, M .I. Strikman and H. Liu, Phys. Rev. Lett. **61**, 686 (1988).

[5] L. L. Frankfurt, W. R. Greenberg, G. A. Miller and M. I. Strikman, Phys. Rev. **C46**, 2547 (1992).

[6] W. Melnitchouk, A. W. Schreiber, and A. W. Thomas, Phys. Rev. **D49**, 1183 (1994).

[7] T. de Forest, Nucl. Phys. **A392**, 232 (1983).

[8] L. L. Frankfurt and M. I. Strikman, (a) Phys. Rep. **76**, 217 (1981); (b) **160**, 235 (1988).

[9] S. Rock et al., Phys. Rev. Lett. **49**, 1139 (1982).

Working Group on

HERA Upgrades and Impacts on Experiments

Conveners:

W. Bartel (DESY), E. Lohrmann (Hamburg, DESY), F. Willeke (DESY)

Participants:

V. Andreev (LPI), D. Barber (DESY), W. Bartel (DESY), R. Brinkmann (DESY), W. Ebeling (DESY), A. Febel (DESY), R. Felst (DESY), V. Garibian (Yerevan), E. Gianfelice-Wendt (DESY), N. Gogitidze (LPI), N. Holtkamp (DESY), M. Kasemann (DESY), G. Knies (DESY), U. Koetz (DESY), R. Kose (DESY), T. Kowalski (Warsaw), M. Kander (DESY), E. Lohrmann (Hamburg, DESY), J. Maidment (DESY), T. Massam (Bologna), B. Parker (DESY), J. Pflueger (DESY), D. Pitzl (Zuerich), U. Schneekloth (DESY), T. Sen (DESY), L. Suszycki (Warsaw), F. Willeke (DESY), K. Zapfe-Dueren (DESY)

HERA Upgrades and Impacts on Experiments

— Working Group Reports:

HERA Luminosity Upgrade

W. Bartel[b], E.Gianfelice[b], N.Holtkamp[a], E. Lohrmann[a], J. Maidment[b], B.Parker[b], D.Pitzlc, F. Willeke[b], HERA-Zeus Upgrade Group[b],

[a] Universität Hamburg
[b] Deutsches Elektronen-Synchrotron DESY, Notkestrasse 85, D-22603 Hamburg, FRG
[c] Inst. for Particle Physics, ETH— Zürich,

Abstract: Ways to increase the luminosity of HERA beyond the design luminosity of $L = 1.5\ 10^{31} cm^{-2} sec^{-1}$ have been explored and investigated: A new design of the interaction region and upgrade of the injector chain. Most promising appears to be a redesign of the IR based on new types of septum magnets. This promises to increase the luminosity by a factor of four if beam deflection and focusing components are integrated in the colliding beam detector. The consequences of such elements for the detectors have been studied.

Contents

1 Introduction

by E. Lohrmann

1.1 Luminosity Upgrade

The HERA e-p storage ring started operating in June 1992. Since then the delivered luminosity has been steadily increasing: The integrated luminosities were $1pb^{-1}$ in 1993,$6pb^{-1}$ in 1994 and 12 pb-1 in 1995 In 1995 a peak luminosity of $L_{peak} = 7 \cdot 10^{30}/cm^2/s$ has been reached,to be compared with the design luminosity of $1.5 \cdot 10^{31}/cm^2/s$. At beam currents of up to $30mA$ for electrons and $55mA$ for protons,the specific luminosity is about two times larger than the design value. As circulating currents increase, there is therefore a very good prospect to reach or slightly surpass the design luminosity. In addition, other improvements in the machine will lead to an increase of the efficiency, so that in the end the machine could deliver an estimated integrated luminosity of $40 - 50pb^{-1}/year$, leading to $200 - 250pb^{-1}$ in a reasonable running time. So far about $20pb^{-1}$ have been collected.

The experiments H1 and ZEUS have made good use of this luminosity. So far,for luminosity reasons,mostly phenomena at values of $Q^2 << M(W)^2$ have been explored,which allows a wide range of studies of QCD. Important results so far are the accurate measurement of F_2,the structure function of the proton, covering four orders of magnitude in both x and Q^2. Its Q^2 dependence can be described in terms of the GLAP evolution equations,which is a big step forward in the understanding of the proton. The large center of mass energy of HERA has also allowed a new look at diffraction, because its spacelike structure can be investigated in great detail.

A number of new QCD tests add to prove HERA a 'QCD-machine'. These results have attracted wide attention. A large international community of experimental physicists from 15 countries have driven this program vigorously,and encouraged by the QCD physics results, have improved the capabilities of the detectors for this type of physics. It must however be noted that this is 'low Q^2 -physics' compared with the electroweak scale of $Q^2 = M(W)^2$. The physics on the electroweak scale has so far been barely touched. This is the region HERA was built to explore. The unique features of HERA,like electron polarization and the capability to compare electron and positron running are relevant only in the electro-weak regime. New important tests of EW interactions will have to be done; in addition new phenomena outside the standard model are more likely to appear.

Whereas the LEP experiments have explored the standard model for time-like momentum transfers up to $Q^2 \geq 8000 GeV^2$, HERA will look into space-like momentum transfers for $Q^2 \geq 10000 GeV^2$. This work has not really begun and it needs large luminosity. So far H1 and ZEUS have each accumulated about charged current (CC)-events, which are characteristic EW interactions. This is to be compared with the number of events available in 'low Q^2' physics for the F_2 studies, which is of order of 0.5 Mio events. An integrated luminosity of $200pb^{-1}$ will give about 4000 CC events, which is still not a large number. In addition, increasing the luminosity will enhance the discovery potential of the machine. Since one investigates effectively electron-quark collisions, and since the quarks have their momentum distributed up to the proton momentum, an increase in luminosity makes statistically larger cm energies

available. The effective center of mass energy increases about like $(luminosity)^{0}.25$. E.g. an increase of luminosity by a factor 4 beyond design will effectively increase the cm energy of the machine from 300 GeV to 420 Gev,and by the same factor increase the mass range which can be probed for discoveries.

All these questions have been studied in great detail in this workshop. They provide a strong motivation to operate HERA at the largest possible luminosity. In addition, the Scientific Council of DESY has, in its session of February 20, 1996, given a strong endorsement for a program of luminosity increase. The following measures are considered to increase the integrated luminosity:

i improve the efficiency of operation

ii improve the emittance of the proton beam by a new proton preaccelerator

iii decrease the beta function at the interaction point

Measures i) and ii) will allow to make optimum use of the machine in its present configuration. Measure iii) can potentially increase the luminosity by another factor 3-4. However, it will involve changes also in the experiments. It requires to position beam deflecting and focusing elements as close to the interaction point as possible. The scheme proposed here requires the beam elements to be placed well inside the H1/ZEUS experiments. Apart from the need to provide the investment and planning for this project, it will require nontrivial changes in these experiments. In addition it will impair certain instrumental capabilities which have been built to investigate 'low Q^2' physics. For example the beam telescopes,which measure protons and neutrons at very small angles, will remain important, and one would like to keep as much of their capability as possible in the new luminosity scheme.

Because of this interrelation of machine- and experiment issues, a joint design team has to work out the details of the proposed scheme. This should be the next step following this workshop.

1.2 Proton Beam Polarization

If polarized proton beams could be stored, this would, in conjunction with polarized electrons, open a number of novel studies of the spin structure of the proton. The physics potential has been studied in detail in this workshop. Accelerating and storing polarized protons in HERA is exceedingly difficult.Progress has been achieved by the studies of the Spin Collaboration, however it is presently not possible to assess realistically the feasibility and the cost of such a development project. The interest of the physics program with such a facility will have to be weighted against the large technical difficulties. If this looks favorable, it would encourage further studies.

1.3 Light and Heavy Ions in HERA

The physics case for storing deuterium and heavier ions in HERA has been studied in detail in this workshop.Deuterium is interesting, because it allows to study the neutron structure, required to obtain a complete picture of the structure of the nucleon.Storing heavy nuclei

would open the way to novel studies of nuclear matter.The physics interest here calls for storing relatively heavy nuclei.

It is in principle possible to store nuclei with Z=A/2. In general, the luminosity will decrease with increasing atomic number A. The changes required in the machine are relatively straightforward. They have not been worked out in great detail, but rough studies indicate, that the cost of the modifications will be appreciable. No schedule for such an upgrade is set at the present time.

2 HERA Luminosity Upgrade Potential

by F. Willeke

2.1 General Remarks

The HERA electron proton collider is the first accelerator of its kind. Two species of charged particles which are stored in two different accelerator rings are brought into collisions. The accelerator is designed for the collisions of $30GeV$ electrons or positrons with $820GeV$ protons. Maximum beam currents are $58mA$ and $160mA$v respectively. Since no experience on such collisions was available, the HERA designers were conservative in the choice of the basic beam parameters and in the layout of the accelerator lattice. This was considered necessary to provide flexibility in case of unexpected difficulties with the collisions of unequal species.

The layout of the interaction point was a particular concern of the designers. They were faced with a number of difficulties and constraints. First, the luminosity depends on the beam size at the interaction point (IP). This is limited by aperture and by chromatic effects of the low β-quadrupole magnets. The beam size thus can only be made small by putting the low-β quadrupoles close to the IP. However, it is obvious that the two beams have first to be separated after collisions before focusing elements for the high energy proton beam can be placed. Thus a quick beam separation is important for high luminosity. But quick separation requires considerable magnetic fields which lead to strong synchrotron radiation from the lepton beam. This is a potential large source of backgrounds for the colliding beam detectors. A number of additional constraints had to be taken into account. The unavoidable dispersion generated in the separators had to be kept to a minimum to avoid strong synchro-betatron coupling by dispersion in the close-by rf cavities. Furthermore, the IR-straight section had to be made spin-transparent to allow for longitudinally polarized lepton beams.

To achieve small proton beam sizes at the IP is thus difficult. The beam sizes of the two beams have to be matched at the IP in order to limit the non-linearity of the beam-beam interaction seen by the proton beam. Given the rather small HERA lepton beam emittance, it turns out to be rather easy to adapt the lepton beam to whatever can be achieved by the protons. The HERA luminosity is thus limited by the ability to strongly focus the proton beam at the IP.

The compromise found between the various constraints to place the first focusing elements for the proton beam at a distance of $22m$ from the IP which allowed for β-functions of $\beta_x^* = 10m$ and $\beta_y^* = 1m$ at the IP. With the normalized beam emittance of $\varepsilon\gamma = 5\pi mradmm$ and the beam intensity of 10^{11} protons per bunch which was expected from the proton injector chain and the maximum lepton current of $I_e = 58mA$ which is limited by the installed rf power of $10.5MW$ a peak luminosity of

$$L_{peak} = 1.5 \cdot 10^{31} cm^{-2} sec^{-1} \tag{1}$$

was expected for HERA.

Experience of four years of colliding beam operation of HERA led to the following conclusions: The synchrotron radiation background in HERA is well tolerable if the beams and

collimator positions are well tuned. The main source of residual synchrotron radiation background comes from tip-scattering from the upstream synchrotron radiation masks. Thus if the upstream synchrotron radiation masks could be avoided, a considerably larger amount of synchrotron radiation generated in the interaction region could be tolerated. This means that the beams could be separated more quickly, low β-quadrupoles for the protons could be placed closer to the IP and the luminosity could be increased by smaller β-functions of the protons at the IP. This is accomplished by separator magnets which are twice as strong as the present ones but which are placed inside the detector close to the IP. Then, the synchrotron radiation will pass through the IR and can be absorbed further downstream. No upstream masks need to placed and one only has to worry about backscattering form the downstream masks.

A second conclusion may be derived from recent HERA experience. The maximum tolerable beam-beam tuneshift levels assumed for the e-p collider in the original design are probably too conservative. As long as the proton beam size is well matched to the size of the lepton beam, the proton beam lifetime in collision is more than $100hours$ and the background from lost protons in the IR is low. The beam-beam tuneshift of the lepton beam is also rather low and might be further increased. Therefore, a brighter proton beam from the injector chain would also help increasing the HERA luminosity.

Consequently, the present study concentrates on two upgrade projects:

- Redesign of the interaction regions with stronger and earlier beam separation in order to further reduce the β-functions of the proton beam.
- Study of the benefit and of the possibilities of increasing the injection energy of the DESYIII proton synchrotron in order to obtain brigher proton beams.

2.2 HERA Performance 1992-1995 and its Limitations

After commissioning in 1991, HERA started to deliver e-p luminosity to the colliding beam experiments H1 and ZEUS in 1992. Since its first year of running, the performance of HERA was steadily improved and the integrated luminosity could be increased by large factors from year to year. The maximum bunch intensity of the proton beam was always limited by the performance of the injector chain and losses in the beam transfer line. Furthermore, the proton beam lifetime in HERA during the 30min injection period and during the early part of the ramp is critical. Usually, the total amount of beam lost in HERA is 10%. Meanwhile, the DESYIII booster synchrotron, where the intensity and the brigthness of the proton beam is limited by space charge effects at injection energy operates at design parameters of 10^{11} protons per bunch and normalized beam emittances of $\varepsilon \cdot \gamma = 8\pi mradmm$ (90% of the beam). The PETRA accelerator has been steadily improved and is now able to deliver routinely about $80mA$ of beam which corresponds to $6 \cdot 10^{10}$ protons per bunch, 60% of the design value. The transfer between HERA and PETRA suffers from the small aperture available in the $40GeV$ proton beam line with a transfer efficiency of at most 90%. About 5% of the beam loss occurs during injection into HERA. From the remaining intensity another 5% is lost due to a beam lifetime of about $3hours$ while HERA is waiting during the 20min filling procedure. The losses during acceleration are usually small. As a result, presently $65mA$ which is $4.5 \cdot 10^{10}$ protons per bunch (180 bunches) can be made available for e-p collisions on average which is about 45% of the design value.

The intensity of the lepton beam suffered in the case of electrons from a breakdown of the beam lifetime due to interactions of the beam with the ion pumps. This problem disappeared when operation was switched to positrons. The beam intensity at this point is limited at about $45mA$ by rf power and reliability constraints. Thus the HERA intensity limitations are well understood. There are not of fundamental nature and measures are being taken for a step-by-step improvement programme.

The beam dimensions at the interaction points of both proton and electron beams are smaller than the desing values. In both accelerators it was possible to give up safety margins in the apertures which allowed for stronger focusing and smaller β-functions at the IP. The β-functions achieved sofar are $\beta^*_{xp} = 7m$; $\beta^*_{yp} = 0.7m$; $\beta^*_{xe} = 1m$; $\beta^*_{ye} = 1m$ which reduces the beam sizes by about 30% of the design. The fact, that the proton beam intensity is still below design has the side effect, that the proton beam emittance is also below design. Usually emittances smaller than $\varepsilon_N = 20\pi mrad\ mm$ can be achieved in HERA in luminosity operation. This is the reason why the specific luminosity is in excess of the design value by almost a factor of two and it gives luminosity peak values of $L_{peak} = 7 \cdot 10^{30} cm^{-2} sec^{-1}$, which is half the design values despite the low beam intensity.

The stability of both beams in collision is very good. This is true in particular for the protons where the beam lifetime during luminosity operation is in the order of several hundreds of hours and there is very little emittance growth ($\dot{\varepsilon}_N/\varepsilon_N = 0.03/hour$). This however requires well matched beam sizes at the IP in order to avoid an enhancement of the nonlinearity of the beam-beam interaction. Under these conditions and with beam-beam tune shifts in the order of $\Delta\nu = 10^{-3}$, the proton beam seems to be not too close to the beam-beam limit.

The stability of the positron beam is very good as well. Its lifetime is given by beam gas bremsstrahlung due to desorbed gas from the beam pipe walls. Due to unavoidable dispersion in the rf regions which are located in each of the straight sections next to the IP, synchrobetatron

resonances are quite strong. They must be avoided which limits the availabe tune space. Good electron spin polarization requires a working point in between of $Q_x+2Q_s = 0$ and $Q_x+3Q_s = 0$ which causes the beam to blow up somewhat in collisions which causes a loss of luminosity of 10%. If the tunes are chosen far from resonances, the leptons may also be considered to be far from the beam-beam limit. The maximum tuneshift values in 1995 were around $\Delta\nu_y = 0.025$.

An important feature of HERA are the spin polarized lepton beams. Since 1995 HERA is operated with one spin rotators pair in the East straight section for longitudinally polarized beam for the HERMES experiments. The polarization degree is routinely above 60% and is not noticeably affected by the beam-beam interaction

The biggest challenge in HERA luminosity operation is to achieve reasonable reliability and availability of the total accelerator complex. On average, the time spent in luminosity operation is only 35% of the scheduled time. The rest of the time is needed for injection, ramping tuning, recovery from technical faults and trouble shooting. These results have to be compared to a maximum possible efficiency of the order of 70%.

2.3 HERA Luminosity Limitations and Constraints

The luminosity of the HERA e-p collider may be written as

$$L = \frac{N_e N_p N_B f_{rev}}{2\pi\sqrt{\sigma_{xp}^2 + \sigma_{xe}^2}\sqrt{\sigma_{yp}^2 + \sigma_{ye}^2}} \tag{2}$$

(N_p is the number of protons per bunch N_e is the number of leptons per bunch, N_B is the number of bunches, f_{rev} is the revolution frequency, $\sigma_{x,y,e,p}$ are the rms beam sizes for protons and leptons respectively). To show the limitations of the luminosity more clearly, this expression may be rewritten in terms of limited quantities and taking into account additional constraints. An important restriction is that the beam cross sections of protons and leptons have to match to limit the nonlinearity of the beam-beam interaction. This is particularly important for the proton beam to avoid emittance blow-up, bad lifetime and large backgrounds. Thus one has $\sigma_{zp}^* = \sigma_{ze}^* = \sigma_z^*$ (z denotes horizontal or vertical, p and e denote positrons or leptons respectively). Furthermore, the total beam current of the lepton beam will be always limited by the available rf power $N_e = I_e/(e \cdot N_B \cdot f_{rev})$. The number of protons per bunch will be ultimately limited by space charge effects in the injector chain. The maximum number of protons per bunch is therefore related to a maximum beam brightness N_p/ε_N. Furthermore, since the two beams have to be separated after collisions before focusing elements for the proton beam can be placed, the beam size at the IP is expected to be limited by the maximum β-function of the protons at the IR low β quadrupole magnets. Taking these considerations into account, the luminosity may be rewritten as

$$L = \frac{I_e \cdot N_p \cdot \gamma_p}{4\pi e\sqrt{\beta_{xp}^* \beta_{yp}^*}\sqrt{\varepsilon_{xN}\varepsilon_{yN}}} \tag{3}$$

One can see that the luminosity is independent of the number of bunches as long as the beam-beam tuneshift limitation of the proton beam is not touched

$$\Delta\nu_{x,y}^p = \frac{r_p I_e \sqrt{\beta_{x,y}^p}}{2\pi e f_{rev} N_B \varepsilon_N (\sqrt{\beta_x^p} + \sqrt{\beta_y^p})}. \tag{4}$$

Since we assume that we are not limited in the β-function of the lepton-beam, the e-beam-beam tuneshift can be always controlled by an appropriate choice of the lepton beam emittance. Fortunately HERA has a big built-in flexibility of focusing in the arcs.

$$\Delta\nu_{x,y}^e = \frac{r_e N_p \sqrt{\beta_{x,y}^p}}{2\pi\gamma_e\sqrt{\varepsilon_{x,y}^e}(\sqrt{\beta_x^p} + \sqrt{\beta_y^p})}. \tag{5}$$

In order to obtain polarized lepton beams, the vertical beam emittance of the lepton beam must be as small as possible. Therefore, the beam cross section at the IP will be flat ($\sigma_x \gg \sigma_y$). Under these circumstances the vertical beam size could be reduced by reducing the emittance of the protons with almost no increase of beam-beam tuneshift.

$$\Delta\nu_{x,y}^p = \frac{r_p I_e}{2\pi e f_{rev} N_B \sqrt{a}(\sigma_x + \sigma_y)} \tag{6}$$

a is a constant geometrical factor for a given lattice. Provided, that the local chromaticity created in the low β quadrupole is not becoming too large, the β-functions in the low β quadrupoles can be increased by the same factor and the β-function at the IP can be correspondingly made smaller without touching the aperture limitation. ($\varepsilon_N/\beta^* \simeq const = a$)

These considerations lead to the following conclusions: HERA luminosity can only be increased by

- reducing the β-functions at the IP by a IR geometry with the proton low-β quadrupoles closer to the IP. Improvement factors of up to four can be reached until a further reduction of the β-functions is limited by the proton bunch length.
- increasing the vertical beam brightness N_p/ε_{yN} by a reduction of the vertical beam emittance of a factor of two.

3 Study of a New Interaction Region for HERA

3.1 Parameters for Upgraded HERA Luminosity Operation

by F. Willeke

The parameters for luminosity operations for an upgraded HERA are optimized around the smallest achievable β-functions namely

$$\beta^*_{xp} = 2.1m;\ \beta^*_{yp} = 0.13m;\ \beta^*_{xe} = 0.75m;\ \beta^*_{ye} = 36m. \tag{7}$$

The value of the vertical β-function of the protons is limited by the proton bunch length. The horizontal β-function of the protons is limited by aperture and the β-functions of the lepton beam are limited by apertures and chromaticities. This will be shown in the following sections. In this study we require an aperture of $12.5\sigma_{x,y}$ for protons and leptons.

We will make the following assumptions on beam intensities, number of bunches, maximum tolerable beam-beam tune shift values and achievable beam emittances:

Electron/Positron Beam Intensity: The beam intensity in HERAe will be always limited by the available rf power. The presently installed rf power does not allow to store the design current of $58mA$ at a beam energy of $30GeV$. Therefore we plan for an 8th rf station with 14 5-cell room temperature cavities which will provide additional $1.5MW$ of rf power. With this system, the rf power will be just sufficient for storing the design current at slightly below the design energy of $30GeV$. We assume, that we will fill the machine with 180 bunches as in present operation. Some 174 are colliding bunches. Six non-colliding bunches are going to be used for background discrimination. Under these circumstances the number of positrons/electrons per bunch will be $N_e = 4.25 \cdot 10^{10}$.

Proton Beam Intensity: The DESYIII booster synchrotron is presently able to deliver a proton bunch intensity of up to $1.25 \cdot 10^{11}$ protons per bunch. Presently, the beam intensity in HERA is limited by instabilities and non-reproducibilities in PETRA and by tight apertures in the beam lines. These are no principle problems. A programme is underway to improve the proton acceleration chain. It is reasonable to assume, that the design bunch intensity of 10^{11} protons per bunch will be reached in the HERA proton ring eventually.

Proton Beam Emittance: The beam brightness N_p/ε_N is limited in DESYIII by space charge effects. The brightness of the proton beams presently exceeds the design values only slightly. We therefore think it is justified to assume the design emittance of $\varepsilon_{xN} = \varepsilon_{yN} = 5\pi mradmm$ for future HERA operation.

Electron/Positron Beam Emittance: In the old lattice, the limitation of the beam sizes at the IP is given by the limited ability to squeeze the proton beam at the IP. It will be shown below , that one can find a favorable geometry for which the vertical β function at the IP can be made as small as the bunch length. The corresponding beam size is that small, that matching the beam sizes can not be achieved by squeezing the electron β function any more unless one wants to place quadrupole magnets inside the colliding beam detector. Therefore it is necessary to make the electron beam emittance smaller by changing the lattice from 60^0 to 90^0 phase advance per FODO cell in the arcs. Under these circumstances, the emittance will be $\varepsilon_{ex} = 16.65nm\ rad$. An emittance ratio of $\varepsilon_{ey}/\varepsilon_{ex} = 0.13$ is necessary to match the vertical sizes of proton and lepton beams at the IP. This should be easily achievable.

Beam-Beam Tuneshifts: The beam-beam tune shift of the protons does not exceed $\Delta\nu_{xp} =$

	e-beam	p-beam
energy	$30GeV$	$820GeV$
bunch charge N	$4.18 \cdot 10^{10}$	$10 \cdot 10^{10}$
Beam Current	$58mA$	$140mA$
normalized emittance ε_N	$1.85 \cdot 10^{-11} mGeV^{-2}$	$5\pi\mu m\ rad$
horizontal emittance	$16.7nmrad$	$6.1nm\ rad$
emittance ratio	0.13	1
horizontal β at IP β^*_x	$0.75m$	$2.10m$
vertical β at IP β^*_y	$0.36m$	$0.13m$
beam size $\sigma_x \times \sigma_y$	$112\mu m \times 28\mu m$	$110\mu m \times 27\mu m$
beam-beam tune shift/IP $\Delta\nu_{x,y}$	.039, .031	.002, .0004
number of colliding bunches	174	
luminosity	$9.37 \cdot 10^{31} cm^{-2} s^{-1}$	
specific luminosity	$2.1 \cdot 10^{30} cm^{-2} s^{-1} mA^{-2}$	
luminosity increase factor	4.63	

Table 1: Parameters for Upgraded IR Lattice

0.002. This is considered within the limits. The vertical tune shift for protons is much less. The necessity to reduce the lepton beam emittance however pushes the lepton beam-beam tune shift close to $\Delta\nu_{xe} = 0.04$ which is quite a large number. It is considered to be close to the limit according to experience with other lepton colliders.

With these parameters, a luminosity of $L = 9.37 \cdot 10^{31} cm^{-2} sec^{-1}$ can be achieved. The parameters described in this section are summarized in table 3.1.

3.2 Layout of the Lattice

by F. Willeke

The purpose of a new HERA IR design is to achieve significantly smaller β-functions for protons and electrons at the IP. This is only possible if the beams are separated more quickly so that the low-β quadrupoles for the protons can be placed closer to the IP. Synchrotron radiation background generated by the beam separator magnets is the main concern if the separation field should become stronger. Since a large contribution from this background however comes from tip scattering at the upstream synchrotron radiation masks, the fields can be significantly increased if these masks can be avoided. This is the case, if the separation fields occur inside the colliding beam detectors. Then the synchrotron radiation can pass through the whole detector region without hitting an absorber. It then can be absorbed further downstream and one only has to worry about backscattered radiation.

Consequently, an agressive luminosity upgrade scheme is based on an air-coil dipole magnet inside the colliding beam detector. With an outer magnet diameter of 190mm we assume that it can be put at a distance of $1.2m$ from the IP. The magnets have a length of $L = 4.4m$ they provide a bending angle of $\theta = 8mrad$ which corresponds to a bend radius of $\rho = 550m$. For

the nominal beam energy of $E = 30GeV$, a bending field of $B = 0.182T$ is required. This fields corresponds to about the maximum field which can be achieved by an air coil magnet.

In the two separator magnets, a synchrotron radiation power of $P_{syn} = 19.2kW$ is generated. The critical energy is $E_{crit} = 109keV$. The corresponding synchrotron radiation fan must pass through the detector and the downstream magnets without striking any material. This requires quite large apertures in the separator magnet. The distance between the synchrotron radiation fan and the centre of the beam at the downstream end of the downstream separator is $90mm$. At the end of the separator magnet, the two beams are separated by $17mm$

Adjacent to the separator magnet are the focusing elements of the electron beam. The focusing is provided by a low-β doublet of conventional quadrupole magnets. These magnets are placed on the axis of the electron beam and they do not contribute to the separation dipole field and only little synchrotron radiation is generated. A speciality of these magnets is that their coils may not occupy any space in the magnet midplane in the ring-outward direction. This space must be kept free for the synchrotron radiation fan generated by the beam separation. This radiation must be absorbed further away from the IP in order to minimize the background from backscattered synchrotron radiation. The synchrotron radiation background of this arrangement will be discussed below. For the vertical low β quadrupole, a pole tip field of $B = 1\ T$ is required. The pole radius is $35mm$. The magnet $1.43m$ long and at its end, the two beams are already separated by $29mm$. The next element is the horizontal focusing quadrupole for the leptons. Since proton and lepton beams are already strongly separated, a large pole radius of $63mm$ is required to accomodate the proton beam. With a pole tip field of $B = 1\ T$ a length of $L = 2.075m$ is sufficient to provide the necessary focusing. At the end of this magnet, the beams are separated by $47mm$. The peak β-functions in this low-β-doublet are $\beta_{x-max} = 300m$ and $\beta_{y-max} = 100m$. The local chromaticity generated in this doublet is $\xi_x = -5.36$ and $\xi_y = -2.17$. The horizontal local chromaticity is quite large. It gives rise to a considerable off energy β-beat which must be carefully considered especially since a 90^0 phase advance is foreseen in the arcs. In fig 1 the proton and electron beam cross sections are shown respectively.

After $11m$ distance from the interaction point, the beams are separated by $58mm$. This is already sufficient separation for a septum-type quadrupole which focuses the protons vertically. This magnet is a new type of iron yoke half quadrupole with a cut in the mirror plate leaving only very little material between the two beams. This quadrupole allows a pole tip field of $B = 0.86\ T$. With a pole radius of $30mm$, a k-value of $k = 0.01m^{-2}$ is achieved. A length of $7.42m$ is required to provide about 65% of the necessary vertical focusing. In fig 2 the proton and electron beam envelopes are shown at the entrance of this magnet. The picture shows the countors of the half quadrupole poles and the mirror plate with the cut schematically. The rest of the vertical focusing is provided by a quadrupole with a septum coil. The electron beam passes in between the septum and the return yoke. This quadrupole has a pole radius of $r = 33mm$ and a pole tip field of $B = 1\ T$. A k-value of $k = 0.011m^{-2}$ is achieved. With a length of $L = 6.36m$, the vertical focusing is completed. At the begin of this magnets, the two beams are already separated by $122mm$ which leaves some $60mm$ thickness for the septum coil. A current density of $11amps/mm^2$ is required in this coil to generate the quadrupole field. Fig 3 shows the beam cross section at the entrance of this element. The $50mm$ wide septum coil is shown schematically. The end of this magnet is at $25.3m$ from the IP. The beams are now separated by $178mm$ so that a conventional quadrupole magnet is forseen for the horizontal focusing. This is accomplished by a ten meter long quadrupole magnet with a pole radius of

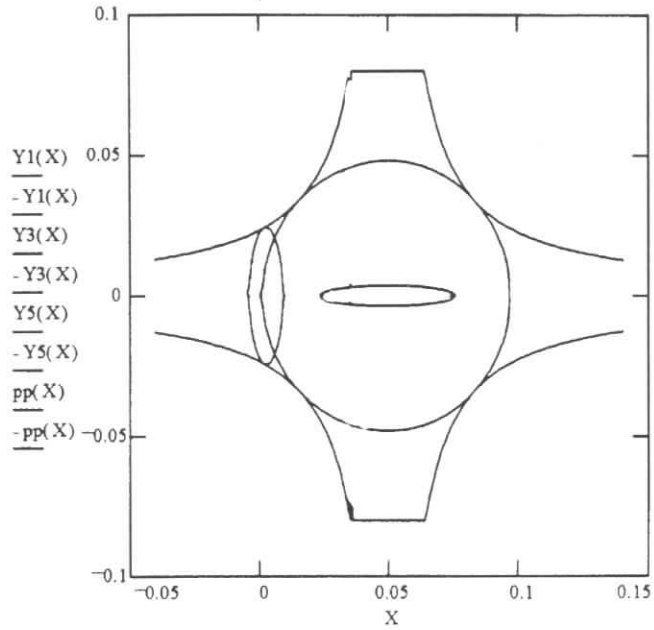

Figure 1: Beam sizes (12.5σ) at the end of the e-beam doublet.

$40mm$ and a pole tip field of $1\ T$. At $35.4m$ from the IP the focusing of the proton beam is accomplished. The maximum β functions in the proton low-β doublet are $\beta_{x-max} = 1807m$ and $\beta_{y-max} = 1639m$. Thus the local chromaticity generated in the doublet compares well with the values of the present HERA lattice. The apertures provide space for 12.5 rms beam sizes and thus has the same margin as the present beam optics.

A complete matching to the arc has not yet been performed. But no problems are expected here. fig 4 shows the β-function in a distance up to 50m from the IP. The geometry with the approximate dimensions of the magnetic elements (top view) is shown in fig 5 in an extended vertical scale.

In the present lattice, there is no compensation foreseen for the changing separator field if the positrons are ramped from $12GeV$ injection to the full energy. This problem can be solved in the following way: First, the proton rf frequency can be phase-locked to the electron rf at a proton beam energy of 400GeV. The two beams have then to be ramped up together to their full energy for which the geometry and the fields are matched. Since there is still a separator field mismatch at electron injection energy because the ratio of $30GeV/12GeV$ is different from $820GeV/400GeV$, some additional compensation of $\theta = 17\mu rad$ is required. This can be provided by the dipole component of the separator half quadrupole field which must be increased by 2%. The corresponding excess quadrupole magnet has to be compensated by the second vertically focusing quadrupole, which has a much smaller dipole component. The course of *beta*-functions is shown is figure 4 and a layout of the IR in extended vertical scale is

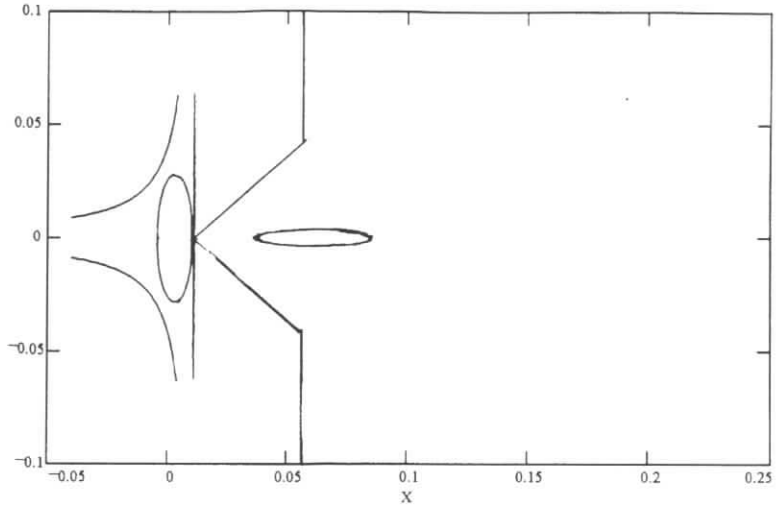

Figure 2: 12.5 σ beam sizes at the entrance of the septum quadrupole

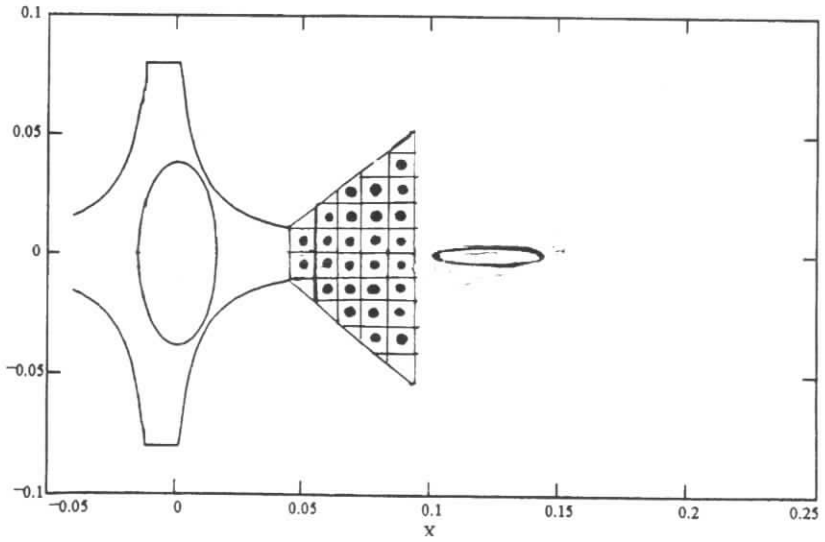

Figure 3: Beam sizes (12.5σ) at the end of the septum coil quadrupole

shown in figure 5.

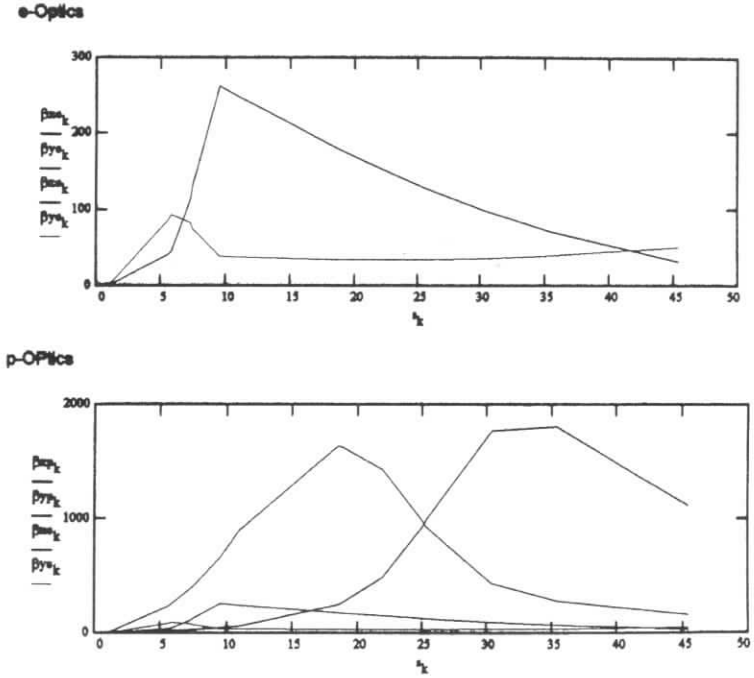

Figure 4: β-functions in meters in the IR region

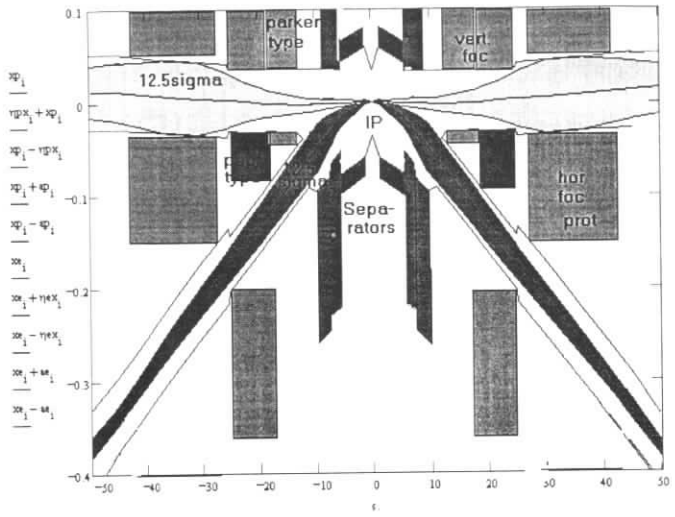

Figure 5: Geometry of the upgraded lattice in the IR. The plot shows the top view of the 12.5σ beam envelopes for proton and electron beam and the limiting magnet apertures. The IP is in the middle of the picture. The boxes represent the magnets which are starting from the IP: the separator magnet, the e-low β-quadrupol doublet, the mirror-plate septum quadrupole, the septum-coil quadrupole (both vertical focusing for protons) and the horizontally focusing quadrupole for the protons. Note that the vertical full scale is only 50cm, the horizontal scale is 100m

3.3 Improved Lattice Design Using a Combined Function Separator Magnet

by B. Parker and F. Willeke

A substantial improvement of the lattice design can be achieved by using a combined function magnet as a separator magnet. A magnet which provides some 35% of the necessary vertical low-β-focusing. A possible design of such a magnets is discussed below. The advantages of this most recent design are:

- The chromaticity of the electron beam is reduced by a large factor. Chromaticity generated in the IR is not an important issue any more.
- The field of the separator is concentrated in a volume occupied by the beam. The volume occupied by the synchrotron radiation fan has only low field. This allows a more economical magnet design.
- The particle beam enters the separator (upstream of the IP) in a high field ($\rho = 450m$). Close to the IP, the field is weaker since the beam has shifted transversely by 15mm($\rho = 650m$). This reduces the synchrotron light background for the luminosity measurement considerably.
- The coils on the ring-outside have to be replaced to produce a quadrupole field. This makes additional room for the synchrotron radiation fan and relaxes the tight aperture conditions in this element.

The disadvantage of the proposed novel solution is an unconventional magnet design, and net forces on the separator due to the detector solenoid field. Since this solution is rather new, these issues have not been studied yet in detail.

Based on such a combined function magnet separator, a self consistent design has been produced which is described below. The β-functions are somewhat relaxed compared to the lattice described in the previous section. Some tribute had to be paid to optics matching to the arcs and realistic magnet apertures. The luminosity improvement factor 4.55 which corresponds to a peak luminosity of $L = 9.2 \times 10^{31} cm^{-2} sec^{-1}$. A Table 2 with updated values is given below. The actual lattices and optics used in defining the magnet design requirements for the e-ring are shown in Fig.6 and for the p-ring in Fig.7. The lattice layout and optics functions are symmetric about the IP so only half of the interaction region magnets are presented.

In this subsection we give an overview of the lattice layout which is followed by more detail descriptions of the magnet parameters and required apetures in later subsections.

The first accelerator magnet starts 1.2 m from the IP and is a combined function (dipole + quadrupole) magnet to provide the horizontal bend for the e-beam to separate it from the p-beam in subsequent magnets and to provide early vertical focusing to help reduce the e-chromaticity. It is followed by a quadrupole doublet which is responsible for the main part of the e-focusing. Care is taken to pass all of the synchrotron radiation generated in the separator magnet completely through these quadrupoles.

The first dedicated p-focusing quadrupole starts at 11 m and incorporates a magnetic septum which isolates the high magnetic field region seen by the p-beam from a very low field region

	e-beam	p-beam
energy	30 GeV	820 GeV
bunch charge N	$4.18 \cdot 10^{10}$	$10 \cdot 10^{10}$
Beam Current	58 mA	140 mA
normalized emittance ε_N	$1.85 \cdot 10^{-11}$ $mGeV^{-2}$	5π μm rad
horizontal emittance	16.65 nm rad	5.72 nm rad
emittance ratio	0.13	1
horizontal β at IP β_x^*	0.83 m	2.4 m
vertical β at IP β_y^*	0.35 m	0.13 m
beam size $\sigma_x \times \sigma_y$	$117\mu m \times 27\mu m$	$117\mu m \times 27\mu m$
beam-beam tune shift/IP $\Delta\nu_{x,y}$	.04, .03	.002, .0004
number of colliding bunches	174	
luminosity	$9.2 \cdot 10^{31}$ $cm^{-2}s^{-1}$	
specific luminosity	$2.0 \cdot 10^{30}$ $cm^{-2}s^{-1}mA^{-2}$	
luminosity increase factor	4.55	

Table 2: Parameters for Upgraded IR Lattice with Combined Function Magnet

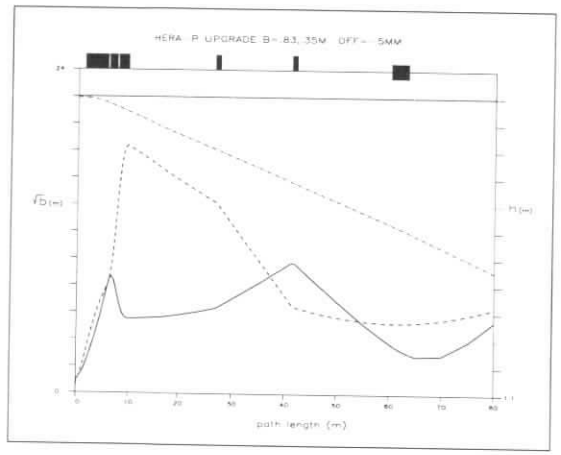

Figure 6: The e-optics for the near IP region are shown here. The horizontal × vertical β^* are 0.83 × 0.35 m respectively and the interaction point is shifted inward by 5 mm. Plotted here is $\sqrt{\beta}_{Hor}$ (solid line), $\sqrt{\beta}_{Ver}$ (dash line) and horizontal beam offset (dash-dot line). In the IR quadrupoles peak-β_{Hor}=74 m and peak-β_{Ver}=337 m. The magnets beyond 26 m can be used to help match to the optics and geometry of the arcs.

for the e-beam. This quadrupole is vertically focusing and is followed by a second vertically focusing quadrupole with a special coil structure.

In this second p-quadrupole all of the excitation current for one coil is made to pass through a limited region between the e- and p-beams. The configuration required is similar to that planned for the PEP-II B-Factory [1] and this special coil configuration yields the quadrupole

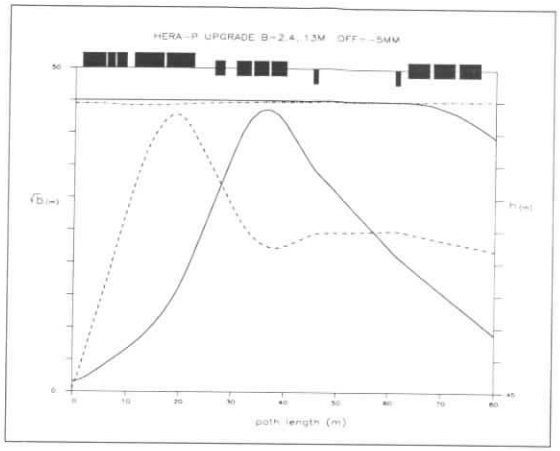

Figure 7: The p-optics for the near IP region are shown here. The horizontal × vertical β^* are 2.4 × 0.13 m respectively and the interaction point is shifted inward by 5 mm. Plotted here is $\sqrt{\beta}_{Hor}$ (solid line), $\sqrt{\beta}_{Ver}$ (dash line), horizontal beam offset (dash-dot line) and vertical beam offset (upper solid line). In the IR quadrupoles peak-β_{Hor}=1900. m and peak-β_{Ver}=1826. m. Additional magnets at 28. m and beyond 40. m can be used to help match to the optics and geometry of the arcs. Note on this plot the sign has been reversed for the vertical deflection given by the BU-dipoles starting at 63. m.

equivalent of a current septum for separating the high field region seen by the p-beam from the reduced field seen by the e-beam.

Together these first two septum magnets provide the bulk of the vertical focusing needed and act together to comprise the first lens of a focusing doublet for the p-beam. The horizontally focusing lens for the p-beam is made up from three already existing standard type quadrupoles which complete the horizontal focusing by 40 m.

There are a few additional secondary magnets, quadrupoles and dipoles, which are useful for optics matching and maintaining the present e- and p-ring geometry. These secondary magnets, whose requirements are not as stringent as the main magnets discussed so far, are addressed in a final subsection.

For aperture plots given in subsequent subsections we indicate the regions for $\pm 20\sigma$ for electrons $\pm 12.5\sigma$ for protons, $\pm(3\sigma+6$ mm) for synchrotron radiation and $\pm 5\sigma$ for neutral vector radiation cone coming from the e-p IP for a luminosity signal. The beam spot sizes are matched according to the parameters given in Table 2. The luminosity upgrade improvement achieved is a factor of 4.55. A vacuum beam pipe wall thickness no less than 1 mm is maintained in all magnets.

The synchrotron radiation criteria, $\pm(3\sigma+6$ mm) used in these plots is only meant to be representative (i.e. as a guide for the eye) as there has been no opportunity to simulate the actual distribution in the Monte Carlo. The synchrotron radiation profiles are plotted coming from the upstream edge of the first separator magnet (gives extreme ring outside limit) and from the middle of this same magnet. As an indicator of where septum masks are required,

synchrotron radiation profiles are indicated from the downstream (gives ring inside limit) on two of the Figures.

3.4 Magnet Design

by B. Parker

3.4.1 Combined Function Separator Magnet

A conceptual design of an air coil dipole magnet is part of the ZEUS report and will not be further described here. Instead we describe an air coil combined function separator as necessary for the improved solution.

An air-coil combined function separator magnet (CFS) provides the bending required to separate the e- and p-beams. In addition if it some provides vertical focusing it is possible to significantly reduce the vertical β-peak in the e-optics and reduce the vertical chromaticity.

A bend of 8.2 mr is assumed with a gradient in the range of 4 to 5 T/m (4.6 T/m used in optics calculations) over a magnetic length of 4.4 m. The the beam separation and synchrotron radiation spread at downstream end of this magnet are shown in Fig.8. A good field region of ± 15 mm horizontally and vertically is required. Because of the 30/820 e/p magnetic rigidity ratios the CFS has only a small effect on the p-beam.

The coil positions indicated in Fig.8 are derived from a brute force approach to achieving the needed field configuration and can certainly be improved upon with further optimization. The required gradient of 4.6 T/m is achieved with a current density of 10.2 amps/mm^2 and has sufficient coil area that the power dissipated per magnet is 100 kW. Over the ± 15 mm horizontal region seen by the beam the gradient is constant to better than 1%. It should be possible to reduce the coil dimensions somewhat and thus to free up more physical aperture as indicated by calculations by Willeke for a somewhat more refined configuration. The example shown is included as a proof of principle.

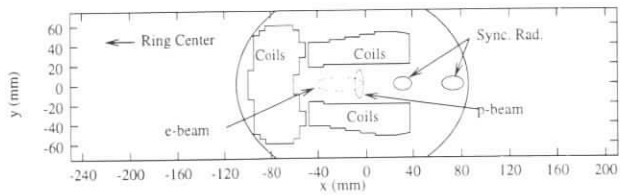

Figure 8: Aperture plot at downstream end of final separator dipole. On this and subsequent plots the coordinate system is such that ring center is to the left (negative numbers) and $\pm 20\sigma$ is indicated for the e-beam and $\pm 12.5\sigma$ for the proton beam. The extreme (ring outside) position of the synchrotron radiation cone is indicated as shown along with one intermediate position. The coil dimensions shown are subject to change and will most likely be reduced in size and moved somewhat further from the beams.

Note that compared to a pure dipole separator it is expected to be possible to eliminate the conductor at the magnet mid-plane on the ring outside to provide extra space for the synchrotron radiation fan.

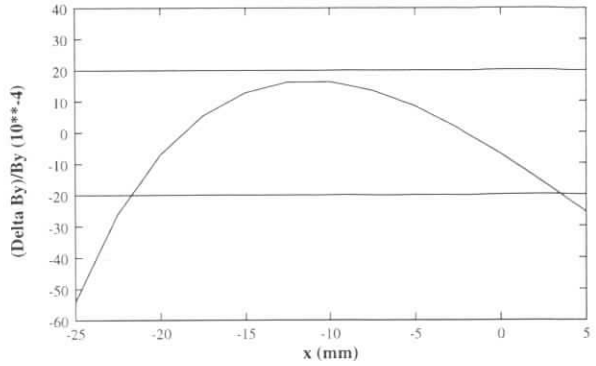

Figure 9: $\Delta B_y/B_y$ as a function of position along the horizontal axis. Note that the field quality is only four times worse that the typical $\pm 5\times 10^{-4}$ even for the preliminary configuration shown. Since on average the β-functions are much smaller in this magnet than in other e- and p-ring magnets, the indicated criteria of $\pm 20\times 10^{-4}$ might be a reasonable design target for this magnet.

3.4.2 Horizontally Focusing e-Ring Quadrupole

After exiting the CFS the beams enter a modified horizontally focusing quadrupole magnet. This quadrupole is centered on the e-beam. The beam positions at the end of this magnet are shown in Fig.10. In order to pass the synchrotron radiation from the separator magnet a gap must be provided in mid-plane of the ring outside coils. The magnetic aperture required for this magnet is driven by the requirement to allow $\pm 12.5\sigma$ for the protons at their outside position.

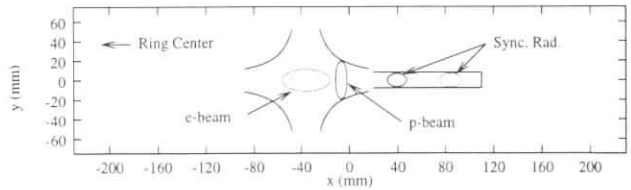

Figure 10: e- and p-beam positions at end of the first horizontally focusing e-ring dipole. This quadrupole is centered on the e-beam however the p-beam is still within the quadrupole aperture. The assumed 35 mm pole radius is indicated as well as a ± 8 mm vertical cutout to pass the synchrotron radiation from the separator magnets.

This magnet has a magnetic length of 1.6 m with a gradient of 28.6 T/m. With a pole radius of 35 mm the pole field reaches 1. T.

It might be possible to construct this magnet from parts of existing HERA QR-type magnets although with such a high pole tip field and compromised coil placement it could be desirable to design a new pole contour and lamination cross section for this magnet.

3.4.3 Vertically Focusing e-Ring Quadrupole

The next magnet outward form the IP is a vertically focusing quadrupole. This quadrupole is also centered on the e-beam. The beam positions at the end of this magnet are shown in Fig.11. As with the previous magnet the ring outside coil must be split along its mid-plane in order to pass the synchrotron radiation from the separator magnet. Here the magnet apeture requirements are completely dominated by the $\pm 12.5\sigma$ for the proton beam.

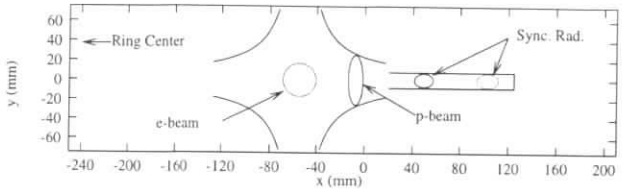

Figure 11: e- and p-beam positions at end of the first vertically focusing e-ring dipole. This quadrupole is centered on the e-beam however the p-beam is still within the quadrupole aperture. The assumed 50 mm pole radius is indicated as well as a ± 8 mm vertical cutout to pass the synchrotron radiation from the separator magnets.

This magnet has a magnetic length of 2.0 m with a gradient of 15.9 T/m. With a pole radius of 50 mm the pole field reaches 0.79 T.

It may be possible to construct this magnet using the laminations from existing HERA QS-type quadrupoles. Since a QS lamination is half that required for this magnet, a full magnet can be constructed that is half the length of a present QS quadrupole. New shorter coils, with the indicated mid-plane split, are however required.

3.4.4 Vertically Focusing Magnetic Septum Quadrupole

The e- and p-beams are separated into two vacuum beam pipes at the magnetic septum quadrupole (MSQ). The beam positions at the beginning of the MSQ are shown in Fig.12. The MSQ provides the same functionality as the QS mirror quadrupoles in the original HERA design. That is it allows having the strongest earliest possible focusing possible for the p-beam while providing an essentially field free region for the e-beam. The MSQ differs from the QS-magnet in that it has a radically cut away mirror plate which enables its placement much closer to the IP than is possible for a QS magnet. In addition because of its closer placement, where the proton beam spot is not as large, it can have a smaller apeture and this translates to having a higher gradient. Thus the net result is to have a stronger quadrupole placed closer to the IP which is precisely what is needed to achieve stronger more effective focusing of the p-beam.

The main challenge in designing the MSQ is to provide adequate field quality for the proton beam which is positioned close to the cutout section of the mirror plate. A scheme for achieving high field quality is outlined in the paper by M. Marx *et.al.*.[2] With proper shaping of the cutout region, a modest field quality, at the few $\times 10^{-3}$ level can be achieved at a fixed excitation current. The trick for achieving standard accelerator magnet field quality, $\Delta B/B \approx 5 \times 10^{-4}$ is to place a small correction coil in the vertex of the cutout as close as possible to the proton

beam. In 2D filed calculations it is found that correction currents which are a very small fraction of the main excitation current lead to good results as shown in Fig.13.

Several correction coil configurations have been studied and the level of achievable correction is approximately the same for the various configurations. The main difference between the different configurations is the optimum amount of trim current. Configurations with the trim current deeper in the "notch" tend to require smaller correction currents for a given degree of field compensation. Smaller currents are desirable because they require less conductor cross-section and result in a thinner septum.

It is important to make the septum thin not only to reach the closest possible e-p beam separations but to limit the solid angle covered by the septum mask needed upstream of the septum to intercept synchrotron radiation coming from the separator magnet. Since this mask is the closest point to the experiment at which synchrotron radiation is absorbed the unavoidable backscatter from this mask could swamp central detector components if sufficient care is not taken to minimize its size. MSQ prototype testing is planned to be made at IHEP Protvino to optimize the trim coil configuration and to provide feedback on mechanical construction and end-field issues.

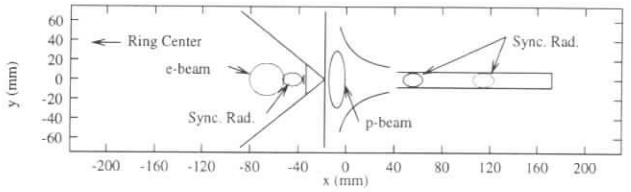

Figure 12: e- and p-beam positions at the start of the MSQ. The assumed 37 mm pole radius, and cut-away mirror with trim coil are indicated as well as a ± 8 mm vertical cutout to pass the synchrotron radiation from the separator magnets. Also indicated is the edge of the synchrotron radiation which passes just inside a collimater/mask just upstream of the septum.

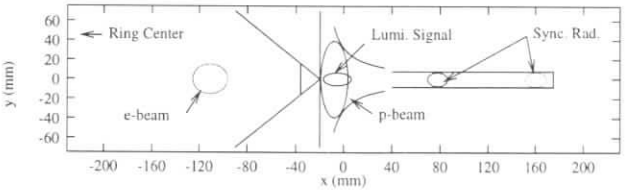

Figure 13: e- and p-beam positions at the end of the MSQ. The assumed 37 mm pole radius, and cut-away mirror with trim coil are indicated as well as a ± 8 mm vertical cutout to pass the synchrotron radiation from the separator magnets. Also indicated is the $\pm 5\sigma$ profile of the neutral vector radiation cone coming from the IP with the divergence of the e-beam at the IP. This is intended to give an indication of the divergence allowed by the MSQ for particles which could be used for a luminosity signal. Note that the $\pm 12.5\sigma$ p-beam + 1 mm assumed vacuum beam pipe (not shown) wall-thickness fills the available magnetic aperture.

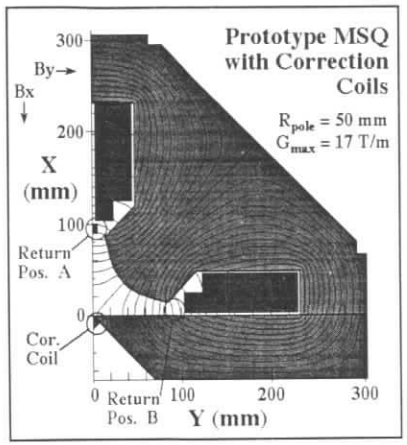

Figure 14: Prototype MSQ with correction coils. The physical geometry and lines of magnetic flux resulting from 2-dimensional calculations of a prototype MSQ. The prototype will be constructed from an existing spare HERA quadrupole and only half of the magnet is shown due to symmetry about the vertical axis. Please note that the coordinate system for this plot is rotated 90$^{\circ}irc$ with respect to the orientation given in Fig.13. Positions are indicated for the correction trim in the septum notch as well as two locations (A and B) for the return loop. In the final magnet only position B is allowed in order to pass the synchrotron radiation from the separator magnets.

This magnet has a magnetic length of 5.6 m with a gradient of 23.2 T/m. With a pole radius of 37 mm the pole field reaches 0.86 T.

The magnetic apeture of this magnet is by definition defined by the $\pm 12.5\sigma$ for the proton beam and the beam positions are shown in Fig.13 along with a $\pm 5\sigma$ for the neutral vector radiation cone from the IP. Once again the ring outside coil is opened up along its mid-plane to accommodate synchrotron radiation form the separator magnet. Monte Carlo simulations indicate that is probably necessary to pass the synchrotron radiation through the coil region in order that it can be absorbed further away from the IP and thus to reduce the solid angle for backscatter from the absorber to central detector components.

It is noted here that due to the use of a combined function magnet, i.e. dipole plus quadrupole, the e-beam initially sees a lower field as it enters the separator magnet from the IP and this results in a much softer synchrotron radiation spectrum impinging upon the septum mask and headed along the proton beam direction. This helps to reduce backscatter from the septum mask and to ease filtering/pre-absorber requirements for the luminosity monitor.

The apeture available for the neutral vector radiation cone from the IP is limited horizontally as shown in the MSQ to roughly $\pm 750\ \mu rad$ and corresponds to $\pm 5\sigma$ of the divergence due to the angular spread of the e-beam at the IP. The MSQ defines the acceptance available for a luminosity monitor.

There is no existing HERA magnet lamination which adequately matches MSQ requirements. If the MSQ were to be made shorter, then a QR-type, 35 mm, profile could be considered

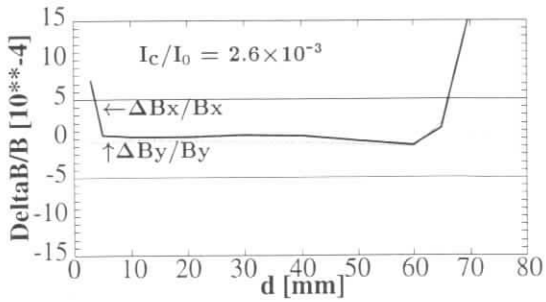

Figure 15: Typical results of MSQ field calculations for prototype configuration (pole radius = 50 mm) with trim correction of 2.6×10^{-3} of the main excitation current. $\frac{\Delta B}{B} = \frac{B-B_l}{B_l}$, in units of 10^{-4}, as function of distance from origin. B_l is field calculated for an ideal quadrupole given by $B_l(d)$ = Gradient×d.

(the same as for the first horizontally focusing e-beam quadrupole); however, then the beam separation would be too small at the next magnet downstream, the current septum quadrupole. On the other hand, too large a pole radius, such as obtained with a QC (or QS) 50 mm pole radius lamination profile, yields too small a quadrupole gradient. Thus the MSQ is expected to require an entirely new profile and should be optimized according to its own requirements.

3.5 Vertically Focusing Current Septum Quadrupole

The next magnet is a current septum quadrupole (CSQ) of the PEP-II type.[1] Here a full quadrupole apeture is available to the p-beam rather than being limited to a half apeture as in the MSQ case and thus the pole radius can be kept smaller for a higher gradient. The tradeoff for this higher gradient is that the e- and p-beams must be separated more than for a MSQ in order to provide space for the full excitation current turns, typically tens of kiloamperes compared to MSQ correction coils with tens of amps. Thus a CSQ cannot be used as a one-for-one replacement for a MSQ; however, when there is sufficient beam separation to use a CSQ, it will perform better.

The CSQ has a magnetic length of 5.6 m with a gradient of 29.2 T/m. With a pole radius of 32 mm the pole field reaches 0.934 T.

The beam positions at the start of the CSQ are shown in Fig.16 along with the edge of the synchrotron radiation that just misses the MSQ septum mask. Note that an additional septum mask is required to protect the septum coil from this synchrotron radiation which is not intercepted by the MSQ septum.

The beam positions at the downstream end of the CSQ are shown in Fig.17. It is assumed that a synchrotron radiation absorber is placed in front of the CSQ so as to shadow the ring outside coils in the mid-plane. While it is conceivable to try to let much of the synchrotron radiation pass through this magnet also by adding a second septum at the ring outside position, such a configuration would cause the magnet to use an excessive amount of electrical power due to reduced conductor cross section.

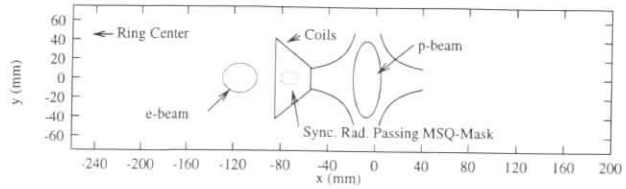

Figure 16: e- and p-beam positions at the start of the CSQ. The assumed 32 mm pole radius is indicated. The synchrotron radiation to the ring outside is assumed to be absorbed in a collimator just upstream of this quadrupole so there is no need for a spit coil in the outside mid-plane. Also indicated is the outline of the area available for the septum coil and a projection for synchrotron radiation which just passes the MSQ septum mask shown in Fig.12. Note that a second septum mask will be needed to protect some of this coil region but the requirements for this mask are not nearly as severe as for the MSQ mask.

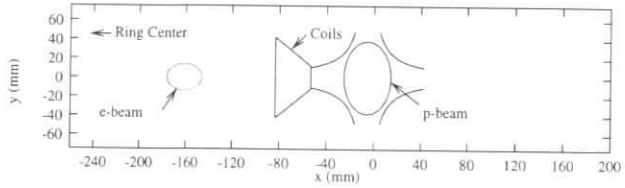

Figure 17: e- and p-beam positions at the start of the CSQ. The assumed 32 mm pole radius is indicated. Any synchrotron radiation which would hit this quadrupole is assumed to be absorbed in upstream collimators. The area available for the septum coil is indicated.

3.5.1 Horizontally Focusing p-Ring Quadrupoles

Once the e-p beam separation is sufficiently large, it is found possible to reuse some of the existing IR magnets to complete the horizontal focusing of the p-beam. Here we use three HERA QR-type magnets connected in series. The beam positions at the first QR quadrupole is shown in Fig.18. The beam separation at the front of this magnet is such that a small amount of material will have to be ground away to make room for the e-vacuum beam pipe.

The beam positions at the middle of the second QR magnet are shown in Fig.19. At this point the e-beam completely clears the outside of the QR magnet. Note also that the $\pm 5\sigma$ for the neutral vector from the IP for reference and it is well inside the region defined by the proton aperture. Thus with a sufficiently large p-ring beam pipe downstream of this magnet it should be possible to pass this cone to the present luminosity monitor location.

The magnetic length assumed for the three QR quadrupoles in series is 3×3=9 m at 24.3 T/m. The QR pole radius of 35 mm then implies a0.85 T pole tip field.

3.5.2 Secondary e- and p-Ring Qudrupoles and Dipoles

Additional quadrupoles, not covered in the previous sections, are desirable for the e- and p-rings

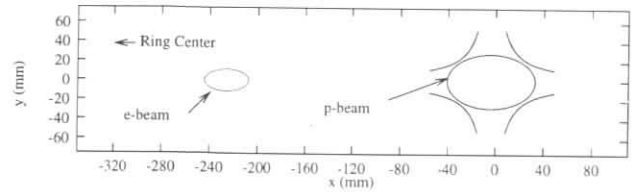

Figure 18: e- and p-beam positions at the start of the first horizontally focusing p-ring quadrupole. The assumed 35. mm pole radius for reusing a HERA QR-type quadrupole is also indicated. Note that some of the material near the e-beam, in the mid-plane of this quadrupole, will have to be cut/grinded away to make room for the e-vacuum beam pipe.

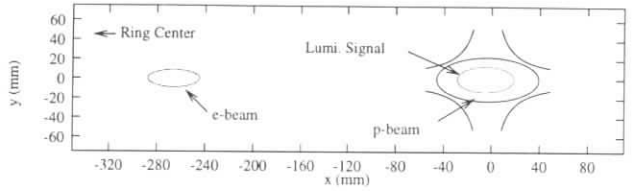

Figure 19: e- and p-beam positions at the center of the second horizontally focusing p-ring quadrupole where the horizontal-β reaches a maximum of 1900. m. The assumed 35. mm pole radius for reusing a HERA QR-type quadrupole is indicated along with the $\pm 5\sigma$ projection of the neutral vector radiation cone from the IP as shown in Fig.13. Note that to this point this cone is always within the 12.5σ of the p-beam. The assertion that the solid angle available for a luminosity monitor is solely limited by the MSQ is subject to a detailed analysis of the aperture provided between this magnet and the present monitor location beyond the vertically bending BU dipoles.

- Completing the IR focusing
- Aiding optics matching to the arc regions

For the e-ring it should be possible to place a HERA QL-type of quadrupole at 27 m which is a position just upstream of the p-ring QR quadrupoles discussed in the last section. Such a quadrupole is useful for giving some additional vertical focusing which does not have to be provided where space is precious close to the IP and facilitates optics matching at an existing QL magnet at about 41 m.

For the p-ring an additional quadrupole placed between 40 to 50 m is useful to complete the vertical focusing after the IR and to aid in optics matching to the arcs. The exact placement is not so critical and can be fixed at a later point in time. It is proposed that a pair of HERA QC-type quadrupoles may be sufficient for this purpose. An additional dipole, not covered in the previous sections is needed in the e-ring to

- Close the ring geometry at an appropriate matching point
- Avoid problems due to synchrotron radiation in the superconducting rf cavities.

The scenario proposed is to reuse one of the BH dipoles which is no longer needed near the IP and place at 62 m next to the superconducting rf region. Since the separator magnet provides 8.2 of the present 10 mr separation angle it is possible to close the ring geometry by adding 0.9 mr bend along with increasing slightly, by the remaining 0.9 mr the bend at an existing dipole in the middle of the rf section. Even it 0.9 mr is not found ideal for dispersion and spin-matching purposes, it should always be possible to find a combination of angles, yielding a net 1.8 mr of bend that closes the ring geometry in the middle of the rf section. Closing the ring at the rf section has the following advantages by:

- Splitting the difference between aperture demands due to a slightly different electron trajectory and the demands due to additional synchrotron radiation from bends close to the rf
- And thus avoids having to move the rf cavities

For the p-ring geometry it is useful to place a dipole near 27 m in the otherwise unused space between the vertically focusing and horizontally focusing p-ring quadrupoles. A BS dipole would fit here and provide 200 μr of bend to partially compensate the kick given to the beam by the MSQ.

References

[1] "PEP-II Conceptual Design Report," Chapter 5, Lawrence Berkeley Lab. PUB-5379, 1993.

[2] M. Marx, B. Parker and H. Wümpelmann, "Concept for a New Magnet Septum Quadrupole," European Particle Accelerator Conference, Barcelona, Spain, June 1996. See DESY Internal Report DESY M 96-13, July 1996 or http://mpy-www.desy.de/parker/EPAC96/mop040g.ps on World Wide Web.

3.6 Impact of the new Interaction Region on e^+/e^- Polarization

by E. Gianfelice-Wendt

The shrinking of the space available with the new IP region design involving the new separator magnets has two important consequences for polarization:

1) the experimantal solenoids will not, as at present, be compensated anymore by antisolenoids;

2) the experimental solenoids must overlap with the last machine magnets.

3.6.1 Effect of antisolenoid suppression

. A magnetic field parallel to the polarization direction $\hat{n}_0$ does not change $\hat{n}_0$. So if rotators are used to get longitudinal polarization at the IP, the solenoidal field does not affect $\hat{n}_0$ (this is not completely true, as we will explain below). There is only a relatively small increase of the betatron resonances due to the betatron motion of the particles in the uncompensated field of the solenoid. This results in a lower polarization level for the ideal machine but the loss is probably negligible wrt depolarizing effects due to the unavoidable machine imperfections.

If rotators are not operating, i.e. $\hat{n}_0$ is nominally vertical and thus perpendicular to the solenoidal field, the field produces a tilt of $\hat{n}_0$. For example the H1 solenoid (B_s=1.5 T, L = 7.333 mt) would tilt $\hat{n}_0$ around the longitudinal axis by about 110 mrad at 29 GeV.

Such a tilt, if not corrected before entering the arcs, would destroy completely the polarization build up mechanism, the Sokolov-Ternov effect.

We could perhaps overcome the tilt by using the scheme invented by K.Steffen for PETRA (1982) and actually applied at LEP. It consists of two vertical bumps, one on each side of the solenoid, involving horizontal bending magnets. For the same purpose one could also use the vertical bending magnets of the rotators. The size of such bumps depends on beam energy and on longitudinal field strength. The feasibility for HERA is still to be proved.

3.6.2 Effect of field overlap

. As mentioned above, even if rotators are operating, the fact that the solenoidal field overlaps with the magnetic field of the last machine elements has as a consequence that $\hat{n}_0$ is not already perfectly longitudinal when the particles enter the solenoidal field. In the following we will assume that the last CoSm magnets before the IP provide together the remaining 10 mrad, which, in the absence of the solenoid, closes the orbit and brings $\hat{n}_0$ in the longitudinal direction. For the ideal case of a "curved" solenoid following the orbit curvature, no orbit distortion is produced, but only a $\hat{n}_0$ distortion.

If the solenoid is straight then both orbit and $\hat{n}_0$ are affected; this is the realistic case that we will discuss here. Thus we need to examine simultanously orbit and spin motion.

On the reference orbit the solenoidal field has a longitudinal as well as a radial component B_x. As long as the solenoid is symmetric wrt the IP the integral of B_x vanishes. The kicks in the fringe field at the entrance and exit of the solenoid cancel. Then there is only a very small effect on the vertical closed orbit due to motion in the solenoid itself since the design orbit is not parallel to the magnet axis. The distortion of $\hat{n}_0$ is negligible too.

If the solenoid is not symmetric $\int ds B_x \neq 0$ and the kicks at the entrance/exit do not cancel. The effect is particularly important for the H1 solenoid, its center being shifted of 1.1 mt. In this case the particles see a vertical kick of 0.2 mrad, whereas the $\hat{n}_0$ is tilted 28 mrad around the radial direction.

This effect can probably be compensated by having different settings for the rotator on the left and right of the North IP.

It remains to be seen whether spin matching against spin diffusion in the straight sections is still possible.

3.7 Investigation of Synchrotron Radiation Background

D. Pitzl

The synchrotron radiation power emitted by the electron beam in a dipole magnet with bending radius R and length ℓ is given by

$$P = \frac{2}{3}\frac{I e}{4\pi\epsilon_0}\frac{\ell}{R^2}(\beta\gamma)^4$$

with $\beta = v/c$ and $\gamma = E/m_e c^2$. Using $\alpha = \ell/R$, the dipole bending angle, the power may be expressed as

$$P[kW] = 14\frac{\alpha[rad]}{R[m]} I[A] E^4[GeV^4]$$

which is proportional to the inverse bending radius for a given bending angle. For $I = 58\,\mathrm{mA}$, $E = 30\,\mathrm{GeV}$, $\alpha = 8\,\mathrm{mrad}$, and $R = 400\,\mathrm{m}$ the emitted power is $13.2\,\mathrm{kW}$ (or $8 \cdot 10^6\,\mathrm{GeV/BC}$) on each side of the interaction region.

The synchrotron radiation spectrum is characterised by the critical energy

$$E_c = \frac{3}{2}\frac{\hbar c}{R}\gamma^3$$

or

$$E_c[keV] = 2.22\frac{E^3[GeV^3]}{R[m]}$$

which amounts to $E_c = 150\,\mathrm{keV}$ for the numbers used above. The photon spectrum is given by

$$N_\gamma(E_\gamma) = \frac{P}{E_c^2}\frac{S(\xi)}{\xi}$$

with $\xi = E_\gamma/E_c$ and the spectral function

$$S(\xi) = \frac{9\sqrt{3}}{8\pi}\xi\int_\xi^\infty K_{5/3}(x)dx$$

where $K_{5/3}$ is a modified Bessel function. At low energies the photon spectrum diverges like $\xi^{-2/3}$. In all simulations a lower cutoff at 10 keV is applied. The rate of photon emission is then $1.2 \cdot 10^{18}\,\mathrm{s}^{-1}$ in the example given above. At high energies ($\xi \gg 1$) the spectrum falls exponentially. Note that half the synchrotron radiation power is carried by photons with energies above the critical energy. In the simulation the synchrotron radiation is emitted tangentially to the path of individual electrons that are tracked through the magnets. The intrinsic angular spread of the radiation is of order $1/\gamma$ (0.017 mrad at 30 GeV), which is much smaller than the divergence of the electron beam.

The number of photons reaching the central detector components must be reduced by 10 orders of magnitude by a system of absorbers and collimators around the interaction region. The central drift chamber of H1, for example, can tolerate at most 10 synchrotron radiation hits per bunch crossing, before the hit occupancy, after integrating over 12 bunch crossings, starts to affect the pattern recognition efficiency. A similar value is obtained from ageing effects in the chamber, using a limit of $0.03\,\mathrm{C/cm}$ of charge accumulated on the sense wires and a

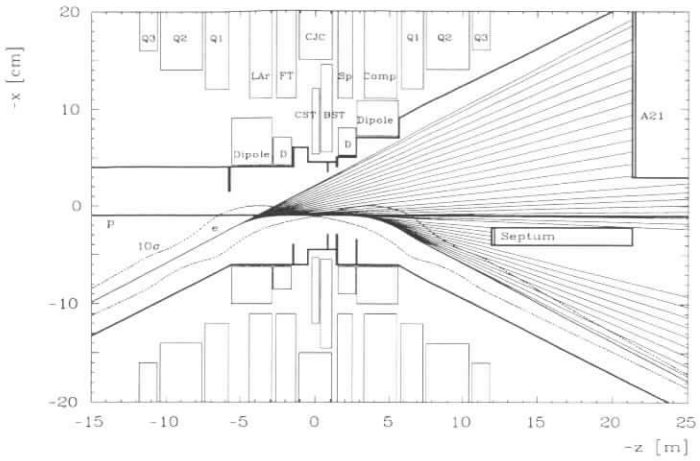

Figure 20: *Layout of a high luminosity interaction region for the H1 experiment in the horizontal plane with the synchrotron radiation fan from the dipole magnets. The beams are displaced by 1 cm horizontally relative to the detector axis. Note the different scales for the z- and x-axes.*

lifetime of 10 years at high luminosity. In the silicon detectors close to the beam pipe a hit rate of $0.01/\mathrm{cm}^2/\mathrm{BC}$ leads to an accumulated dose of 10 krad/y, which can be tolerated for a lifetime of 10 years by the CMOS front end electronics. For the H1 silicon vertex detector the corresponding hit rate is 40/BC, which can be tolerated by the pattern recognition software. In both cases one hit is assumed to deposit 30 keV, and one year of operation is 10^7 s.

3.8 Synchrotron Radiation Shielding

The design of the interaction region is guided by the principle that only doubly scattered radiation may reach the experiment. The direct radiation must not hit the beampipe anywhere inside the detector. It is absorbed by upstream collimators and downstream absorbers. These must be placed as far away as possible to reduce the solid angle for backscattered radiation to reach the central detector. Furthermore, a set of secondary collimators is needed to shield against this backscattered radiation. A possible layout for a high luminosity interaction region with dipole magnets inside the collider experiments is shown fig 20.

3.8.1 Synchrotron RadiationAbsorbers

Absorbers for direct synchrotron radiation must absorb up to 10 kW on an area of a few square centimeters and should have the lowest possible backscattering probability. A detailed simulation of photon interactions in the energy range from 10 to 1000 keV was used to find an optimal absorber. The albedo is defined as the number of backscattered photons devided by the number of incident photons. Fig. 21 shows the albedo as a function of the critical energy of the incident synchrotron spectrum for three different absorbers: pure tungsten, pure copper and a tungsten absorber coated with 0.4 mm silver and 0.2 mm copper. The coated absorber has the lowest albedo (by a factor of 3 at $E_c = 150$ keV) but it requires some development work to ensure that the thin coating is not destroyed by overheating the absorber.

It can be understood qualitatively by inspecting the energy spectra of backscattered photons from the three absorbers (see figure 22). The spectrum from a pure tungsten absorber is dominated by the K_α and K_β fluorescence lines, while the copper absorber shows a Compton continuum (the K-lines of copper are just below the 10 keV cutoff). For the coated absorber the silver layer absorbs the tungsten K-lines and the copper layer in turn absorbs the K-lines of silver (25 keV). The thickness of the layers is a compromise between absorbing the fluorescence from the deeper layer and not generating Compton backscattering of the incident radiation. It is found that the optimum coating is independent of the incident spectrum for critical energies between 30 and 200 keV.

Luminosity Monitor Shielding

3.8.2 Luminosity Monitor Shielding

The photon detector of the luminosity monitoring system is placed 100 m downstream from the interaction point. It has a diameter of about 20 cm and as is therefore exposed to the synchrotron radiation emitted in the last 1 mrad bend. The radiation power is about 2.5 kW, or $1.6 \cdot 10^6$ GeV/BC, which has to be reduced by 6 orders of magnitude in front of the calorimeter. The present photon detector of H1 has a copper-lead-water absorber with a thickness of 3 radiation lengths. This thickness should not be increased in order not to further deteriorate the energy resolution of the calorimeter.

The non-absorbed energy fraction as a function of thickness can be estimated by integrating the photon energy spectrum wheighted by the energy absorption length τ_E

$$F(t) = \frac{1}{N} \int_{E_\gamma,\min}^{E_\gamma,\max} S(E_\gamma)\, e^{-t/\tau_E(E_\gamma)} dE_\gamma$$

whre N is the integral over the incident spectrum. The integrand does not represent the true spectrum at a depth t, since the re-population of the low energy region by scattered photons and fluorescence is not taken into account in detail. However, the tabulated energy absorption lengths include the effects of secondary radiation on average and give a correct description of the overall energy flow. Note that the energy absorption length is larger than the photon mean free path length by up to a factor of 2 in lead and by up to factor of 10 in carbon. A high-Z absorber material is therefore prefered. Figure 23 shows the non-absorbed energy fraction in lead for several critical energies. A reduction of 10^6 in less than $3\,X_0$ is only possible by

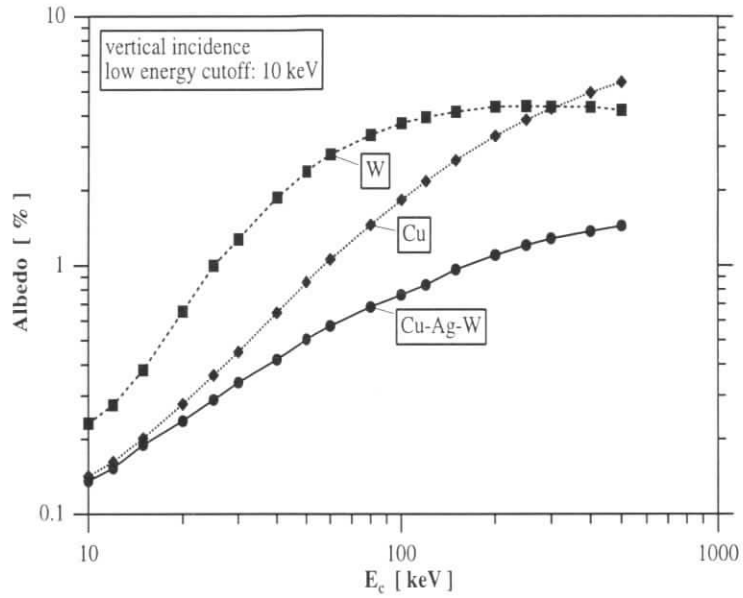

Figure 21: *Backscattered photon fraction for 3 absorbers versus the critical energy of the incident synchrotron spectrum.*

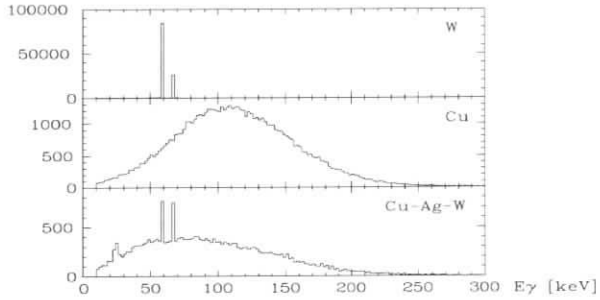

Figure 22: *Energy spectra of backscattered photons for 3 absorbers at $E_c = 150\,keV$. The vertical scale is in arbitrary units.*

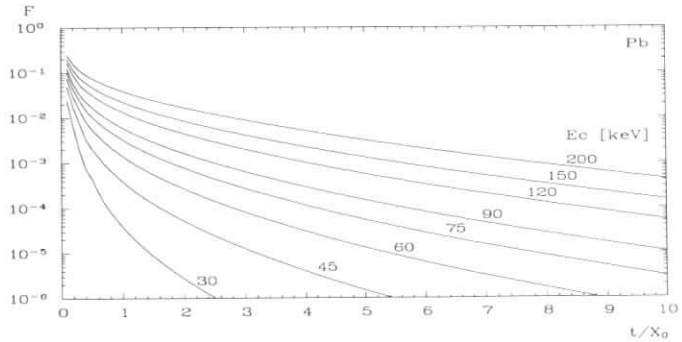

Figure 23: *Non-absorbed energy fraction versus lead thickness for several synchrotron spectra.*

introducing a 'soft bend' with a critical energy below 34 keV for the first 1 mrad. This result is due to the Compton minimum in the photon cross section. Between $E_\gamma = 200$ and 1000 keV the photon mean free path length in lead is larger than than radiation length.

3.8.3 Interaction Region Layout

A possible high luminosity interaction region layout has been developed using the following parameters and considerations:

- The bending angle of 8 mrad is provided by air core dipole magnets inside the experiment.
- The magnets start at ±1.6 m from the interaction point and extend to ±5.6 m. The bend over the first 1 mrad is 'soft' with a radius of 1200 m, which requires a magnet length of 1.2 m. The remaining 7 mrad bend is achieved with a radius of 400 m over a length of 2.8 m.
- The width available for the dipole magnets is limited at the outer radius to 11 cm by the H1 compensator and the liquid argon cryostat. The inner radius is determined by the aperture required for the electron beam and by the outgoing synchrotron radiation fan in the horizontal plane.
- The focussing quadrupoles for the electron beam are placed on-axis and do not contribute to the bending.
- The first focussing element for the proton beam (the septum half-quadrupole) starts at ±12.1 m.
- All synchrotron radiation from the 8 mrad bend passes through the interaction region and is absorbed behind the septum magnet at 21.3 m. The mirror plate of the septum magnet is also exposed to direct synchrotron radiation. Both surfaces are coated for minimum albedo.
- The vacuum tube inside the septum magnet extends up to 20 cm horizontally outward from the beam axis to accomodate the synchrotron radiation fan.
- The central beam pipe section is shielded against backscattering from the absorber and the septum by secondary collimators placed at $z = -0.8$, -1.4, and -2.7 m. These collimators leave an aperture of 20 mm radius required for proton injection and need not be movable.
- The diameter of the central beam pipe is 90 mm such that the existing central and backward silicon tracking detectors of H1 can be accomodated. The critical point is the shielding of the backscattering from the septum magnet with collimators that must not be hit by direct synchrotron radiation.
- The beams are displaced by 1 cm horizontally ring-inwards relative to the axis of the experiment.

This interaction region has been implemented in a simulation program that tracks backscattered photons from the absorber at 21 m and the face of the septum magnet at 12 m. The emission angles are restricted to a solid angle fraction of $7 \cdot 10^{-5}$ of 2π towards the central detector

region. Photons are tracked through any number of scatterings until they are absorbed. With more than 10^6 trajectories followed, an overall sensitivity of better than 10^{-11} is achieved.

The simulation was also performed for H1 interaction region layout of 1996 with a beam energy of 27.5 GeV and for a current of 58 mA. Here, the main absorber at -24 m is a pure copper absorber. The strongest source for scattered radiation is the inner edge of the upstream collimator C_3 at 5.6 m.

Table 3.8.3 the summarizes the beam parameters and simulation results. Two conclusions may be drawn. The absolute prediction for the number of hits in the central drift chamber and the silicon detector are well below the tolerable limits, with a comfortable safety margin. The relative increase for the high luminosity interaction region is roughly a factor of 10 for 58 mA, or a factor of 20 compared to the usual operating current in 1996. The synchrotron radiation background at present is very small and therefore hard to measure. At least, it does not severly exceed the simulation result. It is therefore expected that the present detector can be safely operated in the high luminosity environment.

	HERA 1996	HERA upgrade
E_e [GeV]	27.5	30.0
I_e [mA]	58	58
$\beta^*_{x,e}$ [m]	1.0	0.4
$\beta^*_{y,e}$ [m]	1.0	0.4
bend angle [mrad]	10	8
bend radius [m]	1260	400
E_c [keV]	36	150
P_{tot} [kW]	7	27
$N_\gamma(E_\gamma > 10\,\mathrm{keV})$ [1/s]	$1.2 \cdot 10^{18}$	$2.2 \cdot 10^{18}$
N_γ central BP [1/BC]	10	120
N_{hits} CST, BST [1/BC]	0.02	1
N_{hits} CJC [1/BC]	0.1	2

4 Upgrade of the ZEUS Interaction Region

HERA-ZEUS Upgrade Group:

D.Boscherini, N.Brook, J.Butterworth, A.Caldwell, C.Catterall, R.Cashmore, C.Foudas, J.Hartmann, U.Karshon, R.Klanner, H.Kowalski, M.Kuze, E.Lohrmann, S.Magill, T.Massam, N.McCubbin, K.Piotrzkowski, M.Riveline, R.Saunders, U.Schneekloth, W.Schott, L.Suszycki, J.Tickner, K.Tokushuku, D.C.Williams, F.Zarnecki

Editor: W.Schott

4.1 Summary

We report on the status of the new design of the ZEUS interaction region as discussed in the frame of the HERA Luminosity Upgrade Group and on a first evaluation of the impact on the ZEUS components close to the beam.

4.2 Introduction

As discussed extensively at the workshop, an increase in HERA luminosity above the design value will allow the experiments to extend substantially the current fields of research and even open up new regions of activity. However, most of the parameters that determine the luminosity of the HERA accelerator complex are at their technical limits, and to push them further would need a very major effort of the laboratory. The most promising option is a reduction of the beta functions at the interaction region. A scenario as given in Table 3 would raise the maximum luminosity by a factor of about five above the nominal value of $1.5 \times 10^{31}/\mathrm{cm}^2\mathrm{s}$.

Technically this requires a rearrangement of the HERA magnets in the experimental area. A smaller beta function at the interaction point (IP) leads to a faster growth of the beam envelopes between the IP and the first focusing magnet and the first quadrupole has to be as close as possible to the IP. Therefore the separation of the beams (e, p) with bending dipole magnets should be done as close to the IP as possible.

This means that accelerator magnets have to be installed inside the central part of the existing HERA detectors. This Working Group made a first study of the technical feasibility and the consequences of this concept. The work done by ZEUS members was based on a design study by F.Willeke, that foresees as innermost elements magnets with 8 mrad bending angle, which start at 5.6 m distance from the IP and reach as far as possible into the detector (minimum 1.2 m distance from the IP).

	Present	Proposed
β_x^p	7 m	3 m
β_y^p	0.7 m	0.15 m
β_x^e	1 m	0.4 m
β_y^e	1 m	0.4 m

Table 3: Proposed scheme of beta functions.

The present report gives a first preliminary assessment of the impact of the luminosity upgrade on the ZEUS detector. A more detailed report is to follow.

4.3 The new HERA beam line inside ZEUS

Here we discuss the magnet system for the final 8 mrad bending of the electron beam within ± 5.6 m of the IP. The concept of bringing HERA magnets inside the existing ZEUS detector is subject to several boundary conditions:

- The transverse outer dimensions of the magnets are limited by the 20 cm beam pipe hole of the ZEUS calorimeter.
- The aperture of the magnets has to be wide enough to accommodate the beams and the fan of synchrotron light from the bending of the electron beam.
- The front face of the ZEUS calorimeter should not be shadowed by the magnets, i.e. particles originating from the IP should reach the calorimeter unobstructed.

In addition to these general requirements, consideration has also to be given to aspects like construction of beam pipe, absorption of reflected synchrotron radiation, installation, support etc. Presently two options for the magnet layout are under discussion:

Option 1: An air coil dipole magnet is used on either side of the IP, however, in a somewhat asymmetrical way (see Fig. 24). The magnet on the forward side (ZEUS coordinate $z > 0$) has an outer diameter of 14 cm, an inner diameter of 8 cm, and a length of 400 cm. The magnet ends at $z = 160$ cm, just behind the line-of-sight between IP and FCAL front edge.

The magnet on the rear side (ZEUS coordinate $z < 0$) has an outer diameter of 19 cm, an inner diameter of 12 cm, and a length of 410 cm. The magnet ends at $z = -150$ cm in line with the RCAL front face. It has a wider aperture and is displaced in the horizontal plane by 15 mm to accommodate the fan of direct synchrotron radiation.

Option 2: Here the magnet layout (see Fig. 25) as compared to option 1 is different on the forward side. The air coil dipole magnet has now the same inside and outside diameter as the rear one. However, the length is only 340 cm, ending at $z = 220$ cm.

A permanent SmCo magnet provides a dipole field between $z = 220\,\text{cm}$ and $z = 150\,\text{cm}$. The permanent magnet can be closer to the IP without shadowing the forward calorimeter because the diameter gets smaller towards the IP.

The field of the SmCo is relatively low (approx. 0.1 Tesla) such that it contributes only a 0.5 mrad bend. This has the advantage of reducing the intensity of synchrotron radiation that hits the ZEUS luminosity detector.

4.3.1 Magnet design

Long dipole magnet. Both design options use long dipole magnets (with somewhat varying dimensions). The homogeneous magnetic field is provided by a coil which has a current distribution that is proportional to the cosine of the azimuthal angle. The conductors of the coil are arranged in 3 layers such that they approximate this current distribution along the magnet circumference (see Figs. 26, 27). The coil does not have an iron yoke since it will be inside the ZEUS compensator magnet.

Normal conduction technology is preferred because of space restrictions and in order to keep the infrastructure requirements simple. At a nominal field of approximately 0.2 Tesla the normal conducting coil will use on the order of 100 kW of power. Cooling water is circulated inside the hollow conductor. Several parallel cooling channels are needed to keep the temperature of the magnet below a value that is acceptable for the ZEUS detector. The connections to the coil will be made at the magnet head at $z = \pm 5.6\,\text{m}$. Care must be taken to prevent heating of detector components situated close to the magnet. Safety of this magnet also requires special considerations.

Permanent magnet. The particular feature of option 2 is a permanent magnet on the forward side of the detector. Permanent magnets built from rare-earth-cobalt alloys like SmCo can provide high magnetic field strength at a very compact design. Fig. 25 schematically shows the tapered permanent magnet. It would actually be segmented in the longitudinal direction into several rings. Each ring is made up from blocks of SmCo material (see Fig. 28). The arrangement of the magnetised SmCo blocks in a ring produces a homogeneous dipole field inside with almost no fringe fields outside. One of the difficulties with this design is the need to provide a temperature stabilisation.

4.3.2 Beam pipe

The beam pipe in the experimental area (see Figs. 24, 25) is divided by flanges into three sections. The construction of the front flange is particularly delicate, because the requirement not to put too much inactive material in front of the sensitive ZEUS detector components leaves little space. At least one bellow is needed to give some freedom for relative motion of the beam pipe sections.

The size of the central beam pipe (outer diameter 100 mm) is mainly determined by the synchrotron radiation, i.e. by the direct radiation and the radiation reflected back from downstream absorbers. The synchrotron radiation reflected back into the central ZEUS region has

to be taken care of by dedicated absorbers at $z = -140\,\text{cm}$ (rear flange), $z = -80\,\text{cm}$ and at $z = 150\,\text{cm}$ (front flange).

For a good vacuum pumps are needed inside the beam pipe (see Fig. 26). The magnetic field and the space available inside the large air coil magnet is the same as in the HERA electron dipole magnets. Therefore standard HERA integrated ion getter pumps can be used. Possible negative effects on the electron beam life time, as observed in the HERA electron ring, are not expected, because there is no direct line-of-sight between the anodes of the integrated pump and the beam. The integrated pumps will be in operation only when the air coil magnets are on; additional holding pumps are therefore required between the air coil magnets and the following quadrupole magnets.

The pumping speed can be increased by equipping one of the pumping channels with NEG pumps. The same design can be used as for the HERA dipole pumps, which are in preparation. The advantage is a high pumping speed for active gases independent of the magnetic field.

4.3.3 Support structure

The long dipole magnets which go into the ZEUS interaction region have a mass of about 600 kg each. The forces from the existing ZEUS magnets on the coils are comparatively small (below 100 N).

There are only limited possibilities to support the new magnets, since the experiment has a number of mechanical constraints. As indicated in Figs. 29, 30 the magnets have to be supported mainly from their outside ends, i.e. with relatively long lever arms. The situation is more favourable on the rear side due to the cryo tower structure. On the front side some weight may be supported inside the ZEUS detector by string connections to the spokesplate.

4.3.4 Installation

The magnets, their corresponding beam pipe elements, and related ZEUS detector components will be installed as pre-assembled units. They are installed from the forward side (see Fig. 31). First the rear magnet with the rear beam pipe part is lowered with the hall crane between the opened ZEUS forward calorimeter halves. This unit is then pushed through the central detector to the rear side. Next the central part of the beam pipe is inserted from the forward side. A planned new silicon microvertex detector should have been assembled around the central part of the beam pipe and will then be installed together with it. After installation it will be dismounted from the beam pipe and attached to the CTD inner vessel. Finally the forward magnet with the part of the beam pipe inserted and the FDET assembled around it will be put in place. Removal of the magnets, beam pipe parts, FDET, and microvertex detector will have to be done in the same way as the installation but in reverse order.

4.4 Background conditions

4.4.1 Background from the proton beam

The background from the proton beam will be higher than at present (1996), because a proton current close to the design value of 160 mA is finally expected, to be compared with the

1995 value of 40 mA. However, this increase will come with the general HERA improvement independent of the low beta scheme.

The low beta scheme should not make a big difference, because all apertures near the interaction point are the same as at present, except possibly a synchrotron radiation absorber at $z = -80$ cm and at a horizontal distance of 20 mm from the beam.

The beam gas background will depend on the possibility to install vacuum pumps inside the separator magnets.

4.4.2 Background from the electron beam

Since the collimators C1, C2, C3 and C4 will no longer be there, they cannot be used to limit background from stray electrons. The effect of stray electron on the ZEUS detector is however small, except for the present Beam Pipe Calorimeter (BPC), which will no longer be there.

Again, independent of the low beta scheme, the general increase of the electron current from 30 mA in 1995 to the design value of 58 mA will have to be accommodated.

4.4.3 Synchrotron radiation

Synchrotron radiation is the most critical source of background. There are three potential sources:

i) Backscattered radiation from the main synchrotron radiation absorbers, which are at distances of $12 \cdots 20$ m from the interaction point.

ii) Edge scattering from absorbers near the interaction point which are installed to protect the experiment from source i).

iii) Synchrotron radiation from the quadrupoles, which start about 5.8 m from the interaction point. Under normal circumstances this is a negligible source. However, if the beam is misadjusted, it can make a large contribution.

In the following, we shall only consider source i), the backscattered radiation.

Fig. 24 shows the interaction region with the line marking the boundary of the direct synchrotron radiation. It is not touched by any absorbers, until it hits the main absorbers, which are situated at distances of $12 \cdots 20$ m from the interaction point. In order to minimize reflection from these main absorbers, they have to be covered by an anti-reflecting coating, e.g. 3 mm W, 0.5 mm Ag, and 0.13 mm Cu. The back reflected radiation constitutes the main background for the detector. It delivers a dose rate of about 0.01 Gray/s, and therefore all sensitive parts of the detector including the beam pipe have to be protected from it. This is done by absorbers placed at -0.8 m and -1.4 m (see Fig. 24). All surfaces hit by the reflected radiation need an anti-reflection coating.

In order to assess the radiation load on the CTD, a comparison with the present situation is made. In Table 4 the present situation is compared with the low beta option. For this comparison an electron energy of 30 GeV, an electron current of 58 mA and a field in the last deflection magnet of 0.22 T have been assumed.

The table shows that the background in the CTD will increase about 15-fold. Compared with the situation in 1995, where currents were about 30 mA, one has to expect a 30-fold increase.

In a run with random triggers, less than 1 hit was observed on average in the CTD in 1995 at 30 mA. The hits were distributed uniformly throughout the chamber. This would translate into less than 30 hits on average for the low beta scheme.

In a similar way the number of hits in a Si detector at a radius of 5 cm and of 0.4 mm thickness can be estimated. One gets $10^{-4} \cdots 10^{-3}$ hits/cm^2/bunch-crossing. This corresponds to a dose rate of $10^{-6} \cdots 10^{-5}$ Gray/s.

	present	low beta
Total power (both sides)	9.7 kW	22 kW
Critical energy	44 keV	126 keV
Dist. of main absorber (weighted)	23.5 m	16.3 m eff.
Reflected into experiment (arb. units):		
Total power	1.0	2.3
(distance of main abs.)$^{-2}$	1.0	2.1
Reflection coefficient	1.0	1.6
Missing action of abs. C1 $\cdots$ 3	1.0	2.0
overall factor	1.0	15

Table 4: Comparison of synchrotron radiation background (present values scaled to nominal electron beam parameters, i.e. 30 GeV and 58 mA)

4.5 Luminosity measurement and photon tagging

The consequences of the HERA interaction region upgrade for the present ZEUS LUMI system and for photoproduction tagging are discussed in this section. Also the concept of a future Beam Monitoring Station is proposed.

4.5.1 Present LUMI system

Synchrotron radiation and filter thickness. At an assumed bending radius of 475 m the thickness of the carbon filter in front of the photon calorimeter of the luminosity monitor would have to be increased from $2 \cdots 3$ radiation lengths (r.l.) to 4 r.l. This would deteriorate the resolution from presently $23\%/\sqrt{E}$ (for 2 r.l.) to $>35\%/\sqrt{E}$ and increase the minimum energy that can be measured well from 1 GeV to about 3 GeV. The expected uncertainty of the luminosity measurement due to these effects is about 2 % and is not compatible with ≤ 1 % precision. If, however, a new detector were installed with a preshower detector and better energy resolution, then possibly a 1 % precision could be achieved. Another step to be considered is the use of polyethylene instead of carbon as an absorber.

Event rate. The strongly increased event rate will constitute a problem.

- At a luminosity of $10^{32}/\mathrm{cm}^2\mathrm{s}$ the rate of bremsstrahlung with energy above 1 GeV is 17 MHz. This results in a very high occupancy: on average 2 photons per bunch crossing and only 13 % of bunch crossings without hard bremsstrahlung). Effects of such event pileup, however, can be well simulated, measured and controlled by usage of different energy cuts. Possibly also pileup insensitive measurements (energy flow measurement) can be adopted.
- The present luminosity detector uses PMTs for readout. If one scales the present anode current (already at very low HV) to a luminosity of $10^{32}/\mathrm{cm}^2\mathrm{s}$ one expects 60 μA! Either low gain PMTs (6/8 dynodes) or hybrid PMTs would have to be used.
- Radiation dosage at the worst point is expected to be up to 10 kGray/year and may seriously affect the energy measurement.

Photon acceptance. For the recent Willeke optics the bremsstrahlung cone has a horizontal angular divergence of 0.35 mrad which reduces the photon acceptance from 98 % to 80 %. In such a case systematic effects are much less controlled and may result in an increased error from this source from 0.5 % now to 2 % at the full luminosity. To keep the precision, one can try to either increase the angular acceptance or decrease the electron beam emittance and angular divergence at the IP.

To summarize: A luminosity measurement similar to the one presently used in the ZEUS experiment has an estimated accuracy of 3 %. The accuracy can be possibly improved by ensuring a high photon acceptance and better linearity of the energy measurement. To achieve approximately 1 % precision — desirable for some physics questions — alternative solutions should be considered.

4.5.2 Photoproduction tagging

The present tagging devices are incompatible with the HERA upgrade. There are three possible new locations:

i) About 10 m from the IP, just after the first two quadrupoles; since any extra space (longitudinally) would reduce the luminosity, the detector should be integrated to some extend with the quadrupole/beam pipe — it could be a tungsten spaghetti calorimeter — and use only the typical space available (20···30 cm) between beam line elements. Such a detector would tag photoproduction at high/medium W, at about 180···250 GeV (corresponding to 35···120 mm distance of the scattered electrons from the beam axis).

ii) At a distance >20 m from the IP a low W (about 80 GeV) tagger could be installed using the technique of the present 44 m tagger.

iii) If high W (≥280 GeV) tagging would be required, then a small detector just after the dipole at −5.6 m could be installed using the technique of the present 8 m tagger.

The main difficulty in running the tagging devices at very high luminosity is a large event rate due to e p bremsstrahlung which results in a significant detector occupancy. Therefore, very good vacuum (to avoid a large e-gas contribution) and a high bremsstrahlung photon acceptance (to allow for efficient vetoing) are essential.

4.5.3 Beam monitoring station

Running experience has shown that scintillation counters close to the beam pipe in the outgoing electron beam direction (C5 counters, Beam Pipe Calorimeter) are essential for a quick monitoring of the background conditions at the ZEUS experiment and the precise determination of the mean z position of the e p interaction region and the monitoring of satellite bunches. The present position around $z = -300$ cm will not be free due to the presence of the new dipole magnet. A new extended Beam Monitoring Station (BMS) is proposed at a position around $z = -560$ cm, downstream of the new dipole magnet.

The tasks of the BMS are:

1. Separate measurement of the radiation background from the proton and the electron beam.
2. Measurement of the mean z position (longitudinal) of the e p interaction point from the difference of the arrival times of background particles from the electron and from the proton bunches.
3. Monitoring of the satellite bunches accompanying the main bunches.
4. Measurement of the transverse position of the e p interaction point.
5. Measurement of the luminosity, independent of the present ZEUS luminosity monitor.

A conceptual side view of the BMS is shown in Fig. 32. The main elements are a thin exit window of the vacuum-pipe (i.e. transition from the circular cross section to an elliptical shape), two silicon trackers above and below the beam pipe, each consisting of two microstrip detectors (60 mm × 60 mm) with horizontal strips and two microstrip detectors with vertical strips, and two small compact electromagnetic calorimeters (e.g. $PbWO_4$ crystals). The minimum length required along the beam is 50 cm.

The timing information from the electromagnetic calorimeters is used to obtain the information for topics 1, 2, and 3. The measurement of small angle inelastic e p scattering (angular acceptance 7···12 mrad) and QED Compton scattering ($ep \to e\gamma p$) will provide events to reconstruct the transverse e p interaction point (using the z position obtained from the timing information in topic 2) and to obtain a measurement of the luminosity.

4.5.4 Beam position monitor

A beam position pick-up monitor positioned around $z = \pm 300$ cm (inside of the new dipole) appears highly desirable. No design work has yet been done.

4.6 Impact on other ZEUS components

The impact of the upgrade of the interaction region for components close to the beam is discussed. There are at present only qualitative results.

4.6.1 CAL

There is some fringe field from the new magnets; Table 5 provides a map of the field values from the air coil magnet. The calorimeter PMTs close to the dipole magnet may require improved shielding — this is under study. Possible effects due to the additional material from the new magnet on the calorimeter performance are presently being studied with Monte-Carlo calculations.

$z = 120\,\text{cm}$ (magnet head)

	$x=0$			$x=10$			$x=20$			$x=30$		
$y=0$	0	−1015	0	0	424	0	0	133	0	0	58	0
$y=10$	0	−408	526	−270	−25	216	−86	62	50	−32	42	17
$y=20$	0	−124	131	−80	−64	96	−65	−1	48	−37	15	23
$y=30$	0	−57	58	−30	−42	50	−37	−16	34	−29	0	21

$z = 220\,\text{cm}$

	$x=0$			$x=10$			$x=20$			$x=30$		
$y=0$	0	−2032	0	0	846	0	0	264	0	0	115	0
$y=10$	0	−819	0	−539	−52	0	−172	122	0	−64	81	0
$y=20$	0	−251	1	−160	−130	1	−130	−5	1	−74	28	1
$y=30$	0	−116	1	−61	−85	1	−73	−34	1	−58	−3	1

Table 5: Air coil dipole magnet field map at $z = 120\,\text{cm}$ (magnet head) and $z = 220\,\text{cm}$. The ZEUS coordinates x and y are given in cm, the magnetic field B_x, B_y, B_z in Gauß.

4.6.2 Tracking detector

The additional magnetic field does not pose a problem for the performance of the tracking detector and the track reconstruction. For synchrotron radiation effects see Section 4.4.

4.6.3 Silicon vertex detector

Installation of a vertex detector based on Si detector technology appears compatible with the low beta installation. An inside diameter of 10 cm can be accommodated; the radiation background has been discussed in Section 4.4 and appears to be at a tolerable level. More accurate statements can be made once the design for such a device is available.

4.6.4 FMUON

No impact on the performance of the forward muon system is expected.

4.6.5 PRT

Scintillation counters close to the beam pipe are presently located at $z = 5.4\,\text{m}$ and $z = 25\,\text{m}$ to separate diffractive from non-diffractive events. The place of the counters at 5.4 m will be taken by the new dipole magnet. It presently appears difficult to install new counters at this position unless approximately 20 cm of space is freed along the beam direction. This z position is symmetric to the position in the electron direction of the proposed BMS. The counters at 25 m should not strongly be affected by the modification of the interaction region.

4.6.6 LPS

The main impact of the luminosity upgrade on the performance of the ZEUS Leading Proton Spectrometer (LPS) is due to the increased transverse momentum spread of the proton beam, which, compared to the present situation, increases from 25 MeV to 35 MeV in x and 75 MeV to 160 MeV in y. As the detectors have to be at least $10\,\sigma$ away from the beam this results, for protons with $x_L = 1$, in an increase of the lower transverse momentum cutoff from 250 MeV to 350 MeV. No significant change of the longitudinal momentum resolution is expected. The transverse momentum spread however will result in a significant degradation of the resolution of the measurement of the momentum transfer to the proton.

The installation of the LPS does not present a problem in principle. However, it will represent a major operation both in terms of manpower and money. At present it appears that most detectors have to be rebuilt and that the first three stations S1, S2 and S3 will have to be moved. It should however be possible to leave the beam profile at the later stations S4, S5 and S6 unchanged. Every effort should be made so that this option is viable. This will require a close collaboration between HERA and ZEUS.

The main effects on physics are due to the reduced acceptance and the poorer momentum transfer resolution.

For details we refer to the report "The ZEUS Straight Section Upgrade" (ZEUS-Note 96-087 by T. Massam, August 26, 1996).

4.6.7 FNC

As in the case of the LPS, the main impact on the performance of the ZEUS Forward Neutron Calorimeter (FNC) is due to the increased transverse momentum spread of the proton beam. The angular acceptance of the FNC is determined by the apertures of the HERA beam elements, and no major change is expected if proper care is taken with the new beam design. The measurement of the transverse momentum transfer from the beam proton to the scattered neutron will be much less accurate than at present. Again the optimum design will require a close collaboration between HERA and ZEUS.

Overall no major impact on the physics performance of the FNC is expected in an optimized design.

For details we refer to the report "The ZEUS Straight Section Upgrade" (ZEUS-Note 96-087 by T. Massam, August 26, 1996).

4.7 Impact on physics and conclusions

As can be seen from the physics working group reports included in these proceedings, the upgrade of the HERA accelerator to reach luminosities of $1\,\mathrm{fb}^{-1}$ is necessary to exploit the physics capabilities inherent in HERA. High Q^2 and high P_T physics, as well as the search for rare processes, will greatly benefit from the increase in luminosity.

On the other hand, the luminosity upgrade will impair the capability of the ZEUS experiment to pursue physics processes connected to detecting particles at small forward and backward angles. Components such as the beam pipe calorimeter, electron taggers, the proton remnant tagger, the leading proton spectrometer and the forward neutron calorimeter will be seriously affected, and in some cases will have to be removed completely (e.g., the beam pipe calorimeter). This will mean a reduction in the capability of the ZEUS detector for low Q^2 physics. Studies of diffractive physics, forward jets and energy flows will also be affected (see Sections 4.6.6 and 4.6.7). We will obtain as detailed physics results on these topics as is possible before the implementation of the detector modifications, and efforts will be made to preserve as much capability as possible in the new configuration.

Other implications of the proposed options for the magnet layout within ZEUS are currently under study. The options discussed in Section 4.3.1 have been implemented in the full ZEUS Monte Carlo.

- The effect of the upgrade on the measurement of jets has been studied in both resolved photoproduction and DIS. In both cases $15\cdots30\,\%$ more jets are observed in the new configurations in the region $2 < \eta < 3$ for jets with E_T around 6 GeV. Comparison of jets observed in the calorimeter to "true" jets of final state particles indicates that the extra jets in the calorimeter are not associated with true jets and thus the purity of the sample in the forward region is degraded. However, for jets which are matched to true jets the energy resolution is not significantly degraded. The effects of the two configurations are not significantly different.

- The proton dissociative process $ep \to eX_N p$, where X_N is a system of mass M_N, has also been investigated. The forward calorimeter energy distributions and the tagging acceptance versus M_N^2 show only small differences with respect to the current configuration. The tagging efficiency slightly increases for small values of M_N^2, presumably because of showering in the magnet.

In summary, these preliminary studies indicate some effects in the forward region, which we anticipate can be handled with careful simulation. Detailed studies are currently under way for a wide range of physics processes, and results will be available in a written report. To date, no major impact has been found due to the presence of the dipole magnets in the ZEUS interaction region on the measurements solely performed with the central detector.

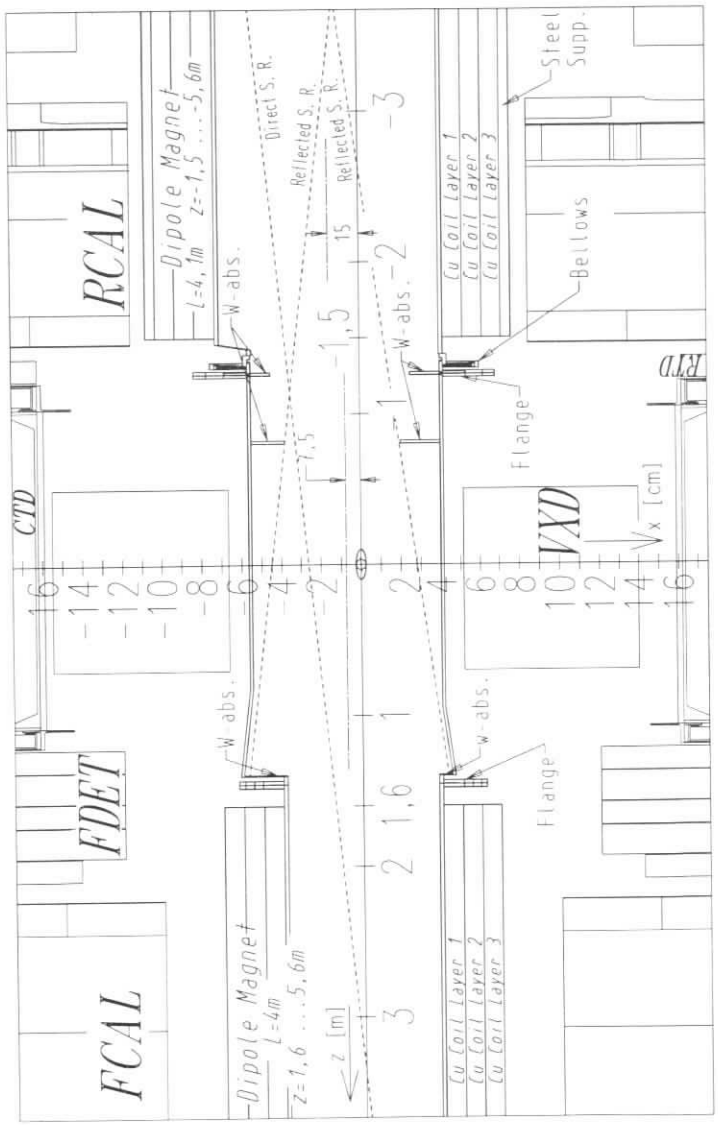

Figure 24: Option 1 — magnet coils, top view.

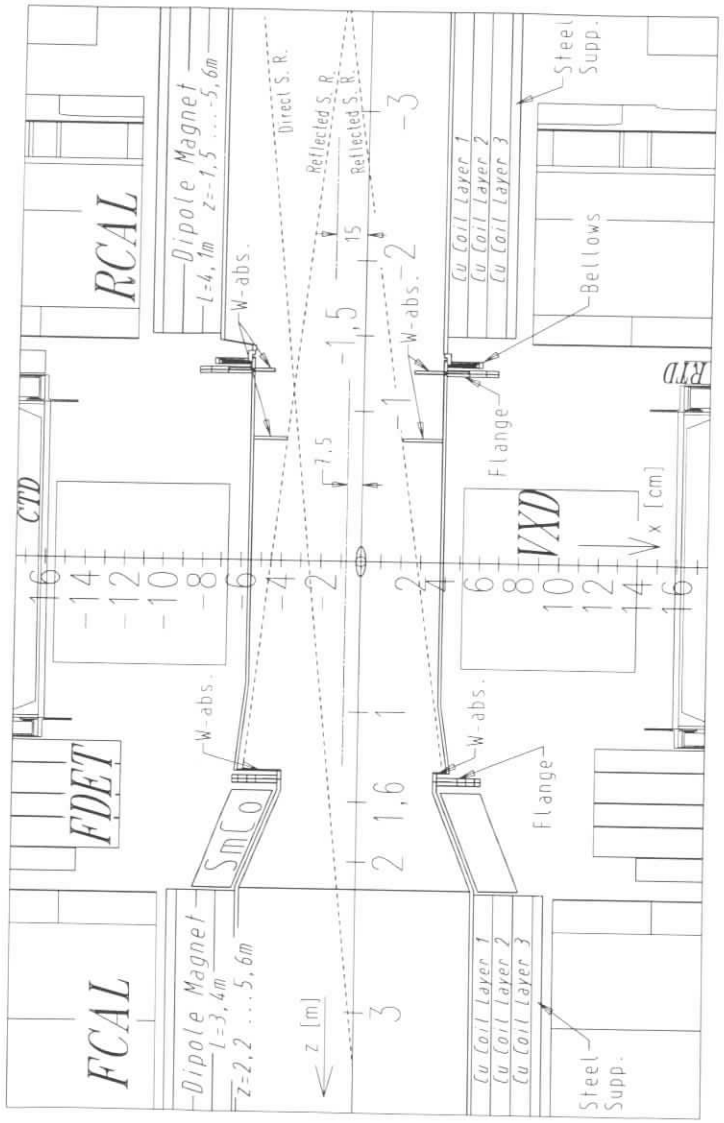

Figure 25: Option 2 — permanent magnet, top view.

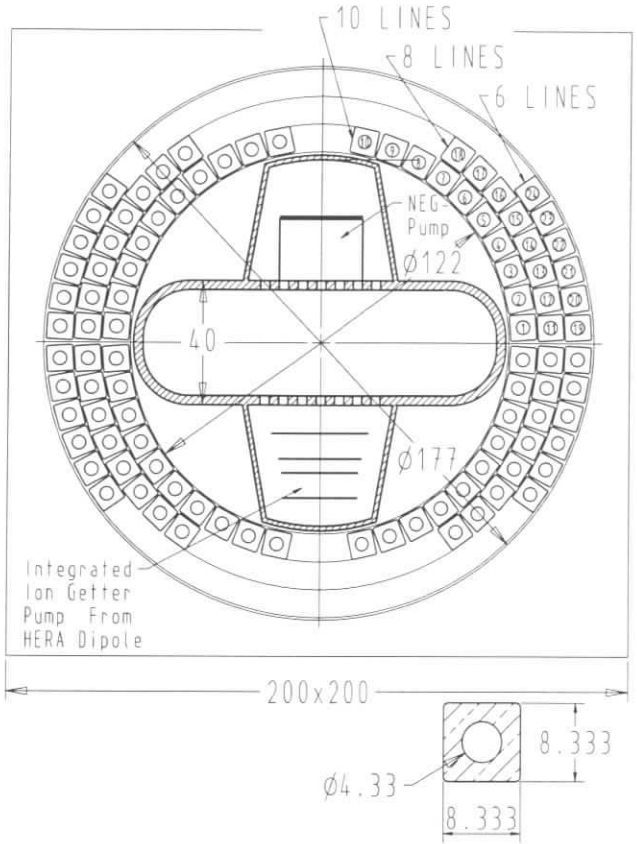

Figure 26: Cross section of magnet coil.

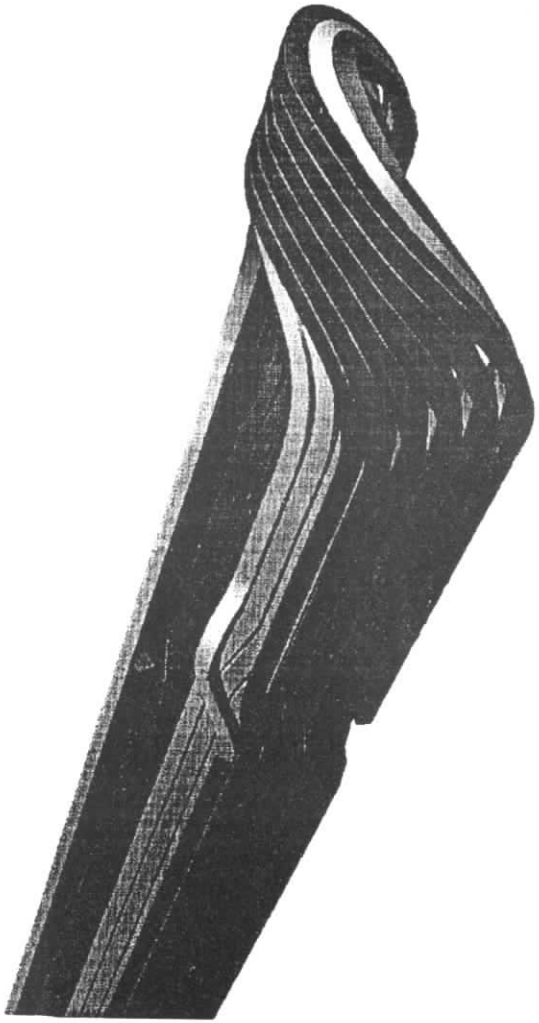

Figure 27: Artist view of magnet coil (upper half).

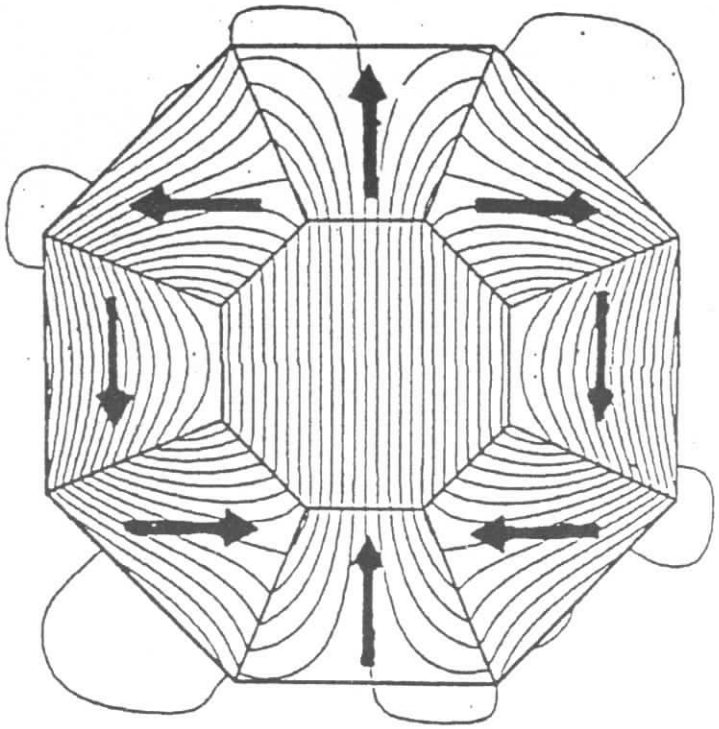

Figure 28: Cross section of permanent SmCo dipole magnet.
A ring-like structure is built from trapezoidal blocks of Sm_2Co_{17}. The block magnetisation and the flux pattern is indicated.

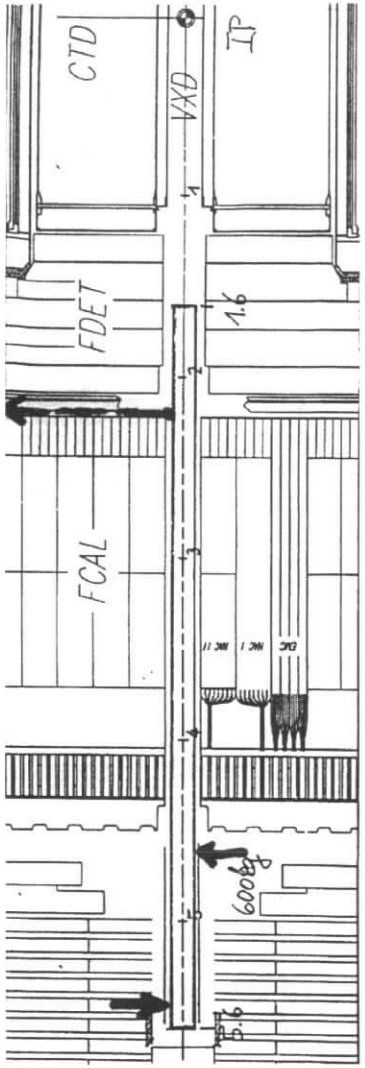

Figure 29: Magnet support on forward side, side view.

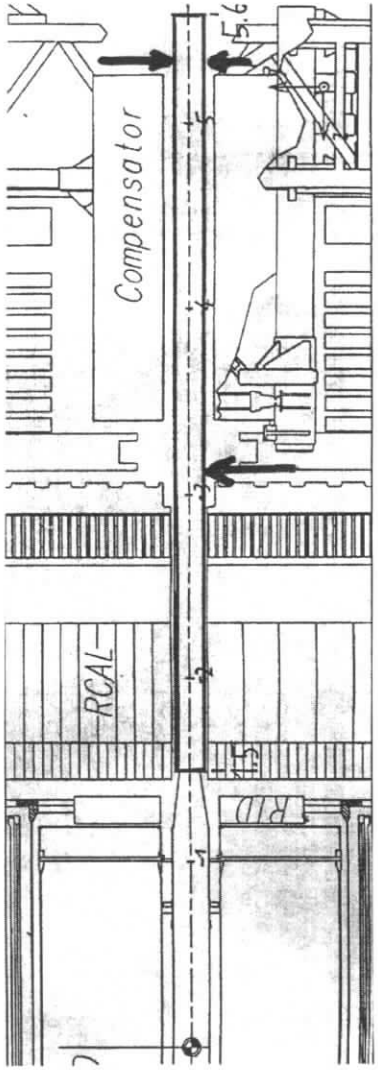

Figure 30: Magnet support on rear side, side view.

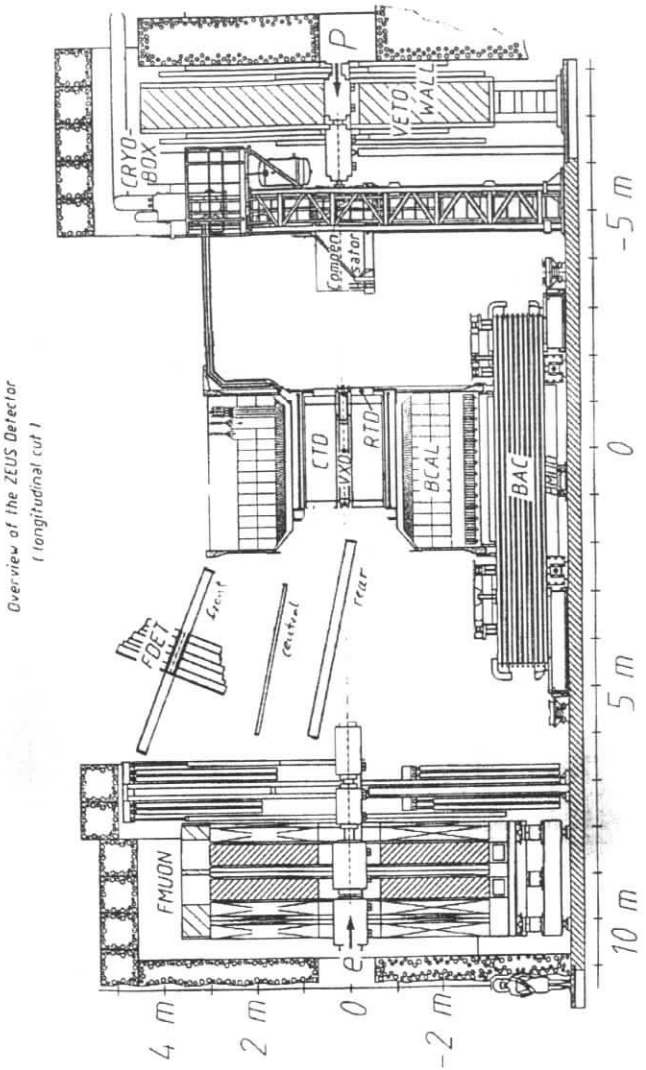

Figure 31: Installation.

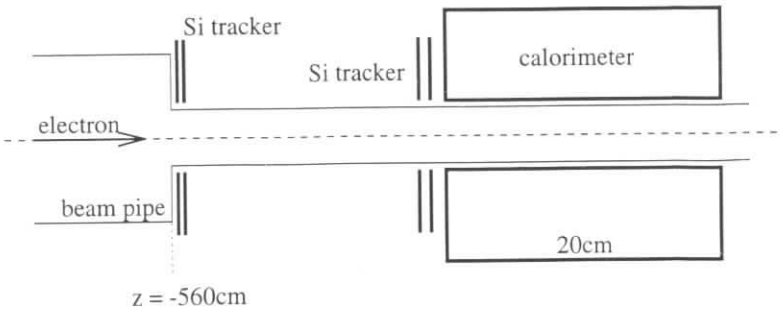

Figure 32: Beam monitoring station, side view.
Conceptual design of a beam monitoring station beyond the separator magnet (side view).

5 Impact of a Luminosity Upgrade on H1

by W. Bartel, H1

Abstract: An attempt has been made to assess the impact of a luminosity upgrade on H1 assuming two warm dipole magnets inserted inside H1. In order to accommodate dipole coils, several ccomponents of the central H1 detector will have to be modified like Silicon trackers, forward and backward tracking chambers, backward Spacal calorimeter, plug calorimeter as well as the support structure for the beam pipe.

5.1 Introduction

High luminosity is the basis for future physics studies with the H1 detector. According to an assessment of the luminosity working group within this workshop, a substantial gain can only be expected by separating the two beams as close to the interaction point as possible by introducing dipole magnets inside the experiments. Such a modification will unavoidably affect the performance of H1. In order to keep the impact on the physics performance as small as possible a scheme was followed which introduces warm dipole magnets with an outer diameter of at most 180 mm.

- The dipole coils with an anticipated outer diameter of 180 mm do not fit into the presently available apertures. Thus H1 has to be reshaped in various places to accommodate the magnets and the beam pipe.
- The deflection of the electrons will create synchrotron radiation, which has to be masked. As a consequence, a new beam pipe has to be designed.
- The luminosity measurement will be affected by the higher level of synchrotron radiation and the modified optics in the interaction point. A new photon calorimeter has to be built.
- The electron tagger needs a new design.
- The space presently taken by the plug calorimeter will be very much reduced and a different instrumentation has to be implemented.
- The detector stations of the FPS have to be moved to different positions.
- The physics performance will change due to the removal of detector elements at small radii, the additional material introduced by the coils and synchrotron radiation absorbers and the change in beam optics.

The detailed studies, which are necessary to investigate the impact of a high luminosity upgrade of H1 were not yet completed by the time of this report so that only a preliminary conclusions can be presented.

5.2 Mechanical installation

A three dimensional view of the H1 detector is displaed in Fig. 33. For a high luminosity interaction region the central beam pipe has to be replaced by a beam pipe surrounded by dipole coils. This device has to fit through the forward aperture of the tank housing the liquid Argon calorimeter, because rebuilding the tank is equivalent to rebuilding H1. This constraint limits the outer diameter to 180 mm.

The Silicon trackers around the beam pipe (CST and BST) are detector elements, which should be kept also for high luminosity operation. Therefore the dipole coil cannot start earlier than $\pm$ 1380 mm from the interaction point, if a symmetric installation of the dipole is maintained as preferred for beam optics considerations.

Having fixed the outer dimensions of the high luminosity dipole magnet a central hole has to be provided, which is wide enough to accommodate it. Thus the central modules of the backward calorimeter (SPACAL) have to be removed, which can be done by reassembling the calorimeter. Furthermore the backward drift chamber has to be rebuilt with a larger central bore hole. In order to support the beam pipe together with the dipole magnet space has to be gained at the position of the first module of the forward tracking module and at the position of the backward drift chamber. Various options are under discussion including one, where a rigid support structure is integrated into the new backward drift chamber and also the first forward tracking module is modified to support the weight of the magnet.

The H1 beam pipe is now pumped by integrated getter pumps of the order of two meters away from the interaction point. For the new beam pipe with collimators and absorbers it will presumably technically more difficult to provide the necessary pumping power close to the interaction point.

The present version of the high luminosity insert assumes that the compensating solenoid is kept, in order to maintain electron and positron polarisation. The compensating solenoid does not move together with the main H1 detector. Therefore the beam pipe with the dipole has to be installed when the experiment sits in the interaction region. The necessary space for inserting can be gained by temporarily removing the HERA quadrupoles next to the interaction point.

5.3 Synchrotron Radiation

All details on the synchrotron radiation generated in the bends next to the interaction point and the way they could be shielded is outlined in D. Pitzls contribution to this workshop [1].

The strategy to protect the experiment against synchrotron radiation is based on a central beam pipe, which is wide enough to pass the synchrotron radiation fan through the experiment and place the principal absorbers as far downstream as possible. Masks close to the interaction point prohibit then scattered photons from reaching the tracking chambers. First background estimates show that an increase by a factor of about ten in the numbers of photons reaching the central drift chamber is expected compared with the present set up, which leads to still tolerable rates.

According to a preliminary study of a beam pipe design, the central Silicon tracker could be kept as it is with the beam passing off center. The backward tracker has in its present version too small an aperture for the beam pipe. It has to be rebuilt.

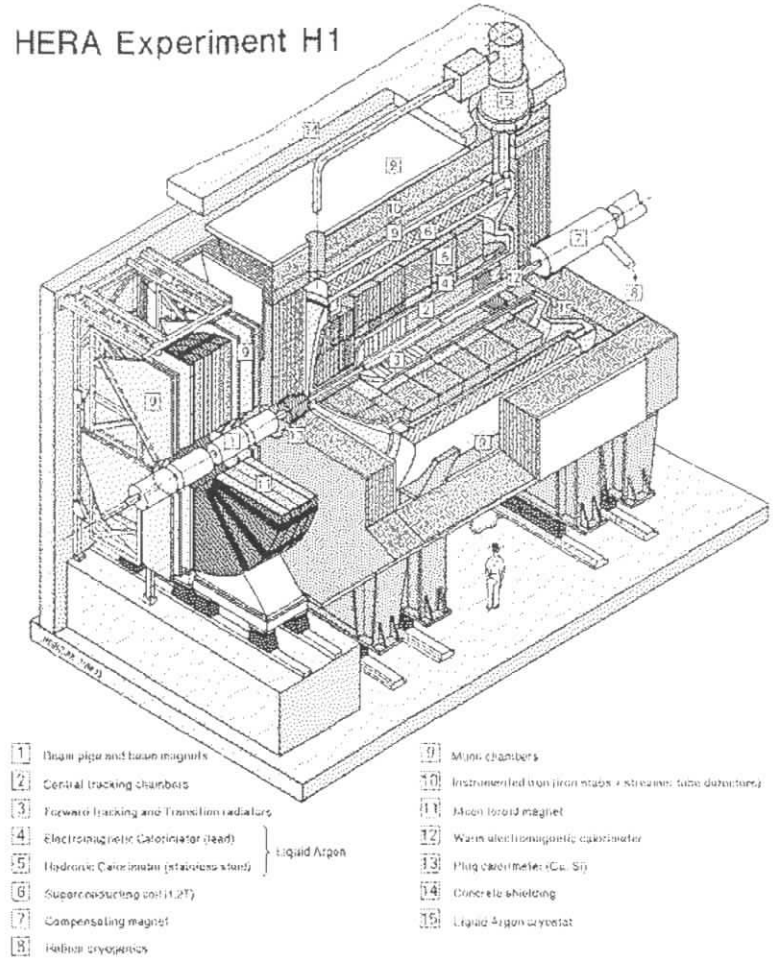

Figure 33: Perspective view of the H1 detecctor.

5.4 Luminosity Measurement

The accuracy of a luminosity measurement by observing ep bremsstrahlung will be degraded in the proposed high luminosity scheme. Two items contribute. First the photon counter due to the larger beam divergence at the interaction point will accept only between 60 and 70% of all bremsstrahlung photons compared with 95% in the prestent set up and second due to the high level of synchrotron radiation the absorber thickness in front of the photon detector has to be increased thus leading to a bad energy resolution. Preliminary studies indicate that the luminosity measurement may not be better than 5%.

At high luminosity, however, other reactions with well known cross sections may be used for normalisation like QED Compton scattering.

In measuring luminosity and for tagging photoproduction events electron taggers are employed. With the new design of the interaction region appropriate new positions for these devices have to be found.

5.5 Plug Calorimeter

The space presently occupied by the plug calorimeter will widely be taken by the forward dipole coil. In addition the material in front of the calorimeter represented by the coil will be too big for a useful energy measurement. Thus a new design for the forward instrumentation has to be made.

Although the calorimetry in this area will be poor it cannot be dropped completely, because another important feature of the plug calorimeter has to be maintained. It provides a timing signal, which is used to suppress background events from beam gas and beam wall scattering.

5.6 Forward Proton Spectrometer

The forward proton spectrometer (FPS) employs the HERA machine magnets downstream of the interaction point for a momentum measurement of small angle protons. Changing the focusing properties of the beamline requires new positions for the detector stations. As an example, 820 GeV protons are most favourably observed at a position, where the phase advance with respect to the interaction point is close to $\pi/2$. The new positions can only be determined after having defined a realistic beam optics scheme. Furthermore it has to be observed that apertures are large enough not to cut into the acceptance of the spectrometer.

Besides these pure geometrical considerations, which have to be observed, the physics performance of the FPS will be affected by the strong focusing and consequently large beam divergence at the interaction point. The transverse momentum thus introduced into the interaction will go up from presently 70 MeV to 160 MeV, which is already close to the natural transverse momentum in diffractive processes of about 350 MeV.

5.7 Physics Performance of H1

The main impact of a high luminosity intersect on the physics capability of H1 is due to the insertion of a massive coil close to the interaction point, which will obscure the region of small angnes (smaller than 100 mrad) in the forward and backward regions. In particular the physics at very low Q^2 ($Q^2 \leq 2\ GeV^2$) and diffractive physics with rapidity gaps above $\eta \geq 3$ will affected. We may, however, assume that by the time the HERA luminosity will be upgraded some 100 pb^{-1} will have been accumulated with the present configuration so that most of these investigations have come to an end. Detailed Mt Carlo studies on the performance of H1 in a high luminosity environment are under way. It is, however, unlikely the main conclusions will change.

By the time H1 and HERA could be upgraded most of the physics processes with large cross sections will have been studied and higher luminosity will be vital for H1 to surwive. Physics

topics, which will come into focus are DIS at high Q^2, electro weak interactions, search for new phenomena and diffractive events with forward going protons at high invariant mass final states.

5.8 Conclusion

Preliminary investigations into an upgrade of the HERA luminosity by introducing a dipole field close to the interaction point inside the H1 detector show that the necessary modifications seem technically feaseble within a reasonable effort. The physics capability of H1 to study ep reactions with the high luminosity machine will not be affected if we assume that the program of large cross section physics is completed by the time of the upgrade. A special effort has to be made to develop a scheme for an accurate luminosity measurement.

An upgrade of H1 and HERA is vital to a physics program beyond the year 2000.

References

[1] D. Pitzl This proceedings

6 Conservative upgrade of the HERA interaction regions

by R. Brinkmann

6.1 Introduction

In this section we discuss the potential for a luminosity upgrade in HERA by modifying the beam optics in the North and South IR's under the boundary condition that the free space for the experiments is left unchanged at $\pm 5.8m$, i.e. without any magnets inside the detector. Such a conservative approach can clearly not provide as much luminosity gain as a more radical lattice modification with separator magnets integrated in the detector, as described in section(...), but the detailed investigation shows that about a factor of two increase in specific luminosity compared to the present optics can be achieved. In this approach, moving the p-beam low-beta quadrupoles closer to the IP is accomplished by the following modifications:

- Reduction of the e-beam bending radius from 1300m (present lattice) to 820m. The critical energy of synchrotron radiation remains unchanged if we limit the e-beam energy to 30 GeV instead of 35 GeV for the original layout.
- Simplification of the e-beam optics by replacing the triplet focussing by a doublet.
- Moving the "BS-type" magnet (used for correcting the influence of the e-magnets on the p-orbit) after the first p-beam focussing element.
- Using a half-quad with "thin" septum plate, as suggested by B. Parker, for the first p-beam focussing element in order to cope with a small beam separation at this position.

The minimum distance of the first p-beam half-quad from the IP is 16.5m with these modifications, down from 27.6m in the present lattice. This allows to reduce the p-beam beta-function at the IP by more than a factor of three. An overview of all relevant parameters is given in table 6. In the following, the beam optics modifications for the electron and proton rings are described in more detail.

6.2 Electron beam optics

The reconfiguration of the e-beam lattice is done by using only existing magnets. The low-beta doublet consists of a pair of QL-quads followed by two QC-quads. As in the present optics, they are positioned off-axis w.r.t. the orbit and act as combined function magnets. The required strengths do not present any problem and the available aperture is safely sufficient for the beams and for the synchrotron light (see fig. 34). After the doublet, a BH-dipole is installed which completes the separation angle to 9 mrad at a bending radius of 820m. An important part of this design is the reduction of the horizontal beam emittance by stronger focussing in the arcs (78 deg. per FODO cell instead of 60 deg.). This reduces the aperture requirement for the e-beam and the chromaticity of the low-beta insertion (same beam size at the IP achieved with

	e-beam	p-beam
energy / GeV	27.5	820
number of colliding bunches	176	176
bunch charge N / 10^{10}	4.18	10
emittances $\epsilon_{x,y}/m$	1.8×10^{-8}	
norm. (2σ) emittance $\gamma\epsilon_{x,y}/m$		20×10^{-6}
Beta at IP $\beta^*_{x,y}/m$	5.5, 0.22	1.8, 0.35
beam size $\sigma^*_{x,y}/mm$	.180, .0324	.178, .0355
tune shift $\Delta Q_{x,y}$	.040, .039	.0017, .0004
specific lumi $/10^{29} cm^{-2} s^{-1} mA^{-2}$	10.7	10.7
gain factor	2.14	2.14
luminosity $/10^{31} cm^{-2} s^{-1}$	4.6	4.6

Table 6: Parameters for the conservative IR upgrade

a larger β^*_x). It will also be beneficial for synchrotron light collimation, since the collimators can be moved closer to the beam axis. Matching of the low-beta insertion to the remaining straight section is in principle no problem, but so far no attempt has been made to include the boundary conditions of spin matching. The optics in the vicinity of the IR is shown in fig.35. The available aperture at the position of the first p-beam half-quad is rather small in the horizontal plane (although sufficient for luminosity operation) and an injection optics with relaxed beta-functions will be required to provide enough acceptance for off-axis accumulation.

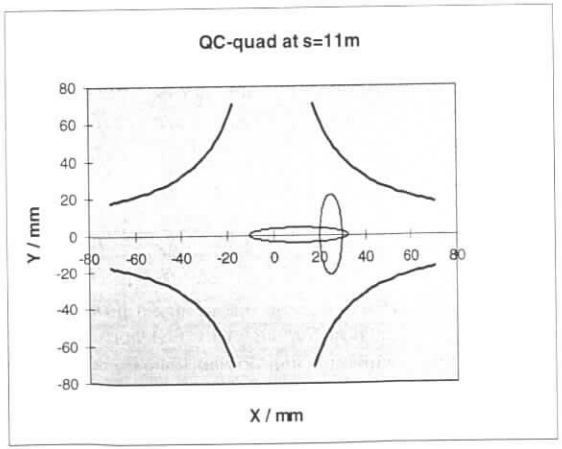

Figure 34: Beamsizes (12-sigma) at the end of the e-beam doublet.

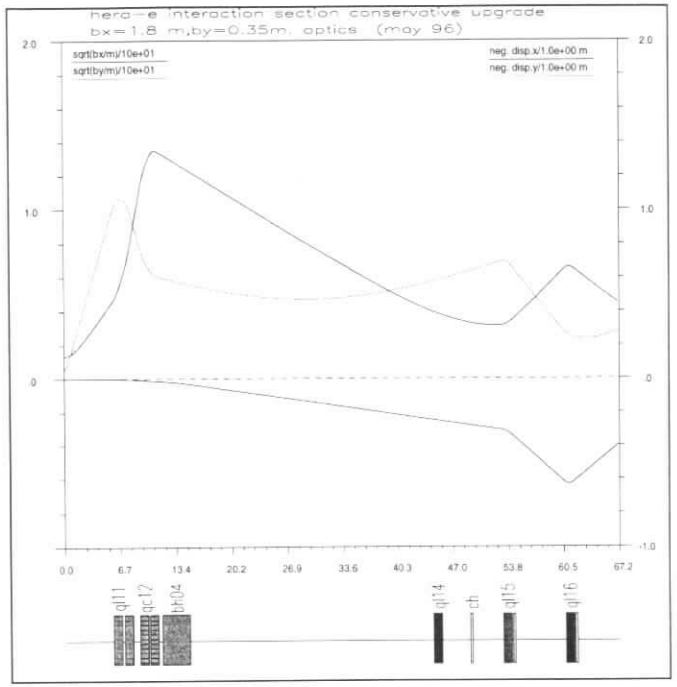

Figure 35: Electron beam optics in the upgraded IR.

6.3 Proton beam optics

The first element of the p-beamline is a "Parker septum half-quad" with an aperture radius of 40 mm. The beam separation is sufficiently large to provide a 12-sigma aperture for both beams (see fig. 36).

The strength of this half-quad corresponds to a pole-tip field of 8 kGauss, which seems conservative. The other p-beam focussing elements are recycled magnets from the present lattice (QS- and QR-magnets) and provide more than the required 12-sigma aperture. A BS-type dipole magnet, with reduced length, is installed between the "Parker-quad" and the first QS-magnet. This correction magnet is foreseen to compensate the variation of the influence of the e-magnets on the p-orbit during the e-ring energy ramp. It is assumed that the p-magnets have to be slightly re-adjusted if the machine is switched from electron to positron operation

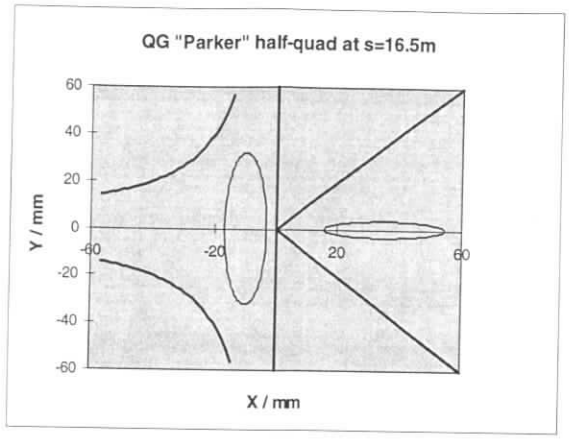

Figure 36: Beamsizes (12-sigma) at the beginning of the Parker half-quad

(or vice versa). The peak beta-functions in the proton optics are even slightly lower than in the present optics and the chromaticity compensation is not a problem. The modified proton optics has been matched to the periodic arcs, which is possible with the available correction quadrupole strengths.

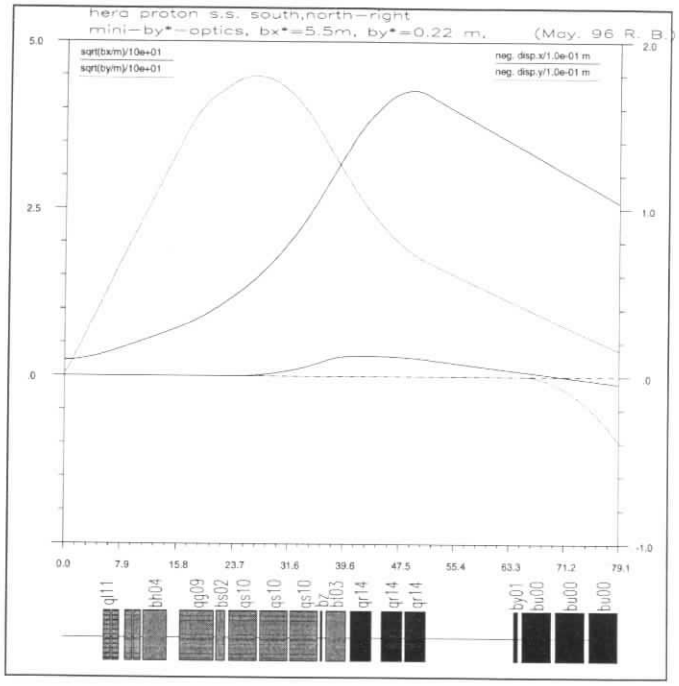

Figure 37: Proton beam optics in the upgraded IR.

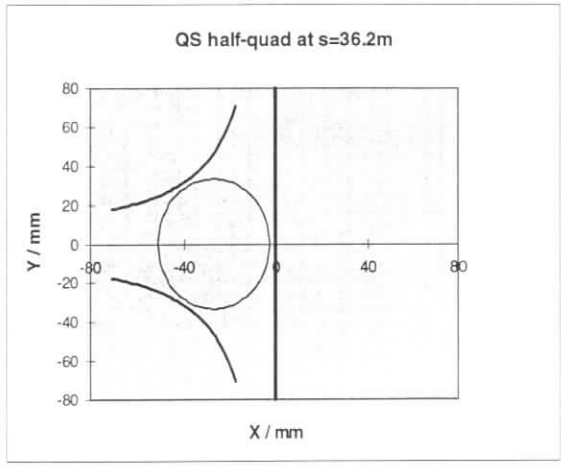

Figure 38: Proton Beamsize (12-sigma) at the end of the 3rd QS half-quad.

6.4 Conclusion

The potential for an IR upgrade in HERA based on an essentially unchanged concept for the beam separation and using many of the presently installed components has been investigated. The proposed beam optics leaves a free aperture of 12 sigma for the p-beam. Tightening the aperture somewhat (say, to 10 sigma) seems conceivable and would allow to bring the vertical beta-function at the IP down to the bunchlength (15 cm) limit, with another 20% gain in luminosity. We therefore conclude that an improved lattice which maintains a free space for the experiments of $\pm$ 5.8 m has a luminosity gain potential of up to a factor of 2.5. Taking into account that such a modification requires a relatively small amount of new components, it seems conceivable that it could be done as the first step of an IR-upgrade on a rather short time scale, and that the full upgrade (as desribed in section (...)) with another gain of about 60 % in luminosity could be viewed as the 2nd step.

7 DESYIII Beam Brightness Limitations

by W. Ebeling and J. Maidment

7.1 Introduction

Desy 3 is the first circular machine in the HERA-p injector chain. It accelerates protons from 50 MeV (kinetic energy) to a momentum of 7.5 GeV/c. Injection into this machine is from a linear accelerator which provides H^- ions. These are stripped using a thin foil which in principle allows accumulation of protons with negligible increase in transverse emittance. Typically the linac pulse current and duration are 10ma and 35μs respectively thus allowing ten turns to be injected. The resultant coasting beam is quasi-adiabatically captured in 11 bunches establishing the longitudinal separation subsequently required in HERA. Acceleration takes approximately 2 seconds. Ten of the 11 bunches are transferred to Petra. The maximum current achieved to date is roughly 200 ma, corresponding to 20% above the HERA single bunch design intensity. In routine operation about $1.1{\cdot}10^{11}$ protons per bunch are accelerated.

7.2 Transverse Space Charge Effects

Space charge is considered to be the most significant effect limiting the beam brightness. It is convenient to use the expression for space charge detuning namely:

$$\Delta Q_v = \frac{N r_p F}{\pi \varepsilon_v \left(1 + \sqrt{\frac{\varepsilon_h}{\varepsilon_v}}\right) B_f \beta \gamma^2}$$

Where N is the total number of circulating protons, F (~ 1) takes account of the image forces, B_f is the bunching factor (average/peak current) and ε is the transverse normalised emittance (2σ). The expression shows that the tune shift (which in reality characterises a spread) is greatest at low energy and increases linearly with brightness.

Measurements of the beam emittances as a function of accelerated current both at peak energy ("flat top") and shortly after injection ("flat bottom"). Figure 39 shows the results for the vertical emittance and Figure 40 those for the horizontal emittance. The solid lines correspond to flat top and the dotted lines to flat bottom. The increase of emittance with increasing beam current is clearly apparent as is also the increasing blow-up from injection to peak energy. More detailed measurements of the variation with time during the cycle together with the corresponding bunch length allow the implied tune shift to be calculated. The (vertical) tune shift so derived is shown in Figure 41.

The variation of tune shift is due not only to the increase in energy but also due to emittance blow-up and particle loss. These latter effects cease at around 0.25s at which time the beam momentum is approximately 1 GeV/c.

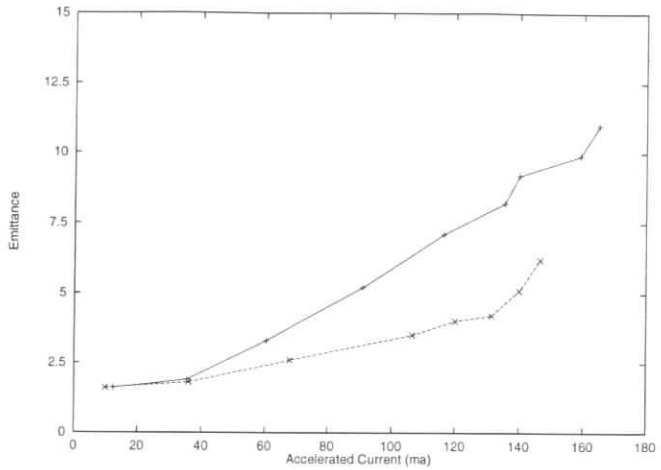

Figure 39: Vertical Emittance vs Accelerated Current

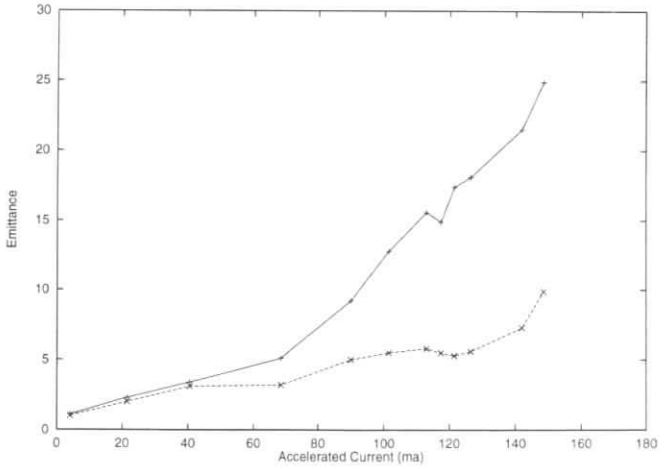

Figure 40: Horizontal Emittance vs Accelerated Current

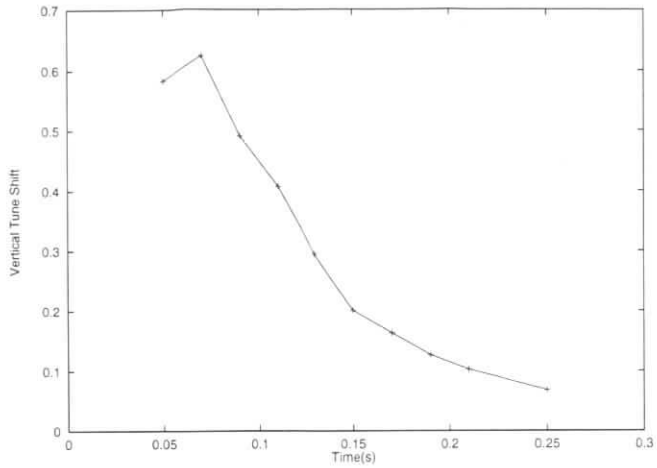

Figure 41: Vertical Tune Shift vs Time

7.3 Future Options

Although there is an ongoing program of machine studies to identify and understand all the contributions to emittance dilution it is clear that space charge is the dominant effect. In this situation an increase in the injection energy would allow potentially brighter beams. Two alternative possibilities have been or are under consideration. One study, in collaboration with INR (Moscow) has proposed an upgrade of the linear accelerator output energy to some 170 MeV. More details of this work may be found elsewhere in this document. In summary this option would require modest modifications to the existing Desy3 systems and yield at most a factor of 2 potential brightness increase.

A further option, namely the use of an intermediate booster, is being investigated in collaboration with IHEP (Protvino). The outline specification is for a 1 Hz repetition rate synchrotron accelerating 2 bunches per cycle to 800 MeV (momentum = 1.46 GeV/c). Five cycles would be used to fill the required 10 bunches in Desy3. Installation of a fast injection kicker system in Desy3 would be required. Use of such a booster may increase the space charge limit in Desy3 by at least a factor of 5.

It is intended that the booster study shall be completed in 6 months. Included will be not only design concepts but also cost estimates. This then allows a decision between the alternative options to be made in mid 1997.

8 LINAC III Upgrade Using a High Gradient Linac

LINACIII Upgrade group; compiled by N. Holtkamp

The conceptual design study which will be presented throughout the next pages is based on a more detailed report which has been worked out in collaboration with the Institute of Nuclear Research in Moscow (Troitsk), the INR. At INR a 600 MeV high duty cycle proton linac is under construction and a proton beam has already been accelerated up to 200 MeV/c [1]. With this expertise in house, the goal of this study was, to investigate the feasibility of an energy upgrade using a higher harmonic accelerating structure which has to be installed in the beam line of the existing LINAC III to the DESY III synchrotron. Given the limited space (length) the maximum energy should be achieved at reasonable investment and operation cost.

8.1 Introduction

Presently the proton linac, which is a 50 MeV Alvarez structure, injects H^- particles into the DESY III proton synchrotron, where multi-turn injection through a stripping foil is used to accumulate sufficient intensity for HERA. This linac is separated into three tanks and powered by a radio-frequency system operating at 202 MHz. The area occupied by the linac and part of the injection beam line which would have to be replaced with new accelerating structures can be seen in 42

The total space available for the installation of the new linac from the end of tank 3 to the injection into the booster synchrotron is roughly 35 m. A scenario which would replace tank 3 in addition and start with a 30 MeV beam to gain somewhat more space for the high gradient structure has been discussed, but will not be presented here. According to the feasibility study a higher harmonic frequency of 810.24 MHz can be used for the upgraded part of the linac. Such a high frequency allows to obtain a large accelerating gradient which will accelerate the H^- beam up to 160 MeV over a distance of $\approx$33 m. This part describes all subsystems of the accelerator leading to a cost estimate for the whole linac.

8.2 Linac III Beam Parameters

The knowledge of the present beam parameters of the Linac III is very important for a suitable design of the upgraded part of the linac. Typically for a low intensity injector into a synchrotron beam profiles and emittances containing 90 % of particles are used. In our case beam emittances containing almost 100 % of particles are used in the design because of the relatively low value of the transverse and the longitudinal acceptance, which is well known for coupled cavity linacs (CCL). Therefore the accelerating and focusing structure of the CCL is designed in order to avoid coupling of the transverse and longitudinal motion as well as non-linear motion. The choice of the harmonic number of the rf system ($\times 4$) of the CCL depends mainly on the longitudinal emittance that can be achieved at the output of the Linac III. The availability of the rf-components of course is a second issue.

In order to determine the emittance from the proton linac precisely, the existing diagnostics equipment in the beam transport line has been used to measure the momentum spread. The harp monitors only provide an rms values which is calculated by fitting a Gaussian curve to the

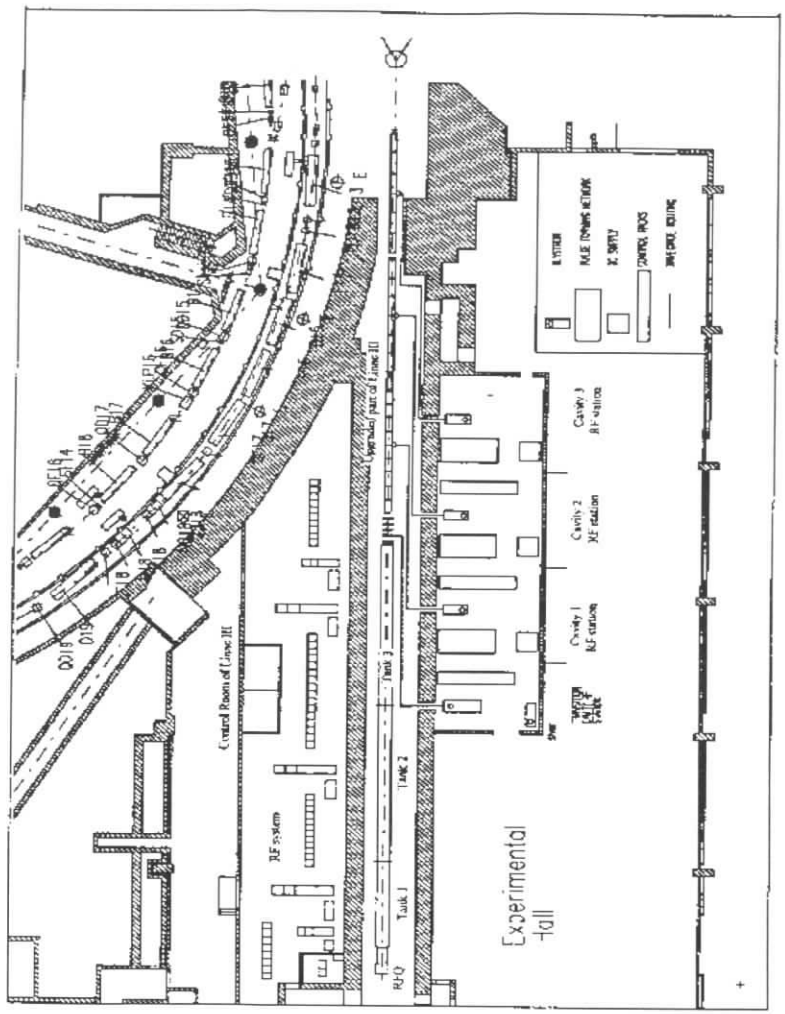

69

Figure 42: Sketch of the present set-up of the H^- linac and the beam transport line into the DESY III synchrotron.

measured data. A more precise measurement will be possible as soon as the new bunch shape and bunch length and velocity monitors are installed in the linac. From the data available and the tests done with off energy beams be dephasing the debuncher cavity at the end of the linac, it can be concluded that $2.5\times\sigma_p$ contains more than 99 % percent of the transmitted particles.

longitudinal emittance data		
long. emittance		ϵ_{eff} / deg×%
rms		1.55
90 %		4.48
Full		9.68
transverse emittance data		
trans. emittance	$\epsilon_x/\pi \cdot mm \cdot mrad$	$\epsilon_y/\pi \cdot mm \cdot mrad$
	2.06	1.81
halo studies $\epsilon_{x,y}$		
rms	2.1	1.8
90 %	9.6	4.1
≈ 100 %	33	29

Table 7: Longitudinal, vertical and horizontal emittance of the 50 MeV beam from the present LINAC III. These values are used for further studies of the upgraded part of the linac.

The fully reconstructed values which are the bases for further beam dynamics simulations are presented in table 7. Similar measurements have been performed for the transverse phase space. Again, in order to increase the spatial resolution on the harp monitors, the beam position has been swept over the wires of the harps. In addition, to measure the beam halo with better resolution, the beam has been focused at the position of the harp. For the transverse phase space, $4\times\sigma$ can be accepted as a maximum beam size which contains more than 99 % of the particles.

8.3 General Criteria for the Beam Dynamics

The beam dynamics in the linac is strongly related to the choice of the accelerating structure. Generally the energy range between 50 MeV to 100 MeV has been covered by Drift Tube Linacs (DTL). Recent studies in Los Alamos as well as in MRTI (Moscow) lead to the development of more efficient rf-structures to be used for acceleration above 100 MeV/c. This type of structure is based on the Coupled Cavity Structures (CCS). In contrast to drift tube linacs, where focusing can only be achieved by using FODO cells with the focusing lenses inside the large diameter drift tubes, the CCS allows to install the magnets outside of the rf cavities. Especially at a multiple of the present LINAC III frequency fabrication becomes easier, the shunt impedance can be significantly increased and strong focusing can be applied between the cavities. A restriction is given by the ratio of the aperture to cavity diameter and the longitudinal emittance which can be achieved at the end of LINAC III in order to match the beam into the smaller phase acceptance of the CCL bucket. In the energy range to be considered in our case (above 50 MeV) there are no efficient operating accelerating structures other than DTL. However, recent studies carried out mainly at Los Alamos resulted in the development of accelerating structures for intermediate energies for light ions in the range of 20-100 MeV[2]. The structure is a combination of the CCS and the DTL - CCDTL (coupled cavity drift tube linac). The data measured so far with the 50 MeV beam and preliminary studies of the beam dynamics show that even for a 50 MeV beam the operating frequency of the CCDTL can be as high as four times the multiple of the DTL frequency. The use of 810 MHz structures is in favor of high accelerating gradients, first of all, due to the well known Kilpatrick law. The choice of the frequency for the upgraded part of the linac has been done also taking into account the availability of 810 MHz klystrons. These klystrons are available, for example, from Litton with minor modifications from the 805 MHz klystrons which have been developed for the Fermi lab linac upgrade [3]. Concerning the beam dynamics, the bucket area reduction is significant for the transition energy of 50 MeV and the problem of proper matching with the acceptance of the upgraded part must be investigated carefully. In contrast to high intensity, high duty cycle linacs, as for example the Moscow Meson Factory, a number of arguments are in favor of the highest possible frequency:

- high accelerating gradients leading to a large vertical size of the separatrix and larger acceptance.
- almost no restrictions for maximum beam loss which can occur due to the reduction of the bucket phase width, other than the intensity required at DESY III.

Providing these high accelerating gradients by using the fourth harmonics on the other hand results in some disadvantages:

- Smaller longitudinal acceptance with respect to the DTL one.
- High accelerating gradients cause coupling of longitudinal and transverse motion in combination with transverse emittance growth.

These effects are more suppressed if the transition energy between the DTL and CCL is low. For all operating two-frequency accelerators (LAMPF, Fermilab, INR (Moscow)) the transition energy is close to 100 MeV which is essentially higher than in case of the proposed

LINAC III upgrade. Therefore the design of the CCL is strongly dependent on the available beam parameters.

Both transverse and longitudinal motion of the particles require a transition region (TR) at the output of the present DTL. Here, the longitudinal emittance has to be matched in order to decrease beam phase spread. In addition beam matching in the transverse phase planes has to be provided, because the periodic length of the focusing structure from $2\times\beta\lambda_0$ to $4\times\beta\lambda_0$ has to be changed, with λ_0 being the wavelength of the DTL operating frequency.Beam diagnostics and steering will be provided at the TR as well.

A number of aspects are carefully investigated for the choice of the accelerating and focusing structure. Following the development of the CCDTL structure, the decision was made to base the upgraded part of the linac on a combination of the CCDTL structure and the more conventional CCL structure. The accelerating cavity consists of $\approx$100 accelerating gaps both for the CCDTL and CCL. To provide proper beam focusing the number of the accelerating gaps per focusing period has to be chosen carefully. Special attention has been given to the choice of inter-section lengths. [1] It is obvious that this length must be as small as possible from the point of view of longitudinal beam motion. In practice nevertheless the length is mainly determined by the installation of focusing lenses, steering magnets as well as beam instrumentation. For operating linacs based on the CCS this space is an odd multiple of $\beta\lambda_0/2$ and a minimum length of $\beta\lambda_0/2$ has been realized for example in the Fermilab linac upgrade. In the energy range of 50-100 MeV this length is not sufficient in order to fit the equipment mentioned before and therefore we decided to choose an inter-section length for the CCDTL cavities equal to $2\beta\lambda_0$. For the CCL this distance is $3\beta\lambda_0/2$.

The considerations presented here resulted in a linac design with 10 accelerating sections and 9 coupling bridges in the CCDTL and 6 accelerating sections and 5 bridges in the CCL. Using the available length of 33 m three accelerating cavities (tanks) can be installed in the beam line. Each cavity is powered by a separate klystron. One CCDTL cavity allows to achieve an energy of 90 MeV and the other two cavities, which are based on the CCS, accelerate the beam up to 160 MeV. The design of the CCS has been made assuming that each accelerating section consists of 16 cells.

For the focusing structure a FODO lattice has been designed. Although it is well known that the FDO structure in the high energy part of the linacs has some advantage from the point of view of transverse beam dynamics, we reject this version. Using the doublet requires longer drift space between the sections which results in a reduction of the longitudinal acceptance. In addition the FDO structure requires a two times higher magnetic field. For our application the FODO structure seems the only solution due to transition from 202.5 to 810 MHz at a comparatively low beam energy.

[1] For the study we assume as well that a cavity consists of accelerating sections coupled by rf bridges, which has some impact on the geometry.

8.4 Accelerating structure

8.4.1 Possibilities for the Accelerating Structure

The choice of the accelerating structure strongly depends on particular requirements of the linac. We are interested in maximum energy gain with the limited space available. The maximum gradient depends on tolerable maximum electric field at the structure surface which is determined by the sparking rate and the reliability of linac operation, assuming that a given fraction of beam pulse will fail due to breakdown. Based on research work [3], performed in FNAL, and strongly referring to the successful experience [4], we have limited the following considerations to a maximum value of the electric field on the surface $E_s max = 1.35\, E_k$, where E_k / [MV/m] is the empirical Kilpatrick sparking limit:

$$f = 1.643 \cdot E_k^2 \cdot exp(-8.5/E) \qquad (8)$$

where f is the operating frequency in MHz. For a frequency of 810.24 MHz the Kilpatrick limit E_k is 26.1 MV/m. With such a high frequency, focusing lenses can not be mounted into the accelerating structure and multi-section design of an accelerating system with focusing elements placed between sections must be considered. Here two main options - a Drift Tube Linac (DTL) structure and a Coupled Cell Structure (CCS) has been considered. The DTL structure was considered in a Bridge Coupled DTL (BCDTL) version [5] with the accelerating cavity consisting of several short sections and each section has 6 accelerating gaps. A general review of CCS has been done, for example, in the [6]. All Coupled Cavity Structures (compare figure 43), - the Side Coupled Structure (SCS), the Disk And Washer (DAW) structure, the Annular-ring Coupled Structure (ACS) and the On-axis Coupled Structure (OCS), have practically the same values for the effective shunt impedance ZT^2. Also for the range of particle velocities between $0.3 \leq \beta \leq 0.55$, similar properties with respect to the maximum electric field at the surface E_{max} can be expected and all of them operate with standing wave field in so-called $\pi/2$ mode. These structures mainly differ in the value of the coupling constant and geometric design. It is well known, that for protons the energy range of 50 to 200 MeV is the called intermediate region for accelerating structures. The rf efficiency of the DTL structure decreases dramatically beyond the energy of 100 MeV. All the details of the DTL study can be found in ref. [7]. For several reasons, the option of using a DTL for particle velocities of $\beta \leq 0.43$ was rejected. On the other hand, the rf efficiency and using a high gradient in a CCS are favorable for energies larger than 100 MeV but they are quite inefficient at low energies. An interesting proposal has been made recently at Los Alamos [2]. To improve the parameters of a CCS in the low energy region, additional drift tubes have been introduced into the accelerating cells. With this geometry a combination of the high efficiency like in a DTL structure at low β (compare fig. 44) with the mode stability properties of the CCSs is possible.

The CCS option has been considered in more details for three type of CCSs, taking into account that for the low energy range of 50 - 90 MeV an intermediate drift tube will be introduced in the cells. Practically there is no difference in the rf parameters between the SCS and the ACS, but the SCS is more developed and investigated. This type of structure is used in LAMPF, at FNAL for the linac upgrade, in the SSCL linac and in many linacs aiming for industrial and medical applications. The outstanding feature of the DAW structure on the other hand are the large coupling constant and high vacuum conductivity [8]. This structure is used at the INR meson facility linac, in linear accelerating systems for TRISTAN, KEK [9] and in a linac for the SIBERIA synchrotron light source [10]. The most important features of CCSs

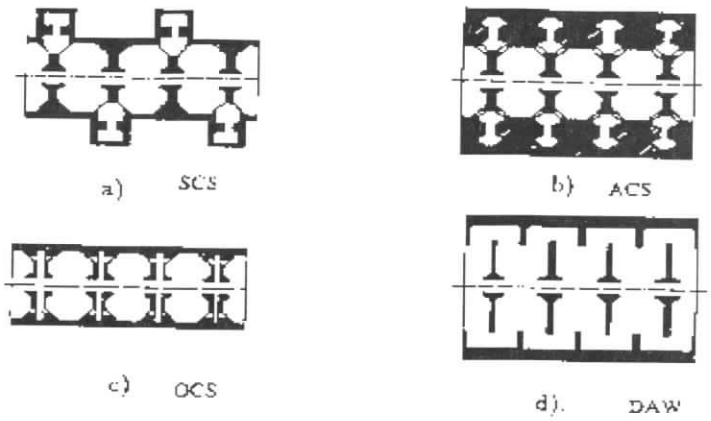

Figure 43: $\pi/2$-mode standing wave Coupled Cavity Cell Structures (CCS). a) - Side-Coupled Structure (SCS), b) - Annular Coupled Structure (ACS), c) - On-axis Coupled Structure (OCS), d) - Disk And Washer structure (DAW).

Structure	Coupling constant	Diameter of the structure (total, with coupling cells)	Remarks	Shunt impedance in the range 50-90 MeV
SCS	(5-7)%	550 mm	Tolerable vacuum conductivity	low
SCSDTL	(1.3- 1.7)%	550 mm	Low coupling constant	satisfactory
DAW	40%	550 mm	High vacuum conductivity	low
DAWDTL	20%	550 mm	Lots of interfering modes	low
OCS	5%	270 mm	Simple design	low
OCSDTL	1.3%	270 mm		satisfactory

Table 8: Parameter study of Coupled Cavity structures for the LINAC III upgrade.

considered for the Linac III upgrade include: (1) mode spectrum without interfering modes in the vicinity of the operating mode, (2)a large value for the cell-to-cell coupling to ensure phase and amplitude stability in long rf-structures with many cells, (3) mechanical properties which allow simple fabrication, (4) simple tuning procedures and an acceptable vacuum conductivity. Table 8 presents a summary of the results. From table 8 one can see that the On-axis Coupled Structure, which has the simplest mechanical design, satisfies most requirements, apart from the strong coupling which is needed because of the large number of cells per structure. Nevertheless, the OCS has the highest potential to increase the coupling constant, because the shunt

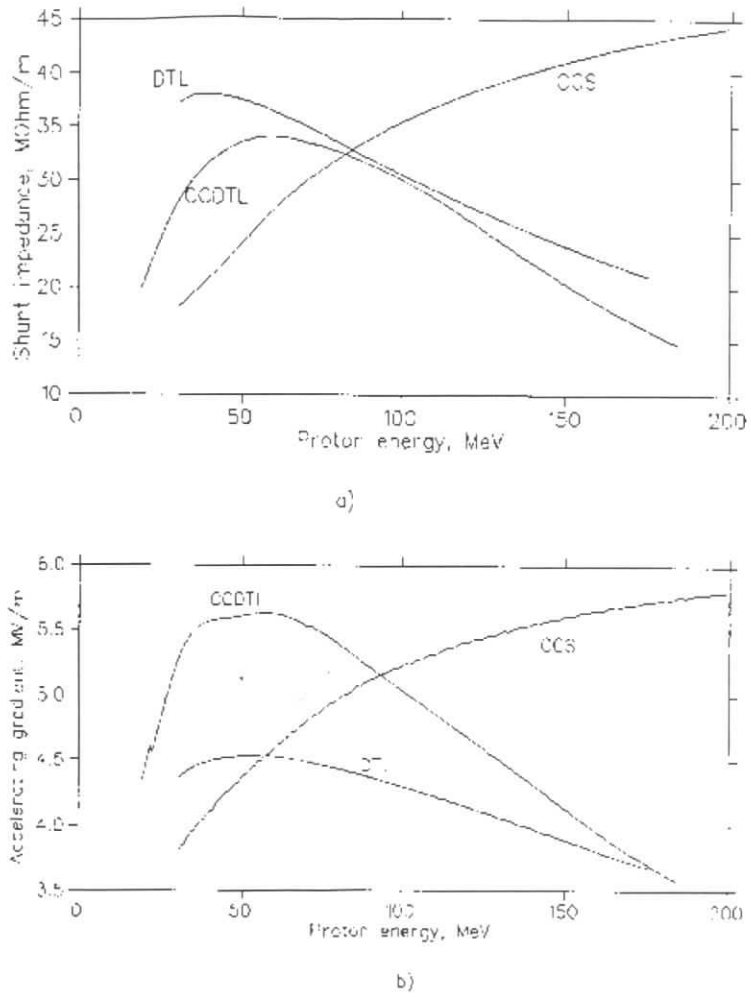

Figure 44: The calculated dependencies of the effective shunt impedance ZT^2 (a) and the corresponding accelerating gradient E_0T for the DTL, CCS and CCDTL structure.

impedance both for the OCS and OCSDTL is a weak function of the coupling as compared to any other known CCS. Therefore the On-axis Coupled Structure is more flexible from this point of view. These reasons lead to the decision to investigate the OCS for the upgraded part of the LINAC III .

8.4.2 Optimization of the Accelerating Structure

The On-axis Coupled Structure has been used mainly for electron linacs at operating frequencies between 1000 - 3000 MHz and comparatively large heat load of a few kW per meter. For a low repetition rate ($\approx$ 60 W/m) of 1 Hz as being used for the LINAC III we do not need internal cooling of accelerating cells. The thickness of the iris can therefore be optimized for maximum coupling and only mechanical constrains have to be considered. A sketch of the OCS and OCSDTL is presented in figure 45. The length of the coupling cell 2 lc is reduced taking into account limitations from the coupling slots and the excitation of the coupling cells. Introduction of the coupling slots reduces the frequency of the cell. For the short coupling cells this influence can be very strong (300 - 400 MHz) and the radius of the coupling cell becomes smaller than radius of the optimal position of the coupling slot. A second point is related to the excitation of the coupling cell. Sparking in the structure can in principle take place in both the accelerating and the coupling cell [11]. The accelerating cells are normally optimized for high gradient operation. In the steady-state regime the coupling cell in a CCSs is not excited at all (or excited at a very low level to provide power flux along the structure for compensation of rf losses in structure walls and for beam acceleration). Nevertheless, significant excitation of coupling cells takes place during transients and may lead to sparking. The maximum electric field value in the coupling cell during such a transient is proportional to the normalized value of $E_{c,max}/\sqrt{(W_c)}$, where $E_{c,max}$ is the maximum electric field on the surface for a given value of the stored energy W_c. In the OCS structure $E_{c,max}/\sqrt{(W_c)}$ is large at two points, at the lower edge of the coupling slot and near the bore hole where the edges have to be rounded as shown in the figure. For both reasons, we have chosen $2\times lc = 7$ mm for the OCS part and $2\times lc = 6$ mm for the OCSDTL, keeping at least a reserve of a factor of two in comparison with ratio of $E_{c,max}/\sqrt{(W_c)}$ for the coupling cell in the FNAL SCS design. This has been verified based on 3 D calculations, using MAFIA. The total thickness is $2\times t+2\times lc = 13$ mm and larger than 7.5 mm web thickness for SCS FNAL design, leading to a reduction in ZT^2 of 10 %. After preliminary optimization the shape of the accelerating cells (Figure 45) has been optimized with a 2 D approximation in more detail for both the OCS and the OCSDTL options. The inside diameter of the cell changes from section to section to compensate for the increasing β, which varies from $0.3 \leq 0.4$ for the OCSDTL and from $0.4 \leq 0.52$ for the OCS.

In order to estimate the required rf-power needed for the cavities, reduced values calculated from a 2 D model have been used. The total reduction of ZT^2 of 17 % for the OCS is given by: 5 % for surface imperfection, 5 % for rf losses in the coupling bridges and 7 % reduction due to coupling slots) and by 25 % (5 % + 4 % + 7 % + 9 %) for the OCSDTL part (with additional 9 % due to rf losses on the stems of the drift tubes). In the OCSDTL part the drift tube is supported by a single stem. At the intermediate tube 6 W of the rf power is dissipated, assuming 1 Hz repetition rate and 35 % from total value of rf losses in the full cell. To simplify the temperature control system and to reduce the rf losses in the stems, we have chosen a water cooled stem with 1.2 cm diameter. The coupling slots have been optimized using the 3 D MAFIA code (Figure 46 and 47). There are two coupling slots at each wall between an

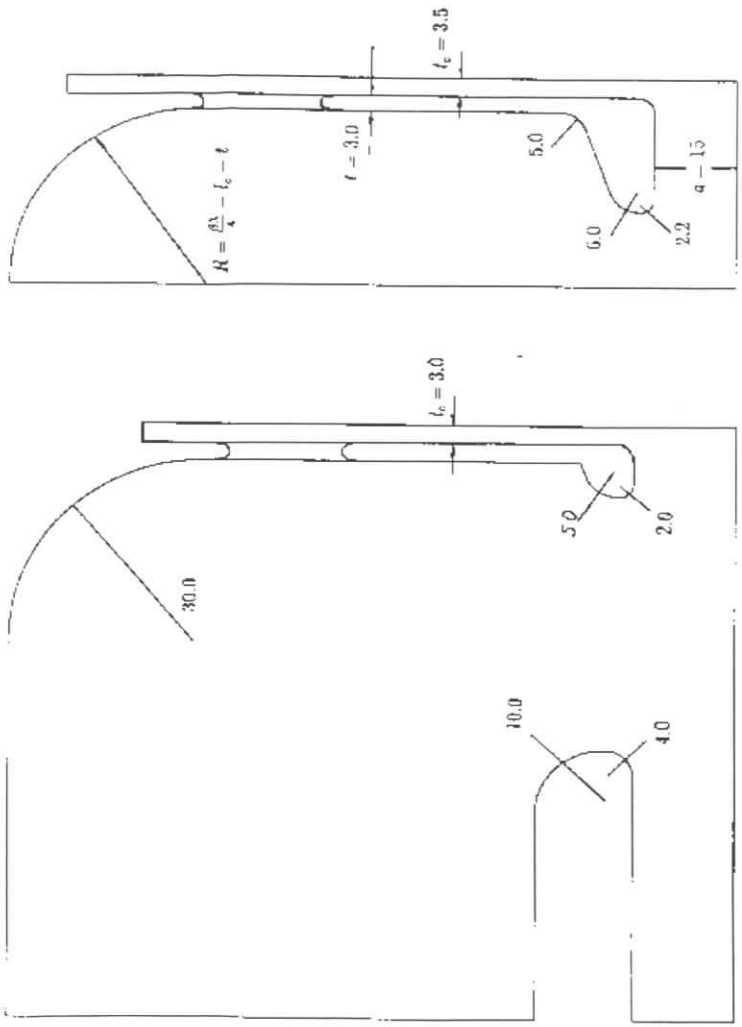

Figure 45: The optimized shape of the cells for the OCDTL structure and the OCS structure is shown. The final parameters od the geometry are given in mm.

accelerating and a coupling cell. The reduction in shunt impedance due to the comparatively large coupling slot is 5 to 7 % for the OCS and 6 to 7 % for the OCSDTL.

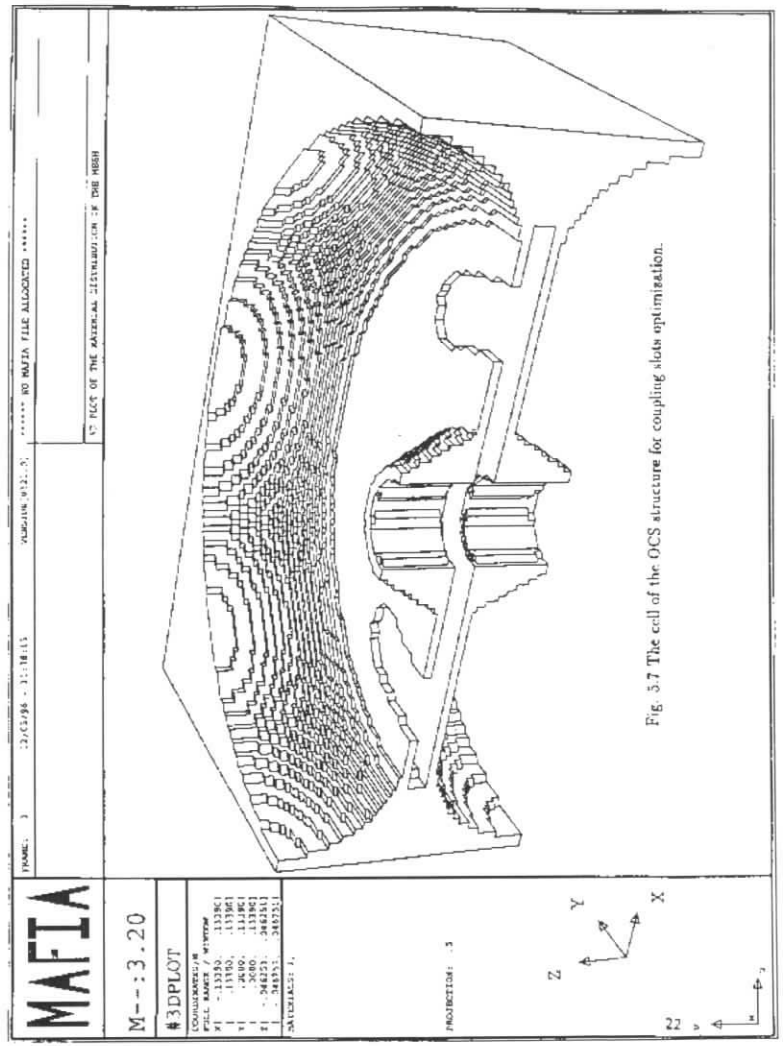

Fig. 3.7 The cell of the OCS structure for coupling slots optimisation.

Figure 46: The geometry of the cell of the OCS structure with the coupling slots in a 3 D MAFIA model.

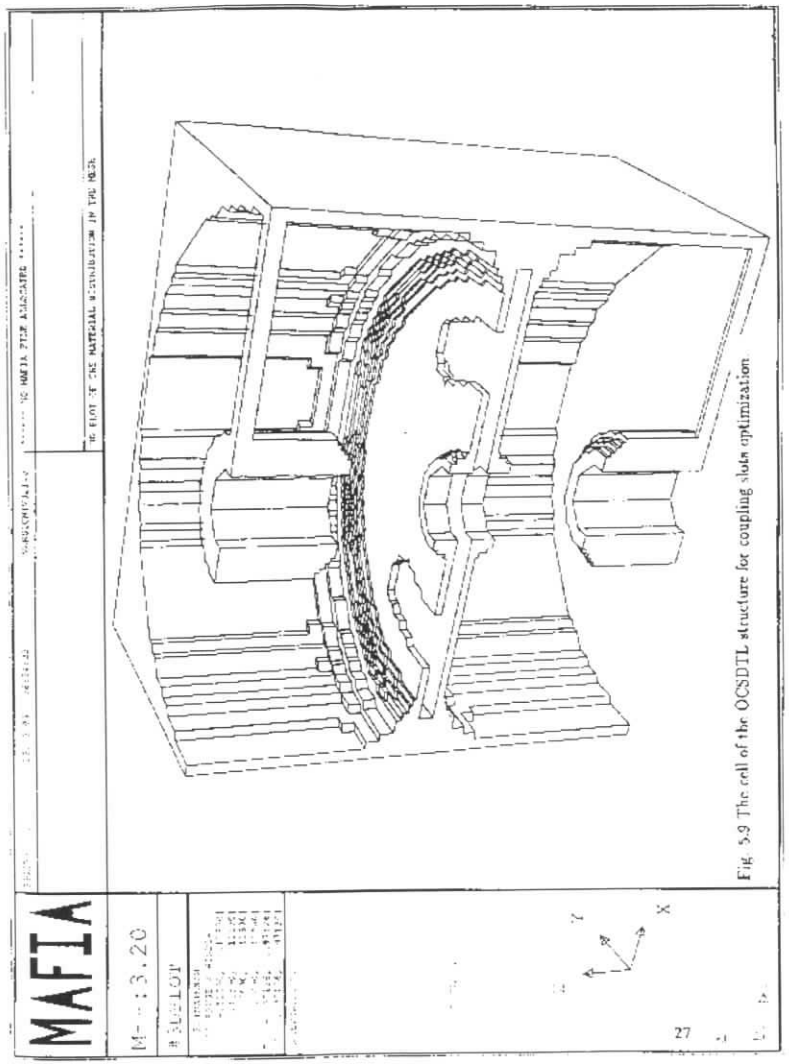

Figure 47: The geometry of the cell of the OCSDTL structure with the coupling slots in a 3 D MAFIA model.

8.4.3 Design of Coupling Bridges

Rectangular bridges operating in the TE_{11n} mode are foreseen to couple the accelerating sections installed in one cavity. This type of bridges was proposed for the accelerating structures of high energy proton linacs, tested at high rf power levels both with DAW and ACS structures [8] and successfully operated in the main part of the INR linac. The original design idea (compare 48) of a TE_{11n} bridge is to provide the space required for diagnostics equipment and can provide both π and $2 \cdot \pi$ phase shift between accelerating sections. The proposed bridges are made from standard rectangular waveguide WR975 and will have a total length of $\approx 2\lambda = 55.6$ cm for the first cavity ($2\beta\lambda$ space between sections, 2π phase shift, TE112 operating mode) and $3\lambda/2 = 83.4$ cm for the second and third cavity ($3\beta\lambda/2$ space between sections, π phase shift, TE113 operating mode). Here $\lambda = 55.6$ cm is the wavelength in a WR975 waveguide at the design operating frequency.

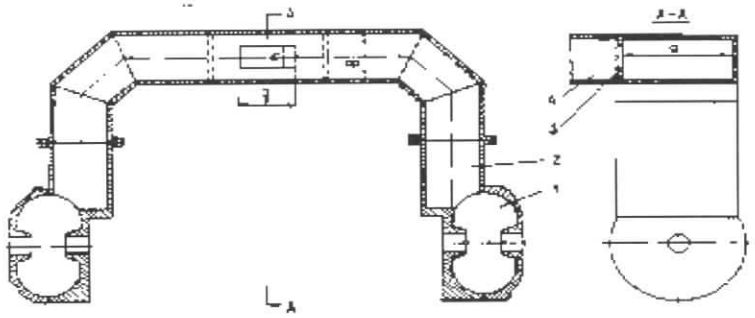

Figure 48: The rectangular bridge with a TE_{10n} operating mode. 1) - the accelerating cell, 2) - the bridge, 3) - matching iris, 4) - rf waveguide

The coupling bridge is attached directly to an accelerating cell and may be considered as an enlarged coupling cell. The additional rf power losses in the bridge is small and does not exceed 3- 5 % compared to the rf power loss in the accelerating sections. The power is fed from the klystron through the middle of on bridge into the cavities. For the tuning of the bridges the plungers which are required are similar to the ones described in [12]. Each bridge coupler is equipped with two plungers, placed symmetrically with respect to the middle of the bridge.

8.4.4 Accelerating Structure Tuning

The tuning of the accelerating cavity consisting of a number of sections connected by the bridges is divided into two more or less independent procedures: first the tuning of the single section and then the tuning of the cavity as a whole. The section tuning procedure involves setting the following values of the parameters: During the tuning procedure, the accelerating mode frequency has to be shifted to the design value under well controlled environmental conditions. Then the coupling mode frequency and the accelerating mode frequency have to tuned to the

same value. Simultaneously the field flatness should be approximately 3 %. The complete method of tuning the section, the cavity and the cavity with the bridges as well as the results are described in [13, 14, 15] in more detail. Many of the methods proposed here, have been developed and tested for both the sections and the multi-section cavities during the construction and installation of the INR linac.

Parameter	Cavity 1	Cavity 2	Cavity 3
Initial kinetic energy	50 MeV	85.412 MeV	119.86 MeV
Final kinetic energy	85.412 MeV	119.86 MeV	159.75 MeV
Total length	10.630 m	9.112 m	10.084 m
Frequency	810.24 MHz	810.24 MHz	810.24 MHz
Repetition rate	1 Hz	1 Hz	1 Hz
Pulse length	30 μs	30 μs	30 μs
Beam pulse current	20 mA	20 mA	20 mA
Synchronous phase	-35°	-35°	-35°
Number of sections	10	6	6
Number of cells per section	4	16	16
Type of structure	OCSDTL	OCS	OCS
Transverse focusing structure	FODO	FODO	FODO
Intersection drift	$2\beta\lambda$	$3/2\beta\lambda$	$3/2\beta\lambda$
Section length	$6\beta\lambda$l	$8\beta\lambda$l	$8\beta\lambda$l
Length of focusing period	$16\beta\lambda$	$19\beta\lambda$	$19\beta\lambda$
Cavity bore radius	1.5 cm	1.5 cm	1.5 cm
Power consumption	9 MW	8.5 MW	9.0 MW
copper loss	8.288 MW	7.816 MW	8.196 MW
beam power	0.708 MW	0.689 MW	0.798 MW

Table 9: Main parameters of the upgraded linac.

8.4.5 The Beam Dynamics Study

The accelerating structure geometry has been generated using the functions of the effective accelerating gradient E_0T, the shunt impedance Z_{eff} and the gap ratio α_g with respect to the relative beam velocity β as being obtained from the rf structure design calculations. The properties of the focusing structure have been compared for two different schemes: FODO and FDO. In Figure 49 a minimum for the maximum value of the transverse Courant-Snyder function β_{tr}, the transverse phase advances Φ_{tr} per focusing period and the required quadrupole gradients G are plotted versus the number of accelerating cells per section. The calculation have been done for a focusing period at the beginning of the upgraded part of the linac.

8.4.6 Segmentation of the Structure

Using the functions $E_0T(\beta)$, Z_{eff} (b), $\alpha_g(b)$ for the CCDTL and the OAS and taking into account the rf power consumption as well, the structure was divided into three cavities. A list of main parameters for each cavity is given in the table 9.

Due to the different transverse periodicity of the focusing structure in cavity 1 ($16\beta\lambda$) and cavity 2 ($19\beta\lambda$), transverse matching is necessary between these two cavities. The matching can be provided with the help of the four last quadrupole lenses of cavity 1.

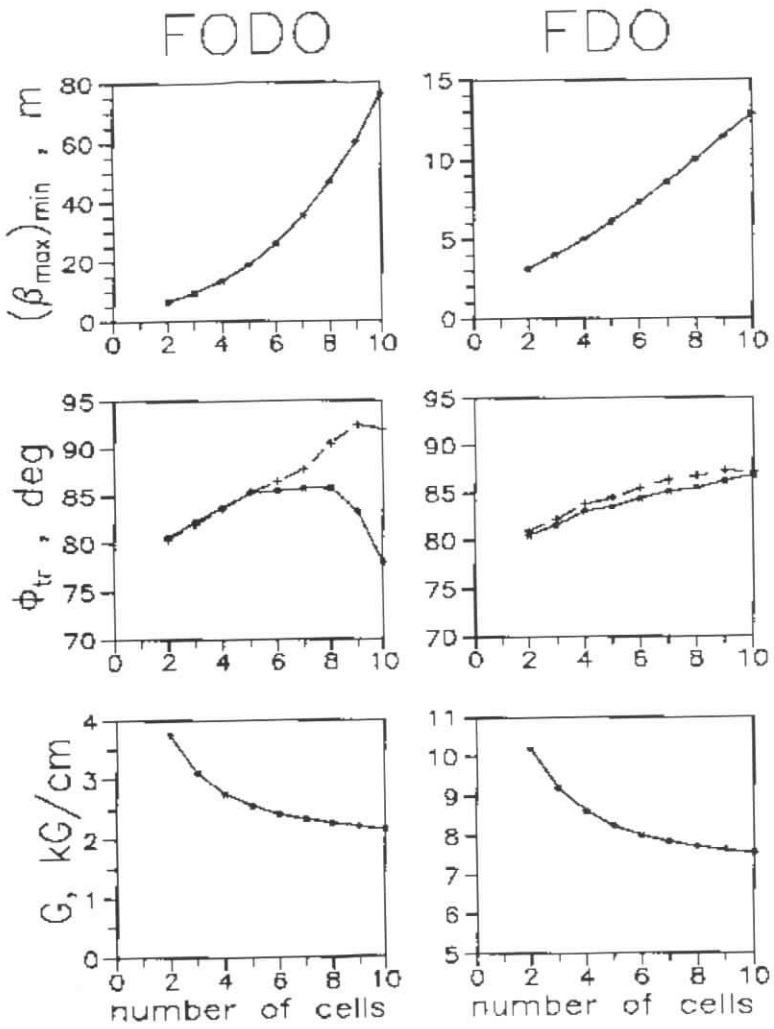

Figure 49: Comparison of FODO and FDO focusing structures.

Buncher parameters:	
number of cells	1
cell type	OCSDTL
effective field E_0T	4.6 MV/m
gap ratio α_g	0.3305
frequency	810.24 MHz
synchronous phase	- 90°
peak power	140.1 kW
drift length	2.335 m
Number of quads	4
Total transition region length	2.729 m

Table 10: Main parameters of the transition region.

8.4.7 Transition region

The main component in the transition region (TR) is a buncher cavity [16] followed by a drift space in order to reduce the phase spread of the 202.56 MHz bunches from ±13° to ±4° as it is required for the matching conditions at the entrance of the upgraded linac. The TR must contain at least four quadrupoles to match the transverse phase space parameters. The buncher length and its electric field strength are determined from the bunch length and longitudinal emittance of the 50 MeV beam. These values have been taken from experimental data (see table 7, first row). The general parameters of the transition region and the elements are listed in the table 10.

The buncher rf-power supply must have some reserve for the matching of unusual beam parameters. In our proposal the rf field can be increased approximately by 20 % which requires ≈200 kW peak power. In the table 51 the general beam matching specifications are presented.The longitudinal dynamics design of the transition region has been performed using the 90 % emittances in the 2-dimensional phase space ($\Delta\phi - \Delta W/W$). However the TR can transport 100 % of the incoming beam particles.

8.4.8 Generation of the Initial Particle Distribution

The present LINAC III beam emittance values found from experiments are presented in the first paragraph of this chapter. If we assume that real beam in the 6-dimensional phase space has an ellipsoidal structure, it is possible to reproduce this distribution using a 6- dimensional uniform distribution. Practically, for beams without intra-beam interaction two or three 6-dimensional uniform distributions will be enough to achieve a sufficiently smoothed 2-dimensional projected phase space. According to the above mentioned assumptions a model of the initial particle distribution has been created. The projections of the 6-dimensional distribution have the same value as compared to the two dimensional emittances mentioned which are listed in table reftab3n1. For further studies particle distributions consisting of the 90 % emittance is called a *main distribution*, whereas the particles outside of this ellipsoid are part of the *background distribution*. The total number of particles in the model distribution is ≈25.000.

Kinetic energy	50 MeV
Pulse current	20 mA
Longitudinal emittance (90 %) ϵ_L	$20.46\pi \times^\circ \times(810MHz) \times \%(\Delta W/W)$
Transverse emittance (90 %, unnorm.) ϵ_x	$9.6\pi \times mm \times mrad$
ϵ_y	$4.1\pi \times mm \times mrad$
Drift tube linac	
frequency	202.56 MHz
effective gradient E_0T (exit)	1.57 MV/m
equilibrium phase ϕ_s	-25°
FODO half-period (linac exit)	46.46 cm
aperture radius	1.5 cm
structure parameters	
β_x	1.692 m/rad
α_x	- 0.01
β_y	0.636 m/rad
α_y	0.00
Upgrade linac	
frequency	810.24 MHz
effective gradient E_0T (entrance)	5.526 MV/m
equilibrium phase ϕ_s	-35°
FODO half-period (entrance)	94.62 cm
aperture radius	1.5 cm
structure parameters (entrance)	
β_x	3.716 m/rad
α_x	3.946
β_y	0.809 m/rad
α_y	- 0.908

Table 11: The 50 MeV beam matching specifications.

		Normalized emittance growth factor			
		x - x'		y - y'	
	$\beta\gamma$	rms	90 %	rms	90 %
TR exit	0.33069	1.00	1.00	1.00	1.00
Exit of cavity 1	0.43616	1.13	1.17	1.17	1.17
Exit of linac	0.60769	1.17	1.20	1.22	1.22

Table 12: Beam performance at the Upgrade Linac.

Parameter	Error range
Average accelerating field over a section	±3 %
Non-uniform distribution of the accelerating field along a section	±3 %
Inter-section distance	±100 μm
Quadrupole gradient	±3 %
Quadrupole displacements: vertical and horizontal directions	±50 μm
longitudinal direction	±150 μm
Quadrupole axis tilt	±0.50°

Table 13: The types of errors included in the studies.

8.4.9 Beam Dynamics Simulation

In figure 50 and figure 52 the beam envelopes (x-plane is solid line, y-plane is dashed line), the relative velocity spread $\Delta\beta/\beta$ and the phase spread $\Delta\phi$ are presented along the linac structure for the main and the total (*main + background*) distributions respectively. In figure 51 and figure 53 the phase space portraits for the main and the total distribution at certain characteristic points along the linac are plotted. The simulation has been done for all 100 % particles including the beam halo and the beam loss is less than 0.04 %. In tablerefftab6n4 the beam emittance growth in the transverse phase planes is given. The main contribution to the beam emittance growth is caused by rf defocusing.

8.4.10 Accelerating Field Distortions and their Effect on Beam Parameters

The imperfections of the accelerating and focusing fields have some influence on the beam parameters. The beam dynamics has been simulated using a Monte Carlo technique for 1000 random seeds of possible deviations of linac parameters from the design values. The range of the deviations are shown in the table 13. The simulation results are shown in the Table 14, which shows that the tolerances given in the Table 13 can be achieved.

In this table the percentage of the particle loss, the emittance (90 % of particles) calculated from all random seeds for all three planes and the energy deviation of the bunch center $(\Delta W/W)c$ are listed. The subscript 0 corresponds to design values. Another source of accelerating field distortions in the long coupled cell structure is:1) a natural drop of the rf power

	Average values	The values obtained with 90 % probability
Particle loss, %	0.481	1.032
ϵ_x /ϵ_{x0} (90 %)	1.073	1.185
ϵ_y /ϵ_{y0} (90 %)	1.085	1.226
ϵ_L /ϵ_{L0} (90 %)	1.009	1.026
$(\Delta W/W)_c$, 10^{-3}	-0.176	3.819

Table 14: The results of the beam dynamics simulation.

along the long cavity containing large number of coupled cells and 2) transient beam loading and compensation. Under steady state condition a power drop along the cavity containing N cells produces accelerating field tilts which are given by [16]:

$$\frac{\Delta E}{E} = \frac{2N^2}{k^2 Q_a Q_c} \tag{9}$$

Where k is the coupling constant and Q_a and Q_c are the quality factors for the accelerating and coupling cells correspondingly. For the OCS the following ratio $Q_c \approx Q_a/4$ can be assumed. Therefore:

$$\frac{\Delta E}{E} = \frac{8N^2}{k^2 Q_a^2} \tag{10}$$

Using a MAFIA simulation a value of $Q_a \approx 2.110^3$ and $k = 0.15$ was calculated. From these values and the previous formulae we can conclude for the second and the third cavity of the linac, that the energy spread is:$\Delta E/E = 0.1\,\%$. This value is negligible for our application.

The transient beam loading causes electric field distortions on the cavity axis due to excitation of modes from the complete passband. The beam is turned on after the steady state condition of the accelerating field is achieved. In order to compensate the beam loading the generator power to resonator increases simultaneously with the beam pulse. During the transient the whole spectrum of the non-operating modes is excited while the beam loads the operating mode only. The total electric field distortion is determined as a complex sum of the electric fields of all excited modes. The total electric field on the axis and the distortions can be found analytically under the following assumptions [17]:

- for the beam loading compensation the generator power P_g is increased by the amount of power extracted from the beam P_b: $P_g = P_{g0} + P_b$
- a linear dispersion law in the range of 0 to π mode instead of sinusoidal law
- only consider a time scale larger than power propagation time along the cavity length L_c. The filling time is $\approx 1\,\mu$sec.

For the linac parameters we can obtain 2.7 % of maximum field distortion for 20 mA beam during the transient. A numerical simulation of the field distortion has been done on the base of a coupled oscillators model. The small field amplitude distortion from the cell to cell inside a section has been ignored and the average value of the field over the section has been calculated during the transient. This model shows 1.6 % for the distortion of the accelerating field amplitude. We expect that the filed distortion results in a small increase of the momentum spread for a very small part of the beam, but detailed studies of the beam dynamics are required.

Part	Section	E0T MV/m	β output	L_{sec} m	L_{dr} m	G kG/cm	P_{cu} kW	P_b kW
Transition region					0.200[1]			
	Buncher	4.6	0.31397	0.174	2.355	2.6158	140.1	-
						1.8620		
						2.2392		
						2.1529		
Cavity 1	1	5.526	0.31857	0.707	0.239	2.4800	757.7	64.03
	2	5.536	0.32765	0.727	0.246	2.4800	774.4	65.97
	3	5.538	0.33665	0.747	0.252	2.4800	793.3	67.81
	4	5.528	0.34555	0.767	0.259	2.4800	811.3	69.47
	5	5.501	0.35433	0.786	0.265	2.4800	827.4	70.90
	6	5.460	0.36297	0.806	0.272	2.4800	841.3	72.08
	7	5.428	0.37145	0.824	0.278	2.3949	858.4	73.33
	8	5.371	0.37978	0.843	0.284	2.2841	867.5	74.19
	9	5.310	0.38792	0.861	0.290	2.4000	875.4	74.92
	10	5.246	0.39588	0.879	0.296	2.2590	882.9	75.53
Cavity 2	1	5.344	0.40512	1.199	0.228	2.3700	1235	105.0
	2	5.400	0.41564	1.230	0.234	2.3700	1260	108.8
	3	5.458	0.42611	1.261	0.239	2.3700	1287	112.8
	4	5.524	0.43652	1.292	0.245	2.3700	1319	116.9
	5	5.574	0.44687	1.323	0.251	2.3700	1345	120.8
	6	5.622	0.45713	1.353	0.257	2.3700	1370	124.6
Cavity 3	1	5.491	0.46714	1.383	0.262	2.3700	1310	124.4
	2	5.521	0.48652	1.412	0.267	2.3700	1329	127.7
	3	5.566	0.48652	1.440	0.273	2.3700	1355	131.3
	4	5.603	0.49600	1.468	0.278	2.3700	1378	134.8
	5	5.631	0.50500	1.496	0.283	2.3700	1398	138.0
	6	5.675	0.51475	1.524	-	2.3700	1426	141.7

Table 15: Summary of parameters for the high energy part of the LINAC III .
(1) distance to the last quadrupole of the LINAC III .

8.4.11 Summary of Beam Dynamics Design

A detailed list of the parameters for the high energy part of the LINAC III above 50 MeV is presented in table 15.

In table 14 the following definitions are used: E_0T is the effective accelerating field; L_{sec} is the section length; L_{dr} is the drift space between the sections; G is the gradient of quadrupole located downstream of the section; P_{cu} is the power loss in the copper surface of the section; P_b is the power transmitted to the beam in the section. In order to keep the total power consumption in each cavity less than 9 MW the maximum possible electric field in the first and third cavity has been reduced by a factor of 0.984 and 0.967 respectively. The effective magnetic length for all quadrupoles is equal to 8.2 cm in the beam dynamics simulation. The

total number of quads is 26.

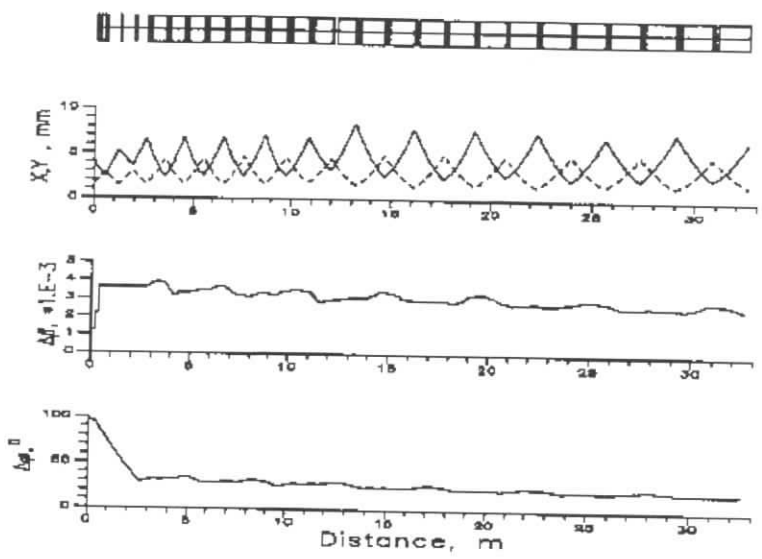

Figure 50: Beam envelopes along the linac (90 % emittance).

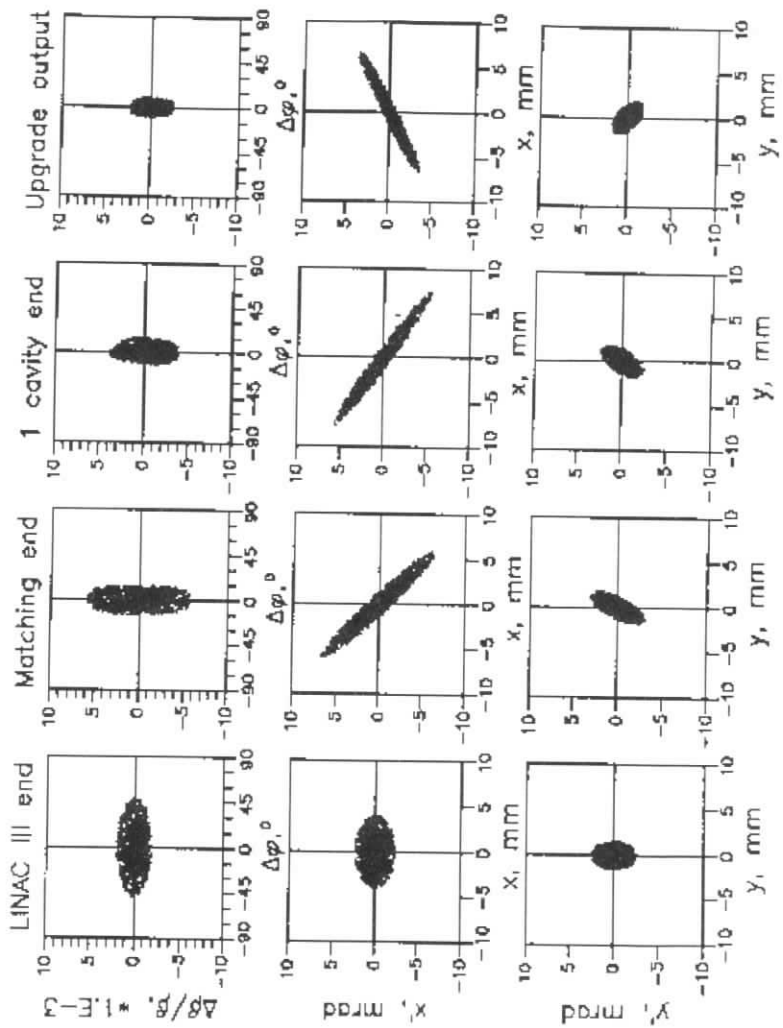

Figure 51: Beam Phase portraits (90 % emittance).

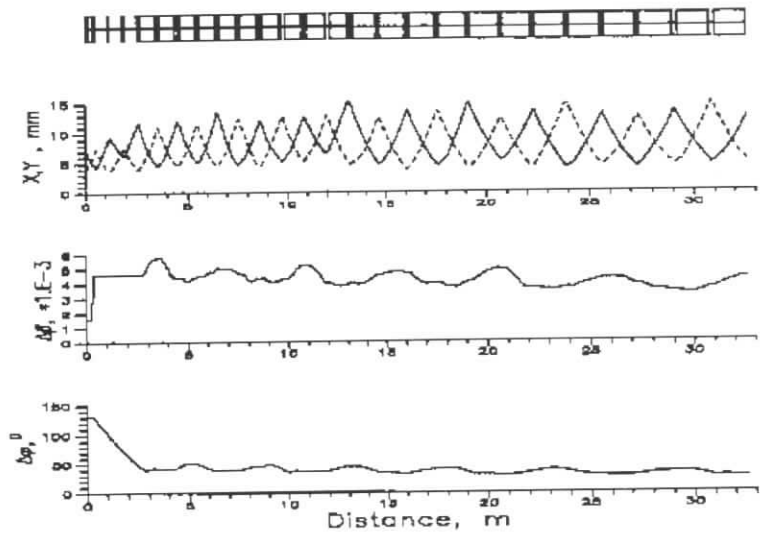

Figure 52: Beam envelopes along the linac (90 % emittance).

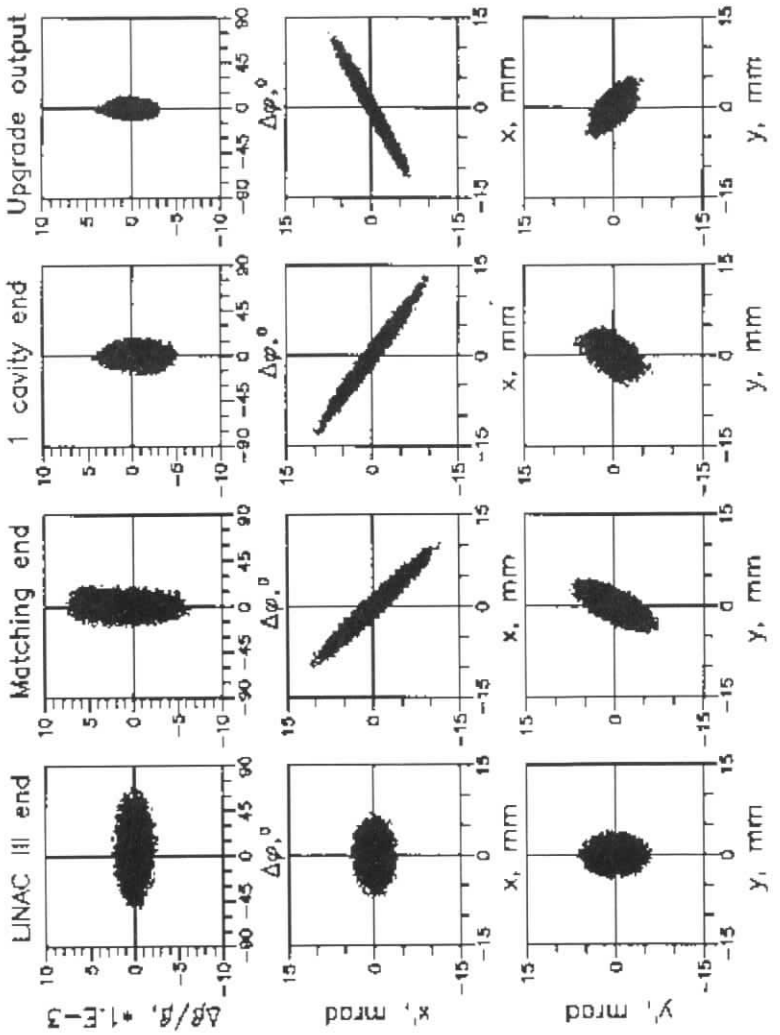

Figure 53: Beam envelopes along the linac (90 % emittance).

8.5 Radio Frequency Power System

8.5.1 Power Requirements

The 810 MHz Linac III upgrade high power rf system consists of three high power klystron and modulator systems. The copper loss and beam power for each of the three modules and the matching cavity are shown in table 15. Table 16 gives a more complete specification for the power requirements, which takes into account additional items (waveguide loss and reserve for feedback loop regulation). This adds up to 11.5 MW total peak power required for the present design. For example, a Litton L-5859 klystron specification together with the Linac III upgrade requirements are shown in Table 17. Since the peak power requirement for the Linac III upgrade is slightly below the nominal klystron rating, the Litton L-5859 klystron should be an adequate power tube. The RF power requirement for the transition section is only 200 kW which can be supplied by different today available tubes. The WR975 waveguide lines will

Typical power, accelerating 20 mA beam	9.8 MW
Waveguide run (WR 975), VSWR	0.65 MW
10 % for feedback loop regulation	1.05 MW

Table 16: Power specifications for the LINAC III upgrade program.

Parameter	Klystron specification	Linac requirements
Peak power output	12 MW	11.5 MW
Pulse length	125 msec	60 msec
Pulse repetition rate	15 Hz	1 Hz
Duty factor	0.1875 %	0.006 %
Average RF power	22.5 kW	0.69 kW
Efficiency	50	
Gain	50 db	
Voltage	170 kV	170 kV
Current	141 A	141 A
RF output	WR975 waveguide	

Table 17: L-5859 klystron specifications and linac requirements.

transport RF power from the klystron to the accelerator. A total length of the waveguide system for three RF stations is about 80 m. Waveguide lines include directional couplers and cavity vacuum windows. Careful design of the transmission line between the klystron and the cavity is necessary. Microwave windows should be placed at the minima of the VSWR in both the klystron and the coupler. The reflection during cavity field build-up should present a low impedance to the klystron output gap.

8.5.2 The RF Modulator

The Fermi lab RF modulator specifications along with the Linac III upgrade requirements are shown in Table 18. The main difference is the average power requirement which is approximately a factor of 30 lower, which decreases the DC power supply. The number of PFN (pulse forming network) sections can be reduced by a factor of two, due to the shorter RF pulse. The main

Parameter	Fermi lab modulator	Linac requirements
Peak power	24 MW	24 MW
Voltage	170 kV	170 kV
Current	141 A	141 A
Pulse repetition rate	15 Hz	1 Hz
Pulse length	125 μs	60 μs
Rise time	9 μs	7 μs
Fall time	18 μsec	12 μsec
Average power	50 kW	1.53 kW
Pulse flatness	$\pm$0.5 %	$\pm$0.5 %
Voltage regulation	$\pm$0.05 %	$\pm$0.05 %
DC power supply	9.0 kV	9.0 kV
DC average current	6.5 A	0.22 A
DC average power	58.5 kW	1.98 kW

Table 18: Modulator specifications and Linac requirement.

parameters calculated for the LINAC III upgrade are: 1) a load impedance of 1206 Ω; 2) a pulse transformer ratio of 20:1 and 3) a total capacitance of the PFN of 9.4 μF. The pulse transformer primary voltage is 9 kV, the charging voltage across the PFN capacitors is 18 kV and the primary current of pulse transformer is 2820 A. With L_P the primary inductance, T_{CH} the charging time of the PFN and ω the circuit resonance frequency the parameters for the charging circuit are given in table 19. The average charging current from the power supply is

I_{DC} / A	L_P / H	T_{CH} / ms	ω / 1/sec	R / Ω
2	194	135	23	225
4	48.6	68	46	110
6	21.6	45	69	75
8	12.2	34	92	56
10	7.8	27	115	45

Table 19: Calculated charging circuit parameters at different DC peak current.

0.18 A and the DC power consumption will only be 1.6 kW. The modulator consists of three main units: the PFN, the charging supply and the HV assembly, which includes the oil tank, the pulse transformer and the klystron. Figure 54 and 55 contain the schematics.

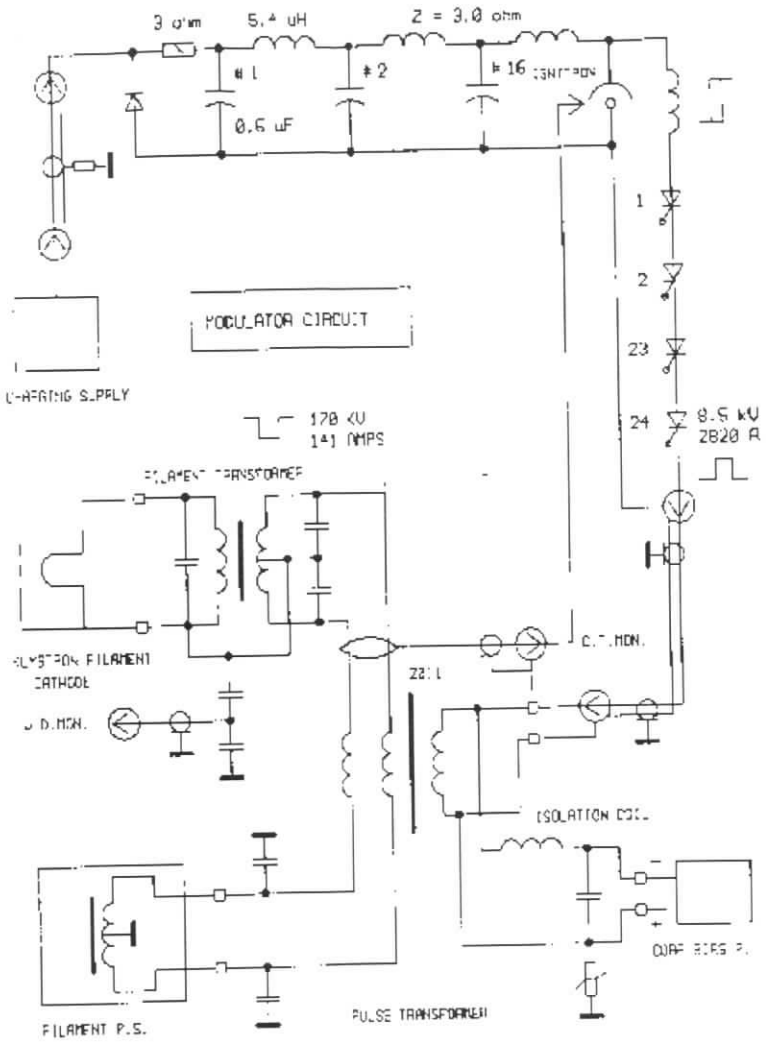

Figure 54: RF modulator circuit.

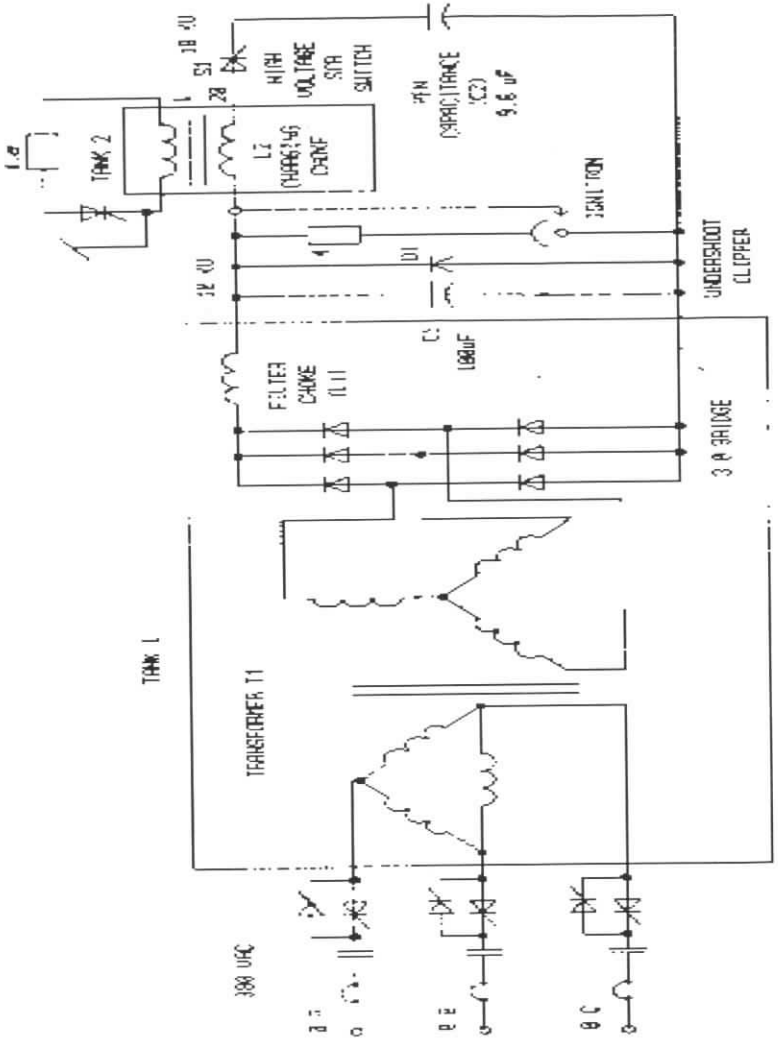

Figure 55: Simplified layout for the charging supply.

8.5.3 Low-Level RF System

The RF drive/distribution system consist of the 202.56 MHz master oscillator, a factor of four frequency multiplier, transistor preamplifiers and 810.24 MHz and 202.56 MHz reference lines. Special phase locking schemes and a motor driven mechanical, trombone type, phase shifter keeps the phase difference between RF signals in two reference lines constant. It provides a stable capture of the accelerated beam into the first 810.24 MHz accelerating tank. As mentioned above, the amplitude and phase of the accelerating fields within the cavities are regulated using a feedback control system. The system includes two feedback loops, one for the phase and another one for amplitude of cavity field. Both controlling loops use a feedback

signal from a small measuring loop probe placed in one of the accelerating section. The system is compatible to the one installed at the LINAC III already and is described in more in [18].

8.5.4 The Cooling System

Each klystron dissipates ≈6.1 kW of heat (5 kW for the solenoid, 1 kW collector and 0.1 kW klystron body), which is 18.3 kW in total for the three stations. A separate cooling system for each station will be used for individual control of the stations. The main components are the heat exchanger, the electronically controlled valve to mix the required water temperature, water flow meters and thermometers. The full amount of heat from the secondary of the heat exchanger flows into the primary water circuit and is removed by the main laboratory cooling circuit. The temperature of the cooling water can be changed within a range of 23 - 30 C°. A temperature stabilization system is introduced into the cooling system to feedback on the measured temperature of the cavities. A remote controlled valve will keep the temperature at the output of the secondary of the heat exchanger at 33 C° with an accuracy of ±1 C°. Apart from the fast mixing valve and a comparatively fast and flexible temperature regulation system, this part is very conventional.

Aperture radius	2 cm
Beam pipe inside radius	1.7 cm
Beam pipe outside radius	1.8 cm
Maximum transversal size	20 cm
Iron core length	7.0 cm
Effective magnetic length	8.2 cm
Field gradient	3.1 kG/cm
Field nonlinearity at radius 1.5 cm	0.1 %
Number of turns per pole	20
Half-Sine pulse current	250 A
Resistance per quad	65 mW
Inductance per quad	1.0 mH
Peak voltage	600 V
Stored energy	36 J
Duty factor	0.14 %
Pulse power	2000 W
Average power	2.8 W

Table 20: Magnetic field parameters of the quadrupole lens.

8.6 Focusing System and Magnets

The focusing of the H^- beam will be provided with magnetic quadrupoles which are placed in each drift interval between the accelerating sections as well as between the cavities. The total number of quadrupoles is 26. Four of them are installed in the 50 MeV matching region between the existing LINAC III and the new part. The quadrupoles are powered with pulsed power supplies. Two options for the repetition rate are foreseen - 1 Hz for tuning and commissioning and 0.25 Hz for injection into the DESY III synchrotron.

Quadrupoles Due to the restricted space between sections and cavities the quadrupoles are operated with a gradient of 3 kG/cm with an aperture radius of 4 cm. Comparable designs have been realized for Fermi lab Linac Upgrade project [3]. Due to the significantly smaller duty cycle the design for the LINAC III upgrade could be even more compact. The main parameters for the quadrupole are shown in Table 20.

Equipment imperfections, instabilities, alignment errors and geometrical displacements will excite coherent oscillations. Overall nine standard type corrector magnets are foreseen to correct the beam orbit. With a maximum energy of 170 MeV the required dipole field is 0.026 T for a magnetic length of 7.5 cm.

8.7 Beam Instrumentation

For the successful commissioning and operation of the machine it is very important to have a good, reliable beam diagnostics. A rather delicate study should be done especially in the transition region (TR). Good beam matching has to be performed at the entrance of the

upgraded part of the linac both in the transverse and the longitudinal phase space. New diagnostics for the upgraded linac will be arranged in the 2.6 m long transition region together with a buncher cavity and four regular quads, in the intersection drifts of the cavities and in the transfer line (TL) to the DESY III synchrotron (see Figure 56).

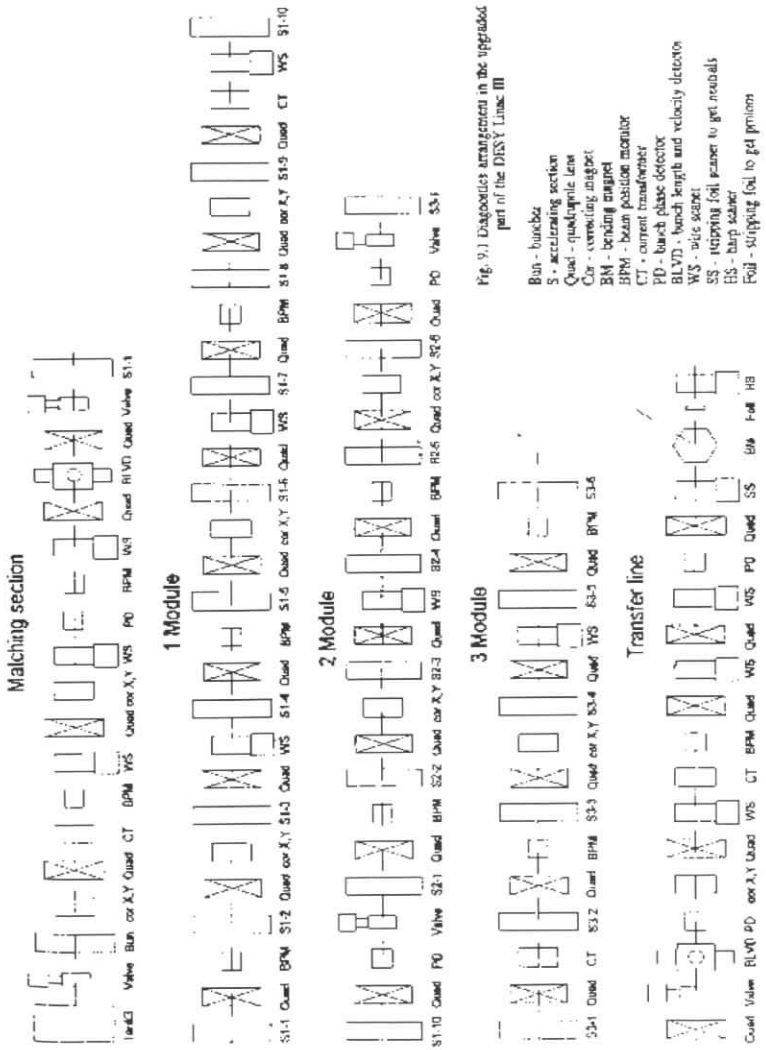

Figure 56: Diagnostics equipment in the upgraded part of the LINAC III .

N section	1-1	1-2	1-3	1-4	1-5	1-6	1-7	1-8	1-9	1-10	
L=2$\beta\lambda$/ mm	239	246	252	259	265	272	278	284	290	296	
L_{diag}/ mm	74	81	87	94	100	107	113	119	125	131	
N section	2-1	2-2	2-3	2-4	2-5	2-6	3-1	3-2	3-3	3-4	3-5
L=3$\beta\lambda$/2 / mm	228	234	239	245	251	257	262	267	273	278	283
L_{diag}/ mm	64	70	75	81	87	93	98	103	109	114	119

Table 21: The intersection drifts L and the possible length L_{diag} to be used for diagnostics equipment .

There will be 3 additional accelerating modules consisting of 10 and 2 times 6 sections. The intersection drifts of $2\beta\lambda$ are chosen for the first module and $2\beta\lambda/2$ for the second and the third module. The geometrical set-up leads to strict limitations for length of the diagnostics equipment along the beam line (see Table 21). The beam diagnostics equipment will serve for the following requirement:

- Beam current measurement;
- Beam center of mass position monitoring;
- Beam transverse position correction by means of steering magnets;
- Beam profile periodically observation along the linac in order to find out the quadrupole setting;
- Measurements aiming the transverse emittance evaluation;
- Measurement of the momentum spectrum at the linac output;
- Bunch width measurements and the longitudinal emittance restoration at the TR and TL;
- Beam-induced rf signals generation for the time-of-flight measurements.

8.7.1 Beam Diagnostics Equipment

Standard technology will be used for the beam position monitors, the wire scanners and the energy measurement. Overall nine BPM's are foreseen which are close to the nine correctors and allow to have approximately 4 corrections per 2π phase advance. The required resolution is $25\,\mu$m. The wire scanners could be similar to the harps installed right now in the LINAC III , although the resolution is not very good. Overall 11 wires are foreseen which are installed close to the waists in the horizontal or vertical plane. With the wires the transverse emittance can be determined.

A momentum spectrometer which is currently used for the 50 MeV beam provides very good momentum resolution: $\Delta p/p = 0.0526 \times \Delta x$, where $\Delta p/p$ is in units of % and Δx is in units of mm. In the beam line a H^- ions are scattered on a wire and the positive ions are detected on screen behind the bending magnet. It is desirable to raise spatial resolution of the harp

by adding wires or replacing the harp by wire scanners for precise detection of the momentum halo with the high energy beam.

In order to control the longitudinal emittance and matching, Beam Shape Monitors will be used [18]. In addition Bunch length and Velocity detectors will be installed, to determine the momentum of the particles [18]. This type of monitors has been successfully operated in many proton accelerators already and will be installed in the 50 MeV part of the LINAC III in 1996.

8.8 Vacuum System

Accelerating sections are combined in cavities using resonant bridge couplers. There are 10 accelerating sections, each having four resonant (accelerating + coupling) cells in the first cavity and 6 accelerating sections each having sixteen resonant (accelerating + coupling) cells in the second and third cavities 57. To decrease the number of titanium pumps a vacuum

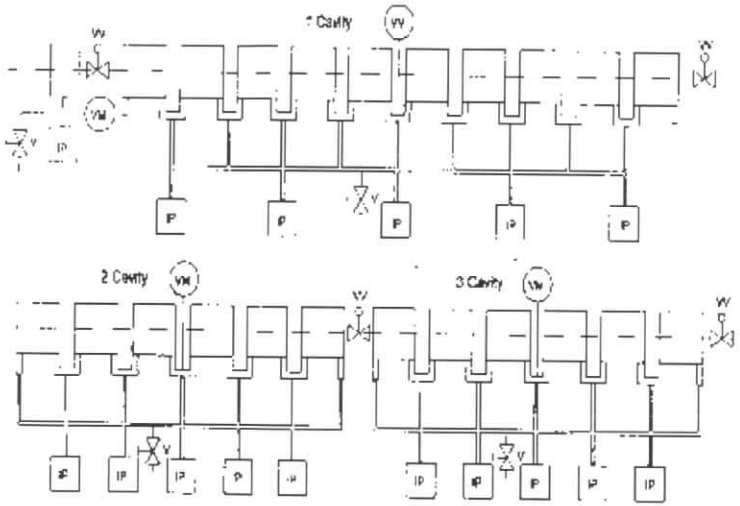

Figure 57: Vacuum system layout.

manifold will be used for each cavity. The vacuum manifold will be connected to the bridge couplers as well as to quarter wavelength shorts which have high vacuum conductivity. Five ion pumps are connected to each cavity plus one pump for the matching cavity. The manifold pipe diameter is 180 mm. The diameter of the pipes connected is 60 mm. Estimates for the vacuum conductivity of a single (accelerating + coupling) cell deliver a value 85 l/s. The effective pumping speed will therefore be ≈ 10.6 l/s. With the out gassing rate of a single cell of approximately $2.6 \cdot 10^{-7}$ l·torr/sec the calculated pressure is $2.5 \cdot 10^{-8}$ torr. The debuncher should operate at 202.54 MHz and allows to decrease the beam momentum spread approximately 10 times in order to fit to the ± 120 keV energy window of the synchrotron bucket.

8.9

The l
matcl
energ
before
after
dispe
debur
10 tir
prelin
must

t and
large
space
talled
ı-zero
The
pread
n our
which

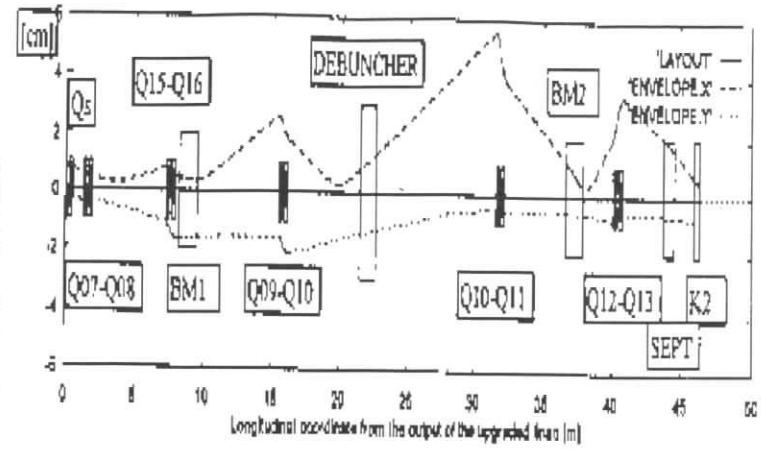

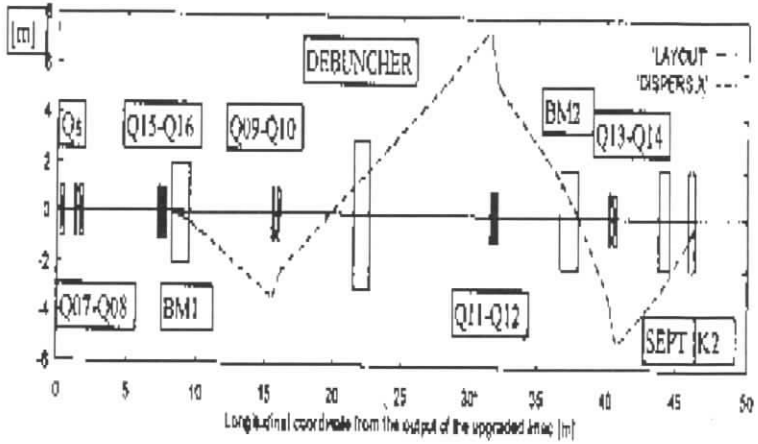

Figure 58: Beam envelopes and linear dispersion along the transport line to the synchrotron.

References

[1] *Commissioning/Operation of the Moscow Meson Factory Linac*, S.K. Esin, L.V. Kravchuk, V.A. Matveev, P.N. Ostromov and V.L. Serov, Proceedings of the 1994 Linac conference, August 1994, Tsukuba, Japan.

[2] J. H. Billen et al. A New rf Structure for Intermediate-Velocity Particles. Proc. of the 1994 Linac Conf., p. 341, 1994.

[3] Fermilab Linac Upgrade Conceptual Design Report, FNAL, November 1989.

[4] K. Jungk et al. Commissioning and First Operational Experience of the 400 MeV Linac at Fermilab. Proc. 1994 EPAC, v.1, p. 751, 1994.

[5] R. W. Garnett et al. Design and Simulation of a Bridge-Coupled DTL Structure for the 20-80 MeV Region of a Proton Linac for Accelerator Transmutation of Waste. Proc. of the 1992 Linac Conf. , p.802, 1992.

[6] Y. Yamazaki. Recent Technological Development in Accelerating Structures. Proc. of the 1992 Linac Conf., p 580, 1992.

[7] V. V. Paramonov. Accelerating Structures Study for Proton Linacs. INR Preprint (to be published).

[8] V. G. Andreev et al. The Test Results of the Experimental Module of the Second Part of the Meson Factory Linac. RTI AS USSR, Moscow, n. 25, 1976 (in Russian).

[9] S. Ignaki. Disk-and-Washer Cavities for an Accelerator. NIM A251, p. 47, 1986.

[10] V. Korchuganov et al. Status of the Siberia-2 Preinjector. Proc. of the 1994 EPAC, p.739, 1994.

[11] T. Kroc et al. Fermilab Linac Upgrade - Modul Conditioning Results. Proc. of the 1992 Linac Conf., p. 187, 1992.

[12] S. V. Isaenko et al. Preprint INR P-0372, Moscow, 1984 (in Russian).

[13] L. V. Kravchuk et al. Preprint INR P-0600, Moscow, 1989 (in Russian).

[14] S. V. Isaenko et al. Preprint INR P-0608, Moscow, 1989 (in Russian).

[15] Yu. V. Bylinski et al. Moscow Meson Factory Accelerating Structure Tuning. 1988 European Particle Accelerator Conference (Rome). Proc., Singapore, World Scientific Publishing Co. Plc. Ltd. Vol. 2, p. 1202, 1989.

[16] E. A. Knapp et al. Resonantly Coupled Accelerating Structure for High Current Proton Linacs. IEEE Transactions on Nuclear Sciences, p. 159 - 165, June 1965.

[17] L. L. Filipchikov. Beam Loading Study in Proton Linacs. Thesis for Candidate Degree. Moscow, 1974.

[18] Yu. V. Bylinski, A. V. Feschenko, P. N. Ostroumov. Longitudinal Emittance Measurement of the 100 MeV Proton Beam. Proc. of the PAC91, Chikago, Il, USA, 1991.

9 Conclusions

by F. Willeke

The studies performed in the last months may be summarizes as follows:
The layout of the HERA colliding beam interaction regions can be upgraded by means of new and unconventional magnets and focusing concepts. A first feasibilty study showed, that such magnets can be provided and operated with a reasonable effort. The maximum improvement factor compared to the luminosity which can be presently achieved amounts to about four. The most aggressive design requires machine magnets to be introduced in the available aperture inside the colliding beam detectors. The impact of such a magnet on the performance of the detector has been studied. The detector performance will be degraded but this will reduce the advantage of higher luminosity only slightly. The synchrotron radiation background conditions will become somewhat more stringent but are believed to be tolerable. The effect on auxiliary systems such as luminosity monitors are severe and optimum solutions remain to be found.

For the proposed new lattice, the design proton beam brightness parameters are assumed. The luminosity could profit -though only moderately- from an increase of the beam brightness by an upgrade of the accelerator chain to avoid space charge limitations in the DESYIII synchrotron. The studies of beam brightness limitation in DESYIII are inconclusive so far. Nevertheless, a feasibility study for an upgrade of LINACIII has been performed, which shows that the kinetic energy of the proton injection energy of DESYIII can be increased by a factor of three. In view of the large effort for such a linac upgrade it should be considered as an additional option which might become more important if the design beam brightness in HERA cannot be achieved.

Polarized Protons in HERA

D.P. Barber[a], K. Heinemann[a], G.H. Hoffstätter[b], and M. Vogt[a]

[a] Deutsches Elektronen-Synchrotron DESY, Notkestrasse 85, D-22603 Hamburg, FRG
[b] Institute of Applied Physics, D-64289 Darmstadt, FRG

Abstract: This article outlines the implications of obtaining polarized protons at high energy in HERA and presents some results of calculations of the equilibrium spin distribution at high energy.

1 Introduction

In May 1994 longitudinal spin polarization was achieved at the HERA electron ring [1] and longitudinal polarization is now provided on a regular basis for the HERMES experiment.

Following this success one should investigate whether we can complement the polarized $e^{\pm}$ beam with polarized protons. For the high energy physics justification see the contributions by the Polarized Protons and Electrons Working Group in these Proceedings.

However, owing to their high mass in comparison to electrons, protons at HERA-p emit almost no synchrotron radiation so that there is no natural polarization process analogous to the Sokolov-Ternov effect, which is used to generate the $e^{\pm}$ polarization [2]. So the attainment of polarized protons in storage rings must proceed along lines very different from those for electrons.

The first ideas on how to approach this task emerged at DESY in 1994 and since then extensive studies of spin motion at high energy in HERA have been made by DESY [3, 4, 5, 6, 7] and by the Institute for Nuclear Research, Troitsk, Russia [8].

Early in 1996 we were joined by the SPIN Collaboration, a very large group dedicated to topics in the high energy physics of proton polarization and the machine physics of providing polarized protons and accelerating them [9]. The results of a study by the SPIN collaboration and the DESY team will appear soon [10]. In addition, polarization specialists from the Budker Institute of Nuclear Physics in Novosibirsk are participating.

As we will see in subsequent sections, the attainment of stored high energy protons in HERA will not be simple and will require extensive additions to the DESY accelerators. Thus at least four requirements must be fullfilled in order for this project to be realised. It must be demonstrated by preliminary tests and by simulations that the machine physics is feasible, the high energy physics community must present a strong case, there must be sufficient luminosity, and of course the money and infrastructure must be available.

This article will explore some aspects of the feasibilty and the luminosity. No attempt will be made to present a final solution — we are still in the process of identifying problems. Instead, the minimum modifications to the HERA complex likely to be necessary to obtain polarized protons will be described together with some results of calculations for high energy spin motion.

2 Obtaining high energy polarized protons

Currently, the only promising way to obtain high energy polarized protons in HERA is to accelerate polarized protons provided by a source of polarized H^- ions. This is far from being straightforward, but polarized protons of a few GeV have been in regular use for many years and polarized protons have been accelerated to above 20 GeV at the Brookhaven AGS [11]. See Table 1.

Table 1: The quest for high energy polarized protons.

Accelerator	Energy
ZGS	12 GeV
KEK PS	12 GeV
AGS	22 GeV
IUCF	1 GeV
Saturn II	3 GeV
PSI Cyclotron	0.59 GeV
TRIUMF Cyclotron	0.5 MeV
LAMPF	0.8 MeV

So one might claim that acceleration of polarized protons up to a few tens of GeV is understood, at least in principle. But as we will see in the following sections, acceleration beyond the top energy of PETRA up to about 1 TeV is a much more demanding exercise. Fortunately, other studies of the problems have already been made and help to show the way. These are listed in Table 2.

Table 2: Other high energy accelerators whose polarized proton capability has been analyzed.

Accelerator	Energy
Fermilab Main Injector	120 GeV
Fermilab TEVATRON	900 GeV
LISS	20 GeV
RHIC	250 GeV

A key aspect of HERA is the fact that the protons must remain polarized at ≈ 820 GeV, without replenishment of the polarization, for the lifetime of the beam, namely about ten hours.

Furthermore, no extensive spin tracking studies of acceleration to the 1 TeV domain have been made previously. These are now underway at DESY. Therefore the strategy adopted at DESY is to separate the investigations conceptually into three parts:

- The polarized source and the acceleration process to $\approx 39GeV$.
- Acceleration in HERA to high energy.
- The phase space distribution of the polarization at high energy and its lifetime.

Naturally, much effort could be saved if there were a way to polarize the high energy proton beam *in situ*. This would also have the potential advantage of continually 'topping up' the polarization if there were significant depolarization (e.g. by the beam–beam interaction). Indeed, two alternative concepts based on polarizing the beam at high energy have been suggested [3]. But since the alternatives do not appear to be promising at present we will limit the discussion to exploration of the conventional route, namely acceleration of a polarized beam from low energy.

2.1 The source and acceleration from low energy

The acceleration chain for HERA consists of:
$SOURCE \rightarrow RFQ(750KeV) \rightarrow LINAC\ III(50MeV) \rightarrow DESY\ III(7.5GeV/c) \rightarrow PETRA\ II(39GeV/c) \rightarrow HERA(820GeV/c)$.

Now we discuss some of these systems. For polarized protons one needs a new H^- source. There are two basic types: the 'atomic beam' and the 'optically pumped' sources [9]. They supply up to 80 percent polarization. So far currents of 1.6 mA, DC, have been reached with an optically pumped source [9, 10, 12]. But it is expected that a pulsed current of 20 mA could be reached after some further development [10]. If the transmission efficiency of the low energy beam transport line and the LINAC could be brought close to 100%, there would probably be no loss of luminosity with respect to the luminosity currently available. Thus the existing radio frequency quadrupole (RFQ) might have to be replaced with a new version with much greater acceptance.

Spin precession in electric and magnetic fields is described by the T–BMT equation [13, 14]:

$$\frac{d\vec{S}}{ds} = \vec{\Omega} \times \vec{S} \tag{1}$$

where $\vec{\Omega}$ depends on the electric and magnetic fields, the velocity and the energy. In magnetic fields equation (1) can be written as:

$$\frac{d\vec{S}}{ds} = \frac{e\vec{S}}{mc\gamma} \times ((1+a)\vec{B}_{\|} + (1+a\gamma)\vec{B}_{\perp}) \ , \quad a = \left(\frac{g-2}{2}\right) \tag{2}$$

where $\vec{B}_{\|}$ and $\vec{B}_{\perp}$ are the magnetic fields parallel and perpendicular to the trajectory. The arc length is denoted by s and the other symbols have the usual meanings. The gyromagnetic anomaly, $\frac{g-2}{2}$, for protons is about 1.79. The full T–BMT equation contains terms depending on the electric field but these vanish if the electric field is parallel to the velocity as in a linac.

The T–BMT equation shows that for motion transverse to the magnetic field, the spin precesses around the field at a rate which is $a\gamma$ faster than the rate of rotation of the orbit direction. Thus

$$\delta\theta_{spin} = a\gamma\delta\theta_{orbit} \tag{3}$$

in an obvious notation. So in one turn around the design orbit of a flat storage ring a non–vertical spin makes $a\gamma$ full precessions. We call this latter quantity the 'naive spin tune' and denote it by ν_0. It gives the natural spin precession frequency in the vertical dipole fields of the ring. At 820 GeV, ν_0 is about 1557. Therefore a 1 mrad orbit deflection will cause about 90 degrees of spin precession. Thus spin is extremely sensitive to perturbing fields and in particular to the radial fields in the quadrupoles.

To reach DESYIII the spins pass through the off–axis horizontal and vertical fields of the various quadrupoles in the LINAC and the transfer line only once. But acceleration in DESY, PETRA, and HERA requires that the spin ensemble passes through the complex structure of quadrupole fields many millions of times. This is the point at which a detailed understanding of spin dynamics in storage rings becomes necessary.

If a circular accelerator only had vertical (dipole) fields, vertical spins would not be affected. But the spins 'see' radial fields in the quadrupoles or combined function magnets since the beam has a non–zero height and even in a nominally flat ring the periodic (closed) orbit is offset vertically owing to unavoidable magnet misalignments. According to the T–BMT equation these fields tend to tilt the spins away from the vertical. The disturbance is different for each spin since it depends on the position of the particle. For particles circulating for many turns the total disturbance can grow to become very big if there is coherence between the natural spin motion and the oscillatory motion in the beam characterized by the spin–orbit resonance condition:

$$\nu_{spin} = m + m_x \cdot Q_x + m_z \cdot Q_z + m_s \cdot Q_s \tag{4}$$

where the m's are integers and the Q's are respectively the horizontal, vertical and longitudinal tunes of the orbital oscillations. Here, ν_{spin} is the real (i.e. not naive) spin tune. In the presence of misalignments, rotators and snakes (see below), the unit vector describing the periodic spin direction on the closed orbit, $\vec{n}_0(s)$, is not vertical so that the concept of spin tune must be generalised to be the effective number of spin precessions around $\vec{n}_0$ per turn. In general $\nu_{spin} \neq \nu_0$ but in a nominally flat ring ν_{spin} will not deviate very far from $a\gamma$. The vector $\vec{n}_0(s)$ also describes the direction of the average spin vector of a bunch i.e. of the polarization direction of a bunch.

Now we can see the difficulty: during acceleration, ν_{spin} passes through the resonance condition many thousands of times since ν_0 increases by one unit for every 523 MeV increase in energy. There is therefore a good chance that the beam loses polarization at each resonance so that by full energy the polarization has vanished. Even at fixed nominal beam energy, there are longitudinal (energy) oscillations due to the presence of the RF cavities installed to keep the beam bunched, and the consequent oscillations in the spin tune can, if they have large enough amplitude, also cause resonance crossing.

Thankfully, the situation is not as bad as it might appear: in 1975 Derbenev and Kondratenko proposed an ingenious class of devices which are now called 'Siberian Snakes' [15, 16]. They consist of magnet systems designed to rotate spins (and $\vec{n}_0$) by 180 degrees around an axis in the horizontal plane independently of the particle energy. With such devices it can be arranged that ν_{spin} is *independent* of the particle energy and that at least the first order

resonance condition, ($|m_x| + |m_z| + |m_s| = 1$ in eqn.4) is never satisfied. Thus at one stroke depolarization during acceleration or due to energy oscillations is eliminated — at least if the effect of higher order resonances can be ignored. Typically one would arrange to set $\nu_{spin} = 1/2$. For detailed sketches of spin motion in the presence of snakes the reader is referred to [17]. From those sketches one can obtain a helpful view of the resonance suppression mechanism. The spin perturbations accumulated during one turn tend to be cancelled on the next turn after the snake has flipped the spins by 180 degrees. This is very reminiscent of the spin echo effect used in spin–magnetic resonance investigations in materials.

From the T–BMT equation it is clear that at high energy, transverse magnetic fields are much more efficient than solenoid fields for rotating spins. For transverse fields the T–BMT equation takes the form

$$\frac{d\vec{S}}{ds} = \frac{e\vec{S}}{mc} \times (1/\gamma + a)\vec{B}_{\perp} \tag{5}$$

from which it is clear that for protons at high energy the spin precession rate is essentially independent of energy and proportional to the field. We have seen that at 820 GeV with $\nu_0 \approx 1557$ the field needed to give a 1 mrad orbit deflection will cause about 90 degrees of spin precession. Equivalently, a simple rotation of 90 degrees requires a field integral of 2.74 Tesla metres. So at high energy, snakes should be built from strings of interleaved horizontal and vertical dipoles which generate a small local closed bump in the orbit but produce, via the noncommutation of large spin precessions, the required overall 180 degree spin rotation. Since the HERA electron spin rotators operate on this principle, expertise in building such devices already exists at DESY [18]. Since the snake fields are independent of energy, a key problem in snake design is to find solutions for which the orbit excursion at low energy is small, i.e. one or two centimetres. The ultimate in 'interleaving' is a superconducting helical dipole, as for example, in the design proposed for RHIC [19, 20]. It is not yet clear how many snakes will be needed for suppression of depolarization during ramping to 820 GeV in HERA.

An aspect of the HERA proton ring that has nontrivial implications for spin motion is that there are sets of interleaved vertical and horizontal bends on each side of the North, South, and East interaction points. These serve to adjust the height of the proton ring to that of the electron ring at the collision points. Coming from the arc, a proton is first bent 5.74 milliradians downwards, then 60.4 milliradians towards the ring center and finally the orbit is made horizontal by a 5.74 milliradians upward bend. The structure is repeated with interchanged vertical bends on the far side of the interaction point at the entrance to the arc. It is easy to see that with $a\gamma \approx 1557$ the interleaved vertical and horizontal bends cause a large disturbance to the spin motion. In a perfectly aligned ring without vertical bends the equilibrium spin direction on the design orbit is vertical. With vertical bends $\vec{n}_0$ is no longer vertical and strongly energy dependent. Thus the vertical bends must be compensated. One way to do this, proposed by V. Anferov [10], would be to insert a radial Siberian Snake at the midpoint of the 60.4 mrad horizontal bends. More details can be found in [10, 7].

Naturally, spin rotators are also needed to provide a choice of spin orientations at the interaction points.

A suggestion for a snake layout in PETRA can be found in [10].

DESYIII poses a special problem. Down at a few GeV, dipole fields of the magnitude needed for snakes would cause unacceptable orbit distortions. A detailed discussion of spin preservation in DESYIII is beyond the intended scope of this article but more details can be

found in [3, 4]. Suffice it to say that devices called 'Partial Snakes' and techniques like orbit and spin tune jumping are under investigation [10, 19, 21]. We have also not discussed the transfer lines.

But one topic deserves special mention, namely proton polarimetry. One clearly needs a polarimeter at the final energy in order to make sense of the measurements of the experimenters [22]. But polarimeters, each chosen for its suitability to handle its energy range, are needed on the low energy part of the chain. Otherwise one will be accelerating 'blindly'.

So far we have dealt only with protons but there is some interest in the particle physics community in obtaining polarized high energy deuterons [23]. For deuterons, $\frac{g-2}{2}$ is only about –0.14 and the deuteron mass is about twice that of the proton. So there are far fewer spin–orbit resonances to cross. But equivalently, the influence of dipole fields on deuteron spins is very small and the design of spin rotators would be far from simple. Nevertheless the possiblity should be kept in mind. In summary, the following modifications, marked by the underlining, to the acceleration chain will be needed.

- The source: atomic beam or optically pumped source of polarized H^- ions.
- Radio frequency quadrupole (RFQ) to 750 KeV: better optimization.
- Proton LINAC to 50 MeV.
- Transfer line to DESY III.
- DESY III: stripping foil injection, $50MeV \rightarrow 7.5GeV$: partial snake and pulsed quads.
- Transfer line DESY III to PETRA II: snakelike spin direction tuner.
- PETRA II: $7.5GeV/c \rightarrow 39GeV/c$: two Siberian Snakes.
- Transfer line PETRA II to HERA: snakelike spin direction tuner.
- HERA: $39GeV/c \rightarrow 820GeV/c$: Siberian Snakes and spin rotators.
- Polarimeters.

This completes the outline of the modifications needed for acceleration from low energy. More information can be found in [3, 4, 10].

Clearly, before embarking on the kinds of upgrades described above one should make computer simulations of the acceleration from low energy and storage at high energy by integrating the equations of combined spin–orbit motion for an ensemble of particles. This is currently the main thrust of the work at DESY. Some results from such calculations are presented in the next section.

3 The equilibrium polarization distribution

The polarization at a point $\vec{z} = (x, p_x, y, p_y, \delta t, \delta E)$ in phase space and azimuth θ in a spin 1/2 beam in an accelerator is defined by the phase space density distribution $\rho(\vec{z};\theta)$, the *value* of the polarization at each point in phase space $\mathcal{P}(\vec{z};\theta)$, and the *direction* of the polarization at each point $\hat{\mathcal{P}}(\vec{z};\theta)$. Once we know these three functions we have a complete specification of the polarization state of the beam.

Since the T-BMT equation is linear in the spin, $\vec{\mathcal{P}}(\vec{z};\theta) = \mathcal{P}\cdot\hat{\mathcal{P}}$ obeys the T-BMT equation [24] which we now write in the form

$$\frac{d\vec{\mathcal{P}}}{d\theta} = \vec{\Omega}(\vec{z},\theta)\times\vec{\mathcal{P}}\ . \tag{6}$$

Because equation (6) describes precession, $\mathcal{P}(\vec{z},\theta)$ is constant along a phase space trajectory.

High energy physics experiments require that the particle bunches look the same from turn to turn, i.e. that they are in equilibrium. Thus in this section we will examine the equilibrium polarization at high energy.

At equilibrium $\rho(\vec{z};\theta)$ is periodic in θ. Furthermore, at equilibrium $\vec{\mathcal{P}}(\vec{z},\theta)$ not only obeys the T-BMT equation, but it is also periodic in θ. We write the equilibrium $\vec{\mathcal{P}}$ as $\vec{\mathcal{P}}_{eq}$ and we denote the unit vector along $\vec{\mathcal{P}}_{eq}(\vec{z},\theta)$ by $\vec{n}(\vec{z},\theta)$. $\vec{n}$ also obeys equation (6) and thus behaves like a spin. The vector $\vec{n}$ was first introduced by Derbenev and Kondratenko [25] in the theory of radiative electron polarization.

The maximizing of the equilibrium polarization of the ensemble implies two conditions:

1. The polarization at each point in phase space should be high.
2. The equilibrium polarization vector at each point in phase space should be almost parallel to the average polarization vector of the beam.

We have seen that at the very high proton energy of HERA the spin motion is extremely sensitive to disturbances and that the quadrupole fields can have a strong influence. As we will see later it can then happen that on average the equilibrium polarization vector deviates by tens of degrees from the average polarization vector of the beam [3]. So even if each point in phase space were 100% polarized the average polarization could be limited to a value much smaller than 100%. The first condition requires that the source delivers high polarization and that the polarization is maintained during acceleration. That was the topic of the last section. The second condition is an intrinsic property of the arrangement of the magnets in the ring, the energy, and the optic. At the interaction points the average direction should, of course, be oriented according to the requirements of the experiments. If it were to be demonstrated that the ring and the optic do not permit a high parallelism, there would be little point in striving to fulfill condition 1.

Clearly, it is very important to have accurate and efficient methods for calculating $\vec{n}(\vec{z},\theta)$.

3.1 Computational techniques

Much of the background to the following material has been covered in several other reports [3, 4, 5, 6] and they should be consulted for mathematical details. Furthermore, an extensive study based mainly on long term spin-orbit tracking can be found in [8]. This also gives examples of spin-orbit motion for various Siberian Snake schemes.

3.1.1 Straightforward polarization tracking

One can try to get information about the spread of the equilibrium spin directions over phase space by tracking a completely polarized beam for many turns. This is illustrated in figure 1. There are no geometrical distortions and the vertical bends are turned off so that the simulation represents a perfectly aligned flat ring. Particles at 100 different phases on a 1 sigma vertical phase space ellipse and zero longitudinal and horizontal emittance have been tracked through HERA for 600 turns while the beam was initially 100% polarized parallel to $\vec{n}_0$ [5, 7]. Similar kinds of tracking results have been presented in [8]. The polarization of the ensemble is defined as the average of the unit spin vectors across phase space. We see that the polarization oscillates wildly. This polarization distribution is obviously not an equilibrium distribution and this implies that the $\vec{n}$-axes are widely spread out away from $\vec{n}_0$. The bold horizontal line is the turn by turn polarization obtained when each spin is initially set parallel to $\vec{n}(\vec{z},\theta)$ (calculated using the code SPRINT-see below) for a particle at its phase space position $\vec{z}$. Now the averaged polarization stays constant at 0.765. This latter value is consistent with the fact that the average deviation of $\vec{n}$ from $\vec{n}_0$ is about 40 degrees. Therefore, by starting simulations with spins parallel to the $\vec{n}$-axis one can perform a much cleaner analysis of beam polarization in accelerators. In effect one is now able to study the effect of spin perturbations (for example due to field noise, beam-beam effect etc) by searching for small deviations away from the 'stationary state' of the beam instead of having to detect long term drifts in a strongly fluctuating average polarization.

3.1.2 Stroboscopic averaging

The first estimates of the distribution of the $\vec{n}$-axis were made using the SLIM formalism [3]. Further estimates were made using normal form theory [4, 8]. However, those calculations indicated that in a very high energy accelerator such as HERA, $\vec{n}$ can be widely spread out away from $\vec{n}_0$ in confirmation of the results presented in figure 1. Since the SLIM formalism and the normal form formalism are both based on perturbation theory and assume that the tilt of $\vec{n}$ from $\vec{n}_0$ is small it was clear that they were potentially unreliable and that a non-perturbative algorithm was needed.

Thus, a new method for obtaining $\vec{n}$ called stroboscopic averaging [5] has been developed. It is based on multi-turn tracking and the averaging of a special choice of spins viewed stroboscopically from turn to turn. Since this innovative approach only requires tracking data from *one particle*, it is fast and very easy to implement in existing tracking codes. Probably the main advantage over other methods is the fact that stroboscopic averaging does not have an inherent problem with either orbit or spin orbit resonances due to its non-perturbative nature. This allows the analysis of the periodic spin solution close to resonances. This algorithm has

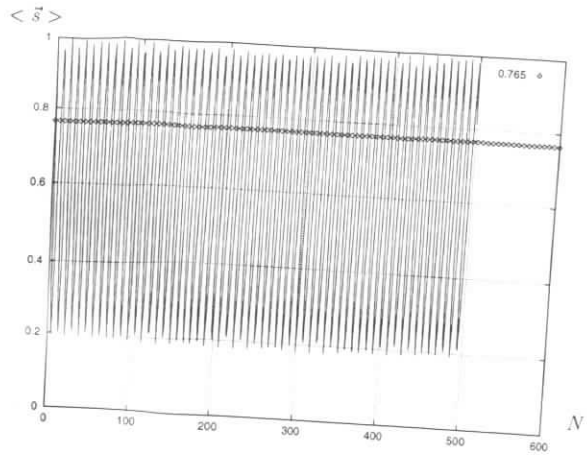

Figure 1: Propagation of a beam that is initially completely polarized parallel to $\vec{n}_0$ leads to a fluctuating average polarization. For another beam that is initially polarized parallel to the periodic spin solution $\vec{n}$ the average polarization stays constant, in this case equal to 0.765.

been implemented in the program SPRINT [5]. This is the code used to calculate the initial $\vec{n}$-axes before propagating the equilibrium distribution in figure 1.

By means of this new tool we are now able to make reliable calculations of $\vec{n}$-axes. We find confirmation of the predictions of SLIM and the normal form analysis, for the basic HERA layout, that the average tilt of $\vec{n}$ from $\vec{n}_0$ can be large, of the order of 60 degrees or more.

However, as mentioned before, Siberian Snakes are not only essential for suppressing depolarization during acceleration but also help at fixed beam energy. In particular they are essential for suppressing spin flip effects due to resonance crossing as the energies of individual particles execute (slow) synchrotron oscillations [8]. Snakes also stabilize the spin motion due to betatron oscillation since the orbital tunes can be chosen so as not to coincide with the fixed real spin tune generated by properly chosen snake layouts.

The next task is then to find snake configurations which indeed counteract the effects of synchrotron and betatron motion. Towards this goal a 'filter' algorithm has been developed which allows the most effective snake layouts to be selected from a starting set [4]. This filtering method has enabled us to identify configurations which strongly reduce the deviation of $\vec{n}$ from $\vec{n}_0$. Figure 2 shows the energy dependence of the average opening angle of the $\vec{n}$-axis for a snake configuration selected by filtering and for two representative orbit amplitudes. The technical details for this example can be found in [7].

4 Further investigations

Apart from the obvious need to find adequate and practical snake schemes, to decide on the best way to realize the compensation of the vertical bends and to design and position the spin

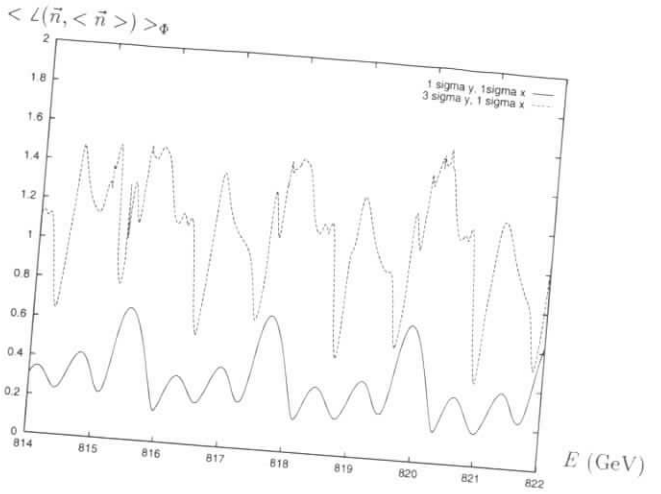

Figure 2: The average opening angle of the equilibrium spin distribution for energies between 814 and 822 GeV after the installation of the snake arrangement found by filtering. The two curves refer to particles with one sigma in the horizontal direction and one or three sigma in the vertical direction respectively.

rotators needed to provide various polarization directions for the experiments at the interaction points, the following topics must be addressed.

1. Understand the effects of misalignments. Find cures. (The most important additional limitation to the polarization is likely to be the spread in the $\vec{n}$-axes caused by misalignments.)
2. Include linear and nonlinear synchrotron oscillations.
3. Determine the maximum allowed emittances.
4. Study the efficacy of the chosen snake scheme for controlling the spin 'equilibrium' during the adiabatic acceleration.
5. Determine the influence of the beam-beam effect.
6. Understand the influence of noise in power supplies.
7. Calculate with optical nonlinearities and optical coupling.
8. Evaluate the effect of intra-beam scattering, if any.
9. Investigate the relevance and feasibility of spin matching [26] and in particular the 'strong spin matching' proposed by K. Steffen [27].
10. Evaluate the advantages of increasing the symmetry of the ring and the optic.

5 Conclusion

The HERA $e^{\pm}$-p colliding beam facility is unique. It provides a high energy, high quality and highly polarized electron (positron) beam for collisions with 820 GeV protons. As a next step one should attempt to polarize the proton beam.

Much work has already been invested in studying ways to accelerate polarized protons up to high energy and most of those ways could be adapted for HERA. It is clear that preparations must begin now.

6 Acknowledgements

We thank members of the HERA machine group and also V. Balandin, N. Golubeva, and G. Ripken for their contributions to this study. We also thank members of the SPIN collaboration.

References

[1] D.P. Barber et al. The first achievement of longitudinal polarization in a high energy electron storage ring. *Physics Letters*, **B343**, 436 (1995).

[2] A.A. Sokolov and I.M. Ternov. *Soviet Physics Doklady*, **8**, N°12 1203 (1964).

[3] D. P. Barber. Possibilities for polarized protons at HERA. In *Prospects of spin physics at HERA*, DESY-Zeuthen, August 1995. DESY Report 95-200, November 1995.

[4] G. H. Hoffstätter. Polarized protons in HERA. In *Proceedings of the DESY Accelerator Group Seminar*, St.Englmar, January 1996. DESY Report 96-05, May 1996.

[5] K. Heinemann and G. H. Hoffstätter. A tracking algorithm for the stable spin polarization field in storage rings using stroboscopic averaging. DESY Report 96-078, May 1996. Accepted for publication in Physical Review E.

[6] D. P. Barber, K. Heinemann, G. H. Hoffstätter and M. Vogt. The phase space dependent spin polarization direction in the HERA proton ring at high energy. In *The Proceedings of the 1 996 European Particle Accelerator Conference*, Sitges, Spain, May 1996.

[7] D. P. Barber, K. Heinemann, G. H. Hoffstätter and M. Vogt. The polarization at high energy in HERA. DESY HERA Report 96-07, September 1996.

[8] V. Balandin, N. Golubeva, and D. P. Barber. Studies of the behaviour of proton spin motion in HERA-p at high energies. DESY Report M-96-04, February 1996.

[9] SPIN Collaboration. Acceleration of Polarized Protons to 120 GeV and 1 TeV at Fermilab. University of Michigan Report UM-HE 95-09, July 1995.

[10] SPIN Collaboration and the DESY Polarization Team. Acceleration of Polarized Protons to 820 GeV at HERA. University of Michigan Report UM-HE 96-20, November 1996.

[11] Z. Khari et al. *Physical Review*, **D39**, 45 (1989).

[12] A. N. Zelenski et al. *Proc. 6th Int. Conf. on Ion Sources (Whistler). Rev. Sci. Instrum.*, **67**, 1359 (1996).

[13] L. Thomas. The kinematics of an electron with an axis. *Philosophical Magazine*, **3**, 1 (1927).

[14] V. Bargmann, L. Michel and V. L. Telegdi. Precession of the polarization of particles moving in a homogeneous electromagnetic field. *Physical Review Letters*, **2**, 435 (1959).

[15] Ya. S. Derbenev and A. Kondratenko. *Soviet Physics Doklady*, **20**, 562 (1976).

[16] Ya. S. Derbenev et al. *Particle Accelerators*, **8**, 115 (1978).

[17] B. Montague. Polarized beams in high energy storage rings. *Physics Reports*, **113**, (1984).

[18] J. Buon and K. Steffen. *Nuclear Instruments and Methods*, **A245**, 248 (1986).

[19] K. Brown et al. Conceptual Design for the Acceleration of Polarized Beams in RHIC. Brookhaven Report May 1993.

[20] V. I. Ptitsin and Yu. M. Shatunov. *Proceedings of 3rd Workshop on Siberian Snakes and Spin Rotators*, Brookhaven September 1994, BNL 52453 (1994).

[21] Yu. N. Filatov et al. *Proc. 5th Workshop on High Energy Spin Physics*, Protvino, Russia 1993.

[22] See for example the contributions by G. Igo and by N. Akchurin et al. in these Proceedings.

[23] See for example the contribution by M. Düren in these Proceedings.

[24] K. Heinemann. Private communication.

[25] Ya. S. Derbenev and A. M. Kondratenko. Diffusion of particle spins in storage rings. *Soviet Physics JETP*, **35**, 230 (1972).

[26] D.P. Barber, et al. A solenoid spin rotator for large electron storage rings. *Particle Accelerators*, **17**, 243 (1985).

[27] K. Steffen. Strong spin matching with and without snakes: a scheme for preserving polarization in large ring accelerators. *Particle Accelerators*, **24**, 45 (1988).